Lecture Notes in Nanoscale Science and Technology 16

Xiaodong Wang
Zhiming M. Wang *Editors*

Nanoscale Thermoelectrics

Springer

Lecture Notes in Nanoscale Science and Technology

Volume 16

Series Editors

Zhiming M. Wang
State Key Laboratory of Electronic, Thin Film and Integrated Devices,
University of Electronic Science and Technology,
Chengdu, People's Republic of China

Andreas Waag
Institut fur Halbleitertechnik, TU Braunschweig, Braunschweig, Germany

Greg Salamo
Department of Physics, University of Arkansas, Fayetteville, AR, USA

Naoki Kishimoto
Quantum Beam Center, National Institue for Materials Science, Tsukuba,
Ibaraki, Japan

Stefano Bellucci
Laboratori Nazionali di Frascati, Istituto Nazionale di Fisica Nucleare,
22 Frascati, Italy

Young June Park
School of Electrical Engineering, Seoul National University, Shinlim Dong,
26 Kwanak-Gu, Seoul, Korea

For further volumes:
http://www.springer.com/series/7544

Xiaodong Wang • Zhiming M. Wang
Editors

Nanoscale Thermoelectrics

Editors
Xiaodong Wang
Engineering Research Center
for Semiconductor Integrated
Technology
Chinese Academy of Sciences
Beijing, China, People's Republic

Zhiming M. Wang
Engineering Research Center
for Semiconductor Integrated
Technology
Chinese Academy of Sciences
Beijing, China, People's Republic

ISSN 2195-2159 ISSN 2195-2167 (electronic)
ISBN 978-3-319-02011-2 ISBN 978-3-319-02012-9 (eBook)
DOI 10.1007/978-3-319-02012-9
Springer Cham Heidelberg New York Dordrecht London

Library of Congress Control Number: 2013953700

© Springer International Publishing Switzerland 2014
This work is subject to copyright. All rights are reserved by the Publisher, whether the whole or part of the material is concerned, specifically the rights of translation, reprinting, reuse of illustrations, recitation, broadcasting, reproduction on microfilms or in any other physical way, and transmission or information storage and retrieval, electronic adaptation, computer software, or by similar or dissimilar methodology now known or hereafter developed. Exempted from this legal reservation are brief excerpts in connection with reviews or scholarly analysis or material supplied specifically for the purpose of being entered and executed on a computer system, for exclusive use by the purchaser of the work. Duplication of this publication or parts thereof is permitted only under the provisions of the Copyright Law of the Publisher's location, in its current version, and permission for use must always be obtained from Springer. Permissions for use may be obtained through RightsLink at the Copyright Clearance Center. Violations are liable to prosecution under the respective Copyright Law.
The use of general descriptive names, registered names, trademarks, service marks, etc. in this publication does not imply, even in the absence of a specific statement, that such names are exempt from the relevant protective laws and regulations and therefore free for general use.
While the advice and information in this book are believed to be true and accurate at the date of publication, neither the authors nor the editors nor the publisher can accept any legal responsibility for any errors or omissions that may be made. The publisher makes no warranty, express or implied, with respect to the material contained herein.

Printed on acid-free paper

Springer is part of Springer Science+Business Media (www.springer.com)

Preface

Thermoelectric materials have attracted much interest for decades because of the application to electricity generation and cooling based on the famous Seebeck and Peltier effects. Compared with traditional generators and refrigerators, thermoelectric devices have several advantages, such as solid-state operation, zero radiation, pollution-free performance, and long operating lifetime. However, interest from the integrated circuit (IC) industry has lagged behind expectations since the potential of these materials was first reported in the 1950s. One reason is that the figure of merit for most thermoelectric materials and structures is quite low, and the other is that the compatibility of the materials and processes with ICs is not satisfying.

About 20 years ago, the theoretical work of Lyndon Hicks and Mildred Dresselhaus changed the situation. It was found that dimensionality had profound implications for thermoelectric efficiency beyond initial expectations. In subsequent research, low-dimensional materials and structures were revealed to have a much higher figure of merit than bulk materials because of size effects and quantum confinement, which then stimulated research interest in nanoscale thermoelectric materials and devices. To date, a variety of low-dimensional thermoelectric structures, such as superlattices, nanowires, nanotubes, and nanocomposites, have been reported with improved performance.

This book explores the latest research results on the physics and materials science, including low-dimensional characteristics, of thermoelectrics at the nanoscale. Chapters 1–6 focus on the theoretical calculation of some nanoscale thermoelectric materials. In Chap. 1, dimensionless figure of merit *ZT*, Seebeck coefficient, electrical conductivity, and thermal conductivity are deduced for metals and semiconductors from the Boltzmann transport equation. Various nanoscale structures embedded in bulk materials could enhance the thermoelectric energy conversion efficiency, which is investigated in Chaps. 2 and 3. Chapter 2 focuses on the impact of nanostructures on the electron transport in the host material, while Chap. 3 addresses the impact of particle shape and size on the composite thermal conductivity. Chapter 4 reviews some prominent techniques for fabricating the relevant nanostructured materials systems. An overview of the concepts and techniques for theoretical modeling of the charge carrier and phonon transport mechanisms in the

interfacial regions is also presented. Chapter 5 reviews recent experimental and theoretical advances in the study of thermal conductivity and thermoelectric property of nanowires. Chapter 6 discusses how specific surface disorder structure can enhance thermoelectric efficiency of nanowires.

Chapters 7–16 introduce various thermoelectric materials. Chapter 7 addresses recent developments in Bi-based nanostructured thermoelectric materials, mainly nanowires, nanotubes, and heterostructures. $Bi_{88}Sb_{12}$ alloy doped with Cerium, Samarium, and Holmium is discussed in Chap. 8. The synthetic approaches used to create skutterudite nanocomposites, and the effects of nanostructures on thermoelectric performance, are summarized in Chap. 9. Chapter 10 reports the high-temperature thermoelectric properties of various skutterudites filled by various group 13 elements, including Ga-filled $CoSb_3$, TI-filled $CoSb_3$, and In/TI double filled $CoSb_3$. Chapter 11 introduces several important oxide thermoelectric candidates with specific focus on self-assembled nanocomposites of ZnO. The effects of nanoscale inclusion in the Ca–Co–O system ($Ca_3Co_4O_9$) and natural superlattices in $SrO/SrTiO_3$ are also discussed. Chapter 12 investigates the thermoelectric properties of carbon nanotubes, graphene nanoribbons, and carbon nanowires using nonequilibrium molecular dynamics simulations and nonequilibrium Green's function method. Graphene is subsequently discussed in Chap. 13. How to enhance the thermoelectric properties in the 1D graphene-based nanostructures through the geometry-decorated method is elucidated and some novel results are presented. Chapter 14 describes the good potential of nanostructured silicon as a thermoelectric material. A top-down process for the reliable fabrication of very complex and large area arrays of silicon nanowires is shown and discussed. Chapter 15 investigates the strain effect on the thermoelectric figure of merit of *n*-type Ge nanowire-Si host nanocomposite materials. Finally, Chap. 16 reviews the most recent progresses in $Si_{1-x}Ge_x$ alloy nanowires with tunable Ge concentration, core-shell structures, and multiple axial junctions.

The editors wish to thank all of the authors for their excellent chapters. We are sure that this book will be a useful reference not only for scientists and engineers exploring thermoelectrics at the nanoscale but also for graduate and postgraduate students specializing in semiconductor physics and devices. We are also grateful to Ms. Zhen Wang and Ms. Yangyang Qi for expert editorial assistance. Without their warmhearted efforts from cold winter to hot summer, this book would not have been completed so satisfactorily. We would also thank Springer staff for their support. Finally, the editors are pleased to acknowledge the support of the National Natural Science Foundation of China under Grant No. 61076077.

Beijing, China, People's Republic — Xiaodong Wang
Beijing, China, People's Republic — Zhiming M. Wang

Contents

1 **Thermoelectric Effects: Semiclassical and Quantum Approaches from the Boltzmann Transport Equation** 1
Andrés Cantarero and F. Xavier Àlvarez

2 **Electron Transport Engineering by Nanostructures for Efficient Thermoelectrics** 41
Je-Hyeong Bahk and Ali Shakouri

3 **Thermal Conductivity of Particulate Nanocomposites** 93
Jose Ordonez-Miranda, Ronggui Yang, and Juan Jose Alvarado-Gil

4 **Nano Bulk Thermoelectrics: Concepts, Techniques, and Modeling** 141
Nikhil Satyala, Payam Norouzzadeh, and Daryoosh Vashaee

5 **Control Thermal Conductivity of Semiconductor Nanowires: Phononics Engineering** 185
Gang Zhang and Yong-Wei Zhang

6 **Thermoelectric Efficiency of Nanowires with Long Range Surface Disorder** 211
Gursoy B. Akguc

7 **One-Dimensional Bi-Based Nanostructures for Thermoelectrics** . . . 237
Liang Li and Guanghai Li

8 **Cerium-, Samarium-, Holmium-Doped $Bi_{88}Sb_{12}$** 255
Cyril P. Opeil and Kevin C. Lukas

9 **Thermoelectric Properties of p-Type Skutterudite Nanocomposites** 271
Chen Zhou, Long Zhang, and Jeffrey Sakamoto

10 Thermoelectric Properties of $CoSb_3$ Based Skutterudites Filled by Group 13 Elements 301
Ken Kurosaki, Adul Harnwunggmoung, and Shinsuke Yamanaka

11 Nanoscale Self-assembled Oxide Bulk Thermoelectrics 327
Yu Zhao, Ashok Kumar, Céline Hin, and Shashank Priya

12 Thermoelectric Properties of Carbon Nanotubes and Related One-Dimensional Structures 363
H.J. Liu

13 The Thermoelectric Properties in Graphene and Graphene Nanoribbons 393
Changning Pan, Zhongxiang Xie, and Keqiu Chen

14 Silicon Nanostructures for Thermoelectric Applications 427
Massimo Totaro and Giovanni Pennelli

15 Modeling and Analysis of Strain Effects on Thermoelectric Figure of Merit in Si/Ge Nanocomposites 451
Y. Xu and G. Li

16 SiGe Nanowires for Thermoelectrics Applications 497
Michele Amato, Maurizia Palummo, Stefano Ossicini, and Riccardo Rurali

Index 517

Contributors

Gursoy B. Akguc Department of Physics, Bilkent University, Ankara, Turkey

Juan Jose Alvarado-Gil Department of Applied Physics, Centro de Investigación y de Estudios Avanzados del I.P.N-Unidad Mérida, Mérida, Yucatán, Mexico

F. Xavier Àlvarez Physics Department, Autonomous University of Barcelona, Bellaterra, Catalonia, Spain

Michele Amato Institut d'Electronique Fondamentale, UMR8622, CNRS, Universitè Paris-Sud, Orsay, France

Je-Hyeong Bahk Birck Nanotechnology Center, Purdue University, West Lafayette, IN, USA

Andrés Cantarero Materials Science Institute, University of Valencia, Valencia, Spain

Keqiu Chen Department of Applied Physics, Hunan University, Changsha, China

Adul Harnwunggmoung Faculty of Science and Technology, Thermoelectric and Nanotechnology Research Center, Rajamangala University of Technology Suvarnabhumi, Huntra, Phranakhon Si Ayutthaya, Thailand

Céline Hin Materials Science and Engineering and Mechanical Engineering, Virginia Tech, Blacksburg, VA, USA

Ashok Kumar Center for Energy Harvesting Materials and Systems (CEHMS), Virginia Tech, Blacksburg, VA, USA

Ken Kurosaki Division of Sustainable Energy and Environmental Engineering, Graduate School of Engineering, Osaka University, Suita, Osaka, Japan

G. Li College of Engineering and Science, Clemson University, Clemson, SC, USA

Guanghai Li Key Laboratory of Materials Physics, Anhui Key Lab of Nanomaterials and Nanostructure, Institute of Solid State Physics, Chinese Academy of Sciences, Hefei, China

Liang Li Key Laboratory of Materials Physics, Anhui Key Lab of Nanomaterials and Nanostructure, Institute of Solid State Physics, Chinese Academy of Sciences, Hefei, China

H.J. Liu Key Laboratory of Artificial Micro- and Nano-structures of Ministry of Education and School of Physics and Technology, Wuhan University, Wuhan, China

Kevin C. Lukas Department of Physics, Boston College, Chestnut Hill, MA, USA

Payam Norouzzadeh Department of Electrical and Computer Engineering, Oklahoma State University, Tulsa, OK, USA

Cyril P. Opeil Department of Physics, Boston College, Chestnut Hill, MA, USA

Jose Ordonez-Miranda Laboratoire d'Énergétique Moléculaire et Macroscopique, Combustion, UPR CNRS 288, Ecole Centrale Paris, Châtenay, Malabry, France

Stefano Ossicini "Centro S3", CNR-Istituto di Nanoscienze, Modena, Italy

Dipartimento di Scienze e Metodi dell'Ingegneria, Centro Interdipartimentale En&Tech, Universitá di Modena e Reggio Emilia, Reggio Emilia, Italy

Maurizia Palummo Dipartimento di Fisica, European Theoretical Spectroscopy Facility (ETSF), Università di Roma, "Tor Vergata", Roma, Italy

Changning Pan Department of Applied Physics, Hunan University, Changsha, China

Giovanni Pennelli Dipartimento di Ingegneria dell'Informazione, Università di Pisa, Pisa, Italy

Shashank Priya Center for Energy Harvesting Materials and Systems (CEHMS), Virginia Tech, Blacksburg, VA, USA

Yangyang Qi Engineering Research Center for Semiconductor Integrated Technology, Institute of Semiconductors, Chinese Academy of Sciences, Beijing, China

Riccardo Rurali Institut de Ciència de Materials de Barcelona (CSIC), Bellaterra, Spain

Jeffrey Sakamoto Department of Chemical Engineering and Materials Science, Michigan State University, East Lansing, MI, USA

Nikhil Satyala Department of Electrical and Computer Engineering, Oklahoma State University, Tulsa, OK, USA

Ali Shakouri Birck Nanotechnology Center, Purdue University, West Lafayette, IN, USA

Massimo Totaro Center for Micro-BioRobotics @SSSA, Istituto Italiano di Tecnologia, Pontedera, PI, Italy

Dipartimento di Ingegneria dell'Informazione, Università di Pisa, Pisa, Italy

Daryoosh Vashaee Department of Electrical and Computer Engineering, Oklahoma State University, Tulsa, OK, USA

Zhen Wang Engineering Research Center for Semiconductor Integrated Technology, Institute of Semiconductors, Chinese Academy of Sciences, Beijing, China

Zhongxiang Xie Department of Applied Physics, Hunan University, Changsha, China

Y. Xu College of Engineering and Science, Clemson University, Clemson, SC, USA

Shinsuke Yamanaka Division of Sustainable Energy and Environmental Engineering, Graduate School of Engineering, Osaka University, Suita, Osaka, Japan

Ronggui Yang Department of Mechanical Engineering, University of Colorado, Boulder, CO, USA

Gang Zhang Institute of High Performance Computing, A*STAR, Singapore, Singapore

Key Laboratory for the Physics and Chemistry of Nanodevices, Department of Electronics, Peking University, Beijing, China

Long Zhang State Key Laboratory of Metastable Materials Science and Technology, Yanshan University, Qinhuangdao, Hebei, China

Yong-Wei Zhang Institute of High Performance Computing, A*STAR, Singapore, Singapore

Yu Zhao Center for Energy Harvesting Materials and Systems (CEHMS), Virginia Tech, Blacksburg, VA, USA

Chen Zhou MEDA Engineering and Technical Services, LLC, Southfield, MI, USA

Chapter 1
Thermoelectric Effects: Semiclassical and Quantum Approaches from the Boltzmann Transport Equation

Andrés Cantarero and F. Xavier Àlvarez

Abstract The thermoelectric efficiency of a material depends on its electronic and phononic properties. It is normally given in terms of the dimensionless figure of merit $ZT = \sigma S^2 T/\kappa$. The parameters involved in ZT are the electrical conductivity σ, the Seebeck coefficient S, and the thermal conductivity κ. The thermal conductivity has two contributions, $\kappa = \kappa_e + \kappa_L$, the electron thermal conductivity κ_e and the lattice thermal conductivity κ_L. In this chapter all these parameters will be deduced for metals and semiconductors, starting from the Boltzmann transport equation (BTE). The electrical conductivity, the Seebeck coefficient, and the electronic thermal conductivity will be obtained from the BTE for electrons. Similarly, the lattice or phonon thermal conductivity will be given from the BTE for phonons. The ab initio approaches to obtain both the electronic and phononic transport via the BTE will also be analyzed. All the theoretical studies are based on the relaxation time approximation. The expressions for the relaxation times for electrons and phonons will be discussed. The results will be particularized to nanostructures whenever is possible.

1.1 Introduction

Solid matter is composed basically by ions and electrons. Electrons move in a metal or semiconductor through the laws of Quantum Mechanics, although for many purposes they can be treated as classical particles. In a first approximation, electrons move in a perfect lattice (Born–Oppenheimer approximation), within a periodic

---

A. Cantarero (✉)
Materials Science Institute, University of Valencia, PO Box 22085, 46071 Valencia, Spain
e-mail: Andres.Cantarero@uv.es

F.X. Àlvarez
Physics Department, Autonomous University of Barcelona, 08193 Bellaterra, Catalonia, Spain
e-mail: Xavier.Alvarez@uab.es

X. Wang and Z.M. Wang (eds.), *Nanoscale Thermoelectrics*, Lecture Notes in Nanoscience and Technology 16, DOI 10.1007/978-3-319-02012-9_1,
© Springer International Publishing Switzerland 2014

potential given by the crystal periodicity of the solid. Phonons are a consequence of the ion movement and thus are related to the disorder or the lack of periodicity in real lattices. They can also be treated as particles, actually called quasi-particles, since we can assign a momentum or quasi-momentum $\hbar \boldsymbol{q} = h/\lambda_{\text{ph}}$, λ_{ph} being the phonon wavelength. In a real lattice, electrons can interact with lattice imperfection or boundaries, a phenomenon known as scattering. The main source of lattice imperfections is temperature dependent, it is thus related to a thermodynamic quantity, the temperature. At low temperature, the main source of electron scattering is the presence of impurities or the existence of boundaries, the last factor being extremely important in nanometric size materials. The scattering of electrons by impurities is elastic, i.e. there is momentum and energy conservation. At high temperatures, electron–phonon interaction is the most important scattering process. Scattering by acoustic phonons is elastic, while that by optical phonons is inelastic, momentum is conserved but the electron after the scattering process absorbs (loses) the phonon energy, i.e. the electron energy is not conserved in the scattering process. In the analysis of electron–phonon scattering, phonons are necessarily treated as quasi-particles. On the other hand, electrons are fermions and obey the Fermi–Dirac statistics, the distribution function f_0 being

$$f_0 = \frac{1}{e^{(\varepsilon(\boldsymbol{k})-\mu)/k_B T} + 1}, \tag{1.1}$$

where $\varepsilon(\mathbf{k})$ is the electron energy, μ the chemical potential (the Fermi energy at 0 K), k_B the Boltzmann constant, and T the absolute temperature. The electronic transport is governed by the changes in the distribution function. Phonon transport also depends on Statistics Mechanics, since they can be treated as quasi-particles obeying the Bose–Einstein statistics

$$N = \frac{1}{e^{\hbar\omega(\boldsymbol{q})/k_B T} - 1}, \tag{1.2}$$

where $\hbar\omega(\boldsymbol{q})$ is the phonon energy. The variation of the phonon distribution function giving rise to phonon transport is produced by a temperature difference and the presence of scattering, no external forces can give rise to phonon transport. A real phonon is not a normal mode of the lattice since it has a lifetime and a mean free path associated. Phonons interact with electrons, lattice imperfections, and other phonons. There is an important difference between electron and phonon scattering. In the case of electron scattering, a given electron with wave function $|\Psi_{n,\,\mathbf{k}}(\boldsymbol{r},\, t)\rangle$, after the scattering process exchange momentum with, for instance, an impurity, and the final electron state will be $|\Psi_{n',\,\mathbf{k}'}(\boldsymbol{r},\, t)\rangle$. The electron is scattered at the point $\boldsymbol{r}$ at the time t, and possibly it will change to a new band or subband ($n \longrightarrow n'$) and change the traveling direction ($k = k'$, since the scattering is elastic). If the electronic transport is, to simplify, through a nanowire, the electrons entering in the nanowire from the left will exit at the right end. In other words, the number of electrons is a conserved quantity.

The number of phonons in a transport experiment is not conserved. The phonon population depends on the temperature and there are more phonons in the hot region of a material than in the cold region. Thus, if there is a temperature gradient, there is a phonon flux from the hot side to the cold side. During this transport, phonons are scattered by impurities or other phonons. After a scattering process, a phonon with wave number $\boldsymbol{q}_1$ and energy $\hbar\omega_1$ is scattered, for instance, by an impurity (wave number $\boldsymbol{K}$), it is annihilated and a new phonon with wave number $\boldsymbol{q}_2$ and energy $\hbar\,\omega_2$ is created. The energy is conserved in the scattering process, $\hbar\omega_1 = \hbar\,\omega_2$, the total wave number is also conserved, $\boldsymbol{q}_1 + \boldsymbol{K} = \boldsymbol{q}_2$, and the number of phonons. But in the case of phonon–phonon scattering, clearly the number of phonons cannot be conserved.

In the analysis of material properties at equilibrium, most of the theoretical approaches used nowadays to relate mechanical to thermodynamic magnitudes had been developed in the first half of last century. When the systems apart from equilibrium, the particles or quasi-particles behave differently depending on the volume element where we look at some physical observable. If we are not so far from equilibrium, the so-called local equilibrium hypothesis allows to generalize the results obtained for equilibrium statistical mechanics, although additional terms are needed depending on first or second derivatives in a similar mathematical analog to a Taylor expansion.

However, the technological advances in the development of new materials and nanostructures, and the accuracy in the measurement of physical observables will put in evidence the fails in the theoretical models developed in the past. From the thermodynamics point of view, many properties measured at the nanoscale apart the system from local equilibrium since the imposed gradients are extremely large. The locality should be revisited in order to completely understand the huge amount of experimental data.

In this chapter we will analyze the main approaches, based on the Boltzmann equation, to quantitatively describe transport phenomena related to thermoelectricity. The electrical conductivity and the Seebeck coefficient are directly related to the electronic transport. The electrons also carry energy or heat, contributing to the thermal conductivity. Finally, the amount of heat transported by phonons is governed by the lattice thermal conductivity. All these quantities will be analyzed here, on the basis of the Boltzmann transport equation.

1.2 The Boltzmann Transport Equation for Electrons

The distribution function $f(\boldsymbol{r}, \boldsymbol{k}, t)$ gives the probability of occupation of a state by an electron located at $\boldsymbol{r}$ with a wave number $\boldsymbol{k}$ at time t. Both $\boldsymbol{r}$ and $\boldsymbol{k}$ can be assumed to be within a given interval $\Delta\boldsymbol{r}$ and $\Delta\boldsymbol{k}$, respectively, in order to fulfill the Heisenberg's principle. The number of electrons occupying the volume element $d^3\boldsymbol{k}$ in $\boldsymbol{r}$ at t per unit volume of the crystal is [1]:

$$dn(\boldsymbol{r}) = \frac{2}{(2\pi)^3} f(\boldsymbol{r}, \boldsymbol{k}, t) d^3\boldsymbol{k}, \tag{1.3}$$

where the factor 2 assumes spin degeneracy. In equilibrium, the distribution function can be written as:

$$f_0(\boldsymbol{r}, \boldsymbol{k}) = \frac{1}{1 + e^{[\varepsilon(\boldsymbol{k}) - \mu(\boldsymbol{r})]/k_B T(\boldsymbol{r})}}\ , \tag{1.4}$$

where the dependence on $\boldsymbol{k}$ is given by the electronic band structure of the solid (the band index has been omitted for simplicity) and that on $\boldsymbol{r}$ via a possible gradient of the temperature or carrier concentration (via the chemical potential). The distribution function can change in time due to the existence of internal or external forces. The rate of variation of the distribution function can be written, using the chain rule, as

$$\frac{df}{dt} = \nabla_r f \cdot \frac{d\boldsymbol{r}}{dt} + \frac{1}{\hbar} \nabla_k f \cdot \frac{d\boldsymbol{p}}{dt} + \frac{\partial f}{\partial t} = \boldsymbol{v} \cdot \nabla_r f + \frac{1}{\hbar} \nabla_k f \cdot \boldsymbol{F}_a + \frac{\partial f}{\partial t}\ , \tag{1.5}$$

$\boldsymbol{F}_a$ being the set of applied forces, which can be divided into external ($\boldsymbol{F}$) and internal forces ($\boldsymbol{F}_D$), that last due to the existence of impurities, defects, phonons, etc. Since the total number of states is constant, $df/dt = 0$, the previous equation can be written as:

$$\boldsymbol{v} \cdot \nabla_r f + \frac{1}{\hbar} \boldsymbol{F} \cdot \nabla_k f + \frac{1}{\hbar} \boldsymbol{F}_D \cdot \nabla_k f = -\frac{\partial f}{\partial t} = -\left(\frac{\partial f}{\partial t}\right)_{\text{drift}} - \left(\frac{\partial f}{\partial t}\right)_{\text{scatt}}\ , \tag{1.6}$$

divided into the time variation due to the presence of external fields (drift) and to internal fields (scattering). Attending the origin of the forces, we can separate the previous equation into two equations,

$$-\left(\frac{\partial f}{\partial t}\right)_{\text{scatt}} = \frac{1}{\hbar} \boldsymbol{F}_D \cdot \nabla_k f \tag{1.7}$$

and

$$-\left(\frac{\partial f}{\partial t}\right)_{\text{drift}} = \boldsymbol{v} \cdot \nabla_r f + \frac{1}{\hbar} \boldsymbol{F} \cdot \nabla_k f; \tag{1.8}$$

1.2.1 The Scattering Integral

For the scattering term, an analytical expression can be derived, called scattering or collision integral. The probability per unit time that a particle in a state ($\boldsymbol{r}$, $\boldsymbol{k}$) goes to a state ($\boldsymbol{r}'$, $\boldsymbol{k}'$) due to a scattering event can be named $W(\boldsymbol{r}, \boldsymbol{k}; \boldsymbol{r}', \boldsymbol{k}')$.

Obviously, $\boldsymbol{r} \sim \boldsymbol{r}'$ since the scattering process will change the electron wave number at a given position, i.e. W does not depend on $\boldsymbol{r}$ (in an homogeneous medium): $W(\boldsymbol{r},\boldsymbol{k};\boldsymbol{r}',\boldsymbol{k}') = W(\boldsymbol{k},\boldsymbol{k}') \equiv W_{\boldsymbol{k}}^{\boldsymbol{k}'}$, i.e. the scattering processes can be analyzed in $\boldsymbol{k}$ space.

Considering two volume elements $d^3\boldsymbol{k}$ and $d^3\boldsymbol{k}'$ around $\boldsymbol{k}$ and $\boldsymbol{k}'$, the number of occupied states within these volume elements is

$$f_{\boldsymbol{k}} \frac{1}{4\pi^3} d^3\boldsymbol{k} \quad \text{and} \quad f_{\boldsymbol{k}'} \frac{1}{4\pi^3} d^3\boldsymbol{k}' \tag{1.9}$$

while the number of empty states would be

$$[1-f_{\boldsymbol{k}}] \frac{1}{4\pi^3} d^3\boldsymbol{k} \quad \text{and} \quad [1-f_{\boldsymbol{k}'}] \frac{1}{4\pi^3} d^3\boldsymbol{k}' , \tag{1.10}$$

where we have also written $f_{\mathbf{k}}$ instead of $f(\boldsymbol{k})$ to save space. In $d\,t$, an electron with wave number $\boldsymbol{k}$ is scattered and acquires a wave number $\boldsymbol{k}'$; the number of occupied states will change by an amount

$$dt\left\{-W_{\boldsymbol{k}}^{\boldsymbol{k}'} f_{\boldsymbol{k}}[1-f_{\boldsymbol{k}'}] + W_{\boldsymbol{k}'}^{\boldsymbol{k}} f_{\boldsymbol{k}'}[1-f_{\boldsymbol{k}}]\right\} \frac{1}{4\pi^3} d^3\boldsymbol{k}' \frac{1}{4\pi^3} d^3\boldsymbol{k}; \tag{1.11}$$

Extending the integral to the whole Brillouin zone (BZ), and assuming that the direct and inverse probabilities are equivalent (time reversal symmetry), $W_{\boldsymbol{k}}^{\boldsymbol{k}'} = W_{\boldsymbol{k}'}^{\boldsymbol{k}}$, the variation of the total number of occupied states in dt is:

$$dt \frac{1}{4\pi^3} d^3\boldsymbol{k} \int W_{\boldsymbol{k}}^{\boldsymbol{k}'} [f_{\boldsymbol{k}} - f_{\boldsymbol{k}'}] \frac{1}{4\pi^3} d^3\boldsymbol{k}'; \tag{1.12}$$

On the other hand, the variation in the number of occupied states given by $f_{\mathbf{k}} d^3\boldsymbol{k} / 4\pi^3$ in dt due to scattering is

$$\left(\frac{\partial f}{\partial t}\right)_{\text{scatt}} dt \frac{d^3\boldsymbol{k}}{4\pi^3}; \tag{1.13}$$

Comparing both equations, the scattering integral can be written as

$$\left(\frac{\partial f}{\partial t}\right)_{\text{scatt}} = \int W_{\boldsymbol{k}}^{\boldsymbol{k}'} [f_{\boldsymbol{k}} - f_{\boldsymbol{k}'}] \frac{1}{4\pi^3} d^3\boldsymbol{k}'. \tag{1.14}$$

In the stationary case

$$\frac{\partial f}{\partial t} = \left(\frac{\partial f}{\partial t}\right)_{\text{drift}} + \left(\frac{\partial f}{\partial t}\right)_{\text{scatt}} = 0 \tag{1.15}$$

and the Boltzmann equation reads

$$\boldsymbol{v} \cdot \nabla_{\boldsymbol{r}} f + \frac{1}{\hbar} \boldsymbol{F} \cdot \nabla_{\boldsymbol{k}} f = - \int W_{\boldsymbol{k}}^{\boldsymbol{k}'} [f_{\boldsymbol{k}} - f_{\boldsymbol{k}'}] \frac{1}{4\pi^3} d^3\boldsymbol{k}'; \tag{1.16}$$

The left side of this equation is related to the classical evolution of the system due to the application of external fields. On the other hand, the right side of the equation contains the probability that an electron be scattered and change its wave number from $\boldsymbol{k}$ to $\boldsymbol{k}'$. This probability can be calculated using Quantum Mechanics techniques (scattering theory), once we know the scattering mechanism.

1.2.2 *Relaxation Time Approximation*

Since a quantum treatment of the scattering integral is a cumbersome problem, we need to assume a simple hypothesis to deal with Eq. (1.16). If the external fields are suppressed in $t = 0$, the system will return to equilibrium due to the existence of scattering. The drift term will disappear and the scattering will produce a random movement of the electrons. In that case, the time evolution of f would be

$$\left(\frac{\partial f}{\partial t}\right) = \left(\frac{\partial f}{\partial t}\right)_{\text{scatt}}. \tag{1.17}$$

If the system is not too far from equilibrium, the rate of evolution of the distribution function can be assumed to be proportional to the difference between the equilibrium and out of equilibrium distribution functions:

$$\left(\frac{\partial f}{\partial t}\right) = \left(\frac{\partial f}{\partial t}\right)_{\text{scatt}} = -\frac{f(\boldsymbol{r},\boldsymbol{k},t) - f_0(\boldsymbol{r},\boldsymbol{k})}{\tau(\boldsymbol{k})}, \tag{1.18}$$

$1/\tau(\boldsymbol{k})$ being the proportionality constant. The solution of this equation is

$$f(\boldsymbol{r},\boldsymbol{k},t) - f_0(\boldsymbol{r},\boldsymbol{k}) = [f(\boldsymbol{r},\boldsymbol{k},0) - f_0(\boldsymbol{r},\boldsymbol{k})]e^{-t/\tau(\boldsymbol{k})} \tag{1.19}$$

i.e. the relaxation time $\tau(\boldsymbol{k})$ indicates how fast the system returns to equilibrium once the effect of the external fields has been removed. Since that

$$\left(\frac{\partial f}{\partial t}\right)_{\text{scatt}} = \int W_{\boldsymbol{k}}^{\boldsymbol{k}'} [f_{\boldsymbol{k}} - f_{\boldsymbol{k}'}] \frac{1}{4\pi^3} d^3\boldsymbol{k}' = -\frac{f - f_0}{\tau(\boldsymbol{k})} \tag{1.20}$$

In terms of $\tau(\boldsymbol{k})$, the Boltzmann equation can be written as

$$\boldsymbol{v} \cdot \nabla_r f + \frac{1}{\hbar} \boldsymbol{F} \cdot \nabla_k f = -\frac{f(\boldsymbol{r}, \boldsymbol{k}) - f_0(\boldsymbol{r}, \boldsymbol{k})}{\tau(\boldsymbol{k})} \tag{1.21}$$

1.2.3 The Linearized Boltzmann Equation

The relaxation time approximation allows an analytical solution of the Boltzmann equation for the stationary case. If we assumed $\boldsymbol{F}_a = e\boldsymbol{E}$, and consider space homogeneity, the Boltzmann equation can be written as

$$\frac{e}{\hbar} \boldsymbol{E} \cdot \nabla_k f = -\frac{f(\boldsymbol{k}) - f_0(\boldsymbol{k})}{\tau(\boldsymbol{k})}. \tag{1.22}$$

Rewriting the equation in terms of $f(\mathbf{k})$,

$$f(\boldsymbol{k}) = f_0(\boldsymbol{k}) - \frac{e}{\hbar} \tau(\boldsymbol{k}) \boldsymbol{E} \cdot \nabla_k f. \tag{1.23}$$

In principle, this equation can be solved iteratively, but, if we are interested in linear phenomena on the electric field $\boldsymbol{E}$, an approximated solution is obtained replacing the distribution function $f(\boldsymbol{k})$ by the equilibrium distribution function $f_0(\boldsymbol{k})$ in the $\boldsymbol{k}$ derivative:

$$f(\boldsymbol{k}) \approx f_0(\boldsymbol{k}) - \frac{e}{\hbar} \tau(\boldsymbol{k}) \boldsymbol{E} \cdot \nabla_k f_0. \tag{1.24}$$

Thus, for a linear problem or weak electric fields, the Boltzmann equation can be interpreted as a linear expansion of the distribution function around $\boldsymbol{k}$. Since $f(\boldsymbol{k})$ is not far from equilibrium,

$$f(\boldsymbol{k}) \approx f_0\left(\boldsymbol{k} - \frac{e}{\hbar} \tau(\boldsymbol{k}) \boldsymbol{E}\right). \tag{1.25}$$

The distribution function resulting from the application of an electric field $\boldsymbol{E}$, including the effect of scattering through $\tau(\boldsymbol{k})$ has been drawn in Fig. 1.1. The difference with the equilibrium distribution function is concentrated in the region around the Fermi energy μ, and it is described as a constant shift of $eE\lambda$, in energy units. λ is the mean free path of the electron at the Fermi energy, $\lambda = v_F \tau(\boldsymbol{k}_F)$.

Another particular case of the Boltzmann equation is that corresponding to a temperature gradient in the absence of applied fields. The BTE, in the relaxation time approximation, can be written as

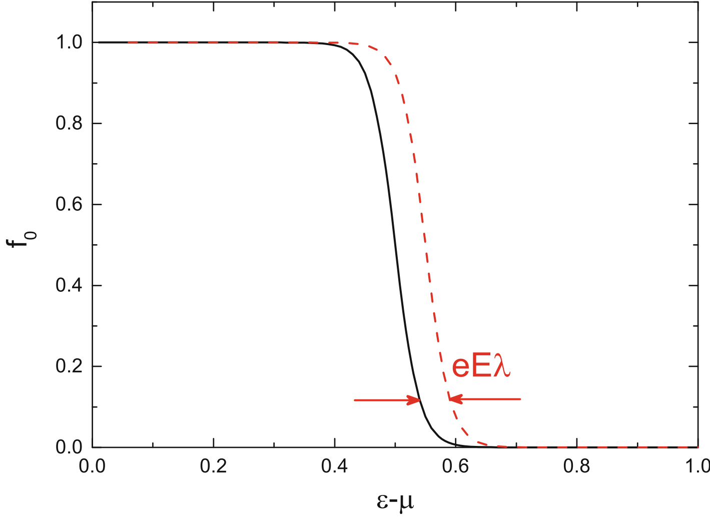

Fig. 1.1 Electron distribution in an electric field. The *solid line, black*, represents the equilibrium distribution function, while the *dotted red line* is f_0 shifted an amount $\boldsymbol{\Delta k}_0 = e\tau\boldsymbol{E}/\hbar$ ($eE\lambda$ in energy, as explained in the text)

$$\boldsymbol{v} \cdot \nabla_r f = -\frac{f(\boldsymbol{r},\boldsymbol{k}) - f_0(\boldsymbol{r},\boldsymbol{k})}{\tau(\boldsymbol{k})}. \tag{1.26}$$

Again, linearizing the equation,

$$f(\boldsymbol{r},\boldsymbol{k}) = f_0(\boldsymbol{r},\boldsymbol{k}) - \frac{\partial f_0}{\partial \varepsilon}(\varepsilon - \mu)\tau(\boldsymbol{k})\boldsymbol{v} \cdot \nabla \ln T. \tag{1.27}$$

Writing the velocity in terms of the energy gradient and that in terms of the gradient of the distribution function,

$$f(\boldsymbol{k}) \approx f_0(\boldsymbol{k} - \tau(\boldsymbol{k})(\varepsilon - \mu)\nabla \ln T/\hbar). \tag{1.28}$$

In Fig. 1.2, the equilibrium distribution function is represented as a black solid line. The blue line is the perturbed distribution function in the presence of a temperature gradient, in the linearized approximation. For energies above the Fermi energy, the electron population is over the equilibrium value, while above the Fermi energy is below equilibrium. There is an increase of the number of carriers above the Fermi energy (and a depopulation below the Fermi energy) due to the thermal gradient. If we change the sign of the thermal gradient, the shape of curve will be the opposite, there will be an increase of the electron population below the Fermi energy as a consequence of the fact that the region is colder.

Returning to the complete expression of the Boltzmann equation in the relaxation time approximation, Eq. (1.26), but writing it in the linearized form,

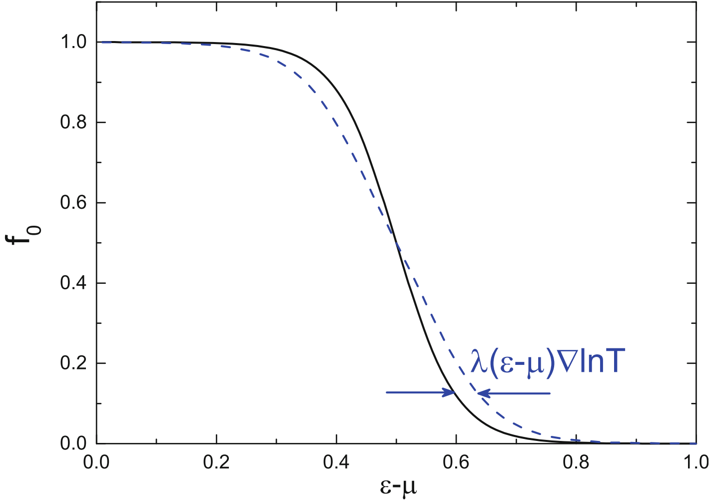

Fig. 1.2 Electron distribution in the presence of a temperature gradient. The *black solid line* represents the equilibrium distribution function, while the *blue line* represents the perturbed distribution function. The energy shift due to the temperature gradient is, approximately, $\lambda(\varepsilon - \mu) \nabla \ln T$, where λ is the electron mean free path at the Fermi energy

$$\boldsymbol{v} \cdot \nabla_r f_0 + \frac{e}{\hbar}\boldsymbol{E} \cdot \nabla_k f_0 = -\frac{f(\boldsymbol{r},\boldsymbol{k}) - f_0(\boldsymbol{r},\boldsymbol{k})}{\tau(\boldsymbol{k})} \equiv -\frac{f^{(1)}(\boldsymbol{r},\boldsymbol{k})}{\tau(\boldsymbol{k})}. \tag{1.29}$$

The label "(1)" in the distribution function may be interpreted as the first order term in a Taylor expansion. The spatial derivative can be written as

$$\nabla_r f_0 = -\frac{e^{(\varepsilon-\mu)/k_BT}}{[1 + e^{(\varepsilon-\mu)/k_BT}]^2}\frac{1}{k_BT}[-\nabla_r\mu - (\varepsilon - \mu)\nabla_{\boldsymbol{r}} \ln T]. \tag{1.30}$$

This equation can be written in a simplified manner using the derivative $\partial f/\partial \varepsilon$:

$$\nabla_r f_0 = -\frac{\partial f_0}{\partial \varepsilon}[\nabla\mu + (\varepsilon - \mu)\nabla \ln T]. \tag{1.31}$$

The gradient with respect to **k** can also be written, using the chain rule, as

$$\nabla_k f_0 = \frac{\partial f_0}{\partial \varepsilon}\nabla_{\boldsymbol{k}}\varepsilon(\boldsymbol{k}) = \frac{\partial f_0}{\partial \varepsilon}\hbar\boldsymbol{v}. \tag{1.32}$$

Thus, the Boltzmann equation, in the linear approximation, can be written as

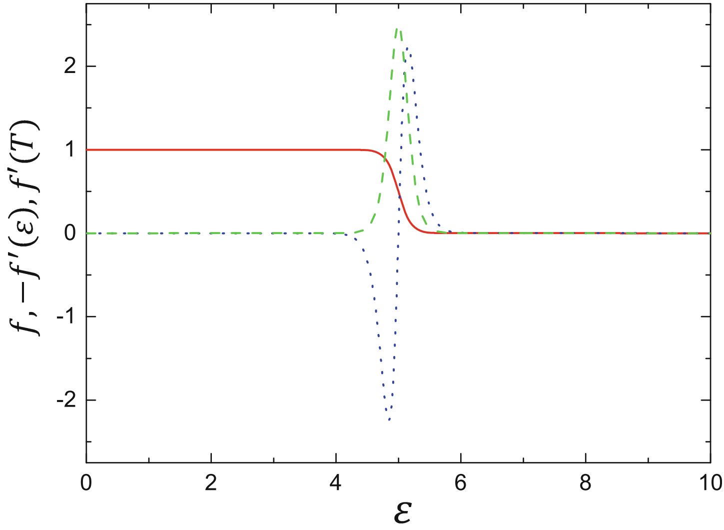

Fig. 1.3 The *solid line* (*red online*) represents the Fermi–Dirac distribution at $k_BT = 0.\ 1$ in units of energy with $\mu = 5$. The *dashed line* (*green online*) is the derivative $-\ \partial f/\partial E$, while the *dotted line* (*blue online*) is the derivative $\partial f/\partial T$

$$f^{(1)}(\boldsymbol{r}, \boldsymbol{k}) = -\frac{\partial f_0}{\partial \varepsilon}\tau(\boldsymbol{k})\boldsymbol{v} \cdot [\nabla(e\phi + \mu) + (\varepsilon - \mu)\nabla \ln T], \tag{1.33}$$

where we have used the fact that the electric field, $\boldsymbol{E} = -\ \nabla\phi$, can be written in terms of the electrostatic potential. It is convenient to leave the expression in terms of $\partial f/\partial \varepsilon$, since this has a deltaic behavior around the Fermi energy at low temperatures. At higher temperatures, the shape of $\partial f/\partial \varepsilon$ is similar to a Lorentzian, restricting the integration to a small region around μ. In Fig. 1.3 we have represented the behavior of f_0, $-\partial f_0/\partial\ \varepsilon$ and $\partial f_0/\partial\ T$. The value of $k_BT = 0.1$ eV (corresponding to ~1,100 K) and $\mu = 5$ eV. Equation (1.33) can be written in short as:

$$f^{(1)}(\boldsymbol{r}, \boldsymbol{k}) = -\frac{\partial f_0}{\partial \varepsilon}\tau(\boldsymbol{k})\boldsymbol{v} \cdot \boldsymbol{A}(\boldsymbol{r}, \boldsymbol{k}) \tag{1.34}$$

where

$$\boldsymbol{A}(\boldsymbol{r}, \boldsymbol{k}) = [\nabla(e\phi + \mu) + (\varepsilon - \mu)\nabla \ln T]. \tag{1.35}$$

If there is only an electric field present in the material, $\boldsymbol{A} = e\nabla\phi = \ -\ e\boldsymbol{E}$ is the Coulomb force.

1.2.4 The Effect of a Magnetic Field on the Boltzmann Equation

Following Ziman [2], a magnetic field does not produce drift on the electrons (it does not produce work), but deviates the electron path due to the Lorentz force. Thus, the time variation of the distribution function due to the presence of a magnetic field (the Lorentz force),

$$\left(\frac{\partial f}{\partial t}\right)_{\boldsymbol{B}} = \frac{e}{\hbar}\boldsymbol{v} \times \boldsymbol{B} \cdot \nabla_{\boldsymbol{k}} f^{(1)} \tag{1.36}$$

cannot be included in the drift, but in parallel with the scattering terms: the deviation of the electrons due to the magnetic field is equivalent to a scattering process. However, we cannot linearized the previous equation since $\mathbf{v} \cdot \mathbf{v} \times \boldsymbol{B} = 0$ and the effect of the magnetic field is neglected. The Boltzmann equation, including the effect of the magnetic field, is

$$\boldsymbol{v} \cdot \nabla_{\boldsymbol{r}} f + \frac{1}{\hbar}\boldsymbol{F} \cdot \nabla_{\boldsymbol{k}} f = -\frac{f^{(1)}(\boldsymbol{r}, \boldsymbol{k})}{\tau(\boldsymbol{k})} + \frac{e}{\hbar}\boldsymbol{v} \times \boldsymbol{B} \cdot \nabla_{\boldsymbol{k}} f^{(1)}. \tag{1.37}$$

The solution for $f^{(1)}(\boldsymbol{r}, \boldsymbol{k})$ can be assumed to have the same form as in Eq. (1.33), but generalizing the $\boldsymbol{A}$ vector to a new amount, Ξ:

$$f^{(1)}(\boldsymbol{r}, \boldsymbol{k}) = -\frac{\partial f_0}{\partial \varepsilon}\tau(\boldsymbol{k})\boldsymbol{v} \cdot \Xi\ . \tag{1.38}$$

If there is no magnetic field, the solution must be reduced to $\Xi = \boldsymbol{A}$. The first derivative of the distribution function can be found to be:

$$\nabla_{\boldsymbol{k}} f^{(1)} = -\frac{\partial f_0}{\partial \varepsilon}\tau\hbar \boldsymbol{M}^{*-1}\Xi\,, \tag{1.39}$$

$\boldsymbol{M}^*$ being the effective mass tensor and a dependence of $\boldsymbol{k}$ through the energy has been assumed for τ and Ξ. In that case, the derivative with respect to $\boldsymbol{k}$ would contain the velocity, which is perpendicular to $\boldsymbol{v} \times \boldsymbol{B}$. We arrive to the equation

$$\Xi = \nabla(e\phi + \mu) + (\varepsilon - \mu)\nabla \ln T + e\boldsymbol{M}^{*-1}\Xi \times \boldsymbol{B} = \boldsymbol{A} + e\boldsymbol{M}^{*-1}\Xi \times \boldsymbol{B}; \tag{1.40}$$

Assuming an isotropic effective mass for simplicity, the solution is:

$$f^{(1)} = -e\tau\frac{\partial f_0}{\partial \varepsilon}\boldsymbol{v} \cdot \frac{\boldsymbol{A} + (e\tau/m^*)^2(\boldsymbol{A} \cdot \boldsymbol{B})\boldsymbol{B} + (e\tau/m^*)\boldsymbol{A} \times \boldsymbol{B}}{1 + (e\tau/m^*)^2 B^2} \tag{1.41}$$

1.2.5 Current and Energy Flux Densities

The current density can be written as:

$$\boldsymbol{j} = \frac{e}{4\pi^3} \int \boldsymbol{v} f(\boldsymbol{r}, \boldsymbol{k}) d^3\boldsymbol{k} = \frac{e}{4\pi^3} \int \boldsymbol{v} f^{(1)}(\boldsymbol{r}, \boldsymbol{k}) d^3\boldsymbol{k} \tag{1.42}$$

Substituting the value of $f^{(1)}(\mathbf{r}, \mathbf{k})$,

$$\boldsymbol{j} = \frac{e}{4\pi^3} \int \left(-\frac{\partial f_0}{\partial \varepsilon}\right) \tau \boldsymbol{v}(\boldsymbol{v} \cdot \Xi) d^3\boldsymbol{k}. \tag{1.43}$$

The movement of charged particles not only carries a current but also transfers energy. The energy flux, i.e. the energy amount crossing a unit cross section per unit time is given by the expression:

$$\boldsymbol{j}_Q = \frac{1}{4\pi^3} \int \varepsilon(\boldsymbol{k}) \boldsymbol{v} f^{(1)}(\boldsymbol{r}, \boldsymbol{k}) d^3\boldsymbol{k} \tag{1.44}$$

The expression, in terms of $\boldsymbol{\Xi}$, is

$$\boldsymbol{j}_Q = \frac{1}{4\pi^3\hbar^2} \int \left(-\frac{\partial f_0}{\partial \varepsilon}\right) \varepsilon(\boldsymbol{k}) \tau \boldsymbol{v}(\boldsymbol{v} \cdot \Xi) d^3\boldsymbol{k}. \tag{1.45}$$

In the absence of magnetic fields,

$$\Xi = e\boldsymbol{E} - \nabla\mu - \frac{\varepsilon - \mu}{T} \nabla T = \boldsymbol{E} - \nabla \frac{\mu}{T} - \frac{\varepsilon}{T} \nabla T. \tag{1.46}$$

The expression for the electric current becomes

$$\boldsymbol{j} = \frac{e}{4\pi^3} \int \left(-\frac{\partial f_0}{\partial \varepsilon}\right) \tau \boldsymbol{v} \left[\boldsymbol{v} \cdot \left(\boldsymbol{E} - \nabla \frac{\mu}{T} - \frac{\varepsilon}{T} \nabla T\right)\right] d^3\boldsymbol{k}. \tag{1.47}$$

For an isotropic medium,

$$\boldsymbol{j} = \frac{4e}{3m^*} \int \left(-\frac{\partial f_0}{\partial \varepsilon}\right) \tau \varepsilon D(\varepsilon) \left(e\boldsymbol{E} - \nabla \frac{\mu}{T} - \frac{\varepsilon}{T} \nabla T\right) d\varepsilon \tag{1.48}$$

Introducing the notation

$$\mathcal{L}_{ij} = \frac{4}{3m^*} \int \left(-\frac{\partial f_0}{\partial \varepsilon}\right) \tau^j \varepsilon^i D(\varepsilon) d\varepsilon\,, \tag{1.49}$$

the electrical current becomes

$$\boldsymbol{j} = e\mathcal{L}_{11}\left(e\boldsymbol{E} - T\nabla\frac{\mu}{T}\right) - e\mathcal{L}_{21}\nabla\ln T, \tag{1.50}$$

Similarly,

$$\boldsymbol{j}_Q = e\mathcal{L}_{21}\left(e\boldsymbol{E} - T\nabla\frac{\mu}{T}\right) - \mathcal{L}_{31}\nabla\ln T. \tag{1.51}$$

From Eq. (1.48) and the definition of the transport coefficients, Eq. (1.49),

$$e^2\mathcal{L}_{11} = \sigma\,, \tag{1.52}$$

the electrical conductivity. If there is no electrical current circulating through the semiconductor (open circuit), $\boldsymbol{j} = 0$, and the electric field is

$$\boldsymbol{E} = \frac{1}{e}\nabla\mu + \frac{\mathcal{L}_{21} - \mu\mathcal{L}_{11}}{e\mathcal{L}_{11}T}\nabla T \tag{1.53}$$

If there are no gradients of concentration, from the definition of the Seebeck effect, the Seebeck coefficient $S = dV/dT$ is given by

$$S = \frac{\mathcal{L}_{21} - \mu\mathcal{L}_{11}}{e\mathcal{L}_{11}T}. \tag{1.54}$$

We can introduce in Eq. (1.51) the electrical current. The result is

$$\boldsymbol{j}_Q = \frac{\mathcal{L}_{21}}{e\mathcal{L}_{11}}\boldsymbol{j} + \left(\frac{\mathcal{L}_{21}^2 - e\mathcal{L}_{31}\mathcal{L}_{11}}{e\mathcal{L}_{11}}\right)\nabla T = \Pi\boldsymbol{j} - \kappa_e\nabla T\,, \tag{1.55}$$

where the Peltier coefficient

$$\Pi = \frac{\mathcal{L}_{21}}{e\mathcal{L}_{11}} = ST \tag{1.56}$$

and the electron thermal conductivity

$$\kappa_e = \frac{\mathcal{L}_{21}^2 - e\mathcal{L}_{31}\mathcal{L}_{11}}{e\mathcal{L}_{11}}. \tag{1.57}$$

The opposite relations are

$$\mathcal{L}_{11} = \frac{\sigma}{e^2}\,, \quad \mathcal{L}_{21} = \frac{\sigma ST}{e}\,, \quad \mathcal{L}_{31} = ST - \kappa_e. \tag{1.58}$$

1.2.6 Relaxation Times for Electron Scattering

The transport coefficients are, in general, second range tensors. In the absence of magnetic fields,

$$\mathcal{L}_{ij}^{\gamma\zeta} = \frac{1}{4\pi^3} \int \left(-\frac{\partial f_0}{\partial \varepsilon} \right) \tau^j v_\gamma v_\zeta \varepsilon^{i-1} d^3\boldsymbol{k}. \tag{1.59}$$

Although it is possible to deduce a general expression in tensorial form, we will assume an isotropic semiconductor to escape from the tensor notation. The integral in $\boldsymbol{k}$ can be split in the usual way in an integral in energy times the integral over a surface of constant energy. The resulting expression after integration in dS_ε is

$$\mathcal{L}_{ij} = \frac{4}{3m^*} \int \left(-\frac{\partial f_0}{\partial \varepsilon} \right) D(\varepsilon) \tau^j \varepsilon^i d\varepsilon = \frac{4}{3k_B T m^*} \int f_0 D(\varepsilon) \tau^j \varepsilon^i d\varepsilon \tag{1.60}$$

in a non-degenerate semiconductor ($-\ \partial f_0 / \partial \varepsilon = f_0 / k_B T$). Since the electron concentration can be defined as

$$n = 2 \int f_0 D(\varepsilon) d\varepsilon = \int dn(\varepsilon)\,, \tag{1.61}$$

we can define the average

$$\langle \varepsilon^i \tau^j \rangle = \frac{2}{3nk_B T} \int \varepsilon^i \tau^j dn(\varepsilon) \tag{1.62}$$

and the transport coefficients can be written in terms of $\langle \tau \rangle$ as:

$$\mathcal{L}_{ij} = \frac{n}{m^*} \langle \varepsilon^i \tau^j \rangle. \tag{1.63}$$

Very often, the relaxation time can be written as a function of the electron energy in the way $\tau = \tau_0 \varepsilon^\lambda$. In that case the average of the relaxation time

$$\langle \tau \rangle = \tau_0 \Gamma(5/2 + \lambda) / \Gamma(5/2) \tag{1.64}$$

can be written in terms of the Γ-function. The exponent depends on the scattering mechanism [3]: 3/2 for scattering by ionized impurities and $-\ 1/2$ for acoustical phonons. In the case of optical phonons, the electron scattering is not elastic and the relaxation time approximation cannot be applied [1].

1.2.7 The Thermal Conductivity in a Semiconductor

The expression for the electronic thermal conductivity, in terms of the transport coefficients, is given by Eq. (1.57). An explicit expression can be obtained for a semiconductor with some common assumptions. In semiconductors with parabolic bands, the relaxation time can be written as

$$\tau = \tau_0 \varepsilon^{\lambda} , \tag{1.65}$$

where λ is a exponent which depends on the scattering mechanism. In terms of Eq. (1.63),

$$\mathcal{L}_{11} = \frac{n}{m^*} \langle \varepsilon \tau \rangle , \quad \mathcal{L}_{21} = \frac{n}{m^*} \langle \varepsilon^2 \tau \rangle , \quad \mathcal{L}_{31} = \frac{n}{m^*} \langle \varepsilon^3 \tau \rangle . \tag{1.66}$$

From Eq. (1.64) and following the expression for the electronic thermal conductivity, it can be written explicitly in terms of Γ-functions:

$$\kappa_e = \frac{n}{m^*} \frac{5 k_B^2 T \tau_0}{4} \left[7 \frac{\Gamma(9/2+\lambda)}{\Gamma(9/2)} - 5 \frac{\Gamma^2(7/2+\lambda)\Gamma(5/2)}{\Gamma^2(5/2+\lambda)\Gamma(7/2)} \right] . \tag{1.67}$$

The expression of κ_e contains the unknown factor τ_0, which is also included in the electrical conductivity. Actually, we can calculate the amount $\kappa_e / \sigma T \equiv L$, the Lorentz number:

$$L = \frac{\kappa_e}{\sigma T} = \frac{\mathcal{L}_{31}\mathcal{L}_{11} - \mathcal{L}_{21}^2}{e^2 \mathcal{L}_{11}^2 T^2} = \frac{k_B^2}{e^2} (5/2 + \lambda) , \tag{1.68}$$

which is independent of τ_0. Thus, the thermal conductivity can be written in terms of the electrical conductivity and the Lorentz number:

$$\kappa_e = \sigma L T = \frac{k_B^2 T^2}{e^2} (5/2 + \lambda) \sigma . \tag{1.69}$$

In a semiconductor, the thermal conductivity of the electrons is proportional to the electronic conductivity. The expression $\kappa_e / \sigma = L \ T$ is known as Wiedemann–Franz law. As it is well known, in the case of metals, or a degenerate semiconductor, the Lorentz number is a constant:

$$L = \frac{\kappa_e}{\sigma T} = \frac{\pi^2}{3} \frac{k_B^2}{e^2} , \tag{1.70}$$

which is not the case in real metals. Actually, this was one of the drawbacks of Drude's model.

1.2.8 The Seebeck Coefficient in a Semiconductor

In the case of a metal or a degenerate semiconductor, the transport coefficients

$$\mathcal{L}_{ij} = \frac{4}{3m^*} \int \left(-\frac{\partial f_0}{\partial \varepsilon} \right) \tau^j \varepsilon^i D(\varepsilon) d\varepsilon \approx \frac{4e^2}{3m^*} \tau^j(\varepsilon_F) \varepsilon_F^i D(\varepsilon_F) \tag{1.71}$$

and the Seebeck coefficient is zero. It is necessary to take the first term in the development of the Fermi integral, giving

$$S = \frac{\pi^2}{3} \frac{k_B^2 T}{e} \frac{\partial \ln \sigma(\varepsilon)}{\partial \varepsilon} \bigg|_{\varepsilon=\varepsilon_F} = \frac{\pi^2}{3} \frac{k_B^2 T}{e\varepsilon_F}. \tag{1.72}$$

The Seebeck coefficient for a typical metal, Cu ($\varepsilon_F = 7.0$ eV), is $S = 1.05$ μV/K at 300 K.

For a semiconductor, assuming an energy dependence of the relaxation time as $\tau(\varepsilon) = \tau_0 \varepsilon^\lambda$, the expression of S can be rewritten as

$$S = \frac{1}{eT} \left[\frac{\mathcal{L}_{21}}{\mathcal{L}_{11}} - (\mu - \varepsilon_c) \right] = \frac{k_B}{e} \left[\frac{5}{2} + \lambda - \frac{\mu - \varepsilon_c}{k_B T} \right]. \tag{1.73}$$

Instead of the chemical potential, it is more useful to write the expression in terms of the electron concentration:

$$S = \frac{k_B}{e} \left[\frac{5}{2} + \lambda - \ln \frac{N_c}{n} \right]. \tag{1.74}$$

We can quantify the Seebeck coefficient for a typical semiconductor. At low temperature, $T \sim 100$ K, $k_B T \approx 8.64$ meV. If we assume for simplicity that, at this temperature, the chemical potential is 8.64 meV below the conduction band, and that impurities are the dominant scattering mechanism, $S \approx 5k_B/e \approx 0.4$ meV/K. Typical values are at least one order of magnitude larger than in metals.

From Eq. (1.72) we can argue that the Seebeck coefficient, roughly, is proportional to

$$S \propto \frac{\partial D(\varepsilon)}{\partial \varepsilon} \bigg|_{\varepsilon=\varepsilon_F}. \tag{1.75}$$

This expression is fulfilled for a metal and looking at the function $\partial f_0 / \partial \varepsilon$ as shown in Fig. 1.3, it is a good approximation in the case of a semiconductor at low temperatures. If the density of states changes around the chemical potential, the Seebeck coefficient will be high. If the density of states is smooth around the chemical potential, the Seebeck coefficient will be low. In semiconductor nanostructures, mainly quantum wires and quantum dots, where the density of

states can be very sharp (varying with energy as $(\varepsilon - \varepsilon_n)^{-1/2}$ or $\delta(\varepsilon - \varepsilon_n)$, respectively, if the Fermi energy is around ε_n around a band or subband minimum ε_n), a huge increase in the Seebeck coefficient is expected.

1.3 The Boltzmann Transport Equation for Phonons

The purpose of this section is to describe how phonons carry heat through the material, i.e. to evaluate the phonon thermal conductivity (κ_L). The phonon thermal conductivity varies two or three orders of magnitude in a wide temperature range [4]. At high temperatures, the main factor limiting the thermal conductivity is the phonon–phonon scattering. At low temperatures, however, size effects are extremely important, even in macroscopic samples. Phonons can travel over millimeters and are finally scattered by the boundary. As pointed out by Ziman [2], the ultimate scattering mechanism at low temperatures is the boundary scattering, since the phonon mean free path is very long.

The thermal conductivity in nanostructures at low temperatures departs from bulk values due to size effects [5]. But at nanometer sizes, it is not clear if quantum confinement could be more important than boundary. There are several approaches in the literature trying to predict the thermal conductivity at all temperatures and size ranges. Although in the case of quantum wires, it is clear that quantum confinement is important for wire diameters of a few nanometers [6], most of the theoretical works on thermal conductivity mix both perspectives (classic and quantum) in a way that still remains unclear the origin of this reduction. Very recently, the authors have published a work clarifying the limits of classical models [5].

The reduction of the thermal conductivity due to the size effects is known from the middle of last century, when researchers like Callaway [7], Holland [8], and Guyer [9] measured and modeled the thermal conductivity of semiconductor materials of millimeter sized samples. They observed how at temperatures below 10–20 K, the thermal conductivity started to decrease showing a T^3 behavior. They concluded that this behavior was due to the scattering of the phonons by the boundaries, which is a constant, and thus the thermal conductivity behaves in temperature like the specific heat. All the models developed in this period are useful to understand boundary scattering.

Phonons are also scattered by impurities. In very pure samples, isotopic disorder (also called mass-defect scattering) limits the thermal conductivity [4]. Since phonons in general do not carry charge, an impurity produces the same effect that an isotope. It is well known the increase of the thermal conductivity in isotopically enriched samples [4]. Finally, the role of N- and U-processes must be deeply studied to quantify their contribution in the thermal conductivity.

1.3.1 Lattice Thermal Conductivity

The Boltzmann equation relates the changes in the distribution function due to the drift to the changes in the distribution function due to scattering processes. The general form of this equation in the stationary state is, as in the case of electrons,

$$\left(\frac{\partial N}{\partial t}\right) = \left(\frac{\partial N}{\partial t}\right)_{\text{drift}} + \left(\frac{\partial N}{\partial t}\right)_{\text{scatt}}, \tag{1.76}$$

where N is the phonon distribution function. The equilibrium distribution function corresponds to a Bose–Einstein distribution function:

$$N_\nu^0(\boldsymbol{q}) = \frac{1}{e^{\hbar\omega_\nu(\boldsymbol{q})/k_BT} - 1}, \tag{1.77}$$

for phonons from the ν-branch with energy $\hbar\,\omega_\nu(\boldsymbol{q})$ and wave number $\boldsymbol{q}$. Differently from electrons, phonons cannot experience external forces ($\boldsymbol{F} = 0$). Thus, only spacial variations of the distribution function must be taken into account. In that case, Eq. (1.76) can be written as

$$\boldsymbol{v_q} \cdot \nabla_{\boldsymbol{r}} N_{\boldsymbol{q}} = \left(\frac{\partial N_{\boldsymbol{q}}}{\partial t}\right)_{\text{scatt}}, \tag{1.78}$$

where $\boldsymbol{v}_{\mathbf{q}} = \nabla\omega_{\mathbf{q}}$ is the phonon group velocity. The phonon branch index has been omitted for clarity. The scattering integral depends on scattering processes due to electrons, impurities, boundaries, and other phonons. In local equilibrium approaches, the usual way to proceed is to consider the relaxation time approximation, in a parallel treatment as that shown for electron scattering. The rate of change of the distribution function $N_{\mathbf{q}}$ depends on the difference of the distribution out of equilibrium with that of equilibrium N_0. In terms of the relaxation time $\tau_{\mathbf{q}}$, Eq. (1.78) can be written as

$$\boldsymbol{v_q}\nabla_{\boldsymbol{r}} N_{\boldsymbol{q}} = -\frac{N_{\boldsymbol{q}} - N_{\boldsymbol{q}}^0}{\tau_{\boldsymbol{q}}}. \tag{1.79}$$

If the inhomogeneities disappear, the distribution function will decay exponentially to ${N_{\mathbf{q}}}^0$ with a time decay $\tau_{\mathbf{q}}$. This approximation allows us to obtain a solution for the thermal conductivity in terms of an integral expression depending on the relaxation time.

Combining Eqs. (1.78) and (1.79) we can obtain the local equilibrium distribution function in terms ${N_{\mathbf{q}}}^0$. Again, linearizing the equation, i.e. approaching $\nabla_{\mathbf{r}} N_{\mathbf{q}} \simeq \nabla_{\mathbf{r}} {N_{\mathbf{q}}}^0$,

$$N_{\boldsymbol{q}} \simeq N_{\boldsymbol{q}}^0 - \tau \boldsymbol{v} \cdot \nabla_{\boldsymbol{r}} N_{\boldsymbol{q}}^0. \tag{1.80}$$

The thermal conductivity can be obtained from Eq. (1.80) by using the definition of energy flux, that is the integral over the phonon population of the energy times the group velocity. In the general case, the thermal conductivity is a second rang tensor and the direction of the current does not necessarily coincide with the thermal gradient.

$$\boldsymbol{j}_Q = \frac{\hbar}{(2\pi)^3} \int \frac{\partial N_{\boldsymbol{q}}^0}{\partial T} \omega_{\boldsymbol{q}} \boldsymbol{v}_{\boldsymbol{q}} \left[\tau_{\boldsymbol{q}} \boldsymbol{v}_{\boldsymbol{q}} \cdot \nabla_{\boldsymbol{r}} T \right] d^3 \boldsymbol{q}; \tag{1.81}$$

The dot product $\mathbf{v_q} \cdot \nabla_{\mathbf{r}} T = v_{\mathbf{q}} \nabla_{\mathbf{r}} T \cos\theta_{\mathbf{q}}$, $\theta_{\mathbf{q}}$ being the angle between a given velocity $\boldsymbol{v}_{\mathbf{q}}$ and the temperature gradient. In the particular case of an isotropic medium, we have to select the velocity component along the thermal gradient since the current will be along $\nabla_{\mathbf{r}} T$. The final result is

$$\boldsymbol{j}_Q = \left[\frac{1}{(2\pi)^3} \int \frac{\partial N_{\boldsymbol{q}}^0}{\partial T} \hbar \omega_{\boldsymbol{q}} \tau_{\boldsymbol{q}} v_{\boldsymbol{q}}^2 \cos^2 \theta_{\boldsymbol{q}} d^3 \boldsymbol{q} \right] \nabla_{\boldsymbol{r}} T \,. \tag{1.82}$$

The expression for the lattice thermal conductivity is

$$\kappa_L = \left[\frac{1}{(2\pi)^3} \int \frac{\partial N_{\boldsymbol{q}}^0}{\partial T} \hbar \omega_{\boldsymbol{q}} \tau_{\boldsymbol{q}} v_{\boldsymbol{q}}^2 \cos^2 \theta_{\boldsymbol{q}} d^3 \boldsymbol{q} \right], \tag{1.83}$$

that can be expressed in terms of the frequency of the phonons by the use of the density of states $D(\omega)$ (DOS) and phonon frequency specific heat $C_{\mathrm{ph}}(\omega)$:

$$\kappa = \frac{1}{3} \int v^2 \tau C_{\mathrm{ph}}(\omega) D(\omega) d\omega. \tag{1.84}$$

The phonon frequency specific heat is defined as

$$C_{\mathrm{ph}}(\omega) = -\frac{\partial N^0}{\partial T} \hbar \omega = k_B \left(\frac{\hbar \omega}{k_B T} \right)^2 N^0 (N^0 + 1); \tag{1.85}$$

The phonon branch ν and wave vector $\boldsymbol{q}$ is included through the definition of the density of states:

$$D(\omega) = \frac{1}{3N} \sum_{\nu, \boldsymbol{q}} \delta(\omega - \omega_{\nu \boldsymbol{q}}) \,, \tag{1.86}$$

N being the number of atoms in the crystal. In the case of phonon confinement, as in a quantum wire, the number of branches in a real nanowire will depend on the number of atoms in the section of the nanowires, since there is only translational

symmetry along the wire (there will be only q_z). If the nanowire has more than a few nanometers, the confinement does not contribute differently to the thermal conductivity, the branches are so closed that the phonon subband can be considered as a continuum (i.e. there is no difference with the bulk DOS).

In most phenomenological theories of the phonon thermal conductivity, the relaxation time approximation has been extensively used. There are some important differences with electron relaxation times that must be carefully analyzed.

1.3.2 Relaxation Time Approximation

Phonons can be scattered in a crystal by lattice imperfections, electrons, crystal boundaries, or by other phonons. It is possible to describe the different scattering processes by their corresponding relaxation times. In the case of electrons, the relaxation time is a measure of the time the system needs to reach the equilibrium once the external forces have been removed. In the case of phonons, however, no external forces drive the phonon conduction, only temperature gradients (or differences in carrier concentration, which can modify the phonon–carrier interaction). The relaxation time is basically the phonon lifetime, which contains the several contributions mentioned above. There is another difference between an electron scattering process and a phonon scattering process. In the case of an electron scattering process, in most cases the energy is conserved (elastic scattering); the exception being the electron–optical phonon interaction, where energy is not conserved (inelastic scattering). Concerning the electron quasi-momentum $\hbar\boldsymbol{k}$, it is always conserved in a scattering process, independently if the scattering is elastic or inelastic. The electron, after the scattering process, is the same electron, in another quantum state. In a phonon scattering process however, a phonon is annihilated and a new phonon is created. The total energy in the scattering process is conserved, but there is not, in general, quasi-momentum conservation. For a phonon–phonon scattering process (also known as phonon anharmonicity), the quasi-momentum conservation law is:

$$\boldsymbol{q}_1 + \boldsymbol{q}_2 = \boldsymbol{q}_3 + \boldsymbol{G}\,, \tag{1.87}$$

where $\boldsymbol{G}$ is any reciprocal lattice vector. If $\boldsymbol{G} = 0$, the process is called normal, N-process, while in the general case, $\boldsymbol{G} \neq 0$ and the process is called Umklapp (flip over), U-process. In Fig. 1.4 we show the quasi-momentum conservation law for phonons. Both N- and U-processes are shown. In the case of phonon scattering by imperfections, the quasi-momentum distribution will be randomly distributed in the space. Even if the initial phonon has a preferred direction due to a temperature gradient, after the scattering process the direction could be whatever. The case of U-processes is similar, when we add a reciprocal lattice vector distributed along any possible direction in the space, the resulting direction of the phonon resulting from the scattering is randomly oriented. Phonon-impurity scattering and U-scattering

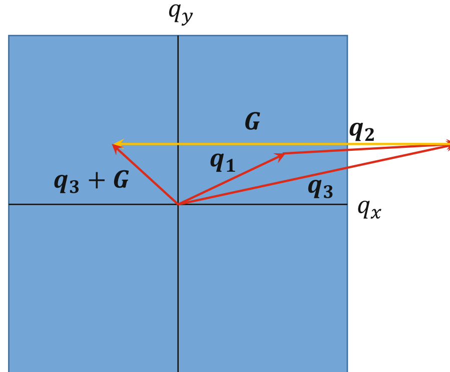

Fig. 1.4 Phonon wave number conservation in a plane square lattice. In an N-process, the wave number $\boldsymbol{q}_1 + \boldsymbol{q}_2 = \boldsymbol{q}_3$ is conserved, while in a U-process, any additional vector of the reciprocal space is added in the conservation law: $\boldsymbol{q}_1 + \boldsymbol{q}_2 = \boldsymbol{q}_3 + \boldsymbol{G}$

contribute to the thermal resistance in a similar way as electron scattering gives rise to the electrical resistance. In the case of N-processes, if there is a temperature gradient, the phonons are diffusing to the cooler region and the scattered phonon will have a net quasi-momentum $\hbar \boldsymbol{q}$ in the opposite direction of the temperature gradient. The phonon quasi-momentum is transferred to the other phonons.

Most of the models describing the thermal conductivity were developed along the sixties of last century. The same models are used nowadays to fit the experimental results of the thermal conductivity in nanostructures. In particular, the thermal conductivity in silicon nanowires has been calculated using the Callaway model [7] and different approximations for the relaxation times. Unfortunately, the Callaway model (CM) does not describe properly N-processes and the effort in giving a good fit in a wide temperature region has moved the researchers to deal with different approximation for the relaxation times, or even the introduction of new relaxation times. We will limit our description of thermal conductivity models to that of Callaway and the model developed by Guyer and Krumhansl [9] (GKM), which gives a more realistic description of N-processes.

1.3.3 The Callaway Model

The Callaway model [7, 8, 10] is based on the BTE within the relaxation time approximation. Callaway splits the scattering term into two, one depending on the relaxation time of N-processes and the other related to the relaxation time of resistive processes (the remaining scattering processes: U-processes, impurities, boundary, and so on):

$$\frac{\hbar\omega_{\boldsymbol{q}}}{k_B T} N^0_{\boldsymbol{q}}(N^0_{\boldsymbol{q}}+1)\boldsymbol{v}_{\boldsymbol{q}}\cdot\nabla\ln T = \frac{N_{\boldsymbol{q}}-N^0_{\boldsymbol{q}_0}}{\tau_N} + \frac{N_{\boldsymbol{q}}-N^0_{\boldsymbol{q}}}{\tau_R}. \quad (1.88)$$

The resistive scattering will relax the distribution function to that given by Eq. (1.77), while in the case of N-processes, the relaxed distribution function is given by

$$N^0_{\boldsymbol{q_0}} = \frac{1}{e^{(\hbar\omega(\boldsymbol{q})+\lambda\cdot\boldsymbol{q_0})/k_B T}-1} \approx N^0_{\boldsymbol{q}} + N^0_{\boldsymbol{q}}(N^0_{\boldsymbol{q}}+1)\frac{\lambda\cdot\boldsymbol{q_0}}{k_B T}. \quad (1.89)$$

In terms of ${N_{\mathbf{q}}}^{(1)} = N_{\mathbf{q}} - {N_{\mathbf{q}}}^0$, the BTE can be written as:

$$N^0_{\boldsymbol{q}}(N^0_{\boldsymbol{q}}+1)\left[\frac{\hbar\omega_{\boldsymbol{q}}}{k_B T}\boldsymbol{v}_{\boldsymbol{q}}\cdot\nabla\ln T + \frac{1}{\tau_N}\frac{\lambda\cdot\boldsymbol{q_0}}{k_B T}\right] = \frac{N^{(1)}_{\boldsymbol{q}}}{\tau_c}, \quad (1.90)$$

where

$$\frac{1}{\tau_c} = \frac{1}{\tau_N} + \frac{1}{\tau_R}, \quad (1.91)$$

τ_c being a combined relaxation time. The procedure of Callaway is to neglect the second term containing the relaxation time for N-processes and compensate this fact with the introduction of a overall relaxation time α. In this approximation,

$$N^{(1)}_{\boldsymbol{q}} = -\alpha N^0_{\boldsymbol{q}}(N^0_{\boldsymbol{q}}+1)\frac{\hbar\omega_{\boldsymbol{q}}}{k_B T}\boldsymbol{v}_{\boldsymbol{q}}\cdot\nabla\ln T \quad (1.92)$$

On the other hand, $\boldsymbol{\lambda}$ is a constant vector, in the opposite direction of the temperature gradient. It can be written in terms of a constant β with dimensions of relaxation time:

$$\lambda = -\hbar\beta v^2_{\boldsymbol{q}}\nabla\ln T; \quad (1.93)$$

Introducing this definition and the value of $N^{(1)}$ into Eq. (1.90), the value of α can be obtained:

$$\alpha = \tau_C(1+\beta/\tau_N) \quad (1.94)$$

Finally, the thermal conductivity has the expression [10]

$$\kappa = \frac{k_B}{2\pi^2 v}\left(\frac{k_B T}{h}\right)^3\int_0^{\theta/T} dx\frac{x^4}{4\sinh^2 x}\left[\beta + \tau_c\left(1-\frac{\beta}{\tau_R}\right)\right] \quad (1.95)$$

where $\beta = \langle \tau_c / \tau_N \rangle / \langle \tau_c / \tau_R \tau_N \rangle$ [10]. In the integral, the term in β represents the drift and that on $\tau_c(1 - \beta / \tau_R)$ corresponds to the diffusive contribution. An isotropic medium has been considered, v is the average group velocity, and θ the Debye temperature. This model was extended later by Holland, incorporating the transversal and longitudinal phonon branches [8].

The Callaway model leads to an overestimation of the thermal conductivity of nanometric-size samples at room temperature due to the inclusion of spurious terms in the conductivity expressions. Several authors have tried to reduce this over-prediction introducing additional relaxation times or phonon confinement.

1.3.4 Guyer–Krumhansl Model

The BTE can be written in terms of operators acting over the occupation probability $N_{\mathbf{q}}$ as

$$\left[\frac{\partial}{\partial t} + \boldsymbol{v_q} \cdot \nabla - \mathcal{S}\right] N_{\boldsymbol{q}} = 0 \,, \tag{1.96}$$

where $\mathcal{S}$ is the scattering operator. The formal solution of the linearized BTE in the steady-state is:

$$N_{\boldsymbol{q}} = \mathcal{S}^{-1}\left[\frac{\hbar\omega_{\boldsymbol{q}}}{k_B T} N^0_{\boldsymbol{q}}(N^0_{\boldsymbol{q}} + 1)\boldsymbol{v_q} \cdot \nabla \ln T\right]. \tag{1.97}$$

The scattering operator can be written in terms of two operators, that dealing with N-processes, and that which accounts for resistive processes:

$$\mathcal{S} = \mathcal{N} + \mathcal{R} \tag{1.98}$$

Formally, if the complete solution (eigenvalues and eigenvectors) of the scattering operators is known,

$$\mathcal{S}|\mu\rangle = g_\mu|\mu\rangle \quad \Rightarrow \quad \mathcal{S} = \sum_\mu g_\mu |\mu\rangle\langle\mu| \quad \Rightarrow \quad \mathcal{S}^{-1} = \sum_\mu \frac{1}{g_\mu}|\mu\rangle\langle\mu| \,, \tag{1.99}$$

we can calculate $\mathcal{S}^{-1}$ and $N_{\mathbf{q}}$ through Eq. (1.97). This information is not available. However, in the low temperature limit when N-processes dominate ($\mathcal{R} \ll \mathcal{N}$) we can assume $\mathcal{S} \cong \mathcal{N}$). We have partial information on the properties of $\mathcal{N}$. In particular, we know that the distributions

$$N(\delta T) = \frac{1}{e^{\hbar\omega/k_b(T+\delta T)} - 1} \quad \text{and} \quad N(\lambda) = \frac{1}{e^{(\hbar\omega + \lambda\cdot\boldsymbol{q})/k_b T} - 1} \tag{1.100}$$

are unaffected by the operator $\mathcal{N}$. If δT and $\boldsymbol{\lambda}$ are small, we can expand the deviations and obtain

$$|\eta_0\rangle = \mu\sqrt{N^0(N^0+1)} \tag{1.101}$$

and

$$|\eta_1\rangle = \frac{1}{k_B T}\begin{pmatrix}\lambda_x q_x\\ \lambda_y q_y\\ \lambda_z q_z\end{pmatrix}\sqrt{N^0(N^0+1)}; \tag{1.102}$$

For an isotropic dispersionless medium the quantities μ and λ can be shown to be, from the normalization conditions [9]:

$$\mu^2 = \frac{k_B}{C_v} \quad \text{and} \quad \lambda^2 = \frac{3k_B\hbar^2 v^2}{C_v}; \tag{1.103}$$

It is straighforward to show that these eigenvectors have null eigenvalues:

$$\mathcal{N}|\eta_0\rangle = 0|\eta_0\rangle \quad \text{and} \quad \mathcal{N}|\eta_1\rangle = 0|\eta_1\rangle\,, \tag{1.104}$$

the first due to energy conservations and the second due to translational symmetry. The linearized BTE may be symmetrized by using $N^\star_{\boldsymbol{q}} = N_{\boldsymbol{q}}/\sqrt{N^0(N^0+1)}$. In this new basis the scattering and drift operators are self-adjoint:

$$[\mathcal{N}^\star + \mathcal{R}^\star]N^\star_{\boldsymbol{q}} = \mathcal{D}N^\star_{\boldsymbol{q}} \tag{1.105}$$

This equation can be solved by writing

$$|N_{\boldsymbol{q}}\rangle = \sum_\mu a_\mu(\boldsymbol{r},t)|\eta_\mu(\boldsymbol{q})\rangle \tag{1.106}$$

The form of the matrices can be easily derived. Since $\mathcal{N}^\star$ has four null eigenvalues, the corresponding matrix must have the form

$$\mathcal{N}^\star = \left(\begin{array}{c|ccc|cccc} 0 & 0 & 0 & 0 & 0 & & & \\ \hline 0 & 0 & 0 & 0 & 0 & & & \\ 0 & 0 & 0 & 0 & 0 & & & \\ 0 & 0 & 0 & 0 & 0 & & & \\ \hline & & & & \lambda_1 & & & \\ & & & & & \lambda_2 & & \\ 0 & 0 & 0 & 0 & & & \lambda_3 & \\ & & & & & & & \ddots \end{array}\right) \equiv \begin{pmatrix} 0 & 0 & 0\\ 0 & 0 & 0\\ 0 & 0 & \mathcal{N}^\star_{22}\end{pmatrix}, \tag{1.107}$$

written in short as a block matrix whose dimensions are 1, 3, and ∞. The matrix is diagonal. Concerning the $\mathscr{R}^*$ matrix, although $|\eta_0\rangle$ is a null eigenvector, $|\boldsymbol{\eta}\rangle$ are not eigenvectors of $\mathscr{R}^*$ due to the lack of quasimomentum conservation and $\mathscr{R}^*$ is not diagonal. The final form of the BTE, in matrix representation, is:

$$\left[\begin{pmatrix} 0 & 0 & 0 \\ 0 & 0 & 0 \\ 0 & 0 & \mathcal{N}^\star_{22} \end{pmatrix} + \begin{pmatrix} 0 & 0 & 0 \\ 0 & \mathcal{R}^\star_{11} & \mathcal{R}^\star_{12} \\ 0 & \mathcal{R}^\star_{21} & \mathcal{R}^\star_{22} \end{pmatrix} - \begin{pmatrix} \mathcal{D}_{00} & \mathcal{D}_{01} & 0 \\ \mathcal{D}_{10} & \mathcal{D}_{11} & \mathcal{D}_{12} \\ 0 & \mathcal{D}_{21} & \mathcal{D}_{22} \end{pmatrix}\right] \begin{pmatrix} a_0 \\ \boldsymbol{a}_1 \\ \boldsymbol{a}_2 \end{pmatrix} = 0 \tag{1.108}$$

where a_0 is an scalar, $\mathbf{a}_1$ a vector, and the dimension of $\mathbf{a}_2$ is basically ∞. The set of equations can be summarized as:

$$\begin{aligned} &\mathcal{D}_{00}a_0 + \mathcal{D}_{01}\boldsymbol{a}_1 = 0 \\ &(\mathcal{R}_{11} - \mathcal{D}_{11})\boldsymbol{a}_1 + (\mathcal{R}_{12} - \mathcal{D}_{12})\boldsymbol{a}_2 = \mathcal{D}_{10}a_0 \\ &(\mathcal{R}_{21} - \mathcal{D}_{21})\boldsymbol{a}_1 + (\mathcal{N}_{22} + \mathcal{R}_{22} - \mathcal{D}_{22})\boldsymbol{a}_2 = 0 \end{aligned} \tag{1.109}$$

The first equation can be expressed as

$$\frac{\partial \varepsilon}{\partial t} + \nabla \cdot \boldsymbol{j}_Q = 0 \tag{1.110}$$

and it corresponds to the energy conservation (continuity equation). The other two equations can be combined to eliminate the unknown quantity $\boldsymbol{a}_2$, giving rise to

$$\frac{\partial \boldsymbol{j}_Q}{\partial t} + \frac{v^2}{3}\nabla\varepsilon = -\frac{1}{\tau_{11}}\boldsymbol{j}_Q \tag{1.111}$$

representing the momentum conservation, where

$$\frac{1}{\tau_{11}} = \mathcal{R}_{11} - \frac{\mathcal{R}_{12}\mathcal{R}_{21}}{\mathcal{N}_{22} + \mathcal{R}_{22}} \tag{1.112}$$

is the phonon quasi-momentum relaxation operator. Equation (1.110) and the homogeneous equation (1.111) represent a hydrodynamic wave. If there is a temperature gradient, $\delta\,\varepsilon = C_v\delta\,T$ and Eq. (1.111) can be written as:

$$-\frac{1}{3}v^2C_v\nabla T = \frac{\partial \boldsymbol{j}_Q}{\partial t} + \frac{1}{\tau_{11}}\boldsymbol{j}_Q \tag{1.113}$$

The steady-state thermal conductivity can be expressed as

$$\kappa = \frac{1}{3}v^2C_v\tau_{11} \tag{1.114}$$

and τ_{11} can be calculated with a little algebra, from the derivation of the relaxation times in particular limits. The matrix elements can be identified as

$$\begin{aligned} \mathcal{N}^{\star}_{22} &= 1/\tau_N \\ \mathcal{R}^{\star}_{11} &= \langle \tau_R^{-1} \boldsymbol{q} \rangle \\ \mathcal{R}^{\star}_{22} &\cong \mathcal{R}^{\star}_{11} \\ [\mathcal{R}^{\star -1}]_{11} &= \langle \tau_R(\boldsymbol{q}) \rangle \end{aligned} \tag{1.115}$$

From these definitions, the momentum relaxation time can be written as

$$\tau_{11} = \langle \tau_R \rangle \frac{\tau_N + \langle \tau_R^{-1} \rangle^{-1}}{\tau_N + \langle \tau_R \rangle} \tag{1.116}$$

If we call

$$\Sigma = \frac{\langle \tau_R \rangle}{\tau_N + \langle \tau_R \rangle}, \tag{1.117}$$

the thermal conductivity can be written as

$$\kappa = \frac{1}{3} C_v v^2 \left[\langle \tau_R \rangle (1 - \Sigma) + \langle \tau_R^{-1} \rangle^{-1} \Sigma \right] \tag{1.118}$$

When N-processes are dominant (low temperature), $\tau_N \rightarrow 0$ and the switching factor $\Sigma = 1$. The second term dominates. Oppositely, the normal processes are negligible (high temperature), $\Sigma = 0$ and the first term dominates.

In a later work [11], the authors introduce a geometrical factor $G(R)$ in the previous equation, applicable to wires (cylindrical shape). The final expression for the thermal conductivity reads

$$\Sigma = \frac{\langle \tau_R \rangle}{\tau_N + \langle \tau_R \rangle} \tag{1.119}$$

the thermal conductivity can be written as

$$\kappa = \frac{1}{3} C_v v^2 \left[\langle \tau_R \rangle (1 - \Sigma) + \langle \tau_R^{-1} \rangle^{-1} G(R) \Sigma \right] \tag{1.120}$$

where R is the radius of the wire and the function $G(R)$ can be written in terms of cylindrical Bessel functions.

1.3.5 Non-equilibrium: Extended Irreversible Thermodynamics

The GKM represents a first approximation in the introduction of non-equilibrium effects at a microscopic level. Their arguments can be extended in order to take into account higher-order terms in the derived expressions. This extension can be useful to obtain a general expression of the thermal conductivity valid for general geometries and sizes. Non-equilibrium theories have not been widely used in nanoscale transport modeling, but when the size of a device is reduced, before the observation of quantum phenomenology, non-equilibrium effects influence transport properties as shown in the GKM. These changes have been widely observed in microfluidics, where the roughness at the boundaries can lead the system out of equilibrium.

The generalization of the approach considered in the GKM can be done using Extended Irreversible Thermodynamics (EIT). Extended irreversible thermodynamics predicts the inclusion of non-localities and memory in the transport equations when the system is out of equilibrium. Extended irreversible thermodynamics proposes a hierarchy of evolution equations for the successive increasing tensorial order fluxes (J_0, J_1, J_2, ...). In the case of thermal transport, these fluxes are the inverse of temperature for the zero tensorial order ($J_0 = T^{-1}$), the heat flux for the first order ($\boldsymbol{J}_1 = \boldsymbol{j}_Q = \langle \hbar \omega \boldsymbol{v} \rangle$), the flux of the heat flux for the second order ($\boldsymbol{J}_2 = \langle \hbar \omega \boldsymbol{v} \otimes \boldsymbol{v} \rangle$), and so on. The first order transport equation is

$$\nabla T^{-1} - \alpha_1 \frac{\partial \boldsymbol{j}_Q}{\partial t} + \beta_1 \nabla \cdot \boldsymbol{J}_2 = \mu_1 \boldsymbol{j}_Q, \tag{1.121}$$

and that for the successive orders it can be expressed as

$$\beta_{n-1} \frac{\partial \boldsymbol{J}_{n-1}}{\partial t} - \alpha_n \frac{\partial \boldsymbol{J}_n}{\partial t} + \beta_n \nabla \cdot \boldsymbol{J}_{n+1} = \mu_n \boldsymbol{J}_n. \tag{1.122}$$

where μ_n, α_n, and β_n are phenomenological coefficients related to the transport coefficients, relaxation times and correlation lengths, respectively. The set of Eq. (1.122) can be Fourier analyzed. A Fourier component of the heat flux is simply [12]

$$\boldsymbol{j}_Q(\omega, \boldsymbol{q}) = -jk\kappa(\omega, \boldsymbol{q}) \hat{T}(\omega, \boldsymbol{q}), \tag{1.123}$$

$\hat{T} = \nabla T / |\nabla T|$, and $\kappa(\omega, \boldsymbol{q})$ represents a Fourier component of the thermal conductivity. Particularizing for $\omega = 0$ and dividing by the bulk thermal conductivity, the following form factor can be derived:

$$F(\ell / L_{\text{eff}}) = \frac{\kappa(\omega = 0, 2\pi / L_{\text{eff}})}{\kappa_0} = \frac{1}{2\pi^2} \frac{L_{\text{eff}}^2}{\ell^2} \left(\sqrt{1 + 4\pi^2 \frac{\ell^2}{L_{\text{eff}}^2}} - 1 \right), \tag{1.124}$$

where L_{eff} is the effective size of the sample and it depends on the geometry. By simple considerations it can be deduced that $L_{\text{eff}} = D$ for wires of diameter D, $L_{\text{eff}} = \sqrt{\pi/2}L$ for square wires of size L and $L_{\text{eff}} = 2.\ 25h$ for thin layers of thickness h. The expression (1.124) has several advantages in comparison with that proposed by Guyer and Krumhansl [11]: it is a simple analytical expression, it can be used for different geometries by only changing the effective size of the sample and it takes automatically into consideration the degree of non-equilibrium present in the sample depending on the normal and resistive relaxation times. In terms of $F(L)$, the thermal conductivity, within the Guyer–Krumhansl model, can be finally written as:

$$\kappa = \kappa_k(1 - \Sigma) + \kappa_z F(L)\Sigma; \tag{1.125}$$

This expression will be used later in the calculation of the thermal conductivity of silicon nanostructures. Here we have named κ_k and κ_z to the thermal conductivity in the kinetic and Ziman regime, respectively.

1.3.6 Phonon Relaxation Times

Once an expression for the thermal conductivity has been established, it is important to determine the relaxation mechanisms present in the studied system. In the model of Guyer and Krumhansl, for instance, two phonon–phonon relaxation times are distinguished, those conserving momentum (N-processes) and those non-conserving momentum (resistive processes). The last category includes U-processes, phonon-impurity (or mass defect) scattering, phonon-boundary scattering, and all possible scattering mechanisms which do not conserve momentum.

Boundary scattering is important, as pointed out by Ziman [2], at very low temperatures. As it has been previously discussed, at very low temperatures, the presence of N-processes gives rise to an infinite thermal conductivity, the thermal conductivity is limited by the presence of the boundary, i.e. the phonon mean free path is limited by the sample size ($\lambda = v\,\tau \leq L_{\text{eff}}$). Actually, the expression for the boundary relaxation time can be written in terms of the phonon group velocity as:

$$\tau_B^{-1}(\boldsymbol{q}) = \frac{v(\boldsymbol{q})}{L_{\text{eff}}}, \tag{1.126}$$

where L_{eff} represents the effective dimensions of the sample. Lowering the sample size we decrease the thermal conductivity since the boundary relaxation time is smaller (the scattering is more important). The scattering of phonons by mass defects (isotopic disorder) is the most important mechanisms by imperfections in very pure samples. The expression was firstly deduced by P. G. Klemens [13]:

$$\tau_I^{-1}(\boldsymbol{q}) = A\omega^4(\boldsymbol{q}) \equiv \frac{V_0 g}{4\pi} \frac{\omega^4(\boldsymbol{q})}{v^3(\boldsymbol{q})}, \tag{1.127}$$

where V_0 is the volume of the primitive cell and

$$g = \sum_i f_i \left(\frac{\Delta m_i}{m_i} \right)^2 \tag{1.128}$$

is the mass defect factor, f_i being the fraction of the corresponding isotope i and Δm_i the difference between the average mass and that of the corresponding isotope.

The relaxation times for phonon–phonon scattering can be extracted from a recent work of A. Ward and D. A. Broido [14]. They fitted their ab initio calculations for Si and Ge in the 100–800 K temperature range with a single functional dependence $\sim T[1 - \exp(-3T/\Theta_D)]$, Θ_D being the Debye temperature. In the case of N-processes the energy dependence is $\sim \omega^2$, while for U-processes, it is $\sim \omega^4$. These expressions must be modified to be valid in the low temperature region. In order to keep a $\omega^a T^{5-a}$ law, as argued by C. Herring [15], an extra term must be added in the expression of the relaxation time for N-processes proposed by Ward and Broido [14]:

$$\tau_N^{-1} = \left(\frac{1}{B_N T} + \frac{1}{B'_N T^3} \right)^{-1} \omega^2 [1 - e^{-3T/\Theta_D}]; \tag{1.129}$$

This expression is valid in the whole temperature range. At high temperatures, the term containing T^3 can be neglected and the expression proposed by Ward and Broido can be recovered. At low temperatures, the term in T^3 provides the right temperature dependence (Debye-law). The expression for U-processes may also be modified to be valid at low temperatures. Since, at low temperatures, only phonons with small $\boldsymbol{q}$-vector and small energy participate in the scattering processes, U-processes cannot take place, because the combination of several phonon wave numbers is much smaller than a reciprocal lattice vector. Following Ziman [2], the relaxation time for U-processes must grow exponentially at low temperatures and the exponential expansion approaches linearly to 1. It is necessary to include a term of the form $\exp(\Theta_U/T)$, where Θ_U is some cutoff temperature, which can be derived from the dispersion relations. The relaxation time for U-processes becomes:

$$\tau_U^{-1} = B_U \omega^4 T e^{-\Theta_U/T} [1 - e^{-3T/\Theta_D}] \tag{1.130}$$

At low temperatures, the term $\exp(\Theta_U/T) \to \infty$ and U-processes do not contribute to the scattering, while at high temperatures $\exp(\Theta_U/T) \to 1$ and the expression proposed by Ward–Broido is recovered.

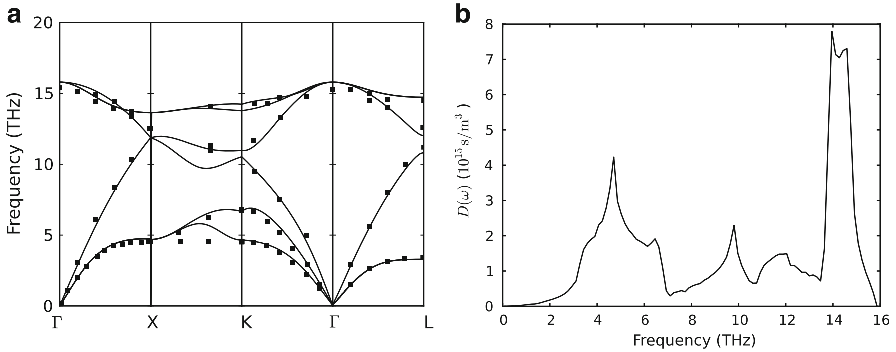

Fig. 1.5 (**a**) Phonon dispersion relation for silicon along high-symmetry directions calculated in the frame of the bond charge model and compared to experimental data from [18]. (**b**) Phonon density of states $D(\omega)$ calculated from bond charge model phonon dispersion relation

1.3.7 Application: Silicon Thermal Conductivity

One of the key points in the calculation of the phonon thermal conductivity is an accurate knowledge of the phonon dispersion relation. Not only the density of states (DOS) is important, the group velocity corresponding to the different branches is also needed for the calculation of the thermal conductivity. In most of the works published in the literature, the Debye model is assumed, and many times two different cutoff frequencies are considered. In order to calculate the thermal conductivity of silicon, as an example, we will use here the bond charge model (BCM), as proposed by Weber [16], since the calculated eigenvalues and eigenvectors agree very well with the experiment. The advantage of the BCM is that the dispersion relations can be obtained with only four force parameters and it can be successfully extended for other tetrahedrally bounded semiconductors [17]. Figure 1.5a shows the dispersion relations obtained for Si bulk using the BCM. The curves fit satisfactorily the experimental data [18] and are similar to those obtained with ab initio methods by Ward and Broido [14]. Additionally, the BCM has the advantage of reproducing very well the TA phonon branches in the BZ boundary. The use of complete dispersion relation includes the role of the optical phonon branches, which are neglected in most of the calculations where the Debye approximation is considered. The parameters used in the calculation of the dispersion relations shown in Fig. 1.5a are that given in the original work of Weber [16]. Figure 1.5b shows the corresponding density of states.

In this section, we will apply the expression deduced in the previous section to silicon nanostructures. In Fig. 1.6a the thermal conductivity κ (solid line) obtained from (1.125) is compared with Si bulk experimental data given by [19]. We have also included the terms $\kappa_z G(\mu)$ (dotted) and κ_k (dashed) corresponding to the kinetic and Ziman contributions. Both curves are affected by the boundary scattering

noticed by the reduction of the conductivity in the low temperature region. This reduction is due to the phonon mean free path included in the kinetic term while in the Ziman term the reduction is due to the form factor. It can be observed how thermal conductivity switches over from κ_z in the high temperature region to κ_k in the low temperature region. The parameters obtained from the fitting of natural silicon are: $B_U = 9 \cdot 10^{-47}\ s^3 K, B_N = 4 \cdot 10^{-19}\ sK, B'_N = 1.7 \cdot 10^{-23}\ s^2 K$ while A can be calculated from its definition, Eq (1.127), $A = 0.7 \times 10^{-45}\ s^3$ and the effective size used is that given in the original paper [19]: $L_{\mathrm{eff}} = 7.1$ mm.

At the lowest temperatures, the boundary scattering present in τ_{RB} is always dominant with respect to τ_N ($\tau_B \ll \tau_N$) and this makes $\Sigma = 1$. In the high temperature regime, near the Debye temperature, Umklapp is expected to be more important than the normal scattering ($\tau_U \ll \tau_N$) so that in this region $\Sigma = 1$. It is only between these limits that N-processes can be dominant. Due to its high Debye temperature, silicon at room temperature is within this region, the thermal conductivity is mainly described by the Ziman regime, providing lower values than those given by the usual kinetic term. This is the main reason for the reduction of the thermal conductivity; the CM overpredicts κ since the Ziman term is not considered in the theory. In a recent work [23], a parameter F, related to the specularity of the boundary, is included as a multiplying factor for the effective length ($L_{\mathrm{eff}} \to F\,L_{\mathrm{eff}}$) to reduce the thermal conductivity and obtain theoretical values closer to the observed data. Considering the GKM which properly considers the role of N-processes makes unnecessary the addition of spurious factors.

In Fig. 1.6 we show the remarkable results given by (1.125) for Si bulk, thin films, and nanowires [5]. The relaxation times used in the calculation of thin films and nanowire at the same as that obtained from the fitting of the bulk. The changes in the thermal conductivity are only due to the effective size of the samples. It can be observed that all the curves are in agreement with the experimental values with the exception of the thinnest nanowire (20 nm) and in some mid temperature region for the 30 nm wire. From this plot we can see that GKM+EIT is able to correctly describe thermal conductivity of general geometry and sizes without the inclusion of confinement effects to an effective size of 30 nm. In the calculation of the thermal conductivity of thin films and nanowire, the bulk dispersion relation has been used.

1.4 Transport Coefficients from First-Principles

The thermoelectric efficiency is given by the figure of merit $Z = \sigma S^2 / \kappa$, where σ is the electrical conductivity, S the Seebeck coefficient, and κ the thermal conductivity. If only the electronic part is considered, $\kappa = \kappa_e$. In the previous sections the transport coefficients are given in a parametric way with empirical inputs, obtained from a fitting with the experiment. The problem of the empirical approaches is the lack of predictability in the exploration of new thermoelectric materials since the information provided by the phenomenological models will be of difficult

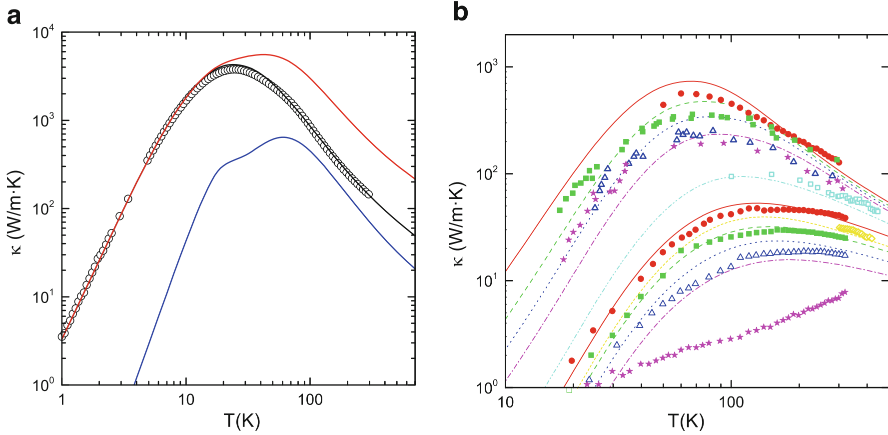

Fig. 1.6 (**a**) The *circles* are the experimental data corresponding to natural silicon [19] and the *black solid line* the fit using the expression (1.125) for the thermal conductivity, and the BCM. The *red and blue lines* represent the kinetic (κ_k) and the Ziman ($\kappa_z G(\mu)$) contributions, respectively. (**b**) The experimental data [19–22] are: TF4.5 μm (*red filled circle*), TF1.6 μm (*green filled square*), TF830 nm (*blue open triangle*), TF420 nm (*magenta filled star*), TF100 nm (*cyan open square*), TF30 nm (*yellow open diamond*), NW115 nm (*red filled circle*), NW 56 nm (*green filled square*), NW37 nm (*blue open triangle*), and NW22 nm (*magenta filled star*). TF refers to thin film and NW to nanowire. The corresponding lines (calculations) are: for TFs, *solid* (*red online*), *dash* (*green online*), *dotted* (*blue online*), *dashed dot* (*magenta online*), *dash dot dot* (*cyan online*), and *short dash* (*yellow online*), respectively. For NWs, *solid* (*red online*), *dash* (*green online*), *dot* (*blue online*), and *dash dot* (*magenta online*), respectively

projection. A different approach is to calculate the transport coefficients for a given material, alloy or nanostructure from first principles or, at least, to reduce the empirical information as much as possible. From the solution of the Boltzmann equation, in the relaxation time approximation, the transport coefficients can be written as [24]

$$\begin{aligned} \sigma &= e^2 \int d\varepsilon \left(-\frac{\partial f_0}{\partial \varepsilon}\right) \Xi(\varepsilon)\,, \\ S &= \frac{e k_B}{\sigma} \int d\varepsilon \left(-\frac{\partial f_0}{\partial \varepsilon}\right) \Xi(\varepsilon) \frac{\varepsilon - \mu}{k_B T}\,, \quad \text{and} \\ \kappa_e &= k_B^2 T \int d\varepsilon \left(-\frac{\partial f_0}{\partial \varepsilon}\right) \Xi(\varepsilon) \left(\frac{\varepsilon - \mu}{k_B T}\right)^2; \end{aligned} \tag{1.131}$$

$\Xi(\varepsilon)$ is called transport distribution. In tensorial form,

$$\Xi = \sum_{\boldsymbol{k}} \boldsymbol{v_k} \otimes \boldsymbol{v_k} \tau_{\boldsymbol{k}} \tag{1.132}$$

The transport distribution needs the electron velocity, which can be obtained from the derivative of the energy. But the approach followed by Scheidemantel et al. [24] is to calculate the velocity as

$$\boldsymbol{v}_{n,\boldsymbol{k}} = \frac{1}{m}\boldsymbol{p}_{n,\boldsymbol{k}} = \frac{1}{m}\langle\psi_{n,\boldsymbol{k}}|\hat{\boldsymbol{p}}|\psi_{n,\boldsymbol{k}}\rangle \tag{1.133}$$

i.e. from the intraband optical matrix elements. They use the WIEN2k-package [25] to calculate the transport coefficients in Bi_2Te_3. Doping is introduced within the rigid-band model approximation, i.e. the bands are considered unchanged (the same effective masses), independently of the doping level. The relaxation times are assumed to be constant, $\tau = 2 \times 10^{-14}$ s, which seems to give a good agreement with the experiment. In principle, besides some assumptions, the only parameter used in the model is the relaxation time, chosen to fit the experimental data. Ir order to get some more information on the behavior of the Seebeck coefficient, taking into account that the integral is limited to a small region given by $\partial f_0 \partial \varepsilon \sim 5\, k_B T$, the transport density has been approximated by

$$\Xi(\varepsilon) = a(\varepsilon - \mu) + b \tag{1.134}$$

and the power factor $PF = \sigma S^2$ can be calculated as

$$\sigma S^2 = \frac{a^2}{b} \tag{1.135}$$

The power factor increases quadratically with the slope of the transport density. The optimum power factor is around 50 meV above the conduction band for n-type doping and 100 meV below the valence band for p-type Bi_2Te_3. The problem is that in highly doped materials the thermal conductivity also increases. Actually, the highest ZT is obtained for p-type doping and is of the order of 0.8. The theoretical model fails for heavily doped Bi_2Te_3. The reason could be the failure of the rigid-band approximation.

In a more recent work, D. J. Singh [26] calculated the doping dependence thermopower in lead telluride. He uses a computer code, BOLTZTRAP, developed for the integration of the transport coefficients within the BZ. The first principle calculations are also done with WIEN2k and the rigid-band approximation is considered through the whole doping variation. Figure 1.7a shows the calculated thermopower of PbTe [26], together with the experimental data provided by [27–29], where PbTe and some nanostructures with different doping levels are analyzed. Figure 1.7b shows the predicted Seebeck coefficient for n-type doping and the approximation given by Harman [30].

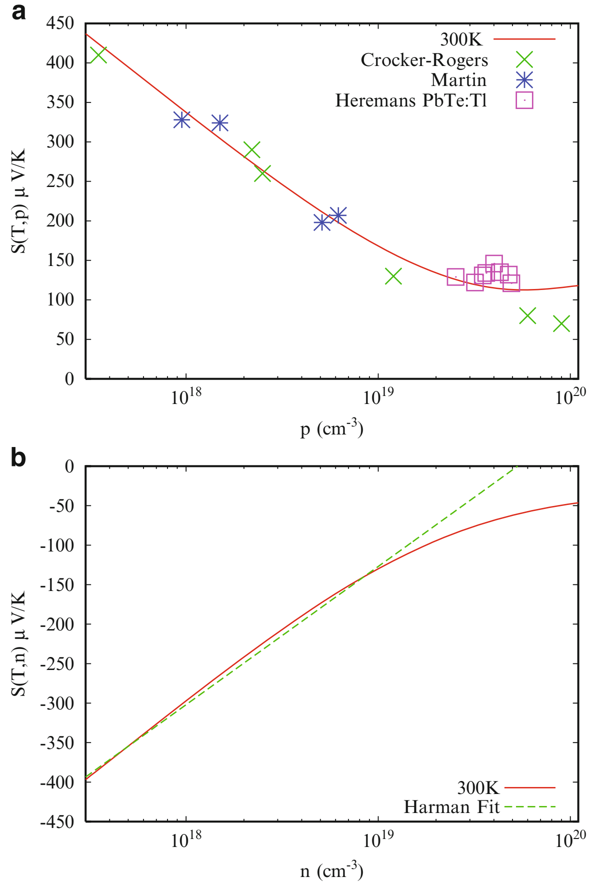

Fig. 1.7 Comparison of the calculated Seebeck coefficient at 300 K [26] with available experimental data (**a**) for *p*-type and (**b**) *n*-type doping, a function of the doping level. The experimental data used for the comparison in (**a**) are from [27–29] and the *dashed line* in (**b**) is a fit given by Harman [30]

1.5 Phonon BTE Using Ab Initio Methods

In the last few years, the calculation of phonon thermal conductivity using *ab initio* techniques has also become possible. The first stage to the calculation of thermal properties due to phonons is the knowledge of the phonon dispersion relations. The dispersion relations are the solutions of the equation

$$\sum_{\beta\kappa'} \frac{1}{\sqrt{M_\kappa M_{\kappa'}}} D_{\alpha\beta}(\kappa,\kappa';\boldsymbol{q})\boldsymbol{e}_{\beta\kappa'}(\boldsymbol{q}) = \omega^2 \boldsymbol{e}_{\alpha\kappa}(\boldsymbol{q}) \,, \tag{1.136}$$

where $D_{\alpha\,\beta}(\kappa,\,\kappa\,';\,\boldsymbol{q})$ is called dynamical matrix and $\mathbf{e}_{\alpha\kappa}$ the phonon eigenvectors (atomic displacements corrected with the square root of the atomic masses). The dynamical matrix has the form

$$D_{\alpha\beta}(\kappa,\kappa';\boldsymbol{q}) = \sum_{l'} \Phi_{\alpha\beta}(l\kappa, l'\kappa') e^{i\boldsymbol{q}\cdot(\boldsymbol{R}_l - \boldsymbol{R}_{l'})}. \tag{1.137}$$

The interatomic force constants (IFC) $\Phi_{\alpha\,\beta}(l\,\kappa,\,l'\,\kappa')$ can be directly calculated from density functional theory. The procedure followed by Ward and Broido [31] is the following: the IFCs in the direct space are calculated using the fast Fourier transform technique on a set of IFCs determined in an uniform grid in the reciprocal space. The matrix of reciprocal space harmonic IFCs is a combination of an electronic and an ionic part:

$$\tilde{\Phi}_{\alpha\beta}(\kappa\kappa',\boldsymbol{q}) = \tilde{\Phi}^{\text{el}}_{\alpha\beta}(\kappa\kappa',\boldsymbol{q}) + \tilde{\Phi}^{\text{ion}}_{\alpha\beta}(\kappa\kappa',\boldsymbol{q}) = \frac{1}{N}\frac{\partial^2 \varepsilon_{\text{tot}}}{\partial u^*_{\kappa,\alpha}(\boldsymbol{q})\partial u_{\kappa',\beta}(\boldsymbol{q})} \tag{1.138}$$

and are given by the second derivative of the total energy with respect to the displacements in the reciprocal space (eigenvectors divided by the square root of the masses). The third order anharmonic IFCs can be evaluated first in the reciprocal space,

$$\tilde{\Phi}_{\alpha\beta\gamma}(\kappa\kappa'\kappa'',\boldsymbol{q}\boldsymbol{q}'\boldsymbol{q}'') = \frac{\partial^3 \varepsilon_{\text{tot}}}{\partial u_{\kappa,\alpha}(\boldsymbol{q})\partial u_{\kappa',\beta}(\boldsymbol{q}')\partial u_{\kappa'',\gamma}(\boldsymbol{q}'')}. \tag{1.139}$$

The anharmonic IFCs are symmetric in the three sets $\{\kappa,\alpha,\boldsymbol{q}\}$ and can be expanded into six terms. As stated by the "$2n + 1$" theorem, it is enough to keep terms in first order perturbation theory in the calculation of second order terms. Once we have the IFCs in the reciprocal space, we can build the IFCs in the real space within the given approximation.

1.5.1 Linearized Boltzmann Transport Equation

The lattice thermal conductivity can be calculated using the linearized Boltzmann transport equation:

$$\boldsymbol{v}_\lambda \cdot \nabla N_{0,\lambda} = \boldsymbol{v}_\lambda \cdot \nabla T\left(\frac{\partial N_{0,\lambda}}{\partial T}\right) = \left(\frac{\partial N_\lambda}{\partial t}\right)_{\text{scatt}} \tag{1.140}$$

where $\lambda \equiv \nu,\,\boldsymbol{q},\,\nu$ being the phonon branch. Three phonon scattering rates are calculated using the Fermi-golden rule:

$$W^{\pm}_{\lambda\lambda'\lambda''} = \frac{\hbar\pi}{4N} N_{0,\lambda}\left(N_{0,\lambda'} + \frac{1}{2} \pm \frac{1}{2}\right) N_{0,\lambda''} \left|\Phi^{\pm}_{\lambda\lambda'\lambda''}\right|^2 \frac{\delta(\omega_\lambda \pm \omega_{\lambda'} - \omega_{\lambda''})}{\omega_\lambda \omega_{\lambda'} \omega_{\lambda''}} \tag{1.141}$$

and the phonon-impurity via

$$W^{\mathrm{imp}}_{\lambda\lambda'} = \frac{\pi}{2} g\omega_\lambda\omega_{\lambda'}N_{0,\lambda}(N_{0,\lambda'}+1)\sum_\kappa |\boldsymbol{e}_{\kappa\lambda}\boldsymbol{e}_{\kappa\lambda'}|^2\delta(\omega_\lambda-\omega_{\lambda'})\,, \tag{1.142}$$

where g, the mass defect parameter has been already defined in (1.128). The total scattering rate is

$$W_\lambda = \sum_{\lambda'\lambda''}\left(W^{+}_{\lambda\lambda'\lambda''}+\frac{1}{2}W^{-}_{\lambda\lambda'\lambda''}\right)+\sum_{\lambda'}W^{\mathrm{imp}}_{\lambda\lambda'} \tag{1.143}$$

and a relaxation time τ_λ can be defined as

$$\tau_\lambda = \frac{N_0(N_0+1)}{W_\lambda}; \tag{1.144}$$

The lattice thermal conductivity can be calculated through the expression

$$\kappa_L = \frac{1}{3}\frac{1}{(2\pi)^3}\sum_\nu\int C(\omega_{\nu,\boldsymbol{q}})v_{\nu,\boldsymbol{q}}\tau_{\nu,\boldsymbol{q}}d^3\boldsymbol{q}\,, \tag{1.145}$$

where $C(\omega_\lambda)$, the phonon heat capacity, has already been defined in Eq. (1.85).

Even when the solution of the Boltzmann equation for phonons is more complex than for electrons, it is also possible to analyze thermal transport by phonons in nanostructures using the BTE. Recently, W. Li et al. [32] have calculated the phonon thermal conductivity in silicon and diamond nanowires using the theory described above. The additional difficulty comes from the fact that the nanowires are limited in the space. Several approximations have been made. First, only phonon–phonon scattering and boundary scattering have been considered. The boundaries are assumed to be completely rough, the specularity parameter being $p = 0$. Finally, an average of the relaxation time in the section of the nanowire is considered. Figure 1.8 shows the results of the calculations for several diamond and silicon nanowires are shown. Obviously, the thermal conductivity decreases with decreasing diameter and size effects are more important in diamond. The thermal conductivity is larger in the [001] direction, while in silicon they are similar and actually the larger thermal conductivity is temperature dependent. Finally, the maximum in the thermal conductivity in diamond is around 200 K, while in silicon is around 70 K. This is due to the fact that phonons are more energetic in diamond and a higher temperature is needed to have a similar phonon–phonon scattering rate in comparison with silicon. This result can be also related to the different Debye temperatures, looking at the expressions of the relaxation times for N- and U-processes given by Eqs. (1.130) and (1.129).

In conclusion, we have analyzed the thermal properties of semiconductors and metals in bulk and some semiconductor nanostructures, based on the Boltzmann

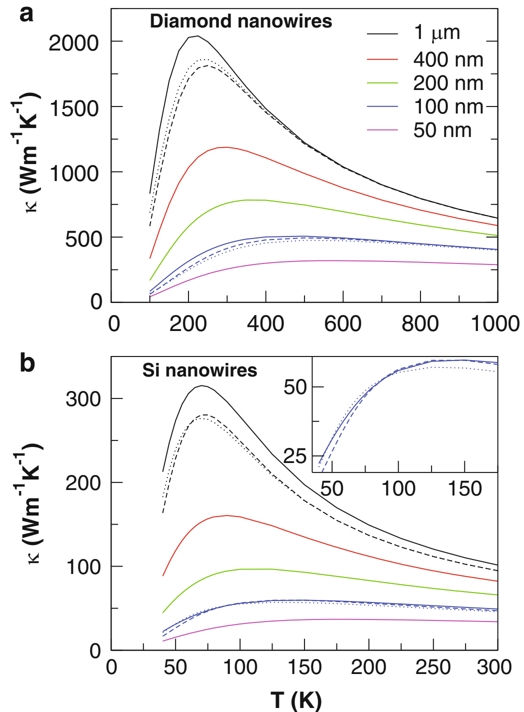

Fig. 1.8 κ_L versus temperature for (**a**) diamond NWs and (**b**) Si NWs along the growth direction [001] (*solid lines*), [011] (*dotted lines*), and [111] (*dashed lines*) for several diameters. The *inset* shows a zoom-in for the silicon nanowire with 100 nm diameter

transport equation. A similar treatment can be assumed in the transport of electrons and phonons, based on the relaxation time approximation. Some ab initio approaches have also been considered to calculate thermal properties related to electron and phonon transport. Although first principles are still far from giving a complete physical approach to the problem, it helps to understand the origin of the increase or reduction in the thermal conductivity in nanostructures.

Acknowledgements We would like to acknowledge the financial support from the Ministry of Finances and Competetiveness of Spain through the Programme Consolider Ingenio 2010 (Grant No. CSD2010-0044) and project MAT2012-33843.

References

1. Nag, B.R.: Electron Transport in Compound Semiconductors. Springer, Berlin (1980)
2. Zimann, J.M.: Electrons and Phonons. Oxford University Press, London (1960)
3. Cantarero, A., Martinez-Pastor, J., Segura, A., Chevy, A.: Transport properties of bismuth sulfide single crystals. Phys. Rev. B **35**, 9586–9590 (1987)

4. Asen-Palmer, M., Bartkowski, K., Gmelin, E., Cardona, M., Zhernov, A.P., Inyushkin, A.V., Taldenkov, A., Ozhogin, V.I., Itoh, K.M., Haller, E.E.: Thermal conductivity of germanium crystals with different isotopic composition. Phys. Rev. B **56**, 9431–9447 (1997)
5. de Tomas, C., Cantarero, A., Lopeandia, A.F., Alvarez, F.X.: Lattice thermal conductivity of silicon nanowires, J. Thermoelectricity 4, 11 (2013)
6. Comas, F., Trallero-Giner, C., Cantarero, A.: Phonons and electron–phonon interaction in quantum wires. Phys. Rev. B **47**, 7602–7605 (1993)
7. Callaway, J.: Model for the lattice thermal conductivity at low temperatures. Phys. Rev. **113**, 1046–1051 (1959)
8. Holland, M.G.: Analysis of lattice thermal conductivity. Phys. Rev. **132**, 2461–271 (1963)
9. Guyer, R.A., Krumhansl, J.A.: Solution of the linearized phonon Boltzmann equation. Phys. Rev. **148**, 766–778 (1966)
10. Krumhansl, J.A.: Thermal conductivity of insulating crystals in the presence of normal processes. Proc. Phys. Soc. **85**, 921–930 (1965)
11. Guyer, R.A., Krumhansl, J.A.: Thermal conductivity, second sound, and phonon hydrodynamic phenomena in nonmetallic crystals. Phys. Rev. **148**, 778–788 (1966)
12. Alvarez, F.X., Jou, D.: Memory and nonlocal effects in heat transport: From diffusive to ballistic regimes. Appl. Phys. Lett. **90**, 083109 (2007)
13. Klemans, P.G.: In: Seitz, F., Turnbull, D. (eds.) Thermal Conductivity and Lattice Vibrational Modes. Solid State Physics, vol. 7, p. 1–98. Academic Press, New York (1958)
14. Ward A., Broido D.A.: Intrinsic phonon relaxation times from first-principles studies of the thermal conductivities of Si and Ge. Phys. Rev. B **81**, 085205 (2010)
15. Herring C.: Role of low-energy phonons in thermal conduction. Phys. Rev. **95**, 954–965 (1954)
16. Weber, W.: The adiabatic bond charge model for the phonons in diamond, Si, Ge and $\alpha -$ Sn. Phys. Rev. B **15**, 4789–4803 (1977)
17. Camacho, J., Cantarero, A.: Phonon dispersion in CdSe: the bond charge model. Phys. Stat. Sol. (b) **211**, 233–236 (2000)
18. Nilsson, G., Nelin, G.: Study of the homology between silicon and germanium by thermal-neutron spectrometry. Phys. Rev. B **6**, 3777–3786 (1972)
19. Glassbrenner, C., Slack, G.: Thermal conductivity of Silicon and Germanium from 3 K to the melting point. Phys. Rev. A1058–A1069 (1964)
20. Song, D., Chen, G.: Thermal conductivity of periodic microporous silicon films. Appl. Phys. Lett. **84**, 687–690 (2004)
21. Li, D., Wu, Y., Kim, P., Shi, L., Yang, P., Majumdar, A.: Thermal conductivity of individual silicon nanowires. Appl. Phys. Lett. **83**, 2934–2937 (2003)
22. Asheghi, M., Leung, Y.K., Wong, S.S., Goodson, K.E.: Phonon-boundary scattering in thin silicon layers. Appl. Phys. Lett. **71**, 1798–1801 (1997)
23. Mingo, N.: Calculation of Si nanowire thermal conductivity using complete phonon dispersion relations. Phys. Rev. B **68**, 113308 (2003)
24. Sheidemantel, T.J., Ambrosch-Draxl, C., Thomhauser, T., Badding, J.V., Sofo, J.O.: Transport coefficients from first-principles calculations. Phys. Rev. B **68**, 125210 (2003)
25. Blaha, P., Schwarz, K., Madsen, G.K.H., Kvasnicka, D., Luitz, J.: WIEN2k, An Augmented Plane Wave1Local Orbitals Program for Calculating Crystal Properties. Karlheinz Schwarz, Techn. Universität Wien, Austria, 2001. ISBN 3-9501031-1-2
26. Singh, D.J.: Doping-dependent thermopower of PbTe from Boltzmann transport calculations. Phys. Rev. B **81**, 195217 (2010)
27. Crocker, A.J., Rogers, L.M.: Interpretation of the Hall coefficient, electrical resistivity and Seebeck coefficient of p-type lead telluride. Br. J. Appl. Phys. **18**, 563–573 (1967)
28. Martin, J., Wang, L., Chen, L., Nolas, G.S.: Enhanced Seebeck coefficient through energy barrier scattering in PbTe nanocomposites. Phys. Rev. B **79**, 115311 (2009)
29. Heremans, J.P., Jovovic, V., Toberer, E.S., Saramat, A., Kurosaki, K., Charoenphakdee, A., Yamanaka, S., Snyder, G.J.: Enhancement of termoelectric efficiency in PbTe by distortion of the electronic density of states. Science **321**, 554–557 (2008)

30. Harman, T.C., Spears, D.L., Manfra, M.J.: High thermoelectric figures of merit in PbTe quantum wells. J. Electron. Math. **25**, 1121–1127 (1996)
31. Ward, A., Broido, D.A., Stewart, D.A., Deinzer, G.: *Ab initio* theory of the lattice thermal conductivity in diamond. Phys. Rev. B **80**, 125203 (2009)
32. Li, W., Mingo, N., Lindsay, L., Broido, D.A., Stweart, D.A., Katcho, N.A.: Thermal conductivity of diamond nanowires from first principles. Phys. Rev. B **85**, 195436 (2012)

Chapter 2
Electron Transport Engineering by Nanostructures for Efficient Thermoelectrics

Je-Hyeong Bahk and Ali Shakouri

Abstract We theoretically investigate nanoscale structures such as nanoparticles embedded in bulk materials as a means of improving the thermoelectric energy conversion efficiency. We focus on the impact of such nanostructures on the electron transport in the host material, and discuss the enhancement of the thermoelectric power factor and thus the figure of merit. Nanostructures embedded in thermoelectric materials can create potential variations at the nanoscale due to the hetero-interfaces, which can alter the transport of charge carriers in the host material to enhance the Seebeck coefficient and the power factor. The energy-dependent electron scattering times induced by nanoparticles are calculated using the partial wave method. Thermoelectric transport properties are then calculated based on the linearized Boltzmann transport theory with the relaxation time approximation for various thermoelectric materials such as ErAs:InGaAs, PbTe, and Mg_2Si. The effects of different kinds of nanoparticles including single-phase ionized metallic nanoparticles and core–shell nanoparticles embedded in semiconductors are investigated in these semiconductors. Finally the electron energy filtering scheme is discussed to further enhance the thermoelectric energy conversion efficiency.

2.1 Introduction

In the past few decades, thermoelectric energy conversion has drawn keen attention as a viable candidate for waste heat recovery and hotspot cooling applications [1, 2]. More than 55 % of energy generated in the society is rejected as a form of heat [3]. Thermoelectric (TE) devices directly convert heat energy into electricity

Je-H. Bahk (✉) • A. Shakouri
Birck Nanotechnology Center, Purdue University, 1205 W. State Street,
West Lafayette, IN 47907-2057, USA
e-mail: jbahk@purdue.edu; shakouri@purdue.edu

X. Wang and Z.M. Wang (eds.), *Nanoscale Thermoelectrics*, Lecture Notes in Nanoscale Science and Technology 16, DOI 10.1007/978-3-319-02012-9_2,
© Springer International Publishing Switzerland 2014

or vice versa, so they can be used in conjunction with heat engines such as in automobiles and enhance the fuel efficiency greatly. However, one of the reasons that TE devices have not been largely employed in many practical applications is their low energy conversion efficiency primarily limited by the inherent thermoelectric properties of the materials used. The thermoelectric efficiency is determined by the unitless figure of merit of the TE material, $ZT = S^2\sigma T/(\kappa_{lat} + \kappa_{elect})$, where S is the Seebeck coefficient, σ is the electrical conductivity, T is the absolute temperature, and κ_{lat} and κ_{elect} are the lattice and electronic thermal conductivities, respectively. Conventional TE materials have $ZT \sim 1$ in their optimal temperature range. Recently, significant enhancements of ZT have been reported for various nanostructured TE materials [4–6]. This breakthrough is mainly due to significant reduction of the lattice thermal conductivity of the TE materials via effective phonon scattering at the boundaries of nanostructures.

However, there have not been many reports so far on the enhancement of the numerator of ZT, the so-called power factor, $S^2\sigma$. Since the power factor is related to charge carrier transport while the lattice thermal conductivity is to phonon transport, the enhancement of power factor requires completely different approaches. Also, the well-known trade-off relation between the Seebeck coefficient and the electrical conductivity renders such enhancement of power factor to be very difficult. Recently, band engineering through alloying and doping has been reported to be an effective way of achieving significant enhancement of power factor over the conventional bulk materials. Pei et al. [7] showed that the band convergence of more than 12 valence valleys in doped p-type $PbTe_{1-x}Se_x$ alloys can achieve a large power factor enhancement and thus $ZT \sim 1.8$ at 850 K. Band convergence enhances the Seebeck coefficient by increasing the electronic density of states near the Fermi level without much sacrificing the carrier mobility. The effect of band convergence has also been demonstrated in n-type $Mg_2Si_{1-x}Sn_x$ alloys, in which Sn contents of 0.6–0.7 showed the highest power factor, and achieved $ZT \sim 1.3$ at 700 K along with a reduction of lattice thermal conductivity by enhanced phonon alloy scattering [8]. Resonant impurities such as Tl in PbTe can also modify the density of states (DOS) in the bulk to enhance the power factor [9]. The Tl impurity levels create resonances within the valence band of PbTe, and these resonant states are non-localized to contribute to the density of states. The sharp feature in DOS by the resonances increases the asymmetry in DOS around the Fermi level, so the Seebeck coefficient could be greatly enhanced. Another interesting strategy for power factor enhancement that was recently reported is the modulation doping in bulk nanocomposite materials. Zebarjadi et al. [10] demonstrated that by separating a carrier-donating nanograin phase from the bulk phase, they were able to confine the impurity scattering centers within the nanograins while carriers are transported through the rest of the material with less scattering, so that the electrical conductivity of the nanocomposite was greatly enhanced with a relatively small reduction of the Seebeck coefficient.

In this chapter, we investigate various nanostructures as additional carrier scattering centers in bulk materials as a way to modify the electron transport and enhance the power factor. This work is based on, but not limited to, a series of the authors'

previous papers: Refs. [11–14]. In Sect. 2.2, we summarize the fundamental electron transport theory based on the Boltzmann transport with relaxation time approximation for thermoelectric transport properties calculations. The calculations of electron scattering time off of spherical nanoparticles based on the partial wave method are also discussed in this section. In Sect. 2.3, we investigate single-phase nanoparticles having a potential offset at the hetero-interface with the host matrix. Unionized and ionized cases of nanoparticles with and without the Coulomb potential around them are discussed for power factor enhancement over a wide temperature range. ErAs semimetal nanoparticles in InGaAlAs III–V semiconductors are highlighted as an example later in the section. In Sect. 2.4, core–shell structured nanoparticles that create resonances with free electrons in the band are discussed for power factor enhancement at low temperatures. In Sect. 2.5, we discuss the electron energy filtering scheme as a means of improving the Seebeck coefficient over a wide temperature range, and show detailed calculation results for several well-known TE materials such as PbTe and Mg_2Si. Finally we conclude the chapter in Sect. 6.

2.2 Electron Transport in Semiconductors

2.2.1 Boltzmann Transport and Thermoelectric Properties

In thermal equilibrium, the distribution of electrons is given by the Fermi–Dirac distribution,

$$f_0(\mathbf{r},\mathbf{k}) = \frac{1}{1+\exp\left[\frac{E(\mathbf{k})-E_\mathrm{F}(\mathbf{r})}{k_\mathrm{B}T(\mathbf{r})}\right]} \tag{2.1}$$

where k_B is the Boltzmann constant, $E_\mathrm{F}(\mathbf{r})$ is the Fermi level referenced to the band edge, and $T(\mathbf{r})$ is the local temperature. The distribution function is a function of the position $\mathbf{r}$, and wave vector $\mathbf{k}$. This equilibrium distribution is altered by the existence of external fields, diffusion forces (∇E_F), and temperature gradient (∇T). The transport of electrons is affected by collisions in the material.

Assuming the transport process is much slower than the relaxation process, and employing the relaxation time approximation, the nonequilibrium distribution of electrons, $f(\mathbf{r},\mathbf{k})$, is determined by the Boltzmann transport equation [15, 16],

$$-\frac{f(\mathbf{r},\mathbf{k})-f_0(\mathbf{r},\mathbf{k})}{\tau(\mathbf{k})} = \mathbf{v}\cdot\nabla_\mathbf{r}f + \frac{e\mathbf{F}}{\hbar}\cdot\nabla_\mathbf{k}f, \tag{2.2}$$

where $\tau(\mathbf{k})$ is the relaxation time, which is assumed to be only dependent on momentum or energy, and thus independent of position. No magnetic field is assumed from here on.

To evaluate the position and momentum derivatives of the distribution function under the assumption that the local deviation from equilibrium is small,

$$\nabla_{\mathbf{r}} f \approx \nabla_{\mathbf{r}} f_0 = \frac{\partial f_0}{\partial E_{\mathrm{F}}} \nabla E_{\mathrm{F}} + \frac{\partial f_0}{\partial T} \nabla T = -\frac{\partial f_0}{\partial E} \nabla E_{\mathrm{F}} - \frac{\partial f_0}{\partial E} \left(\frac{E - E_{\mathrm{F}}}{T} \right) \nabla T,$$

$$\nabla_{\mathbf{k}} f \approx \nabla_{\mathbf{k}} f_0 = \frac{\partial f_0}{\partial E} \frac{\partial E}{\partial \mathbf{k}} = \frac{\partial f_0}{\partial E} \hbar \mathbf{v}.$$

Then, (2.2) is rewritten as

$$f(\mathbf{r}, \mathbf{k}) = f_0(\mathbf{r}, \mathbf{k}) + \tau(\mathbf{k}) \mathbf{v} \left(-\frac{\partial f_0}{\partial E} \right) \cdot \left[-\frac{E(\mathbf{k}) - E_{\mathrm{F}}}{T} \nabla T - e \left(\mathbf{F} + \frac{1}{e} \nabla E_{\mathrm{F}} \right) \right]. \tag{2.3}$$

The last term in (2.3) indicates the combined effect of the drift and diffusion forces.

A variety of transport flux densities can be calculated using the nonequilibrium distribution function. The electron number flux density $\mathbf{J}_{\mathrm{N}}(\mathbf{r})$, the electric current density $\mathbf{J}_{\mathrm{e}}(\mathbf{r})$, and the energy flux density $\mathbf{J}_{\mathrm{U}}(\mathbf{r})$ are given for a single band by [14]

$$\mathbf{J}_{\mathrm{N}}(\mathbf{r}) = \int \frac{d^3\mathbf{k}}{4\pi^3} \mathbf{v}(\mathbf{k}) f(\mathbf{r}, \mathbf{k}), \tag{2.4}$$

$$\mathbf{J}_{\mathrm{e}}(\mathbf{r}) = \int \frac{d^3\mathbf{k}}{4\pi^3} (-e) \mathbf{v}(\mathbf{k}) f(\mathbf{r}, \mathbf{k}), \tag{2.5}$$

$$\mathbf{J}_{\mathrm{U}}(\mathbf{r}) = \int \frac{d^3\mathbf{k}}{4\pi^3} E(\mathbf{k}) \mathbf{v}(\mathbf{k}) f(\mathbf{r}, \mathbf{k}), \tag{2.6}$$

and the thermal (heat) flux density $\mathbf{J}_{\mathrm{Q}}(\mathbf{r})$ is obtained from the Euler relation in thermodynamics, $\mathbf{J}_{\mathrm{Q}} = \mathbf{J}_{\mathrm{U}} - E_{\mathrm{F}} \mathbf{J}_{\mathrm{N}}$ [17],

$$\mathbf{J}_{\mathrm{Q}}(\mathbf{r}) = \int \frac{d^3\mathbf{k}}{4\pi^3} [E(\mathbf{k}) - E_{\mathrm{F}}(\mathbf{r})] \mathbf{v}(\mathbf{k}) f(\mathbf{r}, \mathbf{k}). \tag{2.7}$$

Substituting (2.3) into (2.5) and (2.7) leads to

$$\mathbf{J}_{\mathrm{e}}(\mathbf{r}) = e^2 L_0 \mathbf{F}' - \frac{e}{T} L_1 (-\nabla T), \tag{2.8}$$

$$\mathbf{J}_{\mathrm{Q}}(\mathbf{r}) = -e L_1 \mathbf{F}' + \frac{1}{T} L_2 (-\nabla T), \tag{2.9}$$

where $\mathbf{F}' = \mathbf{F} + \nabla E_{\mathrm{F}}/e$ is the net electric field combining the external electric field and the electric field induced by the gradient of Fermi level or chemical potential, and the transport coefficients L_n are defined by the following integral:

$$L_n = \int \frac{d^3\mathbf{k}}{4\pi^3} \tau(\mathbf{k}) v^2(\mathbf{k}) [E(\mathbf{k}) - E_{\mathrm{F}}]^n \left(-\frac{\partial f_0}{\partial E} \right). \tag{2.10}$$

From the expressions for $\mathbf{J}_{\mathrm{e}}$ and $\mathbf{J}_{\mathrm{Q}}$, various thermoelectric parameters such as the electrical conductivity, the Seebeck coefficient, the electronic contribution to the thermal conductivity, and the Peltier coefficient can be calculated and expressed with the transport coefficients.

The *electrical conductivity* σ is defined as the proportionality constant between the electrical current density and the electric field including the diffusion forces due to the Fermi level gradient under the condition of uniform temperature such that,

$$\mathbf{J}_{\mathrm{e}} = \sigma \mathbf{F}'. \tag{2.11}$$

By comparing (2.11) with (2.8), the electrical conductivity is found to be

$$\sigma = e^2 L_0. \tag{2.12}$$

The *Seebeck coefficient* S is the proportionality constant between the net electric field and the temperature gradient under the condition of no electric current such that

$$\mathbf{F}' = S \nabla T \big|_{\mathbf{J}_{\mathrm{e}}=0}. \tag{2.13}$$

From (2.8) under the condition that $\mathbf{J}_{\mathrm{e}} = 0$, the Seebeck coefficient is found to be

$$S = -\frac{1}{eT} L_0{}^{-1} L_1. \tag{2.14}$$

The *Peltier coefficient* Π is defined as the proportionality constant between the thermal current density and the electric current density under the condition of uniform temperature such that

$$\mathbf{J}_{\mathrm{Q}} = \Pi \mathbf{J}_{\mathrm{e}} |_{\nabla T=0}. \tag{2.15}$$

By comparing (2.8) and (2.9) with $\nabla T = 0$, the Peltier coefficient becomes

$$\Pi = -\frac{1}{e} L_0{}^{-1} L_1. \tag{2.16}$$

From (2.14) and (2.16), the Seebeck coefficient and the Peltier coefficient are related as

$$\Pi = TS. \tag{2.17}$$

The *electronic thermal conductivity* κ_{elect} is defined as the proportionality constant between the thermal current density and the temperature gradient under the condition of no electric current,

$$\mathbf{J}_{\text{Q}} = \kappa_{\text{elect}}(-\nabla T)\big|_{\mathbf{J}_{\text{e}}=0}. \tag{2.18}$$

From (2.8), (2.9), and (2.18),

$$\kappa_{\text{elect}} = \frac{1}{T}\left(L_2 - L_1 L_0{}^{-1} L_1\right). \tag{2.19}$$

All the transport coefficients can be rewritten as integrals over the electron energy using the relation of $\rho_{\text{DOS}}(E)dE = d\mathbf{k}/4\pi^3$, where $\rho_{\text{DOS}}(E)$ is the density of states as a function of energy, such that

$$L_n = \frac{1}{e^2}\int \sigma_{\text{d}}(E)[E - E_{\text{F}}]^n dE, \tag{2.20}$$

where the *differential conductivity* is defined as

$$\sigma_{\text{d}}(E) = e^2\tau(E)v^2(E)\rho_{\text{DOS}}(E)\left(-\frac{\partial f_0}{\partial E}\right). \tag{2.21}$$

It is convenient to rewrite all the thermoelectric properties as integrals over the electron energy with the differential conductivity as follows,

$$\sigma = \int \sigma_{\text{d}}(E)dE, \tag{2.22}$$

$$S = -\frac{1}{eT}\frac{\int \sigma_{\text{d}}(E)(E - E_{\text{F}})dE}{\int \sigma_{\text{d}}(E)dE}, \tag{2.23}$$

$$\kappa_{\text{elect}} = \frac{1}{e^2 T}\int \sigma_{\text{d}}(E)(E - E_{\text{F}})^2 dE - S^2\sigma T. \tag{2.24}$$

The differential conductivity is a contribution of electrons at energy E to the total conductivity. It is also called the *transport distribution* [18]. In order to increase the electrical conductivity, the differential conductivity within the Fermi

level window ($\partial f_0/\partial E$) should be as large as possible. In other words, the Fermi level should be as high as possible. On the other hand, in order to increase the Seebeck coefficient, the asymmetry in the differential conductivity around the Fermi level should be as large as possible, i.e., larger σ_d for $E > E_F$ and smaller σ_d for $E < E_F$. However, it is difficult to increase both S and σ at the same time because the asymmetry in the differential conductivity becomes smaller as the Fermi level increases in energy in typical bulk semiconductors, so that the Seebeck coefficient decreases, and the electrical conductivity increases with increasing Fermi level.

2.2.2 Band Structure and Multi-band Transport

In typical semiconductors, the dispersion relation in each band can be approximated near the band extremum by modified Kane model [19],

$$E(1 + \alpha E) = \frac{\hbar^2 k^2}{2\mathrm{m}^*}, \tag{2.25}$$

where α is non-parabolicity, and m^* is the effective mass. For low electron energies, the conduction band can be assumed to be parabolic with $\alpha = 0$. But for high carrier density and high temperature transport modeling it is important to use a non-parabolic band because a large amount of carriers could fill up the band to high energies and thus the parabolic band model is no longer valid.

The density of states (DOS) for a non-parabolic band is given by

$$\rho_{\mathrm{DOS}}(E) = \frac{\sqrt{2}(\mathrm{m}^*)^{3/2}}{\pi^2 \hbar^3} \sqrt{E + \alpha E^2} \cdot (1 + 2\alpha E). \tag{2.26}$$

The electron velocity in one direction $v(E)$ used in the differential conductivity for a non-parabolic band is given by

$$v^2(E) = \frac{1}{3}\left(\frac{1}{\hbar}\frac{\partial E}{\partial k}\right)^2 = \frac{2}{3\mathrm{m}^*}\frac{E(1 + \alpha E)}{(1 + 2\alpha E)^2}. \tag{2.27}$$

For small band-gap semiconductors, or in the case of high temperature transport where intrinsic carriers are significant, both the conduction band and the valence band need to be taken into account when transport properties are calculated. Also, many semiconductor materials have multiple valleys for conduction or valence bands. Figure 2.1 shows the band structure of PbTe at 300 K as an example. PbTe has a direct band gap of 316 meV at the L valley in the Brillouin zone at 300 K, and has a secondary valence band at the Σ valley.

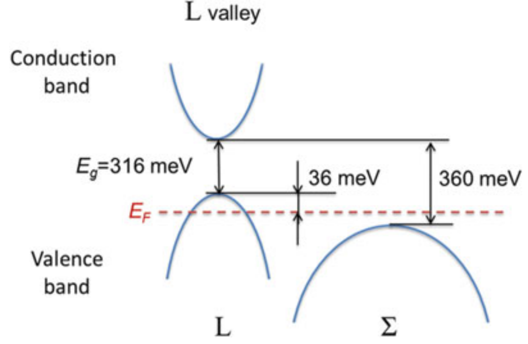

Fig. 2.1 Band structure of PbTe at 300 K [20]. Fermi level (*dotted line*) for hole density of 1×10^{19} cm^{-3} is also displayed

For multiple bands, electron density n and hole density p are obtained by the summation of each valley's carrier density as

$$n = \sum_i \int_0^\infty \rho_{\mathrm{DOS},i}(E) f_{0,i}(E) dE, \tag{2.28}$$

$$p = \sum_j \int_0^\infty \rho_{\mathrm{DOS},j}(E) f_{0,j}(E) dE. \tag{2.29}$$

where $f_{0,i}(E) = 1/[1 + \exp((E - E_{F,i})/k_B T)]$ is the Fermi–Dirac distribution of the i-th conduction valley with the relative position of Fermi level $E_{F,i}$ referenced to the i-th valley edge, and $\rho_{\mathrm{DOS},i}(E)$ is the density of states of the i-th conduction valley. For the valence valleys, an index j is used. For example, as shown in Fig. 2.1, the first valence band of PbTe at L valley has its relative Fermi level at 36 meV from its band edge, and the second valence band has its relative Fermi level at –8 meV from its band edge for 1×10^{19} cm^{-3} hole density at 300 K, since the band offset between the two valence bands is 44 meV.

If there are total N_D^+ ionized donors and total N_A^- ionized acceptors in the material, the charge neutrality gives

$$n + N_A^- = p + N_D^+. \tag{2.30}$$

Conventionally, $(N_D^+ - N_A^-)$ is called the *doping density* for n-type semiconductors, and $(N_A^- - N_D^+)$ is called the doping density for p-type semiconductors. If the doping density is known, one can determine the Fermi level by an iterative search that satisfies (2.30) with calculations of n and p using (2.28) and (2.29).

Once the Fermi level is determined, the electrical conductivity, the Seebeck coefficient, and the electronic thermal conductivity for each carrier type (subscript e for electrons and h for holes), can be calculated by

$$\sigma_e = \sum_i \int \sigma_{d,i}(E) dE, \tag{2.31}$$

$$\sigma_{\mathrm{h}} = \sum_{j} \int \sigma_{\mathrm{d},j}\,(E)\,dE, \tag{2.32}$$

$$S_{\mathrm{e}} = -\sum_{i} \frac{1}{eT}\,\frac{\int \sigma_{\mathrm{d},i}\,(E)(E - E_{\mathrm{F},i})\,dE}{\sigma_{\mathrm{e}}}, \tag{2.33}$$

$$S_{\mathrm{h}} = +\sum_{j} \frac{1}{eT}\,\frac{\int \sigma_{\mathrm{d},j}\,(E)\left(E - E_{\mathrm{F},j}\right)dE}{\sigma_{\mathrm{h}}}, \tag{2.34}$$

$$\kappa_{\mathrm{elect,e}} = \sum_{i} \frac{1}{e^2T} \int (E - E_{\mathrm{F},i})^2 \;\; \sigma_{\mathrm{d},i}\,(E)dE - {S_{\mathrm{e}}}^2\sigma_{\mathrm{e}}T, \tag{2.35}$$

$$\kappa_{\mathrm{elect,h}} = \sum_{j} \frac{1}{e^2T} \int \left(E - E_{\mathrm{F},j}\right)^2 \;\; \sigma_{\mathrm{d},j}\,(E)dE - {S_{\mathrm{h}}}^2\sigma_{\mathrm{h}}T, \tag{2.36}$$

where $\sigma_{\mathrm{d},i}$ ($\sigma_{\mathrm{d},j}$) is the differential conductivity of the i-th conduction valley (the j-th valence valley) calculated with the Fermi level referenced to its valley extremum.

Then, the total electrical conductivity and the total Seebeck coefficient in the bipolar transport are obtained by

$$\sigma = \sigma_{\mathrm{e}} + \sigma_{\mathrm{h}}, \tag{2.37}$$

$$S = \frac{\sigma_{\mathrm{e}}S_{\mathrm{e}} + \sigma_{\mathrm{h}}S_{\mathrm{h}}}{\sigma_{\mathrm{e}} + \sigma_{\mathrm{h}}}. \tag{2.38}$$

The electronic thermal conductivity is not only the sum of the partial electronic thermal conductivity of each type in bipolar transport. Another bipolar term due to the bipolar thermodiffusion effect must be added, which is given by [21]

$$\kappa_{\mathrm{bi}} = \frac{\sigma_{\mathrm{e}}\sigma_{\mathrm{h}}}{\sigma_{\mathrm{e}} + \sigma_{\mathrm{h}}}(S_{\mathrm{e}} - S_{\mathrm{h}})^2T. \tag{2.39}$$

This bipolar electronic thermal conductivity can be significantly large particularly at high temperatures even if the intrinsic carrier densities are much lower than the doping density because the Seebeck coefficients of the two types have opposite signs, so they are added up in (2.39). Also κ_{bi} increases proportionally with temperature.

The total electronic thermal conductivity is thus obtained as

$$\kappa_{\mathrm{elect}} = \kappa_{\mathrm{elect,e}} + \kappa_{\mathrm{elect,h}} + \kappa_{\mathrm{bi}}. \tag{2.40}$$

The electronic thermal conductivity can be a limiting factor in *ZT* at high temperatures and at high doping densities, especially when the lattice thermal conductivity was significantly reduced by nanostructures.

2.2.3 Electron Scattering by Spherically Symmetric Potentials

The scattering time, or relaxation time, $\tau(E)$ is a function of energy, and determined by multiple distinct scattering mechanisms that have different energy dependencies. The acoustic phonon deformation potential scattering $\tau_{\mathrm{AC}}(E)$, the ionized impurity scattering $\tau_{\mathrm{II}}(E)$, the polar optical phonon scattering $\tau_{\mathrm{POP}}(E)$, alloy scattering $\tau_{\mathrm{AL}}(E)$, and defect scattering $\tau_{\mathrm{D}}(E)$ are important scattering mechanisms in most semiconductors. Their reciprocals, or scattering rates, are arithmetically added to make the total scattering rate such that

$$\frac{1}{\tau(E)} = \frac{1}{\tau_{\mathrm{AC}}(E)} + \frac{1}{\tau_{\mathrm{II}}(E)} + \frac{1}{\tau_{\mathrm{POP}}(E)} + \frac{1}{\tau_{\mathrm{AL}}(E)} + \frac{1}{\tau_{\mathrm{D}}(E)} + \cdots \tag{2.41}$$

In this chapter, we are particularly interested in adding a new scattering mechanism by spherical nanoparticles. For this, an accurate calculation of the nanoparticle scattering time is necessary, which can then be added to the total scattering time in (2.41) to study their effects on the transport properties such as Seebeck coefficient, electrical conductivity, and electronic thermal conductivity.

Here, we assume that the nanoparticle scattering is elastic, i.e., momentum and energy are conserved by the scattering. In an elastic scattering, the scattering time τ can be expressed in terms of the total scattering cross section σ_{m}, the concentration of scatterers, i.e., nanoparticle density N_{p}, and the carrier velocity v, which together yield a scattering rate as

$$\frac{1}{\tau} = N_{\mathrm{p}} v \sigma_{\mathrm{m}}, \tag{2.42}$$

Since we are particularly interested in the "momentum" scattering time, which is the average time interval that electron momentum is altered by the scattering, the total *momentum* scattering cross section σ_{m} is used in (2.42) and is given by [22]

$$\sigma_{\mathrm{m}} = \iint D(\theta)(1 - \cos\theta) d\Omega = 2\pi \int_0^{\pi} D(\theta)(1 - \cos\theta) \sin\theta \, d\theta, \tag{2.43}$$

where $D(\theta)$ is the differential scattering cross section that is a function of the angle θ between the incident and the final wave vectors as shown in Fig. 2.2, and $d\Omega = d\varphi d\theta$ from the spherical coordinates (r, θ, φ). Note that the differential scattering cross section is independent of the azimuthal angle φ. The $(1 - \cos\theta)$ term in the integrand of (2.43) is a weighting factor that quantifies the degree to which the incident carrier has its incident momentum deflected.

The differential scattering cross section is defined for a given angle between the incident wave vector $\mathbf{k}_1$ and the final vector $\mathbf{k}_2$ as

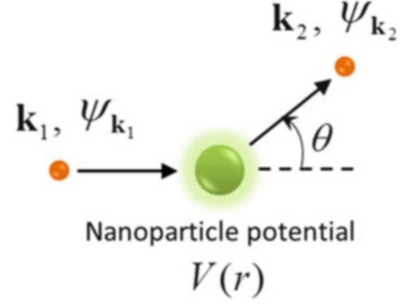

Fig. 2.2 Schematic of an electron scattering off a nanoparticle with a momentum change from wave vector $\mathbf{k}_1$ to $\mathbf{k}_2$ with angle θ between them, and the wave function change from $\psi_{\mathbf{k}1}$ to $\psi_{\mathbf{k}2}$. V(r) is the spherical electrostatic potential around the nanoparticle

$$D(\theta) = \frac{1}{8\pi^3 v}\int_0^\infty R_{12}{k_2}^2 dk_2, \tag{2.44}$$

where k_2 is the magnitude of $\mathbf{k}_2$, and R_{12} is the transition rate from $\mathbf{k}_1$ to $\mathbf{k}_2$.

In the Born approximation, the calculation of the transition rate R_{12} between the two states is based on the Fermi's Golden rule and the energy conservation before and after the transition such that

$$R_{12} = \frac{2\pi}{\hbar}\left|H_{\mathbf{k}_1,\mathbf{k}_2}\right|^2 \delta[U(\mathbf{k}_2) - U(\mathbf{k}_1)]. \tag{2.45}$$

The delta function in (2.45) is the energy conversion before and after the transition. The matrix element or the perturbation Hamiltonian $H_{\mathbf{k}1,\mathbf{k}2}$ is defined by the usual quantum-mechanical expectation value for a potential $V(r)$ as

$$H_{\mathbf{k}_1,\mathbf{k}_2} = \left\langle \psi_{\mathbf{k}_2} \middle| V(r) \middle| \psi_{\mathbf{k}_1} \right\rangle, \tag{2.46}$$

where $\psi_{\mathbf{ki}}$ is the wave function that satisfies the Schrödinger equation for the potential $V(r)$. In the assumption that collisions with a small momentum transfer dominate scattering and the overlap factor is close to unity, then these matrix elements can be solved as

$$H^{\mathrm{Born}}_{\mathbf{k}_1,\mathbf{k}_2} = \int V(\mathbf{r}) e^{i(\mathbf{k}_1-\mathbf{k}_2)\cdot\mathbf{r}} d^3\mathbf{r}. \tag{2.47}$$

As seen in (2.47), the matrix element is the Fourier transform of the potential $V(r)$ from the spatial coordinate to momentum space in the Born approximation. For an arbitrary potential $V(r)$ that is only a function of radial position, the momentum scattering rate is finally calculated in Born approximation using (2.42) along with (2.43)–(2.47) as

$$\frac{1}{\tau^{\text{Born}}} = \frac{8\pi \cdot \text{m}^* N_\text{p}}{\hbar^3} \frac{1}{k^3} \int_0^{2k} \left[\int_0^\infty V(r) \cdot r \frac{\sin(xr)}{x} dr \right]^2 x^3 dx. \tag{2.48}$$

The partial wave (PW) method gives the exact solution to the scattering problem for a spherically symmetric potential $V(r)$ that either vanishes beyond a certain distance or decrease exponentially with r [22, 23]. In the large r region where the potential $V(r)$ can be neglected, the wave function that satisfies the time-independent Schrödinger equation must have both the incident wave $\psi_{\text{in}}(\mathbf{r})$ and the scattered wave $\psi_{\text{sc}}(\mathbf{r})$,

$$\psi(\mathbf{r}) \to \psi_{\text{in}}(\mathbf{r}) + \psi_{\text{sc}}(\mathbf{r}) \quad \text{as } r \to \infty, \tag{2.49}$$

And the scattered wave function ψ_{sc} must represent an outward radial flow of carriers in the form of

$$\psi_{\text{sc}}(\mathbf{r}) = f(k, \theta) \frac{\text{e}^{ikr}}{r}, \tag{2.50}$$

where the amplitude f of the outgoing spherical wave $r^{-1}\exp(ikr)$ is called the *scattering amplitude*, and depends on the magnitude of the wave vector k and the radial direction θ (but independent of the azimuthal angle because the system is completely spherically symmetric). This scattering amplitude determines the differential scattering cross section as

$$D(\theta) = |f(k, \theta)|^2. \tag{2.51}$$

It is noted that the differential scattering cross section is not only a function of the angle between the incident and scattered wave vectors θ, but also a function of k or energy.

For a spherically symmetric potential, the solution to the Schrödinger equation can be expanded in series of Legendre polynomials, which form a complete set in the interval $-1 \leq \cos\theta \leq 1$, as

$$\psi(r, \theta) = \sum_{l=0}^{\infty} R_l(k, r) P_l(\cos\theta), \tag{2.52}$$

where l is the angular momentum quantum number, $P_l(x)$ is the l-th Legendre function. Each term in the series in (2.52) is known as a *partial wave*. Now solving the Schrödinger equation is reduced to find the partial wave amplitude $R_l(k,r)$ for each l.

However, one does not have to find all the partial wave amplitude in order to calculate the scattering amplitude $f(k, \theta)$, and the scattering cross section. Instead, one needs to find a parameter called the *phase shift* $\delta_l(k)$ for each l. The phase shift can be determined by the numerical solution of the Schrödinger

equation inside the nanoparticles and the boundary conditions using the shooting method [24].

Once the phase shift is found, then the scattering amplitude can also be expanded in a series of the partial waves as [23]

$$f(k,\theta) = \frac{1}{k}\sum_{l=0}^{\infty}(2l+1)\mathrm{e}^{i\delta_l}\sin\delta_l P_l(\cos\theta), \tag{2.53}$$

which depends only on the phase shift $\delta_l(k)$. The differential scattering cross section is obtained from (2.51) and (2.53) as

$$D(\theta) = \frac{1}{k^2}\left|\sum_{l=0}^{\infty}(2l+1)\mathrm{e}^{i\delta_l}\sin\delta_l P_l(\cos\theta)\right|^2. \tag{2.54}$$

The total momentum scattering cross section is given from (2.43) and (2.54) to be

$$\sigma_{\mathrm{m}}(\theta) = \frac{4\pi}{k^2}\left[\sum_{l=0}^{\infty}(2l+1)\sin^2\delta_l - \sum_{l=0}^{\infty}2l\cos(\delta_l-\delta_{l-1})\sin\delta_l\sin\delta_{l-1}\right]. \tag{2.55}$$

Finally the partial wave method can give the exact momentum scattering rate using (2.42) and (2.55) for any spherically symmetric potential $V(r)$.

2.3 Single-Phase Nanoparticles

2.3.1 Scattering Potential Around Nanoparticles

Since nanoparticles can donate electrons to the matrix, they can be locally positively charged. The charge neutrality principle may not be observed at small scale around localized charge sources. Due to the positive charge inside the nanoparticles, a coulomb potential is induced outside the nanoparticle, which is proportional to the charge Q inside the nanoparticle, and $1/r$ where r is the radial distance from the center of the nanoparticle. This coulomb potential makes the band edge near the nanoparticle bend upward locally, and makes the potential inside the nanoparticles lower than the surrounding potential.

This band bending, however, attracts a small number of electrons toward the interface because of the coulomb attraction. This charge redistribution is nonuniform with the distance from the interface, but a larger density of electrons is accumulated at closer distance from the interface. The perturbation in potential $\delta V(r)$ due to the local charge redistribution $\delta n(r)$ is governed by the Poisson

equation in a spherical coordinate, assuming only dependence on the radial distance r,

$$\frac{1}{r^2}\frac{d}{dr}\left[r^2\frac{d\delta V(r)}{dr}\right]=\frac{e}{\varepsilon_S\varepsilon_0}\delta n(r), \tag{2.56}$$

where ε_s is the static relative dielectric constant of the matrix. The δn is then related to δV as

$$\delta n=\frac{\partial n}{\partial V}\delta V=\frac{\partial n}{\partial E_F}\frac{\partial E_F}{\partial V}\delta V=\frac{\partial n}{\partial E_F}e\delta V, \tag{2.57}$$

where E_F is the Fermi level, and in the last step, the fact that the Fermi level, which is relative to the conduction band edge, is proportional to the potential such as E_F = const. + $eV(r)$, has been used. The $\delta n/\delta E_F$ in the farthest right hand side of (2.57) is determined by the Fermi–Dirac distribution f_0 as

$$\frac{\partial n}{\partial E_F}=\int_0^\infty \rho_{DOS}(E)\left(\frac{df_0}{dE_F}\right)dE. \tag{2.58}$$

By plugging (2.57) into (2.56),

$$\frac{1}{r^2}\frac{d}{dr}\left[r^2\frac{d\delta V(r)}{dr}\right]=\frac{e^2}{\varepsilon_S\varepsilon_0}\frac{\partial n}{\partial E_F}\delta V=\frac{\delta V}{L_D^2}, \tag{2.59}$$

where the last step defines the screening length L_D, such that

$$L_D=\frac{1}{e}\sqrt{\frac{\varepsilon_S\varepsilon_0}{\partial n/\partial E_F}}, \tag{2.60}$$

The solution to (2.59) is

$$\delta V=\frac{A}{r}e^{-r/L_D}. \tag{2.61}$$

The electric field at the interface of the nanoparticle that has a charge Q inside is determined by the Gauss's law as $|\mathbf{E}(r=a)|=Q/(4\pi r^2\varepsilon_s\varepsilon_0)$, which is in the radial direction. This value of electric field gives a boundary condition for the potential described in (2.61) at $r = a$, which leads to the determination of the proportionality factor A as $A = Q/(4\pi\varepsilon_s\varepsilon_0)\cdot L_D e^{a/LD}/(a + L_D)$. It is noted that A becomes simply $Q/(4\pi\varepsilon_s\varepsilon_0)$ for point-like charge sources ($a \to 0$). The correction factor, $L_D e^{a/LD}/(a + L_D)$, in A is, however, typically close to unity because the screening length is much larger than the size of nanoparticles.

Inside the nanoparticle, potential is assumed to be constant to the first approximation as we assume all net charge lies on the boundary $r = a$. With the potential

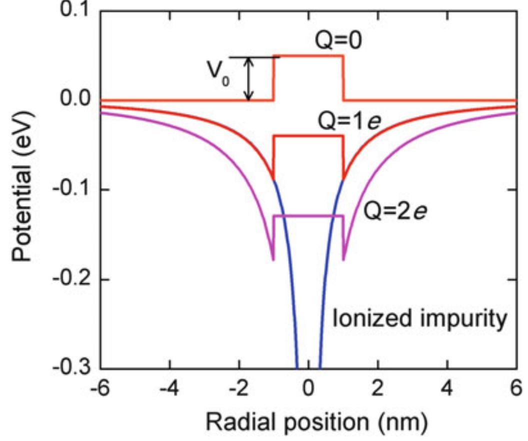

Fig. 2.3 Potential profile $V(r)$ around a nanoparticle with varying $Q = 0$ (unionized), $1e$, and $2e$ and a fixed potential offset $V_0 = 50$ meV. The screened Coulomb potential by an ionized impurity is also shown for comparison

offset, V_0, at the hetero-interface between the ErAs nanoparticle and the matrix, the potential profile becomes

$$\begin{aligned} V(r) &= V_0 - \frac{Q}{4\pi\varepsilon_s\varepsilon_0}\cdot\frac{L_D}{a(a+L_D)} = \text{const.} \quad (0 < r < a). \\ &= -\frac{Q}{4\pi\varepsilon_s\varepsilon_0}\frac{L_D e^{a/L_D}}{a+L_D}\cdot\frac{1}{r}e^{-r/L_D} \qquad (a <). \end{aligned} \tag{2.62}$$

The potential offset (or band offset) V_0 is readily determined as the difference between the Fermi level in the ErAs nanoparticle and the conduction band minimum in the matrix, or the Schottky barrier height. When the nanoparticle Fermi level is higher than the conduction band minimum in the matrix, V_0 is positive (potential barrier). V_0 is negative (potential well) when the Fermi level in the nanoparticle is lower than the conduction band minimum.

Figure 2.3 shows several potential profiles around nanoparticles with $Q = 0$, $1e$ and $2e$ in InGaAs lattice matched to InP. For unionized nanoparticles ($Q = 0$), there is no band bending, and the potential is step-like within the size of nanoparticle. When one charge per particle is transferred to the matrix or $Q = 1e$, the potential outside the nanoparticle is very similar to that of an ionized impurity as the correction factor $L_D e^{a/LD}/(a + L_D)$ is close to unity. Nanoparticles have a finite potential inside, while ionized impurities have a potential diverging to $-\infty$ near the charge center as an ionized impurity is a point charge.

2.3.2 Nanoparticle Scattering Time

Now the electron-nanoparticle scattering time can be calculated for the potential profile given by (2.62), using (2.48) in Born approximation, or using the partial wave method described in Sect. 2.2.3. Here we use the partial wave method for the

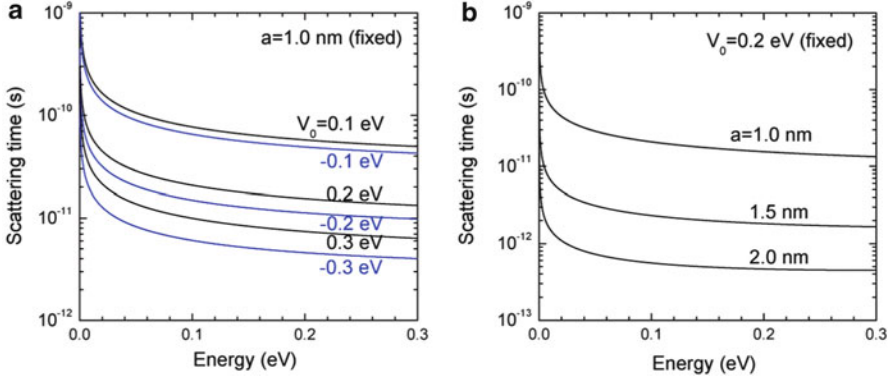

Fig. 2.4 Nanoparticle scattering times as a function of electron energy: (**a**) for varying potential offset (V_0) with a fixed nanoparticle radius $a = 1$ nm, and (**b**) for varying nanoparticle radius a with a fixed potential offset. InGaAs lattice matched to InP with electron effective mass of 0.041 m_0 and the nanoparticle density of 1×10^{18} cm^{-3} were assumed for all the curves

exact scattering calculations. For weak band bending, small band offset, or small size of nanoparticles, the Born approximation is still a good approximation. It has been found that the Born approximation produces the same results as the partial wave method within 5 % errors for the 2.4 nm diameter nanoparticles of 0.6 % volume fraction in InGa(Al)As with band bending as large as 200 meV, and the band offset at the interface as large as ±200 meV. Also, one of the advantages of the Born approximation is that it can easily include a non-parabolic band in the scattering calculations, which is very hard to include in the partial wave method. The partial wave method used in this chapter assumed a parabolic band for the scattering time calculations.

Figure 2.4 shows the calculated nanoparticle scattering times as a function of energy for various potential profiles in the case of no band bending with no ionization of the nanoparticles. Thus, these nanoparticles have only a potential offset at the interface with the host matrix. Two parameters are adjustable for these unionized nanoparticles: one is the potential offset V_0, and the nanoparticle radius a. As one can see in Fig. 2.4a, the larger the magnitude of the potential offset is, the stronger the nanoparticle scattering is. According to the Born approximation from (2.48), the scattering time is inversely proportional to $|V_0|^2$. In the partial wave method, this is roughly true, but the scattering time also depends on the sign of the potential offset. When the potential is a well, i.e., a negative sign of V_0, the scattering is stronger (the scattering time is smaller) than those when the potential is a barrier of the same magnitude but with a positive sign. Since the energies of free electrons are positive above the conduction band minimum, the potential height of a barrier that an electron of positive energy experience is smaller than the potential depth of a well of the same magnitude $|V_0|$ from the electron energy. Therefore, a potential well scatters electrons stronger than a potential barrier does as shown in

Fig. 2.4a. However, the Born approximation does not capture this difference between a well and a barrier, and typically the scattering time calculated using the Born approximation falls in between the exact scattering times calculated by the partial wave method for the well and barrier [23].

Also, the scattering is stronger when the size of the nanoparticle is larger as evidenced by Fig. 2.4b. The scattering rate increases rapidly with the nanoparticle size. For example, from Fig. 2.4b, the scattering time is approximately proportional to $1/a^5$ for the radius range from 1 to 2 nm. This is close to the Rayleigh scattering regime, which has a $1/a^6$ dependency. Note that the nanoparticle density was fixed to be 1×10^{18} cm^{-3} for all the sizes in Fig. 2.4b. The nanoparticle density is proportional to $1/a^3$ for a fixed volume fraction of nanoparticle material, and the scattering time is proportional to the density. Therefore, if we fix the volume fraction of nanoparticles instead of the density, the scattering time becomes proportional to $1/a^2$. In other words, if one uses the same volume fraction of material to form nanoparticles, and finds that different sizes of nanoparticles are formed under different growth conditions, then the larger-size nanoparticle material should have a lower mobility of electron due to the stronger nanoparticle scattering in proportion to the square of the nanoparticle size.

Another important characteristic of unionized nanoparticle scattering time is that the scattering time decreases with increasing energy as shown in Fig. 2.4. In the energy range of interest, the de Broglie wavelengths of electrons are on the order of 100 nm in typical semiconductor materials, which is much larger than the size of nanoparticles of 2–4 nm in diameter. In such a case, the scattering is Rayleigh-like, and the scattering rate becomes approximately proportional to $1/\lambda^4$. Since the electron wavelength is inversely proportional to the energy E, the scattering rate is thus proportional to E^4, or the scattering time is proportional to $1/E^4$ in the Rayleigh scattering regime. This energy dependency is well observed in Fig. 2.4.

When a nanoparticle is ionized, electrons are transferred from the nanoparticle to the host matrix, so that a Coulomb potential is created around the nanoparticle just like ionized impurities as shown in Fig. 2.3. This Coulomb potential is slowly varying in space in contrast to the sharp offset at the interface. These two distinct features, the slowly varying Coulomb potential and the sharp potential offset, determine the scattering time in different energy regions.

From (2.44) and (2.45), the differential scattering cross section is proportional to the magnitude of the matrix element. Also, the matrix element is the Fourier transform of the potential $V(r)$ from the spatial coordinate to the momentum space in Born approximation according to (2.47). For the screen Coulomb potential of an ionized impurity $V(r)$, which is

$$V(r) = -\frac{Q}{4\pi\varepsilon_s\varepsilon_0}\frac{1}{r}\mathrm{e}^{-r/L_D}, \tag{2.63}$$

the matrix element becomes from (2.47)

$$H_{\mathbf{k}_1,\mathbf{k}_2} = \frac{Q}{\varepsilon_r \varepsilon_0 \left[(1/L_D)^2 + (2k \sin(\theta/2))^2 \right]}, \tag{2.64}$$

where $\mathbf{k}_1$ and $\mathbf{k}_2$ have the same magnitude of k, and θ is the angle between the two momentum. Equation (2.64) tells that the matrix element decreases with increasing magnitude of momentum or increasing energy, and also decreases with increasing angle from 0 to π. This indicates that the ionized impurity scattering becomes weaker as the electron energy increases, and favors a small angle scattering. This is because, by the 3D Fourier transform relation between the potential profile and the matrix element, the slowly varying potential in space is transformed into the low-frequency (low-energy) components of the matrix element. On the other hand, the sharp potential offset is transformed into the high-frequency components of the matrix element. As a result, the scattering by the Coulomb potential is dominant in the low-energy region, while the scattering by the potential offset at the interface is dominant in the high-energy region for the ionized nanoparticle scattering.

The comparison of differential scattering cross sections for an unionized nanoparticle ($Q = 0$) and an ionized nanoparticle ($Q = 1e$) reveals the distinct features of the two scatterings as a function of electron energy and scattering angle. As shown in Fig. 2.5a, an unionized nanoparticle scatters higher-energy electrons more strongly than lower-energy ones, and the strength of the scattering is relatively uniform over a wide range of scattering angle. On the other hand, an ionized nanoparticle scatters lower-energy electrons more strongly than higher-energy ones, and only small scattering angles is preferred as shown in Fig. 2.5b. In particular, the low-energy scattering by the Coulomb potential around the nanoparticle is quite much stronger than the scattering by the potential offset as one can see the clear difference in the magnitude of differential cross section by comparing the color bars of the two figures in Fig. 2.5.

Figure 2.6 shows the calculated nanoparticle scattering time as a function of energy for various Q and sizes. In Fig. 2.6, the same carrier density (N_e) of 1×10^{18} cm^{-3} is used for every curve. For a given Q, the required density of nanoparticles (N_p) is obtained from the definition of Q as $Q = e(N_e/N_p)$. When Q is larger than $1e$, indicating that a nanoparticle donates more than one electron, the nanoparticle scattering becomes stronger than the ionized impurity scattering at the same doping density due to the stronger Coulomb potential. However, for $Q = 1e$, the nanoparticle scattering is weaker than the ionized impurity scattering as shown in Fig. 2.6. This is because the nanoparticle potential does not possess the very deep well near the scattering center that strongly attracts electrons to ionized impurities. When the nanoparticle radius is smaller than 0.5 nm, more of the impurity well is present and its scattering time is almost identical to the ionized impurity scattering time. For larger nanoparticles, the scattering time increases with increasing radius over most of the energy range of interest. However, for radii 2.0 nm and larger the scattering time starts to roll over at high energies due to the effect of the potential offset at the hetero-interface, which becomes stronger as the radius increases.

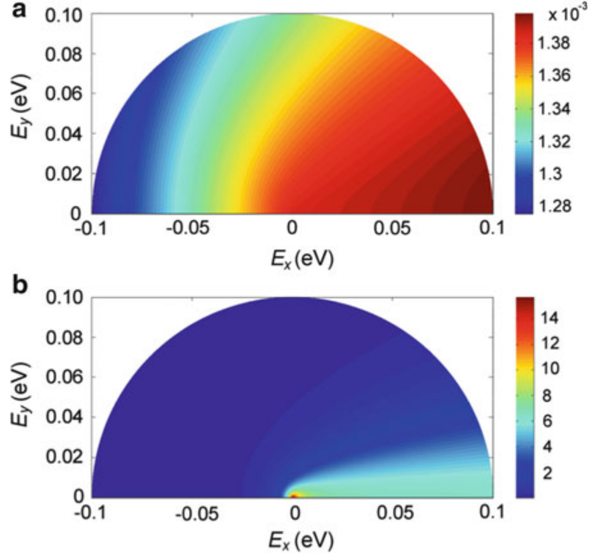

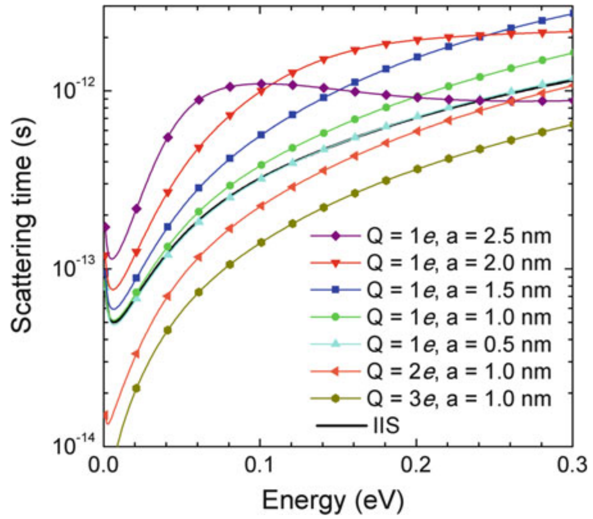

Fig. 2.5 Differential scattering cross section in units of πa^2 (cross section of the nanoparticle) as a function of electron momentum (polar angle and magnitude) for (**a**) an unionized (step-potential) nanoparticle ($Q = 0$) and (**b**) an ionized nanoparticle ($Q = 1e$). $V_0 = 0.2$ eV and $a = 1$ nm for both figures

Fig. 2.6 Nanoparticle scattering times as a function of electron energy for varying Q and radius a in InGaAs lattice matched to InP. (Figure from Ref. 11)

2.3.3 Power Factor Enhancement in III–V Semiconductors

In this section, we show that the power factor can be enhanced by ionized nanoparticles with $Q = 1e$. These ionized nanoparticles can replace the ionized impurities with weaker scatterings, so that the electrical conductivity can be enhanced with a relatively small sacrifice of Seebeck coefficient to enhance the power factor. For Q larger than $1e$, the ionized nanoparticle scattering is stronger

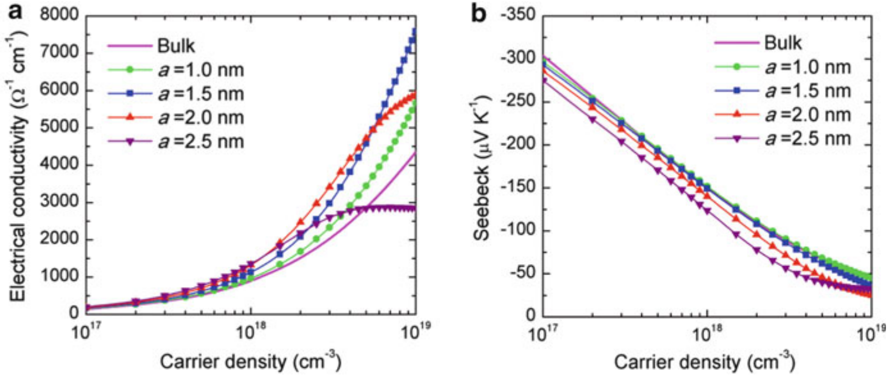

Fig. 2.7 (**a**) Electrical conductivity and (**b**) Seebeck coefficient as a function of electron density for n-type InGaAs with embedded ionized nanoparticles of varying radius a and a fixed $Q = 1e$ at 300 K. Bulk values without nanoparticles are shown together for comparison. (Figure from Ref. 11)

than the ionized impurity scattering. Therefore, the electrical conductivity and power factor are not enhanced over the bulk with conventional ionized single-atom dopants. If the nanoparticles are not ionized, i.e., $Q = 0$, the ionized impurities are still needed to dope the semiconductor, and thus the nanoparticles are only additional scattering centers for carriers, reducing the electrical conductivity. The Seebeck coefficient is not enhanced either because the unionized nanoparticle scattering has its strength increasing with energy. Hot electrons are scattered more than cold electrons in this case, so that the entropy transport per carriers is suppressed, thereby reducing the Seebeck coefficient.

Figure 2.7 shows that the electrical conductivity, and Seebeck coefficient of $In_{0.53}Ga_{0.47}As$ as a function of carrier density at 300 K for various nanoparticle sizes with ionization $Q = 1e$, calculated based on the Boltzmann transport equation under the relaxation time approximation described in Sect. 2.2.1. It has recently been reported that rare-earth doped InGaAlAs has achieved a $ZT \sim 1.3$ at 800 K [13]. In the III–V semiconductor, the ionized impurity scattering can be a dominant scattering in the material so that the replacing nanoparticle scattering can make a big impact in mobility. However, for materials such as PbTe in which phonon scattering is dominant, the nanoparticle scattering effect may not be very large. Other major scattering mechanisms such as polar optical phonon scattering, acoustic phonon scattering, and alloy scattering are included in the total scattering calculation [25]. The relevant material-specific scattering constants are carefully chosen to fit temperature-dependent experimental mobility of bulk Si-doped $In_{0.53}Ga_{0.47}As$. A non-parabolic band model is used for the host material.

Over most of the range of interest, the electrical conductivity is enhanced with nanoparticle scattering compared to the case of ionized impurity scattering. At large degenerate carrier concentrations, the diminished electrical conductivity in materials with large nanoparticles of $a = 2.0$ and 2.5 nm is expected from the scattering time curves in Fig. 2.6, since Rayleigh-like scattering figures prominently for the

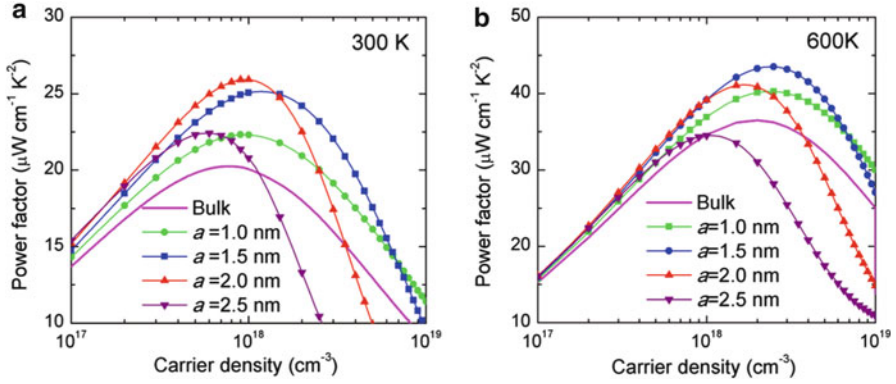

Fig. 2.8 Power factors at (**a**) 300 K and (**b**) 600 K as a function of electron density for *n*-type InGaAs with embedded ionized nanoparticles of varying radius a and a fixed $Q = 1e$. Bulk values without nanoparticles are shown together for comparison. (Figure from Ref. 11)

high-energy electrons near the Fermi surface which dominate conduction. Meanwhile, the Seebeck coefficient is only slightly reduced or even slightly increased for the nanoparticles of 0.5–1.5 nm. This is due to the increase in scattering parameter from nanoparticle scattering.

The power factors calculated using the two properties at 300 K are shown in Fig. 2.8a. The maximum power factor is obtained to be 26 μW/cmK^2 for the particle size of 2.0 nm at the carrier density of 1×10^{18} cm^{-3} at 300 K. This is a 30 % enhancement compared to the maximum power factor, 20 μW/cmK^2, obtained without nanoparticles at this temperature.

At higher temperatures, the enhancement of power factor is still possible with ionized nanoparticles. Figure 2.8b shows the power factors for InGaAs with embedded nanoparticles at 600 K. The maximum power factor at 600 K is obtained to be 43.5 μW/cmK^2 for the particle size of 1.5 nm at the carrier density of 2.5×10^{18} cm^{-3}, which is a 26 % enhancement over the bulk maximum, 34.5 μW/cmK^2. The optimum power factor for the material with nanoparticles with a radius of 2.0 nm becomes smaller than that of 1.5 nm radius at this high temperature, because the Rayleigh scattering has a more substantial contribution at high temperatures for larger nanoparticles. The percentage of enhancement in power factor gradually decreases from 30 to 26 %, and to 15 % with temperature increasing from 300 to 600 K, and to 800 K due to the increased phonon scattering rate at high temperature, which reduces the relative importance of nanoparticle scattering in the total scattering time.

The electronic thermal conductivity also increases at almost the same rate as the electrical conductivity. With the optimal particle size at the optimal carrier density, the electronic thermal conductivity is calculated to increase from 0.6 to 0.8 W/mK at 300 K, while the lattice thermal conductivity is considered fixed at 5 W/mK. Thus, the total thermal conductivity rises from 5.6 to 5.8 W/mK, corresponding to

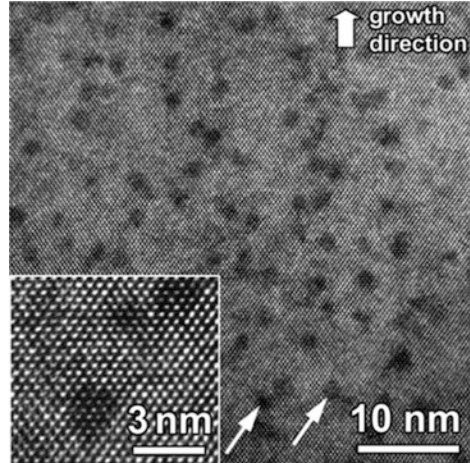

Fig. 2.9 High-resolution cross-sectional transmission electron micrograph (HR-TEM) of randomly distributed ErAs nanoparticles embedded in $In_{0.53}Ga_{0.47}As$. The nanoparticles are seen as almost perfect spheres, and the size of nanoparticles is observed to be 1 ~ 3 nm in diameter. (Figure from Ref. 29)

an increase of just 4 %. Since this change is much smaller than the power factor enhancement of 30 %, the overall *ZT* enhancement remains 25 %. Note that this *ZT* enhancement does not include the lattice thermal conductivity reduction by the nanoparticles. Therefore, the overall *ZT* enhancement could be much larger in nanoparticle materials.

2.3.4 ErAs Nanoparticles in InGaAlAs

ErAs is a semi-metal that has a cubic rock salt structure with the lattice constant of 0.574 nm close to that of InGaAs by 2 % mismatch. An ErAs layer can be grown epitaxially on arsenide semiconductors of the zinc blend structure [26]. Recently, composites of ErAs nanoparticles embedded in epitaxial InGaAs lattice matched to InP substrate or in GaAs have been grown successfully by either overgrowing nanometer sized islands of ErAs, or co-depositing Er during the semiconductor growth using molecular beam epitaxy (MBE) technique [27–29] (Fig. 2.9).

Semi-metal nanoparticles incorporated into a semiconductor can have a large effect on the properties of the semiconductor host. The particles can act as dopants [30, 31], buried Schottky barriers [32], deep states for carrier recombination [33], or enhanced tunneling [34], and phonon scattering centers [35]. This section explores the effect of the ErAs nanoparticles on the thermoelectric properties of InGaAlAs III–V semiconductor alloys over a wide temperature range.

In order to understand the electrical properties of the ErAs:InGaAlAs nanocomposites, the carrier density information of the material is crucial. Figure 2.10 shows the temperature-dependent electron density of 0.3 and 0.6 % ErAs:$(InGaAs)_{0.8}(InAlAs)_{0.2}$ lattice-matched to InP obtained by the Hall effect measurements over a temperature range from 20 to 400 K. They are all n-type.

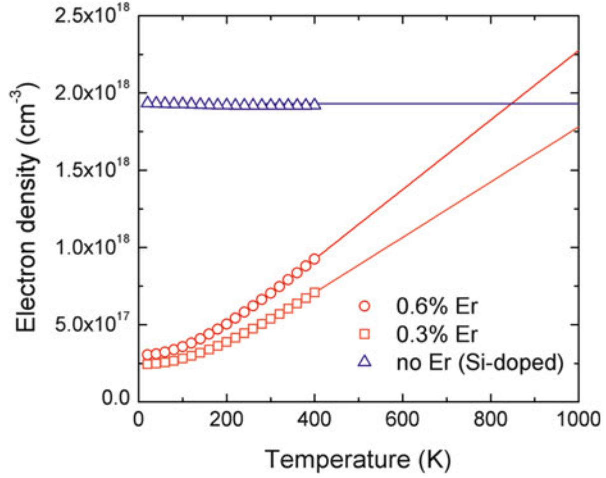

Fig. 2.10 Electron density as a function of temperature for 0.3 and 0.6 % ErAs:$(InGaAs)_{0.8}(InAlAs)_{0.2}$ and a Si-doped control sample. Symbols are experimental data from 20 to 400 K, and curves are linear fits above 400 K

Unlike the conventionally doped InGaAlAs by Si, which has a carrier density constant over a wide temperature range, the ErAs:InGaAlAs nanocomposites exhibit increasing carrier density with temperature. Also, they have unfrozen carriers even at ultra-low temperature. Typically, this kind of carrier donation behavior is seen when there are multiple types of donors. For example, with two types of carriers, one shallow donor and one deep donor, the temperature-dependent carrier density can be modeled as

$$n = N_{\mathrm{DD}} \exp\left(-\frac{E_{\mathrm{DD}}}{k_{\mathrm{B}}T}\right) + N_{\mathrm{SD}}, \tag{2.65}$$

where N_{DD} is the high temperature limit density of the deep donors, E_{DD} is the deep donor energy level below the conduction band minimum, and N_{SD} is the carrier density by the shallow donors. The carriers donated by shallow donors are not frozen at low temperatures, but remain constant over the temperature range. Deep donors are responsible for the increase of carrier density with temperature. ErAs:InGaAlAs nanocomposites have $E_{\mathrm{DD}} \sim 50$ meV for various Al compositions [36]. Although the carrier density by deep donors increases exponentially with temperature according to (2.65), a linear increase assumption of carrier density with temperature is still a good approximation for a small donor energy level. In Fig. 2.10, we extrapolated the carrier density assuming a linear temperature dependence above 400 K for theoretical calculations of the thermoelectric properties.

Figure 2.11 shows the experimental electrical conductivity, Seebeck coefficient, thermal conductivity, and *ZT* as a function of temperature for 0.3 and 0.6 % ErAs:$(InGaAs)_{0.8}(InAlAs)_{0.2}$ and their theoretical fitting calculated by the Boltzmann transport formalism. Since the carrier densities of the ErAs nanocomposites are lower than that of the Si-doped control at room temperature, the electrical conductivity stays lower at low temperatures, but increases with temperature as the carrier

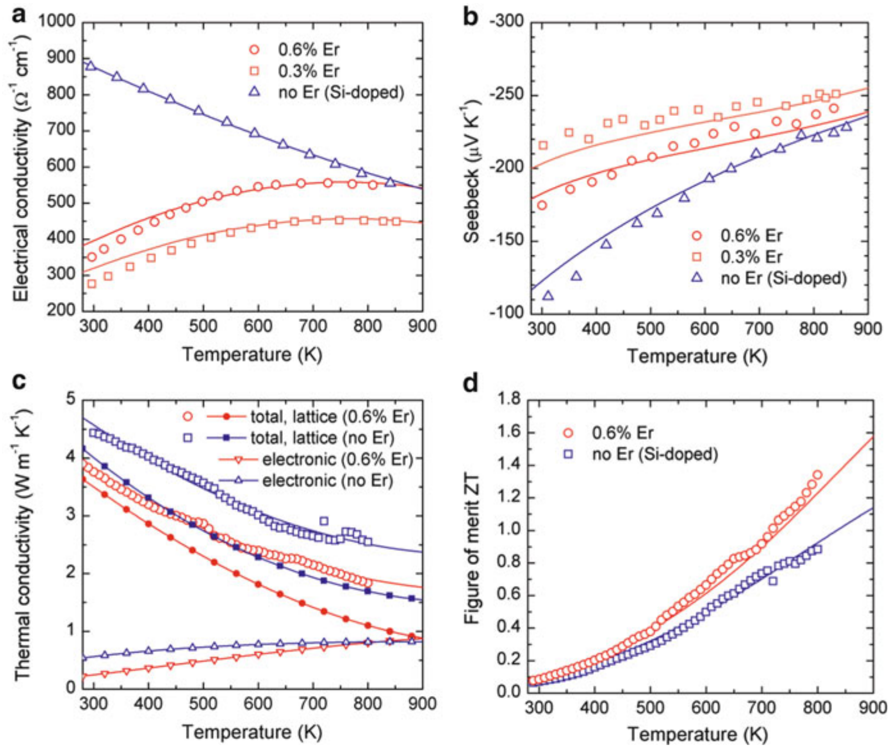

Fig. 2.11 (**a**) Electrical conductivity, (**b**) Seebeck coefficient, (**c**) thermal conductivity, and (**d**) *ZT* as a function of temperature for ErAs:$(InGaAs)_{0.8}(InAlAs)_{0.2}$ nanocomposites. A Si-doped $(InGaAs)_{0.8}(InAlAs)_{0.2}$ with no ErAs at 1.9×10^{18} cm^{-3} doping density is compared. Symbols are experimental data, and curves are theoretical fits. In (**c**), both the lattice and (calculated) electronic components of thermal conductivity are also separately plotted

density increases. The electrical conductivity slowly reaches a maximum and begins to decrease as temperature nears 800 K. This is due to the decrease in mobility with increased phonon scattering, as temperature increases.

Around 800 K, the carrier densities of the Si-doped control and the 0.6 % Er sample are comparable, and also their electrical conductivities are very close to each other. This indicates that the electron mobility in the nanocomposite remains similar to that of the control around this temperature. It was expected that the mobility could be enhanced due to the nanoparticle scattering in the nanocomposite materials, but it turns out that the effect of the nanoparticle scattering was negligibly small in this material. In fact, individual background Er atoms can act as donors in InGaAlAs. Thus, it is uncertain how much carriers of the total number of carriers comes from the ErAs nanoparticles, and how many from the background Er atoms. Also, how many electrons per nanoparticle are donated is also unclear. These uncertainties regarding the donation mechanism of ErAs nanoparticles in this

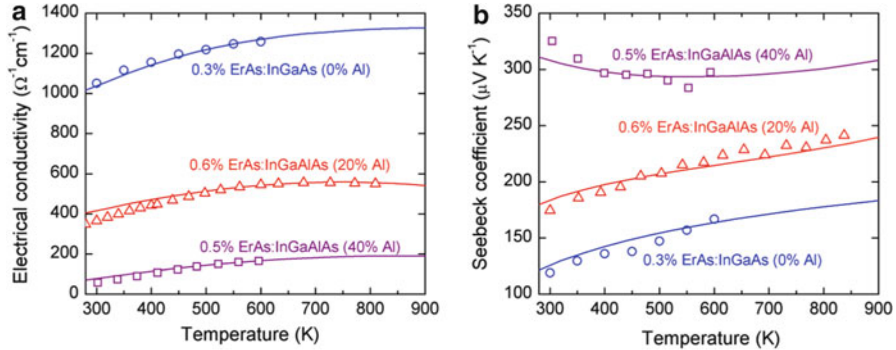

Fig. 2.12 (**a**) Electrical conductivities and (**b**) Seebeck coefficients as a function of temperature for ErAs:$(InGaAs)_{1-x}(InAlAs)_x$ with various Al contents, $x = 0$, 0.2 and 0.4. The ErAs fraction was selected for optimal power factors for each Al content. Symbols are experimental data, and curves are theoretical fits

semiconductor need to be clearly understood in order to study the effect of nanoparticle scattering on the electrical properties.

As shown in Fig. 2.11b, the Seebeck coefficients of the nanocomposites are measured higher than that of the control, mainly due to the reduced electrical conductivity. The power factor is increased by 6 % at 800 K. Once the ErAs nanoparticle scattering is fully understood in this nanocomposite material, further optimization may be possible in terms of power factor, and *ZT*.

An enhancement of *ZT* is obtained for 0.6 % ErAs:InGaAlAs over the Si-doped counterpart mainly due to thermal conductivity reduction. As shown in Fig. 2.11c, the thermal conductivity for the 0.6 % ErAs:InGaAlAs was measured to be 1.8 W/mK at 800 K, while the thermal conductivity of the control was 2.5 W/mK. The reduction in thermal conductivity by 0.7 W/mK came from the reduction of the lattice contribution of thermal conductivity by the additional phonon scattering at the interfaces. The electronic thermal conductivities were very similar between the two samples. As a result, the figure of merit was increased to 1.3 at 800 K for this nanocomposite compared to *ZT* ~ 0.9 of the Si-doped control at the same temperature. The measurements were performed only up to 800 K, but according to the prediction by theory, the figure of merit of the nanocomposite is expected to reach 1.6 at 900 K, and 1.9 at 1000 K.

Further material optimization is possible by varying Al content in the host semiconductor. As the Al content increases in this material, the band gap increases and the effective mass also increases. As a result, the mobility decreases with Al content, and thus the electrical conductivity is reduced. Figure 2.12 shows this trend clearly: ErAs:InGaAs with no Al showed the highest electrical conductivity, and 40 % Al showed the lowest among the three different Al contents. The power factor was highest for the ErAs:InGaAs with no Al due to its much higher electrical conductivity with slightly lower Seebeck coefficient than other compositions over

the entire temperature range. If the thermal conductivity reduction due to the phonon-nanoparticle scattering is similar, then InGaAs with embedded ErAs nanoparticles can achieve higher *ZT* than that of the 0.6 % ErAs:InGaAlAs with 20 % Al shown in Fig. 2.11.

2.4 Core–Shell Resonant Nanoparticles

2.4.1 Resonant Scattering by Core–Shell Nanoparticles

Core–shell nanoparticles embedded in bulk semiconductors can work as resonant scattering centers to suppress conduction in a narrow band of energies and thereby enhance the Seebeck coefficient and thermoelectric power factor. Figure 2.13 shows the three-dimensional structure of resonant core–shell nanoparticles and the potential profile around them in the radial direction, r. The core region ($r < a$) forms a potential well with the well depth V_0 below the band minimum of the host material, and the shell region ($a < r < b$) forms a potential barrier around the core with the finite barrier height V_1 above the host band minimum. With the proper selection of materials for the effective masses of the core and shell regions, quasi-bound states can be formed within the core with evanescent tails that resonantly couple to the continuum of free electron states in the host conduction band.

The use of core–shell nanoparticles has several advantages over the resonant impurities. First, the position and width of resonant levels can be controlled by parameters including the core and shell sizes, the material band offsets which determine the height of the potential barrier and the depth of the inner potential

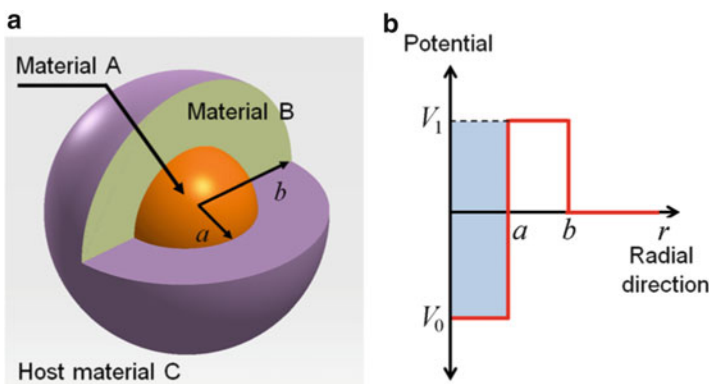

Fig. 2.13 (**a**) Three dimensional schematic of the proposed core–shell nanoparticle structure, and (**b**) the potential profile around the nanoparticles in radial direction. The core region ($r < a$) has heavier effective mass (i.e., 1–1.2 m_0) than those of the shell region and the host material. (Figure from Ref. 12)

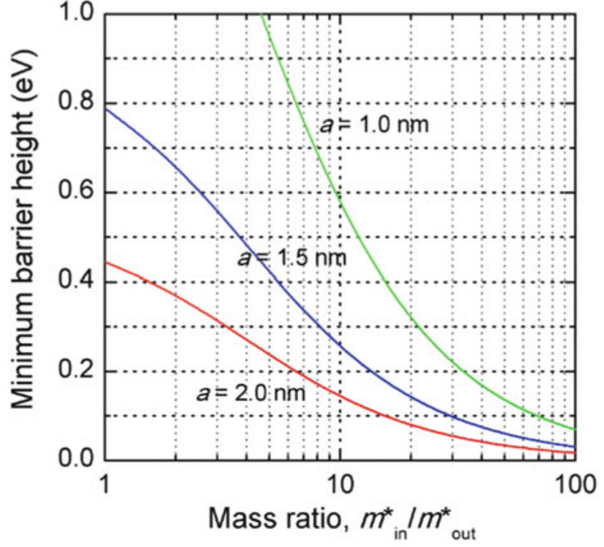

Fig. 2.14 The minimum barrier height required to have at least one bound state as a function of the effective mass ratio, $\alpha = m^*_{in}/m^*_{out}$ with varying core effective mass m^*_{in}, and fixed $m^*_{out} = 0.053m_0$. Results are shown for several core radii, $a = 1$, 1.5, and 2 nm, and are based on a simple model for infinite barrier width described by (2.66)

well, and the effective masses of the constituent materials. In addition, controlling the size distributions of the core–shell nanoparticles provides an additional degree of freedom in designing the width of resonances via inhomogeneous broadening.

Exact quasi-bound states for the potential profile presented in Fig. 2.13b can be obtained by numerically solving the three-dimensional Schrödinger equation with wave-matching boundary conditions. However, a simple model with infinite barrier width ($b \to \infty$) can be conveniently used to design the barrier height V_B ($=V_1 - V_0$) in order to have at least one bound state below the barrier. When the core has an effective mass m^*_{in}, and the shell and the host matrix have the same effective mass m^*_{out}, then the minimum barrier height is given by [22],

$$1 - \alpha = \gamma \cdot \cot \gamma, \tag{2.66}$$

where $\alpha = m^*_{in}/m^*_{out}$ is the effective mass ratio, and γ is the dimensionless barrier height defined by

$$\gamma^2 = \frac{2a^2}{\hbar^2} m^*_{in} \cdot V_B. \tag{2.67}$$

Figure 2.14 shows the minimum barrier height obtained by (2.66) as a function of the effective mass ratio for three distinct values of the core radius, a. Here, we fixed the shell and host effective mass to the DOS effective mass of PbTe at 80 K, $m^*_{out} = 0.053\ \mathrm{m}_0$ [20], where m_0 is the electron mass, and varied the core effective mass m^*_{in} to find the minimum barrier height. Larger core effective mass and larger core size results in lower bound state energy, so the minimum barrier height

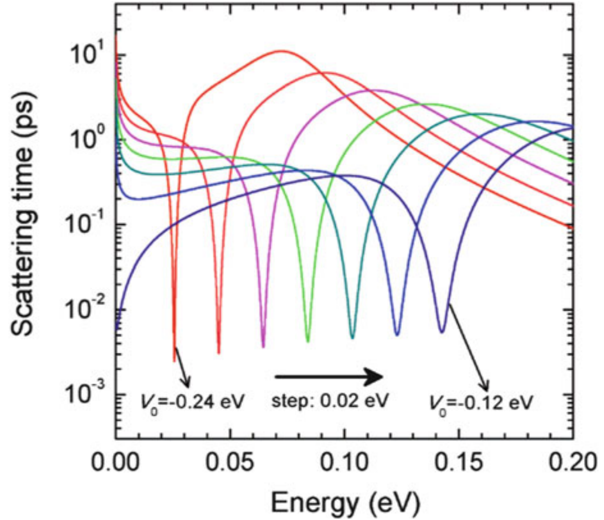

Fig. 2.15 Scattering time of 1×10^{18} cm^{-3} core–shell nanoparticles as a function of electron energy for varying well bottom in the core from $V_0 = -0.24$ eV to -0.12 eV with a step size of 0.02 eV. Other parameters of the core–shell nanoparticles are all assumed to be constants as $V_1 = 0.2$ eV, $a = 1.5$ nm, $b = 3$ nm, $m^*_{in} = 1.2\text{m}_0$, and $m^*_{out} = 0.053\text{m}_0$. (Figure from Ref. 12)

decreases as the effective mass ratio and the core size increase as shown in Fig. 2.14. For example, if one wants the core effective mass to be $10m^*_{out} = 0.53\, m_0$ and the core radius to be 1.5 nm, then we need to use the barrier height higher than 0.25 eV in order to have at least one bound state, according to Fig. 2.14. For finite barrier widths, the minimum barrier height resulting in a bound state is lower than the constraint obtained by (2.66), since the coupling of the quasi-bound state to the continuum lowers its energy.

The scattering properties of the core–shell nanoparticles are calculated using the partial wave method. Figure 2.15 shows the energy-dependent scattering times of the core–shell nanoparticles for varying well depth (V_0) calculated using the partial wave method. All the parameters for the core–shell nanoparticles are carefully chosen to have one quasi-bound state between the matrix conduction band minimum and the barrier height based on (2.66). We used 1.2 m_0 for the core effective mass, and 0.053 m_0 for the shell and host material. The size of the core radius a is chosen to be 1.5 nm, and the shell width ($b-a$) to be 1.5 nm as well. The barrier height V_1 is 0.2 eV, and the well bottom V_0 is varied to control the position of the quasi-bound state. For the core material, metals that have large effective masses around 1–1.2 m_0 can be used. The shell material can be an alloy of the host material with small stoichiometric difference so that the band offset is limited to 0.2 or 0.3 eV, and the effective mass remains similar to the host mass.

In Fig. 2.15, strong scattering dips are observed at the quasi-bound energy levels, which shift to higher energy as V_0 goes up. These sharp scattering dips are clear evidence of the strong resonance between free electrons and the quasi-bound state inside the core–shell nanoparticle. Near the resonance, the energy-dependence of the scattering rate is approximately Lorentzian [37]. The minimum of the resonant dip in scattering time is inversely proportional to the density of the core–shell nanoparticles. The width of the resonant dip comes from the homogeneous

broadening of the resonant level due to the finite lifetime of electron in the quasi-bound state. Electrons remain in the localized quasi-bound state for a certain amount of time, i.e., the state's lifetime, and are ejected out of the state with a randomized momentum. As the electron is confined in the state more weakly, i.e., by thinner and lower barriers, shallower well depth, and/or smaller core size, this lifetime decreases. By the energy–time uncertainty principle, the shorter lifetime in the state results in larger uncertainty of the energy level, and the resonance becomes wider.

The scattering time at energies far away from the resonant levels is determined predominantly by non-resonant scatterings of electrons, such as interface scattering at the potential boundaries. The presence of this additional non-resonant scattering is an important difference between core–shell nanoparticles and impurities that similarly lead to resonant scattering. The sharp potential boundary is associated with the scattering of high energy electrons through the Fourier transform in the Born approximation as described in Sect. 2.3.2. Moreover, since the range of the nanoparticle sizes of interest falls in the Rayleigh scattering regime, the scattering time monotonically decreases with increasing energy for the non-resonant scattering as shown at the energies far away from the resonant dips in Fig. 2.15. Note that another bound state with energy just below the host band edge may dominate over non-resonant scattering at low energies as when $V_0 = -0.12$ eV in Fig. 2.15. The non-resonant scattering rates vary slowly with energy, and diminish the slope of the energy-dependent scattering time at the shoulders of the resonance dips, thereby reducing their enhancement of the Seebeck coefficient. As a result, it is necessary to keep the non-resonant scattering weak with the barrier height sufficiently low (<0.3 eV in most cases) and the size of core–shell nanoparticles sufficiently small (a few nm) in order to gain a large Seebeck enhancement by resonant scattering. This provides a guideline for the selection of the constituent materials and their sizes.

The comparison of the differential scattering cross sections as a function of electron momentum in Fig. 2.16 reveals clear distinction between the resonant scattering and the Rayleigh-like non-resonant scattering. The non-resonant scattering has slowly varying differential scattering cross section with energy and angle. Electrons of greater energy are scattered more, and scattering is primarily by small angles. On the other hand, the resonant scattering is very strong only near the resonant level, and the electron is scattered both forward and backward with almost equal probability since the resonant state is sharply localized in real space.

2.4.2 Power Factor Enhancement in PbTe

Figure 2.17 shows the thermoelectric transport properties of PbTe embedded with the core–shell nanoparticles of 1×10^{18} cm^{-3} density at 80 K, calculated based on the Boltzmann transport theory under the relaxation time approximation described in Sect. 2.2. The core–shell nanoparticle scattering as well as other

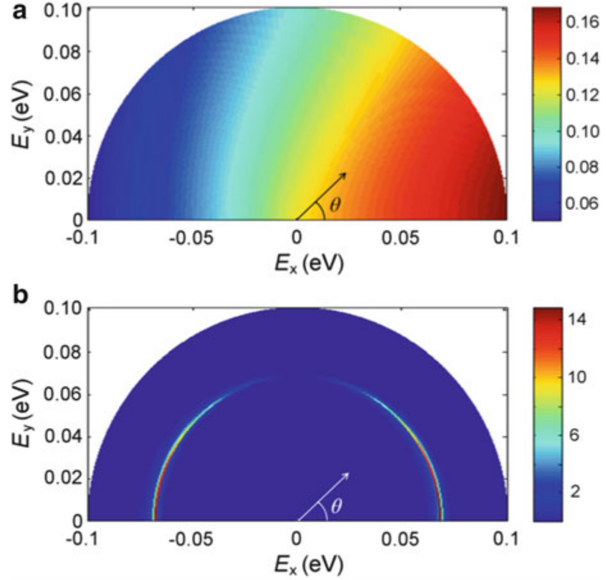

Fig. 2.16 Differential scattering cross section in units of πa^2 (cross section of core region) as a function of final electron momentum (polar angle and magnitude) for core–shell nanoparticles with (**a**) non-resonant scattering and (**b**) resonant scattering with resonant energy level at ~0.07 eV. The incident wave propagates to the + x-direction from left to right. (Figure from Ref. 12)

major scattering mechanisms in PbTe such as polar optical phonon scattering, nonpolar optical phonon and acoustic phonon deformation potential scatterings, alloy scattering, and the screened Coulomb impurity scattering are all included in the calculations using the band and scattering parameters given by the previous literature [20, 38, 39]. We have included the strong dielectric screening effect in the phonon scattering calculations for the IV-VI semiconductor [39]. A non-parabolic band model is used for the bulk PbTe. PbTe is selected as the host material because it has large power factors over a wide temperature range. In addition, the ionized impurity scattering rate in this material is negligibly small even for very high carrier densities, compared to phonon scattering, such that its mobility is relatively unchanged even with strong doping. These characteristics allow us to probe the effects of core–shell nanoparticle scattering over a wide range of doping densities without the need to make idealized assumptions about additional electron scattering processes.

As can be seen in Fig. 2.17c, the Seebeck coefficient sharply increases in a narrow carrier density range for the core–shell nanoparticle materials indicating more than a tenfold enhancement over the bulk value with the equivalent carrier density. As the carrier density is changed from low to high, the Fermi level increases in energy accordingly; when the Fermi level passes by the energy window in which the resonant scattering time has a sharp positive slope, i.e., at the high energy end of the resonant dip, the Seebeck coefficient is drastically enhanced. This is due to the highly selective carrier scattering which allows higher energy electrons to conduct better than lower energy ones, so that the average electron

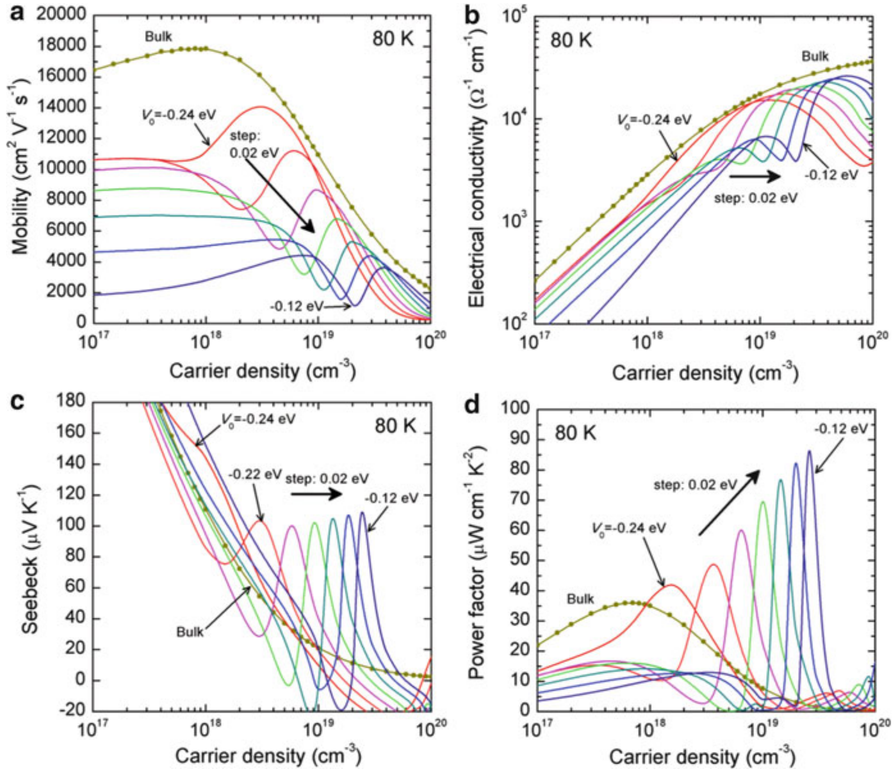

Fig. 2.17 (**a**) Mobility, (**b**) electrical conductivity, (**c**) Seebeck coefficient, and (**d**) power factor of PbTe with 1×10^{18} cm^{-3} embedded core–shell nanoparticles in comparison with bulk PbTe values as a function of carrier density at 80 K. (Figure from Ref. 12)

energy and thus the Seebeck coefficient are increased. This effect is less significant at higher temperatures because the energy distribution of electrons participating in electrical conduction is broader at higher temperatures, proportional to $k_B T$, according to the Fermi–Dirac distribution, so that a larger portion of electrons may not see the much sharper resonance and not benefit from the selective resonant carrier scattering at higher temperatures. In fact, the peak of the Seebeck coefficient in Fig. 2.17c slightly increases with V_0, indicating that further broadening could actually improve the material's power factor. As V_0 increases, the resonant level shifts up and broadens at the same time, so the maximum Seebeck coefficient may keep increasing with increasing V_0 until the broadening of the resonance exceeds the optimal width.

The mobility and the electrical conductivity are suppressed at the resonances due to the strong scattering. However, when the Fermi level is aligned properly at the high-energy shoulder of the resonance, the scattering time retains a large slope

which enhances the Seebeck coefficient, but the scattering time remains sufficiently high across the Fermi window to keep overall mobility high as well. This alignment maximizes the power factor as a function of doping. As shown in Fig. 2.17d, the power factor is enhanced to 65 μW/cmK^2 or higher when the well bottom V_0 is higher than −0.2 eV, which is a more than 80 % enhancement over the maximum bulk power factor 36 μW/cmK^2. The maximum power factor will keep increasing with increasing V_0 until the broadening of the resonance starts to decrease the Seebeck enhancement, or the suppression of mobility at the optimal carrier density outweighs the diminishing Seebeck enhancement.

2.4.3 Effect of Size Distribution

The size distribution of core–shell nanoparticles leads to inhomogeneous broadening of the resonance due to the variation in the resonant energy level. In general, the position of the resonant level is very sensitive to the core size a few nm in average. Figure 2.18 shows the inhomogeneous broadening of the resonant scattering time due to the size distribution. A Gaussian distribution is used for the core radius with a mean value of 1.5 nm and various standard deviations from 0.05 to 0.3 nm as shown in the inset in Fig. 2.18. The shell width $(b - a)$ is kept constant. Even with very small standard deviation of 0.05 nm, inhomogeneous broadening dominates and the FWHM (full width at half maximum) of the resonant dip increases approximately fivefold from 0.01 to 0.05 eV. As a result, the enhancement of the Seebeck coefficient is reduced due to the decreased slope of the broadened scattering time; accordingly the power factor is also reduced as shown in Fig. 2.19. With larger standard deviation of 0.1 and 0.3 nm, the sharp resonant dip almost disappears, and the non-resonant scattering of the nanoparticles result in a power factor worse than that of bulk PbTe. This implies that the core–shell resonant nanoparticles could work only when the size uniformity is very high. However, since the sensitivity of the resonance to the size variation can be largely varied depending on the selection of the materials and the potential profile, further study on the effect of size distribution is necessary.

If proper manipulation of size distribution with extreme sensitivity could be used to filter out the lower half side of the distribution, the power factor could be enhanced beyond that of a material with single-sized core–shell nanoparticles. As shown in Fig. 2.18, with half-Gaussian distribution, the scattering time becomes sharper and stays higher on the high-energy side of the resonance compared to the case of uniform single-sized nanoparticles so that both the Seebeck coefficient and the electrical conductivity can be enhanced further. This effect is related to the electron energy filtering effect, in which electrons having lower energies below the cutoff energy experience stronger resonant scattering by the core–shell nanoparticles, while higher-energy electrons are affected less. The electron energy filtering effect will be discussed in detail later in Sect. 2.5. As shown in Fig. 2.19, the maximum power factor by the half Gaussian distribution is obtained to be

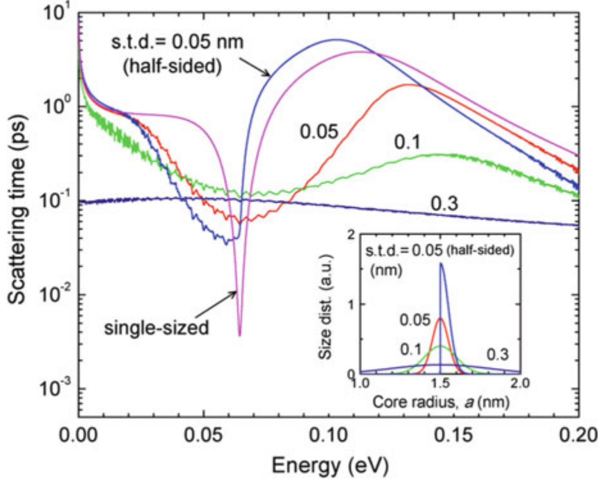

Fig. 2.18 Scattering time for various Gaussian size distributions of the core–shell nanoparticles with mean core radius of 1.5 nm with various standard deviations (s.t.d.) of 0 (single-sized), 0.05, 0.1, and 0.3 nm, and for a special half-Gaussian distribution with standard deviation of 0.05 nm, with the smaller half of the particles removed. All the size distributions are normalized with the total nanoparticle density of 1×10^{18} cm^{-3}. (*Inset*: the normalized size distributions are displayed.)

Fig. 2.19 Power factor of PbTe with core–shell nanoparticles with various size distributions from Fig. 2.18 as a function of carrier density in comparison with bulk PbTe values

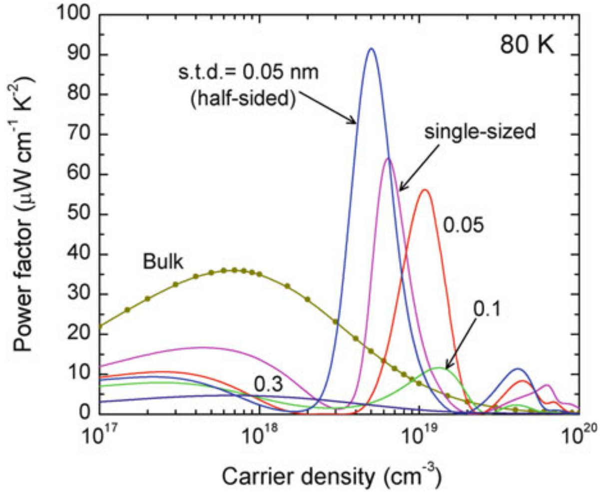

94 μW/cmK^2, which is a 160 % enhancement from the optimal bulk power factor 36 μW/cmK^2 at this temperature.

At room temperature, we obtain a 11 % power factor enhancement from the optimal bulk value of 35–39 μW/cmK^2 for 5×10^{18} cm^{-3} single-sized core–shell nanoparticles in PbTe with $V_0 = -0.1$ eV, $V_1 = 0.2$ eV, $a = 1.5$ nm, $b = 2.5$ nm, $m^*_{\text{in}} = 1.0\ \text{m}_0$, and $m^*_{\text{out}} = 0.079\ \text{m}_0$ (PbTe effective mass at 300 K). A shallower

potential well and a narrower shell width than those at 80 K are used in order to form a wider resonant dip in the energy-dependent scattering time, which is necessary for large Seebeck enhancement at higher temperatures because electrons are distributed over a wider energy range due to thermal excitation at higher temperatures. Also, a larger nanoparticle density is required in order to make resonant nanoparticle scattering the dominant scattering mechanism over phonon scattering, which is stronger at higher temperatures. This power factor enhancement at room temperature has not been fully optimized yet, and a systematic study on the effect of various conditions of the core–shell resonant scattering at high temperatures is necessary.

2.5 Electron Energy Filtering

The idea behind the electron energy filtering scheme is to increase the entropy transport per unit electric current flow by only allowing high-energy or hot electrons to transport while preventing low-energy or cold electrons from participating in the transport. The increased entropy transport results in the increase of Seebeck coefficient. A potential barrier is typically used to block cold electrons to realize the filtering effect, so the electrical conductivity can be reduced at the same time. Optimization of barrier height and carrier density is therefore necessary to maximize the power factor or the figure of merit.

The concept of electron energy filtering was originally proposed in thermionic energy conversion devices. In 1994, vacuum thermionic coolers that utilize a potential barrier between electrode and vacuum were proposed by Mahan [40]. The work function required for efficient cooling at room temperature in the thermionic device was, however, too small (0.3 ~ 0.4 eV) to be practically achieved. Shakouri and Bowers proposed in 1997 to use semiconductor heterostructures for the selective emission of hot electrons over a barrier layer to enhance the cooling performance [41]. By controlling the band offsets in heterostructures, the barrier height was optimized to achieve high cooling power density in the nonlinear thermionic transport regime. Later, Shakouri et al. proposed that tall barrier, highly degenerate multilayers could achieve thermoelectric power factors an order of magnitude higher than bulk values [42].

In the case of electron transport perpendicular to planar barriers, the lateral momentum component is conserved during transport over the barriers analogous to the light refraction in multilayers. This is called lateral momentum conservation. The transverse momentum component needs to be larger than a certain value determined by conduction band offset for the electron to go over the potential barrier. Vashaee and Shakouri [43] found that the key requirement for a large thermoelectric power factor enhancement in planar barrier materials is that the lateral momentum conservation is relaxed, such that the momentum criterion for the transport at the interfaces is replaced by the energy criterion depicting that most of the electrons having energies greater than the cutoff energy are allowed to

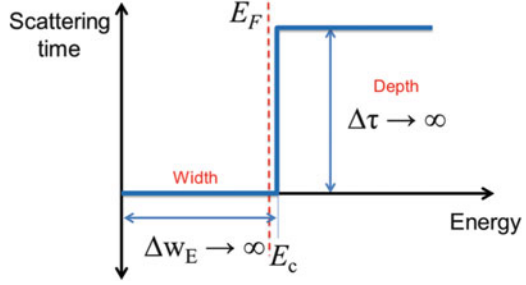

Fig. 2.20 Ideal energy-dependent scattering time for the nonplanar electron energy filtering

participate in transport over the barrier. This lateral momentum non-conservation allows a much larger number of hot electrons to participate in the emission process, so that the suppression of electrical conductivity by barriers is significantly alleviated while a large enhancement of the Seebeck coefficient by hot electron filtering is still achieved. However, Kim et al. [44] recently found that the enhancement in emission current due to the lateral momentum nonconservation could be modest because the smallest number of modes in the well and barrier layers limits the emission current.

Due to these complications in the planar carrier filtering scheme, it is desired to realize a nonplanar carrier energy filtering without extended planar potential barriers, but instead with embedded discrete nanoparticles or impurities. In the latter case, the lateral momentum is not conserved since there is no translational invariance, and thus the power factor can be enhanced in bulk materials.

Figure 2.20 presents an ideal energy-dependent scattering time for the realization of nonplanar electron energy filtering. The scattering time is only a function of energy, independent of the direction of electron momentum, if the scatterers are spherically symmetric in their shape and potential profile. Below a certain energy called the cutoff energy E_C that is slightly above the Fermi level, the scattering time is zero, or the scattering rate is infinitely large, in an ideal case, so that the carriers below the cut-off energy are completely blocked from participating in conduction. The width of the scattering region below the cut-off energy must be sufficiently large, or at least larger than the half width of the Fermi window. Above the cutoff energy, it is ideal that there is no additional scattering other than those that exist naturally in the bulk material such as phonon scatterings.

In this section, we discuss a general theory on electron energy filtering with a cutoff energy in the Boltzmann transport theory under the relaxation time approximation for bulk materials. Power factor enhancement by the electron filtering with an optimal cutoff energy is obtained as a function of the scattering parameter, Fermi level, and temperature. Variations of the electronic thermal conductivity, Lorenz number, and the Hall factor by the filtering effect are also discussed and quantified as functions of the aforementioned parameters. Then the proposed theory is applied to real TE material, PbTe and Mg_2Si, with non-parabolic bands and realistic energy-dependent scattering times taken into account. Later in Sect. 2.5.5, the use of distributed resonant scatterings in Lorentzian shapes is discussed to partially realize the nonplanar electron energy filtering in bulk materials.

2.5.1 Electron Transport with a Cutoff Energy

In an ideal case of nonplanar energy filtering, the modeling of carrier transport becomes simply having a cutoff energy level in the bulk transport calculations, below which all the electrons are completely blocked from participating in conduction. With a cutoff energy level, E_C, the calculations of the transport properties are reduced to the integrals over energy from E_C to infinity such that,

$$\sigma = \int_{E_C}^{\infty} \sigma_d(E) dE, \tag{2.68}$$

$$S = -\frac{1}{eT} \frac{\int_{E_C}^{\infty} \sigma_d(E)(E - E_F) dE}{\int_{E_C}^{\infty} \sigma_d(E) dE}. \tag{2.69}$$

For a parabolic band and $\tau(E) = \tau_0 E^r$, where τ_0 is a constant, and r is called the scattering parameter, (2.68) and (2.69) can be simplified as

$$\sigma = C_1 F_0(E_C), \tag{2.70}$$

$$S = C_2 \left[\frac{F_1(E_C)}{F_0(E_C)} - E_F \right], \tag{2.71}$$

and thus the power factor becomes

$$S^2\sigma = C_1 C_2^2 \frac{[F_1(E_C) - E_F F_0(E_C)]^2}{F_0(E_C)} \tag{2.72}$$

where $C_1 = 2^{3/2} e^2 (m^*)^{1/2} \tau_0 / (3\pi^2 \hbar^3)$ and $C_2 = 1/(eT)$ are all constants, and

$$\begin{aligned} F_s(E_C) &= \int_{E_C}^{\infty} E^{\frac{3}{2}+r+s} \left(-\frac{\partial f_0}{\partial E} \right) dE, \\ &= \left(\frac{3}{2} + r + s \right) \int_{E_C}^{\infty} E^{\frac{1}{2}+r+s} f_0(E) dE + E_C^{\frac{3}{2}+r+s} f_0(E_C), \end{aligned} \tag{2.73}$$

with $s = 0$, 1, or 2. Note that the first term in the second line of (2.73) is an incomplete Fermi–Dirac integral of the order of (½ + r + s).

The scattering parameter r manifests the dominant scattering mechanism in a material. For example, r is -0.5 for the acoustic phonon deformation potential scattering, $r = 1.5$ for the ionized impurity scattering, and $r \approx 0.5$ for the polar

optical phonon scattering. In general, more than a single scattering mechanism are combined together to make the total scattering time. For most semiconductors, r is not a constant, but dependent on energy and temperature, typically ranging from -0.5 to 0.5. Therefore, the constant scattering parameter assumption may not be valid for wide ranges of carrier density and temperature.

The electronic thermal conductivity with a cutoff energy is given by

$$\kappa_e = \frac{C_1}{e^2 T}\left[F_2(E_C) - \frac{[F_1(E_C)]^2}{F_0(E_C)}\right]. \tag{2.74}$$

The electronic thermal conductivity is related to the electrical conductivity via the Lorenz number L by the Wiedemann-Franz law, which is defined as

$$L = \frac{\kappa_e}{\sigma T}. \tag{2.75}$$

Thus, from (2.70) and (2.74), (2.75) becomes

$$L = \frac{1}{e^2 T^2}\left[\frac{F_2(E_C)}{F_0(E_C)} - \left(\frac{F_1(E_C)}{F_0(E_C)}\right)^2\right]. \tag{2.76}$$

The Lorenz number is a function of E_F, although it becomes a constant to be $L_0 = (\pi k_B)^2/(3e^2) \approx 2.44 \times 10^{-8}$ W Ω K^{-2} for metals or in the degenerate limit ($E_F >> 0$) in the bulk ($E_C = 0$). L deviates from L_0, monotonically decreasing, as E_F goes down, or the carrier density decreases in semiconductors. Also the Lorenz number monotonically decreases with increasing E_C, and saturates as E_C goes very high for a given E_F. More details about this are discussed in Sect. 2.5.3.

The Hall effect measurements can be used to obtain the effective carrier density n_e by measuring the Hall coefficient R_H in the case of one-type carrier transport from [45]

$$R_H = \alpha \frac{1}{n_e q}, \tag{2.77}$$

where α is the Hall factor, and q is $-e$ for electrons, and + e for holes. The Hall factor is given by [46]

$$\alpha = \frac{<\tau^2>}{<\tau>^2} = \frac{{F_0}^{r=2r}(E_C){F_0}^{r=0}(E_C)}{[F_0(E_C)]^2}, \tag{2.78}$$

where ${F_0}^{r=2r}(E_C)$ and ${F_0}^{r=0}(E_C)$ are $F_0(E_C)$ defined by (2.73) with $s = 0$, but with r replaced by $2r$, and 0, respectively. The Hall factor is close to unity for the materials with $-0.5 \leq r \leq 0.5$. The effective carrier density measured by the Hall

effect measurements does not include the carriers below the cutoff energy because their overall displacement becomes zero by the cutoff. Thus,

$$n_{\mathrm{e}} = \int_{E_{\mathrm{C}}}^{\infty} \rho_{\mathrm{DOS}}(E) f_0(E) dE, \tag{2.79}$$

which decreases with increasing E_{C}.

In nonideal or practical cases of the energy filtering, the modeling can be more complicated than just having a cutoff energy in the transport calculations. For example, nonplanar potentials created by embedded nanoparticles or impurities of various kinds in a bulk material can be used to modify the transport of charge carriers via energy-dependent scattering times to realize the energy filtering. If these additional energy-dependent scatterings by nanoparticles or impurities are exclusively targeted at the carriers in a specific energy region only, those carriers can be effectively prevented from participating in conduction by the extensive scatterings while others are not affected and allowed to transport, so the energy filtering is realized. In such non-ideal filtering cases, the carriers under strong scatterings may not be completely filtered out of the transport. Instead, their mobilities are slowed down drastically by the extensive scatterings, so that their contribution to transport is significantly reduced compared to those of relatively unaffected higher-energy carriers. Hence the filtering is partially realized. It is noted that in this case, the Hall effect measurements may not thoroughly exclude those carriers under strong scatterings in the measurement of carrier density because their mobilities are not completely zero. Rather, it is possible that the measured carrier density can remain the same as before the filtering effect is included.

2.5.2 Power Factor Enhancement

Figure 2.21 shows the enhancement of power factor by the electron energy filtering as a function of cutoff energy. The Seebeck coefficient monotonically increases with the cutoff energy, while the electrical conductivity monotonically decreases. Due to this trade off, the power factor has a maximum, which is about 250 % larger than the bulk value, when the cutoff is at 0.135 eV in the case of Fig. 2.21.

The optimal cutoff energy, $E_{\mathrm{C,opt}}$, that maximizes the power factor for a given Fermi level, scattering parameter, and temperature can be found by differentiating (2.72) with respect to E_{C} and matching the derivative to zero, which reduces simply to [14]

$$F_1\left(E_{\mathrm{C,opt}}\right)/F_0\left(E_{\mathrm{C,opt}}\right) = 2E_{\mathrm{C,opt}} - E_{\mathrm{F}}. \tag{2.80}$$

Although one can obtain this optimal cutoff energy by numerically solving (2.80) under various conditions, in general the optimal cutoff energy is about one

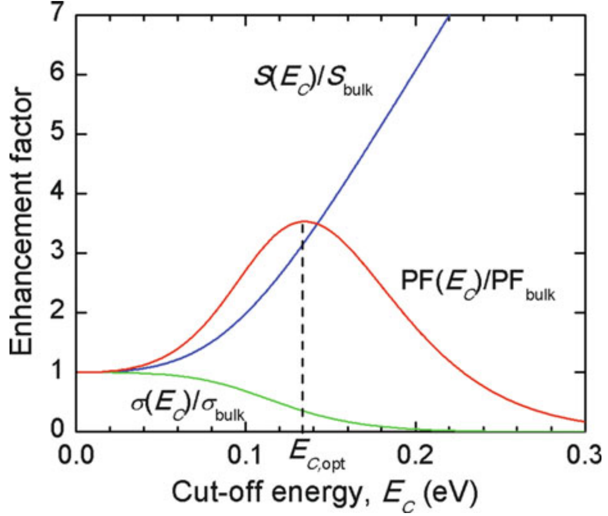

Fig. 2.21 Enhancement factors of Seebeck coefficient (S), electrical conductivity (σ), and power factor (PF) over their bulk counterparts as a function of cutoff energy. $E_F = 0.1$ eV, $r = -0.5$ and $T = 300$ K

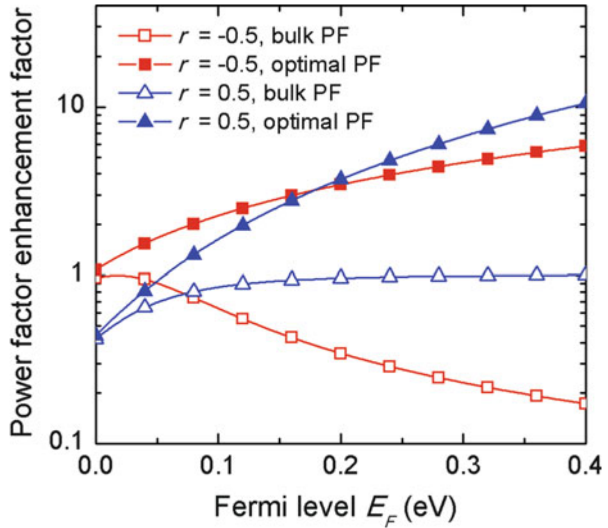

Fig. 2.22 Enhancement of power factor by optimal filtering as a function of Fermi level for scattering parameter $r = -0.5$ and 0.5 at 300 K. All the power factor values are normalized to the maximum bulk value for each r

or two k_BT higher than the Fermi level, depending on the temperature and the scattering parameter.

Figure 2.22 shows the enhancement of power factor by the optimal electron filtering as a function of Fermi level for scattering parameters, $r = -0.5$ and 0.5, at 300 K. For the calculation of the optimal power factors, the optimal cutoff energy obtained from (2.80) for each Fermi level was applied, while no cutoff was assumed for the bulk power factor, i.e., $E_C = 0$. The optimal power factor increases almost linearly with Fermi level for $r = -0.5$, and achieves a factor of 3.5 enhancement

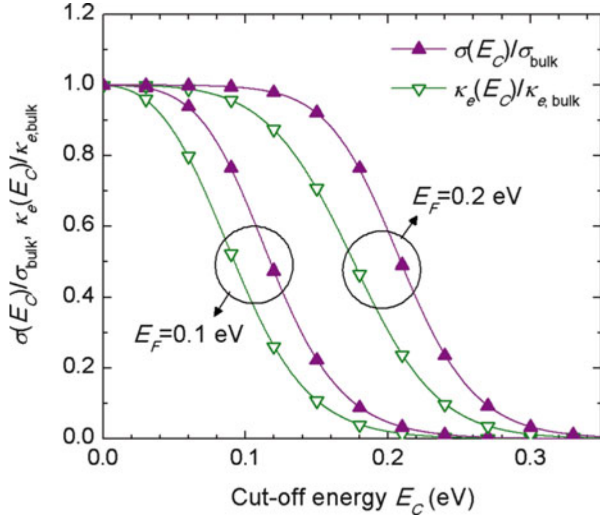

Fig. 2.23 Reduction of the electrical conductivity (σ) and the electronic thermal conductivity (κ_e) from their bulk counterparts by energy filtering as a function of cutoff energy for Fermi level $E_F = 0.1$ and 0.2 eV, and scattering parameter $r = -0.5$ at 300 K

over the maximum bulk value at the Fermi level ~ 0.2 eV, and a factor of 6 enhancement at the Fermi level ~ 0.4 eV. The optimal power factor increases with Fermi level for $r = 0.5$ as well, but at a slower rate than for $r = -0.5$ at the low Fermi level region due to the smaller bulk values. However, as the Fermi level goes further up, the increasing rate for $r = 0.5$ becomes faster than that for $r = -0.5$, and achieves a factor of 10 enhancement over the maximum bulk value at the Fermi level ~ 0.4 eV. In general, a material with a lower scattering parameter can achieve a larger power factor enhancement in the low Fermi level region by the optimal energy filtering condition, but if the Fermi level is high enough, a larger power factor enhancement is possible for a higher scattering parameter material.

Seebeck enhancement factor by optimal filtering is approximately proportional to $1/T$ for a fixed Fermi level. This indicates that the effect of the electron filtering on power factor becomes weaker at higher temperatures, following ~$1/T$.

2.5.3 Electronic Thermal Conductivity, Lorenz Number, and Figure of Merit

Electronic thermal conductivity is lowered from its bulk value by electron energy filtering since the carrier density contributing to the thermal conduction is reduced, similarly as the electrical conductivity is reduced by the filtering. Figure 2.23 shows the electrical conductivity and the electronic thermal conductivity normalized to their bulk values as a function of cutoff energy for $r = -0.5$ at 300 K. It is clearly seen that the electronic thermal conductivity decreases more rapidly than the

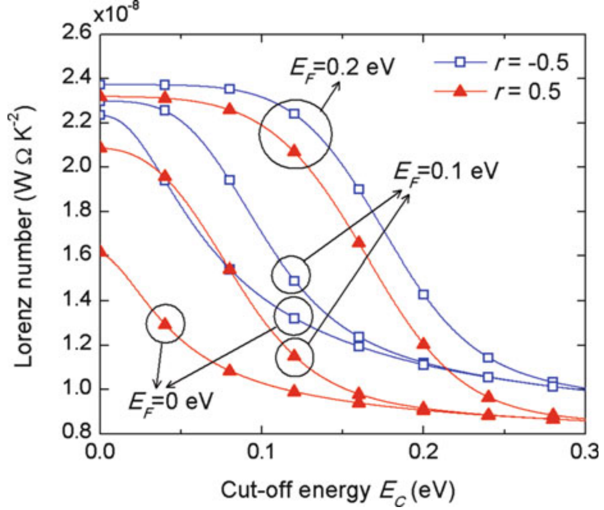

Fig. 2.24 Lorenz number as a function of cutoff energy for Fermi level $E_F = 0$, 0.1 and 0.2 eV, and scattering parameter $r = -0.5$ and 0.5 at 300 K

electrical conductivity does as E_C increases. At the optimal cutoff ($E_{C,opt} = 0.23$ eV) for $E_F = 0.2$ eV, κ_e is merely a 13 % of the bulk value, while σ becomes a 30 % of the bulk value. The Lorenz number has been reduced to a 43 % of the bulk value in this case, which accounts for the difference between the reduction factors of κ_e and σ such that (13 %) = (30 %) × (43 %).

Figure 2.24 shows the Lorenz number given by (2.76) as a function of cutoff energy for two different scattering parameter $r = -0.5$ and 0.5, and two different Fermi levels, $E_F = 0$, 0.1, and 0.2 eV, at 300 K. Lorenz number rapidly decreases when the cutoff energy falls into the range of the Fermi window around the Fermi level. When E_C goes much higher than the Fermi level, the variation of Lorenz number with E_C becomes small, and L saturates to a certain value that depends on the scattering parameter. At higher temperatures, the high cutoff energy limit of Lorenz number slightly increases.

At the optimal cutoff, Lorenz number already becomes significantly lower than the bulk value. As shown in Fig. 2.24, $L = 1.0 \times 10^{-8}$ W Ω K^{-2} when the optimal cutoff energy level $E_{C,opt} = 0.23$ eV is used for $E_F = 0.2$ eV and $r = -0.5$ at 300 K, which is about 43 % of the bulk value, 2.3×10^{-8} W Ω K^{-2}. At 600 K, this Lorenz number at optimal cutoff slightly increases to 1.06×10^{-8} W Ω K^{-2} with $E_{C,opt} = 0.27$ eV, which is about 49 % lower than the bulk value, 2.09×10^{-8} W Ω K^{-2}.

Since the electronic thermal conductivity is suppressed significantly by the optimal filtering to about a 10–20 % of the bulk value, the lattice thermal conductivity can dominate the total thermal conductivity in most cases when the optimal cutoff is applied. In this case, the total thermal conductivity in the denominator of *ZT* becomes almost a constant, and thus the optimal cutoff energy that maximizes the power factor also becomes optimal for maximizing *ZT*. However, it is still possible that the electronic thermal conductivity dominates over the lattice one in

those materials in which the lattice thermal conductivity is enormously suppressed by effective phonon scatterings by nanostructuring. In this case, since the electronic thermal conductivity decreases more rapidly than the electrical conductivity with increasing cutoff energy level, *ZT* will keep increasing as the cutoff energy further increases. Then, the upper limit of *ZT* will be determined when the lattice thermal conductivity limits the decreasing rate of the total thermal conductivity with E_C to be slower than that of the power factor.

2.5.4 Electron Energy Filtering in PbTe and Mg_2Si

A very large *ZT*, greater than 3, can be possible when an appropriate cutoff energy is realized in a good TE material such as PbTe and Mg_2Si. The enhancement comes from two sides: a large enhancement of Seebeck coefficient, and a large reduction of electronic thermal conductivity. Recent advances in material synthesis and growth techniques have enabled the synthesis of novel nanostructured materials with great precision and controllability in their thermoelectric properties. Significant reduction of lattice thermal conductivity has been achieved in these nanostructured materials without much sacrifice in the electron transport part, the power factor from their bulk counterparts, thereby enhancing *ZT* greatly. Recently, the spark-plasma-sintered p-type Na-doped PbTe:SrTe nanocomposites achieved a *ZT* ~ 2.2 at 915 K with a significant reduction of lattice thermal conductivity down to 0.5–0.6 W/mK at the high temperature with comparable power factors with bulk PbTe [47]. A n-type Mg2Si was alloyed with Sn to form natural nanostructures, which reduced the lattice thermal conductivity down to 1 W/mK, in conjunction with the enhanced power factor by the band convergence to achieve a *ZT* ~ 1.3 at 700 K [8].

In this section, we attempt to predict a further enhancement of *ZT* in these two materials, PbTe and Mg_2Si by incorporating the carrier energy filtering effect. First, we modeled complicated band structures of these bulk materials with multiple non-parabolic bands to precisely simulate their bulk properties such as the Seebeck coefficient and electrical conductivity. We have successfully matched the previously reported experimental data with our theoretical model for various compositions and doping densities over a wide temperature range. For PbTe, both n-type and p-type bulk properties were fitted successfully from 300 to 900 K based on the experimental data reported in Refs. [20, 38, 39, 47]. For n- and p-type Mg_2Si and its alloys with Sn, the experimental data from Refs. [8, 48–51] and others were fitted successfully with our model.

Figure 2.25 shows the resulting *ZT* enhancement as a function of doping density in p-type PbTe at 900 K by the carrier energy filtering with optimized cutoff energies at each doping density. A lattice thermal conductivity of 0.5 W/mK is assumed and fixed in this calculation, which is adapted from Ref. 46. The bulk *ZT* of p-type PbTe can reach 2.0 at 2×10^{20} cm^{-3} doping density. With the optimized filtering, the *ZT* can be enhanced beyond 4.0 at doping densities higher than

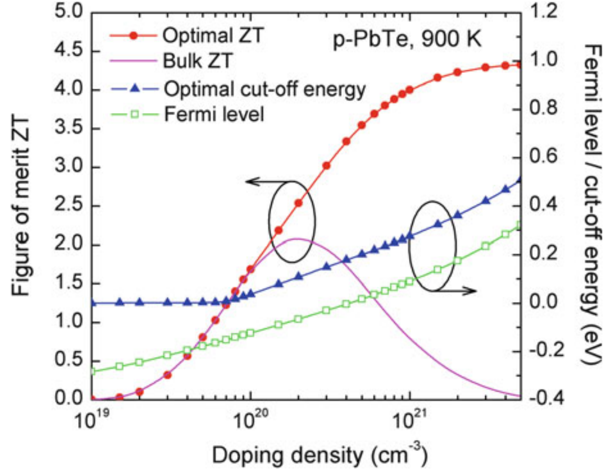

Fig. 2.25 Figure of merit *ZT* by the optimal filtering (*left y*-axis), the Fermi level, and the optimal cutoff energy (*right y*-axis) as a function of doping density in p-type PbTe at 900 K

1×10^{21} cm^{-3}. The optimal cutoff energy as a function of doping density is given in Fig. 2.25 as well. The optimal cutoff energy that maximizes *ZT* at the doping densities is about 0.19 eV higher than the Fermi level of each doping density, which is slightly higher than the optimal cutoff energy that maximizes the power factor obtained from (2.80). This is because by further increasing the cutoff energy level, the electronic thermal conductivity is further reduced, so that even with a slightly sacrifice of the enhancement of power factor, *ZT* was enhanced more. More details about the effect of the optimal cutoff energy on the Seebeck coefficient, the electrical conductivity, and the electronic thermal conductivity are shown in Fig. 2.26.

As shown in Fig. 2.26a, the Seebeck coefficient is greatly enhanced over the bulk value at a given doping density, and maintained as high as 300 μV/K at very high doping densities by the optimal filtering. The electrical conductivity is suppressed significantly at the same time by the filtering, but the power factor remains higher than the bulk value due to the greater enhancement of Seebeck coefficient than the reduction of the electrical conductivity as shown in Fig. 2.26b. At this high temperature, 900 K, the electronic thermal conductivity rapidly increases with doping density. The bipolar electronic thermal conductivity is also very high at the high temperature, and dominant at low doping density region below 1×10^{20} cm^{-3}. Thus, the minimum electronic thermal conductivity including the bipolar term was estimated to be 0.74 W/mK for p-type PbTe at 900 K. This high electronic thermal conductivity becomes a limiting factor that prevents the *ZT* of this material from further enhancing. The optimal filtering can tackle this problem, and suppress the electronic thermal conductivity as low as 0.3 W/mK at high doping densities. In combination of the power factor enhancement, *ZT* can be enhanced beyond 4 with cutoff energies higher than 0.4 eV at doping densities higher than 1×10^{21} cm^{-3} as shown in Fig. 2.25.

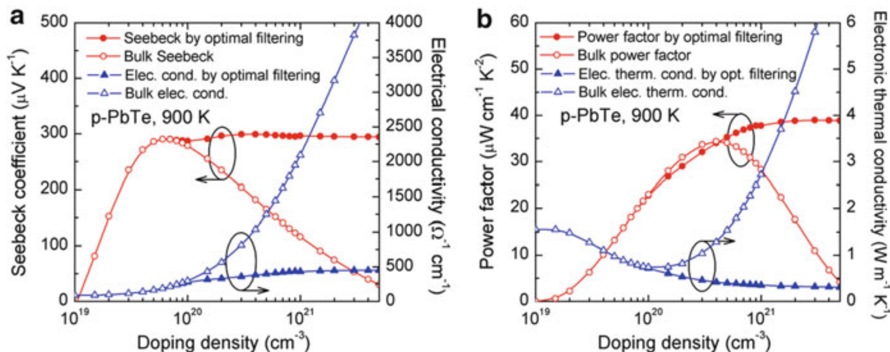

Fig. 2.26 (**a**) Seebeck coefficient (*left* *y*-axis) and electrical conductivity (*right* *y*-axis), (**b**) power factor (*left* *y*-axis) and electronic thermal conductivity (*right* *y*-axis) as a function of doping density by the optimal carrier energy filtering that maximizes *ZT* at each doping density in p-type PbTe at 900 K

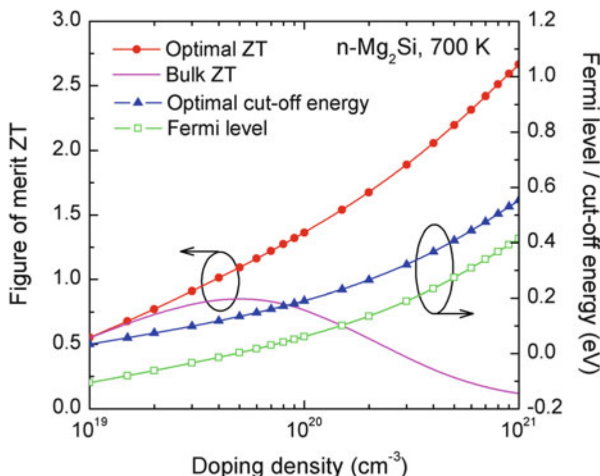

Fig. 2.27 Figure of merit *ZT* by the optimal filtering (*left* *y*-axis), the Fermi level and the optimal cutoff energy (*right* *y*-axis) as a function of doping density in n-type Mg_2Si at 700 K

Similarly, the electron filtering can be applied to n-type Mg_2Si to enhance the *ZT*. The bulk Mg_2Si can reach $ZT \sim 0.8$ at 5×10^{19} cm^{-3} doping density at 700 K if the lattice thermal conductivity of 1.2 W/mK is used at this temperature. By the optimal cutoff energy, this *ZT* can be greatly enhanced beyond 2.0 at doping densities higher than 4×10^{20} cm^{-3} at 700 K as shown in Fig. 2.27. The optimal cutoff energy is found to be about 0.14 eV higher than the Fermi level at each doping density of the range, which is again, higher than the optimal cutoff energy that maximizes the power factor, in order to utilize the further reduced electronic thermal conductivity.

The detailed effects of the optimal filtering on the Seebeck coefficient, electrical conductivity, and electronic thermal conductivity are presented in Fig. 2.28.

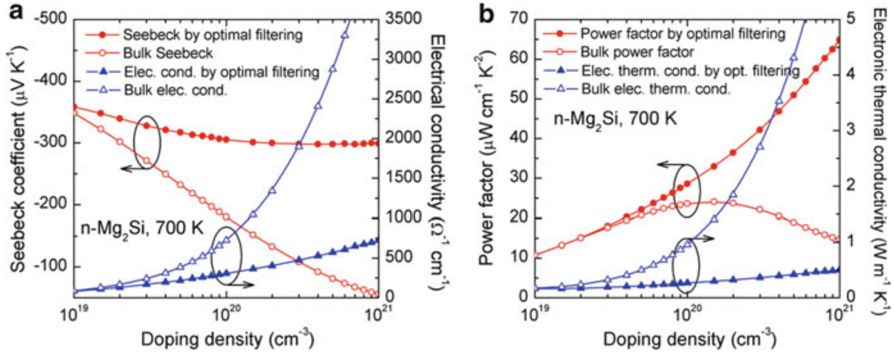

Fig. 2.28 (**a**) Seebeck coefficient (*left y*-axis) and electrical conductivity (*right y*-axis), (**b**) power factor (*left y*-axis) and electronic thermal conductivity (*right y*-axis) as a function of doping density by the optimal carrier energy filtering that maximizes *ZT* at each doping density in n-type Mg_2Si at 700 K

The Seebeck coefficient was greatly enhanced over the bulk value at each doping density and maintained as high as −300 μV/K by the optimal electron energy filtering. The reduction of the electrical conductivity was relatively small, so that the power factor was significantly enhanced over the maximum bulk value, 24 $\mu W/cmK^2$ at high doping densities. The electronic thermal conductivity was significantly reduced down to 0.5 W/mK. As a result, *ZT* could be enhanced beyond 2.0 at this temperature for n-type Mg_2Si. It is expected that a higher *ZT* can be achieved for $Mg_2Si_{1-x}Sn_x$ alloys since their bulk power factor is higher than the binary Mg_2Si, and the lattice thermal conductivity is lower with additional phonon alloy scattering.

2.5.5 *Realization of Nonplanar Electron Filtering*

Now, we turn to a basic and important question: how can we realize the electron energy filtering practically in the materials? One possible way of suppressing electron transport within a certain energy range to realize the desired energy-dependent scattering time shown in Fig. 2.20 is to put an extensive amount of scatterings in that particular energy range, so that electrons experience very slow mobility within the energy region and thus are predominantly prevented from contributing to conduction. Scatterings cannot completely block the electron transport in reality because they cannot be infinitely strong. But a sufficient selectivity in energy can mimic the ideal filtering. Another important requirement for electron filtering is a sharp cutoff in energy selection. Since most of the electrons that participate in conduction are near the Fermi level, only a very sharp edge near the Fermi level in transport can effectively achieve strong energy selection and thus significant Seebeck enhancement.

A single-phase nanoparticle can have a potential offset at the hetero-interface with the host material, which can act as a barrier to filter out electrons having energies below the barrier height. However, this filtering by a 3D step potential does not sharply select electron energy, because the electrons having higher energies than the barrier height are still affected by the existence of the barrier due to the wave nature of electron. Thus, the filtering is not completely on or off, but continuously and slowly modifies the transport. Also, if the nanoparticles are very small, i.e., a few nm in diameter, much smaller than the wavelengths of electrons, then electrons may not be affected much by the potential of the nanoparticle even if their energies are below the barrier height, because the scattering is in Rayleigh regime [11]. That said, an appropriate requirement for sufficient energy filtering by a 3D potential barrier is that the size of the nanoparticle is sufficiently large, typically a few tens nm. However, the nanoparticle cannot be too large, because then the quantum mechanical interaction between the particle and electron becomes negligibly small, and the tranport is bulk-like in the effective composite medium. In fact, Bergman and Levy [52] showed that the effective *ZT* of a composite can never exceed the largest *ZT* value of its components.

One can find energetically sharp scattering times from resonances. The core–shell structured nanoparticles discussed in Sect. 2.4 can have sharp resonant scattering times at the quasi-bound energy states formed inside the core region. The width and position of the resonant scattering dip can be controlled by the well depth in the core region. However, the existence of non-resonant scatterings by potential offsets at the hetero-interfaces can limit the depth of the scattering dip relative to the background level of scattering time near the dip.

A very deep and narrow resonant scattering time can be obtained by resonant impurities. In the 1950s, Friedel found that transition metal impurities can induce a sharp increase of resistivity in a small energy region by their resonant electron scattering [53]. Group III elements such as Tl, and group IV elements such as Sn have also been found to create resonant levels in the band structures of IV–VI semiconductors [54], and Bi_2Te_3 [55], respectively. More thorough review on resonant impurities is found in Ref. [56].

Since the impurities have infinitesimally small sizes, there is no additional non-resonant scattering by potential offsets in contrast to the core–shell nanoparticles, and thus the scattering time can be approximated by the bell-shaped Lorentzian function given by [37]

$$\tau_{\mathrm{res}}(E) = \tau_{0,\mathrm{res}}\left[1 + \left(\frac{E - E_{\mathrm{res}}}{\gamma_{\mathrm{res}}/2}\right)^2\right], \tag{2.81}$$

where E_{res} is the resonant energy level of the impurity, γ_{res} is the full width at half maximum (FWHM) of the resonance, and $\tau_{0,\mathrm{res}}$ is the minimum scattering time reached at $E = E_{\mathrm{res}}$. The parameter $\tau_{0,\mathrm{res}}$ is inversely proportional to the concentration of the resonant impurities. This sharp and deep resonant impurity scattering is a good candidate for creating a sharp cutoff edge near the Fermi level. Also, if

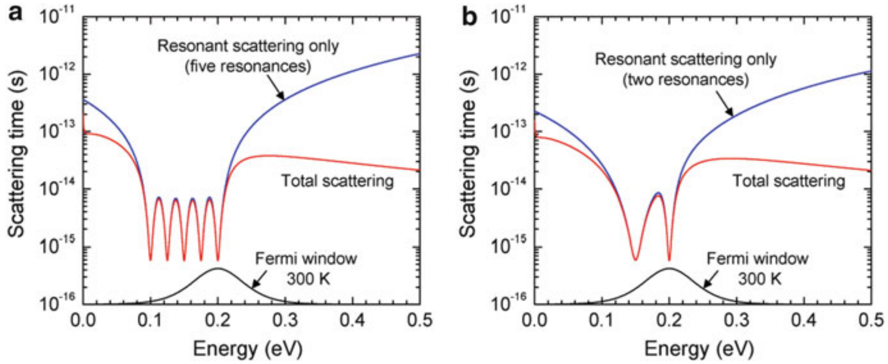

Fig. 2.29 Examples of using distributed resonant scatterings as a means to realize the electron energy filtering by suppressing electron transport in the left half of the Fermi window at 300 K, with (**a**) five resonances and (**b**) two resonances. The total scattering curves includes all other relevant scattering times such as phonon scatterings in PbTe. (Figure from Ref. 14)

different kinds of resonant impurities with different resonant energy levels are put together with appropriate depths and widths and distributed in energy at appropriate positions in a bulk material, a suppression of electron transport over a wide energy range along with a sharp cutoff is possible. A single sharp resonant dip may not be effective in modifying the transport at room temperature or higher, because its width in energy is typically much narrower than that of the Fermi window at high temperatures, so that the major portion of the distribution of conducting electrons is not affected by the resonance. By using multiple resonant dips distributed in energy that cover the half width of the Fermi window, the most of the conducting electrons distributed in the lower-energy half of the Fermi window below the Fermi level could be filtered out to enhance the power factor at high temperatures.

In Fig. 2.29, we show two examples of using distributed resonant scatterings as a means to partially realize the electron filtering. With five 5 meV wide resonances evenly spaced between 0.1 and 0.2 eV as shown in Fig. 2.29a, most of the low-energy half of the Fermi window at 300 K can be effectively covered to suppress electron transport in that energy range. There are local peaks of scattering time between the resonances where the scattering time is much higher than the minimum, such that electron filtering is weak there. In addition, using only two resonances, partial electron filtering is possible as shown in Fig. 2.29b. In this case, the first resonance at the lower energy region can be wider ($\gamma = 15$ meV) than the second resonance at the higher energy region ($\gamma = 5$ meV). The spacing between the two is selected to be larger (50 meV) than that in the case of five resonances (25 meV) to cover as much space as possible with a fewer number of resonances.

Figure 2.30 shows the resulting power factor in n-type PbTe at 300 K for the two cases of distributed resonant scatterings described in Fig. 2.29 in comparison with an ideal electron filtering with a fixed cutoff at 0.2 eV, and with the bulk values. Large enhancements of power factor are achieved using these distributed resonant

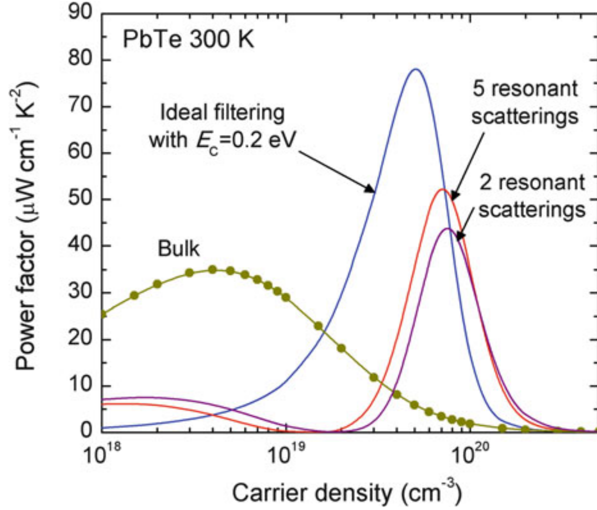

Fig. 2.30 Power factor enhancement in n-type PbTe at 300 K as a function of carrier density for the two cases of distributed resonant scatterings described in Fig. 2.29. For comparison, the properties by an ideal electron filtering with a 0.2 eV cut off, and the bulk values (curve with *filled circles*) are also presented. (Figure from Ref. 14)

scatterings, mainly due to the enhancement of the Seebeck coefficients. However, these enhancements are lower than the enhancement obtained by ideal electron filtering with a similar cutoff energy at 0.2 eV. This is due to the incomplete suppression of electron transport below the cutoff energy by the resonant scatterings, in particular, at the local peaks of scattering time between the resonances. These uncovered energy regions are wider when a smaller number of resonant scatterings are used. As a result, the power factor enhancement can be lower for a smaller number of resonant scatterings. The Fermi window is wider at higher temperature, proportional to T. Hence, a larger number of wider resonant scatterings might be needed to sufficiently cover the lower-energy half of the Fermi window at higher temperatures.

One important note is; if the scattering spectrum is significantly modified to form a band pass or stop, the density of states and dispersion curves can be modified as well. For example, Heremans et al. [9] used a 2 % atomic fraction of Tl impurities in PbTe to enhance the power factor by the modification of the density of states. In order to utilize the resonant scatterings without a significant modification of the band structure, one may need to use a lower amount of impurities than 2 %. When the density of states is modified, the local effective mass at the energy region is also increased, which in turn, may, simultaneously, reduce the mobility and electrical conductivity. Thus, special care might be necessary to achieve a large power factor enhancement at high impurity concentrations.

In addition, the resonant scatterings must be sufficiently stronger than the phonon scatterings to be effectively used at high temperatures. The strength of phonon scatterings increases with temperature as there are increased numbers of phonons at higher temperatures. The main reason that the effect of resonant scatterings was negligibly small at high temperatures is that they are much weaker than the phonon scatterings at the elevated temperatures. Increasing the strength of

resonant scattering may be possible by increasing the number of resonant centers. The amount of impurities to be used must be experimentally determined to be effective at the target temperature, and the effect of the modification of band structure by extensive amount of impurities must also be carefully considered for the realization of the carrier energy filtering.

2.6 Summary and Outlook

In this chapter, we have discussed various nanostructures including nanoparticles as additional carrier scattering centers, and investigated their effects on the thermoelectric properties of various bulk materials. The partial wave method was used to accurately calculate the nanoparticle scattering time, and the transport properties were calculated based on the Boltzmann transport formalism as discussed in detail in Sect. 2. A single-phase nanoparticle has a potential offset at the interface with the host material, which alters the transport of carriers by energy-dependent scatterings. The scattering by a step-like potential offset was stronger at higher carrier energy due to the Fourier transform relation between the spatial potential profile and the differential cross section in momentum space. This scattering cannot enhance the Seebeck coefficient because it reduces the entropy transport per current by scattering hot electrons more strongly than cold electrons. However, when the nanoparticles are ionized by donating carriers to the host material, they can replace the conventional impurity dopants to control the doping density. The ionized nanoparticle scattering turns out to be weaker than the ionized impurity scattering due to the lack of strong Coulomb potential near the particle center. Therefore, they are able to enhance the carrier mobility by replacing the impurity dopants and thus enhance the power factor over a wide temperature range.

Core–shell nanoparticles can create a resonant state within the band with appropriate potential profile and the effective mass control of the constituent materials. This resonant state can effectively scatter electrons in a very narrow energy range near resonant energy level, creating a strong scattering dip. When the Fermi level is aligned at the energies where the resonant scattering time is quickly rising with energy, then the Seebeck coefficient can be greatly enhanced at low temperatures. At high temperatures, this effect may be small due to the much wider electron distribution than the width of the resonance.

Lastly, we discussed the electron energy filtering with nonplanar potentials to further enhance the power factor over a wide temperature range. We found that ZT higher than $2 \sim 3$ can be achieved in PbTe and Mg_2Si semiconductors when an appropriate cutoff energy is realized to filter out the low-energy electrons in the transport to enhance the power factor and suppress the electronic thermal conductivity. A partial realization of electron energy filtering may be possible using multiple distributed resonant scatterings. The power factor enhancement was smaller than that of the ideal filtering, due to the incomplete filtering by the resonant scatterings, but still a large power factor enhancement by more than 50 % can be

achieved using five resonances well distributed in the energy space according to the calculations.

Nanostructured materials thus far have shown a promising future for the thermoelectric energy conversion applications. By combining the excellent control of both phonon and electron transport by using the nanostructures, the realization of a large *ZT* that can compete with conventional heat engines may be possible. Yet, we will have many experimental challenges in realizing such nanostructured materials to meet the theoretical predictions in the future. Interdisciplinary collaborative efforts to tackle those various challenges from various disciplines in science and technologies may only be the solution for the bright future of thermoelectrics.

Acknowledgement The authors thank Zhixi Bian, Mona Zebarjadi, Parthi Santhanam, and Tela Favaloro for their helpful discussion.

References

1. Bell, LE: Cooling, heating, generating power, and recovering waste heat with thermoelectric systems. Science **321**, 1457–1461 (2008)
2. Chen, G, Shakouri, A: Heat transfer in nanostructures for solid-state energy conversion. J. Heat Transf. **124**(2), 242–252 (2002)
3. Lawrence Livermore Nat. Lab., "Estimated U.S. energy use in 2011," https://flowcharts.llnl.gov/, Oct. 2012.
4. Snyder, GJ, Toberer, ES: Complex thermoelectric materials. Nat. Mater. **7**, 105–114 (2008)
5. Vineis, CJ, Shakouri, A, Majumdar, A, Kanatzidis, MG: Nanostructured thermoelectrics: big efficiency gains from small features. Adv. Mater. **22**, 3970–3980 (2010)
6. Shakouri, A: Recent developments in semiconductor thermoelectric physics and materials. Annu. Rev. Mater. Res. **41**, 399–431 (2011)
7. Pei, Y, Shi, X, LaLonde, A, Wang, H, Chen, L, Snyder, GJ: Convergence of electronic bands for high performance bulk thermoelectrics. Nature **473**, 66–69 (May 2011)
8. Liu, W, Tan, X, Yin, K, Liu, H, Tang, X, Shi, J, Zhang, Q, Uher, C: Convergence of conduction bands as a means of enhancing thermoelectric performance of n-type $Mg_2Si_{1-x}Sn_x$ solid solutions. Phys. Rev. Lett. **108**, 166601 (April 2012)
9. Heremans, JP, Jovovic, V, Toberer, ES, Saramat, A, Kurosaki, K, Charoenphakdee, K, Yamanaka, S, Snyder, JF: Enhancement of thermoelectric efficiency in PbTe by distortion of the electronic density of states. Science **321**, 554–557 (2008)
10. Zebarjadi, M, Joshi, G, Zhu, G, Yu, B, Minnich, A, Lan, Y, Wang, X, Dresselhaus, M, Ren, Z, Chen, G: Power factor enhancement by modulation doping in bulk nanocomposites. Nano Lett. **11**, 2225–2230 (2011)
11. Bahk, J-H, Bian, Z, Zebarjadi, M, Santhanam, P, Ram, R, Shakouri, A: Thermoelectric power factor enhancement by ionized nanoparticle scattering. Appl. Phys. Lett. **99**, 072118 (2011)
12. Bahk, J-H, Santhanam, P, Bian, Z, Ram, R, Shakouri, A: Resonant carrier scattering by core-shell nanoparticles for thermoelectric power factor enhancement. Appl. Phys. Lett. **100**, 012102 (2012)
13. Zide, JMO, Bahk, J-H, Singh, R, Zebarjadi, M, Zeng, G, Lu, H, Feser, JP, Xu, D, Singer, SL, Bian, ZX, Majumdar, A, Bowers, JE, Shakouri, A, Gossard, AC: High efficiency semimetal/semiconductor nanocomposite thermoelectric materials. J. Appl. Phys. **108**, 123702 (2010)
14. Bahk, J-H, Bian, Z, Shakouri, A: Electron energy filtering by a nonplanar potential to enhance the thermoelectric power factor in bulk materials. Phys. Rev. B **87**, 075204 (2013)

15. N. W. Ashcroft and N. D. Mermin, *Solid State Physics*, Chap. 12–13 (Thomson Learning Inc., 1976).
16. Shakouri, A, Zebarjadi, M: Nanoengineered materials for thermoelectric energy conversion. In: Volz, S (ed.) Thermal Nanosystems and Nanomaterials. Springer, Berlin (2009)
17. H. B. Callen, *Thermodynamics and an introduction to thermostatistics*, 2nd Ed. (John Wiley & Sons, 1985).
18. Kim, R, Datta, S, Lundstrom, MS: Influence of dimensionality on thermoelectric device performance. J. Appl. Phys. **105**, 034506 (2009)
19. M. Lundstrom, *Fundamentals of Carrier Transport*, 2nd Ed. (Cambridge Univ. Press, 2000).
20. Vineis, CJ, Harman, TC, Calawa, SD, Walsh, MP, Reeder, RE, Singh, R, Shakouri, A: Carrier concentration and temperature dependence of the electronic transport properties of epitaxial PbTe and PbTe/PbSe nanodot superlattices. Phys. Rev. B **77**, 235202 (2008)
21. Nolas, GS, Goldsmid, HJ: "Thermal conductivity of semiconductors", Chap.1.4. In: Tritt, TM (ed.) Thermal Conductivity: Theory, Properties, and Applications. Kluwer, New York (2004)
22. Schiff, LI: Quantum Mechanics. McGraw-Hill, New York (1949)
23. Griffiths, DJ: Introduction to Quantum Mechanics. Prentice Hall, London (1995)
24. Zebarjadi, M, Esfarjani, K, Shakouri, A, Bahk, J-H, Bian, Z, Zeng, G, Bowers, J, Lu, H, Zide, J, Gossard, A: Effect of nanoparticle scattering on thermoelectric power factor. Appl. Phys. Lett. **94**, 202105 (2009)
25. Bahk, J-H, Bian, Z, Zebarjadi, M, Zide, JMO, Lu, H, Xu, D, Feser, JP, Zeng, G, Majumdar, A, Gossard, AC, Shakouri, A, Bowers, JE: Thermoelectric figure of merit of $(In_{0.53}Ga_{0.47}As)_{0.8}(In_{0.52}Al_{0.48}As)_{0.2}$ III-V semiconductor alloys. Phys. Rev. B **81**, 235209 (2010)
26. Palmstrøm, CJ, Tabatabaie, N, Allen, SJ: Epitaxial growth of ErAs on (100) GaAs. Appl. Phys. Lett. **53**, 2608 (1988)
27. Driscoll, DC, Hanson, MP, Mueller, E, Gossard, AC: Growth and microstructure of semimetallic ErAs particles embedded in an $In_{0.53}Ga_{0.47}As$ matrix. J. Cryst. Growth **251**, 243 (2003)
28. Klenov, DO, Driscoll, DC, Gossard, AC, Stemmer, S: Scanning transmission electron microscopy of ErAs nanoparticles embedded in epitaxial $In_{0.53}Ga_{0.47}As$ layers. Appl. Phys. Lett. **86**, 111912 (2005)
29. Zide, JM, Klenov, DO, Stemmer, S, Gossard, AC, Zeng, G, Bowers, JE, Vashaee, D, Shakouri, A: Thermoelectric power factor in semiconductors with buried epitaxial semimetallic nanoparticles. Appl. Phys. Lett. **87**, 112102 (2005)
30. Driscoll, DC, Hanson, M, Kadow, C, Gossard, AC: Transition to insulating behavior in the metal–semiconductor digital composite ErAs:InGaAs. J. Vac. Sci. Technol. B **19**, 1631 (2001)
31. Burke, PG, Lu, H, Rudawski, NG, Gossard, AC, Bahk, J-H, Bowers, JE: Electrical properties of Er-doped $In_{0.53}Ga_{0.47}As$. J. Vac. Sci. Technol. B **29**(3), 03C117 (2011)
32. Dorn, A, Peter, M, Kicin, S, Ihn, T, Ensslin, K, Driscoll, D, Gossard, AC: Charge tunable ErAs islands for backgate isolation in AlGaAs heterostructures. Appl. Phys. Lett. **82**, 2631 (2003)
33. Kadow, C, Fleischer, SB, Ibbetson, JP, Bowers, JE, Gossard, AC: Self-assembled ErAs islands in GaAs: growth and subpicosecond carrier dynamics. Appl. Phys. Lett. **75**, 3548 (1999)
34. Pohl, P, Renner, FH, Eckardt, M, Schwanhausser, A, Friedrich, A, Yuksekdag, O, Malzer, S, Dohler, GH, Kiesel, P, Driscoll, D, Hanson, M, Gossard, AC: Enhanced recombination tunneling in GaAs pn junctions containing low-temperature-grown-GaAs and ErAs layers. Appl. Phys. Lett. **83**, 4035 (2003)
35. Cahill, DG, Goodson, K, Majumdar, A: Thermometry and thermal transport in micro/nanoscale solid-state devices and structures. J. Heat Transf. **124**, 223 (2002)
36. Bahk, J-H: "Electron transport in ErAs:InGa(Al)As metal/semiconductor nanocomposites for thermoelectric power generation," Ph.D. thesis, UC Santa Barbara, 2010.
37. Ravich, YI: "Selective carrier scattering in thermoelectric materials", Chap. 7. In: Rowe, DM (ed.) CRC Handbook of Thermoelectrics, pp. 67–81. CRC Press, Boca Raton, FL (1995)
38. Bilc, DI, Mahanti, SD, Kanatzidis, MG: Electronic transport properties of PbTe and $AgPb_mSbTe_{2+m}$ systems. Phys. Rev. B **74**, 125202 (2006)

39. Ravich, YI, Efimova, BA, Tamarchenko, VI: Scattering of current carriers and transport phenomena in lead chalcogenides. Phys. Stat. Sol. B. **43**, 11–33 (1971)
40. Mahan, GD: Thermionic refrigeration. J. Appl. Phys. **76**, 4362 (1994)
41. Shakouri, A, Bowers, JE: Heterostructure integrated thermionic coolers. Appl. Phys. Lett. **71**, 1234 (1997)
42. Shakouri, A., Labounty, C., Abraham, P., Piprek, J., Bowers, J.E.: Mater. Res. Soc. Proc., **545**, 449– 45 (Mater. Res. Soc., Pittsburgh, 1999).
43. Vashaee, D, Shakouri, A: Improved thermoelectric power factor in metal-based superlattices. Phys. Rev. Lett. **92**, 106103 (2004)
44. Kim, R, Jeong, C, Lundstrom, MS: On momentum conservation and thermionic emission cooling. J. Appl. Phys. **107**, 054502 (2010)
45. Nolas, GS, Sharp, J, Goldsmid, HJ: Thermoelectrics: basic principles and new materials developments. Springer, New York (2001)
46. Smith, RA: Semiconductors, 2nd edn. Cambridge University Press, London (1979)
47. Biswas, K, He, J, Blum, ID, Wu, C, Hogan, TP, Seidman, DN, Dravid, VP, Kanatzidis, MG: High-performance bulk thermoelectrics with all-scale hierarchical architectures. Nature **489**, 414–418 (Sep. 2012)
48. Zaitsev, VK, Fedorov, MI, Gurieva, EA, Eremin, IS, Konstantinov, PP, Samunin, AY, Vedernikov, MV: Highly effective $Mg_2Si_{1-x}Sn_x$ thermoelectrics. Phys. Rev. B **74**, 045207 (2006)
49. Zhang, Q, He, J, Zhu, TJ, Zhang, SN, Zhao, XB, Tritt, TM: High figures of merit and natural nanostructures in $Mg_2Si_{0.4}Sn_{0.6}$ based thermoelectric materials. Appl. Phys. Lett. **93**, 102109 (2008)
50. Tani, J, Kido, H: Thermoelectric properties of Bi-doped Mg_2Si semiconductors. Physica B **364**, 218–224 (2005)
51. Akasaka, M, Iida, T, Matsumoto, A, Yamanaka, K, Takanashi, Y, Imai, T, Hamada, N: The thermoelectric properties of bulk crystalline n- and p-type Mg_2Si prepared by the vertical Bridgman method. J. Appl. Phys. **104**, 013703 (2008)
52. Bergman, DJ, Levy, O: Thermoelectric properties of a composite medium. J. Appl. Phys. **70** (11), 6821–6833 (1991)
53. Friedel, J: On some electrical and magnetic properties of metallic solid solutions. Can. J. Phys. **34**, 1190–1211 (1956)
54. Ahmad, S, Hoang, K, Mahanti, SD: Ab initio study of deep defect states in narrow band-gap semiconductors: Group III impurities in PbTe. Phys. Rev. Lett. **96**, 056403 (2006)
55. Zhitinskaya, MK, Nemov, SA, Svechnikova, TE: Phys. Solid State **40**, 1297 (1998)
56. Heremans, JP, Wiendlocha, B, Chamoire, AM: Resonant levels in bulk thermoelectric semiconductors. Energy Environ. Sci. **5**, 5510–5530 (2012)

Chapter 3
Thermal Conductivity of Particulate Nanocomposites

Jose Ordonez-Miranda, Ronggui Yang, and Juan Jose Alvarado-Gil

Abstract The modeling of the thermal conductivity of composites made up of metallic and non-metallic micro/nanoparticles embedded in a solid matrix is discussed in detail, at both the dilute and non-dilute limits of particle concentrations. By modifying both the thermal conductivity of the matrix and particles, to take into account the strong scattering of the energy carriers with the surface of the nanoparticles, it is shown that the particle size effect shows up on the thermal conductivity of nanocomposites through: (1) the collision cross-section per unit volume of the particles and, (2) the mean distance that the energy carriers can travel inside the particles. The effect of the electron–phonon interactions within metallic particles shows up through the reduction of the thermal conductivity of these particles with respect to its values obtained under the Fourier law approach. The thermal conductivity of composites with metallic particles depend strongly on (1) the relative size of the particles with respect to the intrinsic coupling length, and (2) the ratio between the electron and phonon thermal conductivities. The obtained results have shown that the size dependence of the composite thermal conductivity appears not only through the interfacial thermal resistance but also by means of the electron–phonon coupling. Furthermore, at the non-dilute limit, the interaction among the particles is taken into account through a crowding factor,

J. Ordonez-Miranda
Laboratoire d'Énergétique Moléculaire et Macroscopique, Combustion, UPR CNRS 288, Ecole Centrale Paris, Grande Voie des Vignes, 92295 Châtenay Malabry, France
e-mail: jose.ordonez@ecp.fr

R. Yang (✉)
Department of Mechanical Engineering, University of Colorado, Boulder, CO 80309, USA
e-mail: Ronggui.Yang@Colorado.Edu

J.J. Alvarado-Gil
Department of Applied Physics, Centro de Investigación y de Estudios Avanzados del I.P.N-Unidad Mérida, Carretera Antigua a Progreso km. 6, A.P. 73 Cordemex, Mérida, Yucatán 97310, Mexico
e-mail: jjag@mda.cinvestav.mx

X. Wang and Z.M. Wang (eds.), *Nanoscale Thermoelectrics*, Lecture Notes in Nanoscience and Technology 16, DOI 10.1007/978-3-319-02012-9_3,
© Springer International Publishing Switzerland 2014

which is determined by the effective volume of the particles. The proposed crowding factor model is able to capture accurately the effect of the interactions among the particles for concentrations up to the maximum packing fraction of the particles. The predictions of the obtained analytical models are in good agreement with available experimental and numerical data and they can be applied to guide the design and improve the thermal performance of composite materials.

3.1 Introduction

Composites based on the dispersion of a discontinuous phase of particles embedded in a continuous matrix, have been used for more than a hundred years, due to their outstanding properties that often cannot be obtained with single-phase materials [1, 2]. In many applications ranging from mechanical structures to electronics, it is common to engineer material properties by combining the most useful properties of two or more phases. The prediction and understanding of the composite properties has been a complex subject of research since the properties of composite materials depend on a number of structural parameters and physical/chemical properties including the volume fraction, size, shape and orientation of the particles as well as the interfacial characteristics between the particles and matrix. The two basic configurations of the particles in composites are defined by the random and aligned distribution of particle inclusions, as shown in Fig. 3.1a, b, respectively. The overall thermal conductivity of the first composite can be considered as isotropic, while the thermal conductivity of the second one could be anisotropic.

Since Maxwell [3] who presented a theoretical basis for calculating the effective thermal conductivity of particulate composites, a considerable amount of theoretical and empirical approaches have been employed to analyze the thermal conductivity of composites, as summarized in the books by Milton [1] and Torquato [2], and references therein [4–15], in which most analysis has been performed based on an effective medium approximation (EMA), under the framework of the Fourier law of heat conduction. One of the most widely-used models was recently derived by Nan et al. [8], who considered spheroidal inclusions with interfacial thermal resistance and generalized the previous results of Benveniste [4], and Hasselman and Johnson [5], for spherical, cylindrical and flat-plate inclusions. These EMA models can predict reasonably well the thermal conductivity of composites with small volume fraction of macro/micro-sized particles where heat conduction is governed by the Fourier law.

However, the EMA models developed earlier have not considered the details of heat-carrying carriers and their interaction with microstructures. As a consequence, there are three major drawbacks of these classical models based on the Fourier's law: (1) They are not appropriate for predicting the thermal conductivity of nanocomposites where the particle size could be of the order or smaller than the mean free path of the energy carriers [13, 16, 17]. (2) They do not consider the effect of the electron–phonon coupling and therefore they are not applicable for

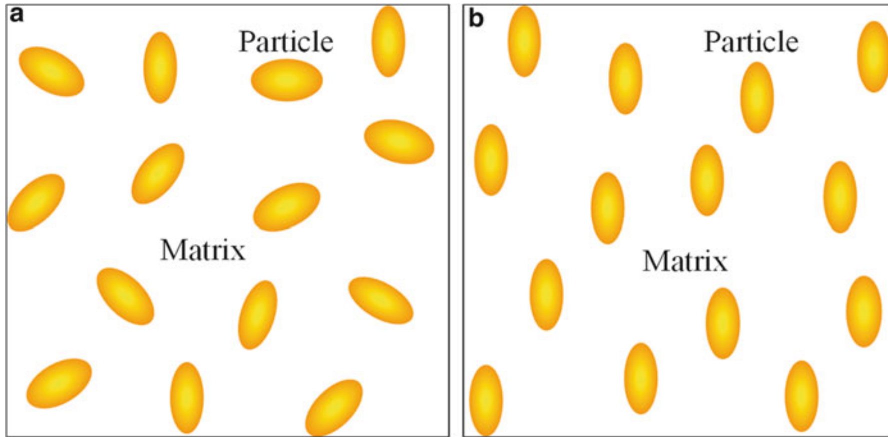

Fig. 3.1 Schematics of a composite with (**a**) random and (**b**) aligned distribution of particles

composites with metallic particles, where the heat conduction is due to the flow of the electron and phonon gases and their interactions. (3) They do not consider the effect of the interaction among the particles and therefore they are not applicable for high concentration of particles (typically larger than 15 %).

In this chapter, we present in detail the modeling of the thermal conductivity of composites made up of metallic and non-metallic micro/nanoparticles embedded in a solid matrix, at both the dilute and non-dilute limits of particle concentrations, which essentially addresses the above drawbacks. Before we present the detailed modeling, we summarize in the rest of this section the basic physics behind the drawbacks identified above. Section 3.2 is dedicated to address the size effects of energy carriers in nanocomposites. A thermal conductivity model for metal-nonmetal composites is developed in Sect. 3.3, which takes into account the effects of both electron–phonon coupling and thermal boundary resistance. In Sect. 3.4, a crowding factor model is presented that can be utilized to extend the thermal conductivity models at the dilute limit to high concentrations. Section 3.5 concludes this chapter.

3.1.1 On the Nanocomposites

Significant interest has recently been given to composites with nano-sized particles (nanocomposites), due to their importance in electronics, structural and energy applications [16]. In contrast to the composites with micro-sized particles, the heat conduction through nanocomposites is expected to be strongly determined by the interface/surface effects. The energy carriers (electrons and phonons) in composites experience multiple scattering processes, which ultimately determine the effective thermal conductivity of the material. One of these scattering

mechanisms is defined by the collision of the energy carriers with the surface of the embedded particles and its effects are strongly determined by the relative size of the particles with respect to the intrinsic mean free path (MFP) associated with the scattering among carriers and carriers with natural impurities. When the size of the particles is much larger than the intrinsic MFP, the collisions of the energy carriers with the surface of the particles is quite infrequent in comparison with the other scattering processes, and therefore their effects can be neglected. By contrast, if the size of the particles is of the order of the MFP or smaller, these collisions can be very frequent and hence their contribution to the heat conduction is significant. Considering that the MFP of electrons and phonons are in the order of a few nanometers to hundreds of nanometers, in a wide variety of materials at room temperature, the effects of the size of the particles are expected to be negligible for micro-sized or bigger particles and become significant for nano-sized particles.

3.1.2 On the Composites with Metallic Particles

Metals usually have much higher thermal conductivities than ceramic or polymer materials. It is expected that metallic nanoparticles can significantly enhance the thermal conductivity of the matrix material [1]. Despite of its importance and practice in using metallic fillers for composite materials, currently there exist no models that can correctly describe the heat transport through nanocomposites with metallic particles in dielectric materials. Heat transport through metallic particles, in contrast to that in nonmetallic materials, is not only due to the phonon gas but also due to the electron gas and their interactions [18]. In addition to the electron–electron and phonon-phonon scatterings, the electron–phonon interactions are also present in metals. In fact, the coupling between electrons and phonons inside the metallic particles and their interaction with the matrix has a dominant role in the heat transport through the composites. In addition, as the size of the particles reduces to nanoscale, the frequent collisions of the electrons and phonons with the surface of the embedded particles significantly shortens their effective mean free path, as shown in Fig. 3.2, which further complicates the modeling of the effective thermal conductivity of metal-nonmetal composite.

3.1.3 On the High Particle Concentrations

Most existing models for thermal conductivity of composites have assumed that the volume fraction of the particles is small enough (typically smaller than 15 %) that the interactions among the particles can be neglected. In such dilute limit, the heat flux lines generated by one particle are not distorted by the presence of the neighboring particles when the distance between neighboring particles is much larger than their size, as shown in Fig. 3.3a. However, for higher particle

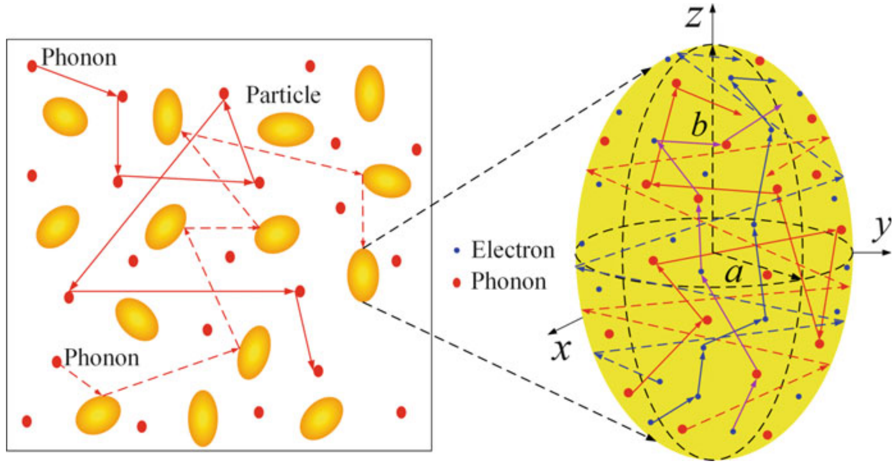

Fig. 3.2 Schematics of the different scattering processes of the energy carriers inside the nonmetal matrix and the metallic particles of a composite

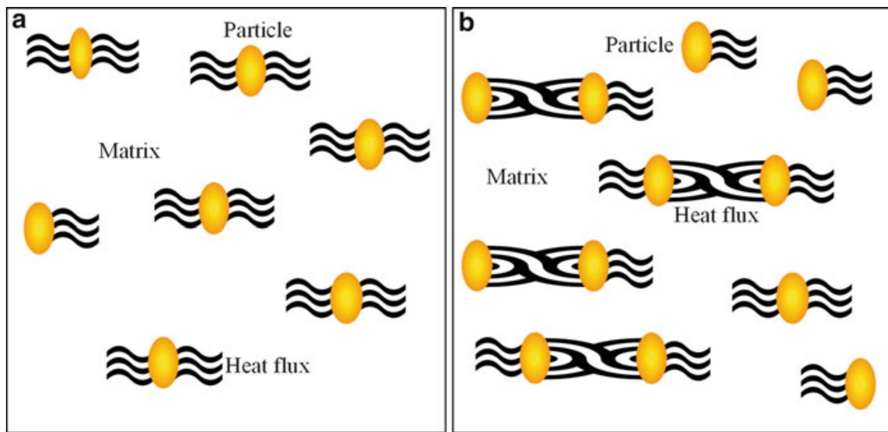

Fig. 3.3 Schematics of the lines of the heat flux inside a composite with a (**a**) dilute and (**b**) non-dilute concentration of particles

concentrations, the distance between neighboring particles can be of the order of the particle size or smaller and the interaction among particles have to be considered, which results in distortion in heat flux that is different from the prediction of single particle assumption, as shown in Fig. 3.3b. Due to this particle interaction, the modeling of the thermal conductivity of composites at the non-dilute limit has been a challenging research problem.

3.2 Size Effects in Nanocomposites

Theoretical models predicting the thermal conductivity of nanocomposites and explaining how the nanoscale structures influence the bulk thermal properties are scarce. Models for thermal conductivity of semiconductor and dielectric nanocomposites just start to emerge. By calculating the scattering cross section and the relaxation time due to a single particle, Khitun et al. [9] derived an expression for the thermal conductivity of a composite with periodically arranged nanoparticles. Even though they reported a particle-size dependence of the effective thermal conductivity, their approach is limited to elastic scattering inside the particles and specular scattering at the interfaces. More recently, based on the phonon Boltzmann transport equation (BTE), Yang et al. [14–16, 19–21] studied the phonon thermal conductivity of a variety of nanocomposites. Their simulations showed that the temperature profiles in nanocomposites are very different from those in conventional composites due to the ballistic phonon transport at nanoscale. This indicates that the dependence of the thermal conductivity on the particle size and volume fraction in nanocomposites can be significantly different from that of macro/micro-composites. Along the same line, Prasher [11, 22] derived semi-analytical expressions for the effective thermal conductivity of nanocomposites with aligned nanowires. More recently, Minnich and Chen [13] proposed a modified EMA formulation based on Nan et al. model [8] by considering the interfacial scattering of phonons in nanocomposites. The predictions of this modified EMA for the thermal conductivity of composites reinforced with spherical and cylindrical particles, as a function of the interface density, are in good agreement with the numerical approaches based on the BTE and Monte Carlo (MC) simulations. We have recently extend the formalism proposed by Minnich and Chen [13] for nanocomposites with spheroidal inclusions. Our results exhibit an explicit dependence of the composite thermal conductivity on the collision cross-section per unit volume of the particles and the average distance that the energy carriers can travel inside the particles.

3.2.1 Modified Effective Medium Approximation (MEMA) Model

In general, the thermal conductivity k of composites can be written as,

$$k = k(k_m, k_I, f, P), \tag{3.1}$$

where k_m and k_I are the thermal conductivities of the matrix and the particles, respectively; f is the volume fraction of the particles and P stands for other properties as the particles size, shape and orientation, and the interfacial thermal resistance. The classical models [4, 5, 8, 12] derived under the framework of the

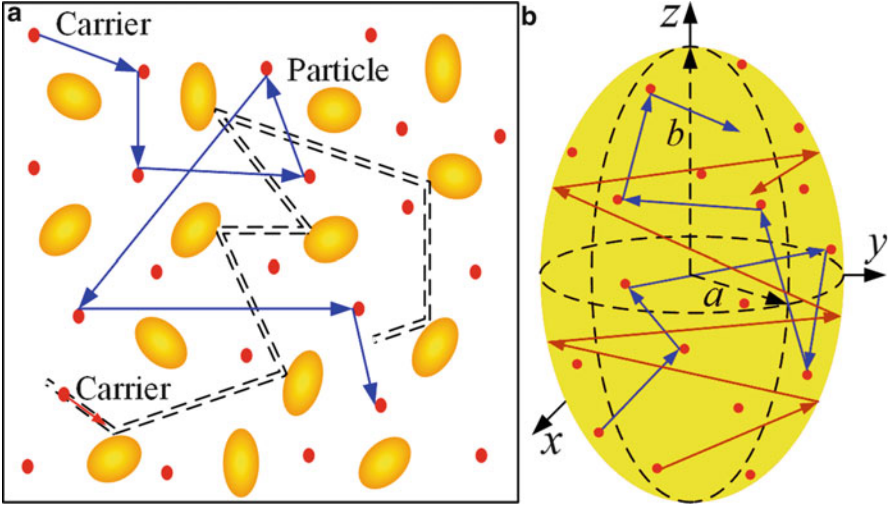

Fig. 3.4 Schematics showing the scattering process of an energy carrier inside (**a**) the matrix and (**b**) the spheroidal particle

Fourier law of heat conduction have the form of (3.1), and they consider k_m and k_I as the bulk thermal conductivity of the constituents. To take into account the particle size effects, the thermal conductivity of the matrix and the particles needs to be modified, by determining the effective mean free path of the energy carriers associated with all the scattering processes. These calculations have been proposed and developed by Minnich and Chen [13] for spherical and cylindrical nanoparticles, and subsequently they have been extended for spheroidal particles by Ordonez-Miranda et al. [23].

According to the kinetic theory [24], the thermal conductivity of a material is given by

$$k_\xi = \frac{1}{3}\int C_\xi(\varepsilon)v_\xi(\varepsilon)l_\xi(\varepsilon)d\varepsilon, \tag{3.2}$$

where C_ξ, v_ξ and l_ξ are the volumetric heat capacity per unit energy, the group velocity and the total MFP of electrons ($\xi = e$) or phonons ($\xi = p$). For a composite as shown in Fig. 3.4a, the MFP of the energy carriers in the matrix is not only determined by the intrinsic carrier-carrier scatterings but also by the carrier-boundary collisions. According to the Matthiessen rule [24], the effective MFP $l_{\xi,m}$ of the energy carriers in the matrix can be written by

$$\frac{1}{l_{\xi,m}} = \frac{1}{l_{\xi\xi,m}} + \frac{1}{l_{\xi I,m}} \tag{3.3}$$

where $l_{\xi I,m}$ is the MFP associated with the collisions of the energy carriers with the outer surface of the particles, and it is assumed to be independent of the intrinsic scattering of the energy carriers represented by $l_{\xi\xi,m}$.

To determine $l_{\xi I,m}$, let us define $A_{\perp}$ as the collision cross-section (the effective area of collision) between an energy carrier and a particle, and n as the number of particles per unit volume of them (the density of particles). If V is the volume of one particle, the volume fraction of particles is $f = nV$. Now if one energy carrier travels a distance L, it collides with particles within the cylindrical swept volume $A_{\perp}L$, which contains $nA_{\perp}L$ particles (see the dashed lines in Fig. 3.3a). The MFP $l_{\xi I,m}$ due to particle inclusions can be thus written as

$$l_{\xi I,m} = \frac{L}{nA_{\perp}L} = \frac{1}{nA_{\perp}} = \frac{1}{\sigma_{\perp} f}, \tag{3.4}$$

where $\sigma_{\perp} = A_{\perp}/V$ is the collision cross-section per unit volume of one particle. After replacing (3.3) and (3.4) into (3.2), it is found that the thermal conductivity $k_{\xi,m}$ of the electron ($\xi = e$) or phonon ($\xi = p$) gases in the matrix material are given by

$$k_{\xi,m} = \frac{K_{\xi,m}}{1 + l_{\xi\xi,m}\sigma_{\perp} f}, \tag{3.5}$$

where $K_{\xi,m}$ is the bulk thermal conductivity of the matrix given by (3.2) with the replacement $l_{\xi} \to l_{\xi\xi,m}$, which, for the sake of simplicity, has been represented by its average value. Equation (3.5) indicates that the size dependence of the effective thermal conductivity $k_{\xi,m}$ of the matrix is related by the collision cross-section per unit volume ($\sigma_{\perp} = A_{\perp}/V$) and not through the total surface area per unit volume of the particles, as was suggested by other researchers [15, 21].

The effective thermal conductivity of the particles can be found similarly. Based on the Matthiessen rule, the effective mean free path $l_{\xi,I}$ of the energy carriers within the particles is given by

$$\frac{1}{l_{\xi,I}} = \frac{1}{l_{\xi\xi,I}} + \frac{1}{c}. \tag{3.6}$$

where c is the average distance traveled by the energy carriers inside the particles, independently of the intrinsic carrier scattering associated with the MFP $l_{\xi\xi,I}$. After replacing (3.6) into (3.2) and assuming that $l_{\xi\xi,I}$ can be represented by its average value, the following thermal conductivity $k_{\xi,I}$ of the particles is obtained

$$k_{\xi,I} = \frac{K_{\xi,I}}{1 + l_{\xi\xi,I}/c}, \tag{3.7}$$

where $K_{\xi,I}$ is the bulk thermal conductivity of the particles, defined by (3.2) with the replacement $l_{\xi} \to l_{\xi\xi,I}$. Equation (3.7) shows that the effective thermal conductivity of the particles can be considerably smaller than its bulk value when $c \leq l_{\xi\xi,I}$, and it

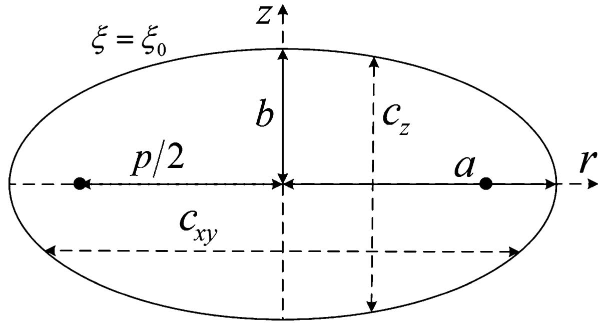

Fig. 3.5 Geometry of the cross-section of an oblate spheroid ($a > b$) with $r^2 = x^2 + y^2$

reduces to its bulk counterpart for $c \gg l_{\xi\xi,J}$. This is expected given that the distance c is directly proportional to the size of the particles, as shown below.

If the particles are aligned spheroids as the one shown in Fig. 3.4b, and the heat flux is in the z-direction (the resultant net direction of the energy carriers), the energy carriers of the matrix "see" an effective area of collision $A_\perp = \pi a^2$, which implies that $\sigma_\perp = \pi a^2/(4\pi b a^2/3) = 3/4b$. Due to the symmetry of the problem, the characteristic length $c = c_z$, can be calculated conveniently using prolate (if $a < b$) or oblate (if $a > b$) spheroidal coordinates (η, ξ, ϕ) [25]. The oblate spheroidal coordinates are related to the Cartesian coordinates (x, y, z) as follows

$$x = \frac{p}{2}\sqrt{(1-\eta^2)(1+\xi^2)}\cos\phi, \tag{3.8a}$$

$$y = \frac{p}{2}\sqrt{(1-\eta^2)(1+\xi^2)}\sin\phi, \tag{3.8b}$$

$$z = \frac{p}{2}\eta\xi, \tag{3.8c}$$

where p is the interfocal distance, as shown in Fig. 3.5. These oblate spheroidal coordinates are defined within the intervals $0 \le \xi < \infty$, $-1 \le \eta \le 1$, and $0 \le \phi < 2\pi$, such that the surface of the spheroid is defined by $\xi =$ contant $= \xi_0$, the plane xy and the z axis are given by $\eta = 0$ and $|\eta| = 1$, respectively [25]. According to these definitions and (3.8a)–(3.8c), the lengths of the axes of the spheroid are determined by $2a = p\sqrt{1+\xi_0^2}$ and $2b = p\xi_0$.

To calculate the mean distance c, we are going to assume that the energy carriers undergo diffusive scattering at the inner surface of the spheroidal particles. This means that the electrons and phonons are reflected from the boundary surfaces with equal probability to any direction, as is the case of rough interfaces, which are usually found in practical applications. In presence of a heat flux along the z axis the distance $c = c_z$, is therefore determined by the average value of $2z_0 = p\eta\xi_0$ (see Fig. 3.5), that is to say

$$c_z = \frac{p\xi_0}{A}\int_A \eta dA, \tag{3.9}$$

where, according to (3.8a)–(3.8c), the differential element of area over the surface of the spheroid is given by $dA = (p/2)^2\sqrt{1+\xi^2}\sqrt{\eta^2+\xi^2}d\eta d\phi$. The integration in (3.9) has to be performed over the total area A of the spheroid, and its result is

$$c_z = \frac{4b}{3\varepsilon}\frac{\sqrt{1+\varepsilon^2}^3 - 1}{\varepsilon\sqrt{1+\varepsilon^2}+\operatorname{arcsinh}(\varepsilon)}, \tag{3.10}$$

where $\varepsilon = \sqrt{(a/b)^2 - 1}$ is the eccentricity of the oblate spheroids. For spherical particles, the characteristic length in (3.10) reduces to the radius of the spheres ($c_z = b = a$), which is consistent with its definition of mean distance. On the other hand, for flat-plate particles ($a \gg b$), (3.10) becomes $c_z = 4b/3 \approx 1.33b$. According to (3.7), this indicates that the thinner the particle, the smaller its thermal conductivity across its plane, as expected.

If the heat flux is parallel to the xy-plane, the cross-section is given by $A_\perp = \pi ab$ and hence $\sigma_\perp = \pi ab/(4\pi ba^2/3) = 3/4a$. Furthermore, according to Fig. 3.4, the distance $c = c_{xy}$ traveled by the energy carriers inside the oblate spheroids is given the average value of $2y_0 = p\sqrt{(1-\eta^2)(1+\xi_0^2)}\sin\phi$, over the surface of the spheroid. The final results is

$$c_{xy} = \frac{8a}{3\pi\varepsilon}\frac{(1+\varepsilon^2)D(-\varepsilon^2) - (1-\varepsilon^2)E(-\varepsilon^2)}{\varepsilon\sqrt{1+\varepsilon^2}+\operatorname{arcsinh}(\varepsilon)}, \tag{3.11}$$

where D and E are the complete elliptic integrals of the first and second kind [26], respectively. For spherical particles, (3.8b) predicts $c_{xy} = b = a$, which agrees with (3.10). On the other hand, for flat-plate particles (3.11) yields $c_{xy} = 8a/3\pi \approx 0.85a$, which is independent of the minor semi-axis and increases linearly with the major semi-axis of the spheroid. By comparing the values $c_z = 1.33b$ and $c_{xy} = 0.85a$, for a flat-plate particle ($a \gg b$), it is clear that its thermal conductivity along its plane is much larger than the one across its plane (see (3.7)).

By using the prolate spheroidal coordinates and following a similar procedure than the one performed for oblate spheroids, a direct calculation shows that for prolate spheroids ($a < b$), (3.10) and (3.11) remains valid after the substitution $\varepsilon \to i\varepsilon$, where $i = \sqrt{-1}$ is the imaginary unit and the new eccentricity is $\varepsilon = \sqrt{1-(a/b)^2}$. Therefore, for cylindrical inclusions ($a \ll b$), (3.10) and (3.11) reduces to $c_z = 8b/3\pi \approx 0.85b$ and $c_{xy} = 32a/3\pi^2 \approx 1.08a$, which indicate that the thermal conductivity along the axis of the particles can be much larger than the one across its axis, as is the case of carbon nanotubes [27], for instance. Figure 3.6a shows that for a fixed semi-axis b, the characteristic

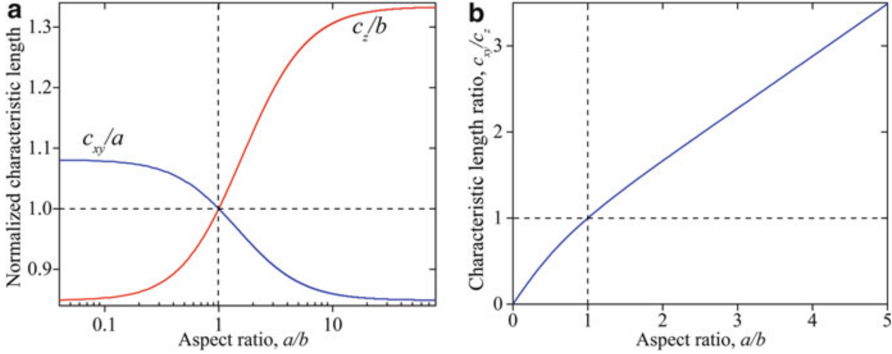

Fig. 3.6 (**a**) Normalized characteristic lengths and (**b**) characteristic length ratio c_{xy}/c_z as a function of the aspect ratio a/b of spheroidal particles

length c_z is bounded and increases with the equatorial radius a of the spheroids. On the other hand, for a given semi-axis a, the characteristic length c_{xy} is also bounded and increases with b. These behaviors are because of the average distance that the energy carriers can travel inside the particles increases with their dimensions. This is confirmed by Fig. 3.6b, which indicates that for prolate spheroids ($a < b$), $c_{xy} < c_z$; while for oblate ones ($a > b$), $c_{xy} > c_z$; as expected.

By replacing the bulk thermal conductivities $K_{\xi,m}$ and $K_{\xi,I}$ involved in a Fourier-law-based model for the thermal conductivity of composites with a defined distribution of particles, with their corresponding modified values given by (3.5) and (3.7), it is expected that the its validity can be extended for composites with nano-sized particles, as is the case of nanocomposites. Given that the modified thermal conductivities are smaller than their corresponding bulk values, it is expected that the modified thermal conductivity of the whole composite is smaller than its unmodified value.

3.2.2 Applications

Now let us consider a composite made up of aligned Si particles embedded in a Ge matrix, where the main heat carriers are the phonons. A suitable model for this case, was derived by Nan et al. [8], who proposed that the components k_i of the thermal conductivity of the composite, along the principal axes ($i = x, z$) of the aligned spheroidal particles are given by

$$k_i = K_m \frac{1 + \beta_i(1 - L_i)f}{1 - \beta_i L_i f}, \tag{3.12}$$

where K_m is the bulk thermal conductivity of the matrix, $2L_x + L_z = 1$, and

$$\beta_i = \frac{\sigma_i - K_m}{K_m + L_i(\sigma_i - K_m)}, \tag{3.13a}$$

$$\sigma_i = \frac{K_I}{1 + RL_i K_I(2/a + 1/b)}, \tag{3.13b}$$

$$L_x = \frac{p^2}{2(p^2 - 1)} - \frac{p}{2\sqrt{p^2 - 1}^3}\operatorname{arccosh}(p), \tag{3.13c}$$

where K_I the thermal conductivity of the inclusions, R the interfacial thermal resistance and $p = b/a$. According to (3.5) and (3.7), the modified thermal conductivity of the inclusions and the matrix are $k_I = K_I/(1 + l_{pp,I}/c)$ and $k_m = K_m/(1 + 3l_{pp,m}f/4d)$, respectively; where $d = a$ (b) for oblate (prolate) spheroids. After replacing these two results into (3.12), (3.13a) and (3.13b), the modified EMA model is obtained.

Figure 3.7a shows the thermal conductivity $k = k_x = k_z$ of the nanocomposite as a function of the volume fraction f for different values of the radius $a = b$ of spherical particles, in comparison with numerical results obtained from the Boltzmann transport equation [13, 15, 21]. Here, the cubic particles studied numerically [21] are represented approximately by spherical particles. The calculations were performed using the data shown in Table 3.1, for the modified (M) and unmodified (UM) models.

Note that the predictions of the modified model are in good agreement with the MC simulations, especially for $a = 5$ and 25 nm, which are much smaller than the phonon MFP, and therefore the interfacial scattering plays an important role. A similar behavior is shown in Fig. 3.7b, for the thermal conductivity of composites in the direction perpendicular to the aligned cylindrical particles ($a \ll$ b), where the predictions of the modified model again agree with the numerical results based on the BTE. A remarkable disagreement between the predictions of the modified and unmodified models is shown in Fig. 3.7a, b, for both spherical and cylindrical particles, respectively. As the size of the particles increases ($a = 100$ nm) and becomes of the same order of magnitude than the MFP, this difference decreases, as a consequence of the reduction of the boundary scattering of phonons.

Furthermore, the modified EMA model can also be used to predict anisotropic thermal conductivity of nanocomposites with spheroidal particles. Figure 3.8a, b show the anisotropic thermal conductivities k_x and k_z of nanocomposites as a function of the volume fraction for three different particles sizes of $a = 5$, 50, 300 nm and $b = 5a$.

Figure 3.8a shows that k_x has a similar decreasing trend than the one for spherical particles shown in Fig. 3.7a. By contrast, Fig. 3.8b shows that the thermal conductivity of the composite can also increase with the volume fraction for $a = 300$ nm. According to (3.12), the increasing (decreasing) of the composite thermal conductivity when the volume fraction increases is determined by $\beta > 0$ ($\beta < 0$). Based on this remark and according to (3.13a) and (3.13b), the thermal conductivity of a composite will decrease independently of the value of the thermal conductivity of

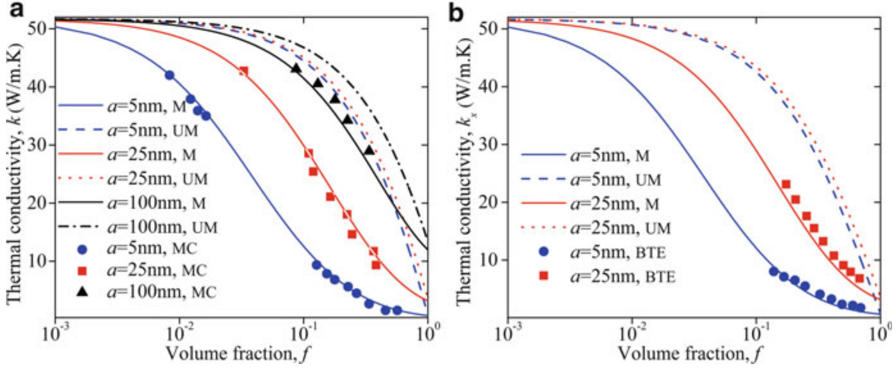

Fig. 3.7 Thermal conductivity of a Si/Ge nanocomposite reinforced with (**a**) spherical and (**b**) cylindrical nanoparticles, as a function of the volume fraction and the particle radius. Calculations were performed with the data reported in Table 3.1

Table 3.1 Material properties used in the calculations [21]

Material	Bulk thermal conductivity (W/mK)	MFP (nm)	Interfacial thermal resistance (m^2K/W)
Si	150	268	6.8×10^{-9}
Ge	51.7	171	

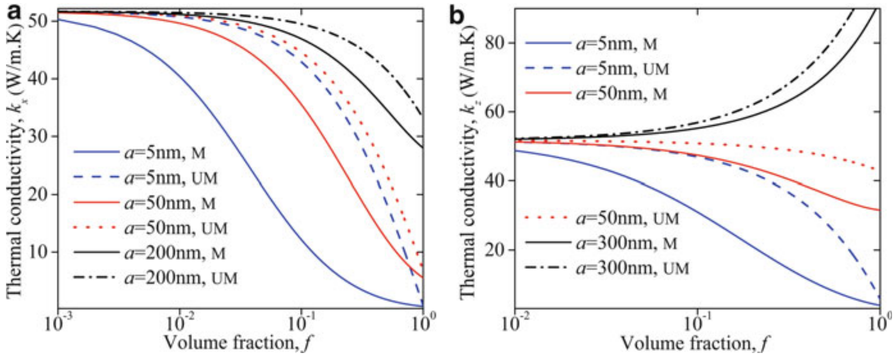

Fig. 3.8 Thermal conductivities (**a**) k_x and (**b**) k_z of a Si/Ge nanocomposite reinforced with prolate spheroids with semi-axes $b = 5a$. Calculations were performed with the data reported in Table 3.1

the particles, when the volume fraction of the particles increases, if the geometry of the particles fulfills the condition

$$\left(\frac{2}{a}+\frac{1}{b}\right)L_i > \frac{1}{a_K}, \tag{3.14}$$

where $a_K = RK_m$ is the so-called Kapitza radius of the composite. Equation (3.14) represents the selection rule to minimize the thermal conductivity of composite

materials by arranging the size and shape of the spheroidal particles properly. For spherical and cylindrical particles of radius a, (3.14) reduces to $a_K > a$, which agrees with the results shown in Fig. 3.7a, b.

3.3 Metal-Nonmetal Composites

In metal-nonmetal composites, heat is conducted by different carriers in the particles and in the matrix. The energy is transport by both electrons and phonons in metallic particles and then coupled to the phonons in the matrix. Both the electron–phonon coupling in the metallic particle and the energy coupling across material interface become important factors that determines the thermal conductivity of composites, especially when the particle size is in the order of the electron–phonon coupling length. In this section, the two-temperature model of heat conduction [28] originally proposed by Kaganov et al. [29] and Anisimov et al. [30] is used to take into account the electron–phonon interactions and to determine the effective thermal conductivity of composites with spheroidal metallic particles embedded in a nonmetallic matrix. The interfacial thermal resistance that accounts for the phonon mismatch between the two phases is included in this model. Our results generalize those obtained by Nan et al. [8] under the framework of the Fourier law of heat conduction and show that the effective thermal conductivity depends strongly on (1) the relative size of the spheroidal particles with respect to the electron–phonon coupling length, and (2) the ratio between the electron and phonon thermal conductivities. It is shown that the composite thermal conductivity has upper and lower bounds, which are determined by the particle size in comparison with the electron–phonon coupling length. For the limiting case of perfect electron–phonon coupling, the proposed model reduces to various previously reported results. This study could be useful for guiding the design of particulate composites with metallic inclusions from macro/micro- to nano-scales.

3.3.1 Theoretical Model

Figure 3.9a shows the particulate composite under consideration, in which coated spheroidal particles with the orientation and geometry shown in Fig. 3.9b are embedded in a dielectric matrix of thermal conductivity k_3. The metallic core of the spheroidal particles has electron and phonon thermal conductivities k_e and k_p respectively, and it is covered by a dielectric layer of thermal conductivity k_2 with variable thickness. Note that the composite shown in Fig. 3.9a, b is a three-phase composite, which can be used to model two-phase composite when the thickness of the dielectric coating goes to zero and the coating is used to represent a finite interfacial thermal resistance. The derivation of the effective thermal conductivity of this composite will be based on finding the temperature profile outside the

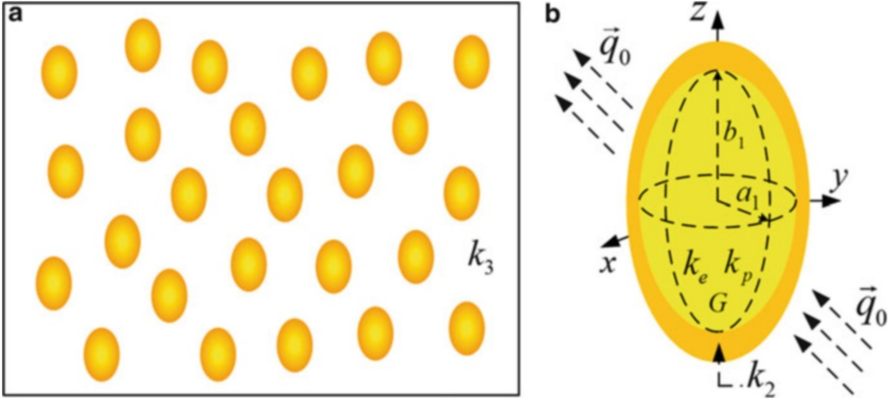

Fig. 3.9 Schematics of (**a**) the composite with aligned coated spheroidal particles and, (**b**) the geometry of one of those particles made of a metallic core with electron thermal conductivity k_e, phonon thermal conductivity k_p and electron–phonon coupling factor G; and a nonmetallic coating layer with thermal conductivity k_2. The semi axes a_2 and b_2 of the outer confocal spheroid satisfy the relation $a_2^2 - b_2^2 = a_1^2 - b_1^2$

particle shown in Fig. 3.9b, when it is exposed to a constant heat flux $\vec{q}_0$. This method is based on the approach developed by Maxwell for an analogous electrostatics problem [3].

In the metallic core, the TTM of heat conduction is used to describe the coupled heat transport due to the electron and phonon gases [31]. This model describes the spatial evolution of electron temperature T_e and the phonon temperature T_p by the following coupled differential equations [28, 31]

$$\nabla^2 T_e - \frac{G}{k_e}\left(T_e - T_p\right) = 0, \tag{3.15a}$$

$$\nabla^2 T_p + \frac{G}{k_p}\left(T_e - T_p\right) = 0, \tag{3.15b}$$

where G is the electron–phonon coupling factor, which takes into account the electron–phonon interactions. Note that if the electron gas is in thermal equilibrium with the phonon gas ($T_e = T_p$), both (3.15a) and (3.15b) reduces to the Laplace equation, which indicates that the difference between TTM and the Fourier law is due to the non-equilibrium state between electrons and phonons inside the metallic particles. According to (3.15a) and (3.15b), the thermal equilibrium between electrons and phonons is reached when $G \to \infty$ (perfect coupling), which indicates that in this limit, the predictions of the current approach should reduce to the results obtained under the Fourier law, as shown below.

We point out that the electron–phonon coupling G in nanostructures is temperature-dependent and could be remarkably different from that in the bulk materials [32–34]. However, many reported results have shown that the predictions

of the TTM with an average constant value of G are in good agreement with experimental data [31–33]. Based on these results and with the objective of keeping solvable the problem, we are going to consider that the coupling factor can be represented by an average constant value to illustrate the importance of G in modeling the thermal conductivity of composites. Phonons dominate the heat conduction in the nonmetallic coating layer and in the matrix and therefore the Fourier law of heat conduction can describe their temperature.

By subtracting (3.15a) and (3.15b), the electron and phonon temperature difference $\psi = T_e - T_p$ can be found by

$$\nabla^2 \psi - \frac{1}{d^2}\psi = 0, \tag{3.16}$$

where d is the electron–phonon coupling length of metals defined by

$$d^2 = \frac{k_a}{G}, \tag{3.17a}$$

$$\frac{1}{k_a} = \frac{1}{k_e} + \frac{1}{k_p}, \tag{3.17b}$$

where k_a is the half of the harmonic mean of the electron and phonon thermal conductivities. It was found that $d \sim 10^{-7}$ m, for a wide variety of metals (as copper, silver, gold and others) at room temperature [28, 31].

Due to the symmetry of the problem, we can use the prolate ($b_1 > a_1$) or oblate ($b_1 < a_1$) spheroidal coordinates (η, ξ, ϕ) to simplify the solution of the problem. Let us now first consider that the uniform heat flux $\vec{q}_0$ shown in Fig. 3.9b is applied in the z-direction. Then, based on the Fourier law and in the relations among the oblate spheroidal coordinates with the Cartesian coordinates defined in (3.8a)–(3.8c), the temperature T_3 far away from the influence of the coated particle, apart from an additive constant, is given by

$$T_3(|z| \to \infty) \equiv T_0 = -\frac{q_0}{k_3} z = -\frac{q_0 p}{2k_3}\eta\xi, \tag{3.18}$$

Taking into account the azimuthal symmetry of the problem, the method of separation of variables indicates that the difference of the electron and phonon temperature can be written as $\psi(\eta,\xi) = S(\eta)R(\xi)$. After replacing this expression into (3.16), it is found that the functions $S(\eta)$ and $R(\xi)$ satisfy the following differential equations

$$\frac{d}{d\eta}\left[\left(1-\eta^2\right)\frac{dS}{d\eta}\right] + \left(\lambda - c^2\eta^2\right)S = 0, \tag{3.19a}$$

$$\frac{d}{d\xi}\left[\left(1+\xi^2\right)\frac{dR}{d\xi}\right]-\left(\lambda+c^2\xi^2\right)R=0, \tag{3.19b}$$

where λ is a separation constant and $c = p/(2d)$. Note that for $c = 0$ ($d = \infty$), the well-behaved solution of (3.19a) and (3.19b) can be expressed in terms of the first and second Legendre polynomials P_l and Q_l, respectively [26]. In this case ($c = 0$), (3.16) reduces to the Laplace equation and therefore it yields the solution for the temperature T under the Fourier law description. Taking into account that $Q_l(\mu) \propto P_l(\mu)F_l(\mu)$ [35], the general solution for T, can be written as follows

$$T(\eta,\xi)=\sum_{l=0}^{\infty}A_lP_l(\eta)P_l(i\xi)[1+B_lF_l(i\xi)], \tag{3.20}$$

where A_l and B_l are constant that depend on the boundary condition of the problem, i is the imaginary unit, and

$$F_l(\mu)=\int_{\mu}^{\infty}\frac{dx}{(x^2-1)[P_l(x)]^2}. \tag{3.21}$$

The temperature profile in the nonmetallic coating layer T_2, and in the matrix T_3, can be therefore written as (3.20), which is a particular case ($c = 0$) of the general solution of (3.19a) and (3.19b).

For the case of $c \neq 0$ ($d \neq \infty$) the solution of (3.19a) is determined by the spheroidal angular functions $S = S_{0l}(c,\eta)$, which are similar to the well-known spherical harmonics and can be expanded in term of Legendre polynomials [25]. Analogously, the solution of (3.19b) is given by the spheroidal radial functions $R = R_{0l}(c,i\xi)$, which have a known expansion in terms of spherical Bessel functions [25]. We can therefore write the general solution of (3.16) as follows

$$\psi(\eta,\xi)=\sum_{l=0}^{\infty}C_lS_{0l}(c,\eta)R_{0l}(c,i\xi), \tag{3.22}$$

where C_l are numerical constants. According to (3.15a), the electron temperature T_e satisfies

$$\nabla^2T_e=\frac{G}{k_e}\psi, \tag{3.23}$$

which is an inhomogeneous partial differential equation, whose general solution is given by the superposition of its complementary (T_{ec}) and particular (T_{ep}) solutions ($T_e = T_{ec} + T_{ep}$) [26]. Taking into account that $\nabla^2T_{ec} = 0$, the solution for T_{ec} is given by (3.20). Furthermore, the combination of $\nabla^2T_{ep} = \psi G/k_e$ with (3.16) yields $T_{ep} = \psi k_a/k_e$. In this way, the general solution of (3.23) is

$$T_e(\eta, \xi) = T(\eta, \xi) + \frac{k_a}{k_e}\psi(\eta, \xi). \tag{3.24}$$

The phonon temperature $T_p = T_e - \psi$ is then found to be

$$T_p(\eta, \xi) = T(\eta, \xi) - \frac{k_a}{k_p}\psi(\eta, \xi). \tag{3.25}$$

Note that (3.24) and (3.25) shows that the temperature profiles predicted by the TTM are given by the superposition of the Fourier law prediction (the common term) and a non-equilibrium term, which takes into account the effects of the coupling among the electrons and phonons of the metallic core of the particle shown in Fig. 3.9b.

After writing out the solutions for temperature distributions inside the particle [(3.24) and (3.25)], in the coating layer and in the matrix [(3.20)], we now need to specify interface and boundary conditions to find the required specific solutions. In general, there are two possible pathways for energy transport across metal-nonmetal interfaces, namely: (1) coupling between electrons and phonons within the metal, and then subsequently coupling between phonons of the metal and phonons of the nonmetal, and (2) coupling between electrons of the metal and phonons of the nonmetal through anharmonic interactions at the metal–nonmetal interfaces.

Even though the direct electron–phonon coupling at metal-nonmetal interfaces is always present (pathway 2), experimental or theoretical methodologies to quantify its contribution are scarce [28, 36]. The description of this channel of heat transport is complicated, and the mechanism is not well understood, especially when the electrons of the metal are not in equilibrium with the phonons of the dielectric material [37, 38]. The authors of these latter works also suggested that contribution of the pathway 2 to the total heat flux through the metal-dielectric interface could be small in comparison to that of the phonon-phonon interactions for a wide variety of metals. Based on these facts and for keeping the problem analytically solvable, we only consider the pathway 1 in this chapter.

Given that the metallic particles are embedded in a nonmetallic matrix, it is reasonable to consider that the electrons are mainly isolated inside the particles. We therefore assume that the electrons inside the core particle do not interact directly with phonons in nonmetals and focus our study on the effect of electron–phonon coupling on the effective thermal conductivity of the composite. Under this condition, the boundary conditions for the temperature and heat flux continuity at the interfaces, can be written as

$$\left.\frac{\partial T_e}{\partial \xi}\right|_{\xi=\xi_1} = 0, \tag{3.26a}$$

$$T_p\big|_{\xi=\xi_1} = T_2\big|_{\xi=\xi_1}, \tag{3.26b}$$

$$k_p \frac{\partial T_p}{\partial \xi}\bigg|_{\xi=\xi_1} = k_2 \frac{\partial T_2}{\partial \xi}\bigg|_{\xi=\xi_1}, \tag{3.26c}$$

$$T_2|_{\xi=\xi_2} = T_3|_{\xi=\xi_2}, \tag{3.26d}$$

$$k_2 \frac{\partial T_p}{\partial \xi}\bigg|_{\xi=\xi_2} = k_3 \frac{\partial T_3}{\partial \xi}\bigg|_{\xi=\xi_2}, \tag{3.26e}$$

where ξ_1 and ξ_2 represent the surfaces of the inner and outer spheroids, respectively. The boundary conditions expressed in (3.18) and (3.26a)–(3.26e) determine the temperature profiles everywhere in the space. An enormous amount of algebraic calculations can be saved during the evaluation of these boundary conditions, by recognizing that the general form of the temperature profiles is dictated by the form of the external thermal excitation [39]. Given that (3.18) has a linear dependence on η, the response of the materials should also have the same dependence, which implies that $l = 1$ in (3.20) and (3.22). Therefore (3.20), (3.24) and (3.25) can be written as

$$T_e(\eta, \xi) = AT_0(\eta, \xi)\left[1 + B\frac{k_a}{k_e}\frac{i_1(c\xi)}{\xi}\right], \tag{3.27a}$$

$$T_p(\eta, \xi) = AT_0(\eta, \xi)\left[1 - B\frac{k_a}{k_p}\frac{i_1(c\xi)}{\xi}\right], \tag{3.27b}$$

$$T_2(\eta, \xi) = CT_0(\eta, \xi)[1 + DF(\xi)], \tag{3.27c}$$

$$T_3(\eta, \xi) = T_0(\eta, \xi)[1 + EF(\xi)], \tag{3.27d}$$

where T_0 is defined by (3.18), $F(\xi) = iF_1(i\xi)$, $i_1()$ is the modified spherical Bessel function of the first kind and order one, and A, B, C, D and E are constants, which are determined by substituting (3.27a)–(3.27d) into the five boundary conditions given in (3.26a)–(3.26e). For the purposes of this work, just the temperature T_3 outside of the spheroid is required and its explicit expression is

$$T_3(\eta, \xi) = T_0(\eta, \xi)\left[1 + \beta_{33}\frac{F(\xi)}{\xi_2 F'(\xi_2)}\right] = T_0(\eta, \xi)\left[1 - \beta_{33}L_{33}^{(2)}\frac{F(\xi)}{F(\xi_2)}\right], \tag{3.28}$$

where the prime ($'$) indicates derivative of F with respect to its argument, and

$$\beta_{33} = \frac{k_{33} - k_3}{k_3 + (k_{33} - k_3)L_{33}^{(2)}}, \tag{3.29a}$$

$$\frac{k_{33}}{k_2} = \frac{1 + \alpha_{33}\left(1 - L_{33}^{(2)}\right)\nu}{1 - \alpha_{33}L_{33}^{(2)}\nu}, \tag{3.29b}$$

$$\alpha_{33} = \frac{k_1 - k_2}{k_2 + (k_1 - k_2)L_{33}^{(1)}}, \tag{3.29c}$$

$$k_1 = \frac{k_e + k_p}{\chi}, \tag{3.29d}$$

$$\chi = 1 + \frac{k_e}{k_p}\frac{d}{b_1}\frac{i_1(b_1/d)}{i'_1(b_1/d)}, \tag{3.29f}$$

$$L_{33}^{(j)} = \left(1 + e_l^{-2}\right)\left(1 - \frac{\arctan\left(e_j\right)}{e_j}\right), \tag{3.29g}$$

where $\nu = a_1^2 b_1 / a_2^2 b_2$ is the volume fraction of the core spheroid relative to the total volume of the coated particle, $e_j = \sqrt{\left(a_j/b_j\right)^2 - 1}$ is the eccentricity of the $j = 1, 2$ oblate spheroid ($a_j > b_j$) and all other parameters have been defined before. In deriving (3.29a)–(3.29g), the relations $a_j = \left(p_j/2\right)\sqrt{1 + \xi_j^2}$ and $b_j = p_j \xi_j / 2$ have been used [25]. It is worthwhile to point out the following remarks on (3.29a)–(3.29g): (1) In absence of the coating layer ($\nu = 1$) and without considering the interfacial thermal resistance, the thermal conductivity k_{33} reduces to the thermal conductivity of the inner spheroid ($k_{33} = k_1$). This indicates that in presence of the coating layer, the thermal conductivity k_{33} can be considered as the effective thermal conductivity of the coated spheroidal particle. (2) The effect of the electron–phonon coupling appears in the parameter χ through the ratio between the minor semi-axis of the inner spheroid and the coupling length d defined in (3.17a). Thus, the relative size of the particles with respect to the coupling length plays an important role in the process of heat conduction. (3) Equation (3.29g) defines the well-known geometrical factor [39], along the minor z axis of the oblate spheroids.

The effective thermal conductivity of the composite can be derived using the temperature profile given by (3.28). To do that, let us consider a large spheroid with semi-axes a_0 and b_0, and surface $\xi = \xi_0$, composed by N aligned small spheroids (see Fig. 3.9a), with the geometry and thermal conductivities shown in Fig. 3.9b, embedded in a matrix of thermal conductivity k_3. Assuming that the volume fraction of the N spheroids $f = N a_2^2 b_2 / a_0^2 b_0$ is small enough to neglect the interaction among them (dilute limit), at distances much larger than the major semi-axis a_0, the heat flux (and therefore the temperature) is simply the superposition of the heat fluxes due to each small spheroid. Under this condition, (3.28) indicates that the temperature profile due to the system of N particles can be written as follows

$$T_3(\eta, \xi) = T_0(\eta, \xi)\left[1 + N\beta_{33}\frac{F(\xi)}{\xi_2 F'(\xi_2)}\right]. \tag{3.30a}$$

By considering the large spheroid as a homogeneous spheroid with effective thermal conductivity K_{33} along its minor axis (z-direction), the temperature profile generated at a large distance is

$$T_3(\eta,\xi) = T_0(\eta,\xi)\left[1 + \beta_{33}^* \frac{F(\xi)}{\xi_0 F'(\xi_0)}\right], \tag{3.30b}$$

where β_{33}^* is defined by (3.29a) with the replacement $k_{33} \to K_{33}$. After equating (3.30a) with (3.30b), it is found that $\beta_{33}^* = \beta_{33} f$, where $f = N\xi_0 F'(\xi_0)/\xi_2 F'(\xi_2)$ is the volume fraction of the N particles. The solution of the former equation for K_{33} yields

$$\frac{K_{33}}{k_3} = \frac{1 + \beta_{33}\left(1 - L_{33}^{(2)}\right) f}{1 - \beta_{33} L_{33}^{(2)} f}. \tag{3.31}$$

Note that (3.31) has a similar mathematical form as (3.29b), which indicates that the effective thermal conductivities of the composite and the coated particles are determined by the same mathematical equation with different physical parameters.

So far, the calculations have been performed considering that the applied heat flux $\vec{q}_0$ is along the z axis of the aligned oblate spheroidal inclusions. When this heat flux is parallel to the x or y axis, we can follow a similar procedure to find the effective thermal conductivities K_{11} and K_{22}, along the x and y axes, respectively. Indeed we find that $K_{11} = K_{22}$, as expected; due to the symmetry of the coated spheroids and they are given by (3.31) with the replacement of the all subscripts $33 \to 11$, while the geometrical factors $L_{11}^{(j)}$ satisfy the relation

$$2L_{11}^{(j)} + L_{33}^{(j)} = 1, \tag{3.32}$$

which implies that none of the (positive) geometrical factors of the spheroidal particles is larger than the unity.

If the particles are prolate coated spheroids ($b_1 > a_1$), we can derive the effective thermal conductivities $K_{11} = K_{22}$ and K_{33} of the anisotropic composite along the principal axes of the aligned spheroids using the prolate spheroidal coordinates [25] and following a similar procedure as that we have performed for the oblate spheroids. The results are indeed still given by equations of the form of (3.31), with minor changes on the geometrical terms defined in (3.29f) and (3.29g) that are specified below.

In summary, the effective thermal conductivities of the particulate composite along the principal axes of the aligned oblate or prolate coated spheroids can be written as follows

$$\frac{K_{ii}}{k_3} = \frac{1 + \beta_{ii}\left(1 - L_{ii}^{(2)}\right) f}{1 - \beta_{ii} L_{ii}^{(2)} f}, \tag{3.33a}$$

$$\beta_{ii} = \frac{k_{ii} - k_3}{k_3 + (k_{ii} - k_3)L_{ii}^{(2)}}, \tag{3.33b}$$

$$\frac{k_{ii}}{k_2} = \frac{1 + \alpha_{ii}\left(1 - L_{ii}^{(2)}\right)\nu}{1 - \alpha_{ii}L_{ii}^{(2)}\nu}, \tag{3.33c}$$

$$\alpha_{ii} = \frac{k_1 - k_2}{k_2 + (k_1 - k_2)L_{ii}^{(1)}}, \tag{3.33d}$$

$$k_1 = \frac{k_e + k_p}{\chi}, \tag{3.33e}$$

$$\chi = 1 + \frac{k_e}{k_p}\begin{cases} \dfrac{d}{b_1}\dfrac{i_1(b_1/d)}{i'_1(b_1/d)}, & \text{Oblate spheroids} \\ \dfrac{d}{a_1}\dfrac{i_1(a_1/d)}{i'_1(a_1/d)}, & \text{Prolate spheroids} \end{cases} \tag{3.33f}$$

$$L_{33}^{(j)} = \begin{cases} \left(1 + e_j^{-2}\right)\left(1 - \dfrac{\arctan\left(e_j\right)}{e_j}\right), & \text{Oblate spheroids} \\ \left(1 - e_j^{-2}\right)\left(1 - \dfrac{\arctan\ h\left(e_j\right)}{e_j}\right), & \text{Prolate spheroids} \end{cases} \tag{3.33g}$$

where $e_j = \sqrt{\left(a_j/b_j\right)^2 - 1}$ for oblate spheroids and $e_j = \sqrt{1 - \left(a_j/b_j\right)^2}$ for prolate spheroids, and the prime ($'$) indicates derivative of $i_1()$ with respect to its argument. It is important to note that as a result of the electron–phonon interactions at the metallic particle, its total thermal conductivity (electron + phonon contributions) is reduced by the factor χ, which can be much larger than the unity when the size of the particles is of the same order of magnitude than the coupling length, as established in (3.33f). This reduction is reasonable, given that these interactions represent a scattering process between the electrons and phonons, which reduces their total mean free path and therefore the corresponding thermal conductivity [24, 40].

When the applied heat flux $\vec{q}_0$ is not parallel to any of the principal axes of the coated spheroids, we can generalize (3.33a)–(3.33g). In this case, the heat flux $\vec{q}_3$ due to the temperature T_3 outside of the spheroids is determined by the principle of superposition and can be written as follows

$$\vec{q}_3 = -k_3\left(\hat{x}\frac{\partial T_3}{\partial x}\bigg|_{\beta_{11}, q_{0,11}} + \hat{y}\frac{\partial T_3}{\partial y}\bigg|_{\beta_{22}, q_{0,22}} + \hat{z}\frac{\partial T_3}{\partial z}\bigg|_{\beta_{33}, q_{0,33}}\right), \tag{3.34}$$

where $q_{0,ii}$ for $i = 1, 2, 3$ are the components of $\vec{q}_0$ relative to the coordinate system (x, y, z) defined as the principal axes of the coated spheroids, and T_3 is given by (3.28), for the appropriate parameters specified as subscripts. The components of the heat flux vector $\vec{q}_3$ relative to the (x',y',z') coordinate system, where the applied heat flux vector $\vec{q}_0$ is parallel to the z' axis (for example), can be obtained with the equation $\left(\vec{q}_3\right)' = M\left(\vec{q}_3\right)$, where M is the transformation matrix and the parenthesis indicate that the heat flux vector is written in matrix form [41]. Note that this latter equation represents the way in which the coordinates of any vector transform from its original coordinate system to a rotated one. This relation together with (3.34) implies that the parameters β_{ii} and $\beta_{ii}L_{ii}^{(2)}$ (see (3.28)) transform according to [41]

$$(\beta)' = M(\beta)M^{-1}, \tag{3.35a}$$

$$\left(\beta L^{(2)}\right)' = M\left(\beta L^{(2)}\right)M^{-1}, \tag{3.35b}$$

where

$$(\beta) = \begin{pmatrix} \beta_{11} & 0 & 0 \\ 0 & \beta_{11} & 0 \\ 0 & 0 & \beta_{33} \end{pmatrix}, \tag{3.36a}$$

$$\left(\beta L^{(2)}\right) = \begin{pmatrix} \beta_{11}L_{11}^{(2)} & 0 & 0 \\ 0 & \beta_{11}L_{11}^{(2)} & 0 \\ 0 & 0 & \beta_{33}L_{33}^{(2)} \end{pmatrix}. \tag{3.36b}$$

Let us now consider that the z axis of the coated spheroids forms an angle θ with the direction of propagation of the applied heat flux (z' direction), as shown in Fig. 3.10. When the coated spheroids are randomly distributed in the plane $x'y'$, this angular displacement between the z and z' axes can be described by a single rotation along the x axis. Therefore the transformation matrix M takes the form [41]

$$M = \begin{pmatrix} 1 & 0 & 0 \\ 0 & \cos\theta & \sin\theta \\ 0 & -\sin\theta & \cos\theta \end{pmatrix}. \tag{3.37}$$

After inserting (3.36a), (3.36b) and (3.37) into (3.35a) and (3.35b), the parameters β'_{ii} and $(\beta L^{(2)})'_{ii}$ can be found. The substitution of these latter results into (3.33a) shows that the components of the effective thermal conductivity K_{ii}^{*} along the x', y' and z' axes (the laboratory coordinate system) are determined by

$$\frac{K_{11}^{*}}{k_3} = \frac{K_{22}^{*}}{k_3} = \frac{2 + \left[\beta_{11}\left(1 - L_{11}^{(2)}\right)(1+\gamma) + \beta_{33}\left(1 - L_{33}^{(2)}\right)(1-\gamma)\right]f}{2 - \left[\beta_{11}L_{11}^{(2)}(1+\gamma) + \beta_{33}L_{33}^{(2)}(1-\gamma)\right]f}, \tag{3.38a}$$

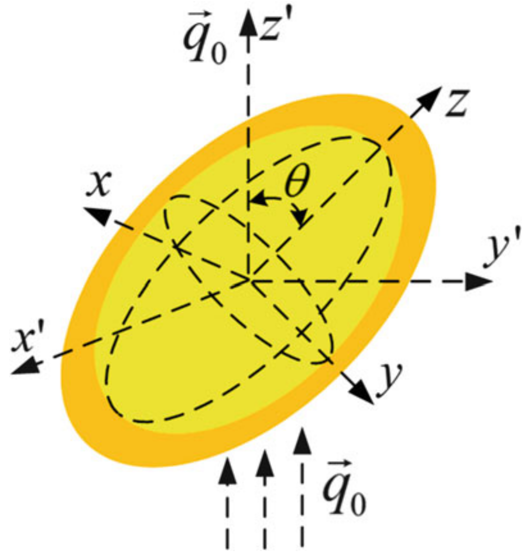

Fig. 3.10 Local (x, y, z) and global (x', y', z') coordinate systems of a coated spheroid

$$\frac{K_{33}^*}{k_3} = \frac{1 + \left[\beta_{11}\left(1 - L_{11}^{(2)}\right)(1-\gamma) + \beta_{33}\left(1 - L_{33}^{(2)}\right)\gamma\right]f}{1 - \left[\beta_{11}L_{11}^{(2)}(1-\gamma) + \beta_{33}L_{33}^{(2)}\gamma\right]f}, \tag{3.38b}$$

where $\gamma = \cos^2\theta$. Note that when $\theta = 0$ ($\gamma = 1$), (3.38a) and (3.38b) reduces to (3.33a), as expected. Equations (3.38a) and (3.38b) determine the effective thermal conductivity of particulate composites that are isotropic in the perpendicular directions to the applied heat flux and anisotropic under the heat flux direction. Thus, the obtained results involve the effects of the coupling length, size, shape, orientation and volume fraction of the particles.

We point out that the primary constituents of the composites under consideration are the matrix and the metallic particles, which are separated by a coating layer, as shown in Fig. 3.9b. This coating layer, as mentioned before, has been introduced to model the lack of thermal coupling at the interface between the matrix and metallic particles [42, 43]. Many experimental results have shown that this phenomenon establishes a discontinuity on the temperature between two dissimilar materials [42]. This temperature jump characterizes the interfacial resistance to the thermal flow and is usually described by means of the interfacial thermal resistance R defined by

$$R = \lim_{\substack{\delta \to 0 \\ k_2 \to 0}} \frac{\delta}{k_2}, \tag{3.39}$$

where $\delta \equiv \sqrt{a_2^2 - a_1^2} = \sqrt{b_2^2 - b_1^2}$ (see the caption of Fig. 3.9). Note that (3.39) differs slightly from the usual definition of R, where the parameter δ is the constant

thickness of the coating layer [8]. In the present case, even though the modeling of the particles as confocal spheroids (see Fig. 3.9b) has allowed us to determine the temperature profiles and the effective thermal conductivity of the composites analytically, the thickness of the coating layer is not constant. Therefore despite (3.51) provides a convenient form of introducing the interfacial thermal resistance, it introduces a small variation in R due to the generic geometry of the particles we chose in this study. Equation (3.51) combines the geometry and the thermal conductivity of the coating layer in just one parameter, which takes into account the interfacial mismatch between the phonons of the matrix and metallic particles. Under these conditions, the coating layer disappears, the inner and outer spheroids have the same geometry, and therefore they have the same geometrical factors ($L_{ii}^{(1)} = L_{ii}^{(2)} \equiv L_{ii}$), the phases of the composite shown in Fig. 3.9a, b decrease to only two constituents, and (3.33c) reduces to

$$k_{ii} = \frac{k_1}{1 + Rk_1L_{ii}(2/a_1 + 1/b_1)}, \tag{3.40}$$

which, in absence of the interfacial thermal resistance, is equal to k_1. The combination of (3.33b) and (3.40) yields

$$\beta_{ii} = \frac{(1 - a_k\gamma L_{ii})k_1 - k_3}{[1 + a_k\gamma(1 - L_{ii})]k_1 + (1 - L_{ii})k_3}, \tag{3.41}$$

where $\gamma = 2/a_1 + 1/b_1$ and $a_K = Rk_3$ is the so-called Kapitza radius [8, 44]. This radius a_K can be interpreted as the equivalent thickness of a layer of the matrix around the spheroidal particles, with a thermal resistance $R = a_K/k_3$. It is important to note that in this limit and in absence of the effect of the electron–phonon coupling ($\chi = 1$) (3.38a) and (3.38b) reduce to the results derived by Nan et al. [8].

To have further insights on the predictions of (3.38a), (3.38b), (3.40) and (3.41), we analyze the following four limiting cases of potential interest:

3.3.1.1 Spherical Particles: $a_1 = b_1$

In this case, $L_{11} = L_{33} = 1/3$, and both (3.38a) and (3.38b) become independent of the direction parameter γ and reduce to

$$\frac{K_{11}^*}{k_3} = \frac{K_{22}^*}{k_3} = \frac{k_1(1 + 2r) + 2k_3 + 2[k_1(1 - r) - k_3]f}{k_1(1 + 2r) + 2k_3 - [k_1(1 - r) - k_3]f}, \tag{3.42}$$

where $k_1 = (k_e + k_p)/\chi$ and $r = a_K/a_1$. In absence of the coupling factor ($\chi = 1$), (3.54) reduces to the result derived by Hasselman and Johnson [5] and Nan et al. [8].

3.3.1.2 Aligned Cylindrical Particles: $a_1 \ll b_1$

For large cylinders aligned parallel to the z axis ($\theta = 0$), $L_{11} = 1/2$, $L_{33} = 0$ and (3.38a) and (3.38b) take the form

$$\frac{K_{11}^*}{k_3} = \frac{K_{22}^*}{k_3} = \frac{k_1(1+r) + k_3 + [k_s(1-r) - k_3]f}{k_1(1+r) + k_3 - [k_s(1-r) - k_3]f}, \tag{3.43a}$$

$$K_{33}^* = k_3(1-f) + k_1 f, \tag{3.43b}$$

In the absence of the coupling factor ($\chi = 1$), (3.43a) reduces to the results presented by Hasselman and Johnson [5] and Nan et al. [8], and (3.43b) is just the simple mixture rule for inclusion arranged in series, as shown by Torquato [2].

Note that a common feature of the effective thermal conductivities of composites reinforced with spheres and cylinders ((3.42) and (3.43a)) is that they both reduce the thermal conductivity of the matrix, independently of the volume fraction of the particles, for a critical radius $a_1 = a_c$ defined by $k_1/k_3 = 1/(1-r)|_{a_1=a_c}$. This relation implies

$$r_c \equiv \frac{a_K}{a_c} = 1 - \chi_c \frac{k_3}{k_s}, \tag{3.44}$$

where $k_s = k_e + k_p$ and χ_c is defined in (3.33f) for $a_1 = a_c$. In terms of the critical ratio r_c, both (3.42) and (3.43a) can be rewritten in the following compact form

$$\frac{K^*}{k_3} = \frac{1 + \sigma\lambda f}{1 - \lambda f}, \tag{3.45}$$

where $\sigma = 1$ and 2, for cylinders and spheres, respectively; and

$$\lambda = \frac{(1-r)\chi_c - (1-r_c)\chi}{(1+\sigma r)\chi_c + \sigma(1-r_c)\chi}, \tag{3.46}$$

Equations (3.44)–(3.46) express that the thermal conductivity of composites reinforced with spheres or cylinders, is totally ruled by the relative radius of these particles with respect to their critical radius a_c, the Kapitza radius a_K and the coupling length d, involved in the parameters χ and χ_c. This shows explicitly that the behavior of K^* is determined by the size scale of the particles. Note that in absence of the interfacial thermal resistance ($r = r_c = 0$), (3.46) reduces to $\lambda = (\chi_c - \chi)/(\chi_c + \sigma\chi)$, which; in contrast to the models developed under the Fourier law approach [1, 2, 4, 5, 12], still depends on the particle size. This reaffirms that not only the interfacial thermal resistance but also the coupling term has an important effect on the thermal conductivity of composites.

The critical radius a_c is determined by (3.44), which in general cannot be solved analytically (see (3.33f)). However if $a_c \ll d$, $\chi_c \approx 1 + k_e/k_p$ and (3.44) yields

$$r_c \equiv \frac{a_k}{a_c} = 1 - \frac{k_3}{k_s}\left(1 + \frac{k_e}{k_p}\right), \quad (3.47a)$$

which indicates that the critical radius a_c is independent of the coupling length d, and is greater than the Kapitza radius a_k ($a_c > a_k$). On the other hand, for $a_c \gg d, \chi_c \approx 1 + (k_e/k_p)/(a_c/d - 1)$ and (3.44) roughly reduces to

$$a_c = \frac{1}{k_s/k_3 - 1}\left(\frac{k_s}{k_3}a_K + \frac{k_e}{k_p}d\right). \quad (3.47b)$$

Equation (3.47b) shows a linear dependence of the coupling length d and suggests that a_c can be interpreted as a weighted average between the Kapitza radius a_c, and d; where the weights are determined by the ratios of thermal conductivities. In general, (3.47a) and (3.47b) establish the minimal and maximum values of the critical radius, respectively.

3.3.1.3 Aligned Flat Plates: $a_1 \gg b_1$

When the particles are laminate flat plates oriented perpendicular to the z axis ($\theta = 0$), $L_{11} = 0, L_{33} = 1$, and (3.38a) and (3.38b) becomes

$$K_{11}^* = k_3(1-f) + \frac{k_s}{\chi}f, \quad (3.48a)$$

$$\frac{1}{K_{33}^*} = \frac{1-f}{k_3} + (\chi + \rho)\frac{f}{k_s}, \quad (3.48b)$$

where $\rho = Rk_s/b_1$. Without taking into account the effect of the coupling factor ($\chi = 1$), the (3.48a) and (3.48b) are identical to the results derived by Torquato [2] and Nan et al. [8].

It is important to note that even though the coupling factor G could be different for spherical, cylindrical and flat plates particles, the obtained results remains valid when an average value of G is used, for each case; as explained in the text underneath (3.15b).

3.3.1.4 Randomly Oriented Spheroidal Particles

This case can be modeled by averaging the direction parameter γ over all possible orientations of the spheroidal particles ($0 \le \theta \le \pi/2$). The calculation of this average is straightforward and is found to be $< \gamma > = 1/3$. After inserting this value into (3.38a) and (3.38b), both equations reduces to

$$\frac{K^*}{k_3} = \frac{3 + [2\beta_{11}(1 - L_{11}) + \beta_{33}(1 - L_{33})]f}{3 - [2\beta_{11}L_{11} + \beta_{33}L_{33}]f}, \tag{3.49}$$

which is the generalization of the Maxwell result [3], for isotropic composites with spheroidal particles. Given that the leading coefficients of the volume fraction f (the quantities in square brackets) in the numerator and denominator of (3.49) are different, the concept of critical radius as was defined by spherical and cylindrical particles, cannot be applied to the case of general spheroidal particles.

3.3.2 Numerical Results and Discussions

First of all, we would like to note the validity of our model. Given that the microscopic electron–phonon interactions requires a space to take place, in general, the TTM is suitable to study the heat conduction in materials with a physical size greater than the mean free path (MFP) of the energy carriers ($2a_1$, $2b_1 > \text{MFP}$). This constraint was the assumption made by Qiu and Tien [31] to derived this model from the Boltzmann transport equation, by evaluating its scattering term using quantum mechanical and statistical considerations. It was found that the coupling length d for a wide variety of metals (as the copper, silver, gold and others) is of the order of hundreds of nanometers (10^{-7} m) [28, 31], and the mean free path of the energy carriers is of the order of nanometers (10^{-9} m) [18] at room temperature. Usually the phonon mean free path, in the order of a few nanometers to tens of nanometer, [45–47] is much longer than the electron mean free path, which could pose constraints on the validity of the model. However, by taking into account the interfacial phonon thermal resistance, the TTM could be extended into a validity regime for spheroidal particles with sizes as small as 5×10^{-9} m [48, 49]. We thus can conclude that the model could be useful for studying the impact of electron–phonon coupling effect on the thermal conductivity of metal-nonmetal materials with a thickness as small as a few nanometers.

The results presented in Sect. 3.3.1 indicate that the major differences of thermal conductivity of metal-nonmetal composites with previously published results is given by the parameter χ, which introduces the effects of the electron–phonon coupling through: (1) the ratio between one semi-axis (size) of the spheroids and their associate coupling length, and (2) the ratio between the electron and phonon thermal conductivities (see (3.33f)). For the limiting case where the particles are nonmetallic, $k_e/k_p < < 1$ or $d \to \infty$ ($G \to 0$), χ reduces to unity ($\chi = 1$), which is its value used under the Fourier approach, and (3.42)–(3.49) reduce to the results obtained by Nan et al. [8]. However, when the particles are metallic ($\chi > 1$), (3.42)–(3.49) exhibit remarkable differences with those results.

Figure 3.11 shows the coupling term χ as a function of the relative size of the particles. Note that the effects of the coupling factor G can only be neglected ($\chi \to 1$) if the dimensions of the spheroidal particles are much larger than the

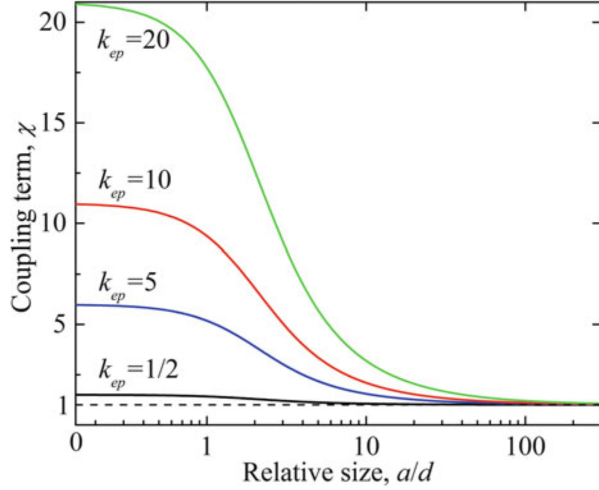

Fig. 3.11 The normalized coupling term χ as a function of the relative size of the spheroidal particles, for different $k_{ep} = k_e/k_p$ values. $a = a_1$ for prolate spheroids, and $a = b_1$ for oblate spheroids

coupling length ($a \gg d$). However, as size of these particles becomes of the same order or smaller than the coupling length ($a \leq d$), the coupling term increases and tends to the limit of $\chi \to 1 + k_e/k_p$, when $a \ll d$. This indicates that the effects of χ should be considered, especially when the electron thermal conductivity is much greater than the phonon thermal conductivity ($k_e > > k_p$), as is the case of metallic particles. Taking into account that for most metals the coupling length is of the order of hundreds of nanometers ($d \sim 10^{-7}$ m) [28, 31], Fig. 3.11 shows that the Fourier law-based models fail when one is dealing with composites with metallic nanoparticles. Another important parameter that determines the effective thermal conductivity of composites involving spherical and cylindrical particles is given by the critical radius a_c, defined in (3.44). Figure 3.12 shows that a_c increases with the Kapitza radius and decreases when the ratio k_s/k_3 of thermal conductivities increases. a_c reaches its minimal value $a_{c,\min} = a_K$ when $k_s/k_3 \to \infty$. This behavior of a_c with a_k indicates that the composites thermal conductivity decreases as a_c increases.

Figure 3.13 shows the influence of the relative particle size with respect to the coupling length on the effective thermal conductivity as a function of the volume fraction of spherical particles. Even though the derived formulas are likely not valid for high volume fractions ($f \to 1$), the lines for the entire range of values of the volume fraction has been plotted simply for completeness. Note that the thermal conductivity of the composite increases when the normalized radius a/d of the spheres increases, such that for $a/d \to \infty$, the thermal conductivity reaches its maximum values, which is predicted by the Fourier law (see Fig. 3.11). As the normalized radius is scaled down, the thermal conductivity of the composite decreases, and it reaches its minimal value for $a/d = 0$. The change of the composite thermal conductivity due to the relative size of the spheres with respect to the coupling length is bounded by $K^*|_{a/d=0} \leq K^* \leq K^*|_{a/d=\infty}$, for any value of the volume fraction. These bounds are determined by the two asymptotic values of

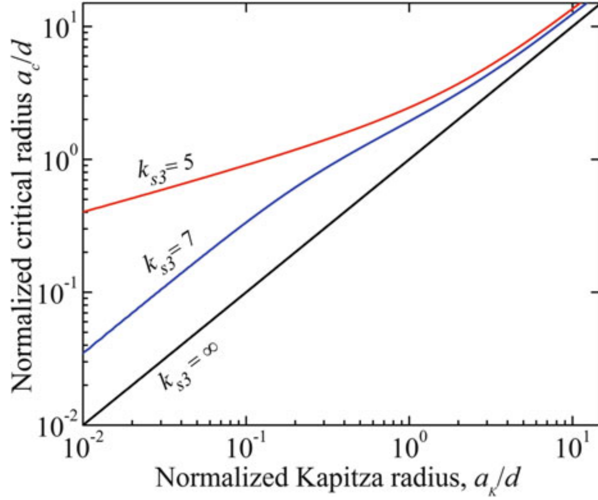

Fig. 3.12 Normalized critical radius a_c/d, as a function of the normalized Kapitza radius a_k/d and the ratio $k_{s3} = k_s/k_3$. Calculations were performed for $k_e/k_p = 4$

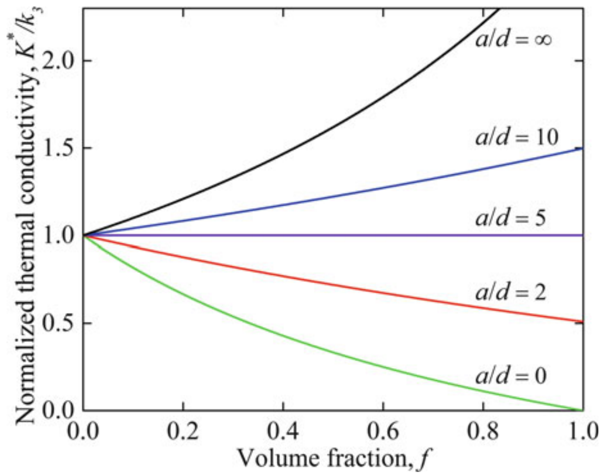

Fig. 3.13 Normalized thermal conductivity of composites with spherical particles as a function of their volume fraction, for different values of the normalized radius a/d. Calculations were performed using $a_c = 5d$, $a_k = 2d$ and $k_e = 3k_p$

the coupling term $\chi = 1, 1 + k_e/k_p$. Note that $K^* > k_3$ for $a > a_c$, $K^* < k_3$ when $a < a_c$, and $K^* = k_3$ at $a = a_c$, for any volume fraction. These features of the effective thermal conductivity are true for any value of the critical and Kapitza radii (see Fig. 3.14a), and they are not only valid for the case of spheres but also for cylinders, as can be shown from (3.45) and (3.46). This indicates that to increase the thermal conductivity of the matrix, the thermal and geometrical properties have to be selected such that, the radius of the particles is larger than their critical radius.

The normalized thermal conductivity of composites with spherical particles as a function of their normalized radius and Kapitza radius is shown in Fig. 3.14a, b, respectively; by comparing the predictions of the proposed approach in presence (solid lines) and absence (dashed lines) of the electron–phonon coupling

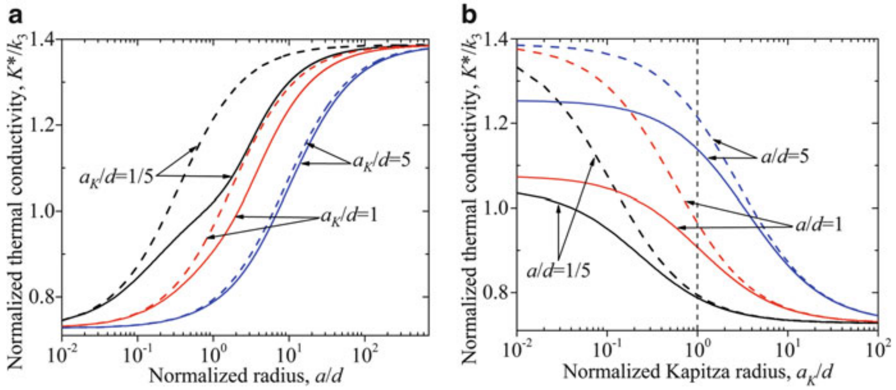

Fig. 3.14 Normalized thermal conductivity of composites as a function of (**a**) the normalized radius of the spherical particles, and (**b**) the normalized Kapitza radius, for different values of the Kapitza and particle radius, respectively. The *continuous* and *dashed lines* correspond to the predictions of the proposed model in presence and absence of the electron–phonon coupling, respectively. Calculations were performed for $k_s = 5k_3$, $k_e = 3k_p$ and $f = 20\ \%$

factor G ($d = \sqrt{k_a/G}$). Figure 3.14a shows that the thermal conductivity of composites is strongly determined by the size of the particles and the Kapitza radius with respect to the coupling length. For a particle radius of the order of the coupling length ($a \sim d$), the effects of G show up remarkably when the Kapitza radius is comparable or smaller than the coupling length ($a_K \leq d$). On the other hand, according to Fig. 3.14a, b, for a fixed Kapitza radius $a_K > d$, those effects become remarkable for a particle radius inside the interval $d \leq a \leq 10d$, and they reduce for other particles sizes. Based on these remarks, it is clear that the contribution of the coupling factor, for particles sizes within this interval ($d \leq a \leq 10d$), is not only present for a small Kapitza radius ($a_K \leq d$) but also for large values ($a_K > d$). Taking into account that the typical values of the coupling length and Kapitza radius are $d \sim a_K \sim 10^{-7}$ m for metal-dielectric interfaces; this indicates that the effect of the electron–phonon coupling on the thermal conductivity of composites could be observed for the case of micro-sized metallic particles, and possibly be overshadowed by the interfacial thermal resistance for nanoparticles.

Figure 3.15a–c show the effective thermal conductivity as a function of the volume fraction of the particles. The comparison of the effective thermal conductivity k of a composite, predicted by the current approach, the models by Nan et al. [8] and by Duan and Karihaloo [12] is shown in Fig. 3.15a, for two relative values of the coupling length d with respect to the radius a of the spherical particles. For a fixed particle radius, k increases when the coupling length decreases, such that for $d \ll a$, it approaches to the predictions of the Nan et al. and Duan and Karihaloo models. Figure 3.15b, c show that the change of the composites thermal conductivity with the volume fraction of randomly oriented oblate (pancake-shaped) or prolate (cigar-shaped) spheroids, respectively. Note that, as in the case of spherical

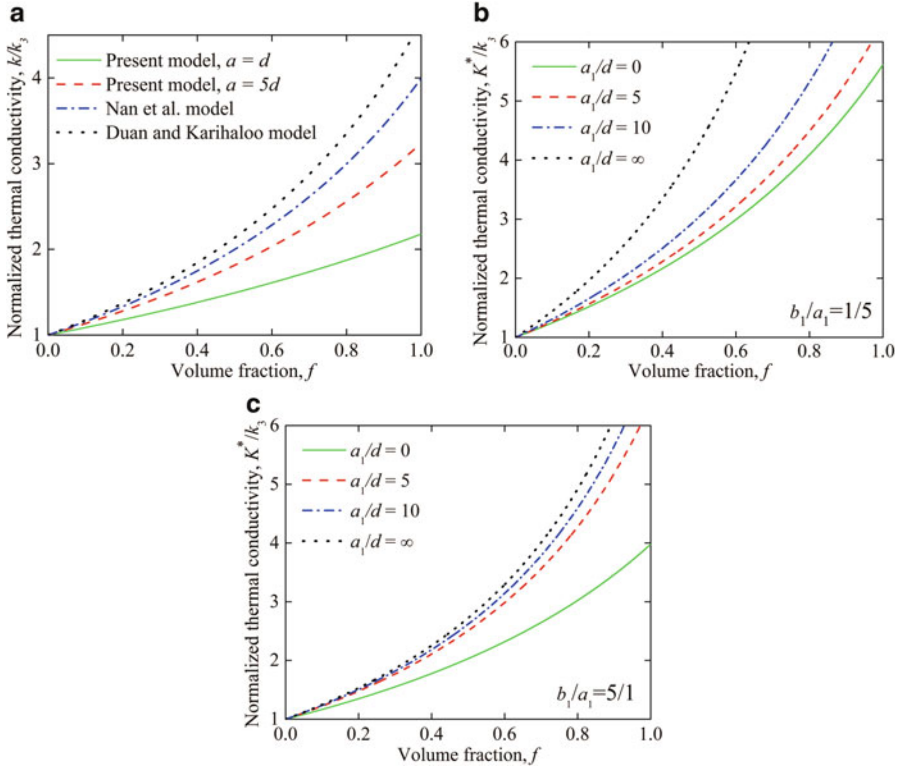

Fig. 3.15 Normalized thermal conductivity of composites as a function of the volume fraction of (**a**) spherical particles, and (**b**) and (**c**) ellipsoidal particles with aspect ratios of $b_1/a_1 = 1/5$, and $b_1/a_1 = 5/1$, respectively. Calculations were performed using $k_s = 25k_3$, $k_e = 3k_p$ and $a = 5a_K$

particles (Fig. 3.13), the effective thermal conductivity is still bounded by its lower values at $a_1/d = 0$, and higher values at $a_1/d = \infty$. This means that the effective thermal conductivity increases when the electron–phonon coupling factor G increases ($d \rightarrow 0$). The corresponding bounds associated with the oblate spheroids are higher than those of the prolate spheroids for any volume fraction. This points out that the composites with randomly oriented oblate spheroids have higher thermal conductivities than those with prolate spheroids.

The effect of the normalized thermal resistance $\rho = Rk_s/b_1$, on K^*/k_3 for oblate ($b_1/a_1 < 1$) and prolate ($b_1/a_1 > 1$) spheroids is shown in Fig. 3.16a, b, respectively. Note that when the interfacial thermal resistance is large enough, the thermal conductivity may not only increases but also decreases with the volume fraction, no matter whether the value of b_1/a_1 is 1/5 or 5. The effective thermal conductivity is largest when the interface thermal resistance is negligible, i.e. $\rho = 0$. According to Figs. 3.15b, c, and 3.16a, b, both the coupling length and the interface thermal resistances impose bounds for the maximum and minimum values of the thermal conductivity of the composite. However, while the thermal conductivity K^* of the

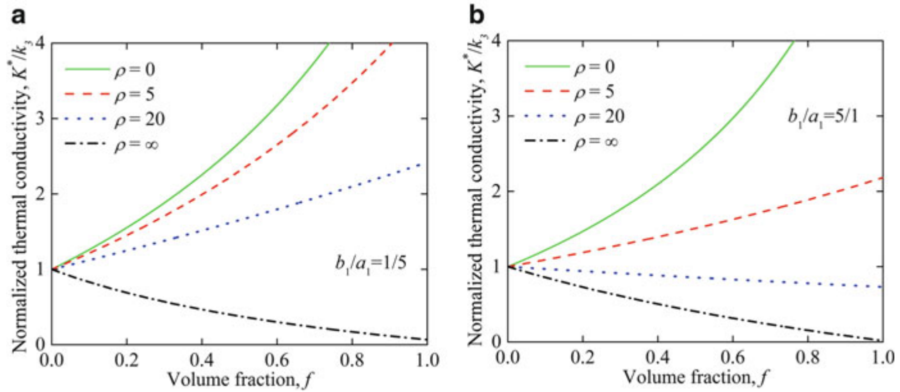

Fig. 3.16 Normalized thermal conductivity of composites as a function of volume fraction for different values of the normalized interfacial thermal resistance and aspect ratios of (**a**) $b_1/a_1 = 1/5$, and (**b**) $b_1/a_1 = 5/1$. Calculations were performed using $k_s = 25k_3$, $k_e = 3k_p$ and $a_1/d = 1/2$

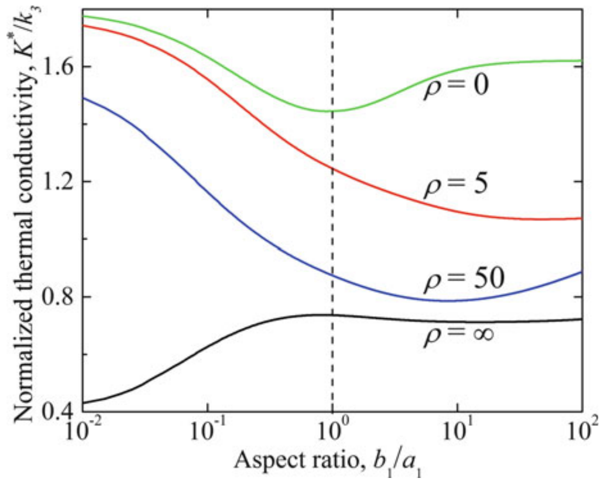

Fig. 3.17 Normalized thermal conductivity of composites as a function of the aspect ratio b_1/a_1, for different values of the normalized interfacial thermal resistance. Calculations were performed using $k_s = 25k_3$, $k_e = 3k_p, f = 20$ % and $a_1/d = 1/2$

composite just increases with the volume fraction, for any value of the coupling length (for $k_s > k_3$), the interfacial thermal resistance may lead to an effective thermal conductivity of the composite that is lower than the one of the matrix ($K^* < k_3$), as was reported by in the literature [8, 23, 50]. This latter feature represents a key difference between the contributions of the interfacial thermal resistance and the coupling length.

Figure 3.17 shows the thermal conductivity of composites as a function of the aspect ratio b_1/a_1 of randomly oriented spheroidal particles and the normalized interfacial thermal resistance ρ. When $\rho = 0$, the thermal conductivity of composites with oblate spheroids is larger than the one with prolate spheroids. The thermal conductivity reaches its minimum value when the particles are spherical ($b_1/a_1 = 1$).

This suggests that the thermal conductivity can be maximized if laminate flat plates are used instead of cylinders or spheres. On the other hand, in presence of the interface thermal resistance ($\rho > 0$) and for a wide range of its values, the effective thermal conductivity increases when the aspect radio b_1/a_1 decreases. However, this trend may be inverted when the interfacial thermal resistance is large enough. K^*/k_3 can be significantly modified by the shape and relative size of the particles with respect to the coupling length, and the Kapitza radius, as shown in Fig. 3.16a, b.

3.4 Composites with High Concentration of Particles

The discussions of Sects. 3.2 and 3.3 are applicable only when the interactions among the particles can be neglected. In such dilute limit, the heat flux lines generated by one particle are not distorted by the presence of the neighboring particles when the distance between neighboring particles is much larger than their size. However, for higher particle concentrations, the distance between neighboring particles can be of the order of the particle size or smaller and the interaction among particles have to be considered, which results in distortion in heat flux that is different from the prediction of the single particle assumption.

One of the first tries to address the problem of the non-dilute concentration of particles was reported by Nielsen [51], who proposed an empirical model for the thermal conductivity of composites based on the analogy between the elastic and thermal properties, which is claimed to be valid for volume fractions of particles up to their maximum packing fraction. One of the key features of this model is the introduction of the maximum volumetric packing fraction of particles, whose effects on the thermal conductivity of the composites increases with the volume fraction of the particles [51–53]. Even though the predictions of this model are in good agreement with a wide variety of experimental data involving composites with spherical and cylindrical particles [51, 52], its semi-empirical nature does make it difficult to explain how the model takes into account the particle interactions, which are strongly present at high particle concentrations. On the other hand, by using the differential effective medium theory proposed by Bruggeman [54], Norris et al. [55], Every et al. [56], and more recently Ordonez-Miranda et al. [57, 58] have reported different models that can potentially be used for the prediction of thermal conductivity in composites with high volume fractions of particles. These Bruggeman theory-based models explain clearly how the composite can be built up by means of a process of incremental homogenization, provided that the matrix remains as a continuous medium and the particles are disconnected. These models agree reasonably well with the experimental data for thermal conductivity of various composites [55–58] and porous media [59], even when the particles are non-uniform as long as the particles do not form large clusters [2, 58]. However, the Bruggeman-based models do not involve the maximum packing fraction of the particles, which plays an increasingly important role on the thermal conductivity of composites with high volume fractions of particles [51, 52]. Despite the limitations of these two approaches,

Nielsen [51] and Bruggeman-based models [55–57], represent the major efforts to describe the thermal conductivity of composites with high concentrations of particles. Thus, a more general approach that takes into account the particle interactions and the maximum packing fraction of the particles is highly desirable.

3.4.1 A Crowding Factor Model

To extend the applicability of the model developed in Sects. 3.2 and 3.3 to higher concentrations, we have recently used the concept of crowding factor to take into the particle interactions [60]. The concept of crowding factor has been introduced in economy as a population density to explain the flow of capital in open and closed economies [61]. In this area of research, the crowding factor determines how different economical agents such as the government and private entities crowd each other with similar solutions to a particular financial problem. Furthermore, the crowding factor is also involved in crowding theory of viscosity of a concentrated suspension of spherical particles [62, 63]. To take into account the particles interactions, in this theory the crowding factor γ is defined as the effective volume fraction of the suspended particles, such that spheres with a partial concentration f_1 crowd other spheres into the remaining free volume fraction $1 - \gamma f_1$. The analytical results of this theory and its generalization have shown good agreement with experimental and simulation data reported in the literature for both low and high concentrations of suspended spherical particles [63]. We extend the use of the crowding factor to describe the thermal conductivity of composites made up of particles with an arbitrary size, shape and orientation within the matrix. The effect of this factor is expected to be important at high particle concentrations, where the crowding among particles is strongly present.

As shown in Fig. 3.18, the composite with volume fraction f of particles can be viewed as embedding particles successively into the matrix with two volume fractions f_1 and f_2, i.e. $f = f_1 + f_2$. We can then analyze the effect of such a homogeneous addition. The addition of the first fraction f_1 of particles increases (or decreases) the thermal conductivity of the matrix by the factor $k_1/k_m = F(f_1)$, where k_1 and k_m are the thermal conductivities of the matrix in presence and absence of particle inclusions, respectively. When $f_1 \to 0$, the function F should reduce to a dilute-limit model. If the second fraction f_2 is added beyond the first fraction, the thermal conductivity will have a further increase (or decrease). This second addition of particles with respect to the first one is to homogeneously place particles with volume fraction f_2 in the available space not occupied by the particles with concentration f_1. By defining the crowding factor γ as the effective volume of particles per unit "real" volume of them, such as γV_1 is the effective volume of the particles in V_1, which is "seen" by the particles in V_2. Therefore, the second addition of f_2 fraction of particles further changes the effective thermal conductivity to $k/k_1 = F(f_{21})$, where $f_{21} = V_2/(V_T - \gamma V_1) = f_2/(1 - \gamma f_1)$ is the volume fraction of V_2 in the accessible volume $V_T - \gamma V_1$, where V_T is the total volume of the composite. The contribution of the crowding factor

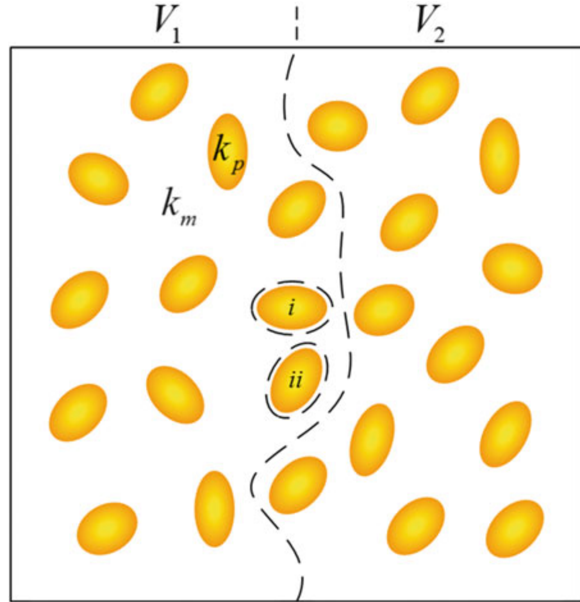

Fig. 3.18 Diagram of the composite under consideration with a total volume of particles $V_1 + V_2$

γ is particularly clear for high volume fractions of particles. For instance, given that a particle of V_2 does not fit in between particles i and ii (see Fig. 3.18), the effective volume of the particles should be slightly larger than its "real" volume. Therefore, it is expected that the parameter γ depends strongly on the geometry and maximum packing volume fraction of particles.

Taking into account that the introduction of f_2 also reduces the free volume available for f_1, the crowding factor for fractions f_1 and f_2 is mutual and therefore the effective concentration of f_1 in the composite is $f_{12} = f_1/(1 - \gamma f_2)$. To account for this mutual effect, the function $F(f_1)$ must be replaced by $F(f_{12})$. We can then determine the normalized thermal conductivity $k/k_m = (k_1/k_m)(k/k_1)$ of the composite with a total concentration $f = f_1 + f_2$ of particles by

$$F(f_1 + f_2) = F\left(\frac{f_1}{1 - \gamma f_2}\right) F\left(\frac{f_2}{1 - \gamma f_1}\right), \tag{3.50}$$

which is a functional equation for the function $F(f) = k/k_m$. Equation (3.50) establishes that this function satisfies these two conditions: $F(0) = 1$ and $F(2x) = F^2(x/(1 - \gamma x)) > 0$, which implies that $F(f)$ is always positive. The solution of (3.1) can be determined by noting that: (1) For the limiting case of $\gamma \to 0$, (3.1) reduces to Cauchy's exponential equation [64], whose solution is given by $F(x) = \exp(Cx)$, where C is an arbitrary constant. (2) Based on this asymptotic solution and on the Wentzel-Kramers-Brillouin-Jeffreys method [65], which is usually applied to solve the one-dimensional

Schrodinger equation with a position-dependent potential, the general solution of (3.1) when $\gamma \neq 0$ can be written as

$$F(f) = \exp(CfG(f)), \tag{3.51}$$

where the function $G(f)$ reduces to the unity when the parameter $\gamma = 0$. By combining (3.50) and (3.51), it is found that G satisfies a functional equation, which for $f_1 = f_2 = x$, takes the form

$$G(2x) = \frac{1}{1-\gamma x} G\left(\frac{x}{1-\gamma x}\right). \tag{3.52}$$

Since $G(f)$ should be a well-behaved function of f, we can seek a solution for (3.52) in the form of

$$G(x) = \sum_{n=0}^{\infty} A_n (\gamma x)^n, \tag{3.53}$$

where $A_0 = 1$ to guarantee that (3.51) reduces to the solution of the Cauchy's exponential function for $\gamma = 0$. Equation (3.53) represents the well-known power series method, which is usually applied to find the solution of second-order ordinary differential equations [26, 66]. After inserting (3.53) into (3.52), the following relation is found for the coefficients A_n,

$$\sum_{n=0}^{\infty} A_n (2\gamma x)^n = \sum_{n=0}^{\infty} \frac{A_n (\gamma x)^n}{(1-\gamma x)^{n+1}}. \tag{3.54}$$

By applying the binomial theorem to expand the factor $(1 - \gamma x)^{-(n+1)}$ in the power series of γx, and rearranging the resulting double series in (3.54), one finds that A_n are determined by the following recurrence relation,

$$2^n A_n = \sum_{l=0}^{n} \frac{n! A_l}{l!(n-l)!}, \qquad A_0 = 1. \tag{3.55}$$

Based on mathematical induction, it is easy to find that all the coefficients determined by (3.55) are given by $A_n = 1$. This simple result transforms the right-hand side of (3.53) into a geometric series [26], which allows writing the solution of (3.52) in the closed form $G(x) = (1 - \gamma x)^{-1}$. Thus, the general solution for the function $F(f)$ of (3.50) is given by

$$F(f) = \frac{k}{k_m} = \exp\left(\frac{Cf}{1-\gamma f}\right), \tag{3.56}$$

where C is a constant that should depend on the thermal properties and the geometry of matrix and particles. Based on (3.56), it is easy to verify that

$$F(f)=\prod_{n=1}^{N}F\left(\frac{f_n}{1-\gamma(f-f_n)}\right), \tag{3.57}$$

if the volume fraction f is divided into N small fractions, such that $f=f_1+f_2\ldots+f_N$. This means that the functional form of (3.56) is independent of the number of small volume fractions used to derive it.

Equation (3.56) establishes that the effect of the crowding factor γ increases with the volume fraction f of the particles, as expected. Taking into account that the heat conduction through composites depends on the thermal, geometrical and interfacial properties of their components, (3.56) indicates that the combined effect of these properties can be unified in two parameters γ and C, which are usually proportional, as shown in the next section. Furthermore, according to (3.56), a higher crowding factor is expected when the thermal conductivity of the particles is higher than that of the matrix and the interfacial thermal resistance between the matrix and particles is not so high, as shown below. This is physically reasonable, given that in this case, the particles represent favorable pathways for the heat conduction through them.

The crowding factor γ should vary with f, because the physical process of filling the matrix with particles depends on their volume fraction. We can therefore re-write the crowding factor as $\gamma(f)=\gamma_0\psi(f)$, such that $\gamma(0)=\gamma_0$ $(\psi(0)=1)$. However, the constants C and γ_0, should then be determined by comparing (3.56) with a dilute-limit model, as shown in the next sub-section, to find the final form of the effective thermal conductivity at the non-dilute limit.

3.4.2 Applications

We apply the generalized crowding factor approach, as derived above, to specific model systems where a dilute-limit model of effective thermal conductivity of composites is available. After finding constants C and γ_0 for specific models, this generalization will extend the applicability range of the existing dilute-limit model for both low and high volume fractions of particle inclusions. Two composites of potential interest are dielectric or metallic particles embedded in a dielectric matrix.

3.4.2.1 Dielectric/Dielectric Composites

Typical examples of dielectric/dielectric materials are ceramic and semiconductor particles/fillers in polymer matrix. For these composites with a low volume fraction of spherical particles (dilute limit), the experimental data on the thermal conductivity agree well with the model derived by Nan et al. [8], whose result can be written as

$$\frac{k}{k_m} = \frac{1 + 2Af}{1 - Af}, \tag{3.58}$$

where

$$A = \frac{1 - \left(k_m/k_p + a_K/a\right)}{1 + 2\left(k_m/k_p + a_K/a\right)}, \tag{3.59}$$

where $a_K = Rk_m$ is the so called the Kapitza radius [8], R is the interfacial thermal resistance between the matrix and the particles of radius a. Note that the composite thermal conductivity depends equally on the ratios k_m/k_p and a_K/a of thermal conductivities and particle size with the Kapitza radius, respectively.

By expanding (3.56), for a first-order approximation (low volume fractions of particles) and comparing the obtained result with (3.58), it is found that $C = 3A$ and $\gamma_0 = A$. Therefore the thermal conductivity of the dielectric/dielectric composites for both low and high volume fractions of particles is determined by

$$\frac{k}{k_m} = \exp\left(\frac{3Af}{1 - A\psi f}\right). \tag{3.60}$$

The function $\psi(f)$ in (3.60) should also satisfy the following limiting values: $\psi(0) = 1$ and $\psi(f_0) = f_0^{-1}$, where f_0 is the maximum packing fraction of the particles. The values of f_0 are reported in literature for different types of particles and packing [51]. For instance, for spherical particles with a random distribution, $f_0 = 63.7\%$. The first of these conditions ensures the agreement between (3.58) and (3.60), at low volume fractions ($f \ll f_0$); and the second one guarantees the maximum increase (or decrease) of the thermal conductivity of the composite is at $f = f_0$ [51, 53]. This last fact can be seen in the denominator of the exponential function in (3.60), which indicates that the maximum ($A > 0$) or minimum ($A < 0$) value of the composite thermal conductivity occurs for $\psi(f_0)f_0 = 1$. The simplest function that satisfies both conditions is given by the equation of a straight line, as follows

$$\psi = 1 + \frac{(1 - f_0)}{f_0^2} f. \tag{3.61}$$

Equation (3.61) shows that the effect of the maximum packing fraction of the particles on the thermal conductivity of the composite appears through the function ψ. Even though this function is not unique, under the current approach, it is expected that (3.61) represents a good approximation given that the crowding factor $\gamma(f) = \gamma_0\psi(f)$ depends slightly on the volume fraction f, as was shown by Lewis and Nielsen [52], to modify the Kerner equation. Note also that the first-order approximation of (3.60) resembles to the semi-empirical model of these last researchers, which

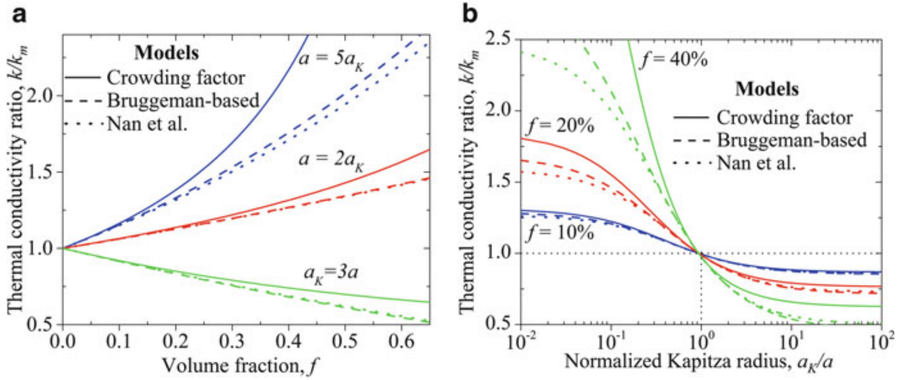

Fig. 3.19 Comparison of the predictions of the crowding factor model, a Bruggeman-based model [57] and the model by Nan et al. [8] for the thermal conductivity ratio of composites with spherical dielectric particles as a function of their (**a**) volume fraction and (**b**) normalized Kapitza radius. Calculations were performed for $k_p = 15k_m$ and $f_0 = 64\ \%$

indicates that the proposed approach provides a consistent extension of Nan et al. [8] and Lewis and Nielsen [52] models, who also generalize previous results.

Figure 3.19a, b shows the comparison of the predictions of the current crowding factor model, a Bruggeman-based model [57] and the model by Nan et al. [8] for the thermal conductivity of dielectric/dielectric composites with spherical particles, as a function of their volume fraction and normalized Kapitza radius, respectively.

Note that for low volume fractions of particles ($f < 15\ \%$), the predictions of the three models are in good agreement. For higher particles concentrations ($f > 15\ \%$), however, the predictions of the crowding factor model are larger than the ones of the Bruggeman-based model and the model by Nan et al., especially when the ratio a/a_K between the particle and Kapitza radii increases. This is expected for $k_p > k_m$ (in this case $k_p = 15k_m$), given that the current model takes into account the interactions among the particles through the crowding factor, which increases the overall thermal conductivity of the composite. For a particles radius of the order of or smaller than the Kapitza radius ($a/a_K = 2,\ 1/3$, in Fig. 3.19a), the predictions of the Bruggeman-based model and the model by Nan et al. are almost overlapped, due to the strong effect of the interfacial thermal resistance. Both the Bruggeman-based model and the crowding factor model take into account the particle interactions. However, both Fig. 3.19a, b show that predictions of the crowding factor model are larger than the ones of the Bruggeman-based model, which suggests that the crowding factor model considers a stronger contribution of the particles interactions than that of the Bruggeman-based model.

For $a_K/a < 1 - k_m/k_p$ ($a_K/a > 1 - k_m/k_p$), Fig. 3.9b shows that the composite thermal conductivity predicted by the three models increases (decreases) when the volume fraction of the particles increases, as reported in the literature [7, 40]. On the other hand, the composite thermal conductivity becomes

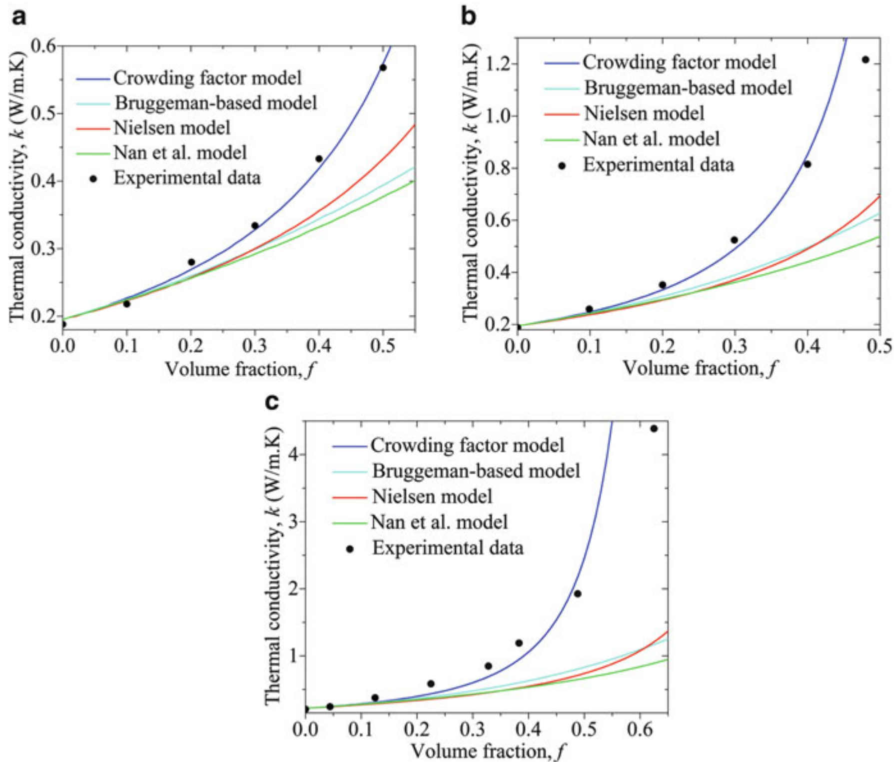

Fig. 3.20 Comparison of the theoretical curves and experimental data [67, 68] for the thermal conductivity of (**a**) silica/epoxy, (**b**) alumina/epoxy and (**c**) aluminum nitride/polyimide composites, as a function of the volume fraction of the spherical particles

independent of f and equals to the matrix thermal conductivity, for $a_K/a = 1 - k_m/k_p (= 1 - 1/15$, in Fig. 3.19b).

Figure 3.20a–c shows the experimental data reported for the thermal conductivity of silica/epoxy [67], alumina/epoxy [67], and aluminum nitrate/polyimide [68] composites as a function of the volume fraction f f, in comparison with the theoretical predictions of the crowding factor model in (3.60), the Bruggeman-based model [57], the models by Nielsen [51] and Nan et al. [8]. The required physical properties at room temperature of each phase used for the calculations are given in Table 3.2. The radius of the spherical particles reported here stands for the average value.

Based on Fig. 3.20a–c, it is clear that the predictions of the three models reported in the literature remarkably underestimate the composite thermal conductivity, while the crowding factor model shows much better agreement with the experimental data. We also note that better agreements are found in Fig. 3.20a and that in Fig. 3.20c, especially for the experimental point of highest volume fraction. We can attribute the discrepancy to the fact that the aluminum nitrate particles were not

Table 3.2 Material properties used in the calculations [50, 67, 68]

Properties	k_p (W/mK)	k_m (W/mK)	a (μm)	a_K (μm)
Silica/Epoxy	1.5	0.195	13.5	1.89
Alumina/Epoxy	36	0.195	13.5	1.34
Al nitrate/Polyimide	200	0.22	2	0.146

totally spherical. The effect of particles shape becomes stronger as the volume fraction of particles increases. The good general agreement of the crowding factor model with experimental data at low as well as at high volume fractions of particles shows that this model represents a remarkable improvement with respect to the dilute-limit models, which are not able to describe the thermal conductivity of composites at high volume fractions of particles.

3.4.2.2 Metal-Nonmetal Composites

To extend the validity of the results obtained in the Sect. 3.3 to concentrations of particles up to the maximum packing fraction, we need to apply the developed crowding factor model. This can be done by equating the first-order expansion $k/k_m = 1 + Cf/(1 - \gamma_0 f)$ of the crowding factor model in (3.56) with the dilute limit model expressed in (3.38a) and (3.38b), to find the constants C and γ_0.

For the case of spherical metallic particles uniformly distributed within a dielectric matrix, this comparison applied to (3.42) and (3.56) yields $C = 3A$ and $\gamma_0 = A$, where the parameter A is determined by

$$A = \frac{1 - (\chi k_3/k_s + a_K/a)}{1 + 2(\chi k_3/k_s + a_K/a)}, \tag{3.62a}$$

$$\chi = 1 + \frac{k_e}{k_p}\frac{d}{a}\frac{i_1(a/d)}{i_1'(a/d)}, \tag{3.62b}$$

Therefore, according to (3.56), the thermal conductivity of the metallic/dielectric composite for both low and high volume fractions of particles is given by

$$\frac{k}{k_3} = \exp\left(\frac{3Af}{1 - A\psi f}\right), \tag{3.63}$$

which has the same mathematical form than (3.60), derived for dielectric/dielectric composites, but with a different parameter A.

The thermal conductivity of composites with spherical metallic particles as a function of their volume fraction and normalized radius is shown in Fig. 3.21a, b, respectively. The continuous lines correspond to the predictions of the present crowding factor model and the dashed ones to the dilute-limit result in (3.42). As expected, the predictions of the current model are larger than the ones of the

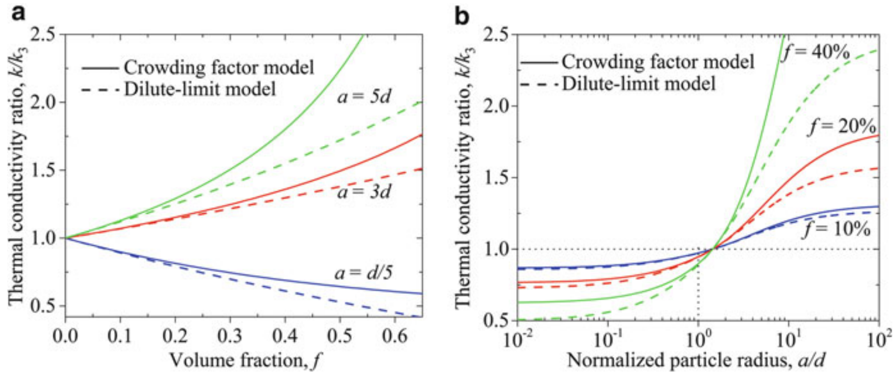

Fig. 3.21 Comparison of the predictions of the crowding factor model and the dilute-limit model for the thermal conductivity of composites with spherical metallic particles as a function of their (**a**) volume fraction and (**b**) normalized radius. Calculations were performed for $k_s = 15k_3$, $k_e = 5k_p$, $a_K = d$ and $f_0 = 64\ \%$

dilute limit model, especially when the volume fraction of the particles increases. Taking into account that the thermal conductivity of the metallic particles is usually much larger than the ones of the dielectric matrix (in this case $k_s = 15k_3$), this increase over the predictions of the dilute limit approach is due to the particle interactions, whose contribution is considered in (3.63). According to both Fig. 3.21a, b, the dilute and non-dilute approaches predict that the composites thermal conductivity increases with the particles volume fractions and size, when $a/d > (1 - \chi k_3/k_p)^{-1} a_K/d (\approx 1.5$, in this case) (see (3.62a) and (3.63)). On the other hand, for $a/d < (1 - \chi k_3/k_p)^{-1}$ a_K/d, the composites thermal conductivity decreases when the particles radius decreases and/or the particles volume fraction increases.

3.5 Conclusions

The thermal conductivity of composites made up of metallic and non-metallic micro/nanoparticles embedded in a solid non-metallic matrix has been modeled and analyzed at both the dilute and non-dilute concentrations of particles. Taking into account the strong scattering of the energy carriers with the surface of the embedded nanoparticles, the thermal conductivity of nanocomposites has been determined in the dilute limit, by modifying both the thermal conductivity of the matrix and particles, accordingly. It has found that the particle shape and size dependence of the composite thermal conductivity shows up through the collision cross-section per unit volume of the particles and the mean distance that the energy carriers travel inside the particles.

The effect of the electron–phonon interactions within metallic particles shows up through the reduction of the thermal conductivity of these particles with respect to its

values obtained under the Fourier law approach. The thermal conductivity of composites with metallic particles depend strongly on (1) the relative size of the particles with respect to the intrinsic coupling length, and (2) the ratio between the electron and phonon thermal conductivities. The obtained results have shown that the particle size dependence of the composite thermal conductivity appears not only through the interfacial thermal resistance but also by means of the electron–phonon coupling.

The applicability of the proposed approach for the dilute limit has been further extended to describe the thermal conductivity of composites with particle concentrations up to the maximum packing fraction of the particles. This has been achieved by considering the particle interactions by means of the crowding factor, which is determined by the effective volume of particles. The comparison of the predictions of the crowding factor model with other non-dilute models reported in the literature has shown that this model not only generalize those models but also capture accurately the effect of the particle interactions. The predictions of the two analytical approaches proposed to describe the particle size and particle interaction effects are in good agreement with experimental and numerical data reported in the literature.

Acknowledgements We acknowledge the financial support for studying thermal and thermoelectric transport in nanostructured materials by AFOSR Thermal Science Program (Grant No. FA9550-11-1-0109), AFOSR STTR programs (PI: Dr. Sayan Naha) and DARPA ACM Program (PI: Dr. Jeff Sharp).

References

1. Milton, G.W.: The Theory of Composites. Cambridge University Press, Cambridge, NY (2002)
2. Torquato, S.: Random Heterogeneous Materials. Springer, New York (2001)
3. Maxwell, J.C.: Electricity and Magnetism. Clarendon, Oxford (1873)
4. Benveniste, Y.: Effective thermal-conductivity of composites with a thermal contact resistance between the constituents—nondilute case. J. Appl. Phys. **61**, 2840–2843 (1987)
5. Hasselman, D.P.H., Johnson, L.F.: Effective thermal-conductivity of composites with interfacial thermal barrier resistance. J. Compos. Mater. **21**, 508–515 (1987)
6. Nan, C.W., Jin, F.S.: Multiple-scattering approach to effective properties of piezoelectric composites. Phys. Rev. B **48**, 8578–8582 (1993)
7. Nan, C.W.: Effective-medium theory of piezoelectric composites. J. Appl. Phys. **76**, 1155–1163 (1994)
8. Nan, C.W., Birringer, R., Clarke, D.R., Gleiter, H.: Effective thermal conductivity of particulate composites with interfacial thermal resistance. J. Appl. Phys. **81**, 6692–6699 (1997)
9. Khitun, A., Balandin, A., Liu, J.L., Wang, K.L.: In-plane lattice thermal conductivity of a quantum-dot superlattice. J. Appl. Phys. **88**, 696–699 (2000)
10. Duan, H.L., Karihaloo, B.L., Wang, J., Yi, X.: Effective conductivities of heterogeneous media containing multiple inclusions with various spatial distributions. Phys. Rev. B. **73**, 174203–174215 (2006)
11. Prasher, R.: Thermal conductivity of composites of aligned nanoscale and microscale wires and pores. J. Appl. Phys. **100**, 034307–034315 (2006)
12. Duan, H.L., Karihaloo, B.L.: Effective thermal conductivities of heterogeneous media containing multiple imperfectly bonded inclusions. Phys. Rev. B. **75**, 064206–064214 (2007)

13. Minnich, A., Chen, G.: Modified effective medium formulation for the thermal conductivity of nanocomposites. Appl. Phys. Lett. **91**, 073105–073107 (2007)
14. Tian, W.X., Yang, R.G.: Thermal conductivity modeling of compacted nanowire composites. J. Appl. Phys. **101**, 054320–054324 (2007)
15. Jeng, M.S., Yang, R.G., Song, D., Chen, G.: Modeling the thermal conductivity and phonon transport in nanoparticle composites using Monte Carlo simulation. J. Heat Trans. Trans. ASME **130**, 042410–042420 (2008)
16. Yang, R.G., Chen, G.: Thermal conductivity modeling of periodic two-dimensional nanocomposites. Physical. Rev. B **69**, 10 (2004)
17. Chen, G.: Thermal conductivity and ballistic-phonon transport in the cross-plane direction of superlattices. Physical. Rev. B **57**, 14958–14973 (1998)
18. Kittel, C.: Introduction to Solid State Physics, 8th edn. Wiley, Hoboken, NJ (2005)
19. Tian, W.X., Yang, R.G.: Phonon transport and thermal conductivity percolation in random nanoparticle composites. Comput. Model. Eng. Sci. **24**, 123–141 (2008)
20. Tian, W.X., Yang, R.G.: Effect of interface scattering on phonon thermal conductivity percolation in random nanowire composites. Appl. Phys. Lett. **90**, 263105–263108 (2007)
21. Yang, R.G., Chen, G., Dresselhaus, S.M.: Thermal conductivity of simple and tubular nanowire composites in the longitudinal direction. Phys. Rev. B **72**, 125418–125424 (2005)
22. Prasher, R.: Thermal boundary resistance of nanocomposites. Int. J. Heat Mass. Tran. **48**, 4942–4952 (2005)
23. Ordonez-Miranda, J., Yang, R.G., Alvarado-Gil, J.J.: On the thermal conductivity of particulate nanocomposites. Appl. Phys. Lett. **98**, 233111–233113 (2011)
24. Chen, G.: Nanoscale Energy Transport and Conversion: A Parallel Treatment of Electrons, Molecules, Phonons, and Photons. Oxford University Press, Oxford. New York (2005)
25. Flammer, C.: Spheroidal Wave Functions. Dover Publications, Mineola, N.Y. (2005)
26. Arfken, G.B., Weber, H.J.: Mathematical Methods for Physicists, 6th edn. Elsevier, Boston (2005)
27. Balandin, A.A.: Thermal properties of graphene and nanostructured carbon materials. Nat. Mater. **10**, 569–581 (2011)
28. Majumdar, A., Reddy, P.: Role of electron-phonon coupling in thermal conductance of metal-nonmetal interfaces. Appl. Phys. Lett. **84**, 4768–4770 (2004)
29. Kaganov, M.I., Lifshitz, I.M., Tanatarov, M.V.: Relaxation between electrons and crystalline lattices. Sov. Phys. JETP **4**, 173–178 (1957)
30. Anisimov, S.I., Kapeliovich, B.L., Perelman, T.L.: Electron emission from metals surfaces exposed to ultra-short laser pulses. Sov. Phys. JETP **39**, 375–377 (1974)
31. Qiu, T.Q., Tien, C.L.: Heat-transfer mechanisms during short-pulse laser-heating of metals. J. Heat Tran. Trans. ASME **115**, 835–841 (1993)
32. Lin, Z., Zhigilei, L.V., Celli, V.: Electron-phonon coupling and electron heat capacity of metals under conditions of strong electron-phonon nonequilibrium. Phys. Rev. B **77**, 075133–075149 (2008)
33. Luh, D.A., Miller, T., Paggel, J.J., Chiang, T.C.: Large electron-phonon coupling at an interface. Phys. Rev. Lett. **88**, 256802–256805 (2002)
34. Melnikov, D.V., Fowler, W.B.: Electron-phonon interaction in a spherical quantum dot with finite potential barriers: The Frohlich Hamiltonian. Phys. Rev. B **64**, 245320–245328 (2001)
35. Byerly, W.E.: An Elementary Treatise on Fourier's Series and Spherical, Cylindrical, and Ellipsoidal Harmonics, with Applications to Problems in Mathematical Physics. Dover Publications, Mineola, NY (2003)
36. Hopkins, P.E., Kassebaum, J.L., Norris, P.M.: Effects of electron scattering at metal-nonmetal interfaces on electron-phonon equilibration in gold films. J. Appl. Phys. **105**, 023710–023717 (2009)
37. Mahan, G.D.: Kapitza thermal resistance between a metal and a nonmetal. Phys. Rev. B **79**, 075408–075413 (2009)

38. Sergeev, A.V.: Electronic Kapitza conductance due to inelastic electron-boundary scattering. Phys. Rev. B **58**, 10199–10202 (1998)
39. Landau, L.D., Lifshits, E.M., Pitaevskii, L.P.: Electrodynamics of Continuous Media, 2nd edn. Pergamon, Oxford, New York (1984)
40. Ordonez-Miranda, J., Yang, R.G., Alvarado-Gil, J.J.: A model for the effective thermal conductivity of metal-nonmetal particulate composites. J. Appl. Phys. **111**, 044319–044330 (2012)
41. Goldstein, H., Poole, C.P., Safko, J.L.: Classical Mechanics, 3rd edn. Addison-Wesley, San Francisco (2002)
42. Swartz, E.T., Pohl, R.O.: Thermal-resistance at interfaces. Appl. Phys. Lett. **51**, 2200–2202 (1987)
43. Swartz, E.T., Pohl, R.O.: Thermal boundary resistance. Rev. Mod. Phys. **61**, 605–668 (1989)
44. Davis, L.C., Artz, B.E.: Thermal-conductivity of metal-matrix composites. J. Appl. Phys. **77**, 4954–4960 (1995)
45. Kanskar, M., Wybourne, M.N.: Measurement of the acoustic-phonon mean free-path in a freestanding metal-film. Phys. Rev. B **50**, 168–172 (1994)
46. Stojanovic, N., Maithripala, D.H.S., Berg, J.M., Holtz, M.: Thermal conductivity in metallic nanostructures at high temperature: electrons, phonons, and the Wiedemann-Franz law. Phys. Rev. B **82**, 075418–075426 (2010)
47. Chantrenne, P., Raynaud, M., Baillis, D., Barrat, J.L.: Study of phonon heat transfer in metallic solids from molecular dynamic simulations. Microscale Thermophys. Eng. **7**, 117–136 (2003)
48. Chen, G., Zeng, T.F.: Nonequilibrium phonon and electron transport in heterostructures and superlattices. Microscale Thermophys. Eng. **5**, 71–88 (2001)
49. Zeng, T.F., Chen, G.: Phonon heat conduction in thin films: impacts of thermal boundary resistance and internal heat generation. J. Heat Tran. Trans. ASME **123**, 340–347 (2001)
50. Hasselman, D.P.H., Donaldson, K.Y., Liu, J., Gauckler, L.J., Ownby, P.D.: Thermal-conductivity of a particulate-diamond-reinforced cordierite matrix composite. J. Am. Ceram. Soc. **77**, 1757–1760 (1994)
51. Nielsen, L.E.: The thermal and electrical conductivity of two-phase systems. Ind. Eng. Chem. Fund. **13**, 17–20 (1974)
52. Lewis, T.B., Nielsen, L.E.: Dynamic mechanical properties of particulate-filled composites. J. Appl. Polym. Sci. **14**, 1449–1471 (1970)
53. Nielsen, L.E.: Generalized equation for elastic moduli of composite materials. J. Appl. Phys. **41**, 4626–4627 (1970)
54. Bruggeman, D.A.G.: Calculation of various physics constants in heterogenous substances. I. Dielectricity constants and conductivity of mixed bodies from isotropic substances. Annalen Der Physik **24**, 636–664 (1935)
55. Norris, A.N., Sheng, P., Callegari, A.J.: Effective-medium theories for two-phase dielectric media. J. Appl. Phys. **57**, 1990–1996 (1985)
56. Every, A.G., Tzou, Y., Hasselman, D.P.H., Raj, R.: The effect of particle-size on the thermal-conductivity of Zns diamond composites. Acta Metall. Mater. **40**, 123–129 (1992)
57. Ordonez-Miranda, J., Alvarado-Gil, J.J.: Thermal conductivity of nanocomposites with high volume fractions of particles. Compos. Sci. Technol. **72**, 853–857 (2012)
58. Ordonez-Miranda, J., Alvarado-Gil, J.J., Medina-Ezquivel, R.: Generalized bruggeman formula for the effective thermal conductivity of particulate composites with an interface layer. Int. J. Thermophys. **31**, 975–986 (2010)
59. Bussian, A.E.: Electrical conductance in a porous-medium. Geophysics **48**, 1258–1268 (1983)
60. Ordonez-Miranda, J., Yang, R.G., Alvarado-Gil, J.J.: A crowding factor model for the thermal conductivity of particulate composites at non-dilute limit. J. Appl. Phys. **114**, 064306–064312 (2013)
61. Chang, W.-y., Tsai, H.-f., Lai, C.-C.: Imperfect competition and crowding out. Econ. Lett. **41**, 73–79 (1993)
62. Vand, V.: Viscosity of solutions and suspensions. J. Phys. Colloid Chem. **52**, 277–299 (1948)

63. Mooney, M.: The viscosity of a concentrated suspension of spherical particles. J. Colloid Sci. **6**, 162–170 (1951)
64. Aczél, J., Dhombres, J.G.: Functional Equations in Several Variables. Cambridge University Press, Cambridge (1989)
65. Hassani, S.: Mathematical Physics: A Modern Introduction to Its Foundations. Springer, New York (1999)
66. Polyanin, A.D., Zaitsev, V.F.: Handbook of Exact Solutions for Ordinary Differential Equations, 2nd edn. Chapman & Hall, Boca Raton (2003)
67. Wong, C.P., Bollampally, R.S.: Thermal conductivity, elastic modulus, and coefficient of thermal expansion of polymer composites filled with ceramic particles for electronic packaging. J. Appl. Polym. Sci. **74**, 3396–3403 (1999)
68. Wang, J.J., Yi, X.S.: Preparation and the properties of PMR-type polyimide composites with aluminum nitride. J. Appl. Polym. Sci. **89**, 3913–3917 (2003)

Chapter 4
Nano Bulk Thermoelectrics: Concepts, Techniques, and Modeling

Nikhil Satyala, Payam Norouzzadeh, and Daryoosh Vashaee

Abstract The beneficial effects of nanostructured material systems have provided a significant momentum to accomplish high-efficiency thermoelectric materials for power generation and cooling applications. The quantum size effects have been widely explored in order to shrink the contribution of lattice thermal conductivity of the thermoelectric systems, thereby enhancing the overall figure-of-merit. Modifying the nanoscale level structural features and the creation of additional phonon scattering sites in the form of grain boundary interfaces became the basis for fabrication of nanostructured materials. The requirement of specific physical features in nanostructured thermoelectrics also brought a variety of changes to the fabrication processes. In this chapter, we review some of the prominent techniques for fabrication of such nanostructured material systems. An overview of the concepts and techniques for theoretical modeling of the charge carrier and phonon transport mechanisms in the interfacial regions is presented. Further, the constructive effects of nanostructuring in thermoelectric materials are discussed based on a theoretical approach via Boltzmann transport equation under the relaxation time approximation. The calculations are used to demonstrate the advantages and disadvantages of nanoscale effects in the well-known material systems of Si_xGe_{1-x} and Mg_2Si.

4.1 Introduction

The unique technique of harvesting waste heat energy for power generation by means of thermoelectric (TE) materials was originally discovered by T. J. Seebeck in 1821 [1]. This effect was later enriched by J. C. A. Peltier and Lord Kelvin via

N. Satyala • P. Norouzzadeh • D. Vashaee (✉)
Department of Electrical and Computer Engineering, Oklahoma State University,
526 N Elgin Ave, Tulsa, OK 74106, USA
e-mail: satyala@okstate.edu; payam.norouzzadeh@okstate.edu;
daryoosh.vashaee@okstate.edu

X. Wang and Z.M. Wang (eds.), *Nanoscale Thermoelectrics*, Lecture Notes in Nanoscale Science and Technology 16, DOI 10.1007/978-3-319-02012-9_4,
© Springer International Publishing Switzerland 2014

their discoveries of the Peltier and Thomson effects, respectively [2, 3]. The Seebeck effect promoted the power generation characteristics of the thermoelectric materials whereas the Peltier effect stimulated the development of the materials and devices for cooling applications. The Thomson effect introduced a comprehensive interrelationship between the Seebeck and the Peltier effects via thermodynamically related coefficients [3]. The thermocouple may have been the most widely used thermoelectric device where a voltage difference generated across the terminals of an open circuit made of two dissimilar metals is used to measure the temperature.

A quantitative characterization of the Seebeck coefficient and the electrical conductivity also paved a path for the identification of many suitable materials for thermoelectric device fabrication [4]. Material systems such as Bi_2Te_3, PbTe, $Si_{1-x}Ge_x$, etc. were originally found to have favorable characteristics for developing high-efficiency thermoelectric materials. However, the initially identified material systems were not adequately efficient for major application areas such as heat engines and refrigeration systems. The pursuit of developing high-efficiency thermoelectric materials was boosted greatly by the emergence of the concept of the dimensionless figure-of-merit (*ZT*), introduced by A. F. Ioffe in 1949 [5, 6]. The figure-of-merit mathematically relates the fundamental properties such as the electrical conductivity (σ), Seebeck coefficient (S), the thermal conductivity due to carriers (κ_e) and the lattice (κ_l) of the TE material, and is defined as [5],

$$ZT = \frac{\sigma S^2}{\kappa_e + \kappa_l} T \tag{4.1}$$

The introduction of the figure-of-merit led to the design and development of numerous optimization techniques for thermoelectric materials that primarily focused on maximizing the (σ/k) ratio while maintaining a substantial Seebeck coefficient. Figure 4.1 illustrates the recently reported *ZT* versus corresponding temperature ranges for various high-performance bulk TE materials [6, 7]. The state-of-the-art bulk TE material systems include many compounds that are suitable for low and medium temperature ranges. However, as indicated by the vertical line in Fig. 4.1, a dearth of high-performance TE materials systems is markedly observed at high temperatures.

4.1.1 Methods to Enhance Efficiency of Thermoelectric Materials

Material systems based on alloys were largely promoted to reduce the lattice thermal conductivity (κ_l) via enhanced scattering of phonons at point defects [5, 8, 9]. Therefore, alloying was employed as the initial technique for thermoelectric material optimization. Later, Slack and Mahan independently defined that in the optimal form the chemical characteristics of a good thermoelectric material essentially

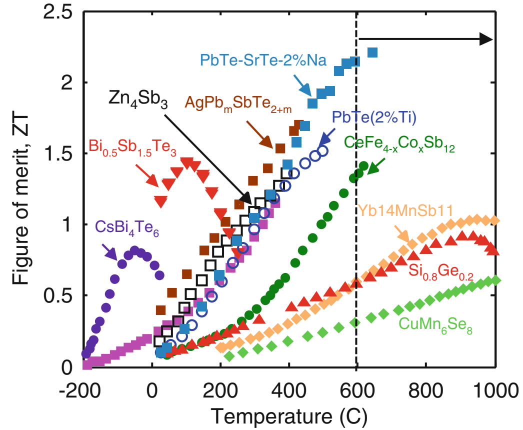

Fig. 4.1 Comparison of the reported maximum figure-of-merit (*ZT*) of various bulk thermoelectric compounds [6, 7]

include phonon–glass/electron–crystal type features [10, 11]. These features include optimum band gap, high mobility, multiple valleys near the Fermi surface, and low thermal conductivity. Such discoveries led to the evolvement of numerous other techniques for optimization of thermoelectric material systems.

The technique of alloying for reducing thermal conductivity was originally proposed in the 1950s [8]. Alloying of compounds with similar band structure was found to reduce the thermal conductivity significantly without disrupting the electrical properties of the compounds. Other methods of introducing point defects through nanoinclusions were also found to have a significantly positive impact on the thermoelectric figure-of-merit. In addition to alloying, further optimization techniques based on material characteristics were also instigated. Techniques such as microstructure modifications [12], bulk nanostructuring [13, 14], energy filtering techniques [15, 16], resonant energy levels [15], quantum wells and superlattices [17], complex material systems [18], etc. have been subsequently introduced.

The nanostructured systems primarily rely on the reduction of lattice and electronic thermal conductivity by enhanced scattering of phonons at the grain boundaries of the same material system. Nanocomposites fundamentally implement the same principle of scattering of phonons; however, the scattering locations are created by nano-sized grains of more than one material compacted to the locations next to each other. Well-known material systems like nanostructured Si_xGe_{1-x} and $Bi_xSb_{2-x}Te_3$ were reported to benefit from very low thermal conductivities ensuing in high figure-of-merit over a wide range of temperatures [13, 19, 20]. However, recent theoretical estimations also revealed that the same nanostructuring techniques could prove to be detrimental to the thermoelectric characteristics of some materials systems such as Mg_2Si owing to the losses incurred in electrical conductivity [21–23].

The techniques of nanostructure modifications were also successfully implemented in material systems like p-type $Bi_{0.52}Sb_{1.48}Te_3$ by means of embedding nanocrystalline domains in an amorphous matrix of the host material [13]. The nanostructure,

also comprised nanocrystals with fine and coherent grain boundaries, and resulted in enhanced electrical conductivity via promoting of selective phonon scattering. The unique structural properties lead to a figure-of-merit of 1.56 at 300 K [13]. Energy filtering methods were also found to enhance the Seebeck coefficient by means of increasing the average energy of the carriers as a result of scattering of low energy carriers at grain boundaries. This type of preferential low energy carrier scattering via energy filtering techniques was employed on materials systems like InGaAs/InGaAlAs superlattices and bulk nanostructured PbTe [16, 24]. A significant enhancement in the power factor ($S^2\sigma$) of the superlattices was attained; however, nanostructured PbTe suffered loss in mobility due to scattering of carriers at grain boundaries.

Modifications in electronic properties such as band structure and density of states (DOS) for optimization of the thermoelectric properties were also reported. It was theoretically demonstrated that sharp features in the DOS close to the Fermi energy result in superior thermoelectric power factor [17]. An impurity-activated resonant level in the DOS is an analogous technique by which additional energy states are generated near to the conduction or valence band edges. The additional states are expected to contribute to the carrier transport and boost the magnitude of the Seebeck coefficient when the Fermi level is considerably close to these states. The enhancement in the Seebeck coefficient by means of impurity-activated resonant levels was reported by Heremans et al. for Tl-doped PbTe [25]. A figure-of-merit of twice that of the undoped bulk PbTe was achieved in Tl-doped PbTe as a direct result of the enhancement of the Seebeck coefficient due to the resonant states created by Tl near to the valence band. Combining the two concepts of bulk nanostructuring and resonant levels can potentially result in both low thermal conductivity and enhanced power factor to make more promising TE materials systems.

Quantum confinement techniques were also explored in the form of low-dimensional quantum wells and superlattices. The methods predominantly aimed at dramatically improving the figure-of-merit by means of controlling the electron and phonon energy spectra via structural alterations. Significant reduction in thermal conductivity and a subsequent enhancement in the figure-of-merit were reported in superlattice structures such as Bi_2Te_3/Sb_2Se_3 and PbTe/PbTeSe quantum-dot superlattices [26, 27]. Other complex material systems such as quantum wires, clathrates, and skutterudites have also been reported to help achieve better thermoelectric properties.

In the recent years, the nanoscale effects in techniques such as nanostructuring and quantum confinement have significantly contributed to the advancement of thermoelectric material systems. Therefore, a thorough understanding of the nanoscale effects pertaining to the structural modifications is required. The emphasis of this chapter is to provide a methodical insight into the nanoscale effects in state-of-the-art thermoelectric materials. In this chapter, the bulk nanostructured material systems will be referred with a new terminology, namely, *Nano Bulk*.

4.2 Comparison of Bulk and Thin Film Thermoelectrics

With the new stimuli of the research community in the thermoelectric (TE) area, TE research has continued in two general directions: (1) theoretical models that predict TE properties and offer superior materials and structural designs and (2) experimental efforts in finding new materials or structures that show enhanced TE properties. The follow-ups to these efforts have been in two main directions. One direction has been in finding new bulk materials and their advanced engineering to achieve a higher *ZT* [28, 29]. Complex crystal structures that yield low lattice thermal conductivity such as $FeCo_3Sb_{12}$ [30], $Yb_{14}MnSb_{11}$ [31], $Ba_8Ga_{16}Ge_{30}$ [32], Zn_4Sb_3 [33], or Ag_9TlTe_5 [34] are several examples of this direction. Other examples of this direction include engineered energy band structures with increased number of energy band minima close to the Fermi surface such as $PbTe_{0.85}Se_{0.15}$: Na or with sharp features in the density of states close to the band edge such as $Tl_{0.02}Pb_{0.98}Te$ [25] that result in the enhancement of the TE power factor [35].

The second direction has been in the use of nanostructures to reduce the thermal conductivity more than the electrical conductivity through the scattering of phonons at interfaces [26, 36]. It has also been possible to maintain or improve the TE power factor through quantum size effects [27, 36, 37] or interface energy filtering [38, 39] while the thermal conductivity was reduced. Some examples of this group are Bi_2Te_3/Sb_2Te_3 superlattices (SL) [27], and PbTe/PbSeTe quantum dot superlattices (QDSL) [26]. The main reason for the improvement in *ZT* in these structures comes from the reduction of the phonon thermal conductivity. For some other cases such as ErAs:InGaAs/InGaAlAs SLs [40], the enhancement in *ZT* was due to the increase of the Seebeck coefficient due to the hot carrier energy filtering [16, 39] and the reduction of the thermal conductivity. Bulk nanostructured $Bi_{0.5}Sb_{1.5}Te_3$ [41], $Si_{0.8}Ge_{0.2}$ [42, 43], and PbTe-SrTe [44] materials have also shown high *ZT* resulting from the reduction of the thermal conductivity due to the increase of the phonon interface scattering.

With the rising demand on new applications of TE materials both for power generation and cooling functions, there is an increasing interest in material structures that are synthesized with cost effective approaches from earth-abundant and environmentally friendly elements. For this reason, superlattice structures made with thin film deposition techniques are usually too expensive for large scale applications and their use is limited to niche applications such as thermal management of telecommunication lasers or micro-power generators for medical or military applications. However, nano bulk materials made with the powder processing and sintering approaches are potentially inexpensive to synthesize and are appropriate for batch processing [20, 39]. They increase the figure-of-merit of the bulk materials typically based on the same principle as in superlattices, that the scattering of phonons should be enhanced relative to electrons. Hence, prior investigations of low-dimensional superlattices have now evolved into research and development of bulk materials containing nanostructured features.

Furthermore, the irreversible losses due to the electrical and thermal contact resistances become predominant factors when the thickness of the TE device is usually less than 100 μm. Thin film superlattices grown by vacuum deposition techniques are typically 5–20 μm thick, versus 200 μm for the thinnest thermoelectric devices based on bulk materials [45]. As a result, TE devices made from bulk materials, even when sliced to a few hundred microns, have shown larger efficiency than the ones made by thin film deposition.

The fabrication of TE modules from thin films also still suffers from a low yield due to the sensitivity to the height variation for making the electrical contacts [46]. Nevertheless, thin film TE devices can address certain thermal management problems in microelectronics that are not often possible through bulk devices. Thermal stabilization of laser diodes, infra-red detectors, charge-coupled devices (CCD), light-emitting diodes (LED), and other optoelectronic devices are among applications that can benefit from a faster response time and cooling power density of on-chip micro-thermoelectric refrigerators.

4.2.1 Significance of the Nano Bulk TE Materials

Bulk material systems such as Bi_2Te_3, Sb_3Te_3, PbTe, $Si_{1-x}Ge_x$, etc. profited majorly in their nano bulk structured forms. For the case of $Bi_{0.5}Sb_{1.5}Te$, the improvement in TE performance was possible owing to the significantly beneficial effect of nanostructuring in this material as shown in Fig. 4.2 [14]. It can be observed from Fig. 4.2a that nano bulk $Bi_{0.5}Sb_{1.5}Te$ demonstrates an approximate 50 % drop in lattice thermal conductivity compared to the bulk crystalline form over a wide range of temperature.

Nano Bulk Si_xGe_{1-x} is also well known for its superior TE properties compared to its bulk crystalline form [47, 48]. The *ZT* of p-type bulk alloy of $Si_{0.8}Ge_{0.2}$ was enhanced from 0.65 (bulk) to 0.95 at 800 °C with the help of nanostructuring. A significant drop in thermal conductivity was demonstrated by nano bulk phosphorous-doped n-type $Si_{0.8}Ge_{0.2}$ resulting in a *ZT* of 1.5 at 900 °C [48]. The thermal and electrical performance of nano bulk $Si_{0.8}Ge_{0.2}$ was recently reported to show significant dependence on the average crystallite size [42]. Theoretical calculations performed on bulk and nano bulk $Si_{0.8}Ge_{0.2}$ demonstrated that the lattice part of the thermal conductivity makes up for 80 % of the total thermal conductivity as shown in Fig. 4.2b. Images from the scanning electron microscopy of the fractured surface of the as-pressed sample and the transmission electron microscopy of the powder are shown in Fig. 4.3a, b, respectively, depicting the crystallite sizes in the nano bulk $Si_{0.8}Ge_{0.2}$ which lead to the low thermal conductivities of less than 3.0 W/mK. Similarly, other highly efficient techniques such as nanoparticle-in-alloy were explored theoretically and a figure-of-merit that is nearly 2.5 times the value of the bulk system of SiGe alloys was predicted [49]. The nanoscale effects owing to the crystallite sizes have been theoretically and experimentally substantiated in many recent reports [19, 42].

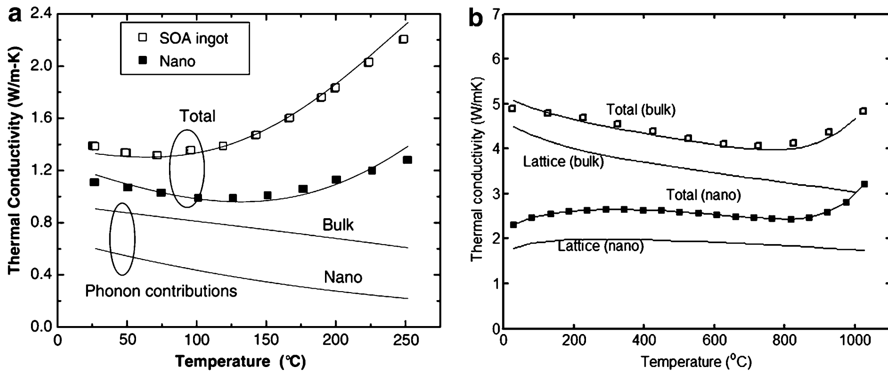

Fig. 4.2 (**a**) Thermal conductivity versus temperature of $Bi_{0.5}Sb_{1.5}Te_3$—state-of-the-art (SOA) bulk ingot compared to nanocrystalline sample [14]; (**b**) Effect of bulk nanostructuring on thermal conductivity of $Si_{0.80}Ge_{0.2}$ [42]

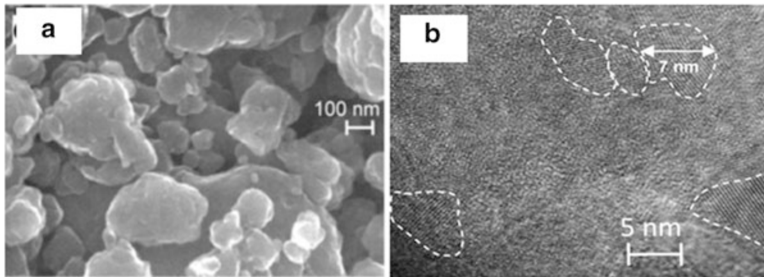

Fig. 4.3 (**a**) Scanning Electron Microscopy (SEM) and (**b**) Transmission Electron Microscopy (TEM) images of nanostructured $Si_{0.8}Ge_{0.2}$ [42]

For a superior synopsis of the recent advances in TE materials through nanostructuring, the readers could refer to the *CRC Handbook of Thermoelectrics* [50] and published review articles [6, 15]. However, within the scope of this chapter, the primary focus will be on the effects of bulk nanostructuring comprehended by means of a theoretical approach as will be discussed in further sections. In order to thoroughly provide insight into the effects of bulk nanostructuring on the TE properties of materials, a simulation based assessment of the TE characteristics of Si_xGe_{1-x} and Mg_2Si follows. In the upcoming sub-sections of this chapter a systematic discussion of the experimental methods for making nano bulk materials, electronic properties of these materials, theoretical approaches to nanostructuring mechanisms, modeling strategies, carrier transport properties, phonon scattering mechanisms and the effect of grain sizes on the TE properties in Si_xGe_{1-x} and Mg_2Si is presented. As the end, the simulation results are critically discussed in order to conclusively show that in certain material systems detrimental effects due to nanostructuring may diminish the overall benefits.

4.3 Fabrication of Nano Bulk Thermoelectrics

Fabrication of nanostructured materials through a bulk process is challenging, but modification of bulk process conditions so that the *ZT* is enhanced is even more difficult. The modification process does not always lead to improved thermoelectric efficiency. Thermal stability of the devices made by nanostructured materials at high temperatures is another influencing factor as the nanoscale features may be removed due to the diffusion and energies of the interfaces. There are two major approaches via top-down and bottom-up methods to fabricate nano bulk thermoelectrics and each of them can be divided in to several branches. These methods are introduced in the following sections and their advantages and disadvantages are briefly discussed.

4.3.1 Top-Down Approach

The top-down methods start from a bulk material and the corresponding nanostructured features are obtained by structural deformations. There are two commonly used techniques which are based on sever plastic deformation (SPD) or thermal processing.

4.3.1.1 Sever Plastic Deformation (SPD)

The basis of the SPD method is to increase the free energy of the polycrystals and generate many more defects and grain boundaries in various nonequilibrium processes so that the microstructure is transformed into nano-sized crystallites while the structure of the coarse-grained material remains unchanged without any associated changes in the cross sectional dimensions of the samples [51]. Key principles of SPD are increasing dislocation density by heavily deforming materials, forming dislocation walls, and making transformation of dislocation walls into grain boundaries. Some known methods in this category are listed below:

- *High pressure torsion*: A small thin disk is placed between two massive anvils under high pressure and intense shear strain is introduced by rotating the two anvils with respect to each other. In this method, the applied hydrostatic pressure is high; therefore, the fracture is suppressed and thus the method is applicable to hard and less ductile materials.
- *Equal channel angular pressing (extrusion)* [52, 53]: In equal channel angular pressing (ECAP) the billet is placed in a die and a high pressure is exerted to it through a punch. It is one of the SPD methods for producing ultra-fine grain structures in nanoscale which applies a large amount of shear strain into the materials without changing the shape or dimensions of the billets.
- *Accumulated roll bonding* [54, 55]: This is another SPD process to produce ultra-fine grain structures in nanoscale which is applicable for continuous

production of the nanostructured materials. In this method 50 % rolled material is cut in two, stacked to make the initial dimension, and then rolled again. By repeating the deformation and bonding processes, the nanostructured materials can be produced.

4.3.1.2 Thermal Processing

Thermal processing techniques have widely been applied to induce nanoscale precipitates [56–58]. In order to fabricate such nanostructures in a metastable solid-solution the starting material is subjected to a thermal processing procedure like spinodal decomposition, nucleation, or the growth mechanism [56]. In the thermal process of matrix encapsulation the liquid mixture is cooled rapidly so that the insoluble minority phase is precipitated, and the embedded nanoparticles in the host material are created [57]. This technique has been applied for n-type $AgPbTe_2$/PbTe [58] and $Pb_{1-x}Sn_xTe$/PbS [56] and p-type $Na_{1-x}Pb_mSb_yTe_{m+2}$ [59] and NaPbTe-SrTe [60].

4.3.2 Bottom-Up Processes

This type of method starts from atoms and molecules as building blocks and the bulk materials are subsequently assembled from elemental constituents. Bottom-up methods are used to assemble nanoparticles into dense solid phases to attain a nanostructured material. The main technique frequently applied for thermoelectric materials consists of powder processing and subsequent consolidation.

4.3.2.1 Powder Processing

The powder characteristics facilitate low temperature sintering, which is a prerequisite for mitigating grain coarsening during the sintering process. The power can be synthesized by a chemical or physics method. The nanoparticles should be preferably non-agglomerating and uniform in size and shape or preferably monodispersed to result in a dense nano bulk material after consolidation. Non-agglomerated nanoparticles are made by wet chemical methods which are usually expensive procedures. The physical method is mainly based on mechanical milling which often results in agglomerated nanoparticles of different sizes in an inexpensive way.

- *Chemical methods*: Several chemical methods have been developed to fabricate metal nanostructured materials with different shapes such as silver (Ag) nanoplates [61], silver nanodisks [62, 63], gold(Au) nanoplates [64], and gold nanodisks [65]. It has been shown that a high-temperature organic solution approach and a hydrothermal process can be used to prepare hexagonal nanoplates of Bi_2Te_3

and Bi_2Se_3 respectively [66]. High-yield two-dimensional micrometer-sized hexagonal nanoplates of Sb_2Te_3 using a solution-based synthesis method have been also produced [67].
- *Mechanical milling*: In this process the powder is milled with different techniques during which the particles are cold welded and fractured many times resulting in ultimate fineness. The most commonly used milling method has been ball milling where the powder mixture is placed in the ball mill and is subjected to high energy collision from the balls. Among these, vibratory ball mills, planetary ball mills, and attritor mills have been common equipment for ball milling.

4.3.2.2 Consolidation

- *Hot pressing* [41, 47, 68, 69]: It is a pressure assisted method for compacting nanopowders to obtain bulk nanostructured materials, which is usually accompanied by sintering at various times, temperatures, and atmospheres. The method of ball milling and hot pressing is cost effective, applicable for many material systems, and can produce nano bulk materials which are thermally stable. Several research groups have reported the implementation of this technique for n-type and p-type $Si_{0.8}Ge_{0.2}$ and some types of $Bi_xSb_{2-x}Te_3$ [41, 42, 70]. Spark plasma sintering [71–73] is a newer technique compared with conventional sintering approach where the heat is provided by an external source. In this method the heat is generated by passing a pulsed DC current through a die and conductive powder. This method creates a very high heating rate (100–1,000 K/min) which leads to a fast sintering process. In a similar approach, a DC current is used for heating the material [41]. The high heating rate allows sintering the material with reducing the grain growth therefore attaining smaller gains in the bulk material.

4.3.3 Theory of Charge Carrier and Phonon Transport at Interfaces

Theoretical studies of phonon transport in superlattices showed that reduction in lattice thermal conductivity does not need a well-defined geometry or a perfect interface at atomistic level [74]. The only requirement is having a high density of interfaces which is present in nano bulk structures. To enhance the *ZT*, the phonons have to be scattered more efficiently than charge carriers. Therefore, as a rule of thumb, the size of nanostructures should be smaller than the phonon mean free path and larger than the charge carrier mean free path. In practice, charge carriers have narrower spectrum than that of phonons. The interface spacing below which the electrical conductivity is reduced considerably can be estimated through the spectrum of the mean free path. If the interface size is larger than a single scattering site, it will have deteriorative impact on charge transport and decreases the *ZT*.

Continued reduction in characteristic lengths in nanostructures has led to increasing importance of interfaces in transport properties of materials. In fact, a large portion of the advances in enhancing *ZT* for nanostructured materials comes from the beneficial effects of the interfaces.

4.3.3.1 Interface Definition and Types

The region in a crystalline or polycrystalline material that separates two crystallites is called interphase boundary or simply interface. The interface represents a discontinuity with a minimum thickness of two atoms. The neighboring grains may have different orientations. A random connection of two different crystallites may lead to dangling bonds, large crystallographic discrepancies, or voids in the interface region. If the crystallites' chemical composition and lattice parameters are the same, the interface is called phase boundary; and if the crystallites belong to different materials, the interface is called heterophase boundary. In an interface, the atoms are shifted from their regular positions as compared to a perfect crystal and introduce defects into crystal structure. Interfaces play an important role in determining the properties of the nano bulk structure due to the large relative fraction of atoms that are present in the interphase boundary. Interfaces decrease the electrical and thermal conductivities of the material and provide preferred places for the precipitation of the new phases from the solid.

To get a sense of the atomic arrangement of the neighboring crystals at an interface, the interfaces can be divided into four classes:

1. Coherent interface: There is a perfect match between two nanocrystals across the interface.
2. Strained coherent interface: Imperfect matching between two nanocrystals causes some strain at the interface, which increases with the size of the crystallites.
3. Semi-coherent interface: Although dislocations contribute to the energy of the system, they reduce the strain energy. The coherent interface with strain is likely to be transformed to a semi-coherent interface with dislocations.
4. Incoherent interface: There is no lattice match between the crystallites across the interface.

As the matching between the crystallites improves, the interfacial free energy becomes smaller. In incoherent interfaces atoms that have more freedom to move are considered mobile, so they have higher energy. Liu et al. [75] established that the coherent interfaces generally exist in nanocrystalline composites, and according to the experimental results, they are largely unaffected by the fabrication process. It is rational that the coherent interfaces play a key role in assembling the composite nanostructures because the coherent interfaces require that the crystal planes from the two adjacent crystallites to have similar basal spacing and that the crystallites bind tightly to form interfaces which are thermodynamically stable. There is currently very little known about the effect of nanoscale coherent interface on energy transport. Nonetheless, some researchers have reported excellent *ZT* for

$Ag_{1-x}Pb_mSbTe_{2+m}$ with $m = 10$ and 18 (2.1 at 800 K) which consist coherent interfaces [58]. The observation of coherent nanointerface in a PbTe/GeTe nanocomposite was also reported at the atomic level and atomistic modeling was applied to characterize the local chemical composition and crystalline structure and the coherency of interfaces was confirmed [76]. It was found that the large value of *ZT* was attributed to the nanoscale coherent interfaces that improved phonon scattering while having minimal effect on the charge carrier transport [76]. The coherent nanointerfaces between the matrix and nanoscale inclusions offer three advantages in thermal design for *ZT* improvement:

(a) The nanoscale inclusions significantly reduce the mean free path of the phonons, thereby reducing the lattice thermal conductivity.
(b) The strain at the coherent interface considerably enhances phonon scattering and causes a large thermal resistance at the interface, which helps to further reduce the overall thermal conductivity.
(c) Electron scattering remains largely unaffected by the coherent interfacial structure, which leads to a very little decrease in the electrical conductivity. Such a combined effect is very favorable for enhancing *ZT*.

Charge carriers and phonons encounter different resistances across an interfacial region. The charge carrier boundary resistance originates from the impact of the charge carriers to a coulomb potential at the interface. This potential depends on the band structure and doping concentration of the interfacial materials. Both a potential barrier and a well can scatter charge carriers due to the disruption of the periodic potential. Charge carriers can tunnel through the barrier or be thermally excited over it depending on the width and height of the barrier [77]. Phonons lose their memory after encountering the interface. The reflectivity or transmission of phonons is determined by density of states and phonon velocities of different modes. The reflected phonons form the phonon boundary resistance which depends on the available energy states at both sides of the interface [78]. The charge carrier and phonon resistances at interfaces lead to nonequilibrium transport properties near the interface and at a distance from the interface, named energy relaxation length, they reach to a new thermal equilibrium.

4.3.3.2 Nano Bulk Structures

In a nano bulk material, grains and interfacial structures may have three distinct types as depicted in Fig. 4.4. Type 1 (Fig. 4.4a) is a nanocrystalline structure made of a single material composition. Type 2 (Fig. 4.4b) consists of embedded nanoparticles inside the lattice. Figure 4.4c is a nanocrystalline structure made from mixture of two or more of different materials or phases. In this structure the grains and/or the grain boundary regions are made from different materials. Experimentally, a nano bulk thermoelectric material may have a structure similar to any of these types or a combination of them. For example, a peak *ZT* of 1.4 at 100 °C was achieved in a p-type nanocrystalline $Bi_{0.5}Sb_{1.5}Te_3$ bulk alloy using the type

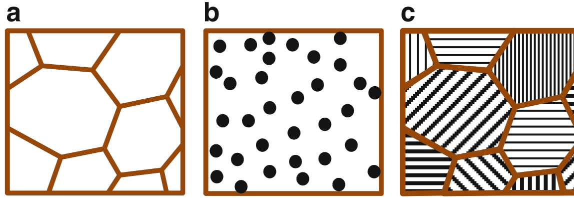

Fig. 4.4 Three types of nano bulk structures: (**a**) single component nanocrystalline material, (**b**) bulk material with embedded nanoparticles, (**c**) multicomponent nanocrystalline material

1 interface, which separates single phase crystallites [41]. Also, the p-type PbTe nanostructured bulk with SrTe precipitates, which demonstrated a *ZT* value of 2.2 at 615 °C, took advantage of the combination of Type 1 and 2 structures to more effectively scatter heat carrying phonons across the integrated length scales [44]. A combination of Type 3 with 1 and/or 2 can make various other structures such as core–shell nanoparticle doped structures, or nanocrystalline structures with embedded nanoparticles. There is yet no report of enhanced *ZT* through Type 3 nano bulk structure.

4.3.3.3 Interfacial Effects on Charge and Phonon Transport

The interface in a nano bulk material is characterized by mismatch in bulk properties and irregularities in the region near the interface. Different carriers of charge and heat encounter different resistances across this interfacial region. Charge carriers encounter a coulomb potential at the interface resulting in the carrier boundary resistance, and phonons hit the interface and lose their memory. The probability of phonon being scattered to one side of the interface or the other is related to the density of states and the phonon group velocity of each vibrational mode. These interfacial resistances at an interface region result in electron and phonon thermal nonequilibrium near the interface, which can affect the thermoelectric properties significantly. The schematic diagram of Fig. 4.5 lists the interfacial effects on charge and heat carriers transport parameters and their connections with the thermoelectric properties.

4.3.3.4 Charge Transport at Interface

There are three major challenges in analyzing the charge transport in nano bulk materials. First, the characteristic lengths in a nano bulk material can become smaller than the charge carrier wavelength as the grains become too small. This will reduce the accuracy of the Boltzmann Transport Equation results as the BTE is valid only if the charge carrier mean free path is much larger than the wavelength [79, 80]. The second difficulty arises from the unknown properties and the composition of the interfaces. As the density of the interfaces increases in the nano bulk

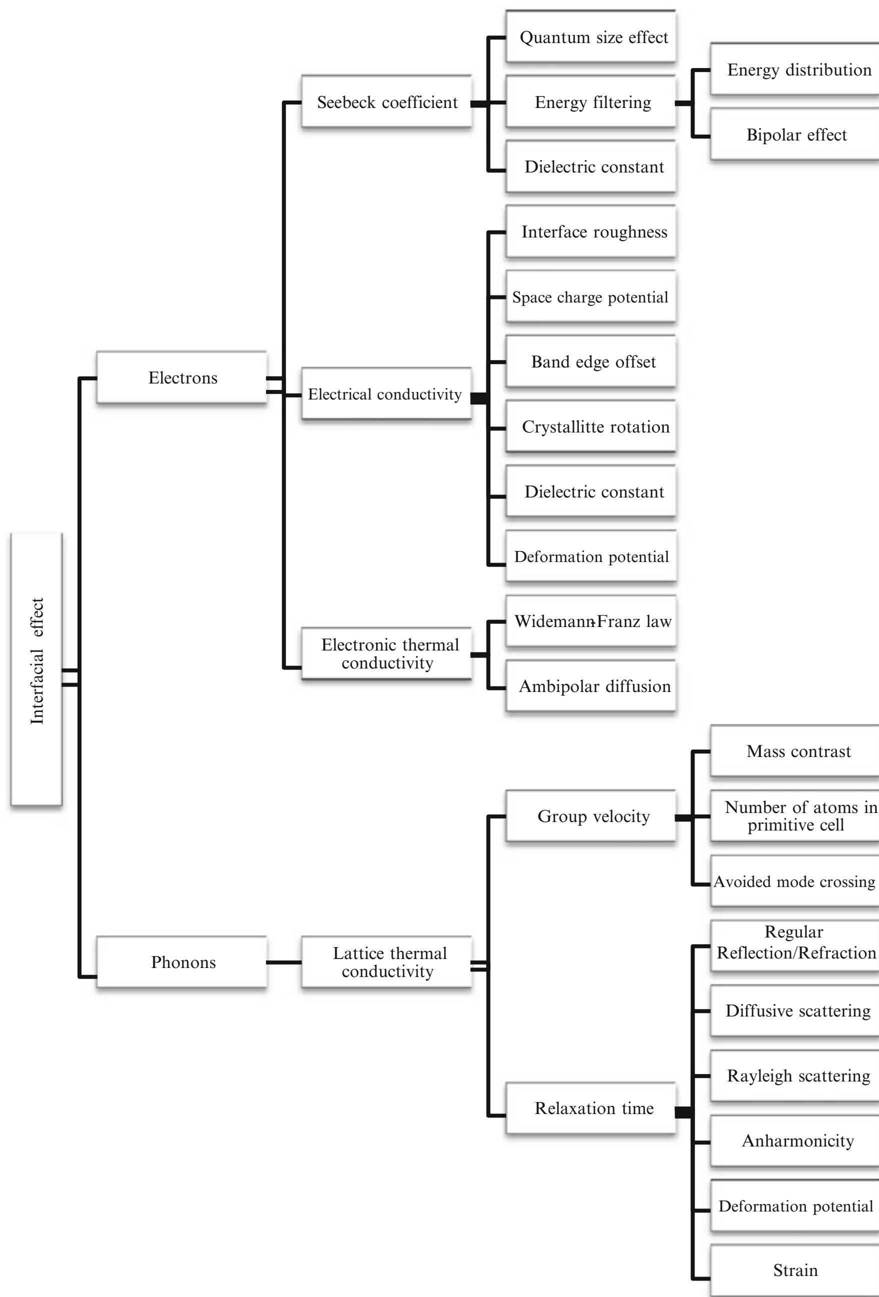

Fig. 4.5 Schematic illustration of the mechanisms that influence charge and thermal transport properties in interfacial regions

material, their volume fractions become comparable with that of the host material; therefore, the transport properties of the material should be derived not just from the scattering processes, but from a new phase of charge and phonon transport making the determination of the interface properties a cumbersome problem.

Interfaces can influence the Seebeck coefficient, electrical conductivity, and the electronic thermal conductivity. In fact, interfaces have negative and positive effects on carrier transport. Although the interface scattering reduces the charge mobility, it can be exploited to improve the Seebeck coefficient through energy filtering and reduce the ambipolar thermal diffusion through preferential scattering of the minority carriers. The following is a brief description of how different concepts and quantities can change the contributions of the interfaces in charge transport properties.

Seebeck Coefficient

As can be seen from the Mott's relation,

$$S = \frac{\pi^2 k_B^2 T}{3e\sigma}\left(\frac{\partial\sigma}{\partial E}\right)E_f = \frac{\pi^2 k_B^2 T}{3e}\left(\frac{\partial \ln g(E)}{\partial E} + \frac{\partial \ln \tau(E) v(E)^2}{\partial E}\right)E_f \tag{4.2}$$

in which $g(E)$ is the electronic density of states and v is the charge group velocity, the interfaces can be beneficial to Seebeck coefficient by three effects as listed below.

- *Quantum size effects* can cause sharp changes in the density of states $g(E)$ which in turn improves S and enhances ZT [37].
- Interfaces can introduce potential barriers that can scatter carriers and affect the thermoelectric efficiency. In the presence of such potential barriers, carriers that are passed over the barriers have higher average energy than carriers far from the barriers. Carrier *energy distribution* function becomes that of the bulk material in a length equal to the energy relaxation length ℓ_E from the barrier. If the grain sizes does not exceed ℓ_E, the carrier distribution function does not return to that of the bulk between GBs, and thus the effective Seebeck coefficient of the nano bulk material is higher than that of the parent single crystalline bulk material. Also, if the momentum relaxation length is much shorter than the distance between the GBs, the behavior of the carriers with energies greater than that of the barrier may be similar to that of carriers in the bulk. In other words, for carriers with energies above those of barriers, the differential conductivity $\sigma(\varepsilon)$ of a material with potential barriers can be approximated by that of the material without potential barriers if $\ell_m << \ell$. Therefore, under the condition of $\ell_m << \ell < \ell_E$, the energy filtering mechanism can increase the effective material Seebeck coefficient. It is also understood that since such defects can reduce the electron mobility, the overall effect appears in the power factor $S^2\sigma$.

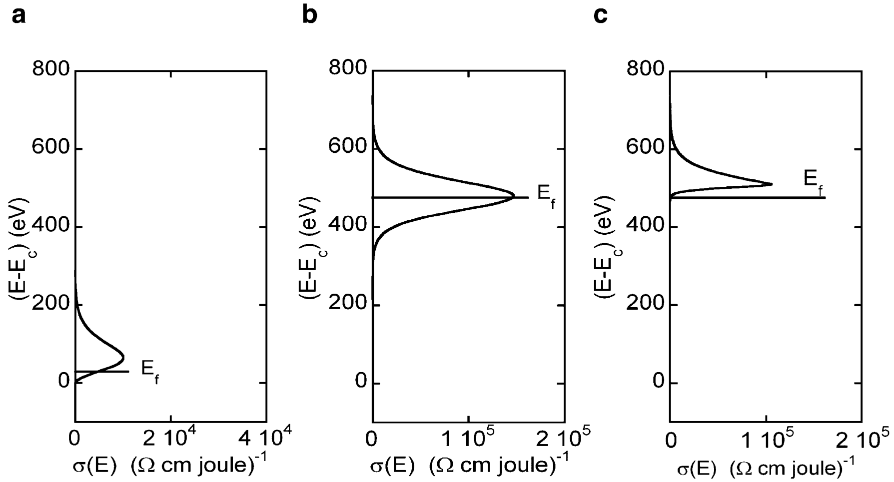

Fig. 4.6 Schematic representation of electron filtering. (**a**) Low doped (**b**) highly doped (**c**) energy filtered highly doped

Figure 4.6a shows the asymmetric contribution of electrons with different energies around the Fermi energy to the conduction process (differential conductivity). A more asymmetric differential conductivity would result in higher Seebeck coefficient. While the Seebeck coefficient is relatively high, the number of conduction electrons is small as the Fermi energy is close to the band edge. Figure 4.6b shows that when the Fermi energy is deep inside the conduction band, the differential conductivity is more symmetric with respect to the Fermi energy resulting in a small Seebeck coefficient. Removing low energy carriers by a potential barrier can lead to an improvement in Seebeck coefficient as shown in Fig. 4.6c. The new scattering mechanism introduced by the interface potential scatters low energy carriers and reduces their contribution to the transport properties so the Seebeck coefficient is increased. The successful implementation of this strategy has been reported for InGaAs/InGaAlAs superlattice [17] and PbTe-based nanostructured materials [18, 81].

Energy filtering improves the Seebeck coefficient through the reduction of *bipolar effect* too. To this end, the minority carriers which have lower energy are affected by fabricating a nanostructure which scatters them more strongly than the majority carriers. Such a reduced bipolar effect has been reported for nanostructured $Bi_{0.5}Sb_{1.5}Te_3$ [41].

- Any change in the dielectric constant caused by the strain or the change of the lattice constant at the interface can appear in ionized impurity, polar optical-mode phonon, and nonpolar optical-mode phonon scattering times [82]. Changes in these scattering times directly affect the Seebeck coefficient according to the Mott's relation.

Electrical Conductivity

Interfaces form two-dimensional networks or line charges in juxtaposition. Interfaces change the electrical conductivity through several possibilities such as:

- *Interface roughness* scattering at the interface decreases the electron mobility in the material [83]. However, the roughness scattering can lead to a significant increase in the thermionic current. A rough interface scattering conserves the energy but not the transverse momentum of the charge carriers. Therefore, the scattering at a rough interface mixes the planar motion of the charge carriers with the longitudinal motion perpendicular to the interface. In this case, the transmission probability depends on the total kinetic energy of the electrons rather than only the perpendicular component to the barrier. This will increase the number of electrons that are transmitted over the barrier, which can significantly increase the electrical conductivity. Non-conservation of transverse momentum does not significantly change the Seebeck coefficient; therefore, optimizing the material parameters (such as doping and barrier height) to gain an overall benefit from the interface roughness scattering is possible. For an accurate treatment of the interface scattering, one needs to develop a comprehensive model that includes all the important effects on the charge mobility and the transmission probability at the interface.
- There are several mechanisms for the existence of an interfacial potential. One is the accumulation of charges at the interface, namely, the space charge electric potential. The broken bounds at the interfaces attract free carriers and form a space charge. The high density of states at interfaces and a space charge on either side of the interface represents a double Schottky barrier at the boundary thereby a high resistance to the lateral current flow. Early works on modeling of the interfaces in polycrystalline materials used a double diode or a two back-to-back diode model [84]. Since then there have been many different models for the effect of the interface space charge on electrical conductivity [85].
- Another mechanism is due to the different orientations of the adjacent grains or simply *crystallite rotation*. Apart from the space charge potential barrier, electrons may experience a potential barrier (or well) due to the rotation of the adjacent grains. For example, an electron moving in L valley in one grain has to enter the Σ valley in the next grain. In a nano bulk material, the grains are randomly distributed with a random orientation. Electrons with sufficiently large energies can pass over the barrier and enter a different valley in the adjacent grain. Electrons with smaller energies may encounter an intervalley scattering and enter an equivalent valley in the adjacent grain (Fig. 4.7). This can happen through electron scattering by phonons or the interface roughness potential. Such scatterings reduce the boundary resistance as they provide alternate means for electron transport between the grains.
- Dielectric constant can be changed due to the permanent dipoles which are induced by the electric field in the interfacial regions. The change in the dielectric

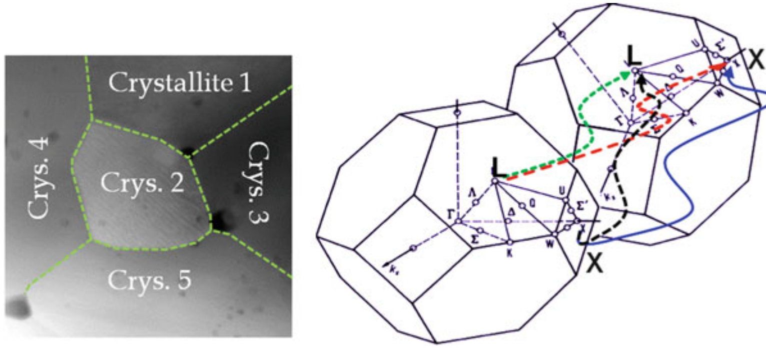

Fig. 4.7 Pictorial depiction of the grain boundary interfaces and intervalley transitions. L–L and X–X lines demonstrate the equivalent intervalley scattering between adjacent grains. L–X line shows transition to a different valley that would disturb the energy spectra of the charge carrier

constant leads to the change in polar optical-mode phonon and nonpolar optical-mode phonon scattering times which in turn alters the electrical conductivity [82].

- Deformation potential theory is a band model to describe the charge transport and works well if the electron–phonon coupling is weak [86]. Deformation potential impacts on the electrical conductivity as well as the total phonon relaxation time. Local deformations in the crystal lattice caused by the interfaces can form an effective electric potential due to the strain and its effects on the band structure. Therefore, the changes in the lattice constant in the interfacial region can also affect the electrical conductivity through the change in the deformation potential [87].

Electronic Thermal Conductivity

The charge carriers also transport heat and add to the thermal conductivity. At first glance it seems that reducing the thermal conductivity through the reduction in the charge mobility or concentration is not favorable as it would adversely affect the *ZT* through electrical conductivity. However, the key is the different value of the Lorenz number in many thermoelectrics. Moreover, the ambipolar diffusion mechanisms can favorably behave differently at the presence of the interfaces. *Wiedemann–Franz law* states that the electronic thermal conductivity k_e and electrical conductivity σ in a metal or degenerate semiconductor are directly proportional as:

$$k_e = L\sigma T \tag{4.3}$$

where L is the Lorenz number with the value $L = 2.45 \times 10^{-8}$ WΩ/K^2, σ is the electrical conductivity, and T is the absolute temperature. Therefore, Wiedemann–Franz law affects the electronic thermal conductivity in two ways. First, k_e is decreased due to the deteriorative effect of the interfaces on the charge

carrier mobility. Second, k_e is a function of the Lorenz number which itself is a function of the relaxation time. Therefore, it is possible to reduce the contribution of carriers in thermal conductivity by reducing the Lorenz number.

If a temperature difference is maintained across a thermoelectric material, a positive concentration gradient of thermally excited electron–hole pair in the direction of the temperature increment occurs. Diffusion causes a net flux of these electron–hole pairs towards the cold side of the material and their subsequent recombination that would heat up the lattice. This process is known as ambipolar thermal diffusion whose strength depends on the band gap and the balance of the electron and hole conductivities. Interfaces can preferentially scatter minority carriers more than majority ones due to the difference in their energy. For example, since the minority carriers have less energy than the majority ones in a bulk material, the former ones are scattered more strongly by the interface potential barriers resulting in an imbalance between the electron and hole electrical conductivities; hence, reducing the ambipolar diffusion.

4.3.3.5 Phonon Transport at Interface

According to the following relation, which is derived from a simple kinetic theory and neglects the normal phonon–phonon interactions, the lattice thermal conductivity can be calculated from [88, 89]:

$$k_{\mathrm{latt}} = \frac{1}{3}\int_0^{\omega_c} C(\omega) v_g(\omega)^2 \tau(\omega) \mathrm{d}\omega \tag{4.4}$$

where C is the heat capacity, v_g is the phonon group velocity, τ is the total relaxation time, and ω_c is the cutoff frequency. It is expected that the interfacial resistance of the grains in a nano bulk material should reduce the lattice thermal conductivity either through the reduction of the group velocity of the phonons or the reduction of the relaxation time. The reduction in relaxation time corresponds to the reduction in phonon mean free path. In nano bulk materials, the reduction of the phonon relaxation time can be achieved through point defects and/or grain boundary scatterings. Due to the complicated interplay of phonon scattering, group velocity, and heat capacity, a frequency dependent analysis of k_{latt} is crucial to design low thermal conductivity thermoelectrics. Some of the main mechanisms affecting the lattice thermal conductivity are introduced briefly in the following.

Group Velocity

The one-dimensional Born–von Karman model, as a chain of atoms connected by springs with linear restoring forces to investigate the effect of the reduction in phonon group velocity on the spectral lattice thermal conductivity, indicates that the decrease in v_g which decreases the $k_{\mathrm{latt}}(\omega)$ occurs in three ways: [90]

- As the mass contrast increases, the optical mode flattens, and if Umklapp scattering dominates, $k_{\text{latt}}(\omega)$ is proportional to $v_g(\omega)^2$; therefore, the $k_{\text{latt}}(\omega)$ is reduced significantly [91].
- As the number of atoms in the primitive unit cell increases, due to their low velocity of optical modes, the $v_g(\omega)^2$ is decreased considerably; hence, the $k_{\text{latt}}(\omega)$ is decreased [92, 93].
- In open framework compounds (such as clathrates and skutterudites) the avoided crossing effect in the vicinity of the guest atom vibrational modes reduces $v_g(\omega)^2$ through the reduction of the acoustic contribution to $k_{\text{latt}}(\omega)$; hence, $k_{\text{latt}}(\omega)$ is decreased [94, 95].

Relaxation Time

Interfaces can scatter phonons via several different possibilities:

- *Regular reflection and refraction*, arising from the difference of the phonon group velocities in the adjacent grains.
- *Diffusive scattering* due to the corrugation of the interface, caused by impurities or interface roughness.
- *Diffraction of waves* when the wavelength is comparable to the particle size. If the interface region is much smaller than the wavelengths of the excited phonons, the problem should be treated as a diffraction process (*Rayleigh scattering*).
- *Anharmonic effects* are also able to extremely decrease the lattice thermal conductivity as reported by Morelli et al. [96]. Anharmonic bands are characterized by Grüneisen parameter γ. Good thermoelectric materials require large γ. Hopkins et al. [97] suggested a new model for thermal conductivity that takes into account the anharmonic coupling, or inelastic scattering events, at the interface of two grains. This is achieved by considering specific ranges of phonon frequency interactions and the conservation of the phonon number density. Their suggested model considered the contributions of the inelastically scattered phonons to the thermal conductivity and provided a good agreement with the experimental results at the Pb–diamond and Au–diamond interfaces.
- *Strain* can be caused by the change of the lattice constant at the interface. The strain affects the vibrational modes and changes the relaxation time [98].
- *Deformation potential*: This potential represents the interaction of charge carriers with phonons. The deformation potential theory has been developed and applied by many researchers [87, 99, 100]. Lattice mismatch at the interfaces can cause a lattice strain that would alter the deformation potential. Therefore, interfaces can affect the lattice thermal (and electrical) conductivity indirectly through the deformation potential.

Figure 4.8 depicts the schematic representation of the scattering mechanisms for phonons. For regular reflection and refraction, the relaxation time has no dependency on angular frequency. If the wavelength is comparable with the particle or

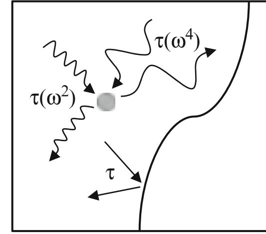

Fig. 4.8 Schematic representation of the scattering mechanisms for phonons from interfaces

the interface size, the relaxation time will be a function of $\omega^2(\lambda \sim d, \tau(\omega^2))$ and if the wavelength is much larger than the particle or the interface size, the relaxation time will be proportional to ω^4 $(\lambda \gg d, \tau(\omega^4))$.

As the characteristic lengths of the nano bulk materials approach the phonon mean free paths, the effect of scattering mechanisms at interfaces becomes much more important than inside the bulk material. Phonon reflection at a boundary leads to the Kapitza resistance, a phenomenon that has been known for a long time but has escaped quantitative description except at very low temperatures when the phonon wavelength is long so that the reflection can be treated based on acoustic wave theory. At room temperature, it is difficult to calculate the phonon reflectivity mainly because of the diffuse phonon reflection as well as the phonon spectrum mismatch between the two sides of the interface.

Phonons have a large range of frequency and relaxation time. Phonons with different frequencies have different effects. Phonons may behave like a plane wave if the interfacial roughness is small compared with the phonon wavelength. They may behave like a particle if their wavelengths are much smaller than the interfacial roughness. Microstructural obstacles like inclusions and precipitates have great effect on the lattice thermal conductivity. Until now, no model has been able to predict the interface thermal conductance except at very low temperatures. The Fourier heat conduction theory, as a common approach to model the effect of interfaces in thermal conductivity, underpredicts the effect of the interfacial scattering. This is mainly because this approach is based on the diffusion picture while the phonon mean free path is longer than the characteristic lengths of the interface region. Phonon transmission and reflectivity are crucial parameters to model the heat conduction in thermoelectric materials. In the case of the nano bulk materials, two major theoretical problems are known for understanding of the phonon transport. First, nano bulks show a lattice thermal conductivity lower than that of their alloy limit. Second, it is not clearly understood how the interface affects the phonon transport. The first problem can be explained by determining the amount of contribution of each wavelength of the phonons to the thermal conductivity. Phonons with short wavelength are strongly scattered by point defects but phonons with long wavelength have a long mean free path. Nevertheless, the contribution of the long wavelength phonons in thermal conductivity is small [101]. If the involved structures have larger characteristic length than that of alloy point defects, interfaces scatter long wavelength phonons that would further reduce the lattice thermal conductivity beyond the alloy limit. Moreover, some researchers believe that the

low limit of thermal conductivity in nano bulk materials is smaller than that of bulk materials modeled by isotropic scattering mechanisms due to the highly anisotropic interfacial scattering in the nanostructures.

Nanoparticles in a host material have multiple interfaces and knowing the amount of the reflected or transmitted phonons from a single interface is crucial for designing nano bulks with reduced thermal conductivity. Available theories do not predict phonon reflectivity and transmission at an interface accurately as they do not clarify the contribution of the phonon scattering inside a nanoparticle or the role of the interface roughness.

4.4 Methods for Modeling Charge Carrier and Phonon Transport at Interfaces

4.4.1 *Modeling by BTE*

The BTE has been used extensively to model the thermoelectric properties of bulk materials. As long as all the scattering mechanisms are elastic and the relaxation time approximation is valid, electrical and thermal properties can be expressed as integrals of the relaxation times [79, 80]. To model the effect of interfaces, one can add an interface scattering time to the scattering times existent in the bulk material using Matthiessen's rule. Therefore, the only thing that one needs is an expression for the interface or the grain boundary scattering, and the general algorithm to solve the BTE is unchanged. Modeling of the interface scattering, however, is not accurate at this stage.

A particular implementation of the BTE is the acoustic mismatch model (AMM) which can be considered as the most simplified and widely used method to treat the phonon transport at the interfaces. AMM compares the impedance ratios at an interface of two crystals. Since this model has been designed for specular elastic scattering of phonons at abrupt interfaces, it is proper for low temperature. The AMM, like other BTE-based models, does not account for the wave nature of the phonon transport that is driven by the underlying lattice dispersion and the boundary conditions on either side. Moreover, it does not take into account the nonequilibrium status of the region between the two thermal reservoirs. In addition, extending this model to cover multiple scattering phenomena in nanostructured materials has not been formulated yet.

4.4.2 *Modeling by Molecular Dynamics (MD)*

MD simulation can provide a deep insight of the mechanisms responsible for phonon transport in nanostructured materials. This method has been extensively developed and has found applications in research on thermal transport in nanoscale

interfaces [102, 103]. After the pioneering work of Maiti et al. [104] using the nonequilibrium molecular dynamics (NEMD) for studying the Kapitza resistance across an interphase boundary, several studies on the interfaces between different phases [105] and nanostructures [106] have been performed. Additionally some researchers have used MD to calculate the thermal conductivity of some thermoelectric materials such as Bi_2Te_3 [107], $Pb_{1-x}Sn_xTe$ [108], $Pb_{1-x}Ge_xTe$ [108], and Si/Ge nanocomposites [109]. Although MD provides some atomistic details, since it is mainly based on empirical potentials, it gives poor estimates of the thermal transport properties.

4.4.3 Modeling by Nonequilibrium Green's Functions (NEGF)

The Nonequilibrium Green's Functions (NEGF) formalism has been extensively used to study the electron transport in nanostructured materials [110–112]. It has been used mainly for structures where characteristic wavelengths of the charge carriers become comparable to, or larger than, the sample size. The method can be readily developed to include the incoherent scattering and the electron–phonon correlation effects. In this method, a two probe system is defined and divided into three regions, left electrode, central region, and right electrode. It is assumed that the electrodes have bulk properties. First, the properties of the electrodes using standard density functional theory (DFT) techniques for periodic systems are calculated. The solution for the electrodes determines boundary conditions for the central region, and then in the second step, DFT equations for the central region are solved self-consistently. The charge carrier transport properties are calculated by using the Kohn–Sham Hamiltonian for propagating each electron.

The NEGF method has been also applied to treat phonon transport across the interfaces in nanostructures. First, some ab initio methods like tight binding, DFT, or MD are used to relax the crystal structures across the interface and to determine the interatomic force constants between the atoms. The computational unit cell should be large enough to get a sufficient number of nearest neighbor interactions. Then the phonon Green's function is computed based on the extracted force constants. Moreover, the converged semiclassical Poisson electrostatic potential is used to calculate the transport properties. For example, the method has been applied to investigate the phonon transport in carbon nanotubes with defects and isotope scattering in carbon and boron-nitride nanotubes [113–115]. It is notable that the strength of the NEGF is its ability to include more complicated incoherent scatterings such as anharmonic phonon mechanisms.

4.5 Nanostructuring in Si_xGe_{1-x} and Mg_2Si

As discussed earlier in Sect. 4.1, nanostructuring techniques have steered the performance of many thermoelectric (TE) compounds towards attaining a $ZT > 1$ in the room to medium temperature ranges. Optimization of device performance was widely achieved through additional scattering mechanisms in the form of grain boundaries and interfaces created via nanostructuring techniques. Nanostructuring techniques were principally designed to scatter mid to long wavelength phonons, a feat that could not be effectively achieved through alloy or point-defect scattering [116]. Consequently, the alloy limit to the reduction of thermal conductivity was overcome by means of restricting the grain sizes to those comparable with the characteristic lengths of phonons.

4.5.1 Properties and Modeling of Silicon Germanium and Magnesium Silicide Nano Bulks

The binary compounds of Si_xGe_{1-x} and Mg_2Si hold favorable thermoelectric (TE) properties for power generation in the high (900–1,100 K) and medium temperature ranges (500–800 K), respectively [43, 117–120]. In addition to being cost efficient and allowing for scalable synthesis methods, both compounds were characterized for having high mobilities, electrical conductivities, Seebeck coefficients, and low lattice thermal conductivities [43, 50, 120]. Table 4.1 shows the important electronic and material properties of silicon germanium (Si_xGe_{1-x}) and magnesium silicide (Mg_2Si).

A favorable feature of $Si_{1-x}Ge_x$ is its ability to facilitate band structure engineering through variation in the alloy composition (x) of the elements. The alloy

Table 4.1 Properties of Si_xGe_{1-x} and Mg_2Si [43, 50, 120]

Property	Si_xGe_{1-x}	Mg_2Si
Energy gap (eV)	$1.12 - 0.41x + 0.008x^2$	0.77
Lattice constant (Å) at 300 K	$5.43(1-x) + 5.66x$	6.34
Dielectric constant	$11.7 + 4.5x$	20
Density (g/cm^3)	$2.329 + 3.493x - 0.499x^2$	1.880
Debye temp. (K)	$640 - 266x$	417
Melting point (K)	$1{,}685 - 738x + 263x^2$	1,375
Thermal conductivity (W/m/K) at 300 K	$4.6 + 8.4x$	7.9
Specific heat (J mol/K)	$19.6 + 2.9x$	68
Effective mass: $m_l^*/m_t^*(m_e)$, $x = 0.8$	X: 0.92/0.19	X_1: 0.86
	L: 1.59/0.08	X_3: 0.14
Mobility (cm^2/V/s) at 300 K	μ_n: 1,396–4,315x	μ_n: 405
	μ_p: 450–865x	μ_p: 65

Semiconductors on NSM, http://www.ioffe.rssi.ru/SVA/NSM/Semicond/SiGe/index.html, Accessed 21st March 2012

composition and the temperature affect both the electrical and thermal properties. Additionally, the similarities between the chemical and the physical properties of Si and Ge make the processing of $Si_{1-x}Ge_x$ relatively simple. $Si_{1-x}Ge_x$ crystallizes with a diamond lattice structure under atmospheric pressure. The type of the conduction and the carrier concentration in $Si_{1-x}Ge_x$ could be controlled by doping with phosphorous (n-type) or boron (p-type). $Si_{1-x}Ge_x$ is an indirect band-gap material with the primary conduction energy gap between the X and L valleys being ~0.8 eV [43, 50].

Among the materials suitable for thermoelectric power generation in the medium temperature range, Mg_2Si stands apart due to the distinctive features of its elemental constituents. The elements of Mg and Si are nontoxic, widely available in nature, and are suitable for making light-weight and recyclable compounds. Additional related intermetallic compounds such as Mg_2Ge and Mg_2Sn are also suitable for thermoelectric power generation in the medium temperature range. Mg_2Ge and Mg_2Si possess semiconducting properties due to the valence electrons in these compounds being equal to the number of states in the Brillouin zone [120]. Mg_2Sn has a very low energy gap and is considered as a semimetal.

Similar to $Si_{1-x}Ge_x$, the bulk crystalline form of Mg_2Si possesses a high melting point, low thermal conductivity, and high electrical conductivity as shown in Table 4.1. Numerous experimental techniques such as mechanical alloying, hot-pressing, and spark plasma sintering have been reported for the preparation and synthesis of Mg_2Si-based thermoelectric materials [121–125]. Recent reports also demonstrate novel methods such as microwave processing to fabricate nano bulk structures of Si_xGe_{1-x} and Mg_2Si [126, 127].

Elements such as antimony, aluminum, and bismuth are typical dopants for synthesis of n-type Mg_2Si. However, the synthesis of p-type Mg_2Si requires dopants such as silver or copper [125, 128]. As cited in the previous subsections, well-known techniques such as mechanical alloying, hot-pressing, and spark plasma sintering have been used to fabricate nano bulk compounds of Si_xGe_{1-x} and Mg_2Si. In some cases, the thermal processing methods such as solid-state reactions were also implemented. Methods to fabricate nano bulk compounds of Mg_2Si were also widely implemented recently [129–132]. In these TE compounds, although a reduction in the thermal conductivity was obtained as a result of nanostructuring, the *ZT* remained lower than one. Unlike compounds such as $Si_{1-x}Ge_x$, the performance trend of nano bulk Mg_2Si illustrated only meager enhancements. In order to understand the physical reasoning behind this unexpected trend, a detailed examination of the electron and phonon transport in these nanostructures is necessary. The primary parameters that are affected by bulk nanostructuring are the phonon mean free path (PMFP) and charge carrier mean free path (CMFP). The mean free path is defined as the distance travelled by the phonon or charge carrier between consecutive scattering events. The PMFP effectively determines the maximum distance of heat transport for each phonon. It is mathematically represented as the product of the phonon relaxation time (τ) and

group velocity (v_g). On the other hand, the lattice thermal conductivity (κ_l) is the magnitude of thermal transport that occurs via the crystal lattice vibrations of the TE material and depends on τ, v_g, and the phonon wavelength. The lattice thermal conductivity is affected by various physical characteristics of the material such as point defects in the lattice, ionized impurity sites, grain boundaries, etc. In particular, as the crystallite size reduces to feature sizes of the electrons and phonons in the nanocrystalline materials, interfacial sites and barrier potentials at the grain boundaries modify the typical behavior of the transport mechanisms by affecting the phonon and electron mean free paths. It should also be noted that the electrical transport properties are also a function of the defect density, impurity concentration, and the size of the crystallite in the TE material systems. Therefore, the effects of nanostructuring could be perceived by a reduction in both the electrical and the lattice thermal conductivities due to enhanced interface scatterings. Additional effects of nanostructuring may include selective carrier filtering which increases the Seebeck coefficient. In order to quantitatively comprehend the electrical and thermal transport properties of the nanostructured TE materials, semiclassical theoretical models have been implemented under the relaxation time approximation [43].

An effective calculation methodology to describe the nano bulk effects in Mg_2Si and $Si_{1-x}Ge_x$ is based on solving the Boltzmann transport equation coupled with the relaxation time approximation [21, 22]. The Debye model can further be applied simultaneously in order to determine the thermal conduction properties of the two materials being discussed. Such a rigorously simulation-tested modeling methodology was presented in detail in [22] and [43] for Mg_2Si and $Si_{1-x}Ge_x$, respectively.

4.5.2 Modeling Methodology

For the material systems in discussion, a multiband transport mechanism is taken into account in order to efficiently estimate the thermoelectric properties [22, 120]. The sequence of the steps included in the modeling and simulation strategy are shown in Fig. 4.9. Under the assumption that the band structure-related and electronic properties of the material are supplied, the calculation methodology primarily includes the following stages:

1. Under the assumption of the charge conservation, calculation of the Fermi level, E_F, based on (4.5a and 4.5b).
2. Calculation of the charge carrier and phonon relaxation times based on scattering mechanisms.
3. Estimation of the charge carrier mobility, Seebeck coefficient, and electrical conductivity.
4. Estimation of the electronic and bipolar thermal conductivities.
5. Determination of the lattice thermal conductivity based on the Debye model.

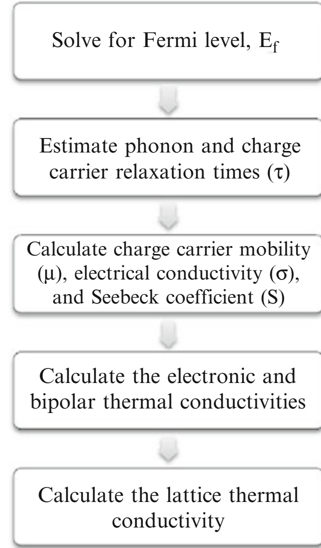

Fig. 4.9 Flow diagram of the methodology of modeling of TE properties

$$n_{\mathrm{o}} = \int_0^\infty f_{\mathrm{o}}(E, E_{\mathrm{f}}) D(E) \mathrm{d}E \tag{4.5a}$$

$$f_{\mathrm{o}} = \left(\exp\left[\frac{E - E_{\mathrm{f}}}{k_{\mathrm{B}} T} \right] + 1 \right)^{-1} \tag{4.5b}$$

Where n_{o} is the charge carrier concentration. For a given temperature and doping concentration, the Fermi level is determined by solving (4.5a and 4.5b). The Matthiessen's rule shown in (4.6) determines the total relaxation times for phonon and carriers where i in represents the type of scattering mechanism [120].

$$\frac{1}{\tau} = \sum\nolimits_i \frac{1}{\tau_i} \tag{4.6}$$

The model is strongly established on the material parameters related to the physical properties such as the lattice properties and the band structure parameters.

Mg_2X-based compounds, where $X = \mathrm{Si}$, Ge, or Sn, are known to have face centered cubic lattice structure. The forbidden energy gap for Mg_2Si is indirect (Γ_{15}–X_3) with $E_{\mathrm{g}}^{\mathrm{in}} = 0.77$ eV and forms the primary energy gap [133]. The multiband assumption for Mg_2Si is justified from the fact that Mg_2Si has three conduction band minima located at X_3, X_1, and L_1 points [80]. However, there is only one valence band maximum which is located at Γ_{15}. The inter-band distances such as the X_1 and X_3 gap (0.4 eV) and the X_3–L_1 separation of 0.5 eV are also provided as the input based on the band structure [133]. Band structural features such as the non-parabolicity are considered for all bands and are implemented under a modified *E(k)* relation shown in (4.7) [43],

Table 4.2 Parameters for simulation of TE properties of $Si_{0.8}Ge_{0.2}$ and Mg_2Si [21, 22]

Parameter	Mg_2Si	$Si_{0.8}Ge_{0.2}$
Energy gap E_g (eV)	0.77	0.8
Temp. dependence of E_g, (eV/K)	$\alpha = -3.5 \times 10^{-4}$ $\beta = 0$	$\alpha = 4.7 \times 10^{-4}$ $\beta = 636$(Si), 235(Ge)
Conduction band effective mass	$m_t = 0.86$, $m_l = 0.14$ (X_1 and X_3)	X: $m_l = 0.92$, $m_t = 0.19$ L: $m_l = 1.59$, $m_t = 0.082$
Conduction band non-parabolicity (e/V)	X_1: 1.0, X_3: 1.0	X: 1.2
Valence band effective mass	$m_{lh} = 1.00$, $m_{lh} = 2.00$	$m_{lh} = 1.20$, $m_{lh} = 1.55$
Valence band non-parabolicity	0	1.25
Debye temp. (K)	417	640
Acoustic phonon deformation potential (eV)	$D_c = 12$, $D_v = 4.5$	$D_c = 10.5$, $D_v = 4.8$
Strain parameter	7	39
Grüneisen parameter	1.4	0.9
Higher order phonon scattering	1.5	1.4
GB potential, P_g (meV)	100	100

$$E(1+\alpha E) = \frac{\hbar^2}{2}\left(\frac{{k_l}^2}{{m_l}^*} + 2\frac{{k_h}^2}{{m_h}^*}\right) \tag{4.7}$$

where k_l and k_t are the longitudinal and transverse components of the electron wavevector, respectively; m_l and m_t are the longitudinal and transverse components of the effective mass of each valley, and α is the non-parabolicity coefficient.

Analogous to the parameters for Mg_2Si, the calculation model for $Si_{0.8}Ge_{0.2}$ was built based on the band structure properties, physical and structural characteristics, and electronic and lattice parameters [43]. The simulation parameters for both materials are summarized in Table 4.2.

4.5.2.1 Scattering Mechanisms

The doped compound of bulk $Si_{0.8}Ge_{0.2}$ is known to accommodate phonon scatterings due to acoustic phonon, intravalley phonon, ionized impurities, and point defects. In the nano bulk structures, the calculations account for an additional scattering mechanism in the form of grain boundary scattering. Similarly, in the crystalline form of doped bulk Mg_2Si, scattering mechanisms are dominated by acoustic phonons and ionized impurities in the lattice. The energy dependent relaxation times can be estimated based on the Brooks–Herring formula via Thomas–Fermi approximation defined in (4.8) [80],

$$\frac{1}{\tau_{IIS}(E)} = \frac{z^2 e^4 n_I}{16\pi\varepsilon^2\sqrt{2m^*}} E^{-\frac{3}{2}}\left[\log\left(1+\frac{8m^*\lambda_s^2 E}{\hbar^2}\right) - \frac{8m^*\lambda_s^2 E/\hbar^2}{1+8m^*\lambda_s^2 E/\hbar^2}\right] \tag{4.8}$$

where λ_s is the Debye screening length and is defined as,

$$\lambda_{\mathrm{s}}^{-2} = \frac{4\pi e^2 z}{\varepsilon_\infty} \int_0^\infty \left(-\frac{\partial f_{\mathrm{o}}}{\partial E}\right) D(E) \mathrm{d}E \tag{4.9}$$

where n_{I} is the number of ions, E is the energy relative to the band edge, z is ionization number, m^* is the effective mass, e is the charge of electron, f_{o} is the Fermi–Dirac distribution obtained from (4.5b), ε is the low frequency dielectric constant, ε_∞ is the high frequency dielectric constant, and $\hbar$ is the Planck's constant. Likewise, the intravalley acoustic and optical phonon deformation potential scattering rates can be estimated using the equations [80],

$$\tau_{\mathrm{DP}}^{-1} = \tau_{\mathrm{o}}^{-1} \left\{ \left(1 - \frac{\alpha E}{1 + 2\alpha E}\left(1 - \frac{D_{\mathrm{v}}}{D_{\mathrm{A}}}\right)\right)^2 - \frac{8}{3} \frac{\alpha E(1 + \alpha E) D_{\mathrm{v}}}{(1 + \alpha E)^2 D_{\mathrm{A}}} \right\} \tag{4.10}$$

$$\tau_{\mathrm{o}}^{-1} = \frac{\pi k_{\mathrm{B}} T D_{\mathrm{A}}^2}{\rho v_{\mathrm{s}}^2 \hbar} D(E) \tag{4.11}$$

where E is the energy relative to the band edge, D_{A} and D_{v} are acoustic phonon deformation potentials for the scattering of electrons and holes, respectively. T is the temperature, α is the non-parabolicity parameter, $D(E)$ is the density of states, ρ is the density, and v_{s} is the speed of sound.

For the calculations of TE properties of nano bulk systems, a potential barrier due to the presence of the grain boundary (GB) locations and/or due to the presence of the nanoparticles can be considered as shown in Fig. 4.10. The shaded circles schematically indicate the situations where nanoparticle doping such as nanoparticles dispersed in the host matrix is applicable. The randomly oriented lines in Fig. 4.10 specify the additional interfaces created due to the crystallite boundaries. These boundaries act as scattering regions for phonons and charge carriers. The potential barrier in these two cases can be modeled as shown in Fig. 4.10. The grain boundary

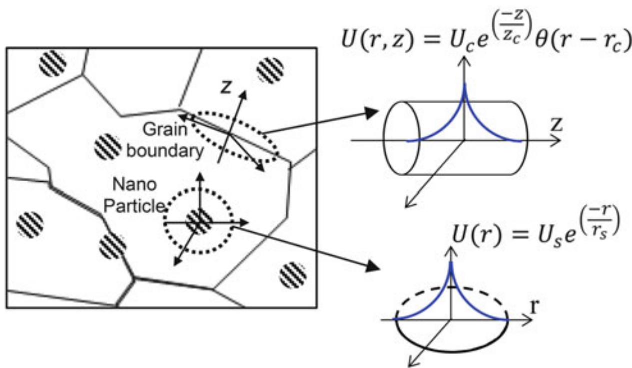

Fig. 4.10 The schematic of the potential barriers due to the grain boundaries (*cylindrical*) and nanoparticle (*circular*) scattering zones

region can be modeled as a location consisting of a space charge region with a cylindrical symmetry and width indicated by the height of the cylinder (*z*-axis). The barrier potential can be modeled to be exponentially decaying towards the edges of the space charge region. The mathematical functions that define the variation of the potential barriers in the direction perpendicular to the grain boundary and/or the nanoparticle are shown in (4.12) and (4.13), respectively. In (4.12) and (4.13), U_c and U_s is the heights of the grain boundary potential and r_o is a constant in the order of the screening length. The Fermi's Golden rule can be applied in order to estimate the effective scattering rate for a chosen grain boundary potential. The grain boundary potentials typically vary in the range of tens of meV to eV. As shown in Table 4.2, a constant value of 100 meV was assumed in these calculations for both material systems to emulate the effect of nanostructuring.

$$U(r,z) = U_c e^{-\frac{|z|}{z_c}} \theta(r - r_c) \tag{4.12}$$

$$U(r) = U_s e^{-\frac{r}{r_s}} \tag{4.13}$$

An effective implementation of this model accounts for the assumption of coherent carrier scattering at the grain boundaries. It is known that in typical nano bulk TE material systems, the crystallite sizes vary in a wide range. In order to estimate the TE characteristics efficiently, a Gaussian distribution of grain sizes with a certain average crystallite size can be considered. In the calculation results to be discussed in the next sub-sections, a Gaussian distribution of grain sizes with an average size of 20 nm was implemented.

4.5.2.2 Relaxation Time

In order to account for the effect of phonon and carrier energies in conjunction to the type of scattering mechanisms, the energy dependent scattering rates for each scattering mechanism were individually estimated. The scattering rates were then combined using the Matthiessen's rule. Figure 4.11 shows the variation of the relaxation times for various scattering mechanisms in Mg_2Si. As indicated by Fig. 4.11, the acoustic phonons dominate in the scattering of electrons with energies higher than 0.1 eV. The ionized impurity scattering (IIS) is only dominant at lower energy levels.

It is indicative from Fig. 4.11 that the grain boundary scattering mechanism introduces additional scattering and is relatively dominant for carriers with lower ($<$0.1 eV) energies. Analogous to this situation, for carriers with energies greater than 0.1 eV, the ionized impurity and acoustic phonon scattering are dominant. It can also be inferred from Fig. 4.11 that in highly doped systems the mechanism of grain boundary scattering may be ineffective for a majority of carriers due to their high energy ranges.

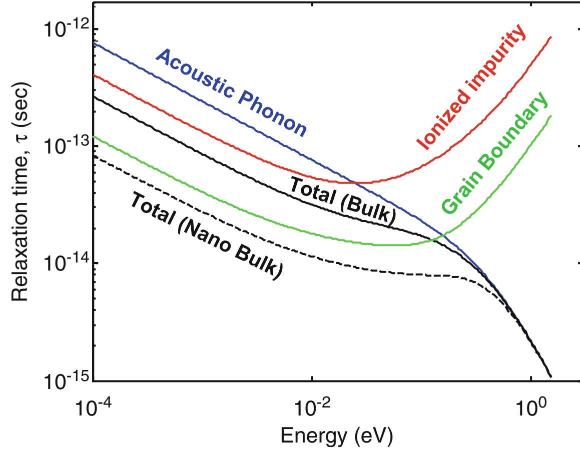

Fig. 4.11 Calculated relaxation time versus energy for various scattering mechanisms in n-type Mg_2Si [21]

4.5.2.3 Estimation of Lattice Thermal Conductivity

The thermal conductivity characteristics for both Mg_2Si and $Si_{0.8}Ge_{0.2}$ can be calculated accurately under the contributions of the phonon scattering mechanisms such as 3-phonon, phonon–electron, alloy scattering, and grain boundary scattering. The relaxation times can be estimated for each scattering mechanism and the lattice thermal conductivity, κ_l, the electronic contribution to thermal conductivity, κ_e, and bipolar thermal conductivity can be estimated using (4.14)–(4.19) [21, 22, 43, 120]

$$k_l = \frac{k_B}{2\pi^2 v_s}\left(\frac{k_B\theta_D}{\hbar}\right)^3\left(I_1 + \frac{I_2^2}{I_3}\right) \tag{4.14}$$

$$I_1 = \int_0^1 \tau x^2 \frac{v^2x^2e^{vx}}{(\exp(vx)-1)^2}\mathrm{d}x \tag{4.15}$$

$$I_2 = \beta\int_0^1 \frac{\tau}{\tau_U}x^2\frac{v^2x^2e^{vx}}{(\exp(vx)-1)^2}\mathrm{d}x \tag{4.16}$$

$$I_3 = \beta\int_0^1 \frac{1}{\tau_U}\left(1-\frac{\beta\tau}{\tau_U}\right)x^2\frac{v^2x^2e^{vx}}{(\exp(vx)-1)^2}\mathrm{d}x \tag{4.17}$$

$$k_c = \left(\frac{k_B}{e}\right)^2 T\sum\nolimits_i L_i\sigma_i \tag{4.18}$$

$$k_b = T\sum\nolimits_{i,j}\sigma_i\sigma_j\left(S_i - S_j\right)^2 \tag{4.19}$$

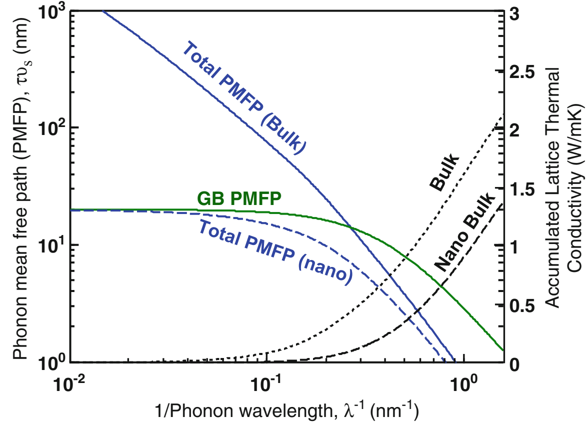

Fig. 4.12 Calculated phonon mean free path (PMFP) and lattice thermal conductivity versus the inverse of the phonon wavelength for bulk and nano bulk n-type Mg_2Si [21, 22]

in which $x = \omega/\omega_D$, where ω_D is the Debye frequency, $v = (\theta_D/T)^\eta$, θ_D is the Debye temperature, η is a fitting parameter to incorporate the effect of higher order phonon scattering (see Table 4.2), β is the ratio of Umklapp to normal-mode scattering, τ and τ_U are the total and Umklapp relaxation times, respectively, T is absolute temperature, i, j are the valleys indices, σ is the conductivity, and S is the Seebeck coefficient. L is the carrier concentration dependent Lorentz number that can be numerically calculated to estimate the electronic part of the thermal conductivity as discussed earlier via (4.3). Lastly, the total thermal conductivity k_{total} can be estimated as the sum of all three components $\kappa_{total} = \kappa_l + \kappa_c + \kappa_b$.

Figure 4.12 shows the variation of the calculated phonon mean free path (PMFP) in n-type Mg_2Si plotted versus the inverse of the phonon wavelength that is proportional to the phonon energy. It is indicative from the plot that the slope of PMFP varies with phonon energy. It is also known that PMFP is a function of the scattering type [21]. At very low energies of phonons, it is known that electron–phonon (e–p) scattering is dominant and PMFP has a frequency dependency of $1/\omega$. With the increasing energy of phonons, the slope sharply increases with $1/\omega^2$ dependency as the 3-phonon (3-p) scattering dominates. At higher energies, the PMFP has a $1/\omega^4$ dependency due to the dominancy of the point defect scattering [21]. Figure 4.12 also shows the dependency of the accumulated lattice thermal conductivity, κ_l, on the phonon energy. The κ_l remains at a very low magnitude for low energy phonons, but increases rapidly with phonon energy after a certain energy. The effect of nanostructuring on the PMFP and κ_l is comprehensively shown in Fig. 4.12. The calculations were performed after assuming an average crystallite size of 20 nm. It can be observed in Fig. 4.12 that at very low phonon energies, the PMFP saturates to approximately the chosen size of the grains. The line labeled GB PMFP also suggests the dominance of the grain boundary scattering resulting in such saturation. The resultant drop in κ_l in the nano bulk Mg_2Si is also presented in comparison with the bulk crystalline system.

4.5.2.4 Estimation of the Electrical Conductivity and the Seebeck Coefficient

In the multiband transport model for both Mg_2Si and $Si_{0.8}Ge_{0.2}$, the electrical conductivity and Seebeck coefficient assume the forms shown in (4.20–4.22).

$$\sigma_{\mathrm{tot}} = \sum_i \sigma_i \tag{4.20}$$

$$\sigma = q\left(\sum_i \mu_{\mathrm{n}_i} \mathrm{n}_i + \sum_j \mu_{\mathrm{p_j}} \mathrm{p}_j\right) \tag{4.21}$$

$$S_{\mathrm{tot}} = \frac{\sum_i \sigma_i S_i}{\sum_i \sigma_i} \tag{4.22}$$

In Equations (4.20–4.22), i and j represent the valleys; q is the charge of the carrier; μ_{n} and μ_{p} are the carrier mobilities for electrons and holes, respectively; n and p indicate the electron and hole concentrations, respectively.

4.5.3 *The Effect of the Grain Size on the TE Properties of Mg_2Si and $Si_{0.8}Ge_{0.2}$*

To better understand the benefits and secondary effects of nanostructuring, the thermoelectric characteristics of bulk (solid lines) and nano bulk (dashed lines) n-type $Si_{0.8}Ge_{0.2}$ and n-type Mg_2Si are calculated with the best fitting models shown in Table 4.2. The predicted accumulated electrical conductivity (σ) and lattice thermal conductivity (κ_{l}) plotted as a function of wavelength in n-type $Si_{0.8}Ge_{0.2}$ (calculated at $T = 1{,}300$ K) and n-type Mg_2Si (calculated at 850 K) are shown in Fig. 4.13a, b. A grain size of 20 nm and a GB potential of 100 meV were assumed for both the material systems.

Figure 4.13a, b shows a comparison of the effects of nanostructuring in both the material systems. As can be observed from Fig. 4.13a, the electrical conductivity (σ) in Mg_2Si suffers significantly with a drop of nearly 40 % in the nano bulk system as compared to the bulk crystalline system. Such an unfavorable effect in nano bulk Mg_2Si is a result of the loss in carrier mobility as will be discussed later in this section. In the corresponding calculations for $Si_{0.8}Ge_{0.2}$ the deterioration in electrical conductivity (σ) is a mere ~10 % of the bulk crystalline system.

The lattice thermal conductivity depicted in Fig. 4.13b shows that the short wavelength phonons carry most of the heat. It can be observed that phonons with wavelengths in the range of 0.5–10 nm contribute significantly to κ_l in both $Si_{0.8}Ge_{0.2}$ and Mg_2Si. The thermal conductivity increases rapidly with cumulative contribution from the short wavelength phonons and remains almost unchanged with adding the contribution of the long wavelength phonons. However, the limitation of grain size to 20 nm leads to ~60 % reduction in κ_{l} of $Si_{0.8}Ge_{0.2}$, whereas the

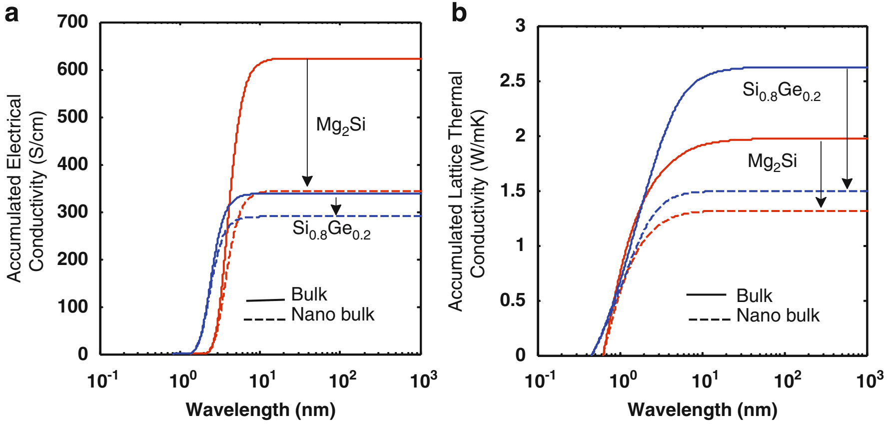

Fig. 4.13 Comparison of (**a**) accumulated electrical conductivity and (**b**) accumulated thermal conductivity in bulk (*solid lines*) and nano bulk (*dashed lines*) n-type $Si_{0.8}Ge_{0.2}$ (calculated at 1,300 K) and n-type Mg_2Si (calculated at 850 K)

same in Mg_2Si is only ~35 %. Considering the loss in σ for the same range of grain size in Mg_2Si, the corresponding loss in power factor could nearly cancel out the effect of the reduction in κ_l, eventually leading to little or no improvement in the ZT.

The detrimental effect of the nanostructuring in Mg_2Si is primarily due to the reduction of charge carrier mobility due to the enhanced scattering at the grain boundaries. Such an effect is the result of the PMFP and CMFP falling in the same range for Mg_2Si [21]. In order to carefully perceive this effect, the differential electrical conductivity and differential lattice thermal conductivity plotted versus energy for both the material systems are shown in Fig. 4.14a, b. The area under each curve is indicative of the corresponding total contribution of each component.

It can be observed from Fig. 4.14a that more than 50 % drop in differential electrical conductivity is resulted from restricting the grain size to 20 nm. This magnitude of drop is less than that of $Si_{0.8}Ge_{0.2}$ shown in Fig. 4.14b. Similarly, the magnitude of the reduction in differential thermal conductivity is not comparable to $Si_{0.8}Ge_{0.2}$ as indicted by the *green lines* in Fig. 4.14a, b.

Carrier filtering effects, which result in the increase of the average energy of the carriers, were seen from the predicted electrical conductivity plots. A slight increase in the Seebeck coefficient was estimated using (4.23) where ΔE is the change in the energy of the carrier and T is the temperature. The estimated increase of the Seebeck coefficients was 15 μV/K and 13 μV/K for Mg_2Si and $Si_{0.8}Ge_{0.2}$, respectively [22].

$$\Delta S = \frac{\Delta E(\mathrm{eV})}{T(\mathrm{K})} \tag{4.23}$$

Figure 4.15a, b shows a comparison of the calculated Hall mobility versus temperature in bulk and nano bulk Mg_2Si and $Si_{0.8}Ge_{0.2}$ at selected optimum

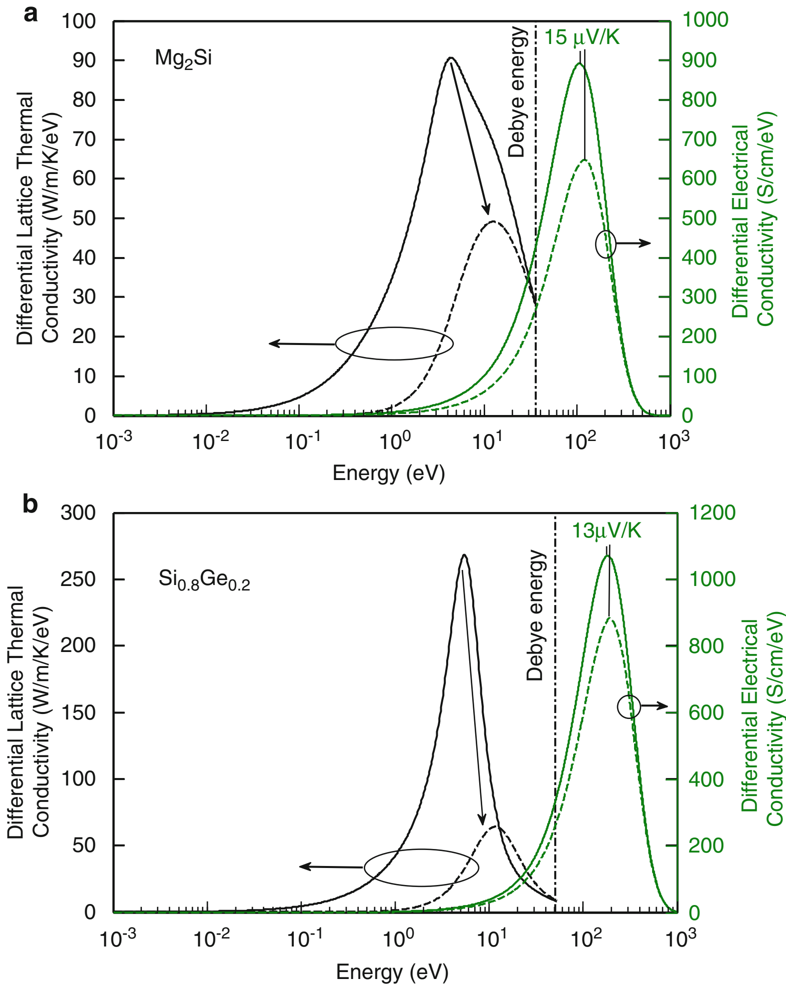

Fig. 4.14 Comparison of the differential electrical and thermal conductivities in bulk (*solid lines*) and nano bulk (*dashed lines*) systems of (**a**) n-type $Si_{0.8}Ge_{0.2}$ at 1,300 K and (**b**) n-type Mg_2Si at 850 K [22]

doping concentrations for n-type and p-type systems, respectively. The carrier mobility linearly decreases with temperature pertaining to the carrier scattering by acoustic phonons which increases with temperature. The introduction of the grain boundaries worsens the magnitude of the mobility, particularly in both n-type and p-type Mg_2Si. In comparison, the n-type and p-type $Si_{0.8}Ge_{0.2}$ suffer a lower magnitude loss in mobility and the loss is much lower at high temperatures where the acoustic phonons are dominant carrier scatterers. Subsequently, an Mg_2Si system gets adversely affected over the entire temperature range.

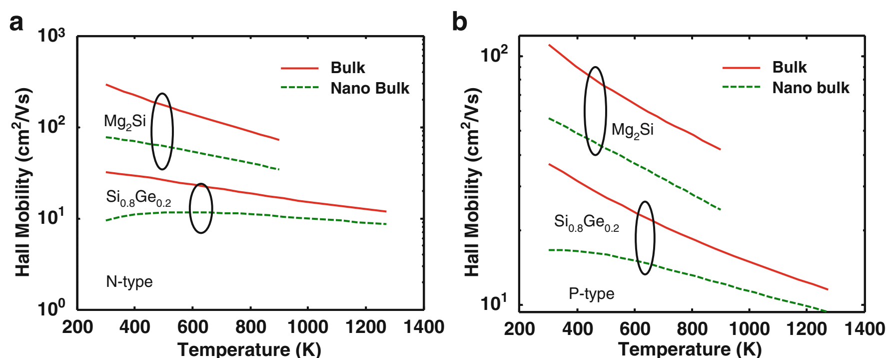

Fig. 4.15 Comparison of the Hall mobility versus temperature at optimum doping concentrations adapted from [22] and [43] (**a**) n-type (Mg_2Si: 5.4 × 10^{19} cm^{-3}; $Si_{0.8}Ge_{0.2}$: 1.6 × 10^{20} cm^{-3}) and (**b**) p-type (Mg_2Si: 4 × 10^{20} cm^{-3}; $Si_{0.8}Ge_{0.2}$: 1.6 × 10^{20} cm^{-3})

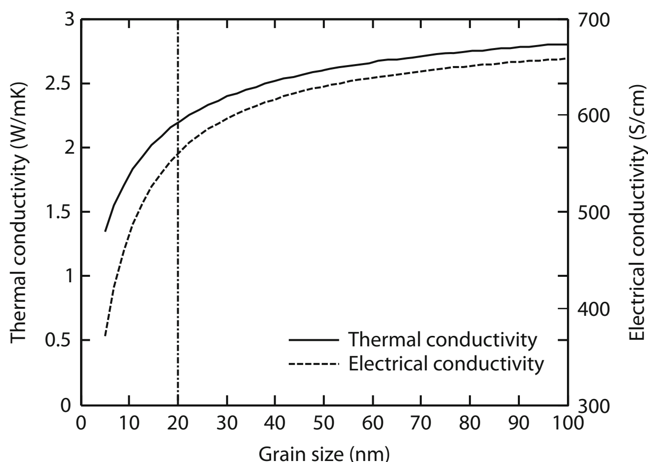

Fig. 4.16 Comparison of calculated electrical and thermal conductivity versus grain size in bulk and nanostructured n-Mg_2Si at 850 K [22]

Figure 4.16 shows the electrical and thermal conductivity of Mg_2Si plotted against the grain size. It is estimated from Fig. 4.16 by means of a sudden descent at grain sizes less than 20 nm that the electrical conductivity is affected more severely compared to the reduction in thermal conductivity in nano bulk Mg_2Si. An unfavorable 35 % drop in electrical conductivity was predicted as a result of the decrease in the grain size from 20 to 5 nm. Such deterioration in the electrical conductivity is expected to affect the power factor negatively given the fact that the carrier filtering effect also leads to a very slight increase in the Seebeck coefficient as discussed earlier via Fig. 4.14.

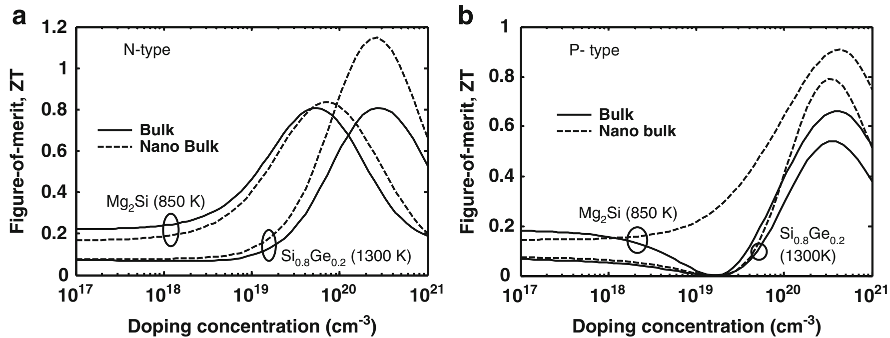

Fig. 4.17 Comparison of the calculated figure-of-merit versus temperature for (**a**) n-type and (**b**) p-type bulk and nanostructured Mg_2Si at 850 K

Figure 4.17a, b depicts the predicted *ZT* versus doping concentration for bulk and nano bulk systems in n-type and p-type Mg_2Si. The results are shown in comparison to n-type and p-type $Si_{0.8}Ge_{0.2}$. It is evident from Fig. 4.17a that the nanostructuring does not show any significant effect on the maximum attainable *ZT* of Mg_2Si over the chosen doping concentration range. Similar calculation for the p-type materials shows that nanostructuring of p-type Mg_2Si enhances the *ZT* to a maximum value of 0.9 at an optimum carrier concentration of 4.3×10^{20} cm^{-3}.

4.6 Future Directions

A fundamental understanding of the transport properties of the charge carriers and phonons in nanoscale can lead to more practical developments and better material designs. A proper theory should be able to explain how the nanoscale structure or structural dependencies at atomistic level such as the crystallite size, crystallite orientation, energy band discontinuity, and the randomness associated with these parameters in nanocrystalline structures affect the bulk properties. Moreover, the calculations of the dispersion curves, momentum, and energy relaxation times are necessary. The enhancement of *ZT* in nano bulk materials has been achieved through the reduction in thermal conductivity below that of the bulk material, so the next improved materials will feature both the reduction in thermal conductivity and improvement in power factor. It is also necessary to quantify the contribution of different geometries of the nanostructures in the reduction of the lattice thermal conductivity and the improvement of the power factor. This effort should address the role of nanostructures, grain and nanoparticle sizes, grain and nanoparticle size distributions, and finally grain and nanoparticle orientations.

It is expected that the theoretical calculations have a major role in providing techniques for the design and optimization of the new materials and their synthesis

processing parameters. Material synthesis parameters should allow for prevention of the grain growth during processing and maintaining the properties of the materials at their working temperature or other required working conditions.

Acknowledgement We acknowledge the support of Air Force Office of Scientific Research (AFOSR) High Temperature Materials program under grant no. FA9550-10-1-0010 and the National Science Foundation (NSF) under grant no. 0933763.

References

1. Seebeck, T.J.: Magnetische Polarisation der Metalle und Erze Durch Temperatur-Differenz. Ostwald's Klassiker der Exakten Wissenshaften Nr. **70**, 1822–1823 (1895)
2. Peltier, J.: Nouvelles Experiences sur la Caloriecete des Courans Electrique. Ann. Chim. **LVI**, 371–387 (1834)
3. Thomson, W.: On the dynamical theory of heat. Trans. R. Soc. Edinb. **3**, 91–98 (1851)
4. Haken, W.: Beitrag zur Kenntnis der thermoelektrischen Eigenschaften der Metallegierungen. Ann. Phys. **333**(7), p291–p336 (1910)
5. Ioffe, A.: Semiconductor Thermoelements and Thermoelectric Cooling. Infosearch, London (1957)
6. Vineis, C.J., Shakouri, A., Majumdar, A., Kanatzidis, M.G.: Nanostructured thermoelectrics: big efficiency gains from small features. Adv. Mater. **22**, 3970–3980 (2010)
7. Sootsman, J.R., Chung, D.Y., Kanatzidis, M.G.: New and old concepts in thermoelectric materials. Angew. Chem. Int. Ed. **48**, 8616–8639 (2009)
8. Ioffe, A.: The revival of thermoelectricity. Sci. Am. **199**, 31–37 (1958)
9. Walker, C.T., Pohl, R.O.: Phonon scattering by point defects. Phys. Rev. **131**, 1433–1442 (1963)
10. Slack, G.A.: New materials and performance limits for thermoelectric cooling. In: Rowe, D.M. (ed.) CRC Handbook of Thermoelectrics, p. 407. CRC, Boca Raton, FL (1995)
11. Mahan, G.D., Sofo, J.O.: The best thermoelectric. Proc. Natl. Acad. Sci. U. S. A. **93**, 7436–7439 (1996)
12. Mahan, G.D.: Good Thermoelectrics, Solid State Physics, vol. 51, pp. 82–157. Academic, New York (1997)
13. Xie, W., Tang, X., Yan, Y., Zhang, Q., Tritt, T.M.: Unique nanostructures and enhanced thermoelectric performance of melt-spun BiSbTe alloys. Appl. Phys. Lett. **94**, 102111 (2009). doi:10.1063/1.3097026
14. Poudel, B., Hao, Q., Ma, Y., Lan, Y., Yan, X., Wang, D., Vashaee, D., Dresselhaus, M., Chen, G., Ren, Z.F.: High-thermoelectric performance of nanostructured bismuth antimony telluride bulk alloys. Science **320**, 634–638 (2008)
15. Minnich, A.J., Dresselhaus, M.S., Ren, Z.F., Chen, G.: Bulk nanostructured thermoelectric materials: current research and future prospects. Energy Environ. Sci. **2**, 466–479 (2009)
16. Vashaee, D., Shakouri, A.: Improved thermoelectric power factor in metal-based superlattices. Phys. Rev. Lett. **92**(10), 106103 (2004)
17. Shakouri, A., et al.: Demonstration of electron filtering to increase the Seebeck coefficient in In0.53Ga0.47As/In0.53Ga0.28Al0.19As superlattices. Phys. Rev. B **74**, 205335 (2006)
18. Snyder, G.J., Toberer, E.S.: Complex thermoelectric materials. Nat. Mater. **7**(2), 105–114 (2008). doi:10.1038/nmat2090
19. Pichanusakorn, P., Bandaru, P.: Nanostructured thermoelectrics. Mater. Sci. Eng. R **67**, 19–63 (2010)
20. Dresselhaus, M.S., Chen, G., Tang, M.Y., Yang, R.G., Lee, H., Wang, D.Z., Ren, Z.F., Fleurial, J.-P., Gogna, P.: New directions for low-dimensional thermoelectric materials. Adv. Mater. **19**, 1043–1053 (2007). doi:10.1002/adma.200600527

21. Satyala, N., Vashaee, D.: The effect of crystallite size on thermoelectric properties of bulk nanostructured magnesium silicide (Mg_2Si) compounds. Appl. Phys. Lett. **100**, 073107 (2012)
22. Satyala, N., Vashaee, D.: Detrimental influence of nanostructuring on the thermoelectric properties of magnesium silicide. J. Appl. Phys. **112**(9), 093716–093716-11 (2012)
23. Pshenai-Severin, D.A., Federov, M.I., Samunin, A.Y.: The influence of grain boundary scattering on thermoelectric properties of Mg_2Si and $Mg_2Si_{0.8}Sn_{0.2}$. J. Electron. Mater. (2013). doi:10.007/s11664-012-2403-0
24. Heremans, J.P., Thrush, C.M., Morelli, D.T.: Thermopower enhancement in lead telluride nanostructures. Phys. Rev. B **70**, 115334 (2004)
25. Heremans, J.P., Jovovic, V., Toberer, E.S., Saramat, A., Kurosaki, K., Charoenpakdee, A., Yamanaka, S., Snyder, G.J.: Enhancement of thermoelectric efficiency in PbTe by distortion of the electronic density of states. Science **32**, 554 (2008)
26. Harman, T.C., Taylor, P.J., Walsh, M.P., LaForge, B.E.: Quantum dot superlattice thermoelectric materials and devices. Science **297**(5590), 2229 (2002)
27. Venkatasubramanian, R., Silvona, E., Colpitts, T., O'Quinn, B.: Thin-film thermoelectric devices with high room-temperature figures of merit. Nature **413**, 597 (2001)
28. Nolas, G.S., Slack, G.A., Modeli, D.T., Tritt, T.M., Ehrlich, A.C.: The effect of rare-earth filling on the lattice thermal conductivity of skutterudites. J. Appl. Phys. **79**, 4002 (1996)
29. Fluerial, J.P., Caillat, T., Borshchevsky, A.: Skutterudites: a new class of promising thermoelectric materials. In: Proceedings of the 13th International Conference on Thermoelectrics, p. 40, Kansas City, Missouri (1994)
30. Sales, B.C., Mandrus, D., Williams, R.K.: Filled skutterudite antimonides: a new class of thermoelectric materials. Science **272**, 1325 (1996)
31. Brown, S.R., Kauzlarich, S.M., Gascoin, F., Snyder, G.J.: Yb14MnSb11: new high efficiency thermoelectric material for power generation. Chem. Mater. **18**, 1873–1877 (2006)
32. Toberer, E.S., Christensen, M., Iversen, B.B., Snyder, G.J.: High temperature thermoelectric efficiency in $Ba_8Ga_{16}Ge_{30}$. Phys. Rev. B **77**, 075203 (2008)
33. Caillat, T., Fleurial, J.P., Borshchevsky, A.: Preparation and thermoelectric properties of semiconducting Zn_4Sb_3. J. Phys. Chem. Solids **58**, 1119–1125 (1997)
34. Kurosaki, K., Kosuga, A., Muta, H., Uno, M., Yamanaka, S.: Ag_9TITe_5: a high-performance thermoelectric bulk material with extremely low thermal conductivity. Appl. Phys. Lett. **87**, 061919 (2005)
35. Pei, Y., Wang, H., Snyder, G.J.: Band engineering of thermoelectric materials. Adv. Mater. **24**, 6125 (2012). doi:10.1002/adma.201202919
36. Chen, G.: Thermal conductivity and ballistic-phonon transport in the cross-plane direction of superlattices. Phys. Rev. B **57**, 14958 (1998)
37. Hicks, L.D., Dresselhaus, M.S.: Effect of quantum-well structures on the thermoelectric figure of merit. Phys. Rev. B **47**, 12727 (1993)
38. Vashaee, D., Zhang, Y., Shakouri, A., Zeng, G., Chiu, Y.: Cross-plane Seebeck coefficient in superlattice structures in the miniband conduction regime. Phys. Rev. B **74**, 195315 (2006)
39. Vashaee, D., Shakouri, A.: Electronic and thermoelectric transport in semiconductor and metallic Superlattices. J. Appl. Phys. **95**(3), 1233–1245 (2004)
40. Zide, J.T.M., Klenov, D.O., Stemmer, S., Gossard, A., Zeng, G.H., Bowers, J.E., Vashaee, D., Shakouri, A.: Thermoelectric power factor in semiconductors with buried epitaxial semimetallic nanoparticles. Appl. Phys. Lett. **87**, 112102 (2005)
41. Poudel, B., Hao, Q., Ma, Y., Lan, Y., Yan, X., Wang, D., Vashaee, D., Dresselhaus, M., Chen, G., Ren, Z.F.: High thermoelectric performance of nanostructured bismuth antimony telluride bulk alloys. Science Express Research Articles (2008). doi:10.1126/science.1156446
42. Zamanipour, Z., Shi, X., Dehkordi, A.M., Krasinski, J.S., Vashaee, D.: The effect of synthesis parameters on transport properties of nanostructured bulk thermoelectric p-type silicon germanium alloy. Physica Status Solidi (a) **209**(10), 2049–2058 (2012)
43. Minnich, A.J., Lee, H., Wang, X.W., Joshi, G., Dresselhaus, M.S., Ren, Z.F., Chen, G., Vashaee, D.: Modeling study of thermoelectric SiGe nanocomposites. Phys. Rev. B **80**, 155327 (2009)

44. Biswas, K., He, J., Blum, I.D., Wu, C.-I., Hogan, T.P., Seidman, D.N., Dravid, V.P., Kanatzidis, M.G.: High-performance bulk thermoelectrics with all-scale hierarchical architectures. Nature **489**, 414–418 (2012)
45. Thermion Company: Implemented conventional bulk technologies to fabricate thermoelectric devices of ~200μm thick. http://www.thermion-company.com (2005)
46. Gould, C., Shammas, N.: A review of thermoelectric MEMS devices for micro-power generation, heating and cooling applications. In: Takahata, K. (ed.) Micro Electronic and Mechanical Systems. Available from: http://www.intechopen.com/books/micro-electronicand-mechanical-systems/a-review-of-thermoelectric-mems-devices-for-micro-power-generation-heating-andcooling-applications
47. Joshi, G., Lee, H., Lan, Y., Wang, X., Zhu, G., Wang, D., Gould, R.W., Cuff, D.C., Tang, M. Y., Dresselhaus, M.S., Chen, G., Ren, Z.: Enhanced thermoelectric figure-of-merit in nanostructured p-type silicon germanium bulk alloys. Nano Lett. **8**(12), 4670 (2008)
48. Bathula, S., Jayasimhadri, M., Singh, N., Srivastava, A.K., Pulikkotil, J., Dhar, A., Budhani, R. C.: Enhanced thermoelectric figure-of-merit in spark plasma sintered nanostructured n-type SiGe alloys. Appl. Phys. Lett. **101**, 213902 (2012)
49. Mingo, N., Hauser, D., Kobayashi, N.P., Plissonnier, M., Shakouri, A.: Nanoparticle-in-alloy approach to efficient thermoelectrics: silicides in SiGe. Nano Lett. **9**(2), 711–715 (2009)
50. Rowe, D.M. (ed.): CRC Handbook of Thermoelectrics. CRC, Boca Raton, FL (1995)
51. Zhu, Y.T., Langdon, T.G.: The fundamentals of nanostructured materials processed by severe plastic deformation. J. Miner. **56**(10), 58–63 (2004)
52. Segal, V.M.: Engineering and commercialization of equal channel angular extrusion (ECAE). Mater. Sci. Eng. **A386**, 269 (2004)
53. Saravanan, M., Pillai, R.M., Pai, B.C.: Equal channel angular pressing of aluminum alloys and composites—an overview. Aluminum India **5**(2), 3–14 (2005)
54. Slarnova, K.: Accumulative roll-bonding: first experience with a twin-roll cast AA8006 alloy. J. Alloys Compd. **378**(1–2), 322–325 (2004)
55. Tsuji, N., Saito, Y., Lee, S.-H., Minamino, Y.: ARB (accumulative roll-bonding) and other new techniques to produce bulk ultrafine grained materials. Adv. Eng. Mater. **5**(5), 338 (2003)
56. Androulakis, J., Lin, C.H., Kong, H.J., Uher, C., Wu, C.I., Hogan, T., Cook, B.A., Caillat, T., Paraskevopoulos, K.M., Kanatzidis, M.G.: Spinodal decomposition and nucleation and growth as a means to bulk nanostructured thermoelectrics: enhanced performance in Pb1-xSnxTe–PbS. J. Am. Chem. Soc. **129**, 9780 (2007)
57. Sootsman, J.R., Pcionek, R.J., Kong, H., Uher, C., Kanatzidis, M.G.: Strong reduction of thermal conductivity in nanostructured PbTe prepared by matrix encapsulation. Chem. Mater. **18**, 4993 (2006)
58. Hsu, K.F., Loo, S., Guo, F., Chen, W., Dyck, J.S., Uher, C., Hogan, T., Polychroniadis, E.K., Kanatzidis, M.G.: Cubic $AgPb_mSbTe_{2+m}$: bulk thermoelectric materials with high figure of merit. Science **303**, 818 (2004)
59. Poudeu, P.F.P., D'Angelo, J., Downey, A.D., Short, J.L., Hogan, T.P., Kanatzidis, M.G.: High thermoelectric figure of merit and nanostructuring in bulk p-type $Na_{1-x}Pb_mSb_yTe_{m+2}$. Angew. Chem. Int. Ed. **45**, 3835 (2006)
60. Blum, I.D., Isheim, D., Seidman, D.N., He, J., Androulakis, J., Biswas, K., Dravid, V.P., Kanatzidis, M.G.: Dopant distributions in PbTe-based thermoelectric materials. J. Electron. Mater. **41**(6), 1583–1588 (2012)
61. Chen, S., Carroll, D.L.: Synthesis and characterization of truncated triangular silver nanoplates. Nano Lett. **2**, 1003 (2002)
62. Maillard, M., Giorgio, S., Pileni, M.P.: Silver nanodisks. Adv. Mater. **14**, 1084 (2002)
63. Hao, E., Kelly, K.L., Hupp, J.T., Schatz, G.C.: Synthesis of silver nanodiscs using polystyrene meso-spheres as templates. J. Am. Chem. Soc. **124**, 15182 (2002)
64. Ibano, D., Yokota, Y., Tominaga, T.: Preparation of gold nanoplates protected by an anionic phospholipid. Chem. Lett. **32**, 574 (2003)

65. Simakin, A.V., Voronov, V.V., Shafeev, G.A., Brayner, R., Bozon-Verduraz, F.: Nanodisks of Au and Ag produced by laser ablation in liquid environment. Chem. Phys. Lett. **348**, 182 (2001)
66. Lu, W., Ding, Y., Chen, Y., Wang, Z.L., Fang, J.: Formation of PbSe nanocrystals: a growth toward nanocubes. J. Am. Chem. Soc. **127**, 10112 (2005)
67. Wang, W., Poudel, B., Yang, J., Wang, D.Z., Ren, Z.F.: High-yield synthesis of single-crystalline antimony telluride hexagonal nanoplates using a solvothermal approach. J. Am. Chem. Soc. **127**, 13792 (2005)
68. Bertini, L., Stiewe, C., Toprak, M., Williams, S., Platzek, D., Mrotzek, A., Zhang, Y., Gatti, C., Muller, E., Muhammed, M., Rowe, M.: Nanostructured $Co_{1-x}Ni_xSb_3$ skutterudites: synthesis, thermoelectric properties, and theoretical modeling. J. Appl. Phys. **93**, 438 (2003)
69. Liu, C.J., Yamauchi, H.: Thermoelectric power and resistivity of $La_{1.8}Sr_{0.2}CaCu_2O_6$ and the effects of O_2 hot-isostatic-press annealing. Phys. Rev. B **51**, 11826 (1995)
70. Wang, X.W., Lee, H., Lan, Y.C., Zhu, G.H., Joshi, G., Wang, D.Z., Yang, J., Muto, A.J., Tang, M.Y., Klatsky, J., Song, S., Dresselhaus, M.S., Chen, G., Ren, Z.: Enhanced thermoelectric figure of merit in nanostructured n-type silicon germanium bulk alloy. Appl. Phys. Lett. **93**, 193121 (2008)
71. Kishimoto, K., Koyanagi, T.: Temperature dependence of the Seebeck coefficient and the potential barrier scattering of n-type PbTe films prepared on heated glass substrates by rf sputtering. J. Appl. Phys. **92**(9), 2544 (2002)
72. Wang, H., Li, J.F., Nan, C.W., Zhou, M., Liu, W., Zhang, B.P., Kita, T.: High-performance $Ag_{0.8}Pb_{18+x}SbTe_{20}$ thermoelectric bulk materials fabricated by mechanical alloying and spark plasma sintering. Appl. Phys. Lett. **88**, 092104 (2006)
73. Li, H., Tang, X.F., Su, X.L., Zhang, Q.J.: Preparation and thermoelectric properties of high-performance Sb additional $Yb_{0.2}Co_4Sb_{12+y}$ bulk materials with nanostructure. Appl. Phys. Lett. **92**, 202114 (2008)
74. Chen, G.: Recent trends in thermoelectric materials research III. In: Willardson, R.K., Weber, E.R. (eds.) Semiconductors and Semimetals, vol. 71, pp. 203–259. Academic, New York (2001)
75. Liu, H., Zheng, Z., Yang, D., Ke, X., Jaatinen, E., Zhao, J.C., Zhu, H.Y.: Coherent interfaces between crystals in nanocrystal composites. ACS Nano **4**(10), 6219–6227 (2010)
76. Huang, X., Wang, X., Cook, B.: Coherent nanointerfaces in thermoelectric materials. J. Phys. Chem. C **114**(49), 21003–21012 (2010)
77. Bartkowiak, M., Mahan, G.D.: Heat and electricity transport through interfaces. In: Tritt, T.M. (ed.) Recent Trends in Thermoelectric Materials, vol. 2. Semiconductors and Semimetals, vol. 70, pp. 245–271. Academic, New York (2001)
78. Swartz, E.T., Pohl, R.O.: Thermal boundary resistance. Rev. Mod. Phys. **61**(3), 605–658 (1989)
79. Singh, J.: Physics of Semiconductors and Their Heterostructures. McGraw-Hill, Singapore (1996)
80. Lundstrom, M.: Fundamentals of Carrier Transport, 2nd edn. Cambridge University Press, Cambridge (2000)
81. Heremans, J.P., Thrush, C.M., Morelli, D.T.: Thermopower enhancement in PbTe with Pb precipitates. J. Appl. Phys. **98**, 063703 (2005)
82. Ramu, A.T., Cassels, L.E., Hackman, N.H., Lu, H., Zide, J.M.O., Bowers, J.E.: Thermoelectric transport in the coupled valence-band model. J. Appl. Phys. **109**, 033704 (2011)
83. Jacob, U., Vancea, J., Hoffmann, H.: Surface-roughness contributions to the electrical resistivity of polycrystalline metal films. Phys. Rev. B **41**, 11852–11857 (1990)
84. Taylor, W.E., Odell, N.H., Fan, H.Y.: Grain boundary barriers in germanium. Phys. Rev. **93**, 666–667 (1954)
85. Tanaka, T., Hayashi, S., Shibayama, K.: Thermal-depolarization-current study of composites of epoxy resin containing mica flakes. J. Appl. Phys. **48**, 3478–3483 (1977)
86. Shuai, Z., Wang, L., Song, C.: Theory of Charge Transport in Carbon Electronic Materials. SpringerBriefs in Molecular Science. Springer, Berlin (2012). doi:10.1007/978-3-642-25076-7_4

87. Bardeen, J., Shockley, W.: Deformation potentials and mobilities in non-polar crystals. Phys. Rev. **80**(1), 72–80 (1950)
88. Ward, A., Broido, D.A.: Intrinsic phonon relaxation times from first-principles studies of the thermal conductivities of Si and Ge. Phys. Rev. B **81**, 085205 (2010)
89. Tritt, T.M. (ed.): Thermal Conductivity: Theory, Properties, and Applications. Springer, New York (2005)
90. Toberer, E.S., Zevalkink, A., Snyder, G.J.: Phonon engineering through crystal chemistry. J. Mater. Chem. **21**, 15843 (2011)
91. Pettersson, S.: Calculation of the thermal conductivity of alkali halide crystals. J. Phys. C Solid State Phys. **20**(8), 1047–1061 (1987)
92. Slack, G.A.: Solid State Physics, vol. 34. Academic, New York (1979)
93. Roufosse, M., Klemens, P.G.: Thermal-conductivity of complex dielectric crystals. Phys. Rev. B **7**(12), 5379–5386 (1973)
94. Pohl, R.O.: Thermal conductivity and phonon resonance scattering. Phys. Rev. Lett. **8**(12), 481–483 (1962)
95. Wagner, M.: Influence of localized modes on thermal conductivity. Phys. Rev. **131**(4), 1443–1455 (1963)
96. Morelli, D.T., Jovovic, V., Heremans, J.P.: Intrinsically minimal thermal conductivity in cubic I-V-VI_2 semiconductors. Phys. Rev. Lett. **101**(3), 035901 (2008)
97. Hopkins, P.E., Duda, J.C., Norris, P.M.: Anharmonic phonon interaction at interfaces and contributions to thermal boundary conductance. J. Heat Transfer **133**(6), 062401 (2011)
98. Rath, S., Sanyal, S.P.: Effect of strain on vibrational modes in strained layer superlattices. Pramana **41**(1), 21–29 (1993)
99. Herring, C., Vogt, E.: Transport and deformation-potential theory for many-valley semiconductors with anisotropic scattering. Phys. Rev. **101**(3), 944–961 (1956)
100. Bir, G., Pikus, G.: Symmetry and Strain-Induced Effects in Semiconductors. Wiley, New York (1974)
101. Henry, A.S., Chen, G.: Spectral phonon transport properties of silicon based on molecular dynamics simulations and lattice dynamics. J. Comput. Theor. Nanosci. **5**(2), 141–152 (12) (2008)
102. Chou, F.C., Lukes, J.R., Liang, X.G., Takahashi, K., Tien, C.L.: Molecular dynamics in microscale thermophysical engineering. Annu. Rev. Heat Transfer **10**, 141–176 (1999)
103. Chen, G., Tasciuc, B., Yang, R.: Nanoscale heat transfer. In: Nalwa, H.S. (ed.) Encyclopedia of Nanoscience and Nanotechnology, vol. 7, p. 429. American Scientific Publishers, Stevenson Ranch, CA (2004)
104. Maiti, A., Mahan, G.D., Pantelides, S.T.: Dynamical simulations of non-equilibrium processes—heat flow and the Kapitza resistance across grain boundaries. Solid State Commun. **102**(7), 517 (1997)
105. Stevens, R.J., Zhigilei, L.V., Norris, P.M.: Effects of temperature and disorder on thermal boundary conductance at solid-solid interfaces: nonequilibrium molecular dynamics simulations. Int. J. Heat Mass Transfer **50**(19–20), 3977 (2007)
106. Zhong, H.L., Lukes, J.R.: Interfacial thermal resistance between carbon nanotubes: molecular dynamics simulations and analytical thermal modeling. Phys. Rev. B **74**, 125403 (2006)
107. Kaddouri, H., Benet, S., Charar, S., Makowaska-Janusik, M., Tedenac, J.C., Kityk, I.V.: Simulation of thermoelectric properties of bismuth telluride single crystalline films grown on Si and SiO2 surfaces. Phys. Rev. B **62**(24), 17108 (2000)
108. Chonan, T., Katayama, S.: Molecular-dynamics simulation of lattice thermal conductivity in $Pb_{1-x}Sn_xTe$ and $Pb_{1-x}Ge_xTe$ at high temperature. J. Phys. Soc. Jpn. **75**(6), 064601 (2006)
109. Huang, X., Huai, X., Liang, S., Wang, X.: Thermal transport in Si/Ge nanocomposites. J. Phys. D. Appl. Phys. **42**, 095416 (2009)
110. Datta, S.: Electronic Transport in Mesoscopic Systems. Cambridge University Press, Cambridge (1995)

111. Meir, Y., Wingreen, N.S.: Landauer formula for the current through an interacting electron region. Phys. Rev. Lett. **68**(16), 2512–2515 (1992)
112. Bulusu, A., Walker, D.G.: Modeling of thermoelectric properties of semi-conductor thin films with quantum and scattering effects. J. Heat Transfer **129**(4), 492–499 (2006)
113. Savic, I., Stewart, D.A., Mingo, N.: Thermal conduction mechanisms in boron-nitride nanotubes: few-shell versus all-shell conduction. Phys. Rev. B **78**, 235434 (2008)
114. Savic, I., Mingo, N., Stewart, D.A.: Phonon transport in isotope-disordered carbon and boron-nitride nanotubes: is localization observable? Phys. Rev. Lett. **101**, 165502 (2008)
115. Stewart, D.A., Savic, I., Mingo, N.: First-principles calculation of the isotope effect on boron nitride nanotube thermal conductivity. Nano Lett. **9**(1), 81–84 (2009)
116. Kim, W., Wang, R., Majumdar, A.: Nanostructuring expands thermal limits. Nano Today **2**(1), 40–47 (2007)
117. Tani, J.I., Kido, H.: Thermoelectric properties of Al-doped $Mg_2Si_{1-x}Sn_x$ ($x \leqq 0.1$). J. Alloys Compd. **466**, 335–340 (2008)
118. Choi, S.M., Kim, K.H., Kim, I.H., Kim, S.U., Seo, W.S.: Thermoelectric properties of the Bi-doped Mg_2Si system. Curr. Appl. Phys. **11**(3 Suppl), S388–S391 (2011)
119. Akasaka, M., Iida, T., Matsumoto, A., Yamanaka, K., Takanash, Y., Imai, T., Hamada, N.: The thermoelectric properties of bulk crystalline *n*- and *p*-type Mg_2Si prepared by the vertical Bridgman method. J. Appl. Phys. **104**, 013703 (2008)
120. Satyala, N., Vashaee, D.: Modeling of thermoelectric properties of magnesium silicide (Mg_2 Si). J. Electron. Mater. **41**(6), 1785–1791 (2012)
121. Zaitsev, V.K., Fedorov, M.I., Gurieva, E.A., Eremin, I.S., Konstantinov, P.P., Samunin, A.Y., Vedernikov, M.V.: Highly effective $Mg_2Si_{1-x}Sn_x$thermoelectrics. Phys. Rev. B **74**, 045207 (2006)
122. Mars, K., Ihou-mouko, H., Pont, G., Tobola, J., Scherrer, H.: Thermoelectric properties and electronic structure of Bi- and Ag-doped Mg_2Si_{1-x} Ge $_x$ compounds. J. Electron. Mater. **38**(7), 1360 (2009)
123. Kim, I.-H., Jung, J.-Y., Choi, S.-M., Seo, W.-S., Kim, S.-U.: Synthesis of thermoelectric Mg_2Si by mechanical alloying. J. Korean Phys. Soc. **57**(4), 1005–1009 (2010)
124. Tani, J.-I., Kido, H.: Thermoelectric properties of Sb-doped Mg_2Si semiconductors. Intermetallics **15**, 1202–1207 (2007)
125. Sakamoto, T., Iida, T., Kurosaki, S., Yano, K., Taguchi, H., Nishio, K., Takanashi, Y.: Thermoelectric behavior of Sb- and Al-doped n-type Mg_2Si device under large temperature differences. J. Electron. Mater. **40**(5), 629–634 (2010)
126. Savary, E., Gascoin, F., Marinel, S.: Fast synthesis of nanocrystalline Mg_2Si by microwave heating: a new route to nano-structured thermoelectric materials. Dalton Trans. **39**, 11074–11080 (2010)
127. Dube, D.C., Fu, M., Agrawal, D., Roy, R., Santra, A.: Rapid alloying of silicon with germanium in microwave field using single mode cavity. Mater. Res. Innov. **12**(3), 119 (2008)
128. Nikitin, E.N., Bazanov, V.G., Tarasov, V.I.: Thermoelectric properties of solid solutions Mg_2Si-Mg_2Sn. Sov. Phys. Solid State **3**(12), 2648 (1962)
129. Yang, M., Zhang, L., Shen, Q.: Synthesis and sintering of Mg2Si thermoelectric generator by spark plasma sintering. J. Wuhan Univ. Technol. Mater. Sci Ed **23**(6), 870–873 (2008)
130. Lu, L., Lai, M.O., Hoe, M.L.: Formation of nanocrystalline Mg_2Si and Mg_2Si dispersion strengthened Mg-Al alloy by mechanical alloying. Nanostruct. Mater. **10**(4), 551–563 (1998)
131. Fiameni, S., Battiston, S., Boldrini, S., Famengo, A., Agresti, F., Barison, S., Fabrizio, M.: Synthesis and characterization of Bi-doped Mg_2Si thermoelectric materials. J. Solid State Chem. **193**, 142–146 (2012)
132. Wang, L., Qi, X.Y., Xiong, W., Zhu, X.G.: Fabrication and mechanical properties of bulk nanocrystalline intermetallic Mg_2Si. Mater. Sci. Eng. A **459**, 216–222 (2007)
133. Aymerich, F., Mula, G.: Pseudopotential band structures of Mg_2Si, Mg_2Ge, Mg_2Sn, and of the solid solution Mg_2(Ge, Sn). Physica Status Solidi (b) **42**(697) (1970)

Chapter 5
Control Thermal Conductivity of Semiconductor Nanowires: Phononics Engineering

Gang Zhang and Yong-Wei Zhang

Abstract The field of nanoscale thermoelectrics has progressed enormously recently because of the strong global demand for pollution-free forms of energy conversion. Rapid development and exciting innovative breakthroughs in the field over the last decades have occurred in large part due to newly emerged nanoscale materials with reduced thermal conductivity, and newly developed physical concepts, which make it possible to modify the thermal conductivity of nanoscale materials. We review recent experimental and theoretical advances in the study of thermal conductivity and thermoelectric property of nanowires. We first present several theoretical and experimental results on the reduction of thermal conductivity and the improvement of the thermoelectric figure of merit, including size effect, roughness effect, isotopically doped impurity, surface and interface phonon scattering. We then discuss coherent phonon resonance in core–shell nanowires and its impact on thermal conductivity. Finally, we highlight the importance of these effects on the figure of merit of nanowires.

5.1 Introduction

It is commonly believed that the world is heading towards energy crisis due to the fact that the world's power demands are expected to rise and the availability of conventional energy sources is expected to decline rapidly. A possible way to

G. Zhang (✉)
Institute of High Performance Computing, A*STAR, Singapore, Singapore

Key Laboratory for the Physics and Chemistry of Nanodevices, Department of Electronics, Peking University, Beijing 100871, People's Republic of China
e-mail: zhangg@ihpc.a-star.edu.sg

Y.-W. Zhang
Institute of High Performance Computing, A*STAR, Singapore, Singapore
e-mail: zhangyw@ihpc.a-star.edu.sg

X. Wang and Z.M. Wang (eds.), *Nanoscale Thermoelectrics*, Lecture Notes in Nanoscale Science and Technology 16, DOI 10.1007/978-3-319-02012-9_5,
© Springer International Publishing Switzerland 2014

alleviate or even solve the global energy crisis is to enhance the utilization efficiency of energy. Today, approximately 80 % of the world's power is generated by heat engines that use fossil fuel combustion as a heat source [1], which is believed to be responsible for a large fraction of carbon dioxide (CO_2) emissions worldwide. The heat engines used in most thermal power stations typically operate at 30–40 % efficiency. This means that roughly 10 TW of heat energy is lost to the environment. Thermoelectric modules can potentially convert part of the wasted heat directly into electricity, reducing the usage of fossil fuels and lowering carbon emission.

In addition to waste heat harvesting, thermoelectric materials also can be applied in solar energy conversion. More solar energy hits the earth in 1 h than all the energy consumed by the world in a year. The development of affordable solar cells is therefore one of the most promising long term solutions to the energy crisis. To increase efficiency of the light-harvesting process in converting solar energy to electricity, it is important that the materials used are able to capture a large fraction of the solar spectrum. However, most solar cell materials absorb solar energy only in the visible wavelength range. Therefore, a large fraction (more than 50 %) of the solar spectrum in the near infrared region is not captured, and thus lost as heat energy, leading to low efficiencies. Thermoelectric materials can potentially convert part of the solar heat directly into a high grade form of energy such as electricity.

Moreover, microelectronic processors generate a huge amount of heat in very small areas (called hotspots). Traditionally, this heat is considered as waste and may lead to the partial or total loss of the functionality of the processors. Power dissipation issues have recently become one of the greatest challenges for integrated electronics, which limits the performance of a wide range of electronics from handheld devices to massive data centers, and it is also becoming a bottleneck for the further development of smaller and faster devices. For instance, the energy use of information technology infrastructure in the USA is currently in excess of 20 GW, or 5–10 % of the national electricity capacity. More importantly, the energy consumption in data centers has doubled in the past 5 years. Currently, for every kilowatt-hour of energy consumed by a computer in a data center, another kWh is needed for cooling [2].

In existing commercial silicon chips, hot spot removal is a key for the future generation of IC chips. Circulated liquid cooling is one of current available cooling technologies, which moves heat sink away from the processors by increasing the surface area. However, reliability is a big concern if the liquid hose is leaking. The other widely used technology is thermoelectric (TE) modules. Thermoelectric cooling is a silent and environment friendly solution. However, the hot spots in microprocessors are normally in the order of 300–400 μm in diameter, and thus even the smallest commercial cooling module is still too large to be used in spot cooling. In addition, as the silicon stacked chips or three-dimensional (3D) chips are introduced, this can create even smaller and hotter spots. Nanoscale cooler with

high efficiency is a key enabler to remove small hot spots in IC chips and for the improvements of future IC thermal management.

The performance efficiency of thermoelectric material is best measured by the figure of merit: $ZT = \frac{S^2 \times \sigma}{\kappa} T$ [3], here S is the Seebeck coefficient, σ is the electrical conductivity, T is the absolute temperature, and κ is the thermal conductivity. $\kappa = \kappa_e + \kappa_p$, where κ_e and κ_p are the electron and phonon (lattice vibration) contributions to the thermal conductivity, respectively. In order to make a material competitive for thermoelectric purposes, the ZT of the material must be larger than three. However, the road to achieve this goal has not been very smooth so far. There are several ways to do this. The first approach is to increase the Seebeck coefficient S. However, for general materials, simply increasing S will lead to a simultaneous decrease in electrical conductivity. The second approach is to increase the electrical conductivity. This has also proven to be ineffective, because electrons are also carriers of heat and an increase in the electrical conductivity will also lead to an increase in the thermal conductivity. The ideal case is to reduce the thermal conductivity without affecting the electrical conductivity. It is possible to achieve this in nanoscale materials. Nanoscale materials have been proposed to enhance ZT [3–5] due to their reduced thermal conductivity. Because of the large surface area to volume ratio, the strong phonon surface scattering in nanowires can result in a low thermal conductivity compared to their bulk counterparts [6].

In the novel nanoscale TE materials, silicon nanowires (SiNWs) are appealing choices because of their small sizes and ideal interface compatibility with conventional Si-based technology [7–9]. In SiNWs, the electrical conductivity and electron contribution to Seebeck coefficient are similar to those of bulk silicon, but they exhibit 100-fold reduction in thermal conductivity [6], showing that the electrical and thermal conductivities can be decoupled. Recent experiments [10, 11] have provided direct evidence that an approximately 100-fold improvement of the ZT values over bulk Si are achieved in SiNWs over a broad temperature range. This large increase of ZT is attributed to the decrease of thermal conductivity. This has raised the exciting prospect that SiNWs can be applied as novel nanoscale thermoelectric materials.

It is obvious that the systematic applications of nano thermoelectric materials depend on how well we understand their material properties. Thermal property in nanostructures differs significantly from that in macrostructures because the characteristic length scales of phonons are comparable to the characteristic length of nanostructures.

A large variety of studies on thermal conductivity of nano materials have been undertaken in the past decade, and many quite unexpected phenomena have been observed. This book chapter is to review the recent advances in the study of thermoelectric property of an important class of one-dimensional materials, Si nanowires, focusing on the theories and applications. For comprehensive review of nanoscale thermal conductivity, please refer to the articles [12–21].

5.2 Modify Thermal Conductivity of Silicon Nanowires: Incoherent Mechanism

SiNWs have attracted a great attention in recent years because of their excellent electrical and mechanical properties [22] and their potential applications in many areas including biosensors [23, 24], electronic devices [25], and solar PVs [26].

The size effect on the low temperature thermal conductance of SiNWs has been demonstrated experimentally [6]. Donadio and Galli studied the heat transport in SiNWs systematically, by using molecular dynamics simulation, lattice dynamics, and Boltzmann transport equation calculations [27]. It was demonstrated that the disordered surfaces, nonpropagating modes analogous to heat carriers, together with decreased lifetimes of propagating modes are responsible for the reduction of thermal conductivity in SiNWs. In this section, we discuss various incoherent mechanisms that can lead to reduction in thermal conductivity of SiNW.

5.2.1 Size and Surface Roughness Effects

Due to the size effect and high surface to volume ratio, the thermal conduction properties of silicon nanostructures differ substantially from those of their bulk counterparts. Volz and Chen investigated the thermal conductivity of SiNWs based on molecular dynamic simulations using the Green–Kubo method, and found that the thermal conductivity of individual SiNWs is more than 2 orders of magnitude lower than the bulk value [28, 29]. Li et al. [6] have experimentally demonstrated a significant reduction of thermal conductivity in SiNWs compared to the thermal conductivity in bulk silicon, and a strong diameter dependence was observed as shown in Fig. 5.1. The room temperature thermal conductivity of bulk silicon is 140 W/m K. However, thermal conductivity of SiNW with diameter of 50 nm is only about 20 W/m K, and thermal conductivity decreases with decreasing diameter. This is due to the following facts. Firstly, the low frequency phonons, whose wave lengths are longer than the length of nanowire, cannot survive. Therefore, the low frequency contribution to thermal conductivity, which is very substantial and significant in bulk material, is largely reduced. Secondly, because of the large surface to volume ratio, the boundary scattering in quasi-1D structure is also significant.

The surface area to volume ratio (SVR) increases as the system scales down. It thus plays a more and more important role when the device becomes smaller and smaller. It has also been shown that SVR affects the physical properties of nano materials remarkably. The SVR dependence of thermal conductivity of [100] SiNWs with different cross-sectional areas and geometries have been investigated [30]. Figure 5.2a–c shows the thermal conductivity κ versus SVR at different temperatures. For simplicity, NWs with rectangular, circular, and triangular cross-sectional shapes are named as rect-SiNWs, cir-SiNWs, and tri-SiNWs, respectively. At each temperature, thermal conductivity decreases monotonically

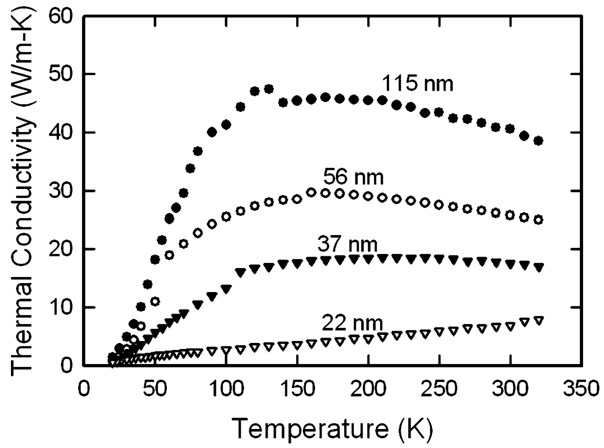

Fig. 5.1 Measured thermal conductivity of Si nanowires (SiNWs) with different diameters. For details please refer to [6]

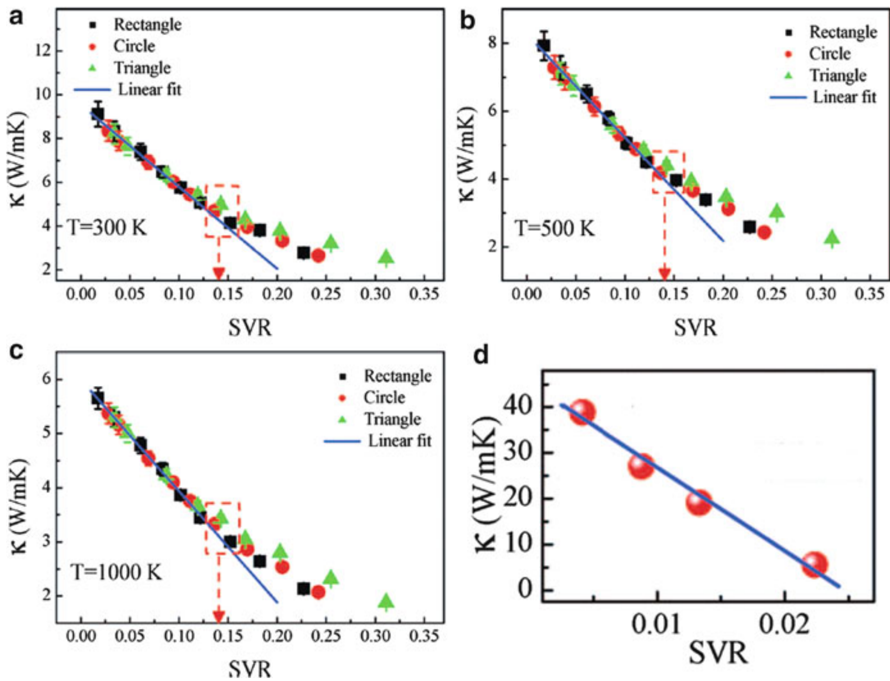

Fig. 5.2 Thermal conductivity (κ) of SiNWs versus surface-to-volume ratio for different temperatures: (**a**) 300 K, (**b**) 500 K, and (**c**) 1,000 K. The *black squares*, *red circles*, and *green triangles* denote thermal conductivity of rect-SiNWs, cir-SiNWs, and tri-SiNWs, respectively. (**d**) Experimental results at 300 K from [6]

with the increase of SVR, which is a consequence of the enhanced surface scattering when SVR increases. More interestingly, for different cross-sectional geometries, thermal conductivity follows the same linear dependence on SVR when the cross-sectional area is greater than certain threshold of about 20 nm^2 (Fig. 5.2). This important feature suggests that SVR can serve as a universal gauge for thermal conductivity of SiNWs, regardless of the specific cross-sectional geometry.

For very thin SiNWs with cross-sectional area below the threshold, the dependence of thermal conductivity on SVR deviates from the universal linear fitted line. We refer to the cross-sectional area above and below this threshold as the "universal region" and "non-universal region," respectively. The threshold in cross-sectional area is found to be about 20 nm^2, which only corresponds to about 5 nm in diameter for SiNWs with circular cross-sectional shape. This dimensional scale for the threshold is very close to the smallest diameter that the current experimental fabrication technique can achieve. Therefore, from practical point of view, SVR can be used as a universal gauge without any restriction of cross-sectional area.

In the universal region, the linear dependence of thermal conductivity on SVR holds for all temperatures above 300 K, while the absolute value of the slope for the linear best fit decreases with the increase of temperature. When the temperature increases from room temperature, κ decreases as a consequence of stronger anharmonic phonon–phonon scattering at high temperatures. The higher SVR value can induce a stronger surface scattering and thus result in more localized phonon modes. The introduction of phonon localization can weaken the temperature dependence of thermal conductivity. As a result, thermal conductivity of the nanowire with a lower SVR decreases more than that of the one with a higher SVR, leading to a decrease in the absolute value of the linear slope with the increase in temperature.

Figure 5.2d shows the thermal conductivity versus SVR relation based on the experimental results from [6] for cir-SiNWs at 300 K. The SiNWs used in [6] are single crystalline with the length of several microns and cross-sectional area up to 1×10^4 nm^2. A good linear dependence of thermal conductivity on SVR also appears from these results. The good agreement of experimental results with the linear fit line further supports the fact that the linear relation between thermal conductivity and SVR is an intrinsic phenomenon in NWs.

An analytical formula including the surface scattering and the size confinement effects of phonon transport is proposed by Liang and Li to describe the size dependence of thermal conductivity in NWs and other nanoscale structures. For SiNWs with length in micrometer scale, the thermal conductivity increases with increasing diameter remarkably until the diameter is larger than about hundreds of nanometers [31]. The quantitative formula for the size-dependent thermal conductivity of SiNW is [31]:

$$\frac{\kappa}{\kappa_{\mathrm{b}}} = p \exp\left(-\frac{d_0}{D}\right)\left[\exp\left(\frac{-(\alpha-1)}{D/\lambda-1}\right)\right]^{3/2} \tag{5.1}$$

Here κ is the thermal conductivity of SiNW, κ_{b} is the thermal conductivity of bulk silicon. The details about this formula can be found in [31].

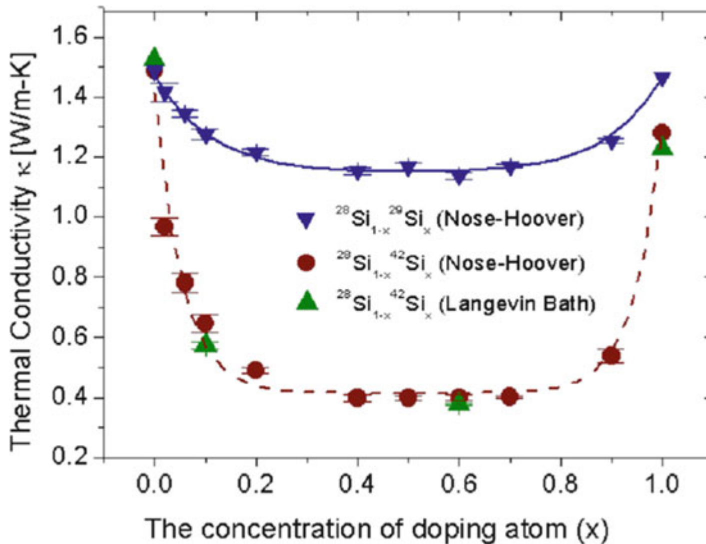

Fig. 5.3 Thermal conductivity of SiNWs versus the percentage of randomly doping isotope atoms at 300 K. The results by Nosé–Hoover method coincide with those by Langevin methods indicating that the conclusions are independent of the heat bath used. Details are given in [32]

5.2.2 Effects of Random Doping

It is indispensable to reduce the thermal conductivity of SiNWs further in order to achieve higher thermoelectric performance. Yang et al. have proposed to dope SiNWs with isotope impurity randomly to reduce thermal conductivity of SiNWs [32]. In silicon isotopes, ^{28}Si is of the highest natural abundance (92 %), followed by ^{29}Si and ^{30}Si with 5 % and 3 %, respectively.

Figure 5.3 shows the effect of randomly distributed isotopic atoms on the thermal conductivity of ^{28}Si NWs. The curve of thermal conductivity decreases first to reach a minimum and then increases as the percentage of isotope impurity atoms increases. At a low isotopic percentage, a small ratio of impurity atoms can induce a large reduction in thermal conductivity. In contrast to the high sensitivity at the two ends, the thermal conductivity versus isotopic concentration curves are almost flat at the central part as shown in Fig. 5.3, where the value of thermal conductivity is only 77 % of that of isotopically pure ^{28}Si NW. The calculated thermal conductivity of SiNW with natural isotopic abundance, 5 % ^{29}Si and 3 % ^{30}Si is around 86 % of pure ^{28}Si NW, which is close to the experimental results of bulk Si. The similar effect of impurities on the thermal conductivity of SiNWs was also reported by using first-principles calculations [33].

The growth of isotopically controlled SiNWs by the vapor–liquid–solid mechanism has been performed successfully [34]. The growth is accomplished by using silane precursors $^{28}SiH_4$, $^{29}SiH_4$ and $^{30}SiH_4$ synthesized from SiF_4 isotopically

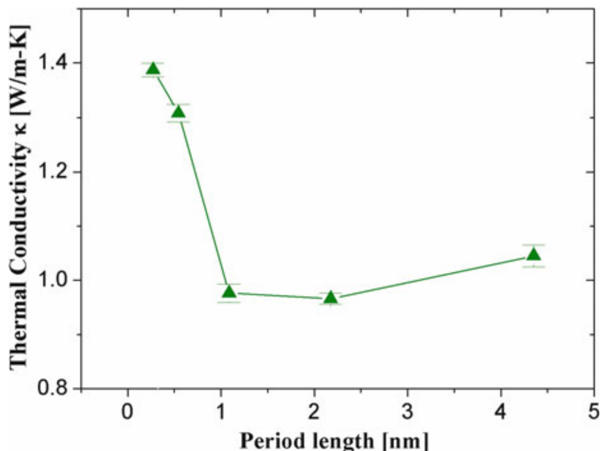

Fig. 5.4 Thermal conductivity of the superlattice SiNWs versus the period length at 300 K. Details of the chosen parameters can be found in [32]

enriched in a centrifugal setup. In addition, the effect of isotope doping on longitudinal optical phonon has also been investigated. The corresponding experimental measurement of thermal conductivity is currently on-going [34].

5.2.3 Interface and Surface Phonon Scattering

It has been shown [35, 36] that superlattice is an efficient structure to achieve ultra low thermal conductivity. However, for structures built from different crystalline materials, the relatively high interface energy will limit the stability of these structures. The isotopic-superlattice (IS) is a good example that the thermal conductivity can be reduced without destroying its stability. The thermal conductivity of IS structured NWs, which consist of alternating ^{28}Si/^{29}Si layers along the longitudinal direction, is shown in Fig. 5.4. As expected, the thermal conductivity decreases as the period length decreases, or the number of interface increases. The thermal conductivity reaches a minimum when the period length is 1.09 nm. This is consistent with the fact that increasing the number of interface for a fixed length will enhance the interface scattering, giving rise to the reduction of the thermal conductivity.

It is seen from Fig. 5.4 that when the period length is smaller than 1.09 nm, the thermal conductivity increases rapidly as the period length decreases. This anomalous increase in thermal conductivity can be understood from the phonon density of states (DOS) as shown in Fig. 5.5. When the period length is 2.17 nm, there is an obvious mismatch in the DOS spectra, both at the low frequency band and high frequency band, resulting in a very low thermal conductivity. On the contrary, the DOS spectra overlap perfectly for IS structured SiNW whose period length is 0.27 nm. The good match in the DOS comes from the collective vibrations of different mass layers, which are harder to be built in superlattice structures with a

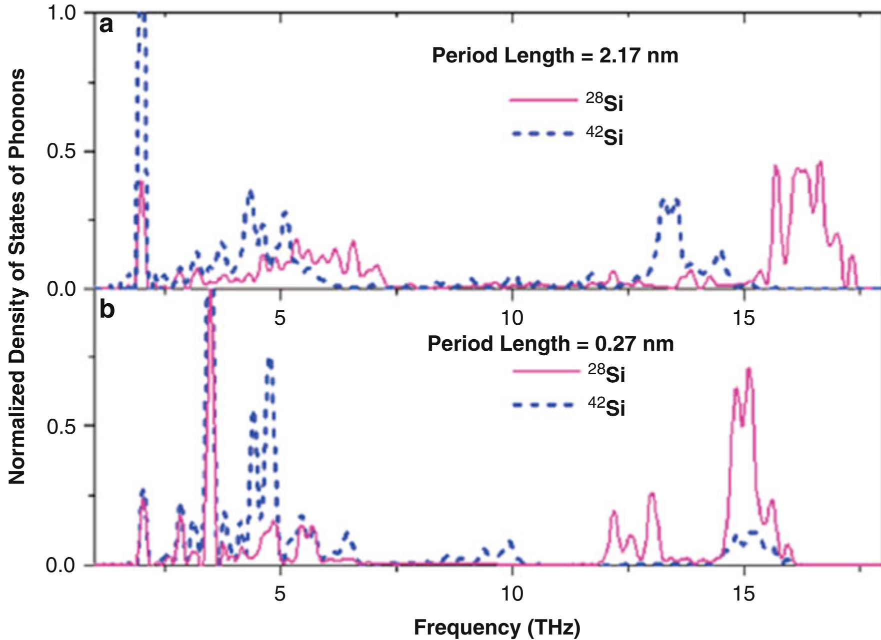

Fig. 5.5 Average normalized density of states of phonons of different mass atoms (^{28}Si or ^{42}Si) along the longitude direction for superlattice SiNW structures. (**a**) The period length of superlattice NW is 2.17 nm. This structure has a low conductivity of 0.42 W/m K. (**b**) The period length of superlattice NW is 0.27 nm. This structure has a high conductivity of 0.85 W/m K

larger period. The match/mismatch of the DOS spectra between the different mass layers controls the heat current. The similar phenomenon is also observed in Si/Ge superlattice structured nanowires [37].

In addition to the interface scatterings of phonon, thermal conductivity of NWs can be reduced further obviously by introducing more surface scattering, for example, by making hallow SiNWs with inner surface, i.e., silicon nanotubes (SiNTs) [38]. Figure 5.6 shows the room temperature thermal conductivity of SiNWs and SiNTs versus cross-sectional area. Even a very small hole, for example, a 1 % reduction in the cross-sectional area, can induce a reduction of thermal conductivity of 35 %. Moreover, with further increasing the hole size, a linear dependence of thermal conductivity on cross-sectional area is observed.

The reduction of thermal conductivity can be understood from the analysis of phonon participation ratio (p-ratio) (Fig. 5.7). The p-ratio measures the fraction of atoms participating in a given mode, and effectively indicates the localized modes with O(1/N) and delocalized modes with O(1). There is a reduction of p-ratio in SiNTs for both low and high frequency phonons, compared with SiNWs. Figure 5.7 shows the normalized energy distribution on the cross-sectional plane for SiNWs and SiNTs at 300 K. For those localized modes with p-ratio less than 0.2, it is clearly seen that the intensity of localized modes is almost zero in the center of the

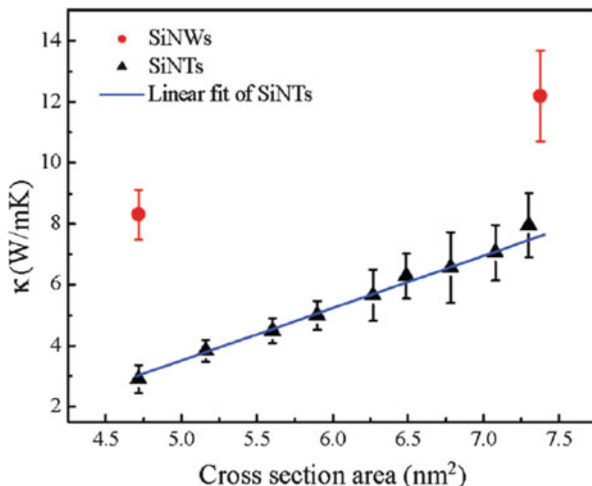

Fig. 5.6 Thermal conductivity of SiNWs and SiNTs versus cross-sectional area at 300 K. The *red dots* and *black triangles* denote SiNWs and SiNTs, respectively. The cross-sectional areas for these two SiNWs are 7.37 nm^2 and 4.72 nm^2, respectively. The *blue line* is drawn to guide the eyes

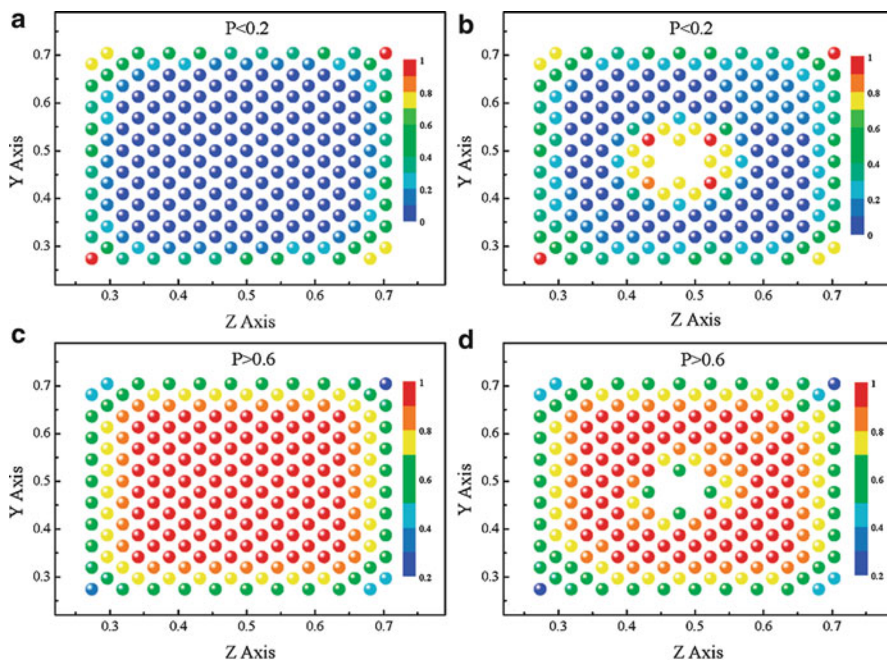

Fig. 5.7 Normalized energy distribution on the cross-sectional plane for SiNWs and SiNTs at 300 K. Intensity of the energy is depicted according to the color bar. (**a**) Energy distribution of SiNWs for modes with $P < 0.2$; (**b**) energy distribution of SiNTs for modes with $P < 0.2$; (**c**) energy distribution of SiNWs for modes with $P > 0.6$; (**d**) energy distribution of SiNTs for modes with $P > 0.6$

NW, while it has a finite value at the boundary. Due to the introduction of inner surface in SiNTs, energy localization also shows up around the hollow region. These results provide direct evidence that localization takes place on the surface region. For those delocalized modes with *p*-ratio greater than 0.6, the majority of energy is distributed inside SiNWs and SiNTs as shown in Fig. 5.7c, d, except for the hollow region in SiNTs. Therefore, from the spatial distribution of delocalized modes, we can conclude that energy is localized on the boundary (surface) region.

Since SiNTs are constructed from SiNWs, the density is approximately the same for these two structures. For SiNWs and SiNTs with the same cross-sectional area and same length, the total number of eigen modes is the same for SiNTs and SiNWs. Compared with SiNWs, SiNTs have a larger surface area, which corresponds to a higher SVR. As a result, there are more modes localized on the surface, which increases the percentage of the localized modes to the total number of modes. In heat transport, the contribution to thermal conductivity mainly comes from the delocalized modes rather than the localized modes. Due to the increased SVR in SiNTs, which induces more localized modes, the percentage of delocalized modes decreases, leading to a reduction of thermal conductivity in SiNTs compared with SiNWs.

5.3 Reduce Thermal Conductivity of Silicon Nanowires: Coherent Mechanism

Most of the above approaches to reduce thermal conductivity, such as introduction of rough surface and defect scatterings, are based mainly on incoherent mechanisms, which cause phonons to lose coherence. In the following, we discuss the phonon coherent resonance to tune thermal conductivity [39].

The coherence of phonons can be described by the heat current autocorrelation function (HCACF). Figure 5.8a shows the typical time dependence of normalized

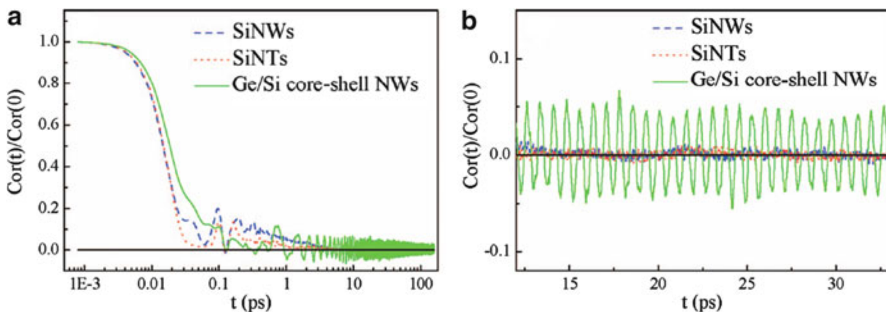

Fig. 5.8 Time dependence of normalized heat current autocorrelation function (HCACF). (**a**) Normalized HCACF for SiNWs (*dashed line*), SiNTs (*dotted line*), and Ge/Si core–shell NWs with Lc/L = 0.65 (*solid line*). (**b**) Long-time region of (**a**)

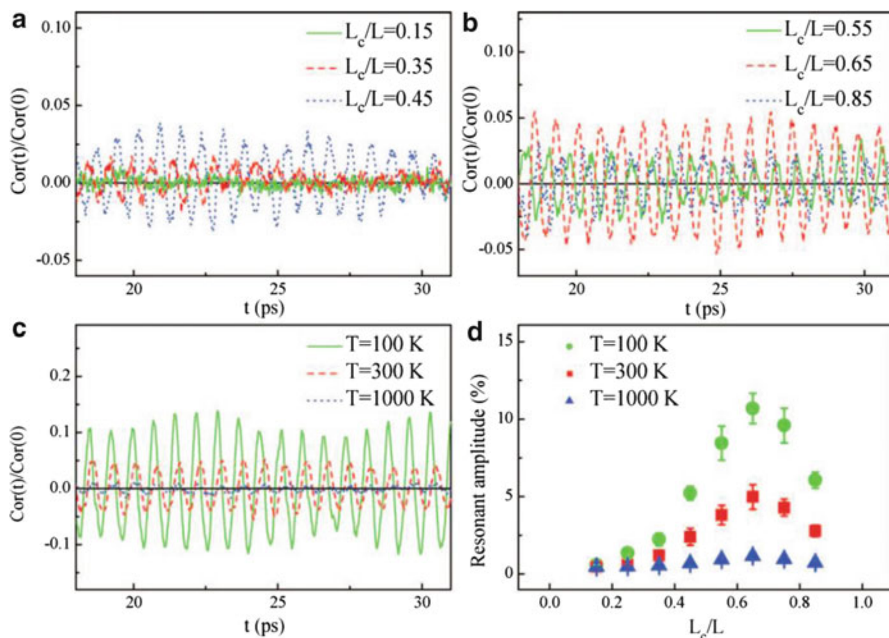

Fig. 5.9 Structure and temperature dependence of the oscillation effect in Ge/Si core–shell NWs. (**a**) Lc/L = 0.15, Lc/L = 0.35, and Lc/L = 0.45 at 300 K. (**b**) Lc/L = 0.55, Lc/L = 0.65, and Lc/L = 0.85 at 300 K. (**c**) Lc/L = 0.65 at 100, 300, and 1,000 K. (**d**) Oscillation amplitude versus core–shell ratio Lc/L at 100, 300, and 1,000 K

heat current autocorrelation function in Ge/Si core–shell NWs, SiNWs, and SiNTs. For both SiNWs and SiNTs, there is a very rapid decay of HCACF at the beginning, followed by a long-time tail with a much slower decay. However, a nontrivial oscillation up to a very long time appears in HCACF for core–shell NWs. The long-time region of HCACF reveals that this nontrivial oscillation is not random but rather periodic.

Figure 5.9 shows the long-time regime of normalized HCACF for Ge/Si core–shell NWs with different core–shell ratios at 300 K. When the core-size increases, the resonance effect becomes stronger, reaches its maximum, and then decreases. Obviously, this resonance effect in core–shell NWs is structure-dependent. Moreover, for a given core–shell structure, the oscillation amplitude is temperature-dependent and becomes larger at lower temperature. This nontrivial oscillation suggests that there exists a coherent mechanism in core–shell NWs, which can cause phonons to have the long-lasting correlation in such heterostructure.

Figure 5.10 shows the fast Fourier transform (FFT) of normalized HCACF for core–shell NWs. The FFT amplitude for Ge/Si core–shell NWs exhibits a dominant peak (f_0) and multiple high frequency resonant peaks with much smaller amplitude. The FFT spectrum of SiNWs and SiNTs looks completely different from that of Ge/Si core–shell NWs: there is no dominant peak over the entire frequency regime,

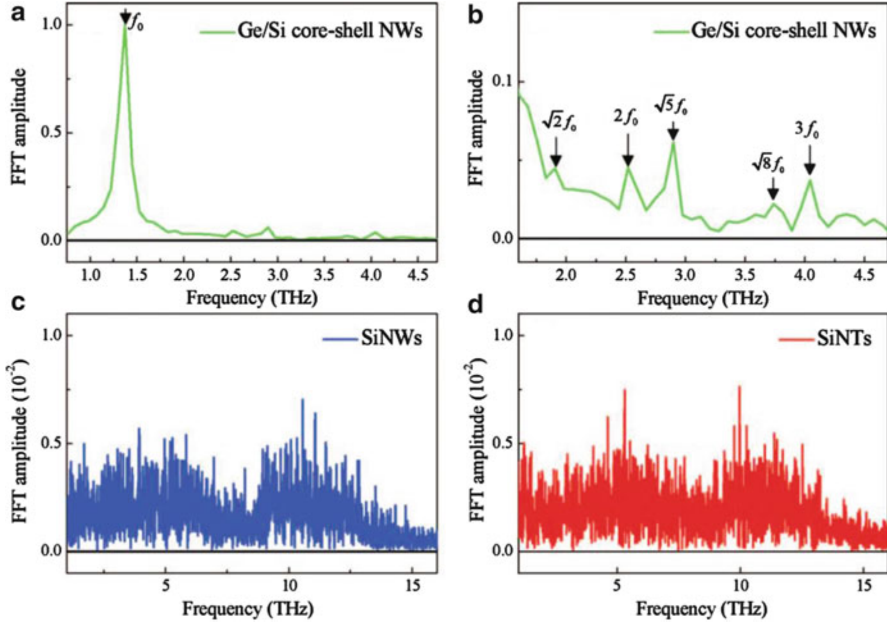

Fig. 5.10 Amplitude of the fast Fourier transform (FFT) of the long-time regime of normalized HCACF. (**a**) Ge/Si core–shell NWs. (**b**) The high frequency oscillation peaks for Ge/Si core–shell NWs. (**c**) and (**d**) show the amplitudes of the FFT of the long-time regime of normalized HCACF for SiNWs and SiNTs, respectively

and the FFT amplitude is more than 2 orders of magnitude smaller than the dominant peak amplitude for Ge/Si core–shell NWs. These two aspects are the typical characteristics of the noise spectrum.

These multiple resonant peaks observed in core–shell NWs are very similar to the frequency spectrum of the coherent resonance effect of the acoustic wave in a confined structure. For a wire with the square cross section and side length L, the eigen-frequency in such confined structure calculated from the elastic medium theory is given by:

$$f_{mn} = \frac{\omega_{mn}}{2\pi} = \frac{C}{2\pi}\sqrt{\left(\frac{m\pi}{L}\right)^2 + \left(\frac{n\pi}{L}\right)^2} = \sqrt{m^2 + n^2}f_0, \tag{5.2}$$

where f_{mn} is the eigen-frequency specified by two integer number m and n, C is the speed of sound, and $f_0 = C/2L$ is the lowest eigen-frequency. As shown in Fig. 5.10b, the theoretical prediction for the high frequency eigen-modes according to (5.2) agrees quite well with the resonant peaks calculated by the actual FFT of the oscillation signal. This good agreement of resonant frequency suggests that the nontrivial oscillation is caused by the phonon coherent resonance effect in the transverse direction.

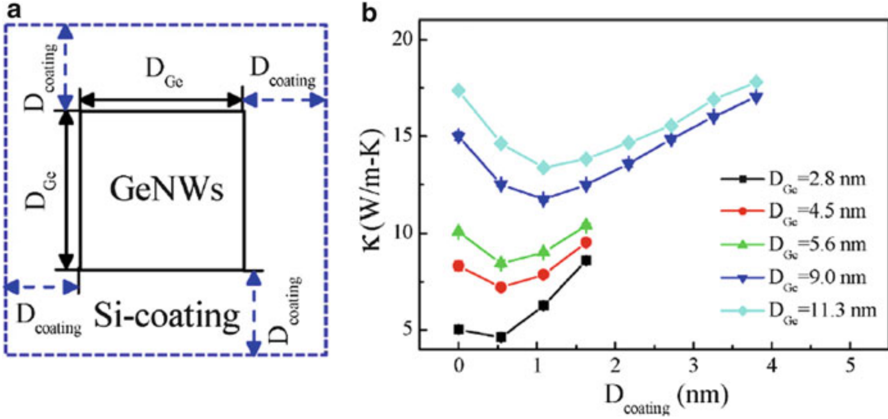

Fig. 5.11 Coating configuration and thermal conductivity. (**a**) Cross section of (100) GeNWs with Si-coating shell. (**b**) Thermal conductivity of GeNWs and Ge/Si core–shell NWs for different D_{Ge} at room temperature

In core–shell NWs, atoms on the same cross-sectional plane have different sound velocities in the longitudinal direction. As a result, atoms near the core–shell interface are stretched due to the different sound velocities. This induces a strong coupling of vibrational motions (modes) between the longitudinal and transverse directions. However, for SiNWs, this mode coupling is weakened because all Si atoms have the same sound velocity. This coupling picture explains that the coherent resonance effect in the transverse direction can indeed manifest itself in HCACF along the longitudinal direction in Ge/Si core–shell NWs, while the same effect is absent in SiNWs and NTs. As the resonance effect of acoustic wave is a coherent process that requires long-time correlation, the stronger anharmonic phonon–phonon scattering at high temperature causes phonon to lose coherence, and leads to the vanishing of the resonance effect at high temperature. When phonons transport along core–shell NWs, their energies are dispersed to the transverse direction due to the coherent resonance effect and mode coupling, which can significantly hinder the heat transport in the longitudinal direction. Therefore, the resonance effect can be used to tune the thermal conductivity.

Very recently, the direct connection between thermal conductivity reduction and coherent resonance was reported [40] in Ge/Si core–shell NWs. The configuration of Ge/Si core–shell NW is shown in Fig. 5.11a. The GeNW is with side length (diameter) denoted by D_{Ge}, and the coating thickness denoted by $D_{coating}$. As shown in Fig. 5.11b, it is obvious that for each GeNW, the coating of Si layers can reduce the thermal conductivity. Further coating leads to an increase of thermal conductivity. When the coating thickness is greater than certain critical value, thermal conductivity of the resultant Ge/Si core–shell NWs becomes larger than that of pristine GeNW without coating. Increasing coating thickness has two opposite effects on thermal conductivity. On the one hand, the creation of core–shell structures will induce the phonon resonance between the transverse and

longitudinal modes, thus offering a coherent mechanism to reduce thermal conductivity. On the other hand, the coating layers increase the entire cross-sectional area and thus the resultant core–shell NWs can contain more phonons contributing to thermal conductivity. Therefore, thermal conductivity of Ge/Si core–shell NWs is determined by these two competing effects. When the coating thickness is less than certain critical value, the suppression of the longitudinal phonon transport is the dominating factor, corresponding to the reduction of thermal conductivity. However, when the coating layer thickness increases further beyond the critical thickness, the phonon enhancement effect dominates the thermal transport, leading to an enhanced thermal conductivity compared to that of pristine GeNW.

The above finding shows that in practical applications, one can control thermal conductivity of NWs by coating with other materials. This approach offers a novel avenue and more flexibility for the design of nanostructures for thermal management. For instance, small diameter NWs are favorable for thermoelectric applications due to their low thermal conductivity, but it is more challenging to synthesize such NWs. Through coating, the low thermal conductivity feature close to a very thin NW can be obtained from a much thicker NW. For instance, thermal conductivity of pristine GeNWs with $D_{\mathrm{Ge}} = 9.0$ nm is close to that of coated GeNWs with $D_{\mathrm{Ge}} = 11.3$ nm and $D_{\mathrm{coating}} = 2.7$ nm. The resultant core–shell NW has a cross-sectional side length of 16.7 nm, which is almost twice of the cross-sectional side length for pristine GeNW with the similar thermal conductivity. As this coating thickness is achievable with atomic layer deposition technology, it offers a practical approach to tune thermal conductivity.

In practical conditions, the interface between the NW and its coating layer is not smooth at the atomistic scale. The interface roughness does not change the qualitative dependence of thermal conductivity on coating thickness, but it can further reduce the thermal conductivity of Ge/Si core–shell NW at a given coating thickness. Moreover, this additional reduction of thermal conductivity increases monotonically with increasing interface roughness.

Figure 5.12 compares the participation ratio (p-ratio) for each eigen-mode in pristine GeNWs, Ge/Si core–shell NWs with perfect interface, and Ge/Si core–shell NWs with rough interface. In the low frequency regime, there is a reduction of p-ratio in coated NW compared to pristine GeNWs. This phonon localization effect is caused by the resonance effect induced by coupling between the transverse and longitudinal phonon modes in core–shell nanostructures. As the strongest resonance peak is related to the eigen-mode with the lowest frequency in the transverse direction, the localization is remarkable for phonons with long wavelength (larger than the NW diameter). The polarization-resolved participation ratio for the longitudinal acoustic (LA) phonons near the Brillouin zone center is shown in Fig. 5.12b. The participation ratio in core–shell NWs shows an overall reduction for very low frequency LA phonons. More importantly, an obvious dip of the participation ratio is observed at around 0.5 THz, which is consistent with the resonance frequency found in FFT of HCACF along the longitudinal direction and thus provides strong evidence that phonon resonance in core–shell NWs leads to localization for low frequency phonons.

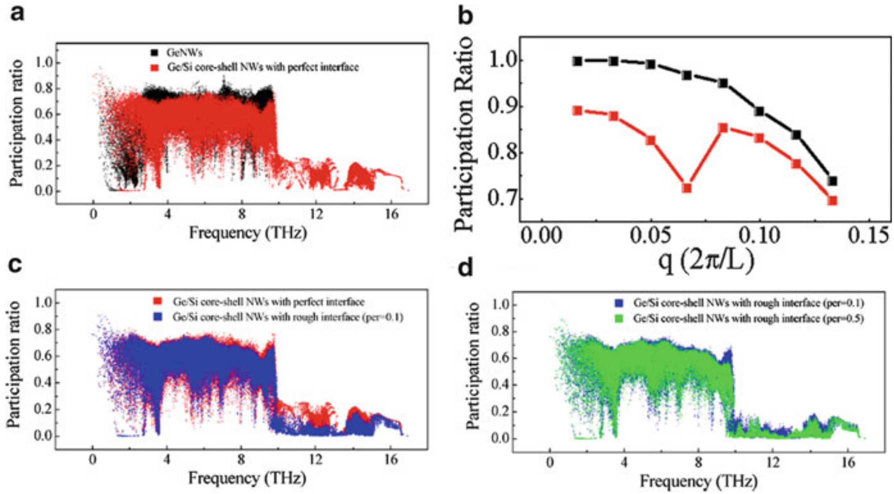

Fig. 5.12 (**a**) Participation ratio for different phonon modes in GeNWs before and after coating. (**b**) The polarization-resolved participation ratio for the LA phonon near the Brillouin zone center in GeNWs (*black*) and Ge/Si core–shell NWs with perfect interface (*red*). (**c** and **d**) Participation ratio for different phonon modes in core–shell NWs with perfect and rough interface, respectively

The p-ratio of the low-frequency phonons is almost unaffected by interface roughness. More interestingly, the additional reduction of p-ratio in the high frequency regime (>10 THz) is observed in core–shell NWs with rough interface (Fig. 5.12c, d), that is, the modes with the wavelength less than the NW diameter are localized by rough edges. Thus, core–shell induces localization for low frequency phonons (wavelength comparable to diameter), while interface roughness localizes the high frequency phonons (wavelength much less than diameter). Thus, the core–shell structure offers the unique opportunity to further reduce thermal conductivity of low thermal conductivity material even coated with high thermal conductivity material. This offers novel avenues and more flexibility for the design of nanostructures. Experimentally, the reduction in thermal conductivity in core–shell NWs has been verified [41].

5.4 Thermoelectric Property of Silicon Nanowires

5.4.1 Thermoelectric Figure of Merit of Silicon Nanowires

Predicting nanoscale effects on the thermoelectric properties of a specific system requires quantitative calculations of the system. Here we consider the diffusive regime, and σ, S, and κ_e are evaluated by only considering elastic scattering processes. The electrical conductivity σ, the electron thermal conductivity κ_e, and

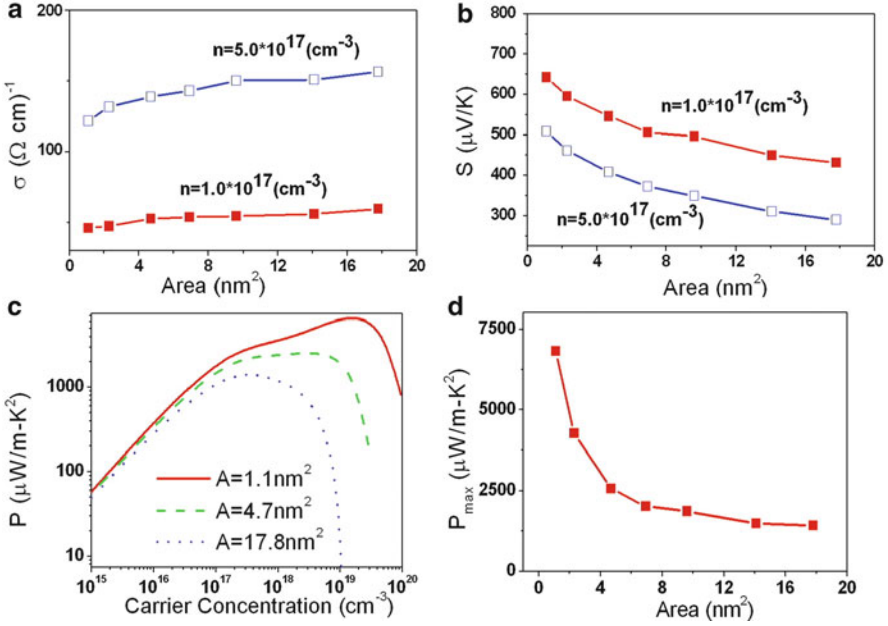

Fig. 5.13 (**a**) Electrical conductivity versus cross-sectional area with different carrier concentrations. (**b**) S versus cross-sectional area with different carrier concentrations. (**c**) Thermal power factor of SiNW versus carrier concentration with three different transverse dimensions. (**d**) Maximum power factor versus cross-sectional area

the Seebeck coefficient S, are obtained from the electronic structure with the solution of one-dimensional Boltzmann transport equation as [42]:

$$\begin{aligned} \sigma &= \Lambda^{(0)} \\ \kappa_{\mathrm{e}} &= \frac{1}{e^2 T}\left[\Lambda^{(2)} - \Lambda^{(1)}\left(\Lambda^{(0)}\right)^{-1}\Lambda^{(1)}\right] \\ S &= \frac{1}{eT}\left(\Lambda^{(0)}\right)^{-1}\Lambda^{(1)} \\ \Lambda^{(n)} &= e^2\tau\frac{2}{m^*}\sum_{E_{\mathrm{k}}}\Delta E\left[\frac{\beta\exp(\beta(E_{\mathrm{k}}-\mu))}{(1+\exp(\beta(E_{\mathrm{k}}-\mu)))^2}\right]D(E_{\mathrm{k}})E_{\mathrm{k}}(E_{\mathrm{k}}-\mu)^n \end{aligned} \tag{5.3}$$

Here e is the charge of carriers, T is the temperature, E_{k} is the electron energy, τ is the relaxation time, m^* is the effective mass of the charge carrier, μ is the electron chemical potential, and $D(E_{\mathrm{k}})$ is the density of states.

Figure 5.13a, b shows the size effects on σ and S with different electron concentrations. σ increases slightly as the diameter increases, while the Seebeck coefficient S decreases remarkably. The size dependence arises from the effect of

quantum confinement on the electronic band structure of SiNWs. The electron band gap converges quickly as the transverse dimension increases, and thus the electronic conductivity only has an obvious size dependence in very small size, and it depends on transverse size weakly when cross-sectional area is larger than 5 nm^2. In contrast to the weak size dependence of electronic conductivity, Seebeck coefficient S decreases with increasing the transverse size remarkably. Besides the electronic band gap, Seebeck coefficient S also depends on the detailed band structure, in which a narrow DOS distribution is preferred. In a bulk material, the continuous electron energy levels give rise to a wide distribution of carrier energies. However, the DOS of SiNW differs dramatically from that of bulk silicon. The large number of electronic states in narrow energy ranges can lead to a large S. With increasing the transverse dimension, the sharp DOS peaks widen, reducing S.

In thermoelectric application, the power factor P, which is defined as $P = S^2\sigma$, is an important factor influencing the thermoelectric performance directly. Figure 5.13c shows the power factor versus carrier concentration for SiNWs with different cross-sectional areas. Increasing carrier concentration has two effects on power factor. On the one hand, the increase of carrier concentration will increase the electrical conductivity. On the other hand, the increase of carrier concentration will suppress the Seebeck coefficient S. The power factor is determined by these two competing effects. Therefore, there exits an optimal carrier concentration, which yields the maximum attainable value of P_{max}. With increasing SiNW diameter (cross-sectional area), the maximum attainable power factor P_{max} decreases (as shown in Fig. 5.13d). Power factor is contributed by both Seebeck coefficient S and electrical conductivity σ. S decreases remarkably with increasing size, while σ increases slowly. So in power factor, the slow increase of σ is offset by obvious decrease in S ($P \sim S^2$), as a result, the power factor reduces with increasing size. When the area increases from about 1 to 18 nm^2, the maximum power factor decreases from about 6,800 to 1,400 μW/m K^2.

The power factor is directly related to the cooling power density (PD) of a thermoelectric cooler. In practical application, the cooling effect at the junction is opposed by Joule heating in the nanowire and by heat conducting from the hot end. The maximal cooling power density is given by [7]:

$$\mathrm{PD}_{max} = \frac{1}{2}\frac{S^2\sigma}{L}T^2, \tag{5.4}$$

where T is the environment temperature around the SiNW, and L is the length of the SiNW. If we consider SiNW with length of 1 μm, which is readily fabricated by current nanofabrication techniques, for thick SiNW with cross-sectional area of 17.8 nm^2, the maximal cooling power density, 6.4×10^3 W/cm^2, is about 6 times larger than that of an SiGeC/Si superlattice cooler, 10 times larger than that of an Si/Si_xGe_{1-x} thin film cooler, and 600 times larger than that of a commercial TE module [3–5].

For SiNWs with length in micrometer scale, the phonon thermal conductivity increases remarkably with increasing diameter until the diameter is larger than

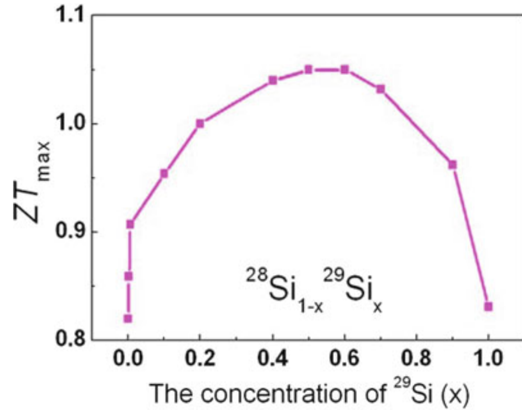

Fig. 5.14 Isotopic concentration-dependent thermoelectric figure of merit, ***ZT***, for SiNWs

about hundreds of nanometers [6, 28–31]. This reflects the fact that scattering at the surface introduces diffuse phonon relaxation in the transverse cross section. After the diameter reaches large values, the portion of phonons experiencing boundary scattering becomes much smaller, as a result, the thermal conductivity tends to be constant and is close to the value of bulk silicon. Combining the size dependence of the power factor as shown in Fig. 5.13d, we can conclude that *ZT* will decrease when the NW diameter increases. Thus, thin SiNWs are preferred for thermoelectric applications.

Isotopic impurities can also enhance the figure of merit. The dependence of thermoelectric figure of merit of SiNW on isotope concentration is shown in Fig. 5.14 [42]. *ZT* increases with ^{29}Si concentration, reaches a maximum and then decreases. This phenomenon is due to the isotope effect on lattice thermal conductivity. At a low isotopic percentage, a small ratio of isotope atoms can induce a large increase in ZT_{max}. For instance, in the case of $^{28}Si_{0.8}{}^{29}Si_{0.2}$ NW, namely, about 20 % ^{29}Si, its ZT_{max} increases with 15 % from that of pure ^{28}Si NW. And with 50 % ^{29}Si doping ($^{28}Si_{0.5}{}^{29}Si_{0.5}$ NW), the ZT_{max} can increase from 0.81 to 1.06. Thus, isotope doping is a promising method to further enhance *ZT* of nanoscale materials.

5.4.2 *Composite-Dependent Thermal Conductivity of SiGe Nanowires and Nanocrystals*

In addition to isotopic doped semiconductor, compound semiconductor is another possible structure that can lower thermal conductivity. Silicon germanium alloys have long been used in thermoelectric modules for deep-space missions to convert radioisotope heat into electricity. Silicon and germanium can form a continuous series of substitutional solid, $Si_{1-x}Ge_x$ over the entire compositional range of $0 \leq x \leq 1$. These semiconductor alloys offer a tunable system with a wide range of crystal lattices and band gaps, leading to fascinating electrical and optical

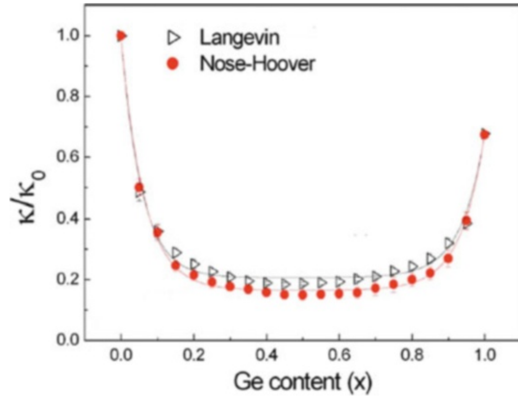

Fig. 5.15 The thermal conductivity versus Ge content x at 300 K. Here κ is the thermal conductivity of $Si_{1-x}Ge_x$ NWs, and κ_0 is the corresponding thermal conductivity of pure Si NW

properties. Recently, single crystalline $Si_{1-x}Ge_x$ NWs have been successfully grown and their electronic band gap modulation with composition has been reported [43]. These $Si_{1-x}Ge_x$ NWs provide intriguing opportunities for the development of novel nano devices.

Figure 5.15 shows the thermal conductivity κ of $Si_{1-x}Ge_x$ NWs versus Ge content at room temperature [37]. The lowest κ is 0.59 W/m K calculated with Langevin heat bath, which is 18 % of that of pure SiNW calculated with the same heat bath. At the two ends of the curves, the thermal conductivity shows a very sensitive dependence on x and follows an exponential decay, which is caused by the localization of high frequency phonons by the impurity. It is quite interesting that the thermal conductivity can be reduced by 50 % with only 5 % Ge atoms ($Si_{0.95}Ge_{0.05}$ NW).

From the calculated low thermal conductivity, it is shown in Fig. 5.16 that the maximal obtainable figure of merit can be increased by a factor of about 4–5 in $Si_{0.5}Ge_{0.5}$ NWs, compared with the corresponding values in pure SiNWs. Combining with the experimental measured ZT of n-type SiNW, which is about 0.6–1.0, it is most likely that we may obtain a high ZT value of about 2.4–4.0 in n-type $Si_{1-x}Ge_x$ NWs [44].

In addition to SiGe nanowires, it has been observed experimentally that when the Ge content in $Si_{1-x}Ge_x$ nanocomposites increases from 5 to 20 %, the thermal conductivity of both p-type SiGe alloy [45] and n-type SiGe alloy [46] decreases obviously. It is found that nano size interfaces are not as effective as point defects in scattering phonons with wavelengths shorter than 1 nm. Figure 5.17 shows that only a 5 at.% Ge replacing Si is very efficient in scattering phonons with wavelength shorter than 1 nm, giving rise to a further thermal conductivity reduction by a factor of 2.

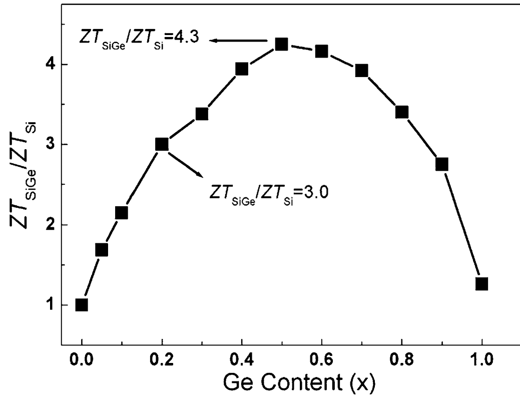

Fig. 5.16 $ZT_{Si_{1-x}Ge_x}/ZT_{Si}$ versus the Ge content x for n-type $Si_{1-x}Ge_x$ nanowires

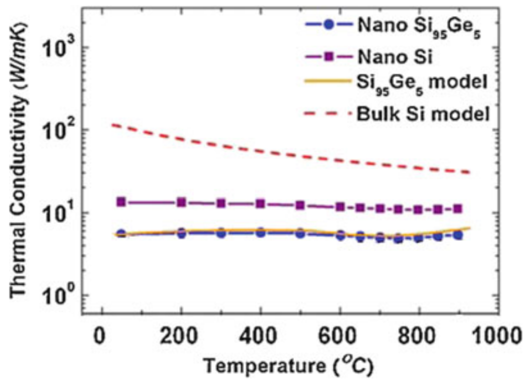

Fig. 5.17 Temperature dependent thermal conductivity of nanostructured Si (*filled squares*), nanostructured $Si_{95}Ge_5$ (*filled circles*) and bulk Si model

5.4.3 High Thermoelectric Figure of Merit in Silicon-Germanium Superlattice Structured Nanowires

Superlattice structured nanowires have recently attracted broad interest due to their fascinating applications in photonics, electronics, and phononics. The superlattice NWs are attractive especially in thermoelectric applications because the interface between two different materials can scatter the phonons strongly, thus reducing the thermal conductivity. Very recently, the thermoelectric property of p-type SiNWs with axial Ge heterostructures was calculated based on a combination of density-functional theory and interatomic potentials [47]. In addition, thermoelectric performance for both n-type and p-type SiGe superlattice NWs were also investigated on the same footing [48].

For the charge transport, a combination of the DFT and NEGF calculations has been used to obtain the electronic transmission. The electronic conductance can be written as [48]:

$$G = e^2 L^{(0)}(\mu) \tag{5.5}$$

The electronic contribution to thermal conductance is:

$$\lambda_e = \frac{1}{T}\left[L^{(2)}(\mu) - L^{(1)}(\mu)\left[L^{(0)}(\mu)\right]^{-1} L^{(1)}(\mu)\right] \tag{5.6}$$

And the Seebeck coefficient is:

$$S = \frac{1}{eT}\left[\left(L^{(0)}(\mu)\right)^{-1} L^{(1)}(\mu)\right] \tag{5.7}$$

with

$$L^{(m)}(\mu) = \frac{2}{h}\int_0^\infty \mathrm{d}E T_e(E)(E-\mu)^m\left(-\frac{\partial f}{\partial E}\right), \tag{5.8}$$

where e is the charge, μ is the chemical potential, h is the Planck constant, T is absolute temperature and E is the electron energy. $T_e(E)$ and $f(E)$ are the charge transmission coefficient and the Fermi–Dirac distribution, respectively.

The lattice thermal conductance is calculated in an analogous way to the electronic conductance, by segmenting the system into a “lead-conductor-lead” model. The phonon thermal conductance is:

$$\lambda_p = \frac{\hbar^2}{2\pi k_B T^2}\int_0^\infty \mathrm{d}\omega \omega^2 T_{ph}(\omega)\frac{e^{\frac{\hbar\omega}{k_B T}}}{\left(e^{\frac{\hbar\omega}{k_B T}} - 1\right)^2} \tag{5.9}$$

where ω is phonon frequency, $T_{ph}(\omega)$ is phonon transmission.

Figure 5.18a shows the P_{max} versus periodic length L for both p-type and n-type NWs. For n-type superlattice NWs, the P_{max} curves firstly increase, reach the maximum value at $L = 0.54$ nm, then decrease. The similar behaviors have been also found in p-type counterparts, but the value of P_{max} for p-type NWs is only about 40 % of that of n-type NWs. Moreover, P_{max} for pristine SiNWs is larger than that for superlattice NWs. The larger P_{max} achieved in SiNWs comes from the higher transmission compared with that in the superlattice NWs.

Figure 5.18b shows the maximum value of ZT (ZT_{max}) versus the periodic length L. The ZT_{max} curves firstly increase, reach the maximum value at the periodic length $L = 0.54$ nm and then decrease with the further increase of the periodic length. The achievable ZT_{max} for n-type NWs is about twice of its p-type counterparts.

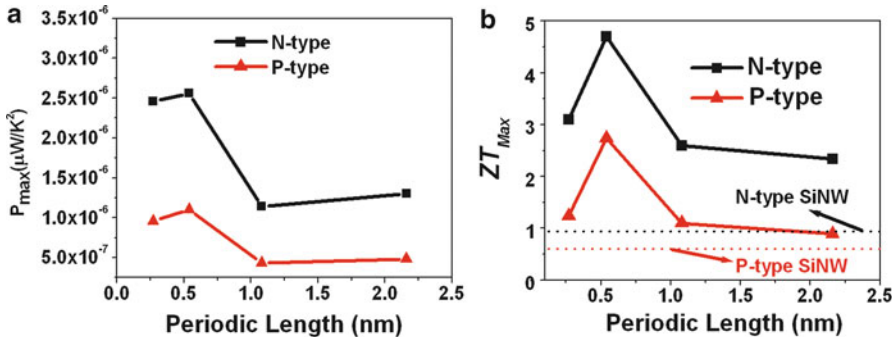

Fig. 5.18 (**a**) P_{max} versus periodic length for p-type and n-type $Si_{0.5}Ge_{0.5}$ superlattice NWs. (**b**) Dependence of ZT_{max} on periodic length for p-type and n-type $Si_{0.5}Ge_{0.5}$ superlattice NWs. The *dotted lines* in (**b**) are for the p-type and n-type pristine SiNWs

Moreover, the values of ZT_{max} for the superlattice NWs are much larger than those of pristine SiNWs because of their ultralow thermal conductance. The maximum value of ZT_{max} for n-type NWs is 4.7 at the period length $L = 0.54$ nm, which is fivefold increase as compared to the equivalent pristine SiNWs ($ZT_{max} = 0.94$); and the maximum value of ZT_{max} for p-type NWs is 2.74 with the same periodic length, which is 4.6 times larger than that of p-type SiNWs ($ZT_{max} = 0.6$) [48].

5.4.4 Defect Effect on Thermal Conductivity and Thermoelectric Property of NWs

Nanostructures such as nanowires often consist of both natural and artificial defects. These defects can lead to the localization of acoustic modes in their vicinity, causing additional scattering to the phonon transport, and a change of the thermal conductance deviating from the ballistic phonon transport. By using the scattering-matrix method, Chen et al. studied the low temperature thermal conductance in nanowire [49]. It was found that the behavior of the thermal conductance versus temperature is qualitatively different for different types of defects. When the defect is void, the universal quantum thermal conductance and the decrease of thermal conductance at low temperature can be clearly observed. However, when the structural defect consists of clamped material, the quantized thermal conductance cannot be observed, and the thermal conductance increases monotonically with increasing temperature.

Based on atomistic simulations of electron and phonon transport, Markussen et al. [50] found that the presence of an alkyl molecule or a nanowire branch can lead to a reduction of both the thermal conductivity $\delta\kappa$ and the electronic

conductivity $\delta\sigma$. At room temperature, the ratio $\delta\kappa/\delta\sigma > 50$ for the alky functionalized SiNWs and $\delta\kappa/\delta\sigma > 20$ for a nanotree. By engineering the SiNW surfaces, it is possible to reduce the phonon thermal conductivity while keeping the electronic conductivity almost unaffected. Thus, the surface-decorated SiNWs are promising candidates for nanoscale thermoelectric applications. Moreover, surface passivation with nitrogen can also reduce the thermal conductivity of nanowires [51].

5.5 Conclusions and Outlook

In this chapter, we have presented the state-of-the-art of thermoelectric properties and related fundamental phonon transport theories of nanowires. Clearly, the study of thermal property of nanowires is an emerging new research topic, which is potentially important for many thermoelectric and thermal management applications, such as waste heat energy harvesting and on-chip cooling. Note that although we mainly focus on SiNWs in this article, the physics discussed here is not limited to this system.

In particular, we have surveyed and discussed various physical mechanisms that are exploited to modify thermal conductivity of nanowires: namely, incoherent and coherent mechanisms. We have firstly reviewed the recent theories and experiments focusing on thermal conductivity of nanowires. Then, we have provided an overview of various effects on thermal conductivity of nanowires, including size effect, roughness effect, isotopically doped impurity, surface and interface phonon scattering. Then coherent phonon resonance in core–shell nanowires and its impact on reduction in thermal conductivity have also been discussed. Finally, we have summarized direct atomistic simulations used to predict the thermoelectric property of nanowires.

Currently, although we have much better understanding on thermal conductivity and thermoelectric property in nanoscale materials, clearly, there are still many open questions and challenges deserving further experimental and theoretical studies.

Experimentally, the primary challenge is how to measure and ultimately get rid of the thermal contact resistances. Currently, a technique called noncontact electron beam heating method was introduced to measure the thermal contact resistance between multilayer graphene and substrate [52]. Theoretically, a comprehensive transport theory for nano-composites is still lacking. In particular, a theory which includes the important long range effect of the Coulomb interaction and other important effects are highly desirable [53–58]. Furthermore, a theoretical model for interfacial thermal resistance arising from incorporating the anomalous thermal conduction is still lacking. Therefore, it is necessary to establish an improved theory to describe thermal transport in practical thermoelectric devices, including interface and complex long range interactions. More experimental and theoretical studies on these fundamental issues are necessary to further advance this fascinating field.

Acknowledgements We are grateful to Baowen Li, Nuo Yang, Jie Chen, Xiaoxi Ni, Lihong Shi, Donglai Yao, ChenXi Yu, Xiuqiang Li, Wanli Ma, Qing Shi, Haishuo Zhang for fruitful collaborations in different stages of this project. This work has been supported by grants from National Natural Science Foundation of China (Grant No. 11274011), the Ministry of Education of China (Grant No. 20110001120133), the Ministry of Science and Technology of China (Grant No. 2011CB933001).

References

1. World Outlook 2004: Paris: IEA, 2004-10-26, ISBN 92-64-1081-73, 13 June 2006
2. EPA Report on Sever and Data Center Energy Efficiency, 22 Sept 2009
3. DiSalvo, F.J.: Science **285**, 703 (1999)
4. Zebarjadi, M., Esfarjani, K., Dresselhaus, M.S., Ren, Z.F., Chen, G.: Energy Environ. Sci. **5**, 5147 (2012)
5. Vineis, C.J., Shakouri, A., Majumdar, A., Kanatzidis, M.G.: Adv. Mater. **22**, 3970 (2010)
6. Li, D., Wu, Y., Kim, P., Shi, L., Yang, P., Majumdar, A.: Appl. Phys. Lett. **83**, 2934 (2003)
7. Zhang, G., Zhang, Q., Bui, C.-T., Lo, G.-Q., Li, B.: Appl. Phys. Lett. **94**, 213108 (2009)
8. Zhang, G., Zhang, Q.-X., Kavitha, D., Lo, G.-Q.: Appl. Phys. Lett. **95**, 243104 (2009)
9. Rowe, D.M. (ed.):Thermoelectrics Handbook: Macro to Nano. Taylor & Francis, London (2006)
10. Hochbaum, A.I., Chen, R., Delgado, R.D., et al.: Nature **451**, 163 (2008)
11. Boukai, A.I., Bunimovich, Y., Kheli, J.T., et al.: Nature **451**, 168 (2008)
12. Dubi, Y., Di Ventra, M.: Rev. Mod. Phys. **83**, 131 (2011)
13. Li, N., Ren, J., Wang, L., Zhang, G., Hänggi, P., Li, B.: Rev. Mod. Phys. **84**, 1045 (2012)
14. Zhang, G., Li, B.: NanoScale **2**, 1058 (2010)
15. Pop, E.: Nano Res. **3**, 147 (2010)
16. Liu, S., Xu, X., Xie, R., Zhang, G., Li, B.: Eur. Phys. J. B **85**, 337 (2012)
17. Balandin, A.A.: Nat. Mater. **10**, 569 (2011)
18. Nika, D.L., Balandin, A.A.: J. Phys. Condens. Matter **24**, 233203 (2012)
19. Mohammad Sadeghi, M., Thompson Pettes, M., Shi, L.: Solid State Commun. **152**, 1321 (2012)
20. Cahill, D.G., Ford, W.K., Goodson, K.E., Mahan, G.D., Majumder, A., Maris, H.J., Merlin, R., Phillpot, S.R.: J. Appl. Phys. **93**, 793 (2003)
21. Yang, N., Xu, X., Zhang, G., Li, B.: AIP Adv. **2**, 041410 (2012)
22. Xia, Y., Yang, P., et al.: Adv. Mater. **15**, 353 (2003)
23. Cui, Y., Wei, Q., Park, H., Lieber, C.M.: Science **293**, 1289 (2001)
24. Zhang, G.-J., Zhang, G., Chua, H.J., Chee, R.-E., Wong, E.H., Agarwal, A., Buddharaju, K.D., Singh, N., Gao, Z., Balasubramanian, N.: Nano Lett. **8**, 1066 (2008)
25. Xiang, J., Lu, W., Hu, Y., Wu, Y., Yan, H., Lieber, C.M.: Nature **441**, 489 (2006)
26. Hu, L., Chen, G.: Nano Lett. **7**, 3249 (2007)
27. Donadio, D., Galli, G.: Phys. Rev. Lett. **102**, 195901 (2009)
28. Volz, S.G., Chen, G.: Appl. Phys. Lett. **75**, 2056 (1999)
29. Volz, S.G., Chen, G.: Phys. Rev. B **61**, 2651 (2000)
30. Chen, J., Zhang, G., Li, B.: J. Chem. Phys. **135**, 204705 (2011)
31. Liang, L.H., Li, B.: Phys. Rev. B **73**, 153303 (2006)
32. Yang, N., Zhang, G., Li, B.: Nano Lett. **8**, 276 (2008)
33. Gibbons, T.M., Estreicher, S.K.: Phys. Rev. Lett. **102**, 255502 (2009)
34. Moutanabbir, O., Senz, S., Zhang, Z., Gösele, U.: Nano Today **4**, 393 (2009)
35. Yu, X.Y., Chen, G., Verma, A., Smith, J.S.: Appl. Phys. Lett. **67**, 3554 (1995)

36. Huxtable, S.T., Abramson, A.R., Tien, C.-L., Majumdar, A., et al.: Appl. Phys. Lett. **80**, 1737 (2002)
37. Chen, J., Zhang, G., Li, B.: Appl. Phys. Lett. **95**, 073117 (2009)
38. Chen, J., Zhang, G., Li, B.: Nano Lett. **10**, 3978 (2010)
39. Chen, J., Zhang, G., Li, B.: J. Chem. Phys. **135**, 104508 (2011)
40. Chen, J., Zhang, G., Li, B.: Nano Lett. **12**, 2826 (2012)
41. Wingert, M.C., Chen, Z.C.Y., Dechaumphai, E., Moon, J., Kim, J.-H., Xiang, J., Chen, R.: Nano Lett. **11**, 5507 (2011)
42. Shi, L., Yao, D., Zhang, G., Li, B.: Appl. Phys. Lett. **95**, 063102 (2009)
43. Yang, J.-E., Jin, C.-B., Kim, C.-J., Jo, M.-H.: Appl. Phys. Lett. **6**, 2679 (2006)
44. Shi, L., Yao, D., Zhang, G., Li, B.: Appl. Phys. Lett. **96**, 173108 (2010)
45. Joshi, G., Lee, H., Lan, Y., et al.: Nano Lett. **8**, 4670 (2008)
46. Zhu, G.H., Lee, H., Lan, Y.C., et al.: Phys. Rev. Lett. **102**, 196803 (2009)
47. Shelley, M., Mostofi, A.A.: EPL **94**, 67001 (2011)
48. Shi, L., Jiang, J., Zhang, G., Li, B.: Appl. Phys. Lett. **101**, 233114 (2012)
49. Chen, K.-Q., Li, W.-X., Duan, W., Shuai, Z., Gu, B.-L.: Phys. Rev. B **72**, 045422 (2005)
50. Markussen, T., Jauho, A.-P., Brandbyge, M.: Phys. Rev. Lett. **103**, 055502 (2009)
51. Li, H.P., De Sarkar, A., Zhang Jr., R.Q.: EPL **96**, 56007 (2011)
52. Wang, Z., Xie, R., Bui, C.T., Liu, D., Ni, X., Li, B., Thong, J.T.L.: Nano Lett. **11**, 113 (2011)
53. Beloborodov, I.S., Lopatin, A.V., Vinokur, V.M., Efetov, K.B.: Rev. Mod. Phys. **79**, 469 (2007)
54. Glatz, A., Beloborodov, I.S.: Phys. Rev. B **79**, 041404R (2009)
55. Glatz, A., Beloborodov, I.S.: Phys. Rev. B **79**, 235403 (2009)
56. Glatz, A., Beloborodov, I.S.: Phys. Rev. B **80**, 245440 (2009)
57. Markussen, T.: Nano Lett. **12**, 4698 (2012)
58. Tian, Y., Sakr, M.R., Kinder, J.M., Liang, D., MacDonald, M.J., Richard, L., Qiu, J., Gao, H.-J., Gao, X.P.A.: Nano Lett. **12**, 6492 (2012)

Chapter 6
Thermoelectric Efficiency of Nanowires with Long Range Surface Disorder

Gursoy B. Akguc

Abstract Thermoelectric efficiency of nanowires is shown to be enhanced when they have disordered surfaces with long range correlations. To show this effect, one needs to solve Schrödinger equation in a surface disordered waveguide geometry as a model for nanowires and employ the resulting transmission to analyze nanowires as feasible heat engines. Using the linear response theory in determining the efficiency of the possible heat engine device based on silicon nanowires is although useful to point out the overall behavior with respect to the continuous incident electron energy, it says nothing about its performance as a heat engine. A nonlinear response theory is proved to be necessary to find out the specific energies at which the nanowire has greater efficiency at max power as a thermoelectric device. The efficiency at the maximum power shows that some nanowires with specific surface disorder structure is more appropriate to use as a heat engine than the others. The possibility of engineering the transmission of electrons in the nanowires to increase their efficiency maybe an answer to the demand of highly efficient thermoelectric semiconductor materials in future.

6.1 Introduction

The model system we use for a long nanowire having a rough surface as a heat engine is illustrated in Fig. 6.1 as a scattering system. Although our approach is pretty general, we will be using silicon nanowires as our model thermoelectric device. A hot electron reservoir with temperature T_h and Fermi–Dirac distribution

G.B. Akguc (✉)
Department of Physics, Bilkent University, 06800 Ankara, Turkey
e-mail: akguc@physics.utexas.edu

X. Wang and Z.M. Wang (eds.), *Nanoscale Thermoelectrics*, Lecture Notes in Nanoscale Science and Technology 16, DOI 10.1007/978-3-319-02012-9_6,
© Springer International Publishing Switzerland 2014

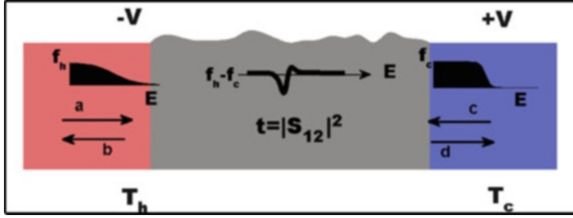

Fig. 6.1 The model of the quantum wire with hot (*red*) and cold (*blue*) reservoirs. The potential bias, + V and − V, and the temperatures of cold, (T_c) and hot, (T_h) reservoirs are indicated. The Fermi–Dirac distribution function of hot (f_h) and cold (f_c) electrons on the corresponding reservoirs and their difference ($f_h - f_c$) on the nanowire with respect to energy, E, are illustrated for a typical case. The incident and the outgoing waves of the electrons illustrated by *arrows* labeled as a, b and c, d used to form the scattering matrix, S, where $| S_{12} |^2$ element of the scattering matrix yields transmission

of electron density f_h is connected through a scattering region to a cold electron reservoir with its own temperature T_c and distribution function f_c. Fermi–Dirac distribution function is given in general,

$$f_{c/h} = \left[1 + \exp\left(\frac{E - \mu_{c/h}}{k_B T_{c/h}}\right)\right]^{-1} \tag{6.1}$$

where $\mu_{c/h}$ is the chemical potential of either cold or hot electrons, respectively. We plot a typical Fermi–Dirac distribution function for hot and cold electrons on the reservoirs, and their difference is shown in the scattering region. We apply a negative potential bias between the hot and the cold ends of the nanowire, and it set symmetrically as $-V$ and $+V$ as depicted in Fig. 6.1. Therefore, we have a symmetrical chemical potential $\mu_{c/h} = \mu \pm V$ while the average μ can be adjusted according to the incident electron energy by using a back gate potential. When there is no electron temperature difference, the electrons flow in the direction of potential (from right to left in Fig. 6.1). In the same way, if no bias applied, then there is a net flow of the electrons from the hot electron to the cold electron reservoir (from left to right in Fig. 6.1) because of the difference in the occupation number density on both sides. Finally, if both temperature difference and a potential bias applied, then there can be a net electron flow to the one of either directions, and the result can be described as the heat engine or the refrigerator regime. When the hot electron moves against to the potential difference (from left to right in Fig. 6.1) hence makes work, it is the heat engine regime, and when the reverse is true (from right to left in Fig. 6.1) the system works as refrigerator, namely a potential difference supplied to the system to make it colder. In this work, we are interested in the heat engine regime.

The silicon nanowires with rough surfaces are shown to perform about 100 times better compared to their bulk form as thermoelectric materials [1, 2]. Electrons in the constricted geometries such as nanowires do not obey the Wiedemann–Franz

rule which states that the electron conductance is proportional to the electron thermal conductance; however, it is generally valid for bulk materials. Consequently, the thermoelectric efficiency described partly as the ratio of these two conductances can be improved better. Furthermore, the significance of the surface randomness is shown to be prominent in both of the experimental and the theoretical studies. Moreover, long range correlations on the surface randomness can be used to engineer the electron transmission spectrum of silicon nanowires [3]. Likewise, the random surface scattering is important in the manipulation of the phonon scattering, and consequently the control of heat conduction, [4, 5]. Accordingly, there are several studies reporting the increase of the overall thermoelectric efficiency in silicon wires [6, 7] and graphene ribbons [8].

The transport of electrons under a thermal gradient can be utilized to convert the heat energy to the electrical energy, i.e. working as a heat engine [9–11], or by supplying the electrical energy to cool the electrons, i.e. as a cooler [12, 13]. The efficiency of a heat engine depends on the electron transmission through the structure and the chemical potential of the electron reservoirs. It is possible to achieve the theoretically maximum efficiency, i.e., the Carnot efficiency, $\eta = 1 - T_C/T_H$ where T_H and T_C are the hot and the cold reservoir temperatures, respectively, at the opening of a new channel in a nanowire [14]. It has been shown that the maximum thermoelectric efficiency can be obtained by adjusting the chemical potential with respect to the incident energy such a way that the transport of electrons without leading to any entropy change [15, 16]. Anyhow, the problem with the heat engine working under adiabatic condition is that it only describes a system with zero power output, hence it does not have practical value. The thermoelectric efficiency therefore needs to be redefined for the finite time process [17–19]. One possible way to do this is to define the efficiency at the maximum power [20, 21]. The efficiency of a heat engine is shown universally approach to $\eta = 1 - \sqrt{T_C/T_H}$ also known as Curzon–Ahlborn limit [17, 22]. In this context, it is interesting to see how efficient to use nanowires as a heat engine depending on the electron transmission spectra.

We model a silicon nanowire with a rough surface as a scattering problem connecting two electron reservoirs at different temperatures. We solve this scattering problem using the reaction matrix method and calculate all the transport coefficients and the efficiency using the Landauer–Buttiker formulation [23–25] of the linear response theory for this system [26]. The efficiency obtained in this way will not give any information about the feasibility of working condition of the wire as a heat engine. A more explicit description involves the calculation of the power generated in the system when it is connected to an external load. We can achieve this using a nonlinear thermodynamic approach [27]. We obtained the efficiency and the power which are both function of the incident electron energy and the applied bias this way. The efficiency at the maximum power is discussed for this system at different regions of operation depending on the transmission of the electrons. Previously, a comparison of the dimensionality has been made for the quantum dots, the perfect quantum wires, and the thermionic materials using

nonlinear thermodynamic methods [27, 28]. Here, we examine the quantum wire case when the electronic transmission can be modulated by adding long range correlation to the surface roughness [3, 5]. We compare two transmission profiles, one being a single window reduced transmission and the other is double window of the reduced transmission in their respective spectrum. It is customary to define figure of merit ZT as dimensionless parameter proportional to the efficiency. We find that the double window transmission has up to ZT $=3$ efficiency peaks away from the threshold energy of the nanowire. In general, the surface engineered nanowires show thermoelectric efficiency larger than ZT $=2$. We compare the linear response efficiency and the efficiency at the maximum power using nonlinear methods. We discuss in general how the transmission profile effects the efficiency and the details of the calculation of the nonlinear thermodynamic result including the effect of nonlinear temperature differences.

The transmission probability of the electrons, t, in the scattering region is crucial to define the device characteristics. We find the scattering matrix for electrons from the nanowire and extract the transmission probability, $t = |S_{12}|^2$, from it. The S-matrix connects the amplitudes of the incoming plane waves a, c to the outgoing ones, b, d, as $(b, d)^T = S(a, c)^T$ where we use transpose of arrays. We use the reaction matrix approach [29] to find S matrix. We give some details of this method next.

6.2 Scattering in Rough Waveguides

We will start with describing a formalism to obtain scattering matrix, hence conductance for a quite general system as sketched in Fig. 6.2. It consists of a flat wave guide of width w that supports N open modes (or channels) with a rather

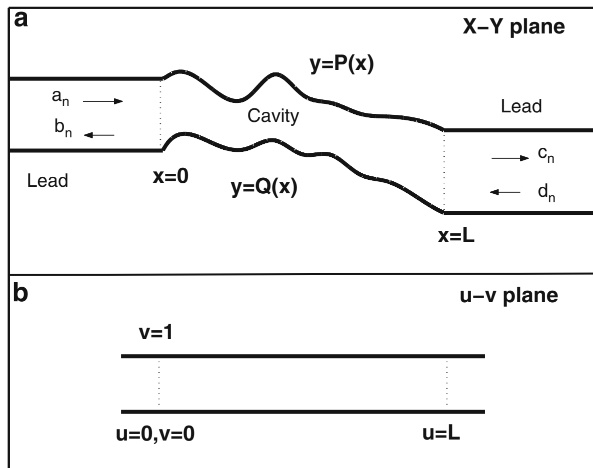

Fig. 6.2 (**a**) An open billiard of length L. (**b**) the scattering cavity is transformed to a rectangular region in u–v plane

general scattering region of length L. The specific method we develop requires two leads (openings are in principle also possible) at opposing ends of a scattering region. We shall arbitrarily fix them to be on the right and on the left, as in the figure. The scattering region between the leads or openings shall be described by two single-valued functions of a coordinate say x defined between the two leads. No additional scatterers in the so defined cavity are allowed. We will assume that the leads have equal width. The latter is not essential for the method but simplifies notation. The scattering problem will be defined in terms of a $2N \times 2N$ scattering matrix S. Having nano structures in mind we can rewrite the S-matrix as

$$S = \begin{pmatrix} r & t' \\ t & r' \end{pmatrix}, \tag{6.2}$$

where r (r') and t (t') are the reflection and transmission matrices for incidence on the left (right) of the scattering region. The dimensionless conductance is obtained from S as

$$T = \mathrm{tr}(\mathrm{tt}^{\dagger}). \tag{6.3}$$

Our calculations will be based on the traditional R-matrix approach [30, 31]. This formalism has been adapted to obtain the S matrix for a wave guide in previous works [32–34]. Until now only a restricted choices of scattering regions have been investigated. For example only one of the walls was taken of sinusoidal shape while the other one was kept flat (ripple billiard). We want to generalize this approach to a generic open two-lead cavity without obstacles, where one can choose any unique differentiable function of $P(x)$ and $Q(x)$ in Fig. 6.2a to represent the upper and lower walls of the scattering cavity.

We wish to remind the reader that the R-matrix approach relates the S-matrix to a matrix R determined by boundary conditions relating internal and external functions at the edges, where the leads are connected to the scattering region, such that

$$\psi|_{\Gamma} = R\nabla\psi|_{\Gamma} \tag{6.4}$$

at $x = \Gamma$ as in of the boundaries represented as dotted lines in Fig. 6.2. R-matrix can be generalized for number of lead connection and number of modes in the leads. R-matrix can be related to S-matrix,

$$S = \frac{1 - ikR}{1 + ikR} \tag{6.5}$$

Rather than recalling the details of R-matrix theory we will evoke the spirit of the method by presenting a trivial one-dimensional example:

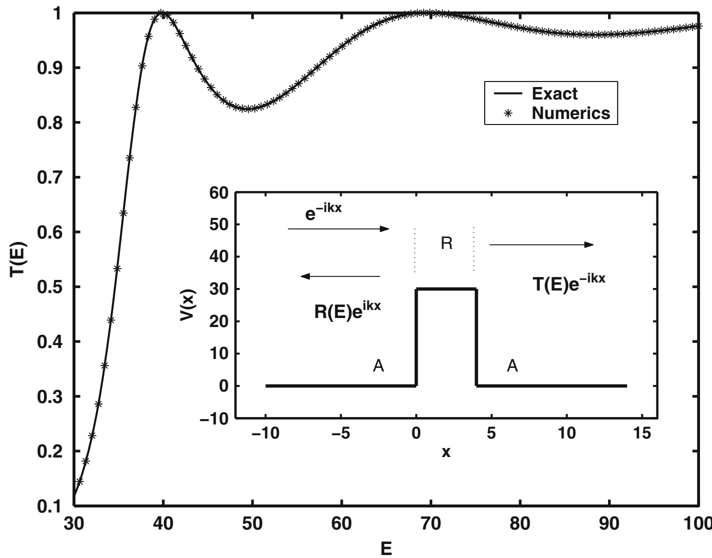

Fig. 6.3 Scattering from a 1D barrier. The *solid line* shows the transmission probability as a function of energy and *stars* are the numerical calculations. In the *inset* the geometry of the scattering system is shown. *I* indicates the interaction region, *A* the asymptotic regions

In Fig. 6.3 we show the 1D example we want to solve using *R*-matrix method. In this example we have two asymptotes as in the general case we discuss but the *r* and *t* are functions instead of a matrices as in the 1 mode case for the real cavity problems. The exact *S*-matrix can be found in this case and the transmission probability is given by

$$T_{\text{exact}}(E) = \frac{1}{\left(1 + \left(\frac{V_0^2}{(E(E-V_0))(2\sin(k))^2}\right)\right)} \tag{6.6}$$

for a constant potential step of height V_0 and length 1.

Numerically we use a basis for the Reaction region, (R in Fig. 6.3), which is given by $cos(m\,\pi\,x)$, $m = 0, 1, \ldots \infty$. $x_l = 0$ and $x_r = 1$ have been chosen. Using this basis, the *R*-matrix elements are given by,

$$R_{rr} = \frac{1}{E - V_0} + \sum_{m=1}^{\infty} \frac{2}{E - m^2\pi^2 - V_0} = R_{ll}$$

$$R_{rl} = \frac{1}{E - V_0} + \sum_{m=1}^{\infty} \frac{2\cos(m\pi)}{E - m^2\pi^2 - V_0} = R_{lr}. \tag{6.7}$$

This series should be truncated at some finite value for a numerical calculation; $m = 1,000$ is used in Fig. 6.3. The S matrix is obtained from R matrix as

$$S = \begin{pmatrix} 1 & 0 \\ 0 & e^{-ik} \end{pmatrix} \frac{\begin{pmatrix} 1 & 0 \\ 0 & 1 \end{pmatrix} - ik \begin{pmatrix} R_{rr} & R_{rl} \\ R_{lr} & R_{ll} \end{pmatrix}}{\begin{pmatrix} 1 & 0 \\ 0 & 1 \end{pmatrix} + ik \begin{pmatrix} R_{rr} & R_{rl} \\ R_{lr} & R_{ll} \end{pmatrix}} \begin{pmatrix} 1 & 0 \\ 0 & e^{-ik} \end{pmatrix} \tag{6.8}$$

Using this S matrix we plot the transmission probability, $|S_{1,2}|^2$ in Fig. 6.3. We note that generalizing the potential in this example to any shape can be done by using a finite difference method [35].

The method to obtain the S-Matrix thus proceeds in two steps: First obtain the solution of the boundary value problem inside the scattering region with Neumann and Dirichlet boundary conditions at lead connections and cavity walls, respectively. Second connect the known solution in the asymptotic region(leads) to the one obtained for the scattering region by imposing continuity of the solution. In the numerical method we present, the most time consuming part will be to obtain a complete set of function to expand the scattering wave function inside the cavity region, which is a prerequisite to the first step.

6.3 An Efficient Method for the Scattering Problem

We shall thus start by presenting a very efficient method to deal with the problem inside the scattering region. This method can also be applied to closed cavities, as we will point out further down. As we will use transformed coordinates the second step will not be entirely trivial and will be presented once we have the internal solutions.

6.3.1 Cavity Region

We want to solve the Schrödinger equation in the cavity with specific boundary conditions, namely Neumann conditions at the open boundaries, and Dirichlet conditions at the walls of the billiard. In other words, the derivative of the wave function is set to be zero at the dotted line in Fig. 6.2 and the wave function itself is set to zero at surface of the billiard. Thus we have the equation

$$H|\Psi(x,y)>= -\frac{\hbar^2}{2m}(\nabla_x^2 + \nabla_y^2)\Psi(x,y) = E_n\Psi(x,y), \tag{6.9}$$

with the boundary conditions $\nabla_x \Psi(x,y)|_{x=0} = 0$, $\nabla_x \Psi(x,y)|_{x=L} = 0$, $\Psi(x,y)|_{y=P(x)} = 0$ and $\Psi(x,y)|_{y=Q(x)} = 0$. The eigenvalues and eigenvectors of this equation are used to represent the scattering dynamics inside the cavity.

The solution of the Schrödinger equation in the coordinates x, y is complicated due to the arbitrary shape of the boundaries so we use the following transformation to new coordinates u, v.

$$
\begin{aligned}
u &= x \\
v &= \frac{y - Q(x)}{P(x) - Q(x)}
\end{aligned}
\tag{6.10}
$$

This change of variable transforms the complicated boundary to a simple one, i.e. a rectangular region. The price we pay is that the form of the Schrodinger equation becomes more complicated. The Hamiltonian operator in the u–v plane can be obtained by using the above transformation and complete derivatives. The final result is

$$
\begin{aligned}
H = \nabla_u^2 &+ \left(\frac{1 + (Q_u + vJ_u)^2}{J^2}\right)\nabla_v^2 - 2\left(\frac{Q_u + vJ_u}{J}\right)\nabla_{u,v} \\
&- \left(\frac{Q_{u,u} + vJ_{u,u}}{J}\right)\nabla_v + 2\left(\frac{(Q_u + vJ_u)J_u}{J^2}\right)\nabla_v
\end{aligned}
\tag{6.11}
$$

where J is defined as $J = P - Q$ and subscripts indicate partial derivatives. In this form the symmetric nature of Hamiltonian is not obvious. Therefore we will represent the same equation in the following matrix form [36],

$$
H = \frac{1}{J}\left(\nabla_\alpha J g^{\alpha,\beta} \nabla_\beta\right) \alpha = u, v \;\; \beta = u, v
\tag{6.12}
$$

where g is a metric and equivalent to,

$$
g \equiv \begin{pmatrix} 1 & \dfrac{-(Q_u + vJ_u)}{J} \\ \dfrac{-(Q_u + vJ_u)}{J} & \dfrac{1 + (Q_u + vJ_u)^2}{J^2} \end{pmatrix}
\tag{6.13}
$$

The meaning of J becomes clear when we notice it is related to the determinant of the metric. It plays the role of Jacobian of the transformation from the x–y to the u–v plane. The wave function in the u–v plane can be expanded in terms of a basis

$$\Psi_k(u,v) = \sum_{n,m} B^k_{n,m}\psi_{n,m} \\ = \sum_{n,m} B^k_{n,m}\frac{1}{\sqrt{J}}\frac{2}{\sqrt{L}}\cos\left(\frac{m\pi u}{L}\right)\sin(n\pi v) \tag{6.14}$$

which satisfies the boundary conditions at $u = 0, u = L$ and $v = 0, v = 1$ automatically. To determine the unknown coefficients $B_{n,\ m}{}^k$ we will use the orthonormality condition. In the original coordinates plane waves are orthonormal; in terms of u,v they must be orthonormal with a weight function given by the metric

$$< \Psi|\Psi > \equiv \int\int dudvJ\Psi_k(u,v)\Psi_{k'}(u,v) = \delta_{k,k'} \tag{6.15}$$

After multiplying the eigenvalue equation with another eigenfunction and integrating we obtain the matrix equation,

$$\sum_l \sum_{l'} H_{ll'}B^k_{l'} = B^k_l \tag{6.16}$$

where we use new indices such that $(n,\ m) \to l$ and $(n',\ m') \to l'$. Eigenvalues E_k correspond to energy and eigenvectors contain the unknown coefficients $B_l{}^k$ of the wave function. Using the matrix form of H we have

$$\int\int dudvJ\psi_l\frac{1}{J}\nabla_\alpha Jg^{\alpha\beta}\nabla_\beta\psi_{l'} = E_k\delta_{l,l'}. \tag{6.17}$$

we can integrate by parts. The surface terms are zero due to the boundary condition we have chosen. We thus find

$$-\int \nabla_\alpha\psi_l Jg^{\alpha\beta}\nabla_\beta\psi_{l'} = E_k\delta_{l,l'}. \tag{6.18}$$

Since the metric is symmetric, the matrix obtained from this equation is real symmetric and positive definite which guarantees positive energy eigenvalues.

Once the eigenvalue equation is solved one can obtain scattering wave function for any energy within the range of wave length we allow. This makes the method efficient compared to direct integration of the differential equation by some mesh-based methods like finite element [33]. The cutoff on the number of basis states determines the accuracy and range of validity of the method. In practice it is necessary to decide how many modes to choose in u and v direction. A corresponding integrable geometry gives an idea about these numbers. Also one needs to choose only the lower part of the eigenvalue spectrum in the bound region to ensure that truncation wont bring errors due to poor solutions of the bounded problem. For example, $m = 90$, $n = 50$ and using the first 3,000 eigenvalues of the 4,500 $\times$ 4,500 matrix is suitable for a rectangular region with length

twice its width. The limit of the highest wavelength that can be attained in leads is connected to the lead size to the scattering size. If the size of the scattering region is much bigger than the size of the leads, then the method is limited to only couple of modes in leads due to the cutoff on the number of eigenvalues that has to be done in cavity region. For a nanowire this is not the case since leads size is same with scattering region. Note also that due to the large number of modes used in the scattering direction, the Fourier transform techniques developed in [29] are especially helpful.

6.3.2 Leads and Scattering Matrix

With the knowledge of states in the cavity region it is possible to couple known asymptotic, such as leads to the cavity. The corresponding solution on the left and on the right leads to

$$\Psi_L^n = \left(\frac{a_n}{\sqrt{k_n}} e^{ik_n x} - \frac{b_n}{\sqrt{k_n}} e^{-ik_n x}\right) \sin\left(\frac{n\pi y}{w}\right)$$
$$\Psi_R^n = \left(\frac{c_n}{\sqrt{k_n}} e^{-ik_n x} - \frac{d_n}{\sqrt{k_n}} e^{ik_n x}\right) \sin\left(\frac{n\pi y}{w}\right) \tag{6.19}$$

where w is the lead width, a_n, b_n, c_n and, d_n are scattering amplitudes and the wave vector is given by

$$k_n = \sqrt{\left(\frac{n\pi}{w}\right)^2 - \frac{2mE}{\hbar^2}}. \tag{6.20}$$

we here assume propagating modes but it is possible to add evanescent modes with complex k vectors to the calculation. Their effect is discussed in [34].

As shown in [32–34] the energy eigenfunctions $|E>$ of the total scattering system have contributions from both cavity and leads.

$$< x, y|E >= \sum_{j=1}^{\infty} \gamma_j \phi_j(x, y) + \sum_{n=1}^{\infty} \left(\Gamma_n^L \Psi_L^n + \Gamma_n^R \Psi_R^n\right) \tag{6.21}$$

where ϕ_j are basis states calculated for the cavity alone.

The continuity of scattering wave functions at the lead boundary gives the connection between the leads and the cavity region:

$$\Psi_n^\alpha = \sum_{n'=1}^{\infty} R_{\alpha L}(n, n') \nabla_x \Psi_n^\alpha|_{x_L}$$
$$- \sum_{n'=1}^{\infty} R_{\alpha R}(n, n') \nabla_x \Psi_n^\alpha|_{x_R} \tag{6.22}$$

where

$$R_{\alpha\beta}(n,n') = \frac{\hbar^2}{2m} \sum_{j=1}^{\infty} \frac{\phi_{j,n}(x_\alpha)\phi_{j,n'}(x_\beta)}{E - \gamma_j} \tag{6.23}$$

is the (n, n')th matrix element of the R matrix. Here $\phi_{j,\,n}$ is the overlap between cavity states and lead functions and given by

$$\phi_{j,n}(x_\alpha) = \sqrt{\frac{2}{L}} \int_0^{\infty} dy \phi_j(x_\alpha) \sin\left(\frac{n\pi y}{w}\right) \tag{6.24}$$

where $\alpha \equiv L$, R and $x_L = 0$, $X_R = L$ in Fig. 6.3.

6.4 Waveguides with Colored Surface Disorder

We treat quantum wires as a long 2D waveguide as illustrated in Fig. 6.4b. The scattering coordinate is denoted x and the transverse coordinate is denoted y. The width of the waveguide is denoted w and the length is denoted L. In all the calculations $L = 100w$ and w is set to be unity. That is, we scale all length by the waveguide width. The upper and lower boundaries of the waveguide are described by $y = P(x)$ and $y = Q(x)$. The case in Fig. 6.4b represents a situation

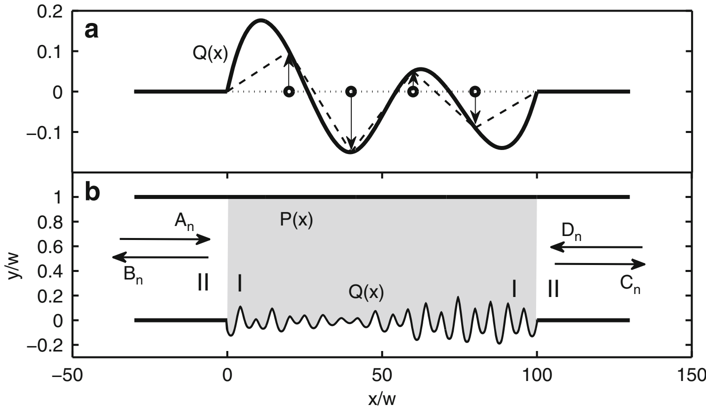

Fig. 6.4 Schematic plot of a 2D rough waveguide that models rough quantum wires. (**a**) The generation of a rough surface is illustrated using $M = 4$ random shifts in the transverse direction. (**b**) One waveguide geometry with a straight upper boundary $y = P(x) = 1$ and a rough lower boundary $y = Q(x)$. Scattering occurs in region I (*gray area*) and region II denotes the left and right leads. *Arrows* indicate the direction of incoming and outgoing electron waves. A_n, B_n, C_n, and D_n are quantum amplitudes

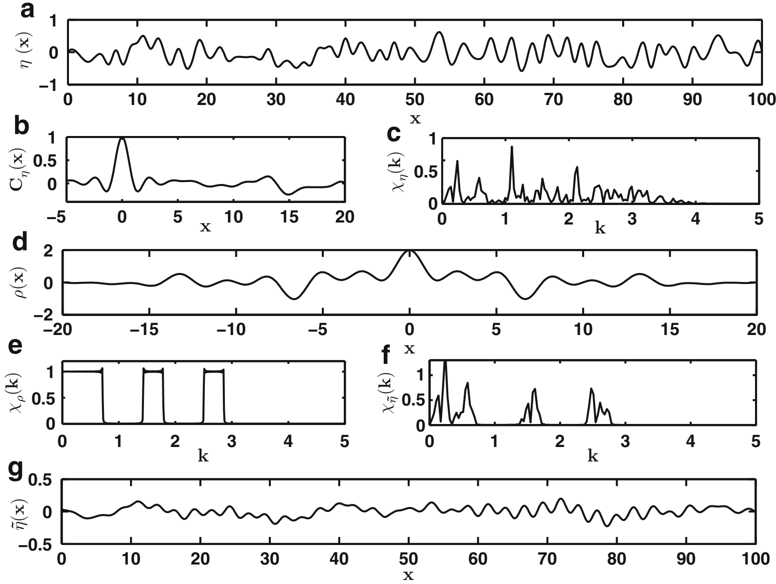

Fig. 6.5 (**a**) One realization of the surface roughness function $\eta(x)$, with the method described in detail in the text. (**b**) The associated autocorrelation function $C_\eta(x)$. (**c**) Surface structure factor $\chi_\eta(k)$ obtained from the $C_\eta(x)$ shown in panel (**b**). (**d**) A function $\rho(x)$ that will be used to introduce additional correlations via convolution. (**e**) The Fourier transform of the $\rho(x)$ shown in panel (**d**). (**f**) The structure factor $\chi_{\tilde{\eta}}(k)$ obtained from a convolution between $\rho(x)$ and $\eta(x)$. (**g**) The new surface roughness function $\tilde{\eta}(x)$, with correlations that are absent in $\eta(x)$

where the upper boundary is a straight line ($P(x) = 1$) and the lower boundary is rough. As in our other studies of rough waveguides [29, 37], we form a rough waveguide boundary in three steps. First, we divide a rectangular waveguide into M pieces of equal length L/M. Second, the end of each piece is shifted in y randomly, with the random y-displacement, denoted η, satisfying a Gaussian distribution. Third, we use spline interpolation to combine those sharp edges to generate a smooth curve $\eta(x)$ for either the upper or the lower waveguide boundary. For the sake of clarity, Fig. 6.4a depicts this procedure with the number of random shifts being as small as $M = 4$. In all our calculations below we set $M = 100$. In Fig. 6.5a we show one realization of the surface roughness function $\eta(x)$.

The function $\eta(x)$ may be characterized by its ensemble-averaged mean $\overline{\eta}$ and its self-correlation function $C_\eta(x - x')$, i.e.,

$$\overline{\eta} = \langle \eta(x) \rangle = 0,$$
$$\langle \eta(x)\eta(x') \rangle = \sigma^2 C_\eta(x - x'), \tag{6.25}$$

where σ is the variance of $\eta(x)$. In the limit of white noise roughness, $C_\eta(x - x')$ is proportional to $\delta(x - x')$. But more typically, $C_\eta(x - x')$ decays at a characteristic

length scale, called the correlation radius R_c. For our case here, because the randomness is introduced after dividing the waveguide into $M = 100$ pieces, the correlation length R_c of the $\eta(x)$ we construct here is of the order of $L/M \sim w$. This length scale is comparable to the wavelength of the scattering electrons in the one-mode regime.

One tends to characterize the strength of the surface roughness by the variance σ defined above. However, in practice it is better to use the maximal absolute value of $\eta(x)$, denoted $|\eta_{\max}|$, to characterize the roughness strength. This is because for strong roughness with a given variance, there is a possibility that some of the random displacements become too large such that the waveguide may be completely blocked. Recognizing this issue, we first set a value of $|\eta_{\max}|$ and then, after having generated a roughness function $\eta(x)$ based on spline interpolation, rescale $\eta(x)$ such that its maximal absolute value is given by $|\eta_{\max}|$.

The roughness function $\eta(x)$ obtained above does not have any peculiar features. There are a number of ways to introduce some structure to the correlation function $C_\eta(x - x')$. In [38] a filtering function method was proposed to produce a power-law decay of $C_\eta(x - x')$ from white noise. Here we adopt the approach used in [39, 40], which is based on the convolution theorem of Fourier transformations. In particular, the discrete form of autocorrelation function of $\eta(x)$ is defined as

$$C_\eta\left(\frac{mL}{N}\right) = c\sum_{n=1}^{N-m-1}\eta\left(\frac{(n+m)L}{N}\right)\eta\left(\frac{nL}{N}\right) \tag{6.26}$$

where $m = -N+1, \cdots, -1, 0, 1, \cdots, N-1$ and c is a normalization constant such that $C_\eta(0) = 1$. In Fig. 6.5b we show the autocorrelation function for the surface roughness function depicted in Fig. 6.5a. The autocorrelation drops from its peak value to near zero at a scale of $R_c \sim 0.7w$.

As will be made clear in what follows, it is important to consider the Fourier transform of $C_\eta(x)$, i.e., the autocorrelation function in the Fourier space. This important quantity is denoted $\chi_\eta(k)$, where k is the wavevector conjugate to x. Using the Fast Fourier transform of $C_\eta(x)$, $\chi_\eta(k)$ can be evaluated as follows:

$$\chi_\eta(k) = \sum_{j=1}^{2N} C_\eta\left(\frac{jL}{2N}\right)\exp\left[\frac{-i2\pi(j-1)(m-1)}{2N}\right], \tag{6.27}$$

where $k = (2(m/2N) - 1)(2\pi N/2L)$. In our calculations we choose $N = 1,024$. Note that $\chi_\eta(k)$ is a real function due to the evenness of $C_\eta(x)$. The real function $\chi_\eta(k)$ is called below the structure factor of the surface roughness. Figure 6.5c shows the structure factor $\chi_\eta(k)$ obtained from the correlation function shown in Fig. 6.5b.

Additional correlations in the surface disorder can now be generated by modulating the structure factor $\chi_\eta(k)$. Because the structure factor $\chi_\eta(k)$ is equivalent to the square of the Fourier transform of $\eta(x)$, we may imprint interesting structures

onto $\chi_\eta(k)$ by convoluting $\eta(x)$ with some filtering function. Consider then the function $\rho'(x) = \sin(ax)/ax$ with $a > 0$. Its Fourier transform is a step function of $|k|$ [39, 40], with a height π/a and the step edge located at $|k| = a$. The Fourier transform (denoted $\chi_\rho(k)$) of a combination of such functions, i.e.,

$$\rho(x) = \sum_n A_n \frac{\sin(|a_n^r|x) - \sin(|a_n^l|x)}{|a_n^r|x}. \tag{6.28}$$

will be π/A_n if $a_n^r > |k| > a_n^l$ or $a_n^r < |k| < a_n^l$; and zero otherwise. If we now consider the following roughness function,

$$\tilde{\eta}\left(\frac{mL}{N}\right) = \sum_n \rho\left(\frac{nL}{N}\right)\eta\left(\frac{(m-n)L}{N}\right), \tag{6.29}$$

then according to the convolution theorem, we have

$$|\chi_{\tilde{\eta}}(k)|^{1/2} \sim |\chi_\rho(k)||\chi_\eta(k)|^{1/2}, \tag{6.30}$$

where $\chi_{\tilde{\eta}}(k)$ is the structure factor for the new surface roughness function $\tilde{\eta}(x)$. As such, the structure of $\chi_\rho(k)$ is directly imprinted on $\chi_{\tilde{\eta}}(k)$. That is, computationally speaking, arbitrary modulation can be imposed on the structure factor by filtering out the unwanted components and magnifying other desired structure components. Below we apply this simple technique to create different kinds of surface roughness correlation windows and then examine the conductance properties. In Fig. 6.5d we show one example of $\rho(x)$. Its Fourier transform amplitude, as shown in Fig. 6.5e, displays two windows. As shown in Fig. 6.5f, this double-window structure is passed to $\chi_{\tilde{\eta}}(k)$ due to (6.30). Finally, in Fig. 6.5g we show the surface roughness function $\tilde{\eta}(x)$, which obviously contains more correlations than the old surface roughness function $\eta(x)$ shown in Fig. 6.5a.

With the mapping between the scattering problem in 2D waveguide and 1D Anderson's model [41, 42], early theoretical work [39–41] established that the localization length L_{loc} of the 2D waveguide problem is given by

$$L_{\text{loc}}^{-1} = \frac{\sigma^2\pi^4}{w^6}\frac{\chi(2k)}{(2k)^2}, \tag{6.31}$$

where $\chi(2k)$ is either the structure factor $\chi_\eta(2k)$ or the new structure factor $\chi_{\tilde{\eta}}(2k)$ after a convolution procedure. If $L_{\text{loc}} > L$, a transmitting state is expected and if $L_{\text{loc}} << L$, then the electron can only make an exponentially small contribution to the conductance. As such, one expects transmitting states when the structure factor $\chi(2k)$ is essentially zero; and negligible conductance if $\chi(2k)$ is significant and if σ is not too small. This suggests that the conductance properties can be manipulated by realizing different surface roughness functions. Equation (6.31) is obtained under

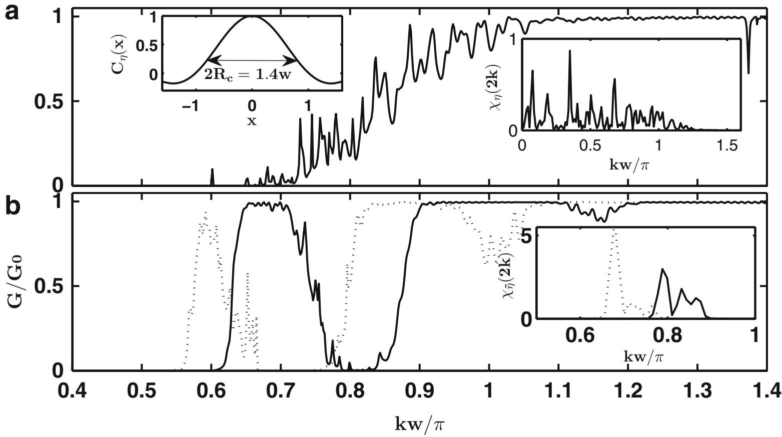

Fig. 6.6 (**a**) Conductance of rough waveguides versus $k = k_1$ (see (6.9)). The upper boundary is flat, i.e., $P(x) = 1$, and the lower boundary is given by $Q(x) = \eta(x)$, with a surface disorder strength characterized by $\sigma = 0.0779w$ or $|\eta_{\max}| = 0.2w$. *Inset* on the right shows the structure factor of the surface roughness in one single realization. (**b**) Same as in panel (**a**), but two cases with different surface structure factor obtained from a convolution approach are plotted, using *solid* and *dashed lines*. All conductance curves here are averaged over three realizations

a weak electron scattering approximation (Born approximation). As such, the theoretical result of (6.31) may not be valid if σ is not small as compared with w or if the scattering electron is close to the threshold value of channel opening. Another assumption in the theory is that L_{loc} should be much greater than R_c, the radius of the surface correlation function $C_\eta(x)$.

However, in our computational studies we will examine some interesting cases that are evidently beyond the validity regime of the theory. For example, the strength of the surface disorder may not be small and the scattering energy may be placed in the vicinity of a shifted channel opening energy.

In Fig. 6.6a we show conductance results averaged over three realizations of a rough waveguide, with a flat upper boundary $P(x) = 1$ and a rough lower boundary $Q(x) = \eta(x)$. The strength of the surface disorder is given by $\sigma = 0.0779w$, which is chosen based on a pre-set value of $|\eta_{\max}| = 0.2w$. As is clear from Fig. 6.6a, there exists a threshold $k \sim 0.6\pi/w$ beyond which the system becomes transmitting (this threshold will be explained below). In the transmission regime the conductance shows a systematic trend of increase as the wavevector k increases. The inset of Fig. 6.6a shows $\chi_\eta(2k)$, one key term in (6.31). The characteristic magnitude of $\chi_\eta(2k)$ for the shown regime of k is ~0.3. Using (6.31), one obtains that the localization length L_{loc} is comparable to $L = 100w$. This prediction is hence consistent with our computational results that demonstrate considerable transmission.

Next we exploit the convolution technique described above to form new rough surfaces described by $\tilde{\eta}(x)$. In particular, the inset of Fig. 6.6b shows two sample

cases with distinctively different surface structure factors. In one case (dotted line) $\chi_{\tilde{\eta}}(2k)$ has significant values in the interval $0.67 < kw/\pi < 0.8$. Indeed, during that regime the value of $\chi_{\tilde{\eta}}(2k)$ is many times larger than the mean value of $\chi_{\eta}(2k)$ in the case of Fig. 6.6a. In the other case (solid line) $\chi_{\tilde{\eta}}(2k)$ is large only in the regime of $0.75 < kw/\pi < 0.9$. For these regimes, the theory predicts that the localization length to be much smaller than the waveguide length and hence vanishing conductance. This is indeed what we observe in our computational study. As shown in Fig. 6.6b, either the dotted or the solid conductance curve displays a sharp dip in a regime that matches the main profile of $\chi_{\tilde{\eta}}(2k)$.

In addition, similar to what is observed in Fig. 6.6a, b also displays a transmission threshold. Take the dotted line in Fig. 6.6b as an example. For $kw/\pi < 0.55$, there is no transmission at all, even though $\chi_{\tilde{\eta}}(2k)$ in that regime is essentially zero. This suggests that this threshold behavior is unrelated to surface roughness details. Rather, it can be considered as a non-perturbative result that is not captured by (6.31). To qualitatively explain the observed threshold, we realize that due to the relatively strong surface roughness, the effective width of the waveguide decreases and as a result, the effective mode opening energy increases. For $|\eta_{\max}| = 0.2w$, we estimate that the effective width of the waveguide is given by $w_{\text{eff}} = w - |\eta_{\max}| = 0.8w$. Hence, the corrected mode opening energy E is now given by $(\hbar^2/2m^*)(\pi/0.8w)^2$. Using (6.20), this estimate gives that, regardless of the surface roughness details, the threshold k value for transmission is $\sim 0.75\pi/w$, which is close to what is observed in Fig. 6.6. Such an explanation is further confirmed below. This also demonstrates that the maximal value of $|\eta(x)|$ is an important quantity to characterize the surface roughness strength.

The results in Fig. 6.6 show that even when the surface roughness is strong enough to significantly shift the threshold energy for transmission, the surface structure factor may still be well imprinted on the conductance curve. Moreover, the resultant windows of the conductance curves in Fig. 6.6 are seen to match the location of the structure factor peak.

As we explain in next section the form of the transmission plays important role in efficiency of nanowires as a thermoelectric device. We establish that it is possible to manipulate the transmission curve by introducing long range correlation into the surface disorder of nanowires, now we look at the effect of two possible surfaces with two different long range correlations on the efficiency of thermoelectric heat engine.

6.5 Efficiency of a Silicon Nanowire Working as a Heat Engine

We use the Landauer approach to calculate the electron transport coefficient for this system. Since the parasitic heat flow decreases the efficiency of the wire as a heat engine drastically when there is more than one mode, we restrict ourselves to the

case where there is only one propagation mode in the nanowire. General quantities governing the transport in the system are the heating and the cooling rates of contacts and the electrical current as a response to the thermal and the potential gradients. They are described for a nanowire with one propagating mode as follows

$$I = \frac{2e}{h}\int t(E)(f_h - f_c)dE \tag{6.32}$$

$$I_{q_h} = \frac{2}{h}\int t(E)(E-\mu_h)(f_h - f_c)dE \tag{6.33}$$

$$I_{q_c} = \frac{2}{h}\int t(E)(E-\mu_c)(f_h - f_c)dE \tag{6.34}$$

where I_{q_h} and I_{q_c} are the heating and the cooling rates of the hot and the cold contacts, respectively, h is the Planck constant, $t(E)$ is the transmission, and f_h and f_c are the equilibrium Fermi–Dirac distributions for the contacts. First, we look at the linearized form of these equations to find the transport coefficient. After that, we calculate the efficiency and the power without using the linear approximation.

6.5.1 Linear Response Theory

In the linear response regime, $I_{q_H} \approx I_{q_C} \equiv I_q$ and we have following approximation

$$I = G\Delta V + SG\Delta T, \tag{6.35}$$

$$I_q = -TSG\Delta V - \kappa\Delta T \tag{6.36}$$

where ΔT is the temperature difference between the contacts, G is the electric conductance, κ is the heat conductance, S is the Seebeck coefficient, and T is the temperature. We set $\mu = \mu_h$ and $f = f_h$, and the transport coefficients in the Landauer–Buttiker formulation are expressed as follows

$$G = -\frac{2e^2}{h}\int_0^\infty dE\frac{\partial f}{\partial E}t(E) \tag{6.37}$$

$$S = \frac{1}{G}\frac{2e^2}{h}\frac{k_B}{e}\int_0^\infty dE\frac{\partial f}{\partial E}t(E)(E-\mu)/k_BT \tag{6.38}$$

$$\frac{K}{T} = -\frac{2e^2}{h}\left(\frac{k_B}{e}\right)^2\int_0^\infty dE\frac{\partial f}{\partial E}t(E)[(E-\mu)/k_BT]^2 \tag{6.39}$$

where f is the Fermi–Dirac distribution function and k_B is the Boltzman constant. Note that the heat conduction is given in terms of K as

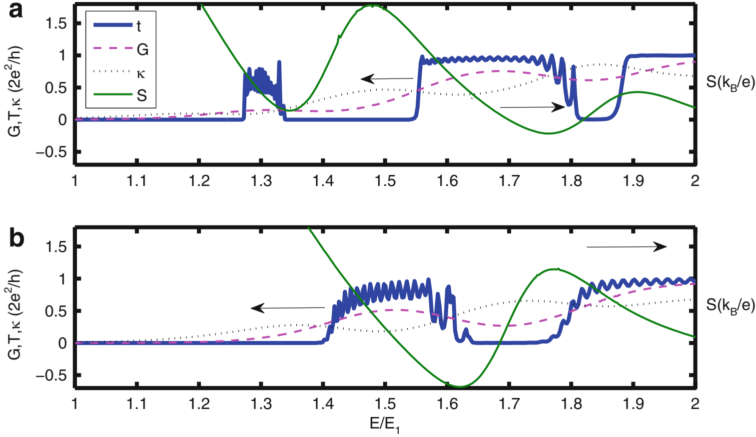

Fig. 6.7 (**a**) Transmission probability (*thick*, *blue*), t, electron thermal conductance (*dotted*, *black*), κ, electron conductance (*dashed*, *magenta*) G in units of conductance quanta, $2e^2/h^2$, are shown with respect to the incident energy of electrons in units of first mode threshold energy, E_1. Thermal power (*red*), S, is also displayed in units of k_B/e. The transmission probability has two windows of transmission dips in energy corresponds to the long range correlated surface $\tilde{\zeta}_d$ (**b**) same as in (**a**) but with a transmission probability which contains single window of transmission dip which corresponds to the correlated surface described by the $\tilde{\zeta}_s$

$$\kappa = -K\left(1 + \frac{S^2 GT}{K}\right) \tag{6.40}$$

we present these transport coefficients in Fig. 6.7 for two different electron transmission spectra. We characterize them according to the transmission hole in energy with one having single well as in Fig. 6.7b and the other has double well of minimal transmission as in Fig. 6.7a. For a perfect wire, the transmission spectrum is unity for the energy range shown here. We have a plateau starting at $E = 1.\ 4E_1$ for a white noise surface transmission with an average amplitude of 0.2 in terms of the wire width taken as unity, see [3]. For the double well transmission spectrum, we use a convolving function, $\rho_d(x) = (\sin(1.2\pi x) - \sin(0.6\pi x))/(1.2\pi x) + (\sin(2.2\pi x) - \sin(1.8\pi x))/(2.2\pi x)$ with corresponding surface structure factor $\tilde{\zeta}_d$, and for the single well spectrum, we have $\rho_s(x) = (\sin(1.8\pi x) - \sin(0.6\pi x))/(1.8\pi x)$ with corresponding surface structure factor $\tilde{\zeta}_s$. It has also been averaged over several generated surfaces for each cases. We use energy units as the opening energy of first channel which is given by $E = \hbar^2/2m(p^2/w^2)$ where the width set to $w = 1$; however, the system is scale invariant. We choose the length of the wire as 100 times of the width, and the temperature is chosen as $k_B T = 0.\ 05E_1$.

We can find the efficiency of the thermoelectric silicon wire from the transport coefficient. First, we define a related quantity known as figure of merit or (ZT) as $\mathrm{ZT} = GTS^2/\kappa$. Accordingly, the efficiency of the thermoelectric material is related to the ZT by

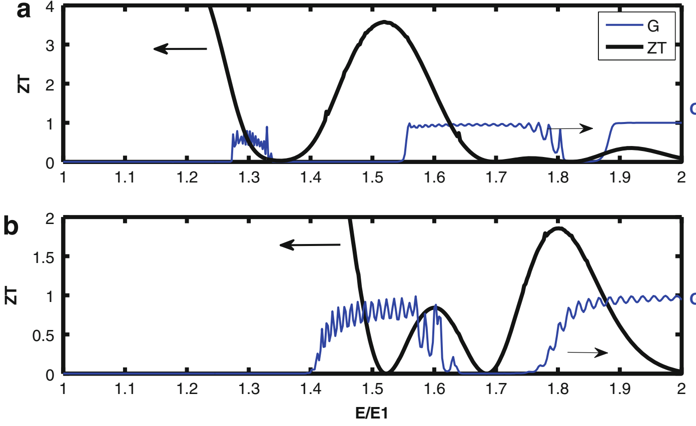

Fig. 6.8 (**a**) The figure of merit ZT (*black*) and the transmission probability are shown for windows of two transmission dips described by the surface structure factor $\tilde{\zeta}_d$. (**b**) same as in (**a**) but for the case when the transmission contains single transmission dip with the surface structure factor $\tilde{\zeta}_s$

$$\eta_{\max} = \eta_C \frac{\sqrt{\mathrm{ZT}+1}-1}{\sqrt{\mathrm{ZT}+1}+1} \tag{6.41}$$

hence the Carnot limit, η_C, is reached when ZT $\rightarrow \infty$. We present the performance of these two nanowires with different surface structures as thermoelectric material ZT for the double well transmission spectrum in Fig. 6.8a and for the single well spectrum in Fig. 6.7b. The ZT has a peak at about 3.3 in the double well spectrum whereas it is about 1.8 in the single well case. In both cases, the ZT goes to very high values at the opening of the first channel. But, we will see that these are not always the best region to make the heat engine work because of negligible power output.

6.5.2 *Efficiency at Maximum Power*

Linear response theory results a continuous efficiency valid for each incident energy, but the feasibility of these efficiencies should be decided based on the power output for a given incident electron energy. For this reason, we use general transport equations without introducing linear approximations. The first parameter we need to set for the model is the temperature difference, ΔT. The temperature should be set accordingly in order to demonstrate the effects we have been seeing in these systems. If we choose very high temperatures for the cold and the hot reservoirs, then the detailed features of the transmission spectrum might be totally

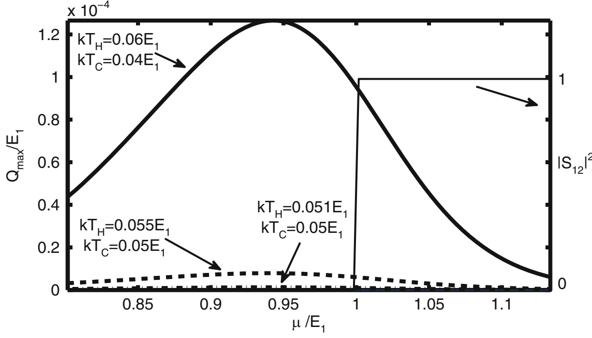

Fig. 6.9 Heat generation rate with varying chemical potential is shown for different temperature differences pointed by *arrows* in the figure. A perfect wire with step function transmission probability has been used, and it has been shown here in units of conductance quanta at the right axis

washed up because of the temperature averaging, and we hardly observe an increase in the thermoelectric efficiency. Also, the temperature difference has nonlinear effect on the overall performance of the device, if it is chosen very large. In Fig. 6.9, we present several choices of the temperature difference, and the resulting maximum heat production rate, $Q_{\max} = I_{q_H} - I_{q_C}$, calculated from (6.5) and (6.6). We choose $T_1 = 0.06E_1$ and $T_2 = 0.04E_1$ where E_1 is the channel threshold energy of the waveguide. Note that we choose $T = 0.05E_1$ for the linear response approach. We see that the peak rate obtained for this temperature difference at a value close to the step function transmission spectrum (valid for a perfect wire), and this is comparable to the width of the transmission wells in the spectrum of the disordered silicon nanowires we used. The peak shifts to the lower energies with the increasing temperature difference, and the heat rate becomes too low for very small energy difference.

Next, we find the power generation and the efficiency for the two systems with different spectra using the temperature differences set at $kT_H = 0.06E_1$ and $kT_C = 0.04E_1$. First, we need to locate the region of power generation. We find the regions of positive power production bounded by open circuit potential, V_{oc}, to determine the region of potential where the heat engine produce work. We determine V_{oc} from

$$I_{q_H} - I_{q_C} = \Delta VI \tag{6.42}$$

where ΔV is the potential difference produced due to the temperature difference of two reservoirs. We can produce power in the system until this potential balanced by the applied bias. We show the power generation, $P = IV$, in Fig. 6.10a, and the efficiency, $\eta/\eta_C = P/I_{q_H}$ in Fig. 6.10b for the case of one well of low transmission in the spectrum. We show the corresponding transmission spectrum in Fig. 6.10b. The limiting thick black curves in Fig. 6.10a, b denote the open circuit potential, V_{oc} and it is a nonlinear function of Fermi–Dirac distribution and transmission curves as well as the temperature difference. As described earlier, we

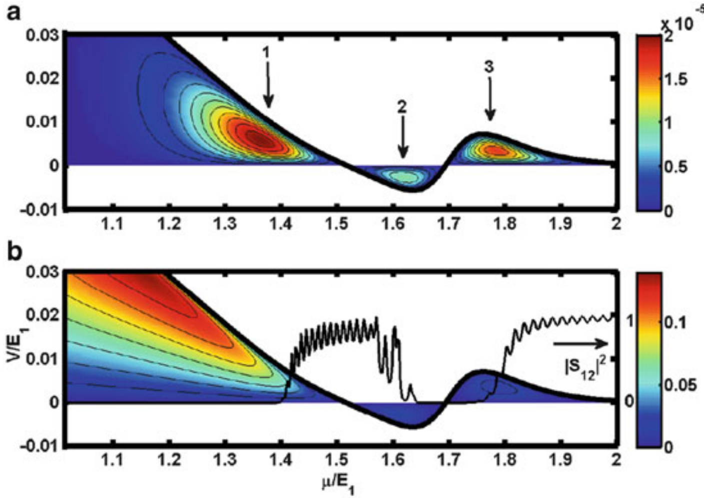

Fig. 6.10 Nonlinear analysis of the case in which the transmission probability contains a window of single dip as a result of used surface structure factor $\tilde{\zeta}_s$. (**a**) The power generation, P, and the potential, V in units of E_1 are shown with varying chemical potential, μ. *Arrows* show each of the local power maximums. (**b**) Normalized efficiency, (η / η_C), is shown for same variables. *Thin black curve* is the transmission probability in units of the conductance quanta. In both graphs, *thick black boundary curve* is the open circuit potential difference, V_{oc}, calculated as described in the text

change the chemical potential by supplying a potential bias to the system with respect to the incident electron energy assuming the average chemical potential can be changed in energy with a back gate potential. There are three regions of high power generation right at the discontinuities of the transmission spectrum. Note that the discontinuities in transmission spectrum is the only way to produce power, for instance a perfect wire there will be no power generation except at the openings of new channels. The sharp increase or decrease in the transmission results in the generation of the heat and the power and increasing the efficiency in general. In the first case, we see the best possible working condition as a heat engine is just before the opening of the channel energy, since at this place both the high power and the efficiency can be achieved.

In Fig. 6.11, we show a similar graph for the second case, i.e. the silicon wire with a surface disorder arranged to produce two transmission wells in the spectrum. The power generation and the efficiency corresponding to the transmission spectrum shown in Fig. 6.11b are plotted with respect to the changing chemical potentials. Yet again, we have peak positions of the power generations near the transmission discontinuities. In this case, we observe that the working condition of a heat engine is actually different than the channel opening but near the second well as shown with arrow 3 in Fig. 6.11a. At this region, the power generation is much higher than the channel opening pointed by arrow 1 in the Fig. 6.11a, and the efficiency is comparable.

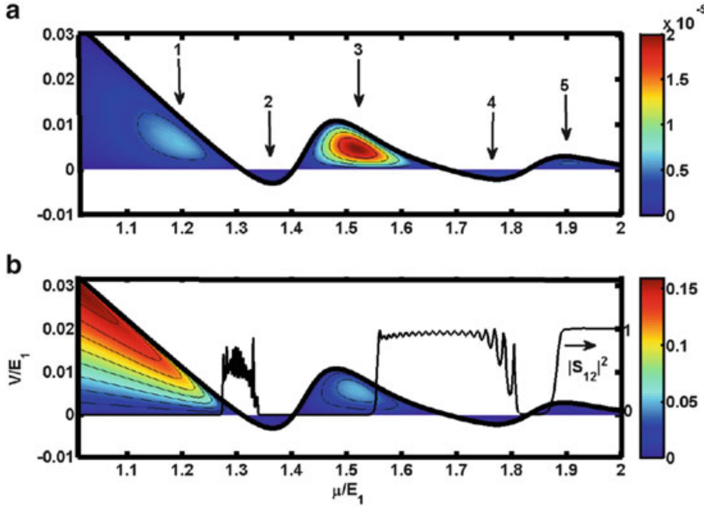

Fig. 6.11 The power generation and the efficiency are shown for the case in which the transmission probability contains windows of two transmission dips produced by surface structure factor $\tilde{\zeta}_d$. (**a**) Positive power regions are shown as a function of potential and energy. (**b**) corresponding normalized efficiency as a function of potential and energy are shown. Thin black curve represents the spectrum for this case. Same parameters are used as in Fig. 6.5

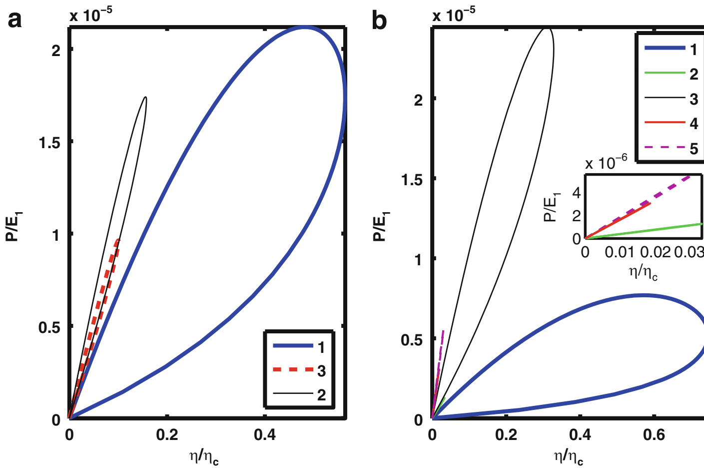

Fig. 6.12 (**a**) The power versus the efficiency at constant μ values shown with *arrows* in Fig. 6.10 with varying potential, (**b**) same as in (**a**) but at the location of *arrows* in Fig. 6.11

We present loop plots of the power versus the efficiency at those incident chemical potentials, μ / E_1, shown with arrows in Fig. 6.10a and in Fig. 6.11a in Fig. 6.12a, b, respectively. Here, we can see the efficiency at local maximum powers. We observe the power buildup and increasing of the efficiency at the

location of 3rd arrow in Fig. 6.11a. Comparison of the efficiencies at the maximum power is in proportion and close to the efficiency one get from the linear response theory. The nanowire with a surface correlation producing double gap near the transmission threshold could be used with an efficiency given by ZT number close to 3.

In this study, we confine our analysis to a simplified system with no thermal effects coming from phonons, and also the electron–electron interaction is not included. It is noteworthy to remark about the connection between our results and the traditional figure of merit for thermoelectric systems

$$\mathrm{ZT} = \frac{GTS^2}{\kappa_e + \kappa_p} = \mathrm{ZT}_e\left(\frac{\kappa_e}{\kappa_p + \kappa_e}\right) \tag{6.43}$$

where T is the average temperature, and κ_e is the electronic and κ_p is the phononic heat conductances. In our calculation, we find the electronic figure of merit ZT_e which is higher than the traditional ZT. Moreover, the electron–phonon interaction causes a further decrease of the electronic conductance due to the phonon drag effect. Interestingly, it has been shown that the phonon drag contributes positively to thermopower with decreasing temperature [2]. The phonon drag contribution is of the form as $S_{\mathrm{ph}} \propto \left(\frac{1}{\kappa_p \mu T}\right)$where μ is electron mobility. If we neglect the electronic contribution and consider only phononic part, then we have $\mathrm{ZT} \propto \frac{n}{\mu T \kappa_p^3}$ which shows that ZT increase with decreasing temperature. This behavior has been found consistent with the experimental results for temperatures around $T = 200K$ for silicon nanowire [2]. Thermopower contribution of phonon drag decreases again for temperatures below $T = 200$ K. Therefore, our results are valid for temperatures much less than $T = 200$ K; however, they underestimate ZT for temperatures around $T = 200$ K. Moreover, since the effect we observe here is mainly due to the increasing thermopower as a result of jumps in the conduction curves, we do not expect significant changes in our results due to an overall decrease in electron conduction.

Another important effect in determining the thermoelectric efficiency is due to the electron–electron interaction. We have not included the electron–electron interaction in our calculations. We give some remarks about this before leaving it to the future work. It has been shown that the conductance dependence on temperature changes with the electron–electron interaction for a perfect wire, and one cannot use simple Onsager relations to find electronic thermal conductance [43]. For low temperatures, Friedel oscillations, Luttinger liquid behavior and 0.7 conductance anomaly can also be observed due to electron–electron interaction. However, the temperature increase undermines these effects due to screening of electron–electron interaction, i.e., $V = \frac{e^2}{4\pi\epsilon r} e^{-r/L}$ with a screening length $L = \sqrt{\epsilon k_B T/(e^2 n)}$ valid for low temperatures. Screening is less effective at high temperatures because of the smaller fractional change of the energy of the electrons. For the silicon wire with a density of electrons as $n = 10^{19}\ \mathrm{cm}^{-3}$, the screening length becomes large for

temperatures greater than $T = 10$ K [44]. Consequently, we can use Onsager relations in our model for temperatures larger than $T = 10$ K and our results remain valid there. Nevertheless, our focus point in this study is the improvements in the thermoelectric efficiency due to the surface changes. Since the effect inherently comes from the rate of change of the transmission probability curve and this can be maintained by changing the surface correlations even in a system with electron–electron interaction, our conclusions are still sound. However, further work is necessary along these lines including the electron–electron interaction.

6.6 Concluding Remarks

Surface randomness with long range correlations introduced to the silicon nanowires increases the thermoelectric efficiency. We find the figure of merit, ZT can be increased by manipulating the transmission spectra of nanowire. It is possible to produce silicon nanowire heat engines by applying an electrical load. We characterize such a system and discussed two cases with different transmission spectrum as a result of two different long range correlations included in their surface generation. The characterization requires the efficiency at a given power generation. We find several of those at the local maximum of power generations. In the case where transmission has double window, we can get better efficiency at maximum power in higher energies than channel opening energy.

There are a variety of ways to manipulate the transmission spectrum. Some examples might be the nanowires with periodic surface potentials resulting gaps in the spectrum or some specific structures with fano resonance type of transmission spectrum [45, 46]. Since the surface randomness is almost unavoidable at nano scale, it should be tried to control by mixing some smooth function with the disorder or one should check the possible correlation on the surface structure to see their effect in transmission spectrum. Nano heat engines can be improved in these structures by looking at the local power maximums and the corresponding efficiencies.

References

1. Hochbaum, A.I., Chen, R., Delgado, R.D., Liang, W., Garnett, E.C., Najarian, M., Majumdar, A., Yang, P.: Nature **451**, 163 (2008)
2. Boukai, A.I., Bunimovich, Y., Tahir-Kheli, J., Yu, J.-K., Goddard, W.A., Heath, J.R.: Nature **451**, 168 (2008)
3. Akguc, G.B., Gong, J: Phys. Rev. B. **78**, 115317 (2008)
4. Pernot, G., Stoffel, M., Savic, I., Pezzoli, F., Chen, P., et al.: Nat. Mater. **9**, 491 (2010)
5. Akguc, G.B., Gong, J.: Phys. Rev. B. **80**, 195408 (2009)
6. Markussen, T., Jauho, A.-P., Brandbyge, M.: Phys. Rev. Lett. **103**, 055502 (2009)
7. Shelley, M., Mostofi, A.A.: Eur. Phys. Lett. **94**, 67001 (2011)

8. Sevincli, H., Cuniberti, G.: Phys. Rev. B. **81**, 113401 (2010)
9. Bell, L.E.: Science **321**, 1457 (2008)
10. DiSalvo, F.J.: Science **285**, 703 (1999)
11. Horvat, M., Prosen, T., Casati, G.: Phys. Rev. E **80**, 010102(R) (2009)
12. Mahan, G.D.: J. Appl. Phys. **76**, 1 (1994)
13. Horvat, M., Prosen, T., Casati, G.: J. Stat. Phys. 10026 (2011)
14. O'Dwyer, M.F., Lewis, R.A., Zhang, C., Humphrey, T.E.: Phys. Rev. B. **72**, 205330 (2005)
15. Humphrey, T.E., Newbury, R., Taylor, R.P., Linke, H.: Phys. Rev. Lett. **89**, 116801 (2002)
16. Humphrey, T.E., Linke, H.: Phys. Rev. Lett. **94**, 096601 (2005)
17. Curzon, F., Ahlborn, B.: Am. J. Phys. **43**, 22 (1975)
18. Izumida, Y., Okuda, K.: Phys. Rev. E **80**, 021121 (2009)
19. Esposito, M., Kawai, R., Lindenberg, K., Van den Broeck, C.: Europhys. Lett. **89**, 20003 (2010)
20. Van den Broeck, C.: Phys. Rev. Lett. **95**, 190602 (2005)
21. Esposito, M., Kawai, R., Lindenberg, K., Van den Broeck, C.: Phys. Rev. Lett. **105**, 150603 (2010)
22. Esposito, M., Lindenberg, K., Van den Broeck, C.: Phys. Rev. Lett. **102**, 130602 (2009)
23. Sivan, U., Imry, Y.: Phys. Rev. B. **33**, 551 (1986)
24. Butcher, P.N.: J. Phys. Condens. Matter **2**, 4868–4878 (1990)
25. Imry, Y.: Rev. Mod. Phys. **71**, s306 (1999)
26. van Houten, H., Molenkamp, L.W., Beenakker, C.W.J., Foxon, C.T.: Semiconductor Sci. Technol. **7**, B215–B221 (1992)
27. Nakpathomkun, N., Xu, H.Q., Linke, H.: Phys. Rev. B **82**, 235428 (2010)
28. Kim, R., Datta, S., Lundstrom, M.S.: J. Appl. Phys. **105**, 034506 (2009)
29. Akguc, G.B., Seligman, T.H.: Phys. Rev. B **74**, 245317 (2006)
30. Wigner, E.P., Eisenbud, L.: Phys. Rev. **72**, 29 (1947)
31. Lane, A.M., Thomas, R.G.: Rev. Mod. Phys. **30**, 257 (1958)
32. Reichl, L.E.: The Transition to Chos, 2nd edn. Springer, Berlin (2004)
33. Akguc, G.B., Reichl, L.E.: Phys. Rev. E **67**, 46202 (2003)
34. Akguc, G.B., Reichl, L.E.: Phys. Rev. E **64**, 56221 (2001)
35. Reichl, L.E., Akguc, G.B.: Found. Phys. **31**, 243 (2001)
36. DeWitt, B.S.: Rev. Mod. Phys. **29**, 377 (1957)
37. Akguc, G.B., Gong, J.B.: Phys. Rev. B **77**, 205302 (2008)
38. Izrailev, F.M., Krokhin, A.A., Makarov, N.M., Usatenko, O.V., Phys. Rev. E **76**, 027701 (2007)
39. Izrailev, F.M., Makarov, N.M.: Opt. Lett. **26**, 1604 (2001)
40. Izrailev, F.M., Makarov, N.M.: Appl. Phys. Lett. **84**, 5150 (2004)
41. Freilikher, V.D., Makarov, N.M., Yurkevich, I.V.: Phys. Rev. B **41**, 8033 (1989)
42. Freilikher, V.D., Gredeskul, S.A.: J. Opt. Soc. Am. **7**, 868 (1990)
43. Rech, J., Micklitz, T., Matveev, K.A.: Phys. Rev. Lett. **102**, 116402 (2009)
44. Renard, V.T., Tkachenko, O.A., Tkachenko, V.A., Ota, T., Kumada, N., Portal, J.-C., Hirayama, Y.: Phys. Rev. Lett. **100**, 186801 (2008)
45. Karlstrom, O., Linke, H., Karlstrom, G., Wacker, A.: Phys. Rev. B **84**, 113415 (2011)
46. Fahlvik Svensson, S., Persson, A.I., Hoffmann, E.A., Nakpathomkun, N., Nilsson, H.A., Xu, H.Q., Samuelson, L., Linke, H.: arXiv:1110.0352 [cond-mat.mes-hall] (2011)

Chapter 7
One-Dimensional Bi-Based Nanostructures for Thermoelectrics

Liang Li and Guanghai Li

Abstract Bi and its alloys are important thermoelectric materials for solid-state refrigeration and power generation. An increase in the thermoelectric figure of merit is predicted due to quantum confinement and phonon scattering at interfaces for one-dimensional (1D) nanostructured thermoelectric materials. This chapter addresses recent developments in Bi-based nanostructured thermoelectric materials focused mainly on nanowires, nanotubes, and heterostructures. In addition, current challenges in preparation and measurement of 1D nanostructured thermoelectric materials are discussed.

7.1 Introduction

Thermoelectric materials, which can generate electrical power from thermal energy or convert electrical power into heating or cooling, are expected to play an increasingly important role in meeting the energy challenge of the future [1–3]. Generally, the performance of thermoelectric materials is qualified by the figure of merit $ZT = S^2\sigma T/\kappa$, where S, σ, T, and κ refer to the Seebeck coefficient, electrical conductivity, temperature, and thermal conductivity, respectively. ZT determines the fraction of Carnot efficiency, and in order to compete with traditional energy conversion technologies which work at 30–40 % Carnot efficiency, thermoelectric materials theoretically should have a $ZT \geq 3$ [4]. Unfortunately, thermoelectric materials have long been too inefficient and their ZT is still too low for fully scalable applications. Therefore, increasing ZT is still the core issue in thermoelectric field.

The key to obtain a higher ZT is to increase the Seebeck coefficient and electrical conductivity and reduce the thermal conductivity simultaneously. However, these

L. Li (✉) • G. Li (✉)
Key Laboratory of Materials Physics, Anhui Key Lab of Nanomaterials and Nanostructure, Institute of Solid State Physics, Chinese Academy of Sciences, Hefei 230031, P.R. China
e-mail: liliangjr@issp.ac.cn; ghli@issp.ac.cn

X. Wang and Z.M. Wang (eds.), *Nanoscale Thermoelectrics*, Lecture Notes in Nanoscale Science and Technology 16, DOI 10.1007/978-3-319-02012-9_7,
© Springer International Publishing Switzerland 2014

three quantities interrelated to each other for conventional three-dimensional crystalline systems which limit the further increase of *ZT* for the best conventional thermoelectric materials. According to Wiedemann–Franz law, an increase in S usually results in a decrease in σ, and a decrease in σ leads to a decrease in the electronic contribution to κ [2, 5]. Normally, two different approaches were developed to increase *ZT*: one is to use new families of advanced bulk thermoelectric materials—the main motivation of this method is to maximize the power factor ($S^2\sigma$); another focus is mainly on reducing phonon-based thermal conductivity by using low-dimensional material systems [2, 6–8].

Hicks and Dresselhaus, who were regarded as the pioneers of low-dimensional thermoelectric materials, predicted a larger *ZT* in low-dimensional systems [9, 10]; since then, one-dimensional (1D) nanostructures have become a hot topic in thermoelectric field. As a class of most widely used thermoelectric materials, Bi and its alloys with some special nanostructures, including nanowires, nanotubes, and 1D heterostructures, could be applicable for commercial applications after further optimizing their *ZT* and thus have been broadly studied.

In this chapter, we review the latest advance in Bi-based nanostructured thermoelectric materials focused mainly on nanowires, nanotubes, and heterostructures. The chapter is organized into four sections. The following section discusses some fabrication strategies of 1D thermoelectric nanostructures, along with physical model on 1D thermoelectric materials. Section three evaluates the thermoelectric properties of 1D thermoelectric materials, including ensemble properties of arrays and thermoelectric properties of single nanowires. At the end, we give some remarks on current challenges in 1D thermoelectrics.

7.2 Fabrications and Characterizations of 1D Nanostructures

In this section, we focus mainly on electrodeposition method. Besides, a new method of 1D nanostructure fabrication, similar to chemical vapor deposition, which is called stress-induced method, is also introduced.

7.2.1 Template-Assisted Electrodeposition

The template-assisted electrodeposition is one of the most cost-effective techniques for the fabrication of 1D nanostructured materials. Compared with other synthetic routes, this method possesses various advantages such as low cost, high deposition rate, low temperature operation, and easy controllability [11].

7.2.1.1 Nanowires

For nanowires, the density of states is increased due to the two-dimensional confinement of electrons which in turn increases the thermoelectric power factor. In addition, the increased phonon scattering from the surface of the wire gives rise to the reduction of lattice thermal conductivity.

Anodic aluminum oxide (AAO) template with highly ordered pores has attracted much attention for nanowire fabrication. Bi, $Bi_{1-x}Sb_x$, Bi_2Te_3, $(Bi_{1-x}Sb_x)_2Te_3$, and $Bi_2(Te_xSe_{1-x})_3$ have been successfully deposited in AAO template by potentiostatic electrodeposition [12–17]. In the fabrication of Sb-related nanowires, it should be noted that Sb salt is very difficult to dissolve in aqueous solutions; high concentrations of complexing agents such as tartaric and $C_6H_8O_7{\cdot}H_2O$ and low pH should be used or switch to organic solvent [13]. Besides AAO template, polymer templates are another attractive membrane for the fabrication of thermoelectric nanowires. Compared to AAO template, polymer templates, such as polycarbonate and polyimide-based Kapton, have a lower thermal conductivity and therefore could be potentially used to build nanowire-based thermoelectric device [18–20].

As one of the mostly used electrodeposition techniques, pulsed electrodeposition has been considered as an effective way for the growth of uniform and single-crystal nanowires for a long time [21, 22]; recently this technique aroused great attention in fabrication of high-quality thermoelectric nanowires [23]. The added "off" time in pulsed electrodeposition compared to conventional direct current electrodeposition allowed the recovery of ion concentration in growth front during deposition making the nanowire growth uniform and homogeneous. Our group developed this technology for the synthesis of single-crystal Bi, $Bi_{1-x}Sb_x$, and Bi_2Te_3 nanowires [24–28]. By adjusting the pore diameter of AAO template, pulsed parameters such as deposition potential, "on" and "off" time, and pH of the electrolyte, Bi nanowires with different diameters and growth orientations were obtained. $Bi_{1-x}Sb_x$ nanowires with controlled composition and growth direction were fabricated via the pulsed technology. The growth of the nanowires follows the 3D-to-2D mode. We found that the effective deposition potential which is defined as $U_{\text{eff}} = T_{\text{on}}/(T_{\text{on}} + T_{\text{off}})U$ affects not only the alloy composition but also the diameter of the nanowires. A typical figure is shown in Fig. 7.1. Bi_2Te_3 nanowires with a preferential orientation along the [015] direction also have been fabricated in aqueous solutions by our group [28]. By carefully modulating the ion concentration of the solution and deposition potential, stoichiometric Bi_2Te_3 nanowires were obtained. In order to study the influence of electrochemical process on the microstructure of the Bi_2Te_3 nanowires, Lee and co-workers did a systematic research on the fabrication of Bi_2Te_3 nanowires by using the pulsed, galvanostatic and potentiostatic electrodeposition and found that Bi_2Te_3 nanowire arrays deposited by pulsed voltage have a highly oriented crystalline structure and were grown uniformly as compared to those grown by other two techniques [29].

Recent works are focused on tuning the size, geometrical, composition, and crystallographic of thermoelectric nanowires simultaneously [30, 31]. Although much work has been done in fabrication unitary and binary nanowires, fabrication

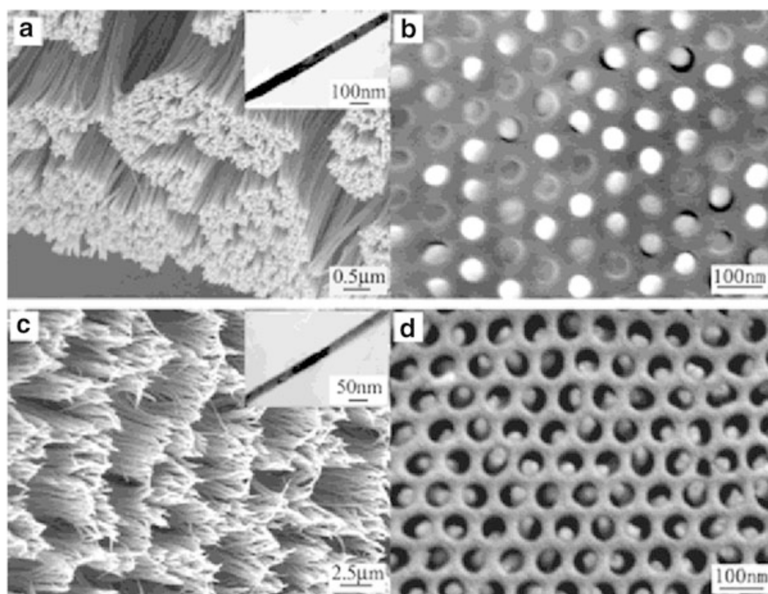

Fig. 7.1 SEM images of $Bi_{1\text{-}x}Sb_x$ alloy nanowire arrays with different diameters deposited at potentials of (**a**, **b**) 0.18 (nanowire diameter: 60 nm) and (**c**, **d**) 0.25 V (nanowire diameter: 28 nm). The *insets* are the corresponding TEM image of a single nanowire. Reproduced with permission from [27] Copyright 2006 Am. Chem. Soc

of high-quality ternary alloy such as $(Bi_{1\text{-}x}Sb_x)_2Te_3$ and $Bi_2(Te_xSe_{1\text{-}x})_3$ with controllable composition and geometrical is still very difficult [11], and further work needs to be done.

7.2.1.2 Nanotubes

Compared to nanowires, the structural feature of both hollow tube channels and two-dimensional tube walls in nanotubes has a stronger phonon blocking effect, which will result in a reduced lattice thermal conductivity and different electronic transport behaviors.

A facile and general method was presented by our group for the fabrication of nanotubes using AAO template [32, 33]. Figure 7.2 shows a typical procedure for the fabrication of Bi nanotubes. The core to obtain nanotubes is to form a mesh-like Au layer on one planar surface of the AAO template before electrodeposition. By tuning the thickness of the coated Au layer and parameters of the current densities, the Bi nanotubes with controlled thickness could be realized [34]. Using this simple method, Bi_2Te_3 and Sb_2Te_3 nanotubes were also fabricated in the following years by other groups [35–37]. However, in the fabrication of Bi-Sb alloy nanotubes, our group found an abnormal growth of the nanotubes during the electrodeposition [38]. As can be seen from Fig. 7.3 the growth of the polycrystalline nanotubes is terminated by

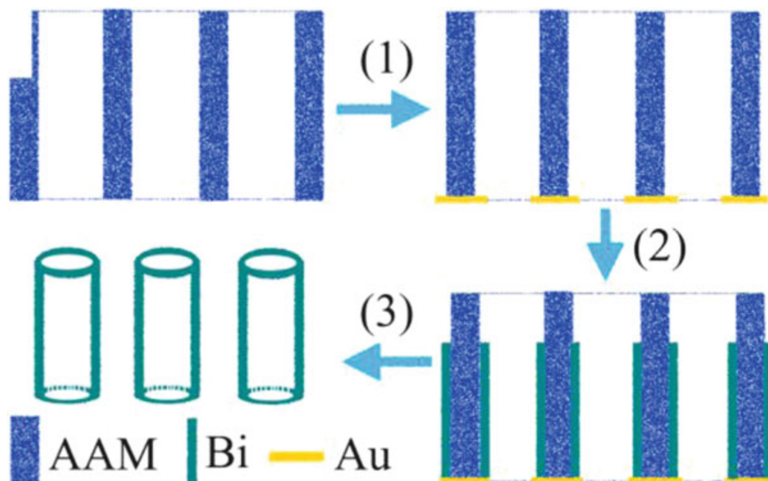

Fig. 7.2 Schematic illustration of the growth processes of Bi nanotube arrays: (1) sputtering thin Au electrode film, (2) electrodepositing Bi nanotube, and (3) removing AAM. Adapted with permission from [33]. Copyright 2006 American Institute of Physics

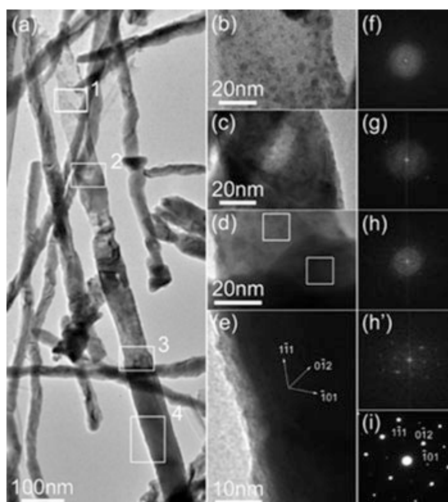

Fig. 7.3 (**a**) TEM image of a nanotube–nanowire junction. (**b–e**) HRTEM images of the area marked with the rectangles 1–4 shown in (**a**). (**f**, **g**) 2D FFT of (**b**) and (**c**). (**h**, **h′**) The FFT of the area marked with the rectangles 1 and 2 shown in (**d**). (**i**) The SAED pattern of (**e**). Reproduced with permission from [38] Copyright 2008 Am. Chem. Soc

polycrystalline nanowires abruptly and then followed by single-crystalline nanowires. We assume that the initial formation mechanism of the nanotubes followed a 3D growth mode, and the transition from the polycrystalline nanotube to polycrystalline nanowire takes place abruptly due to an abnormal grain growth, which is due to the competitive growth of different grains. The change from polycrystalline nanowire to single-crystalline nanowire follows the common 3D-to-2D transition process.

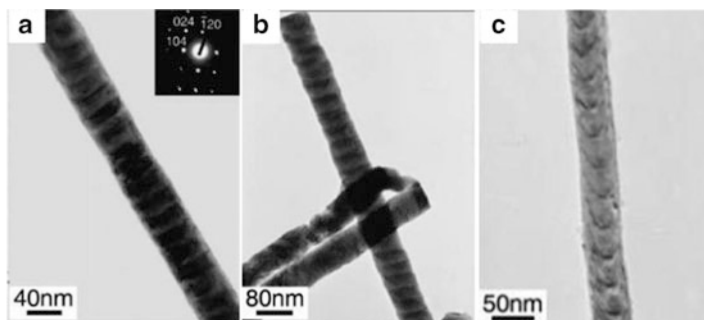

Fig. 7.4 TEM images of (**a**) 2D plane growth mode; (**b**) tilted plane growth mode; (**c**) curved plane growth mode. Adapted with permission from [40] Copyright 2008 Am. Chem. Soc

7.2.1.3 1D Superlattice

Superlattice nanowires (SLNWs) are the structure which integrates the advantages of both quantum wires and quantum dots, and the electronic transport along the wire axis is made possible by the tunneling between adjacent quantum dots, while the uniqueness of each quantum dot and its zero-dimensional characteristics is maintained by the energy difference of the conduction or the valence bands between different materials [39, 40]. The lattice thermal conductivity of the SLNWs is reduced by blocking the phonon along the wire axis due to the abundance of heterogeneous interfaces between the nanodots, while the periodic potential perturbation may be beneficial to the electrical conduction [39]. These features make the SLNWs especially attractive for thermoelectric applications.

Template-assisted electrochemical method is widely used in fabricating SLNWs. A variety of thermoelectric SLNWs, such as Bi/Sb, Bi/BiSb, Bi_2Te_3/Sb, and Bi_2Te_3/BiSbTe, have been fabricated in a single bath using pulsed electrodeposition in AAO templates [40–43]. Among these, our group developed an effective process to synthesize Bi/BiSb SLNWs with controllable and very small bilayer thickness and sharp segment interface by adopting a charge-controlled pulse electrodeposition [40, 44], in which we use millisecond potentiostatic pulses during the electrodeposition of each segment. As well known, the *ZT* of SLNWs generally increases with a decrease in both wire diameter and the segment length before the alloy limit is reached [39]; our synthetic method may play an important role in fabricating high-quality thermoelectric materials. In addition, three different growth modes of the nanowires such as 2D plane growth mode, tilted plane growth mode, and curved plane growth mode were first observed by our group [40], as shown in Fig. 7.4, in which a single-crystal Bi/BiSb nanowire has three different interfaces. We assumed that the 2D plane growth mode is controlled predominantly by thermodynamics, while the tilted plane growth and the curved plane growth modes are controlled mainly by kinetics. An interested thing found in electrodeposited Bi_2Te_3-related SLNWs is that without post-processing the fabricated Bi_2Te_3-related SLNWs are

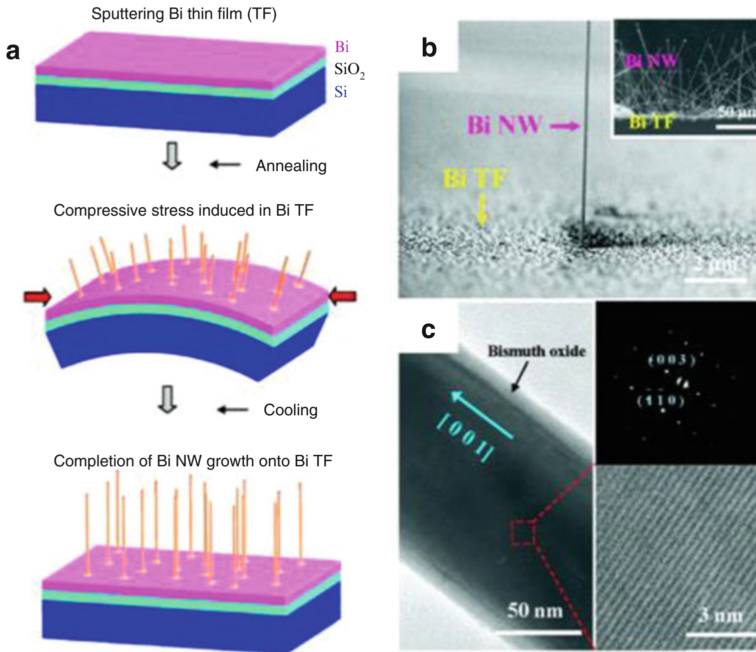

Fig. 7.5 Growth mechanism and structural characteristic of the Bi nanowires. (**a**) A schematic representation of the growth of Bi nanowires by OFF-ON. (**b**) A SEM image of a Bi nanowire grown on a Bi thin film. (**c**) A low-magnification TEM image of a Bi nanowire: the ED pattern (*top right*) and a high-resolution TEM image (*bottom right*) of the Bi nanowire. Reproduced with permission from [46] Copyright 2009 Am. Chem. Soc

polycrystalline. A nanoconfined precipitation reaction was developed by Wang and co-workers for the spontaneous formation of Bi_2Te_3/Te multilayered nanowires in which each segment was single crystalline in AAO template [45]. In this method, the electrodeposited Te-rich supersaturated Bi_xTe_{1-x} nanowires imbedded in AAO were annealed under different conditions, the heterogeneous structure formed due to the confined effect of the nanochannel during the Te crystal growth [45].

7.2.2 *Stress-Induced Method*

Recently, a novel stress-induced method termed as on-film formation of nanowires (OFF-ON) was proposed by Lee's group for the fabrication of single crystalline Bi and Bi_2Te_3 nanowires [46, 47]. This synthesized technology is based on the mismatch of the thermal expansion between the substrate and the film. When annealing at an appropriate temperature, this mismatch acts as a thermodynamic driving force driving the mass flow along grain boundaries to grow nanowires. Figure 7.5a shows the

OFF-ON process for the fabrication of Bi nanowires. A Bi thin film was initially deposited onto a thermally oxidized silicon substrate. Then the film was heated to about 270 °C and kept at this temperature for about 10 h to generate thermal stress. As can be seen from Fig. 7.2b, c, single-crystal Bi nanowire with [001] orientation was obtained after annealing. The diameter of nanowires is tunable by controlling the mean grain size of the film, which is dependent upon the thickness of the film. However in the growth of Bi_2Te_3 nanowires by the same mechanism, the nanowires are single crystalline but with [110] growth orientation. These results demonstrate that the OFF-ON technique can be used to grow wires with different compositions [47].

Bi-Te core/shell nanowires and $Bi/Bi_{14}Te_6$ axial heterostructure nanowires were also fabricated by using this OFF-ON method combined with post-processing [48, 49]. For the synthesis of Bi-Te core/shell heterostructure nanowires, Bi nanowires was first growth from a Bi thin film using the OFF-ON method mentioned above, then Te film with 30 nm in thickness was deposited in situ onto the Bi nanowires using radio frequency magnetron sputtering at room temperature, Bi-Te core/shell nanowires with smooth or rough interface can be achieved just by changing the substrate temperature and the power of radio frequency magnetron sputtering. For the growth of $Bi/Bi_{14}Te_6$ axial heterostructure nanowires, a thin Te layer (in their experiment, the total volume of Te with respect to Bi is limited to approximately 20 %) was first deposited on the fabricated Bi nanowires by tilting and rotating the sample during low power deposition. Next, the Te-coated Bi nanowires were annealed at 310 °C. $Bi/Bi_{14}Te_6$ multi-segmented nanowires were formed based on the thermodynamics of supersaturated phase.

7.2.3 Other Methods

Although the abovementioned two methods are simple and inexpensive in fabricating 1D nanostructures, the low-yield nature of them makes it difficult in the measurement of the thermoelectric property and blocks the further commercial applications. Consequently, the exploration of other methods with large-scale production is needed. Many researchers have devoted to fabricate high-output and high-performance 1D nanostructured materials. For example, Zhang et al. focused their research on Bi_2Te_3-related nanomaterials and developed an ethylene glycol-mediated solution-phase method, and Bi_2Te_3 nanotubes, ultrathin n-Type Bi_2Te_3 nanowires with 5 nm in diameter, and Te-based nanowire heterostructures have been obtained [50–52]. Our group also developed a simple solvothermal for the preparation of large-scale Bi nanowires [53]. However, we are not going to introduce these methods in details; readers can realize these from references [11, 54, 55].

7.3 Thermoelectric Properties of 1D Bi-Based Nanostructures

There are two different methods in measuring thermoelectric properties of 1D Bi-based nanostructures, i.e., the ensemble measurement on 1D nanostructure arrays and measurement on individual 1D nanostructure. Measurements on a single 1D nanostructures are important in studying quantum and classical size effects, while ensemble measurements promote the ultimately realization of the benefits of nano-structured components in thermoelectric devices.

7.3.1 Semimetal-to-Semiconductor Transition

Theoretical investigation reveals a semimetal-to-semiconductor transition appeared in Bi nanowires when the wire diameter shrinks to the order of 40–50 nm at 77 K, which depends on the crystalline orientation of the wires [56]. Consequently, Bi nanowire arrays with different diameters were fabricated in order to investigate the semimetal-to-semiconductor transition phenomenon in Dresselhaus' group, and they found a semimetal-to-semiconductor transition at a diameter of around 65 nm [57], which coincides with the modelling calculations. Temperature-dependent measurements of the resistance of single-crystalline Bi nanowire arrays also were performed by our group, and a clear transition was observed when the diameter of Bi nanowires decreased from 90 to 50 nm [58]. Systematic studies on the physical properties of individual single-crystalline bismuth nanowires are very difficult due to the oxidation nature when the wires are released from the template [59]. Recently, Lee and co-workers grew single-crystalline Bi nanowires with small diameters down to 20 nm by their OFF-ON method, and the measurements of the electrical transport property of individual nanowires and the temperature-dependent resistance of individual Bi nanowires indicate a semimetal-to-semiconductor transition when the diameter of Bi wires turns to 63 nm [60]. Transport measurements on 65 nm $Bi_{1\text{-}x}Sb_x$ show a complex behavior in $R(T)/R(270\ \text{K})$ as a function of x and T, providing a signature of the semimetal-to-semiconductor transition in Bi-based systems [61].

Semimetal-to-semiconductor transition phenomenon was also observed in Bi nanotubes by our group [33]. The temperature dependence of the resistance $R(T)$ of Bi nanotube arrays is shown in Fig. 7.6. From Fig. 7.6a, one can see that all the three kinds of nanotubes that have the same wall thickness but different diameters exhibit obvious negative temperature coefficient of resistance, indicating a semiconductor character. From Fig. 7.6b, one can see that a typical semimetal–semiconductor transition occurs as the wall thickness of Bi nanotubes decreases from 100 to 15 nm. Our following theoretical calculation work conforms to our experiment results nicely [62]. The calculations are based on the Boltzmann transport equation in the constant-relaxation-time approximation. The results predicate a phase diagram of the semimetal-to-semiconductor transition, as shown in Fig. 7.7, in which the

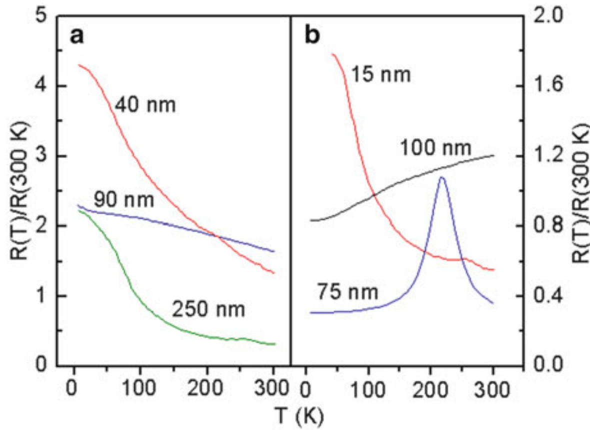

Fig. 7.6 Temperature dependence of the normalized electronic resistances of Bi nanotube arrays (**a**) with the same wall thickness 15 nm and different diameters and (**b**) with the same diameter of 250 nm and different wall thicknesses. Reproduced with permission from [33]. Copyright 2006, American Institute of Physics

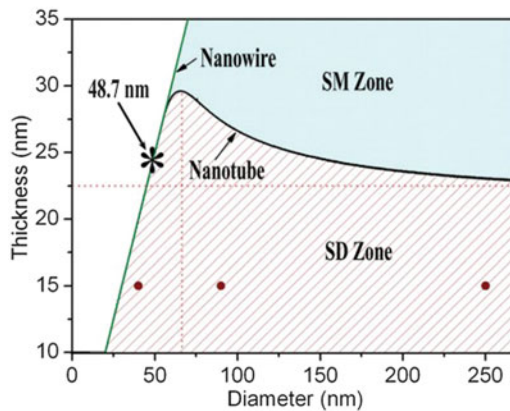

Fig. 7.7 Phase diagram of the semimetal-to-semiconductor transition of Bi nanotubes oriented along the $[10\bar{1}1]$ growth direction at 77 K. The *solid circles* represent the experimental results, the *dotted lines* are two assistant lines, and the symbol * refers to the position of 48.7 nm diameter nanowires in which the semimetal-to-semiconductor transition occurs for Bi nanowires. Reproduced with permission from [62]. Copyright 2011, American Institute of Physics

dependence of the critical thickness on diameter was demonstrated for Bi nanotubes oriented along $[10\bar{1}1]$ growth direction at 77 K. From this figure, one can see that the critical thickness of the transition from semimetal to semiconductor for Bi nanotube first increases and then decreases as the diameter varies from 48.7 to 270 nm, where 48.7 nm is the critical diameter of the transition from semimetal to semiconductor for Bi nanowires oriented along the $[10\bar{1}1]$ direction at 77 K.

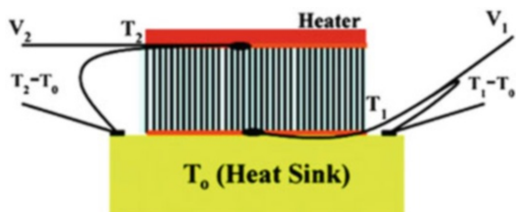

Fig. 7.8 Schematic setup for Seebeck coefficient measurements on nanowire array of AAO. Adapted with permission from [63] Copyright 2010 Am. Chem. Soc

7.3.2 Ensemble Measurements on 1D Nanostructure Arrays

7.3.2.1 Measurements of Seebeck Coefficient

The Seebeck coefficient (S) is defined as $S = \Delta V/\Delta T$, where ΔT is the temperature gradient of the sample, and ΔV is the thermal electromotive force generated by ΔT. Seebeck coefficient measurements on arrays are in theory as similar as single 1D nanostructure measurements since the S measurement is intrinsically independent of the number of nanowires or nanotubes contributing to the signal [61]. A typical measurement on arrays for Bi_2Te_3 nanowires is shown in Fig. 7.8 [63]. Briefly, a gold layer is sputtered for an enhanced electrical and thermal contact. The embedded AAO template is placed between two copper blocks where a temperature gradient is applied. After reaching a constant gradient, the voltage along the nanowires is measured. Using this method, the Seebeck coefficients of Bi, $Bi_{0.95}Sb_{0.05}$ and Bi_2Te_3 nanowire arrays were measured [29, 61, 63–65]. However, an enhancement of Seebeck coefficient in the nanowire arrays could not be observed so far.

7.3.2.2 Thermal Conductivity

Thermal conductivity of Bi-based nanowire arrays has also been studied by some groups. Conventionally, the thermal conductivity of the filled template and empty template are both obtained, and then, the thermal conductivity of nanowire arrays can be calculated using an effective medium mode: $k_c = x\, k_{NW} + (1\text{-}x)\, k_m$ where x is the area packing density of the nanowire array and k_c, k_{NW}, and k_m are the thermal conductivity of filled template, nanowire arrays, and empty template, respectively. Different methods were used to characterize the thermal properties. For example, Chen et al. used laser flash equipment to measure the thermal diffusivity; the thermal diffusivity of Bi_2Te_3 nanowires was calculated based on modified effective medium theory model, the heat capacity was determined by a differential scanning calorimeter, and finally the thermal conductivity of the nanowire arrays was calculated by $\kappa = \lambda\rho\, C_p$ where λ, ρ, and C_p are, respectively, the thermal diffusivity, density, and heat capacity of the nanowires [63]. They got a smaller $\kappa = 0.75$ W/mK at 300 K for nanowires, which is about one-third of that of bulk. In order to reach a nanometric lateral spatial resolution, Rojo et al. performed a versatile and straightforward technique called 3ω-SThM method to measure

composite sample which made of a Bi_2Te_3 nanowires array embedded in an alumina matrix equivalent thermal resistance [66], using the effective medium model shown above, they estimate the thermal conductivity of the nanowires to be 1.37 ± 0.20 W/mK. Considered that the thermal conductivity of AAO template is comparable to that of the Bi_2Te_3 nanowire array, Biswas et al. replaced the AAO matrix with SU-8 to minimize the parasitic thermal conduction [67]. The fabrication details can be found in ref. [67]. Using a photoacoustic technique, the thermal conductivity of the nanowire array composites was measured. The effective thermal conductivity of the Bi_2Te_3 nanowires in the composite is calculated to be 1.45 ± 0.09 W/mK.

7.3.2.3 Harman's Technique for *ZT* Measurement

Harman's technique is a simple method for the direct measurement of the figure of merit (*ZT*). This technique was first used to measure the thermal conductivity using the Peltier effect by Harman et al. [68]; now it has been developed by many groups as a preliminary method for the measurement of *ZT*. In this technique, a constant current is run through the sample until a constant voltage is observed. Due to the Peltier effect a temperature difference is established across the sample which in turn establishes a Seebeck voltage in addition to the Ohmic voltage. The total voltage across the sample is the sum of electrical voltage of Ohm's law and Seebeck voltage. When the current is turned off, the Ohmic voltage disappears instantaneously, while the Seebeck voltage drops slowly because of the heat dissipation and heat capacity of the materials. The ratio of the Seebeck voltage and the electrical voltage provides *ZT* [37, 69]. Using this method, Jennifer Keyani and Angelica M. Stacy get a $ZT = 0.12$ at room temperature for hybrid $Bi_{0.3}Sb_{0.7}$ nanowire array–$Bi_{0.4}Sb_{1.6}Te_3$ bulk thermoelectric device [70], while Penner et al. obtained a maximum $ZT = 0.82$ for a single Bi_2Te_3 nanowire [69].

It should be noted that Harman's technique is not a precise method due to the thermal loss of the nanowires and the restriction in accuracy of the instrument.

7.3.3 Thermoelectric Properties of Individual Nanowires

Along with the advance of the micro-processing techniques, substantial progress has been achieved in the thermoelectric measurements on the individual nanowires [1, 71–76]. Among these techniques, the suspended microelectromechanical system (MEMS) technique developed by Shi et al. aroused much attention [71, 74]. Figure 7.9 shows the microdevice for characterization of single-wire thermoelectric [75]. The device is a suspended structure consisting of two adjacent low-stress SiN_x membranes, each suspended with six SiN_x beams. A platinum resistance thermometer serpentine is designed on each membrane connected to four Pt electrodes. Two additional Pt electrodes are designed on each membrane to provide electrical contact

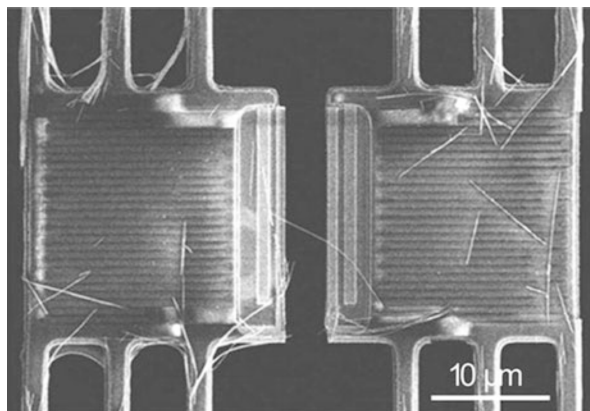

Fig. 7.9 A typical prominent measurement microdevice for individual nanowire thermoelectric characterization. Reproduced with permission from [75]. Copyright 2009, American Institute of Physics

to the nanowire. An individual nanowire can be placed between the two membranes of the suspended device and on top of the four pre-patterned Pt electrodes with a sharp probe, or dropping a nanowire solution for measurements. One common challenge in the microfabrication process is to ensure reliable thermal and electrical contact between the nanowire and electrodes. Focused ion beam (FIB) technique is usually used to remove oxides of the nanowire and deposit small metal pads on top of the nanowire–electrode contacts in order to improve thermal and electrical contact.

A reduction of thermal conductivity in individual 1D Bi-based nanostructure is reported in many studies. For example, Moore et al. find that the thermal conductivity of a single-crystal bismuth nanowire with a diameter of 232 nm is 3–6 times smaller than their bulk counterpart [77]. Their findings also reveal that the crystal structure influences the nanowire thermal conductivity [77]. In order to demonstrate the influence of the growth direction on the nanowire thermal conductivity, Lee and co-workers determined the thermal conductivity of single-crystal Bi nanowires with two different growth directions prepared via OFF-ON method [78]. Their findings show that the thermal conductivity of the Bi nanowires with a growth direction of [110] is about fourfold lower than that of the Bi nanowires with a growth direction of $[\bar{1}02]$ [78]. They also investigated the reduction of the lattice thermal conductivity of Bi-Te core/shell nanowires with rough interfaces by comparison study of the thermal conductivity of Bi-Te core/shell nanowires with smooth and rough interfaces [48]. Their results show that the thermal conductivity can be reduced to 0.43 W/m K by using rough interface Bi-Te core/shell nanowires [48]. In recent research, they demonstrate that a low thermal conductivity of 0.92 W/m K exhibited in 100 nm diameter $Bi/Bi_{14}Te_6$ multi-segmented nanowires [49].

Although a reduction of the thermal conductivity is observed by many researchers, reported values on the thermoelectric power factor of individual Bi-based nanowires are far below the corresponding bulk values. This was mainly attributed to difficulties in controlling the chemical composition of nanowires. Experimentally determined *ZT* values are only 0.02 at 300 K for 88 nm diameter single-crystalline Bi_xTe_{1-x} nanowire and 0.13 at 411 K for 55 nm diameter polycrystalline Bi_xTe_{1-x} nanowire [73, 75].

7.4 Conclusions and Outlook

During the last decade, significant progresses have been achieved in thermoelectric materials for energy conversion both in theory and experiment. 1D nanostructured materials are considered to be a promising strategy for achieving high efficiency. Numerous thermoelectric materials have been developed in recent years. Among them, Bi-based materials are still a dominating material system in thermoelectrics.

Although great progress has been achieved in thermoelectric performance, there are at least three pressing challenges for one-dimensional nanostructured materials. The first and most immediate one is to obtain materials with *ZT* values higher than their bulk counterpart with lower cost [55], since *ZT* determines the conversion efficiency and cost dictates the future commercialization. To address this challenge, novel strategies and synthesis routes should be developed. The second challenge is to measure individual nanowire in a more accurate, convenient, and economic way. The last one is to study and optimize long-term stability, interdiffusion, and coarsening of nanostructures [79], as the thermoelectric materials generally work at high temperatures and temperature gradients.

Acknowledgments The authors greatly appreciate the financial support given by the National Natural Science Foundation of China (No: 11174285).

References

1. Hochbaum, A.I., Chen, R.K., Delgado, R.D., Liang, W.J., Garnett, E.C., Najarian, M., Majumdar, A., Yang, P.D.: Enhanced thermoelectric performance of rough silicon nanowires. Nature **451**(7175), 163–165 (2008)
2. Dresselhaus, M.S., Chen, G., Tang, M.Y., Yang, R.G., Lee, H., Wang, D.Z., Ren, Z.F., Fleurial, J.P., Gogna, P.: New directions for low-dimensional thermoelectric materials. Adv. Mater. **19**(8), 1043–1053 (2007)
3. Li, Z., Sun, Q., Yao, X.D., Zhu, Z.H., Lu, G.Q.: Semiconductor nanowires for thermoelectrics. J. Mater. Chem. **22**(43), 22821–22831 (2012)
4. Hochbaum, A.I., Yang, P.D.: Semiconductor nanowires for energy conversion. Chem. Rev. **110**(1), 527–546 (2010)
5. Bejan A, Kraus AD.: Heat Transfer Handbook. Wiley, New York (2003)
6. Sootsman, J.R., Chung, D.Y., Kanatzidis, M.G.: New and old concepts in thermoelectric materials. Angew. Chem. Int. Ed. **48**(46), 8616–8639 (2009)
7. Zhang, G.Q., Yu, Q.X., Wang, W., Li, X.G.: Nanostructures for thermoelectric applications: synthesis, growth mechanism, and property studies. Adv. Mater. **22**(17), 1959–1962 (2010)
8. Nielsch, K., Bachmann, J., Kimling, J., Bottner, H.: Thermoelectric nanostructures: from physical model systems towards nanograined composites. Adv. Energy Mater. **1**(5), 713–731 (2011)
9. Hicks, L., Dresselhaus, M.: Effect of quantum-well structures on the thermoelectric figure of merit. Phys. Rev. B **47**(19), 12727 (1993)
10. Hicks, L., Dresselhaus, M.: Thermoelectric figure of merit of a one-dimensional conductor. Phys. Rev. B **47**(24), 16631–16634 (1993)

11. Zhang, G., Yu, Q., Li, X.: Wet chemical synthesis and thermoelectric properties of V-VI one-and two-dimensional nanostructures. Dalton Trans. **39**(4), 993–1004 (2009)
12. Jin, C.G., Jiang, G.W., Liu, W.F., Cai, W.L., Yao, L.Z., Yao, Z., Li, X.G.: Fabrication of large-area single crystal bismuth nanowire arrays. J. Mater. Chem. **13**(7), 1743–1746 (2003)
13. Prieto, A.L., Martín-González, M., Keyani, J., Gronsky, R., Sands, T., Stacy, A.M.: The electrodeposition of high-density, ordered arrays of $Bi_{1-x}Sb_x$ nanowires. J. Am. Chem. Soc. **125**(9), 2388–2389 (2003)
14. Sander, M.S., Prieto, A.L., Gronsky, R., Sands, T., Stacy, A.M.: Fabrication of high-density, high aspect ratio, large-area bismuth telluride nanowire arrays by electrodeposition into porous anodic alumina templates. Adv. Mater. **14**(9), 665–667 (2002)
15. Sander, M.S., Gronsky, R., Sands, T., Stacy, A.M.: Structure of bismuth telluride nanowire arrays fabricated by electrodeposition into porous anodic alumina templates. Chem. Mater. **15**(1), 335–339 (2003)
16. Martin-Gonzalez, M., Prieto, A.L., Gronsky, R., Sands, T., Stacy, A.M.: High-density 40 nm diameter Sb-rich $Bi_{2-x}Sb_xTe_3$ nanowire arrays. Adv. Mater. **15**(12), 1003–1006 (2003)
17. Martin-Gonzalez, M., Snyder, G.J., Prieto, A.L., Gronsky, R., Sands, T., Stacy, A.M.: Direct electrodeposition of highly dense 50 nm $Bi_2Te_{3-y}Se_y$ nanowire arrays. Nano Lett. **3**(7), 973–977 (2003)
18. Lim, J.R., Whitacre, J.F., Fleurial, J.P., Huang, C.K., Ryan, M.A., Myung, N.V.: Fabrication method for thermoelectric nanodevices. Adv. Mater. **17**(12), 1488–1492 (2005)
19. Xiao, F., Yoo, B., Lee, K.H., Myung, N.V.: Electro-transport studies of electrodeposited $(Bi_{1-x}Sb_x)_2Te_3$ nanowires. Nanotechnology **18**, 335203 (2007)
20. Li, X.H., Koukharenko, E., Nandhakumar, I.S., Tudor, J., Beeby, S.P., White, N.M.: High density p-type $Bi_{0.5}Sb_{1.5}Te_3$ nanowires by electrochemical templating through ion-track lithography. Phys. Chem. Chem. Phys. **11**(18), 3584–3590 (2009)
21. Nielsch, K., Müller, F., Li, A.P., Gösele, U.: Uniform nickel deposition into ordered alumina pores by pulsed electrodeposition. Adv. Mater. **12**(8), 582–586 (2000)
22. Zhang, Y., Li, G., Wu, Y., Zhang, B., Song, W., Zhang, L.: Antimony nanowire arrays fabricated by pulsed electrodeposition in anodic alumina membranes. Adv. Mater. **14**(17), 1227–1230 (2002)
23. Peranio, N., Leister, E., Töllner, W., Eibl, O., Nielsch, K.: Stoichiometry controlled, single-crystalline Bi_2Te_3 nanowires for transport in the basal plane. Adv. Funct. Mater. **22**(1), 151–156 (2012)
24. Li, L., Zhang, Y., Li, G., Zhang, L.: A route to fabricate single crystalline bismuth nanowire arrays with different diameters. Chem. Phys. Lett. **378**(3), 244–249 (2003)
25. Li, L., Li, G., Zhang, Y., Yang, Y., Zhang, L.: Pulsed electrodeposition of large-area, ordered Bi1-x Sb x nanowire arrays from aqueous solutions. J. Phys. Chem. B **108**(50), 19380–19383 (2004)
26. Zhu, Y.G., Dou, X.C., Huang, X.H., Li, L., Li, G.H.: Thermal properties of bi nanowire arrays with different orientations and diameters. J. Phys. Chem. B **110**(51), 26189–26193 (2006)
27. Dou, X.C., Zhu, Y.G., Huang, X.H., Li, L., Li, G.G.: Effective deposition potential induced size-dependent orientation growth of Bi-Sb alloy nanowire arrays. J. Phys. Chem. B **110**(43), 21572–21575 (2006)
28. Li, L., Yang, Y.W., Huang, X.H., Li, G.H., Zhang, L.D.: Pulsed electrodeposition of single-crystalline Bi2Te3 nanowire arrays. Nanotechnology **17**(6), 1706–1712 (2006)
29. Lee, J., Farhangfar, S., Cagnon, L., Scholz, R., Gösele, U., Nielsch, K.: Tuning the crystallinity of thermoelectric Bi_2Te_3 nanowire arrays grown by pulsed electrodeposition. Nanotechnology **19**(36), 365701 (2008)
30. Muller, S., Schotz, C., Picht, O., Sigle, W., Kopold, P., Rauber, M., Alber, I., Neumann, R., Toimil-Molares, M.E.: Electrochemical synthesis of $Bi_{1-x}Sb_x$ nanowires with simultaneous control on size, composition, and surface roughness. Cryst. Growth Des. **12**(2), 615–621 (2012)

31. Picht, O., Muller, S., Alber, I., Rauber, M., Lensch-Falk, J., Medlin, D.L., Neumann, R., Toimil-Molares, M.E.: Tuning the geometrical and crystallographic characteristics of Bi_2Te_3 nanowires by electrodeposition in ion-track membranes. J. Phys. Chem. C **116**(9), 5367–5375 (2012)
32. Li, L., Xiao, Y.H., Yang, Y.W., Huang, X.H., Li, G.H., Zhang, L.D.: A facile route to fabricate single-crystalline antimony nanotube arrays. Chem. Lett. **34**(7), 930–931 (2005)
33. Li, L., Yang, Y.W., Huang, X.H., Li, G.H., Ang, R., Zhang, L.D.: Fabrication and electronic transport properties of Bi nanotube arrays. Appl. Phys. Lett. **88**(10) (2006)
34. Yang, D.C., Meng, G.W., Xu, Q.L., Han, F.M., Kong, M.G., Zhang, L.D.: Electronic transport behavior of bismuth nanotubes with a predesigned wall thickness. J. Phys. Chem. C **112**(23), 8614–8616 (2008)
35. Li, X.H., Zhou, B., Pu, L., Zhu, J.J.: Electrodeposition of Bi_2Te_3 and Bi_2Te_3 derived alloy nanotube arrays. Cryst. Growth Des. **8**(3), 771–775 (2008)
36. Pinisetty, D., Davis, D., Podlaha-Murphy, E.J., Murphy, M.C., Karki, A.B.., Young, D.P., Devireddy, R.V.: Characterization of electrodeposited bismuth-tellurium nanowires and nanotubes. Acta Mater. **59**(6), 2455–2461 (2011)
37. Pinisetty, D., Gupta, M., Karki, A., Young, D., Devireddy, R.: Fabrication and characterization of electrodeposited antimony telluride crystalline nanowires and nanotubes. J. Mater. Chem. **21**(12), 4098–4107 (2011)
38. Dou, X., Li, G., Huang, X., Li, L.: Abnormal growth of electrodeposited BiSb alloy nanotubes. J. Phys. Chem. C **112**(22), 8167–8171 (2008)
39. Lin, Y.M., Dresselhaus, M.S.: Thermoelectric properties of superlattice nanowires. Phys. Rev. B **68**(7) (2003)
40. Dou, X.C., Li, G.H., Lei, H.C.: Kinetic versus thermodynamic control over growth process of electrodeposited Bi/BiSb superlattice nanowires. Nano Lett. **8**(5), 1286–1290 (2008)
41. Xue, F.H., Fei, G.T., Wu, B., Cui, P., Zhang, L.D.: Direct electrodeposition of highly dense Bi/Sb superlattice nanowire arrays. J. Am. Chem. Soc. **127**(44), 15348–15349 (2005)
42. Yoo, B., Xiao, F., Bozhilov, K.N., Herman, J., Ryan, M.A., Myung, N.V.: Electrodeposition of thermoelectric superlattice nanowires. Adv. Mater. **19**(2), 296–299 (2007)
43. Wang, W., Zhang, G., Li, X.: Manipulating growth of thermoelectric Bi_2Te_3/Sb multilayered nanowire arrays. J. Phys. Chem. C **112**(39), 15190–15194 (2008)
44. Dou, X.C., Li, G.H., Lei, H.C., Huang, X.H., Li, L., Boyd, I.W.: Template epitaxial growth of thermoelectric Bi/BiSb superlattice nanowires by charge-controlled pulse electrodeposition. J. Electrochem. Soc. **156**(9), K149–K154 (2009)
45. Wang, W., Lu, X., Zhang, T., Zhang, G., Jiang, W., Li, X.: Bi_2Te_3/Te multiple heterostructure nanowire arrays formed by confined precipitation. J. Am. Chem. Soc. **129**(21), 6702–6703 (2007)
46. Shim, W., Ham, J., Lee, K., Jeung, W.Y., Johnson, M., Lee, W.: On-film formation of Bi nanowires with extraordinary electron mobility. Nano Lett. **9**(1), 18–22 (2009)
47. Ham, J., Shim, W., Kim, D.H., Lee, S., Roh, J., Sohn, S.W., Oh, K.H., Voorhees, P.W., Lee, W.: Direct growth of compound semiconductor nanowires by on-film formation of nanowires: bismuth telluride. Nano Lett. **9**(8), 2867–2872 (2009)
48. Kang, J., Roh, J.W., Shim, W., Ham, J., Noh, J.S., Lee, W.: Reduction of lattice thermal conductivity in single Bi-Te core/shell nanowires with rough interface. Adv. Mater. **23**(30), 3414–3419 (2011)
49. Kang, J., Shim, W., Lee, S., Roh, J.W., Noh, J.-S., Voorhees, P.W., Lee, W.: Thermodynamic-enabled synthesis of Bi/$Bi_{14}Te_6$ axial heterostructure nanowires. J. Mater. Chem. A **1**(7), 2395–2400 (2013)
50. Zhang, G., Yu, Q., Yao, Z., Li, X.: Large scale highly crystalline Bi_2Te_3 nanotubes through solution phase nanoscale Kirkendall effect fabrication. Chem. Commun. **17**, 2317–2319 (2009)

51. Zhang, G.Q., Kirk, B., Jauregui, L.A., Yang, H.R., Xu, X.F., Chen, Y.P., Wu, Y.: Rational synthesis of ultrathin n-type Bi_2Te_3 nanowires with enhanced thermoelectric properties. Nano Lett. **12**(1), 56–60 (2012)
52. Zhang, G., Fang, H., Yang, H., Jauregui, L.A., Chen, Y.P., Wu, Y.: Design principle of telluride-based nanowire heterostructures for potential thermoelectric applications. Nano Lett. **12**(7), 3627–3633 (2012)
53. Tang, C., Li, G., Dou, X., Zhang, Y., Li, L.: Thermal expansion behaviors of bismuth nanowires. J. Phys. Chem. C **113**(14), 5422–5427 (2009)
54. Xia, Y., Yang, P., Sun, Y., Wu, Y., Mayers, B., Gates, B., Yin, Y., Kim, F., Yan, H.: One-dimensional nanostructures: synthesis, characterization, and applications. Adv. Mater. **15**(5), 353–389 (2003)
55. Zhao, Y.X., Dyck, J.S., Burda, C.: Toward high-performance nanostructured thermoelectric materials: the progress of bottom-up solution chemistry approaches. J. Mater. Chem. **21**(43), 17049–17058 (2011)
56. Lin, Y.M., Sun, X.Z., Dresselhaus, M.S.: Theoretical investigation of thermoelectric transport properties of cylindrical Bi nanowires. Phys. Rev. B **62**(7), 4610–4623 (2000)
57. Zhang, Z.B., Sun, X.Z., Dresselhaus, M.S., Ying, J.Y., Heremans, J.: Electronic transport properties of single-crystal bismuth nanowire arrays. Phys. Rev. B **61**(7), 4850–4861 (2000)
58. Li, L., Yang, Y.W., Fang, X.S., Kong, M.G., Li, G.H., Zhang, L.D.: Diameter-dependent electrical transport properties of bismuth nanowire arrays. Solid State Commun. **141**(9), 492–496 (2007)
59. Cronin, S.B., Lin, Y.M., Rabin, O., Black, M.R., Ying, J.Y., Dresselhaus, M.S., Gai, P.L., Minet, J.P., Issi, J.P.: Making electrical contacts to nanowires with a thick oxide coating. Nanotechnology **13**(5), 653–658 (2002)
60. Lee, S., Ham, J., Jeon, K., Noh, J.S., Lee, W.: Direct observation of the semimetal-to-semiconductor transition of individual single-crystal bismuth nanowires grown by on-film formation of nanowires. Nanotechnology **21**(40), 405701 (2010)
61. Lin, Y.M., Rabin, O., Cronin, S., Ying, J.Y., Dresselhaus, M.: Semimetal–semiconductor transition in Bi 1-x Sb x alloy nanowires and their thermoelectric properties. Appl. Phys. Lett. **81**(13), 2403–2405 (2002)
62. Zhou, G., Li, L., Li, G.H.: Semimetal to semiconductor transition and thermoelectric properties of bismuth nanotubes. J. Appl. Phys. **109**(11) (2011)
63. Chen, C.L., Chen, Y.Y., Lin, S.J., Ho, J.C., Lee, P.C., Chen, C.D., Harutyunyan, S.R.: Fabrication and characterization of electrodeposited bismuth telluride films and nanowires. J. Phys. Chem. C **114**(8), 3385–3389 (2010)
64. Heremans, J., Thrush, C.: Thermoelectric power of bismuth nanowires. Phys. Rev. B **59**(19), 12579 (1999)
65. Lee, J., Kim, Y., Cagnon, L., Gösele, U., Nielsch, K.: Power factor measurements of bismuth telluride nanowires grown by pulsed electrodeposition. physica status solidi (RRL)-Rapid. Res. Lett. **4**(1–2), 43–45 (2010)
66. Munoz Rojo, M., Grauby, S., Rampnoux, J.-M., Caballero-Calero, O., Martin-Gonzalez, M., Dilhaire, S.: Fabrication of Bi_2Te_3 nanowire arrays and thermal conductivity measurement by 3ω-scanning thermal microscopy. J. Appl. Phys. **113**(5), 054308-054308-054307 (2013)
67. Biswas, K.G., Sands, T.D., Cola, B.A., Xu, X.: Thermal conductivity of bismuth telluride nanowire array-epoxy composite. Appl. Phys. Lett. **94**(22), 223116-223116-223113 (2009)
68. Harman, T., Cahn, J., Logan, M.: Measurement of thermal conductivity by utilization of the Peltier effect. J. Appl. Phys. **30**(9), 1351–1359 (1959)
69. Menke, E.J., Brown, M.A., Li, Q., Hemminger, J.C., Penner, R.M.: Bismuth telluride (Bi_2Te_3) nanowires: synthesis by cyclic electrodeposition/stripping, thinning by electrooxidation, and electrical power generation. Langmuir **22**(25), 10564–10574 (2006)
70. Keyani, J., Stacy, A.M., Sharp, J.: Assembly and measurement of a hybrid nanowire-bulk thermoelectric device. Appl. Phys. Lett. **89**, 233106 (2006)

71. Shi, L., Li, D., Yu, C., Jang, W., Kim, D., Yao, Z., Kim, P., Majumdar, A.: Measuring thermal and thermoelectric properties of one-dimensional nanostructures using a microfabricated device. J. Heat Transf. **125**(5), 881–888 (2003)
72. Boukai, A., Xu, K., Heath, J.R.: Size-dependent transport and thermoelectric properties of individual polycrystalline bismuth nanowires. Adv. Mater. **18**(7), 864–869 (2006)
73. Zhou, J., Jin, C., Seol, J.H., Li, X., Shi, L.: Thermoelectric properties of individual electrodeposited bismuth telluride nanowires. Appl. Phys. Lett. **87**(13), 133109-133109-133103 (2005)
74. Mavrokefalos, A., Pettes, M.T., Zhou, F., Shi, L.: Four-probe measurements of the in-plane thermoelectric properties of nanofilms. Rev. Sci. Instrum. **78**(3), 034901-034901-034906 (2007)
75. Mavrokefalos, A., Moore, A.L., Pettes, M.T., Shi, L., Wang, W., Li, X.: Thermoelectric and structural characterizations of individual electrodeposited bismuth telluride nanowires. J. Appl. Phys. **105**(10), 104318-104318-104318 (2009)
76. Zuev, Y.M., Lee, J.S., Galloy, C., Park, H., Kim, P.: Diameter dependence of the transport properties of antimony telluride nanowires. Nano Lett. **10**(8), 3037–3040 (2010)
77. Moore, A.L., Pettes, M.T., Zhou, F., Shi, L.: Thermal conductivity suppression in bismuth nanowires. J. Appl. Phys. **106**(3), 034310-034310-034317 (2009)
78. Roh, J.W., Hippalgaonkar, K., Ham, J.H., Chen, R., Li, M.Z., Ercius, P., Majumdar, A., Kim, W., Lee, W.: Observation of anisotropy in thermal conductivity of individual single-crystalline bismuth nanowires. ACS Nano **5**(5), 3954 (2011)
79. Vineis, C.J., Shakouri, A., Majumdar, A., Kanatzidis, M.G.: Nanostructured thermoelectrics: big efficiency gains from small features. Adv. Mater. **22**(36), 3970–3980 (2010)

Chapter 8
Cerium-, Samarium-, Holmium-Doped $Bi_{88}Sb_{12}$

Cyril P. Opeil and Kevin C. Lukas

Abstract $Bi_{88}Sb_{12}$ alloy has been doped with 0, 0.066, 0.66, 1.32, and 3.91 % Sm and prepared under two different fabrication conditions. The first being ball milled for 12 h and hot pressed at 240 °C and the second ball milled for 6 h and hot pressed at 200 °C. The results are in agreement with previously studied Ce and Ho samples prepared under similar conditions. A slight ZT enhancement is seen due to doping which is an effect of an enhanced Seebeck coefficient as a result of a decrease in the carrier concentration. The enhancement does not appear to be caused by the magnetic moments of Ce, Sm, and Ho based on the similar change to the gap size with the widely varying magnetic moments of the dopants. In addition, lattice thermal transport in these materials was investigated experimentally and theoretically where phonon dispersions were obtained from first principle calculations, and semiclassical models were used to calculate phonon lifetimes. We have not observed a strong thermal conductivity dependence on the type of the impurity.

8.1 Introduction

This chapter discusses the electrical and thermal transport properties of Sm-doped $Bi_{88}Sb_{12}$. Similar studies were done with the addition of both Ce and Ho and show comparable effects on the transport properties.

Bismuth–antimony alloys have long been noted for their beneficial thermoelectric properties below room temperature since the initial measurements by Smith and Wolf [1, 2]. Thus far they have the highest figure of merit, *ZT*, below 200 K making them the best candidate for the n-type leg of thermoelectric refrigeration devices [3].

C.P. Opeil (✉) • K.C. Lukas
Department of Physics, Boston College, Chestnut Hill, MA 02467, USA
e-mail: opeil@bc.edu; lukaske@bc.edu

X. Wang and Z.M. Wang (eds.), *Nanoscale Thermoelectrics*, Lecture Notes in Nanoscale Science and Technology 16, DOI 10.1007/978-3-319-02012-9_8,
© Springer International Publishing Switzerland 2014

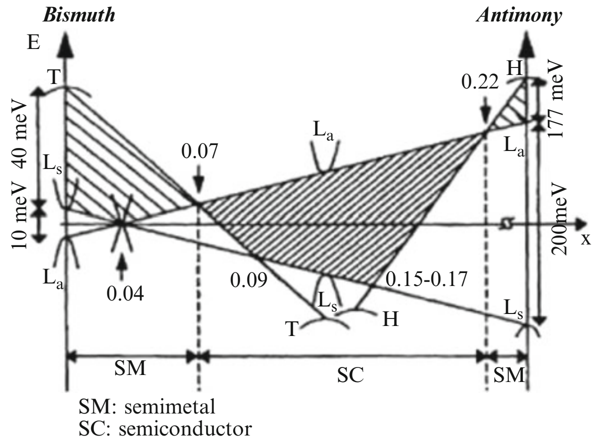

Fig. 8.1 Depiction of energy band structure near the Fermi level for bulk $Bi_{1-x}Sb_x$ alloys at 0 K [4]

As group V semimetals bismuth and antimony form a solid solution over the entire composition range leading to many interesting physical features [4]. Lenoir et al. described in detail the changes in electronic band structure depending on the antimony content for $Bi_{1-x}Sb_x$ alloys [4]. The band structure for bulk $Bi_{1-x}Sb_x$ is shown in Fig. 8.1. The solid solution is semimetallic when the Sb concentration is $x < 0.07$ and $x > 0.22$, while the alloy is semiconducting inside the region $0.07 < x < 0.22$ [4–9]. The best thermoelectric properties are found for single crystals, with $0.09 < x < 0.16$, when measured parallel to the trigonal axis [4, 10, 11]. The very small bandgap in the semiconducting region, specifically the direct energy gap at the L point, along with the quasi-ellipsoidal electron Fermi surface leads to small electron effective masses, high electron mobilities, and a non-parabolic dispersion relation [3]. The small direct energy gap at the L point leads to the dependence of the band structure on many different physical parameters including alloy composition [5, 12, 13], temperature [14], magnetic field [15, 16], and pressure [17, 18].

Single crystals exhibit the best transport properties, but they are difficult to grow and are mechanically weak making them unlikely candidates for commercial use. Several techniques for synthesizing polycrystalline BiSb have been studied, but none demonstrate a higher value for *ZT* than single crystals. These methods include arc plasma [19], quenching [10], mechanical alloying [20], powder metallurgy [21], and doping [22, 23]. Devaux et al. [19] studied the effects of grain size on the thermoelectric properties, specifically investigating the decrease of the lattice component of the thermal conductivity with the reduction of grain size. While the thermal conductivity was reduced due to phonon scattering, there was no benefit to *ZT* due to increased resistivity, as has also been seen in nanosized grains [24, 25]. Though it was initially thought that doping BiSb alloys would not enhance the transport properties, it was demonstrated in a few previous studies that doping impurities into BiSb can be another method for *ZT* enhancement [26].

We doped Ce, Sm, and Ho into $Bi_{88}Sb_{12}$ to study the effects of introducing a magnetic impurity into BiSb alloys [27]. While the ultimate goal was to study the

magnetotransport properties, a slight enhancement was discovered in zero magnetic field. As mentioned above the band structure of BiSb alloys is very sensitive to different physical parameters, and changes at low temperatures have been interpreted as arising from lattice distortion as well as from varying spin–orbit interactions that arise from alloying [4]. Both Ho and Ce have a relatively large magnetic moment which could affect the spin–orbit interaction and therefore the band structure leading to enhanced transport properties. Samarium has a smaller magnetic moment while having an ionic mass in between that Ho and Ce. Therefore any difference in transport properties due to the differences in magnetic moment should be readily noticeable. The present study includes Sm-doped $Bi_{88}Sb_{12}$ alloys synthesized under similar conditions and doping percentages for both Ho- and Ce-doped $Bi_{88}Sb_{12}$. The data for the Ce- and Ho-doped samples are similar to the Sm samples prepared under the same fabrication conditions.

8.2 Experimental

Nano-polycrystalline $Bi_{88}Sb_{12}$ samples were prepared by ball milling and dc hot-pressing techniques described previously [27]. Two sets of samples were prepared using elemental chunks of bismuth (Bi) (99.99 %, Alfa Aesar), antimony (Sb) (99.99 %, Alfa Aesar), samarium (Sm) (99.9 %, Alfa Aesar), cerium (Ce) (99.9 %, Alfa Aesar), and holmium (Ho) (99.9 %, Alfa Aesar) according to the atomic composition $Bi_{88}Sb_{12}Ce_y$ ($y = 0$, 0.07, 0.7, and 4.2), $Bi_{88}Sb_{12}Sm_y$ ($y = 0$, 0.066, 0.66, 1.32, and 3.93), and $Bi_{88}Sb_{12}Ho_y$ ($y = 0$, 1, and 3). One set of Sm samples was prepared, identically to the Ho-doped samples, by ball milling elemental chunks with the proper stoichiometric ratio for 12 h to form a powder which was hot pressed at 240 °C, thereby creating a disk approximately 4 mm thick and 12 mm in diameter. For simplicity these samples are labeled 0.06Sm, 0.6Sm, 1Sm, and 3Sm. The second set of samples was prepared, just as the Ce-doped samples, by melting the constituent elements in quartz tubes for 6 h at 450 °C and then quenching the solution in water to form an ingot. The ingot was then placed in a high-energy ball mill for 6 h and then pressed at a temperature of 200 °C.

From the pressed disks, two samples were cut to measure the thermoelectric properties where all transport properties were measured perpendicular to the pressing direction (parallel to the disk face). Samples cut in dimensions $2 \times 2 \times 4$ mm were then polished, chemically etched in a bromine solution, and metallic contacts were sputtered onto the faces. Gold-coated oxygen-free high conductivity (OFHC) copper disks provided by quantum design were soldered to the sputtered metallic contacts. Thermoelectric transport properties including the Seebeck coefficient (S), electrical resistivity (ρ), and thermal conductivity (κ) were measured in the standard two-probe method, from 5 to 350 K using the thermal transport option of the physical property measurement system (PPMS) from quantum design (QD). A second sample was used to determine the Hall coefficient (R_H). The Hall coefficient was also determined using the PPMS under a magnetic field of 9 T

and a current of 20 mA. The Hall samples were rotated 180° in field using the QD-PPMS AC rotator option, thereby averaging out any anomalous effects on the measurement due to the field. Platinum wires (2 mil) were spark welded to the Hall samples, with typical dimensions of $1 \times 2 \times 11$ mm, in a five-wire configuration. The carrier concentration (n) was determined directly from the Hall coefficient using the relation $R_H = 1/nq$ where q is the electronic charge. Resistivity was measured using a standard four-point probe technique, with the same sample and orientation used to attain the Hall coefficient, and Hall mobility (μ_H) was calculated from R_H/ρ. X-ray diffraction was performed (Bruker AXS) to ensure that the powders were alloyed into a single phase, and SEM (JEOL 7001 F) images were taken from freshly fractured surfaces to observe the effects of grain growth during pressing. The magnetic susceptibility (χ) was measured in a magnetic field of 0.1 T using a vibrating sample magnetometer (VSM) in the PPMS by our collaborators at the National Magnet Lab in Florida and Los Alamos National Laboratory. The lattice portion of the thermal conductivity was measured directly using a classically large magnetic field to completely suppress the electronic portion of κ, as previously described [37].

8.3 Discussion

Sm-doped samples were prepared at various doping concentrations and through both fabrication methods. The 240 °C hot-pressed samples will be discussed in detail in this chapter, and it can be shown that the data matches quite well with the similarly prepared Ho-doped samples. Second the transport properties of the 200 °C hot-pressed samples can be shown to correlate well with what was seen in the study of Ce-doped $Bi_{88}Sb_{12}$. A qualitative analysis similar to that used previously will be given since both the non-parabolic energy-momentum dispersion relation and the narrow bandgap make a quantitative analysis of the transport properties of BiSb alloys very difficult [3, 4].

Figure 8.2 shows the XRD pattern for the samples hot pressed at 240 °C and demonstrates that the material is single phase within the resolution of the system. SEM images are shown in Fig. 8.3 where it is seen that all doping concentrations, other than 3Sm, have similar grain sizes. The highest doping concentration has a much different microstructure where the grains appear to be much smaller. This difference was also seen in the highest percentage of the Ce-doped samples [28]. The difference at the highest doping concentration could be due to the low solubility of Sm in Bi, based on the Bi-Sm phase diagram; therefore, it is reasonable that the solubility would be low in the Bi-rich alloy $Bi_{88}Sb_{12}$.

The magnetic susceptibility of the Ce- and Ho-doped samples is plotted against temperature in Fig. 8.4. The magnetic susceptibility is measured to ensure that the proper ratio of magnetic impurities is, in fact, in the sample. Problems arose in the VSM with our collaborators when trying to measure the Sm samples; based on the results of the Ce and Ho samples shown in Fig. 8.4 and the similarity between

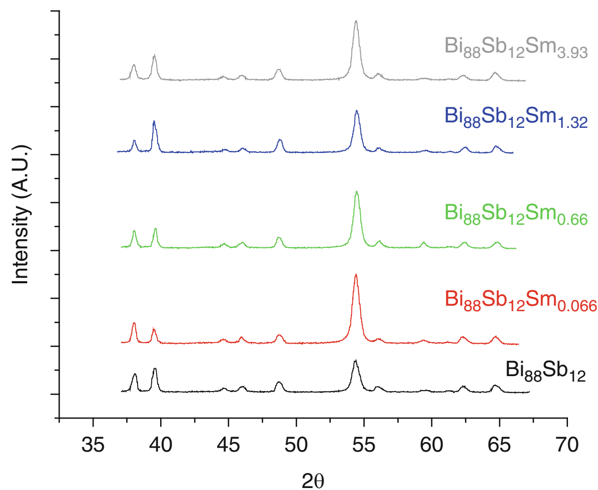

Fig. 8.2 XRD patterns for all Sm-doped samples. Data show that the samples are single phase and alloyed similarly within the resolution of the machine

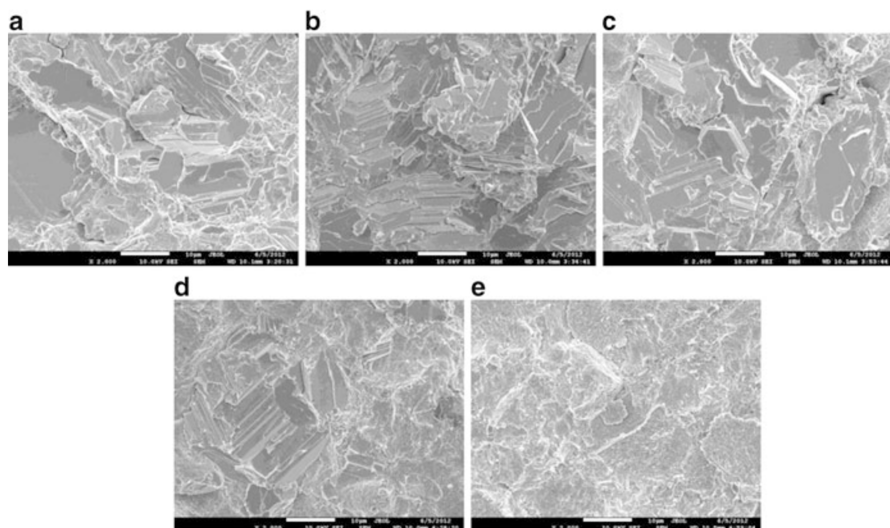

Fig. 8.3 SEM images for samples $Bi_{88}Sb_{12}$ (**a**), 0.06Sm (**b**), 0.6Sm (**c**), 1Sm (**d**), and 3Sm (**e**)

the Ce-Bi, Sm-Bi, and Ho-Bi phase diagrams, it is reasonable to assume as a first approximation that the intended percentage of Sm actually was incorporated into the sample. BiSb is typically diamagnetic; however, it can be seen that the values for χ in Fig. 8.4 are in fact positive demonstrating that the sample is paramagnetic. The shift to paramagnetism is due to the increased number of free carriers; as discussed below, free electrons are known to enhance paramagnetism [29]. The susceptibility is found to increase with increasing Ce and Ho doping concentration, as is expected from the introduction of magnetic impurities, demonstrating that Ce

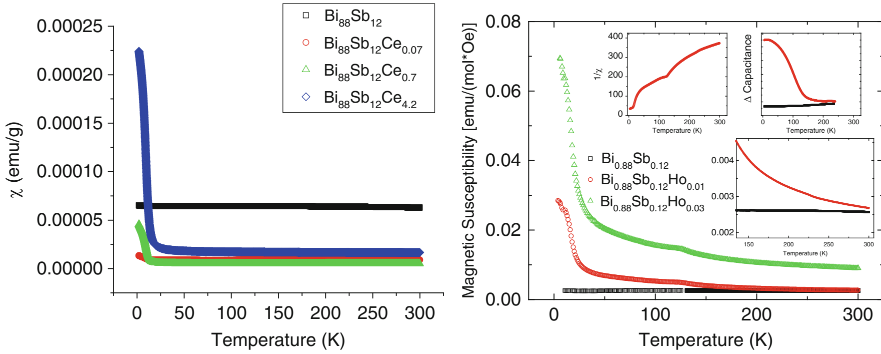

Fig. 8.4 Magnetic susceptibility plotted against temperature for Ce-doped (*left*) and Ho-doped (*right*) $Bi_{88}Sb_{12}$. The *insets of the right figure* show the nonlinearity of $1/\chi$ vs. T as well as measurements made using a homemade torque cantilever magnetometer

and Ho are in fact assimilated into the solid solution. High enough temperatures could not be reached to perform an accurate Curie–Weiss fit for the magnetic susceptibility. However, it is interesting to note that we can still fit the data, though inaccurately, using the Curie–Weiss expression [29]:

$$\chi = \chi_m + \frac{C}{\theta - T} \tag{8.1}$$

where χ_m is the diamagnetic susceptibility, θ is the Curie temperature, T is the absolute temperature, and C is a constant dependent upon the atomic mass of the magnetic impurity, the total J spin state, and concentration of magnetic impurities in the sample. The atomic mass is constant, and the value for J should remain unchanged, leading C to depend only on the impurity concentration. If Fig. 8.4 is fit using (8.1), the values for C can be calculated. While the fit is poor ($1/\chi$ vs. T is nonlinear), the value for C scales with the Ce and Ho impurity concentration. This observation gives confidence that these impurities are not only assimilating into the BiSb solid solution but also being incorporated in the solid solution according to the desired atomic ratios.

Electrical resistivity values for all samples are plotted versus temperature in Fig. 8.5. From 5 K to approximately 100–200 K (depending on doping concentration), values of ρ for all samples, except 3Sm, increase with increasing temperature. This typical metallic-like behavior is due to an impurity band located in the conduction band; this impurity band has been experimentally measured and described by Lenoir et al. [3, 4]. The impurity density dominates ρ values up to a maximum at which point the temperature becomes high enough to excite carriers from the valence band to the conduction band across the thermal energy gap [4]. In this regime the intrinsic carrier concentration begins to dominate and all samples exhibit classical semiconducting behavior.

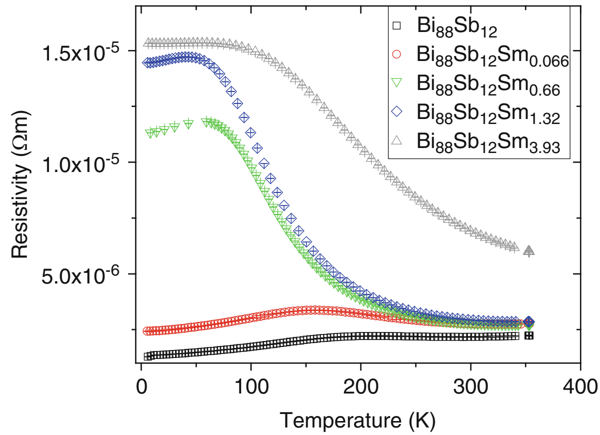

Fig. 8.5 Resistivity plotted vs. temperature for all Sm-doped samples

Table 8.1 Estimated thermal energy gap, E_g, using (8.2) for Ce, Sm, and Ho doped samples under different fabrication conditions for ball milling (BM) time and hot pressing (HP) temperature

Doping %	0 Sm	0.066 Sm	0.66 Sm	1.32 Sm	3.93 Sm	0 Sm	.066 Sm	.66 Sm	1.32 Sm	3.93 Sm	0 Ce	.07 Ce	.7 Ce	34.2 Ce	0 Ho	1 Ho	3 Ho
BM (hours)	12	12	12	12	12	6	6	6	6	6	6	6	6	6	12	12	12
HP (°C)	240	240	240	240	240	200	200	200	200	200	200	200	200	200	240	240	240
E_g(meV)	-	17	40	40	47	-	40	47	44	45	32	41	42	44	30	40	47

Values for ρ increase as the doping concentration is increased. Using a similar analysis to that of Lenoir, the thermal energy gap can be estimated using Arrhenius' law [4]:

$$\rho = \rho_o \exp\left(-\frac{\Delta E_g}{2k_B T}\right) \tag{8.2}$$

where ρ_o is the zero temperature resistivity, k_B is Boltzmann's constant, T is the absolute temperature, and ΔE_g is the thermal gap size. Table 8.1 includes gap sizes from Sm samples as well as the previously studied Ho and Ce samples. It should be noted that the energy gaps for the parent compounds of both the Ce- and Ho-doped samples, 32 meV, are in agreement with previously determined gap sizes for similar stoichiometries [3, 4]. The parent compounds for the Sm-doped samples, however, exhibit more semimetallic behavior and have a negligible gap size. One possible explanation is that the sample is slightly off the desired $Bi_{88}Sb_{12}$ stoichiometry, and, as previously discussed, the band structure of BiSb is highly dependent on Sb concentration [5, 12, 13]. In the present study, it is the relative change that is important, and for that reason each independently prepared set of

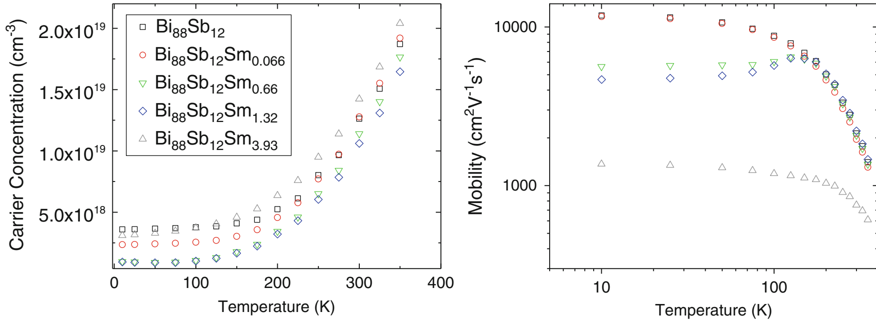

Fig. 8.6 Carrier concentration (*left*) and carrier mobility (*right*) for all Sm-doped samples plotted against temperature

samples (Ho, Ce, Sm) are doped from the same initial batch and the parent for each set is always measured. The addition of the smallest amount of Sm increases the gap size, and the energy gap is further increased with increasing Sm doping, reaching a maximum value of 47 meV for sample 3Sm. Similar results are found for both the Ce- and Ho-doped samples as shown in Table 8.1.

The Hall coefficient is negative for all samples over the entire temperature range, signifying that the dominant carriers are electrons. The carrier concentrations and mobilities plotted in Fig. 8.6 are in agreement with the impurity band model. The carrier concentration values are relatively constant at lower temperatures, where charge transfer is dominated by an impurity band, and the carrier density due to impurities should be independent of temperature. At higher temperatures $k_B T$ is near the energy required to excite carriers from the valence to the conduction band, and electronic conduction is due to both electrons and holes in this intrinsic region of the semiconductor, where values for ρ begin to decrease as the temperature is increased. In the intrinsic region the single-carrier expression for the Hall coefficient, $R_H = 1/nq$, is no longer valid and must be replaced by the two-carrier expression $R_H = 1/(n + p)q$ [30]. The carrier concentration is much higher than previously reported values for single crystals at low temperatures [31] which leads to positive χ values as discussed above. The carrier concentration is slightly decreased with the addition of 0.066 % Sm doping and further decreased with 0.66 % and slightly further with 1.32 % Sm addition. The widening of the bandgap explains the decrease in carrier concentration. Sample 3Sm has a carrier concentration slightly greater than the parent compound which is due to the fact that there is an increased number grain boundaries, as seen in Fig. 8.3, and this increase in grin boundaries leads to an increased number of carriers [34].

The magnitude of the mobility at lower temperature is very high due to the non-parabolic band structure and quasi-ellipsoidal Fermi surfaces of Bi-rich BiSb alloys [4]. From lower temperature, in the metallic-like regime, the mobility slightly decreases as the temperature increases, which leads to increasing values for ρ with T. The mobility is unchanged by the addition of 0.066 % Sm and decreased by the addition of 0.66 and 1.32 % Sm. The introduction of 3.93 % Sm drastically reduces the mobility which could be due to both increased

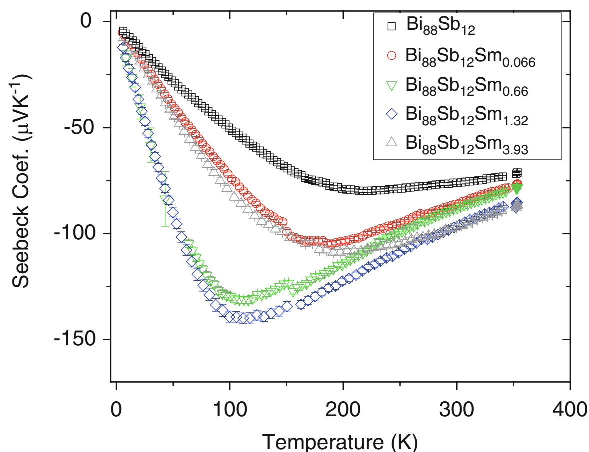

Fig. 8.7 Seebeck coefficient for all Sm-doped samples plotted against temperature

electron–electron interactions from the higher carrier concentration as well as the decreased carrier mean free path due to the smaller grain sizes as seen in the SEM images. It is interesting to note that there is a slight peak in the μ_H versus T plot for samples 0.6Sm and 1Sm, which could be an evidence of a change in the scattering parameter since μ_H is proportional to T^{s-1} where s is the scattering parameter. Another possible explanation for the peak in the mobility, which is found in the temperature range where the electrical conduction is intrinsic, is that there is a slight alteration of the band structure due to the Sm doping; as shown in Table 8.1 the gap size increases with increasing Sm doping. It is possible that initially only highly mobile carriers from the L valence band [4] contribute to electrical transport, and then as the temperature rises above 175 K the other heavier valence H and T bands [4] begin to contribute holes leading to identical mobility values as the parent compound. There are identical peaks in the optimally doped Ho and Ce $Bi_{88}Sb_{12}$ [27, 28].

The Seebeck coefficient versus temperature is plotted in Fig. 8.7 and is negative over the entire temperature range, confirming that electrons are the dominant carriers. The data qualitatively agrees quite well with the impurity band model. At lower temperatures the thermopower for all samples varies linearly with T which is typical of a degenerate system and is expected based on the metallic-like temperature dependence of the resistivity. The Seebeck coefficient increases with decreasing carrier concentration as the doping concentration is altered from 0.06Sm to 1Sm, typical of diffusive transport. As the temperature increases, carriers from the valence band are excited into the conduction band and the intrinsic semiconducting properties begin to dominate leading to a maximum in the S vs. T plot. While in the intrinsic region the electrical conductivity can be written as the simple sum of the hole and electron conductivities, the Seebeck coefficient is given as

$$S = \frac{S_h \sigma_h + S_e \sigma_e}{S_h + S_e} \tag{8.3}$$

Fig. 8.8 Thermal conductivity for all Sm-doped samples plotted against temperature

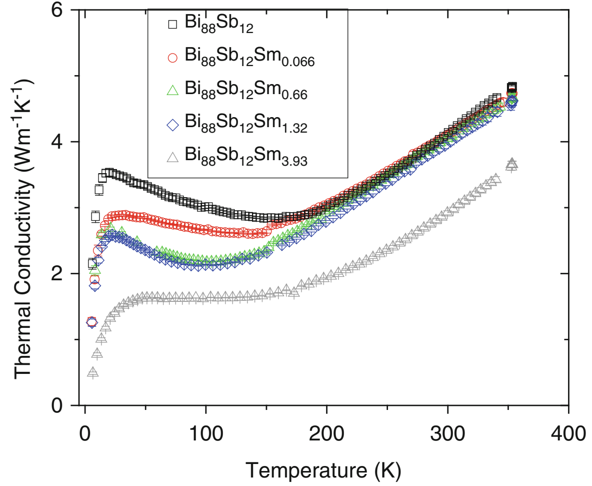

where S_h and S_e are the hole and electron contributions to the Seebeck coefficient and σ_h and σ_e are the hole and electron contributions to the electrical conductivity, respectively. The fact that S remains negative even at higher temperatures is evidence that the hole conductivity is not the dominant contribution to the total electrical conductivity; this is in agreement with previous studies which demonstrate that the hole mobilities are much lower in alloyed BiSb than in pure Bi [4].

The temperature dependence of the total thermal conductivity (κ_{total}) is plotted in Fig. 8.8 for all samples where κ_{total} decreases with increasing Sm doping concentration due to the Sm atoms scattering phonons, and for sample 3Sm the reduction in κ is due to the increased number of grain boundaries as well. The total thermal conductivity is given by the sum of the individual contributions from the lattice and the carriers. For semiconducting materials the carrier contribution is given by the sum of both unipolar and bipolar terms [32]. Therefore κ_{total} can be written as [32]

$$\kappa_{total} = \kappa_\iota + \kappa_e + \kappa_b \tag{8.4}$$

where κ_ι, κ_e, and κ_b are the lattice, electronic, and bipolar thermal conductivities, respectively. The total thermal conductivity rises from lower temperatures up to a maximum at around 20 K and then decreases down to a minimum before rising again as temperature continues to increase. The maximum at lower temperatures is typical of the interplay between different phonon scattering mechanisms [33]. The increase in κ_{total} at higher temperatures is due to the bipolar contribution and can be seen to occur at the same temperature at which the magnitude of the Seebeck coefficient begins to decrease.

ZT is plotted in Fig. 8.9 for all Sm-doped samples, and *ZT* increases with increasing Sm doping for all samples except 3Sm. The enhancement comes from the slight decrease in thermal conductivity as well as the increased Seebeck coefficient which is a result of the decreased carrier concentration. Sample 3Sm

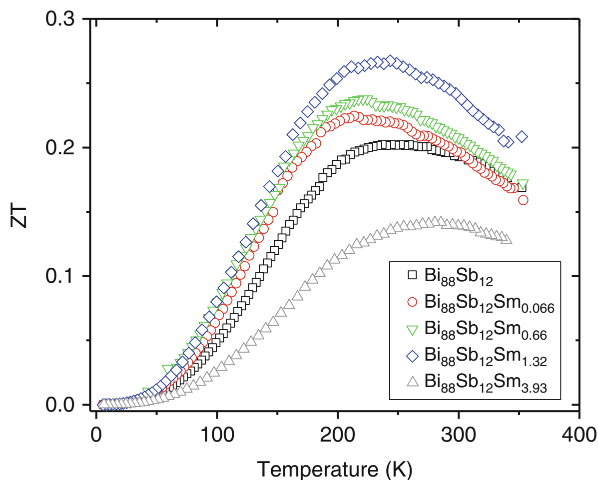

Fig. 8.9 *ZT* for all Sm-doped samples plotted against temperature

has a *ZT* value that is drastically lower than all samples which is completely due to the reduced mobility which both increases ρ and decreases S.

Figure 8.10 plots all transport data for the Sm-doped samples prepared via ball milling for 6 h and hot pressing at 200 °C. The results are similar to the Sm samples that were ball milled for 12 h and presented in Figs. 8.2, 8.3, 8.4, 8.5, 8.6, 8.7, 8.8, and 8.9 and can be analyzed in the same manner. The electrical resistivity, shown in Fig. 8.10a, increases with increasing Sm concentration; the largest change in the resistivity is due to the lowest doping concentration. Figure 8.10b plots the temperature dependence of the Seebeck coefficient where the largest enhancement in the magnitude of S is due to the lowest doping concentration along with a shift in the peak of S to lower temperature. The total thermal conductivity is plotted in Fig. 8.10c and is seen to decrease with increasing Sm doping. The overall effect on *ZT* is plotted in Fig. 8.10d where there is a slight enhancement at the lower doping concentrations based on the enhancement in S and reduction in κ_{total}. The main difference between the two sets of Sm samples lies in that the transport properties are most drastically changed by the lowest doping concentration for the 200 °C hot-pressed samples.

The results in Fig. 8.10 are identical to those of the Ce-doped samples prepared under the same conditions [28], while the results for the Sm-doped samples prepared by ball milling for 12 h and hot pressing at 240 °C are the same as the Ho-doped samples [27]. The difference in the transport properties between the two different preparation methods is most likely due to the difference in ball milling time. It is known that high-energy ball milling enhances the solubility of materials [34]. Also, there is no solubility at room temperature of Ce, Ho, and Sm in Bi according to the phase diagrams. It is likely that Bi-rich $Bi_{88}Sb_{12}$ will have a solubility close to that of pure Bi, and therefore it is reasonable that the transport properties are enhanced at a higher doping concentration with longer ball milling times.

The present study of Ce-, Sm-, and Ho-doped $Bi_{88}Sb_{12}$ shows similar enhancements in thermoelectric transport properties. From the current study it is believed

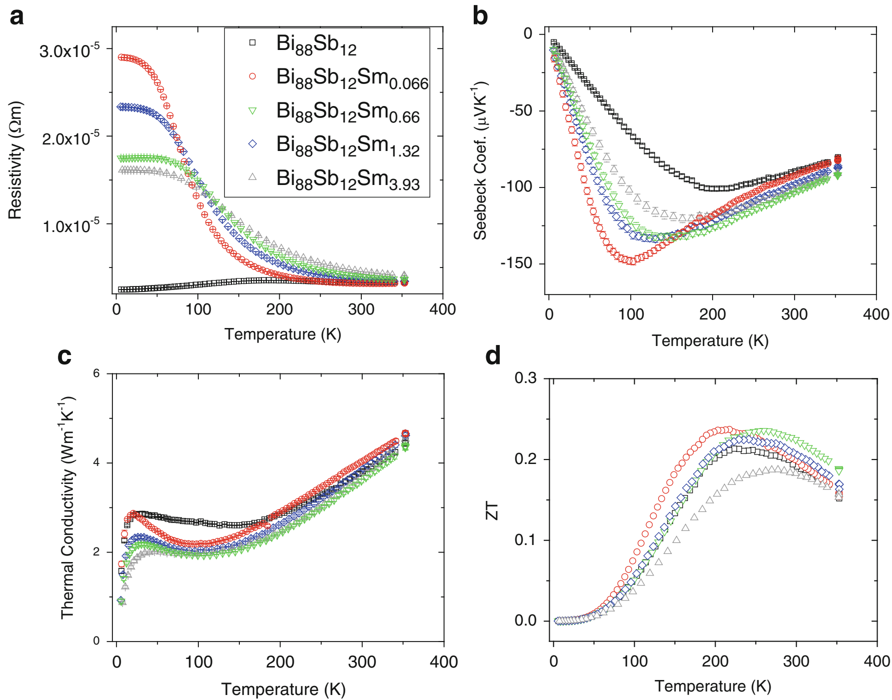

Fig. 8.10 The temperature dependence of the resistivity (*top left*), Seebeck coefficient (*top right*), thermal conductivity (*bottom left*), and *ZT* (*bottom right*) for all Sm-doped samples prepared at a hot pressing temperature of 200 °C

that the differences in the effects of doping percentage are due to the difference in ball milling times. As mentioned previously Ce, Sm, and Ho all have quite different magnetic moments with effective Bohr magneton moments of 2.4, 1.5, and 10.4, respectively [35]. The fact that the transport properties are all similarly affected seems to lead to the conclusion that it is not the magnetic moment that is responsible for this enhancement. Fe has a similar moment to that of Ce and was also doped into the $Bi_{88}Sb_{12}$ alloy. While the resistivity increases, there is no enhancement of the Seebeck coefficient which further confirms that the change in transport properties is not due to the magnetic moments of the impurities. From this study it seems probable that the changes seen in the Ce-, Sm-, and Ho-doped samples are due to some other effect, likely a mass effect, though further investigation is required.

8.4 Separation of κ_{lattice} and κ_{carrier}

At lower temperatures, T < 100 K, the bipolar contribution is negligible and κ_{total} is the sum of κ_{carrier} and κ_{lattice}. Because the mobility is so high in BiSb alloys, the condition for a classically large magnetic field $\mu B >> 1$ is satisfied for an

experimentally accessible magnetic field of 9 T, and $\kappa_{carrier}$ and $\kappa_{lattice}$ can be separated using a magnetic field. This technique, described in detail previously [37], is used to directly measure κ_l below 100 K. At higher temperatures, due to large electron–phonon coupling and low electron mobility, it is challenging to separate the contributions of the electrons and phonons. The data are fitted using a methodology which is previously described by Zebarjadi et al. [36]. The model uses the full phonon dispersion calculated from first principles and combines that with phenomenological models to calculate phonon lifetimes. We have discussed before that such modeling is advantageous to Debye-type modeling and gives more reliable estimation of the phonon mean free path. For the phonon dispersion of the BiSb alloy, first principle and virtual crystal approach were used. First, we calculated force-displacement data in 4 × 4 × 4 supercells of pure Bi and Sb using ABINIT package [38]. Because of strong spin–orbit interaction in Bi and Sb, spin–orbit interaction was included with HGH pseudopotential [39]. Convergence of the results with respect to supercell size, cutoff energy (15 Ha), and k mesh (4 × 4 × 4) was carefully checked. Then, harmonic force constants of pure Bi and Sb were extracted from the force-displacement data sets [40]. Finally, using the virtual crystal approximation, harmonic force constants in BiSb alloy were obtained by interpolating harmonic force constants in pure Bi and Sb [41]. The group velocities (v) were calculated from the dispersion, and they were used to estimate the phonon lifetimes. Three scattering mechanisms are included to calculate the frequency-dependent relaxation times including phonon–phonon scattering (τ_{ph}) [42], boundary scattering (τ_{BC}), and isotope or mass fluctuation scattering (τ_{iso}) [43]:

$$\tau^{-1} = \tau_{BC}^{-1} + \tau_{iso}^{-1} + \tau_{ph}^{-1} = \frac{v}{l_g} + Ax^4T^4 + Bx^2T^2\exp\left(\frac{\theta_D}{2T}\right); x = \frac{\hbar\omega}{k_B T} \tag{8.5}$$

where l_g is the average grain size, k_B is the Boltzmann constant, and A and B are fitting parameters representing the impurity scattering strength and the phonon–phonon coupling, respectively.

Figure 8.11 plots the lattice thermal conductivity as a function of temperature along with the different phonon scattering mechanisms for both the parent compound as well as sample 1Sm. From the plot it is seen that for both samples grain boundary scattering dominates at lower temperatures (T < 10 K) while phonon scattering is dominant at much higher temperatures (T > 100 K). In most of the relevant temperature range (10 < T < 90 K) the impurity scattering from the parent atom is dominant. This is the main reason why the lattice thermal conductivity is not sensitive to the additional dopants. In fact the parent BiSb has too many defects and impurities in it so that the additional dopants only increase the impurity level slightly, resulting in a minor change in the thermal conductivity. The minor change is still visible; note that Fig. 8.11 has logarithmic axis. Refer to Fig. 8.8 for comparing the effect. We found that by slightly changing the impurity scattering strength, we can explain the results for different Sm dopants. This is plotted in Fig. 8.12. Theoretical fits have been shown with solid lines. Numbers in front of the theory indicate the relative strength of the impurity scattering taking the first fit as one.

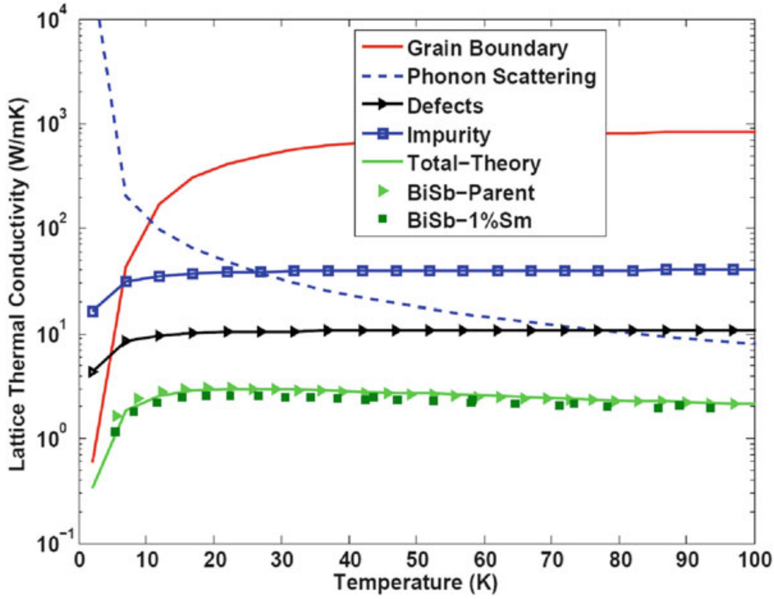

Fig. 8.11 Temperature dependence of the lattice thermal conductivity plotted along with the different phonon scattering mechanisms

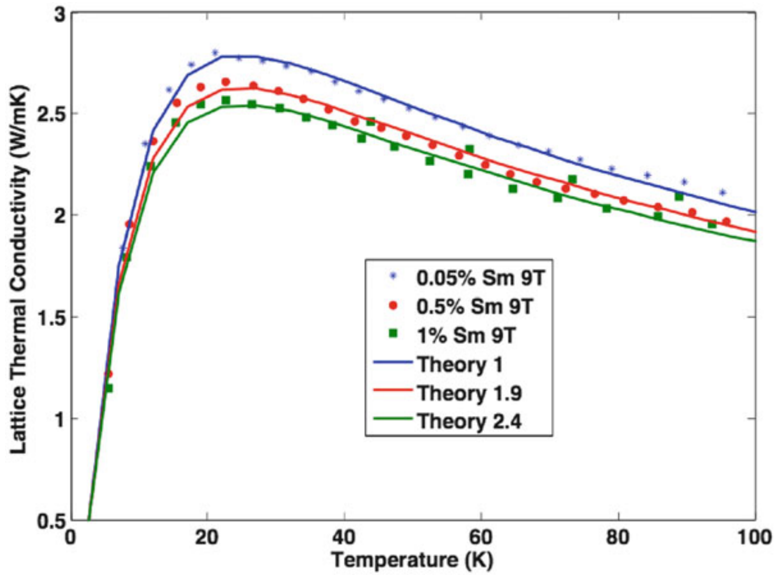

Fig. 8.12 Theoretical fits to thermal conductivity data

Again, the numbers are not directly proportional to the Sm impurity concentration because of the presence of background impurities originally presented in the BiSb parent sample. Results are similar for both the Ce- and Ho-doped samples and are therefore not shown.

8.5 Conclusion

The $Bi_{88}Sb_{12}$ alloy has been doped with 0, 0.066, 0.66, 1.32, and 3.93 % Sm and prepared under two different fabrication conditions, the first being ball milled for 12 h and hot pressed at 240 °C and the second being ball milled for 6 h and hot pressed at 200 °C. The results are in agreement with Ce and Ho samples prepared under similar conditions. A slight *ZT* enhancement is seen due to doping which is the effect of an enhanced Seebeck coefficient as a result of a decrease in the carrier concentration, most likely caused by a widening bandgap. The alteration of the bandgap does not appear to be caused by the magnetic moments of Ce, Sm, and Ho based on the similar change to the gap size with the widely varying magnetic moments of the dopants.

Acknowledgements We gratefully acknowledge funding for this work through the "Solid State Solar-Thermal energy conversion Center (S3TEC)," an energy frontier research center founded by the US Department of Energy, Office of Basic Energy Science, under award number DE-SC0001299/DE-FG02-09ER46577.

References

1. Smith, G.E., Wolfe, R.: J. Appl. Phys. **33**, 84 (1962)
2. Wolfe, R., Smith, G.E.: Appl. Phys. Lett. **1**, 5 (1962)
3. Lenoir, B., Cassart, M., Michenaud, J.P., Scherrer, H., Scherrer, S.: J. Phys. Chem. Solids **59**, 129 (1998)
4. Lenoir, B., Cassart, M., Michenaud, J.P., Scherrer, H., Scherrer, S.: J. Phys. Chem. Solids **57**, 89 (1996)
5. Jain, A.L.: Phys. Rev. **114**, 1518 (1959)
6. Ellet, M.R., Horst, R.B., Williams, L.R., Cuff, K.F.: J. Phys. Soc. Jpn. **21**, 666 (1966)
7. Chao, P.W., Chu, H.T., Kao, Y.H.: Phys. Rev. B **9**, 4030 (1974)
8. Oelgart, G., Schneider, B., Kraak, W., Herrmann, R.: Phys. Status Solidi (b) **74**, K75 (1976)
9. Kraak, W., Oelgart, G., Schneider, G., Herrmann, R.: Phys. Status Solidi (b) **88**, 105 (1978)
10. Kitagawa, H., Noguchi, H., Kiyabu, T., Itoh, M., Noda, Y.: J. Phys. Chem. Solids **65**, 1223 (2004)
11. Yim, W.M., Amith, A.: Solid-State Electron. **15**, 1141 (1972)
12. Golin, S.: Phys. Rev. **176**, 830 (1968)
13. Brandt, N.B., Hermann, R., Golysheva, G.I., Devyatkova, L.I., Kusnik, D., Kraak, W., Ponomarev, Y.G.: Sov. Phys. JETP **56**, 1247 (1982)
14. Mendez, E.E.: PhD Thesis, MIT (1979)
15. Brandt, N.B., Svistova, E.A.: J. Low Temp. Phys. **2**, 1 (1970)
16. Hiruma, K., Kido, G., Kawauchi, K., Miura, N.: Sol. St. Comm. **33**, 257 (1980)
17. Brandt, N.B., Chudinov, S.M.: Sov. Phys. JETP. **32**, 815 (1971)

18. Mendez, E.E., Misu, A., Dresselhaus, M.S.: Phys. Rev. B **24**, 639 (1981)
19. Devaux, X., Brochin, F., Martin-Lopez, R., Scherrer, H.: J. Phys. Chem. Solids **63**, 119 (2002)
20. Martin-Lopez, R., Dauscher, A., Scherrer, H., Hejtmanek, J., Kenzari, H., Lenoir, B.: Appl. Phys. A **68**, 597 (1999)
21. Sharp, J.W., Volckmann, E.H., Goldsmid, H.J.: Phys. Status Solidi (a) **2**, 257 (2001)
22. Belaya, A.D., Zayakin, S.A., Zemskov, V.S.: J. Adv. Mater. **2**, 158 (1994)
23. Ivanov, G.A., Kulikov, V.A., Naletov, V.L., Panarin, A.F., Regel, A.R.: Sov. Phys. Semicond. **7**, 1134 (1973)
24. Liu, H.J., Li, L.F.: J. Alloys Comp. **433**, 279 (2007)
25. Dutta, S., Shubha, V., Ramesh, T.G., D'Sa, F.: J. Alloys Comp. **467**, 305 (2009)
26. Tritt, T.M.: Recent Trends in Thermoelectric Materials Research. Academic, Boston (2001)
27. Lukas, K.C., Joshi, G., Modic, K., Ren, Z.F., Opeil, C.P.: J. Mater. Sci. **47**, 5729 (2012)
28. Lukas, K.C., Zhao, H., Stillwell, R.L., Ren, Z.F., Opeil, C.P.: MRS Online Proc. Library mrss12-1456-jj01-04, doi:10.1557/opl.2012.1368 (2012)
29. Cullity, B.D., Graham, C.D.: Introduction to Magnetic Materials. IEEE Press, New Jersey (2009)
30. Schroder, D.K.: Semiconductor Material and Device Characterization. Wiley, New York (1998)
31. Hattori, T.: J. Phys. Soc. Jpn. **29**(5), 1224 (1970)
32. Nolas, G.S., Sharp, J., Goldsmid, H.J.: Thermoelectrics: Basic Principles and New Materials Developments. Springer, Heidelberg (2001)
33. Tritt, T.M.: Thermal Conductivity. Kluwer Academic/Plenum, New York (2003)
34. Suryanarayana, C.: Prog. in Mater. Sci. **46**, 1 (2001)
35. Ashcroft, N.E., Mermin, N.D.: Solid State Physics. Saunders, New York (1976)
36. Zebarjadi, M., Yang, J., Lukas, K., Kozinsky, B., Yu, B., Dresselhaus, M.S., Opeil, C.P., Ren, Z.F., Chen, G.: J. Appl. Phys. **112**, 044305 (2012)
37. Lukas, K.C., Liu, W.S., Joshi, G., Zebarjadi, M., Dresselhaus, M.S., Ren, Z.F., Chen, G., Opeil, C.P.: Phys. Rev. B **85**, 205410 (2012)
38. Gonze et al., X.: Comput. Phys. Commun. **180** (2009)
39. Hartwigsen, C., Goedecker, S., Hutter, J.: Phys. Rev. B **58** (1998)
40. Esfarjani, K., Stokes, H. T.: Phys. Rev. B **77** (2008)
41. Abeles, B.: Physical Review **131** (1963)
42. Walker, C.T., Pohl, R.O.: Phys. Rev. **131**, 1433 (1963)
43. Klemens, P.G.: Solid State Phys. **7**, 1 (1958), Edited by Seitz, F., Turnbull, D. (Academic, New York)

Chapter 9
Thermoelectric Properties of p-Type Skutterudite Nanocomposites

Chen Zhou, Long Zhang, and Jeffrey Sakamoto

Abstract Skutterudite is a new family of compounds identified to be a promising candidate for thermoelectric applications. Since the early 1990s, skutterudite-based materials have undergone substantial technological development, making its way to the next generation of thermoelectric devices for power generation and waste heat recovery. Nanostructuring is one approach that could enable significant improvements in thermoelectric performance by reducing the thermal conductivity while maintaining the electronic properties. In this chapter, we present progress towards realizing the potential of bulk skutterudites utilizing low dimensionality and nanostructures with an emphasis on p-type skutterudites. We summarized the synthetic approaches used to create skutterudite nanocomposites, namely, ball milling, melt spinning, in situ formation, high-pressure torsion, and solvothermal and hydrothermal synthesis. The effect of nanostructuring on the thermal and electron transport is also discussed.

C. Zhou (✉)
MEDA Engineering and Technical Services, LLC., 17515 W. Nine Mile Road, Suite 1075, Southfield, MI 48075, USA
e-mail: kzhou08@gmail.com

L. Zhang
State Key Laboratory of Metastable Materials Science and Technology, Yanshan University, Qinhuangdao, Hebei 066004, China
e-mail: lzhang@ysu.edu.cn

J. Sakamoto
Department of Chemical Engineering and Materials Science, Michigan State University, East Lansing, MI 48824, USA
e-mail: jsakamot@egr.msu.edu

X. Wang and Z.M. Wang (eds.), *Nanoscale Thermoelectrics*, Lecture Notes in Nanoscale Science and Technology 16, DOI 10.1007/978-3-319-02012-9_9,
© Springer International Publishing Switzerland 2014

9.1 Introduction

Thermoelectric (TE) materials are those that utilize electrons and holes as the working fluid to enable direct energy conversion between heat and electricity. There are numerous benefits offered by TE technology: TE power generators can recover waste heat into useful electricity, thus improving the overall efficiency of energy utilization; TE coolers are silent, reliable, and free of toxic refrigerants and their efficiency is size independent, which means that they can be miniaturized to provide local cooling in places like integrated circuits and car seats.

From a material perspective, the efficiency of TE devices is closely related to the dimensionless TE figure of merit (FOM) ZT, which is defined as

$$ZT = \frac{S^2\sigma}{\kappa}T = \frac{S^2\sigma}{\kappa_l + \kappa_e}T \tag{9.1}$$

where S is the Seebeck coefficient (also known as the thermopower), σ the electrical conductivity, κ the thermal conductivity (κ_l: lattice thermal conductivity; κ_e: electronic thermal conductivity; $\kappa = \kappa_l + \kappa_e$), and T the temperature. Thus, the higher the ZT, the greater the TE performance. The benchmark of a promising TE material is related to many factors. But in terms of ZT, materials with a $ZT = 1$ are generally considered good TE materials. However, nowadays it is not uncommon to find materials with $ZT > 1$ in bulk materials from several material systems [1–11] and even up to $ZT = 2.2$ in Na-doped p-type PbTe that utilizes multiple-scale phonon scattering strategy [12]. The physical quantities of S, σ, and κ are intricately related to each other, which makes increasing ZT much more complicated than the appearance of (9.1). For example, insulators may have a large Seebeck coefficient and low thermal conductivity but have low electrical conductivity; on the other hand, metals are good electrical conductors, but they also conduct heat well and suffer a low Seebeck coefficient of only a few μVK^{-1}. It is found that semiconductors have the best compromise and tunability among S, σ, and κ in order to achieve a high ZT value. For this reason, good TE materials are usually heavily doped semiconductors.

The skutterudite is an example of a semiconductor that was identified as a good candidate for TE applications in the early 1990s [13, 14] and has since progressed into numerous working prototypical systems for waste heat recovery and thermoelectric generators for NASA [15, 16]. The name "skutterudite" originates from a small mining town "Skutterud" in Norway [17] where a common form of skutterudite ($CoAs_3$) is mined. Unfilled skutterudites are binary compounds of the form MA_3, where M is a metal such as Co, Rh, or Ir and A is As, P, or Sb. $CoSb_3$ and $IrSb_3$ have a high carrier mobility and a large effective mass, which result in power factors comparable to and even exceeding the state-of-the-art heritage materials such as Bi_2Te_3 and PbTe [18, 19]. Their thermal conductivities, however, are relatively too large to make them useful TE materials [13, 20].

An early and key finding was the discovery of approaches to significantly reduce the thermal conductivity through doping with filler atoms. In 1980, Braun and

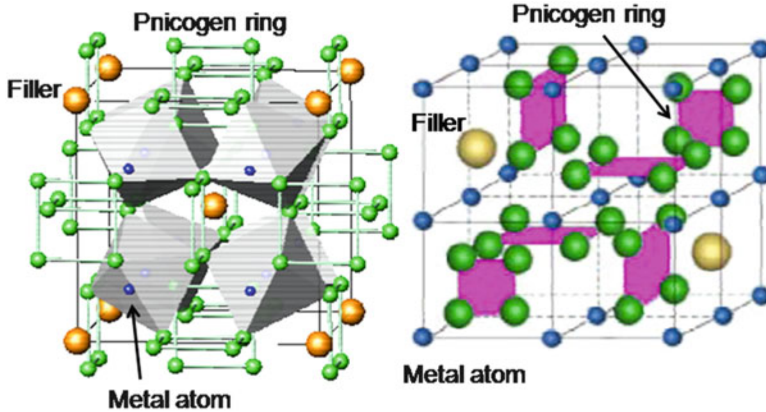

Fig. 9.1 Crystal structure of a filled skutterudite viewed from different perspectives

Jeitschko conducted a detailed structural study of compounds with the prototypical $LaFe_4P_{12}$-type structure [21–23] (shown in Fig. 9.1). Although they did not measure the TE properties of these compounds, they did identify several light rare-earth elements from La to Eu, the first of the kind that could be inserted into the empty cages found in the skutterudite unit cell. In 1994, Morelli and Meisner experimentally showed that the thermal conductivity of $CeFe_4Sb_{12}$ was reduced by nearly an order of magnitude compared to the unfilled skutterudites $CoSb_3$ and $IrSb_3$. They concluded that the reduction was at least partially due to the phonon scattering from the filler atom Ce [13]. Following research has found out that the foreign atom confined in the cage exhibits an Einstein-like mode that provides additional phonon scattering to dampen the lattice thermal conductivity [13, 24, 25]. Creating filled skutterudites has achieved great success especially in reducing the lattice thermal conductivity of this type of material. Today, the filler atoms have expanded from rare-earth, alkali-metal to alkaline-earth elements, and it is not unusual to find double-filled skutterudites with *ZT* greater than 1.3 [5] and triple-filled skutterudites exhibiting *ZT* as high as 1.7 [9].

Unfilled skutterudite $CoSb_3$ exhibits p-type conduction. Adding filler atoms into the void of the skutterudite structure introduces extra electrons and converts the material to n-type semiconductors. In order to create a p-type material, an element with fewer electrons than Co, like Fe, is used to substitute for Co to create holes into the valence band. The resultant chemical formula of p-type skutterudites is usually in the form of $R_yFe_xCo_{4-x}Sb_{12}$ where R represents one or multiple rare-earth, alkali-metal and alkaline-earth elements. The range for y and x is determined by the electronegativity, charge states, and structural stability of the filler atoms. For detailed discussion on this topic, the readers are encouraged to read articles by Shi, Chen, and Meisner [20, 26–28]. Here we offer a succinct illustration using p-type skutterudite $Yb_yFe_xCo_{4-x}Sb_{12}$ as an example (shown in Fig. 9.2) [29]. Other rare-earth filler atoms are expected to follow a similar trend.

The maximum filling fraction for Yb in $CoSb_3$ at ambient pressure was found to be around 0.2 [30]. Fully filled skutterudite has the formula of $YbFe_4Sb_{12}$ [31]. According to Meisner et al. [32], $Yb_yFe_xCo_{4-x}Sb_{12}$ could be considered a solid

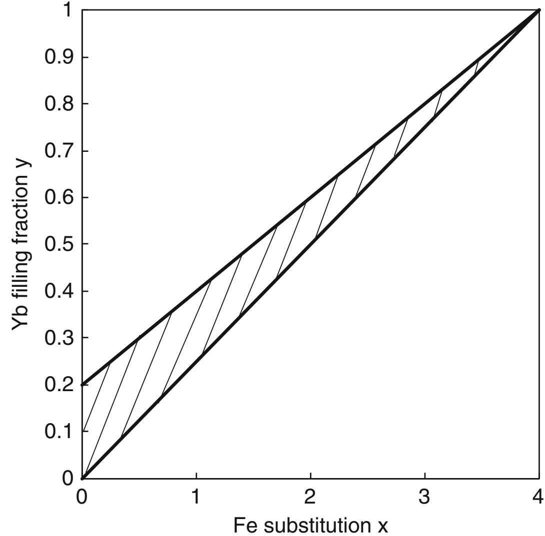

Fig. 9.2 Filling fraction as a function of Fe substitution in $R_yFe_xCo_{4-x}Sb_{12}$ where R = Yb. Other rare-earth fillers are expected to have similar effects

Table 9.1 Some physical properties of $Yb_yFe_xCo_{4-x}Sb_{12}$ at 300 K demonstrating the change of conduction type by varying the Yb filling fraction "y" and Fe substitution for Co "x." Reprinted from reference [29]. Copyright 2011 with permission from Elsevier

Sample composition	y = 0.2, x = 0	y = 0.4, x = 1	y = 0.6, x = 2	y = 0.8, x = 3	y = 1, x = 4
Estimated carrier/f.u.	−0.6 ~ −0.4	−0.2 ~ 0.2	0.2 ~ 0.8	0.6 ~ 1.4	1 ~ 2
Observed carrier/f.u.	−0.07	0.06	0.235	0.325	0.84
Conduction type	n-type	p-type	p-type	p-type	p-type
Carrier density ($\times 10^{20}$ cm^{-3})	1.90	1.48	6.03	8.54	21.5
Carrier mobility (cm^2 V^{-1} s^{-1})	53.9	29.0	14.0	17.3	9.53

solution of α mol% of ($YbFe_4Sb_{12}$) and $(1 - \alpha)$ mol% of Co_4Sb_{12}. The empirical equation for the maximum Yb filling fraction is $y = \alpha + 0.2(1 - \alpha) = \frac{x}{4} + 0.2\left(1 - \frac{x}{4}\right)$. The lower boundary for the minimum filling fraction is constructed by connecting the filling fraction of unfilled skutterudite "y = 0" and that of $YbFe_4Sb_{12}$ "y = 1" in Fig. 9.2. Table 9.1 uses $Yb_yFe_xCo_{4-x}Sb_{12}$ as an example to demonstrate the change of conduction type from n-type to p-type by varying the amount of Yb filling and Fe substitution for Co.

Further optimization of *ZT* relies on new mechanisms that can (1) reduce the lattice thermal conductivity κ_l and (2) increase the power factor $S^2\sigma$. In both directions, introducing discontinuities in the long-range atomic order at the nanometer scale, known as "nanostructuring," could be an effective approach. The κ_l reduction by introducing nanostructures is not hard to understand as the myriad nano-interfaces would offer additional phonon scattering and cap the phonon mean free path. Theoretical calculations on composites of Si_xGe_{1-x} containing Si nanowire have

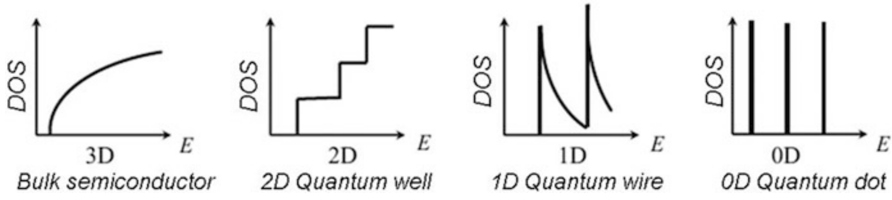

Fig. 9.3 Electronic density of states (DOS) for a bulk 3D crystalline semiconductor, a 2D quantum well, a 1D nanowire or nanotube, and a 0D quantum dot [33]

shown that the thermal conductivity is significantly reduced in the nanocomposites compared to bulk samples of the same composition [33, 34]. Such results have later been confirmed in nanostructured Si–Ge alloys due to the much reduced thermal conductivity [35]. Similar *ZT* enhancement arising from thermal conductivity reduction has also been found in nanostructured Bi–Te alloys [36]. To understand the enhancement of $S^2\sigma$, it is helpful to express the Seebeck coefficient according to the Mott and Jones equation [37]:

$$\begin{aligned} S &= \frac{\pi^2 k^2 T}{3e}\left(\frac{d\ln\sigma(E)}{dE}\right)\Bigg|_{E=E_F} \\ &= \frac{\pi^2 k^2 T}{3e}\left(\frac{d\ln g(E)}{dE} + \frac{d\ln v^2(E)}{dE} + \frac{d\ln\tau(E)}{dE}\right)\Bigg|_{E=E_F} \end{aligned} \tag{9.2}$$

where v is the average electron drift velocity and τ is the relaxation time. For free electrons, $g(E) \propto E^{1/2}$, $v^2 \propto E$, and $\tau \propto E^s$. The first term $d\ ln\ g(E)/d\ E$ suggests that a large S is possible if the Fermi level is positioned near a sharp spike in the density of state (DOS). Theoretical calculations show that the DOS becomes discontinuous when the dimension of the constituent is reduced as illustrated in Fig. 9.3 [33]. This mechanism has been corroborated by the large power factor enhancement in PbTe quantum well structures [38, 39], Si/Ge superlattice [40], PbSeTe-based quantum dot superlattice (ZT ~ 1.3–1.6) [41], and Bi_2Te_3/Sb_2Te_3 superlattice (ZT ~ 2.4) [42]. The third term $d\ ln\ \tau(E)/d\ E$ indicates that it is also possible to enhance the Seebeck coefficient by tweaking the scattering parameter s (also known as the energy filtering effect [43]). In fact, this method has been proposed by Ioffe and his co-workers as a way to search for new TE materials with ionic bonding [44]. Heremans et al. demonstrated that the enhanced Seebeck coefficient is the result of a greater scattering parameter s caused by resonant scattering in PbTe nanostructures [45].

9.2 Fabrication of Bulk Nanostructured Skutterudites

Making nanostructured bulk TE materials that are chemically, thermally, and mechanically stable has proven to be difficult. There are many challenges that researchers often encounter during synthesis. For example, creating nano-sized particles that fall into the desirable size range is difficult. Other examples include preventing agglomeration, removing surface ligands, suppressing grain growth during sintering, and identifying suitable nanoparticles with the appropriate physical properties. Here, we briefly introduce a few synthesis methods commonly used for creating skutterudite-based nanocomposites, although most of these methods are applicable to other TE material systems as well.

9.2.1 Ball Milling and Hot Pressing

Ball milling (BM) is one of the most widely used techniques for producing submicron and nano-sized grains. In the ball milling process, the particle size of the grinding materials is reduced as a result of attrition and impact from the grinding media. During the milling process, many parameters can affect the microstructure of the product, such as the type of mill, milling speed, milling time, ball-to-powder weight ratio (BPR), ball materials, size distribution of the balls, milling environment, process control agent(s), and milling temperature [46].

The technique of BM followed by hot pressing is especially relevant to skutterudites [47–53]. The targets are usually to (1) incorporate precipitates to skutterudite host matrix in order to improve TE performance and retard grain growth [54–61]; (2) obtain nano- or submicron-sized grains and imperfections; and (3) obtain bulk samples of high density and good mechanical properties.

Planetary ball milling is the most popular BM to prepare skutterudite powder. Figure 9.4 shows the schematic illustration of the planetary BM. The shock power P can be expressed as $P = f \times E_k$, where f is shock frequency and E_k is the kinetic energy per hit [62]. f and E_k are functions of the main disk rotation speed, vial rotation speed, ball mass, and radius of disk, vials, and balls [62]. Higher kinetic energy is not necessarily ideal to produce nano-sized skutterudite grains as high kinetic energy could lead to decomposition of skutterudite phase. It is, therefore, very important to optimize the milling conditions. Here we look into how the planetary ball mill works in the context of the formation and decomposition of the skutterudite.

Starting with elemental Co and Sb, $CoSb_3$ was formed after only 2 h of milling when the following conditions were applied: 10 mm balls, main disk rotation speed Rs = 300 rpm, and BPR = 40 %. Figure 9.5 illustrates the formation of $CoSb_3$ under various milling conditions (the volume percentages were estimated from Rietveld refinement) [61]. When larger balls (diameter $\varnothing_b = 10$ mm) were used, a similar tendency was observed. The quantity of $CoSb_3$ increases with ball milling time, reaching a maximum value between 2 and 6 h. The influence of BPR is obvious:

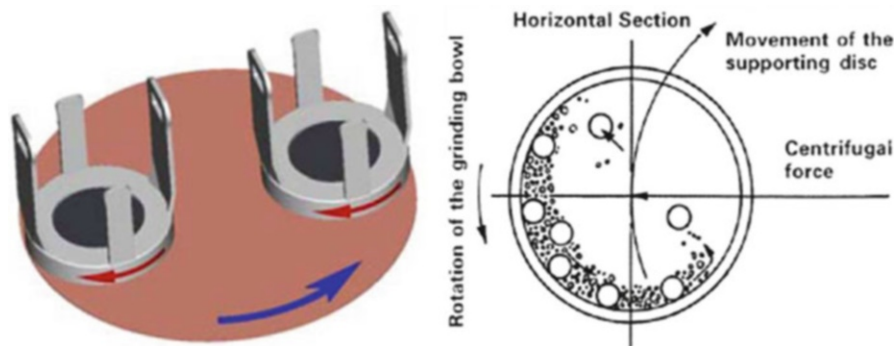

Fig. 9.4 Schematic illustration of a planetary BM

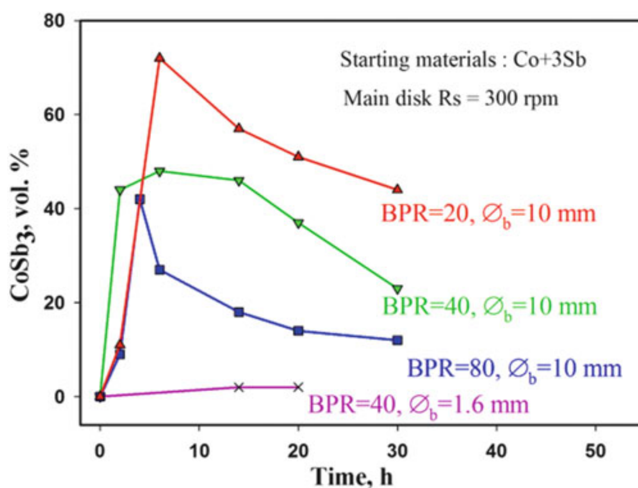

Fig. 9.5 Formation of $CoSb_3$ and volume percentage from Rietveld refinement of $CoSb_3$. Reprinted from reference [61], Copyright 2009 with permission from Elsevier

the percentage of skutterudite phase increases with decreasing BPR. In the case of the small balls with $\varnothing_b = 1.6$ mm, almost no skutterudite was observed, thus indicating that there is insufficient kinetic energy to form $CoSb_3$ [62]. In both cases no pure $CoSb_3$ can be achieved from mechanical alloying (MA). Therefore, BM from pre-reacted skutterudite is normally the way for solid-state nanostructuring. The investigation of decomposition of skutterudite is of critical importance. The influences of milling conditions on decomposition of $CoSb_3$ (performed in PULVERISETTE 4, Fritsch; two chambers with tungsten carbide vessels) have been described in detail in reference [61], including Rs, planetary ratio (PR),

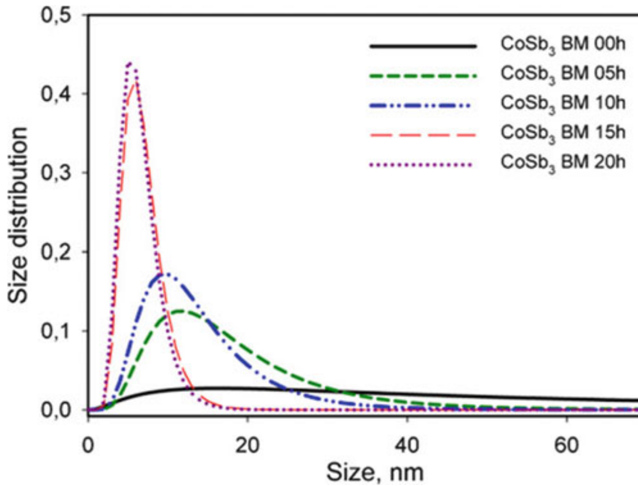

Fig. 9.6 Crystallite size distribution for $CoSb_3$ ball milled for different periods of time. Reprinted from reference [61], Copyright 2009 with permission from Elsevier

$\varnothing_b$, BPR, and a process control agent (PCA). The following is a summary of the key parameters.

1. When Rs changes from 70 to 360 rpm in steps of 10–30 with the increase of milling time, $CoSb_3$ decomposes for the combination of Rs > 200 rpm and $\varnothing_b = 1.6$ mm, but no decomposition occurs for $\varnothing_b = 10$ mm.
2. When PR is higher than a critical value, the decomposition is substantial, e.g., PR = −3.3.
3. Smaller ball diameter achieves finer powder faster. Nevertheless, milling with small balls leads to greater decomposition compared to big balls.
4. Increasing the BPR accelerates the decomposition.
5. Liquid PCA significantly prevents the decomposition of $CoSb_3$ in addition to preventing oxidation and adhesion compared to PCA evolving gases. In other words, liquid PCA reduces kinetic energy.

In conclusion, only moderate milling conditions can achieve nano-sized skutterudites, i.e., Rs = 200 rpm, PR = −2.5, $\varnothing_b = 10$ mm, and PCA = cyclohexane for a milling time of 0, 5, 10, 15, and 20 h. The resulting crystallite size as shown in Fig. 9.6 (evaluated from X-ray powder diffraction) continuously decreases until the saturated minimum is reached after a milling time of 15 h. The dislocation density, however, remains constant at about 10^{12} m^{-2} regardless of the prolonged milling time.

Similar nano-sized skutterudites have also been obtained in a series of p-type samples $E_yFe_4Sb_{12}$ and $E_yFe_3CoSb_{12}$ where E stands for Ba, Ca, didymium (DD), and mischmetal (MM), respectively [63].

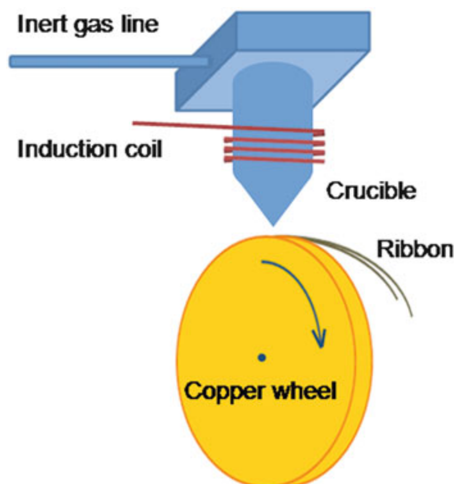

Fig. 9.7 Schematic illustration of melt spinning

9.2.2 Melt Spinning (MS) and Pulsed Electric Current Sintering (PECS)

Melt spinning is a rapid solidification technique that is key to many advanced functional materials [64, 65]. In a typical laboratory melt spinner, as shown in Fig. 9.7, the molten metal is ejected by an inert gas onto a rotating copper wheel and then spun off in the form of ribbon. The assembly is usually enclosed in an inert gas environment. The quench rate is controlled by the surface velocity of the wheel and can be on the order of 10^4–10^7 K/s [66]. The fast quench rate makes it possible to produce fine nano-grain or even amorphous materials and obtain the desired phase without involving the time-consuming annealing process. Li and Tang have reported the synthesis of several nanostructured Yb-filled skutterudites $Yb_xCo_4Sb_{12}$, $Yb_{0.2}Co_4Sb_{12+y}$, and $Yb_{0.3}Co_4Sb_{12+y}$ by using the melt spinning technique [3, 67, 68]. These workers have shown that in melt-spun $Yb_{0.2}Co_4Sb_{12}$ the grain size on the free face ribbons decreases from 100–200 nm at $v_s = 10$ m/s to 20–50 nm at $v_s = 30$ m/s. The contact face has a much higher cooling rate that results in an amorphous skutterudite at $v_s = 30$ m/s [67]. After melt spinning, ribbons were loaded into the graphite die and consolidated by the PECS. PECS, also known as the spark plasma sintering (SPS), is a fast sintering technique that utilizes the joule heating effect by passing pulsed DC current through the graphite die and conductive samples. Compared to hot pressing that relies on the heat convection from the external heating filaments, PECS can achieve a very fast heating rate of 1,000 K/min, which is crucial to suppress grain growth. Li and Tang have shown that the final bulk $Yb_{0.2}Co_4Sb_{12}$ sample prepared by MS + PECS is in fact a nanocomposite consisting of two length scales of 100 nm and 10–20 nm size nanocrystals [67].

9.2.3 In Situ-Formed Nanocomposites

In situ synthesis of nanocomposites utilizes the naturally occurring oxidation, precipitates of metastable filler atom, and secondary phase to form the nano-inclusions. Compared to other nano-synthesis approaches, in situ synthesis excels at simplicity of sample preparation as the nano-inclusions form during certain stage in the solidification or post heat treatment steps. Once formed, these nano-inclusions have already been embedded into the matrix materials and form natural composites. Because the formation of the nano-inclusions is driven by the thermodynamics, they tend to be chemically stable and their heterogeneous nature with respect to the matrix materials makes them less prone to grain growth at elevated temperatures.

Several authors and research groups have reported preparation of skutterudite nanocomposites by the in situ synthesis approach. Zhao et al. have prepared $Yb_{0.21}Co_4Sb_{12}/Yb_2O_3$ nanocomposites where Yb_2O_3 was formed by grinding the composite samples containing unreacted Yb in air for 30 min [70]. Li et al. have reported in situ-formed $In_xCe_yCo_4Sb_{12}$ nanocomposites by melt spinning and PECS, where metastable In filler has led to the formation of InSb nano-inclusions [4]. From the same train of thought, Xiong et al. have synthesized $Yb_{0.26}Co_4Sb_{12}$/yGaSb, where the Ga is driven out of the cage and forms GaSb due to the reduced solubility below the melting point [10]. Turning now to p-type skutterudite nanocomposites, Zhou et al. have reported $Co_{0.9}Fe_{0.1}Sb_3$-based skutterudite nanocomposites with $FeSb_2$ nano-inclusions [69]. $FeSb_2$ is a chemically stable secondary phases found in p-type skutterudites. The nanocomposite samples have chemical formulae of $Co_{0.9}Fe_{0.1+x}Sb_{3+2x}$ where x = 0.05, 0.1, and 0.02. These samples contain less Sb than the normal skutterudite stoichiometry in order to facilitate the formation of $FeSb_2$ during the rapid solidification. Figure 9.8 shows the high-resolution field emission scanning electron microscopy (FESEM) images on the fractured surface of the bulk $Co_{0.9}Fe_{0.1+x}Sb_{3+2x}$ nanocomposites. The inset of Fig. 9.8a shows the zoomed-in observation of the circle region where nano-sized particles can be found. The amount of nanoparticles approximately scales with the nominal content "x" $FeSb_2$ introduced from (a) to (c). Figure 9.8d shows the reference sample $Co_{0.75}Fe_{0.25}Sb_3$ having the same Fe/Co ratio as x = 0.2 sample but has the normal skutterudite composition MA_3. It is very interesting to note that the nanoparticles found in (a)–(c) have almost disappeared and grain boundaries in (d) are much cleaner, which suggests that either Fe atoms were absorbed to form skutterudite or some $FeSb_2$ nanoparticles have grown to the micron size. The same idea was later applied to Yb-filled p-type skutterudite nanocomposites where similar microscopic features have been found [71].

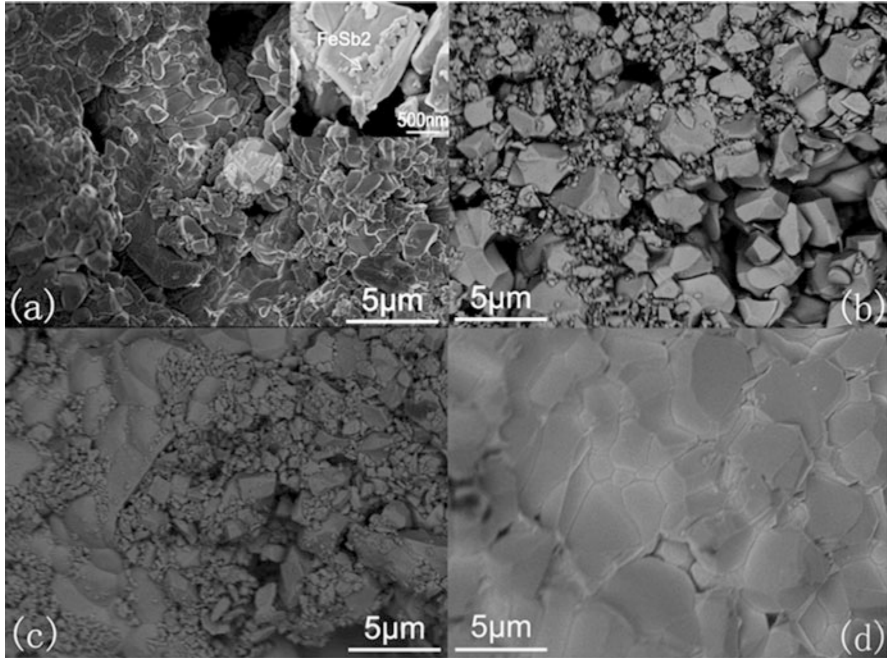

Fig. 9.8 High-resolution FESEM images on fractured surface of nanocomposite samples $Co_{0.9}Fe_{0.1}Sb_3$ + $xFeSb_2$ and control sample $Co_{0.75}Fe_{0.25}Sb_3$. (**a**) x = 0.05, the *inset* image zooms in the *circled area* to reveal the nano-sized particles; (**b**) x = 0.1; (**c**) x = 0.2; (**d**) $Co_{0.75}Fe_{0.25}Sb_3$. Reprinted from reference [69], Copyright 2011 American Institute of Physics

9.2.4 High-Pressure Torsion

High-pressure torsion (HPT) has recently been studied and applied to skutterudites by a research group at University of Vienna, Austria. This method is capable of directly producing ultrafine nano-grains and lattice defects in a bulk sample via severe plastic deformation [72, 73]. During the HPT experiment (apparatus shown in Fig. 9.9), a disk specimen of 10 mm in diameter and 0.8 mm in thickness is clamped in the cavities of the upper and lower anvils. The cavities prevent the loaded specimens from dislodging under high pressure. The upper and lower anvils rotate to apply torsional force while exerting high hydrostatic pressure to prevent cracking [74] and retain the deformation-induced defects that are crucial for the formation of dislocation-induced grain boundaries [73, 75, 76]. The shear strain γ is related to the number of revolution n, specimen radius r, and thickness t by

$$\gamma = \frac{2\pi n r}{t} \tag{9.3}$$

In addition, induction heating can be integrated into the system to induce more shear strain at elevated temperature [72].

Fig. 9.9 High-pressure torsion (HPT) apparatus

The nanoscopic grain boundaries and dislocations induced by HPT are effective in scattering the phonons and hence reduce the lattice thermal conductivity. Although the electrical resistivity is also expected to increase after HPT, the formation of nano-grains may result in an enhanced Seebeck coefficient possibly due to the discontinuities in the DOS.

However, since skutterudites will operate at elevated temperature, the effect of recrystallization and grain growth cannot be dismissed. One approach to improve the microstructural stability is through "orientation pinning," which utilizes brittle nanoparticles precipitated along the grain boundaries and junctions to suppress grain growth [77]. Typical nanoparticles that can serve this purpose are rare-earth oxides. It should be noted, though, that high-volume fraction of oxides may impede sintering and lead to low-density samples, which will in turn affect the electron and phonon transport [61].

9.2.5 Solvothermal/Hydrothermal Synthesis

Solvothermal/hydrothermal (we will use the term "solvo/hydrothermal" in the remaining paragraphs for conciseness) synthesis is a solution-based synthesis technique that is capable of directly precipitating fine crystals at elevated temperature and pressure. Compared to other nano-synthesis techniques, solvo/hydrothermal synthesis boasts the following merits: (1) it can directly precipitate nanocrystals from the solutions without fully melting the reactants and complicated post-processing; (2) it has better control of the particle size and morphology; (3) it has been proven to be very adaptable to synthesize a wide range of inorganic and organic materials, both conventional and novel, provided one can find suitable reactants, solvents, and appropriate thermodynamic and kinetic parameters; (4) because of the abovementioned points, solvo/hydrothermal consumes less energy, has higher throughput, and is relatively inexpensive, which really make it suitable for industrial production [78, 79].

In a general solvo/hydrothermal synthesis, the first step is selection of appropriate chemical precursors and solvents based on the final product. The concentration of precursors could affect the crystallite shape [80], and the type of solvents employed takes an important role in the reaction mechanisms [79]. The second step is to select thermodynamic parameters based on the combination of precursors and solvents, which include pressure, temperature, and time. The underlying mechanisms for controlling crystallite size are nucleation and growth rate and that for morphology is the competitive growth rate along principal direction. For instance, higher temperature and pressure will increase the precursor concentration in solvents, which in turn creates conditions favorable for growth. In addition, non-thermodynamic variables such as stirring can also influence the synthesis outcome [78].

Several research groups have reported solvo/hydrothermal synthesis of nanostructured skutterudites. Mi and co-workers have reported synthesis of $CoSb_3$ using $CoCl_2{\cdot}6H_2O$ and $SbCl_3$ as the precursors and $NaBH_4$ as the reductant. The reactants were dissolved in ethanol and reacted in autoclave at a temperature between 190 and 270 °C for 24–72 h. The influence of temperature is significant as $CoSb_3$ phase is absent in the sample reacted at 190 °C for 24 h but begins to be visible in samples reacted at 220 °C. Samples reacted at 250–270 °C show greatly enhanced skutterudite phase intensities. Extending the reaction time also increases the skutterudite phase. Nearly single-phase $CoSb_3$ was obtained for samples heated at 250 °C for 72 h. SEM images showed that the solvothermal prepared $CoSb_3$ powders were composed of a mixture of small particles of tens of nanometers and larger aggregates of several hundreds of nanometers [54]. Li et al. have conducted similar solvothermal experiments on $CoSb_3$ and $Co_{4\text{-}x}Fe_xSb_{12}$ where they used a different reagent of triethylene glycol. These authors claimed that they have obtained single-phase skutterudite with well-controlled particle size of 10–20 nm at a reaction temperature of 250 °C for only 12 h [81]. Lu et al. have studied the effect of solvents on the solvo/hydrothermal synthesis of filled p-type $LaFe_3CoSb_{12}$, where four aqueous solutions of ethylenediamine-tetra-acetic disodium salt (EDTA), cetyltrimethylammonium bromide (CTAB), ethylenediamine (EDA), and ethylene glycol (EG) were used. They concluded that different solvents not only affected the skutterudite phase formation but also had influence on the morphology of the products. For example, EDTA and CTAB created similar mixture of nanoparticles of 80–100 nm and nanorods of 100–120 nm in diameter and 800–2,000 nm in length. DTA could only create nanorods about 70 nm in diameter, and EG only created nanoparticles of 200 nm [82].

Although the solvo/hydrothermal synthetic approach has many advantages for preparing nanoscale materials over other methods, it unavoidably uses many solvents, reductants, and additives, whose constituents can become contaminants that affect the electronic properties. For example, Mi et al. observed that solvothermally synthesized $CoSb_3$ exhibited n-type conduction, in contrast to the p-type conduction reported in single-crystal $CoSb_3$ [18, 54].

9.3 Effects of Nanostructures on Thermoelectric Performance

The introduction of low-dimensional and heterogeneous nanoparticles has demonstrated the efficacy in improving the thermal and electronic properties of several TE materials. In this section, we discuss the reduction in thermal conductivity and enhancement in TE power factor achieved through various synthesis approaches.

9.3.1 Effects of Nanostructures on Thermal Conductivity

The introduction of nano-interfaces could provide additional phonon scattering that is anticipated to reduce the lattice thermal conductivity κ_l. The lattice thermal conductivity is usually obtained by subtracting the electronic thermal conductivity κ_e from the total thermal conductivity κ. In most cases, κ_e can be estimated by Wiedemann–Franz law $\kappa_e = L\sigma T$, where L is the Lorenz number. Since most TE materials are heavily doped semiconductors and semimetals, a value of $L = 2.44 \times 10^{-8}\ \mathrm{W\Omega K^{-2}}$ has been assumed in most cases. But the actual Lorenz number is related to the scattering mechanism and the doping level and may deviate from the abovementioned value. If this is the case, a more accurate calculation of Lorenz number can be found in the reference [44].

The lattice thermal conductivity κ_l can be expressed by the Debye–Callaway model:

$$\kappa_l = \frac{k_B}{2\pi^2 v}\left(\frac{k_B}{\hbar}\right)^3 T^3 \int_0^{\vartheta_D/T} \tau_c \frac{x^4 e^x}{(e^x - 1)^2} dx$$
$$v = \frac{k_B \vartheta_D}{\hbar(6\pi^2 N)^{1/3}}, \quad x = \frac{\hbar\omega}{k_B T} \tag{9.4}$$

where k_B is the Boltzmann constant, $\hbar$ the reduced Planck constant, θ_D the Debye temperature, ω the phonon frequency, and v the sound velocity. The various phonon scattering mechanisms have been reflected in the term of the phonon relaxation time τ_c, which can be expressed as [83]

$$\tau_c^{-1} = \tau_N^{-1} + \tau_U^{-1} + \tau_E^{-1} + \tau_B^{-1} + \tau_D^{-1} \tag{9.5}$$

where τ_N represents the phonon–phonon normal scattering, τ_U is the phonon–phonon Umklapp scattering, τ_E is the phonon–electron scattering, τ_B is the boundary scattering, and τ_D is the defect scattering. The terms pertinent to the nanostructuring are the τ_B and τ_D. The boundary scattering rate can be expressed as

$$\tau_B^{-1} = v/d \tag{9.6}$$

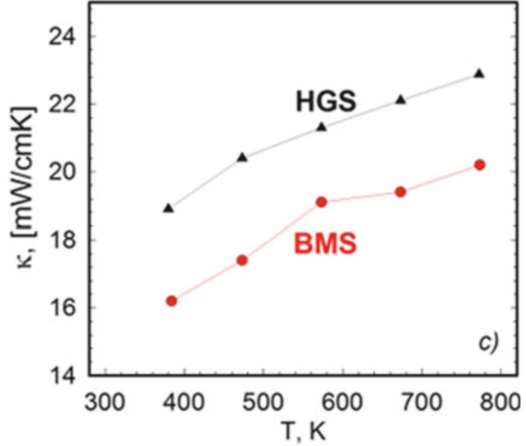

Fig. 9.10 Thermal conductivity κ of bulk p-type skutterudite $Mm_{0.68}Fe_3CoSb_{12}$ prepared from ball-milled (BMS, *circles*) and hand-ground (HGS, *triangles*) powders followed by hot pressing

where d is the grain size of the polycrystalline materials. So the smaller the grain size, the smaller the value of κ_l. The defect scattering rate τ_D can be written as

$$\begin{aligned} &\tau_D^{-1} = \tau_{\text{dis}}^{-1} + \tau_{\text{str}}^{-1} \\ &\tau_{\text{dis}}^{-1} \propto N_D \frac{r^4}{v^2}\omega^3, \quad \tau_{\text{str}}^{-1} \propto N_D \frac{\gamma^2 B_D^2 \omega}{2\pi} \end{aligned} \tag{9.7}$$

where τ_{dis} is the relaxation time of phonon-dislocation scattering, τ_{str} is the phonon-strain scattering, N_D is the number of dislocation lines per unit area, r is the core radius, and B_D is the Burgers vector of the dislocation. Thus more lattice defects would offer stronger phonon scattering as well.

Zhang et al. have prepared $Mm_{0.68}Fe_3CoSb_{12}$ by ball milling followed by hot pressing. In contrast to the hand-ground powders that have a grain size of 20–100 μm, the ball-milled powders have a much finer grain size of only 100–300 nm. In addition, the ball-milled powders often contain small quantities of impurity phases such as Mm_2O_3, $MmSb_2$, $FeSb_2$, and Sb. In the temperature range over the Debye temperature (around 300 K for filled skutterudites [84]), the high-frequency phonons are strongly scattered by point defects while the low-frequency phonons are suppressed by grain boundaries [85]. Consequently, the thermal conductivity of ball-milled materials can be 15 % lower than that of hand-ground sample as shown in Fig. 9.10 [61]. The same effects on skutterudites are also shown in [48, 53, 58, 85].

Zhou et al. have achieved significant thermal conductivity reduction in the in situ-formed $Co_{0.9}Fe_{0.1}Sb_3$ nanocomposites with $FeSb_2$ as the nano-inclusions. As shown in Fig. 9.11, the lattice thermal conductivities of the nanocomposites have been greatly reduced in the whole temperature range compared to the reference sample $x = 0$. Such low κ_l values exhibited in the nanocomposites are even comparable to

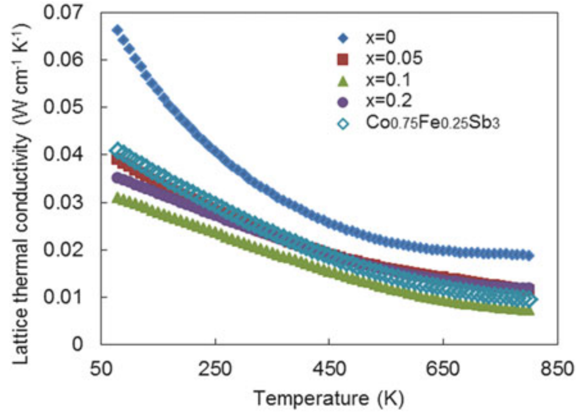

Fig. 9.11 Lattice thermal conductivity κ_l as a function of temperature for skutterudite nanocomposite $Co_{0.9}Fe_{0.1+x}Sb_{3+2x}$. Both samples of x = 0 and $Co_{0.75}Fe_{0.2}Sb_3$ have the nominal skutterudite stoichiometry of MA_3 and serve as the reference formulation. Reprinted from reference [69], Copyright 2011 American Institute of Physics

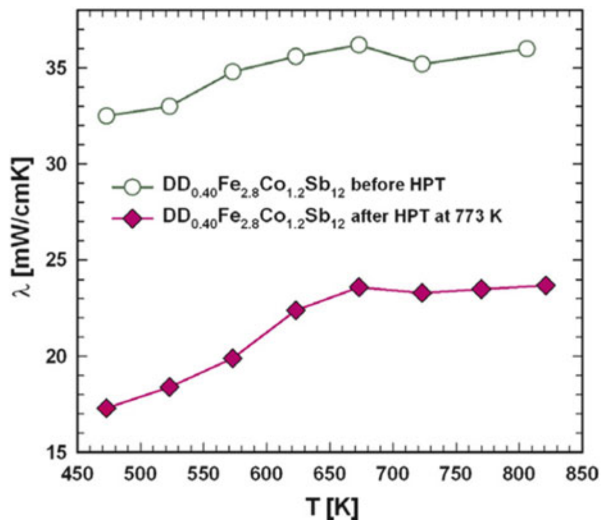

Fig. 9.12 Temperature-dependent thermal conductivity of $DD_{0.4}Fe_{2.8}Co_{1.2}Sb_{12}$ before and after HPT. Reprinted from reference [72], Copyright 2012 with permission from Elsevier

some of the filled skutterudites [86]. It is believed that the reduced thermal conductivities arise from the phonon scattering effect of the $FeSb_2$ nanoparticles [69].

Significant thermal conductivity reduction has also been achieved in the HPT-treated samples. In a given example of $DD_{0.6}Fe_3CoSb_{12}$, the dislocation density has been increased by almost an order of magnitude, and the crystallite size has been reduced from 152 to 53 nm, a factor of three reduction after HPT. As a result, the thermal conductivities were greatly reduced, and in the case of $DD_{0.4}Fe_{2.8}Co_{1.2}Sb_{12}$ (Fig. 9.12), the thermal conductivity after HPT is nearly half the value before HPT [72].

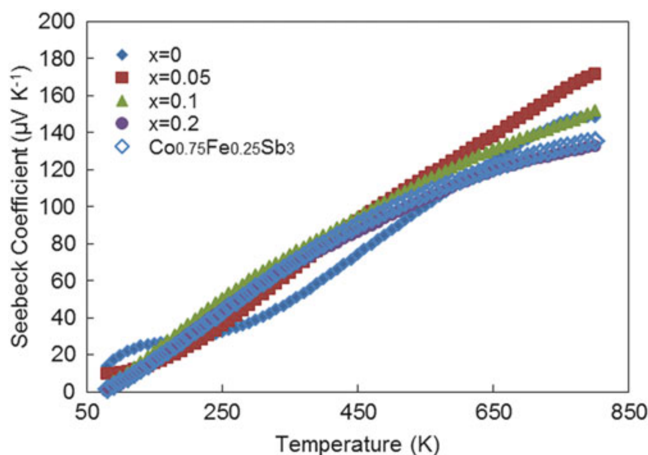

Fig. 9.13 Seebeck coefficient as a function of temperature for skutterudite nanocomposite $Co_{0.9}Fe_{0.1+x}Sb_{3+2x}$. Both samples of x = 0 and $Co_{0.75}Fe_{0.2}Sb_3$ have normal skutterudite stoichiometry of MA_3 and serve as the reference samples. Reprinted from reference [69], Copyright 2011 American Institute of Physics

9.3.2 Effects of Nanostructures on Electronic Properties

Improving the electronic properties by nanostructuring has been proven to be more difficult compared to reducing the thermal conductivity. The increased grain boundaries and heterogeneous nanoparticles embedded in the matrix materials would scatter the charge carriers as well as the phonons and in general increase the electrical resistivity. However, several authors and research groups have demonstrated that it is possible to increase the power factors by enhancing the Seebeck coefficient.

Zhou et al. have reported enhanced Seebeck coefficients in nanocomposites $Co_{0.9}Fe_{0.1+x}Sb_{3+2x}$ (Fig. 9.13). The nanocomposite Seebeck coefficients first increase with increasing $FeSb_2$ nano-inclusions up to x = 0.1 and then start to decrease. The samples with x = 0.05 and 0.1 exhibit a higher Seebeck coefficient compared to the reference x = 0 sample above 250 K. The nanocomposite samples also possess higher electrical resistivities (Fig. 9.14) at low temperature; however, they appear to be saturated at high temperature and are thus lower than the reference sample x = 0 above 500 K. As a result, the overall power factor has been enhanced from 10×10^{-6} Wcm^{-1} K^{-2} in x = 0 to 17×10^{-6} Wcm^{-1} K^{-2} in x = 0.05 using this nanocomposite approach.

Dramatic enhancement of the Seebeck coefficient has also been realized in the $DD_{0.4}Fe_{2.8}Co_{1.2}Sb_{12}$ after HPT. As it is shown in Fig. 9.15, the Seebeck coefficient of the sample that has undergone the most strain during HPT has increased by nearly a factor of two compared to the control sample without HPT. The authors

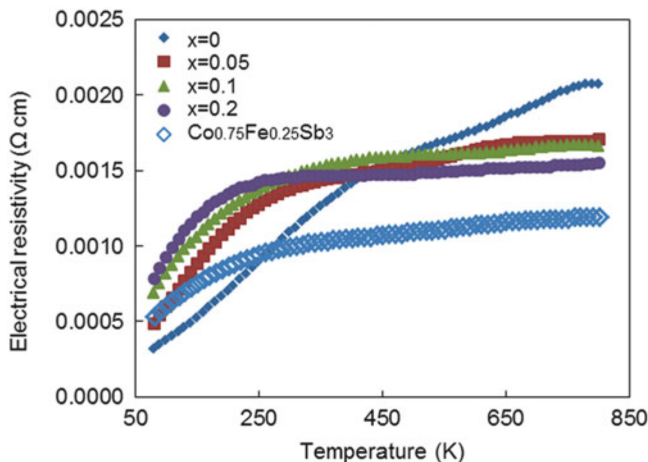

Fig. 9.14 Electrical resistivity as a function of temperature for skutterudite nanocomposite $Co_{0.9}Fe_{0.1+x}Sb_{3+2x}$. Both samples of x = 0 and $Co_{0.75}Fe_{0.2}Sb_3$ have the nominal skutterudite stoichiometry of MA_3 and serve as the reference samples. Reprinted from reference [69], Copyright 2011 American Institute of Physics

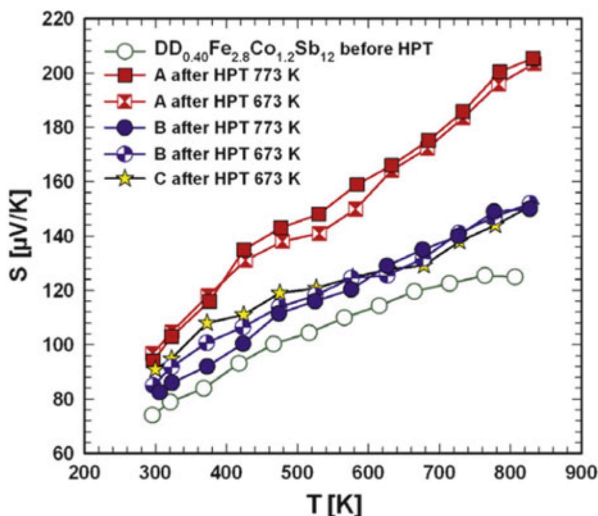

Fig. 9.15 Seebeck coefficient as a function of temperature for $DD_{0.4}Fe_{2.8}Co_{1.2}Sb_{12}$ before and after HPT. A, B, and C represent samples sectioned at different distance away from the center of HPT disk, with A being near the rim, and C near the center. Reprinted from reference [72], Copyright 2012 with permission from Elsevier

attribute the enhancement of Seebeck coefficient to the quantum confinement from the reduced crystallite size [72].

In the abovementioned two examples, we have shown that under certain conditions, the existence of nanostructures indeed can enhance the Seebeck coefficient in p-type skutterudites. However, one should always keep in mind that the impurities or additional elements introduced during the synthesis could potentially dope the matrix material and affect the Seebeck coefficient. To verify whether the enhancement of

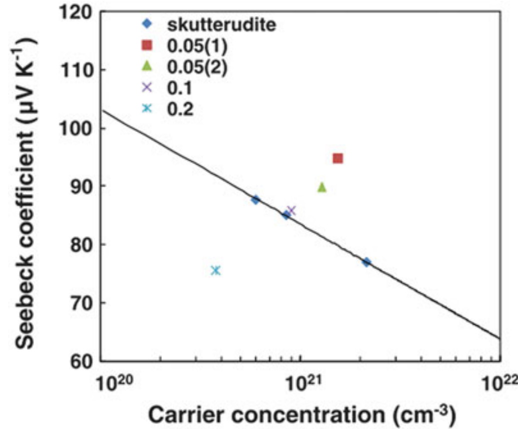

Fig. 9.16 Pisarenko relation of $Yb_{0.6}Fe_2Co_2Sb_{12}/xFeSb_2$ nanocomposites where x = 0.05, 0.1, and 0.2. The *blue diamonds* represent polycrystalline $Yb_yFe_{4\text{-}x}Co_xSb_{12}$ of different hole concentrations. The *fit line* serves as an aid to the eye [71]. With kind permission from Springer Science +Business Media: Journal of Electronic Materials **41**(6), 1030–1035 (2012), Zhou, C., Sakamoto, J., Morelli, D. Fig. 7

the Seebeck coefficient truly arises from the introduction of nanostructures or simply from the doping effect, it is necessary to plot Seebeck coefficient as a function of carrier concentration, known as the "Pisarenko relation" [87]. For degenerate semiconductors, the Seebeck coefficient can be expressed as [87]

$$S = \frac{k}{e}\left(s + 2 + \ln\frac{2(2\pi m^* kT)}{h^3 n}\right) \tag{9.8}$$

where s is the carrier scattering parameter, m^* the density of state effective mass, and n the carrier concentration. For bulk semiconductors, with similar compositions, s and m^* usually have comparable values; thus the Seebeck coefficient is proportional to the logarithm of the inverse carrier concentration. Experimentally, the Pisarenko plot can be constructed by fitting a series of bulk samples of identical chemical compositions but different carrier concentrations. If the enhancement of S is from a different carrier scattering parameter s or a change in the DOS that is reflected as m^*, then S must deviate from the base line constructed by the bulk samples (more specifically, exhibit a higher Seebeck coefficient at the same carrier concentration level).

An example is given in $Yb_{0.6}Fe_2Co_2Sb_{12}/xFeSb_2$ nanocomposites as shown in Fig. 9.16. A series of skutterudites $Yb_yFe_{4\text{-}x}Co_xSb_{12}$ with different hole concentrations form a linear relation between S and ln (n) as suggested by (9.8). Nanocomposites of $Yb_{0.6}Fe_2Co_2Sb_{12}/xFeSb_2$ with x = 0.05(1) and x = 0.05 (2) show higher Seebeck coefficients than those projected by the fit.

The specific contribution of scattering parameter s and the density of state effective mass m^* to the change of Seebeck coefficient can be calculated from

four experimentally measured physical quantities, namely, the Seebeck coefficient S, the electrical conductivity σ, the Nernst coefficient N, and Hall coefficient R_H. This method is known as "the method of four coefficients" and is well documented in the literature. The details of the theoretical derivation can be found elsewhere [88]. Here we only offer the key calculation results based on a generalized non-parabolic band structure following Heremans et al.'s work [45, 89, 90]. $\gamma(E)$ describes the non-parabolic energy of carriers given by (9.9), and E_g is the bandgap:

$$\begin{aligned} \gamma(E) &= \frac{\hbar^2 k^2}{2m_v{}^*} = E\left(1 + \frac{E}{E_g}\right) \\ \gamma' &= 1 + 2\frac{E}{E_g} \\ \gamma'' &= \frac{2}{E_g} \end{aligned} \tag{9.9}$$

The carrier concentration, carrier mobility, Seebeck coefficient, and Nernst coefficient can be expressed by (9.10)–(9.13):

$$n(p) = \frac{[2m^*(E=0)\gamma(E)]^{\frac{3}{2}}}{3\pi^2\hbar^3} \approx \frac{1}{R_H e} \tag{9.10}$$

$$\mu = R_H\sigma = \frac{\sigma}{n(p)e} \tag{9.11}$$

$$S = \pm\frac{\pi^2}{3}\frac{k}{e}kT\left[(s+1)\frac{\gamma''}{\gamma} - 2\frac{\gamma''}{\gamma'}\right] \tag{9.12}$$

$$N = \mu\frac{\pi^2}{3}\frac{k}{e}kT\left[\left(s - \frac{1}{2}\right)\frac{\gamma'}{\gamma} - 2\frac{\gamma''}{\gamma'}\right] \tag{9.13}$$

These equations can be fitted by using mathematical software or solved explicitly as a function of measured parameters to yield Fermi energy E_F, scattering parameter s, and DOS effective mass $m^*(E_F)$ from (9.14)–(9.16):

$$E_F = \frac{E_g}{2}\frac{\left(-A + \frac{\pi^2k^2T}{eE_g}\right) + \sqrt{\left(A - \frac{\pi^2k^2T}{eE_g}\right)^2 + 2\frac{\pi^2k^2T}{eE_g}A}}{A}, \quad A = S - \frac{N}{\mu} \tag{9.14}$$

$$s = \frac{1}{2} + \left(\frac{\frac{3N}{\mu E_g \frac{\pi^2k^2T}{eE_g}} + \frac{4}{E_g + 2E_F}}{1 + 2\frac{E_F}{E_g}}\right)E_F\left(1 + \frac{E_F}{E_g}\right) \tag{9.15}$$

$$m^*(E_F) = m^*(E=0)\gamma'(E_F) \tag{9.16}$$

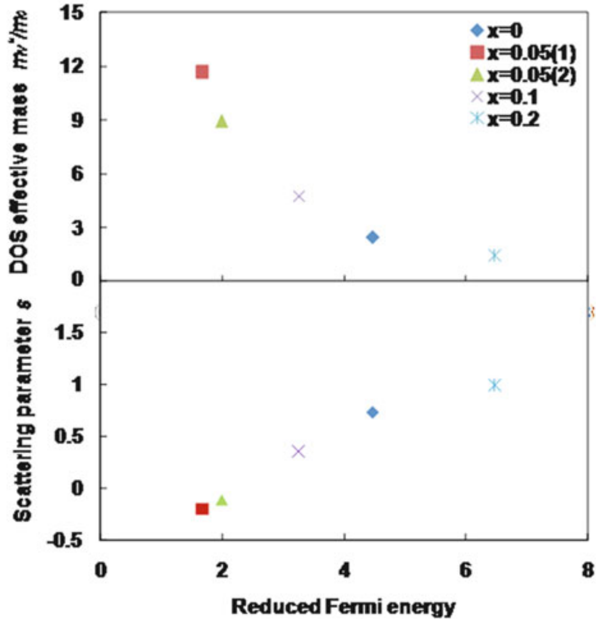

Fig. 9.17 DOS effective mass m_v*/m_0 and carrier scattering parameter s as a function of the reduced Fermi energy for $Yb_{0.6}Fe_2Co_2Sb_{12}$/x$FeSb_2$ nanocomposites [71]. With kind permission from Springer Science+Business Media: Journal of Electronic Materials **41**(6), 1030–1035 (2012), Zhou, C., Sakamoto, J., Morelli, D. Fig. 8

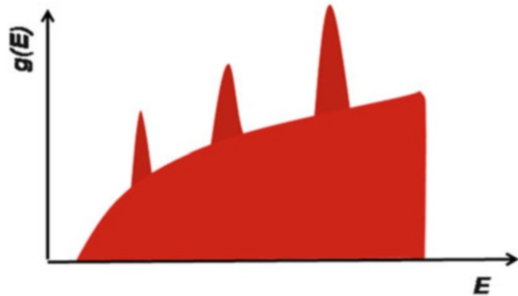

Fig. 9.18 Conceptual model of DOS for nanocomposites

The non-parabolic band model described by (9.9) has been used to study the band structure of $CoSb_3$ [91–93], so it appears to be valid to apply it to the example of $Yb_{0.6}Fe_2Co_2Sb_{12}$/x$FeSb_2$ nanocomposites. The bandgap E_g has adopted the literature-reported value of 0.5 eV from similar composition of $YbFe_4Sb_{12}$ [94, 95]. Therefore, we can calculate s and $m*(E_F)$. As it can be seen in Fig. 9.17, the DOS effective masses for samples x = 0.05(1) and x = 0.05(2) are three to four times greater than the effective mass for the reference sample x = 0. From classical physics, the DOS $g(E) \propto (m*)^{3/2}$, so the energy dependence of $m*$ can be viewed at least as a qualitative reflection of the shape of $g(E)$. The large effective mass obtained in the nanocomposite samples implies that the presence of nanoparticles may have induced a localized sharp peak in the DOS as depicted in the conceptual model in Fig. 9.18, which leads to the enhancement of Seebeck coefficient. The scattering parameter s, on the other hand, does not offer a positive contribution to the Seebeck

coefficient. Thus, based on the results from the method of four coefficients, we have shown that in this example, it is the effective mass rather than the scattering parameter that results in an enhanced Seebeck coefficient and hence power factors for the nanocomposites.

9.4 Conclusions and Outlook

In this chapter, we have focused our discussion mainly on the underdeveloped p-type skutterudites and briefly described several most commonly used synthesis approaches, namely, ball milling, melt spinning, in situ formation, high-pressure torsion, and solvo/hydrothermal synthesis that have been successfully applied to prepare skutterudite nanocomposites. Introducing nanoparticles or reducing the crystallite size has demonstrated promise in offering additional phonon scattering and therefore effectively reducing the thermal conductivity. Under certain conditions, the presence of the nanoparticles could also enhance the Seebeck coefficient to compensate for the reduction in electrical conductivity.

Figure 9.19 illustrates the progress towards higher *ZT* in p-type skutterudites by combining nanostructuring with the conventional void filling strategy. Starting from the basic binary skutterudite variant $Co_{0.9}Fe_{0.1}Sb_3$, nanocomposite $Co_{0.9}Fe_{0.1+x}Sb_{3+2x}$ enhances the *ZT* by almost 100 %. Additionally, using Yb a single filler element also achieves a ZT enhancement by almost 100 % in $Yb_{0.6}Fe_2Co_2Sb_{12}$, and creating $Yb_{0.6}Fe_2Co_2Sb_{12}$ nanocomposite with antimonide nano-inclusions further improve *ZT* by 23 %. The total *ZT* enhancement from $Co_{0.9}Fe_{0.1}Sb_3$ to $Yb_{0.6}Fe_2Co_2Sb_{12}$ nanocomposite represents a 150 % improvement. Table 9.2 summarizes recent *ZT* enhancement of skutterudite nanocomposites over their relative matrix materials that have been prepared by various synthesis techniques.

We also like to point out that although thermal conductivity reduction has been the major contributing factor that governs *ZT* enhancement, the lattice thermal conductivity cannot be reduced indefinitely. The minimum κ_l is estimated to be around 0.2 $Wm^{-1}\ K^{-1}$ for skutterudites assuming a phonon mean free path equal to one interatomic spacing. On the other hand, filled p-type skutterudites that exhibit high *ZT*s are generally very conductive, with an electrical resistivity typically below 1 mΩcm. In some cases, the electronic thermal conductivity is a significant contribution to the total thermal conductivity, sometimes even exceeding 50 %. This implies that the room for further *ZT* enhancement by reducing the lattice thermal conductivity is very limited. Therefore future work needs to seek new materials that exhibit higher Seebeck coefficient *S*:

$$ZT = \frac{S^2\sigma}{\kappa_l + \kappa_e}T = \frac{S^2\sigma}{\kappa_l + L\sigma T}T \Rightarrow S = \sqrt{\left(\frac{1}{T}\right)(LT + \rho\kappa_l)} \tag{9.17}$$

To explicitly show what Seebeck coefficient is needed for certain lattice thermal conductivity and resistivity in order to get a $ZT = 1$, we start from the definition of *ZT*

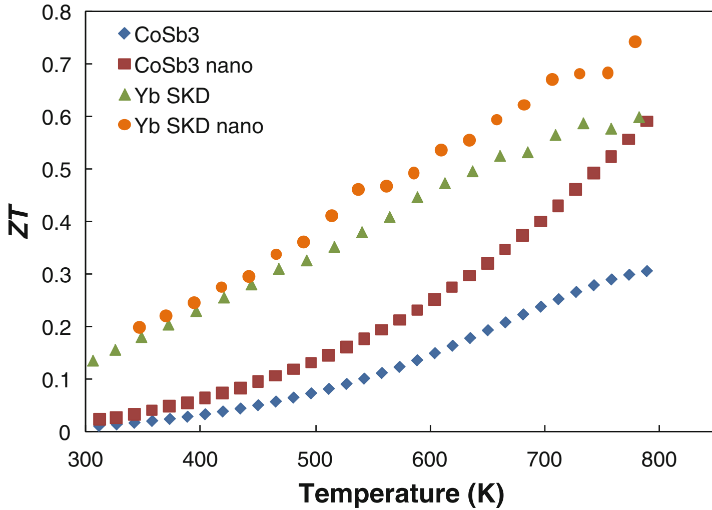

Fig. 9.19 Progress of *ZT* for p-type skutterudites via nanostructuring and void filling. $CoSb_3$ represents $Co_{0.9}Fe_{0.1}Sb_3$, and Yb SKD represents $Yb_{0.6}Fe_2Co_2Sb_{12}$. Nano represents nanocomposites with antimonide nano-inclusions. Data are excerpted from references [69] and [71]

Table 9.2 *ZT* enhancements in skutterudite nanocomposites over their relative matrix materials prepared by various synthesis techniques

Nanocomposite systems	Conduction type	Matrix ZT	Nanocomposite ZT	Percentage of improvement (%)	References
$Yb_xCo_4Sb_{12}/Yb_2O_3$	n-type	1	1.3	30	[70]
$Yb_{0.3}Co_4Sb_{12}$ melt spin	n-type	1	1.22	22	[67]
$In_xCe_yCo_4Sb_{12}/InSb$	n-type	~1.15	1.43	24	[4]
$Yb_{0.26}Co_4Sb_{12}/yGaSb$	n-type	~1.3	1.45	12	[10]
$Co_{0.9}Fe_{0.1}Sb_3/xFeSb_2$	p-type	0.30	0.59	97	[69]
$Yb_{0.6}Fe_2Co_2Sb_{12}/xFeSb_2$	p-type	0.60	0.74	23	[71]
$Mm_{0.68}Fe_3CoSb_{12}$ BM	p-type	0.78	0.86	10	[61]
$DD_{0.6}Fe_3CoSb_{12}$ HPT	p-type	1.2	1.3–1.45	8–21	[72]

and express the Seebeck coefficient S as a function of electrical resistivity ρ and lattice thermal conductivity κ_l as shown in (9.17). If we assume $ZT = 1$ at 800 K and the Lorenz number $L = 2.44 \times 10^{-8}\ V^2\ K^{-2}$, we plot the projected Seebeck coefficient as a function of electrical resistivity ρ and lattice thermal conductivity κ_l as shown in Fig. 9.20. Figure 9.21 shows the minimum Seebeck coefficients needed to attain a certain ZT assuming that κ_l is at minimum theoretical value 0.2 $Wm^{-1}\ K^{-1}$. Taking $ZT = 1$, for example, if we assume $\rho = 1$ mΩcm, then a $S > 164\ \mu VK^{-1}$ is needed.

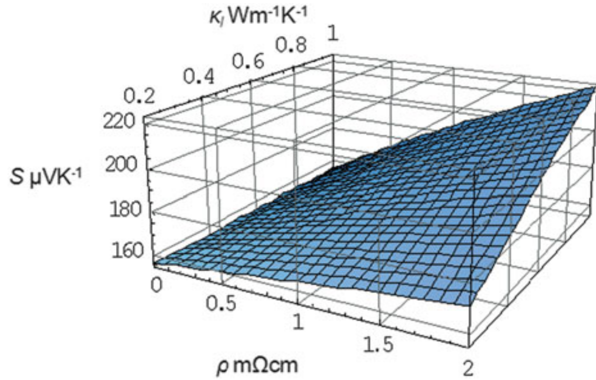

Fig. 9.20 3D graph of the projected Seebeck coefficient S as a function of electrical resistivity ρ and lattice thermal conductivity κ_l

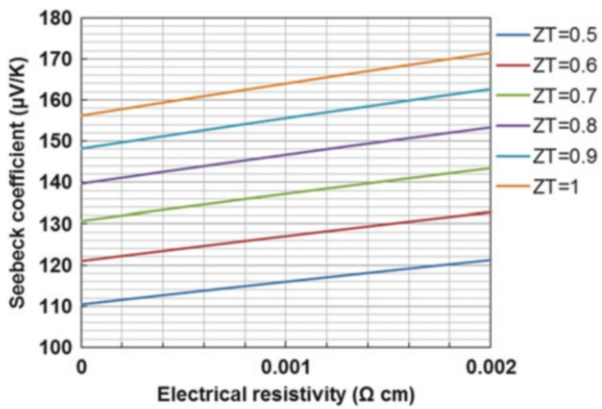

Fig. 9.21 Cross section of $\kappa_l = 0.2\ \mathrm{Wm}^{-1}\ \mathrm{K}^{-1}$ from Fig. 9.20 which is used to identify the minimum Seebeck coefficient needed to attain certain *ZT*

In conclusion, nanostructuring has been proven to provide significant benefits to the thermoelectrics, especially in terms of the thermal conductivity reduction. Future work needs to focus on improving the electronic properties by multiple approaches including nanostructuring so that reproducible $ZT > 2$ can ultimately be achieved in a variety of bulk material systems. In addition, the long-term stability of the nanocomposites has not been validated yet. Last but not least, it is crucial to evaluate the feasibility of transferring the exciting advances produced in the laboratory to thermoelectric generators for space and terrestrial technologies.

References

1. Androulakis, J., Hsu, K.F., Pcionek, R., Kong, H., Uher, C., Dangelo, J.J., Downey, A., Hogan, T., Kanatzidis, M.G.: Nanostructuring and high thermoelectric efficiency in p-type Ag(Pb1-ySny)(m)SbTe2+m. Adv. Mater. **18**(9), 1170 (2006)

2. Hsu, K.F., Loo, S., Guo, F., Chen, W., Dyck, J.S., Uher, C., Hogan, T., Polychroniadis, E.K., Kanatzidis, M.G.: Cubic AgPbmSbTe2+m: bulk thermoelectric materials with high figure of merit. Science **303**(5659), 818–821 (2004)
3. Li, H., Tang, X., Zhang, Q., Uher, C.: Rapid preparation method of bulk nanostructured Yb0.3Co 4Sb12+y compounds and their improved thermoelectric performance. Appl. Phys. Lett. **93**(Compendex), 252109 (2008)
4. Li, H., Tang, X.F., Zhang, Q.J., Uher, C.: High performance InxCeyCo4Sb12 thermoelectric materials with in situ forming nanostructured InSb phase. Appl. Phys. Lett. **94**(10), 102114 (2009)
5. Shi, X., Kong, H., Li, C.P., Uher, C., Yang, J., Salvador, J.R., Wang, H., Chen, L., Zhang, W.: Low thermal conductivity and high thermoelectric figure of merit in n-type Bax Yby Co4 Sb12 double-filled skutterudites. Appl. Phys. Lett. **92**(18), 182101 (2008)
6. Uher, C., Shi, X., Kong, H.: Enhanced thermoelectric figure of merit in BaxYb yCo4Sb12 Skutterudites. In: Boston, MA, United States 2008. Materials Research Society Symposium Proceedings, pp. 191–196. Materials Research Society
7. Bai, S.Q., Pei, Y.Z., Chen, L.D., Zhang, W.Q., Zhao, X.Y., Yang, J.: Enhanced thermoelectric performance of dual-element-filled skutterudites BaxCeyCo4Sb12. Acta Mater. **57**(11), 3135–3139 (2009)
8. Pei, Y.Z., Yang, J., Chen, L.D., Zhang, W., Salvador, J.R., Yang, J.H.: Improving thermoelectric performance of caged compounds through light-element filling. Appl. Phys. Lett. **95**(4), 042101 (2009)
9. Shi, X., Yang, J., Salvador, J.R., Chi, M., Cho, J.Y., Wang, H., Bai, S., Yang, J., Zhang, W., Chen, L.: Multiple-filled skutterudites: high thermoelectric figure of merit through separately optimizing electrical and thermal transports. J. Am. Chem. Soc. **133**((Compendex)), 7837–7846 (2011)
10. Xiong, Z., Chen, X.H., Huang, X.Y., Bai, S.Q., Chen, L.D.: High thermoelectric performance of Yb0.26Co4Sb12/yGaSb nanocomposites originating from scattering electrons of low energy. Acta Mater. **58**(11), 3995–4002 (2010)
11. Xie, W.J., Tang, X.F., Yan, Y.G., Zhang, Q.J., Tritt, T.M.: Unique nanostructures and enhanced thermoelectric performance of melt-spun BiSbTe alloys. Appl. Phys. Lett. **94**(10) (2009)
12. Biswas, K., He, J.Q., Blum, I.D., Wu, C.I., Hogan, T.P., Seidman, D.N., Dravid, V.P., Kanatzidis, M.G.: High-performance bulk thermoelectrics with all-scale hierarchical architectures. Nature **489**(7416), 414–418 (2012)
13. Morelli, D.T., Meisner, G.P.: Low-temperature properties of the filled skutterudite Cefe4sb12. J. Appl. Phys. **77**(8), 3777–3781 (1995)
14. Caillat, T., Borshchevsky, A., Fleurial, J.P.: Investigations of several new advanced thermoelectric materials at the jet propulsion lab. In: Proceedings of the 28th Intersociety Energy Conversion Engineering Conference, August 8, 1993–August 13, 1993, Atlanta, GA, USA 1993. Proceedings of the Intersociety Energy Conversion Engineering Conference, pp. 245–248. Published by SAE
15. Yang, J.H., Caillat, T.: Thermoelectric materials for space and automotive power generation. MRS Bulletin **31**(3), 224–229 (2006)
16. Sakamoto, J.S., Schock, H., Caillat, T., Fleurial, J.P., Maloney, R., Lyle, M., Ruckle, T., Timm, E., Zhang, L.: Skutterudite-based thermoelectric technology for waste heat recovery: progress towards a 1 kW generator. Sci. Adv. Mater. **3**(4), 621–632 (2011)
17. Rowe, D.M.: Thermoelectrics Handbook Macro to Nano. CRC (2005-12-09)
18. Caillat, T., Borshchevsky, A., Fleurial, J.P.: Properties of single crystalline semiconducting CoSb3. J. Appl. Phys. **80**(8), 4442–4449 (1996)
19. Slack, G.A., Tsoukala, V.G.: Some properties of semiconducting Irsb3. J. Appl. Phys. **76**(3), 1665–1671 (1994)

20. Chen, B.X., Xu, J.H., Uher, C., Morelli, D.T., Meisner, G.P., Fleurial, J.P., Caillat, T., Borshchevsky, A.: Low-temperature transport properties of the filled skutterudites CeFe4-xCoxSb12. Phys. Rev. B **55**(3), 1476–1480 (1997)
21. Braun, D.J., Jeitschko, W.: Preparation and structural investigations of anti-monides with the Lafe4p12 structure. J. Less. Common. Met. **72**(1), 147–156 (1980)
22. Braun, D.J., Jeitschko, W.: Ternary arsenides with Lafe4p12-type structure. J. Solid. State. Chem. **32**(3), 357–363 (1980)
23. Jeitschko, W., Braun, D.: Lafe4p12 with filled Coas3-type structure and isotypic lanthanoid-transition metal polyphosphides. Acta Crystallogr. B, Struct. Sci. **33**, 3401–3406 (1977)
24. Rowe, D.M.: CRC handbook of thermoelectrics. CRC Press, Boca Raton, London (1995)
25. Sales, B.C., Mandrus, D., Williams, R.K.: Filled skutterudite antimonides: a new class of thermoelectric materials. Science **272**(5266), 1325–1328 (1996)
26. Meisner, G.P., Morelli, D.T., Hu, S., Yang, J., Uher, C.: Structure and lattice thermal conductivity of fractionally filled skutterudites: solid solutions of fully filled and unfilled end members. Phys. Rev. Lett. **80**(16), 3551–3554 (1998)
27. Shi, X., Zhang, W., Chen, L.D., Yang, J., Uher, C.: Theoretical study of the filling fraction limits for impurities in CoSb3. Phys. Rev. B **75**(23) (2007)
28. Shi, X., Zhang, W., Chen, L.D., Yang, J.: Filling fraction limit for intrinsic voids in crystals: doping in skutterudites. Phys. Rev. Lett. **95**(18) (2005)
29. Zhou, C., Morelli, D., Zhou, X., Wang, G., Uher, C.: Thermoelectric properties of P-type Yb-filled skutterudite YbxFeyCo4-ySb12. Intermetallics **19**(10), 1390–1393 (2011)
30. Nolas, G.S., Kaeser, M., Littleton, R.T., Tritt, T.M.: High figure of merit in partially filled ytterbium skutterudite materials. Appl. Phys. Lett. **77**(12), 1855–1857 (2000)
31. Bauer, E., Galatanu, A., Michor, H., Hilscher, G., Rogl, P., Boulet, P., Noel, H.: Physical properties of skutterudites YbxM4Sb12, M = Fe, Co, Rh, Ir. Eur. Phys. J. B **14**(3), 483–493 (2000)
32. Morelli, D.T., Meisner, G.P., Chen, B.X., Hu, S.Q., Uher, C.: Cerium filling and doping of cobalt triantimonide. Phys. Rev. B **56**(12), 7376–7383 (1997)
33. Dresselhaus, M.S., Chen, G., Tang, M.Y., Yang, R., Lee, H., Wang, D., Ren, Z., Fleurial, J.-P., Gogna, P.: New directions for low-dimensional thermoelectric materials. Adv. Mater. **19**(8), 1043–1053 (2007)
34. Yang, R.G., Chen, G.: Thermal conductivity modeling of periodic two-dimensional nanocomposites. Phys. Rev. B **69**(19) (2004)
35. Joshi, G., Lee, H., Lan, Y.C., Wang, X.W., Zhu, G.H., Wang, D.Z., Gould, R.W., Cuff, D.C., Tang, M.Y., Dresselhaus, M.S., Chen, G., Ren, Z.F.: Enhanced thermoelectric figure-of-merit in nanostructured p-type silicon germanium bulk alloys. Nano Lett. **8**(12), 4670–4674 (2008)
36. Poudel, B., Hao, Q., Ma, Y., Lan, Y.C., Minnich, A., Yu, B., Yan, X.A., Wang, D.Z., Muto, A., Vashaee, D., Chen, X.Y., Liu, J.M., Dresselhaus, M.S., Chen, G., Ren, Z.F.: High-thermoelectric performance of nanostructured bismuth antimony telluride bulk alloys. Science **320**(5876), 634–638 (2008)
37. MacDonald, D.K.C.: Thermoelectricity: an introduction to the principles. John Wiley & Sons, Inc. (1961)
38. Hicks, L.D., Harman, T.C., Sun, X., Dresselhaus, M.S.: Experimental study of the effect of quantum-well structures on the thermoelectric figure of merit. Phys. Rev. B **53**(16), 10493–10496 (1996)
39. Harman, T.C., Spears, D.L., Manfra, M.J.: High thermoelectric figures of merit in PbTe quantum wells. J. Electron. Mater. **25**(7), 1121–1127 (1996)
40. Koga, T., Cronin, S.B., Dresselhaus, M.S., Liu, J.L., Wang, K.L.: Experimental proof-of-principle investigation of enhanced Z(3D)T in (001) oriented Si/Ge superlattices. Appl. Phys. Lett. **77**(10), 1490–1492 (2000)
41. Harman, T.C., Taylor, P.J., Walsh, M.P., LaForge, B.E.: Quantum dot superlattice thermoelectric materials and devices. Science **297**(5590), 2229–2232 (2002)

42. Venkatasubramanian, R., Siivola, E., Colpitts, T., O'Quinn, B.: Thin-film thermoelectric devices with high room-temperature figures of merit. Nature **413**(6856), 597–602 (2001)
43. Thiagarajan, S.J., Jovovic, V., Heremans, J.P.: On the enhancement of the figure of merit in bulk nanocomposites. Phys. Status Solidi. Rapid. Res. Lett. **1**(6), 256–258 (2007)
44. Goldsmid, H.J.: Applications of thermoelectricity. John Wiley & Sons Inc., New York (1960)
45. Heremans, J.P., Thrush, C.M., Morelli, D.T.: Thermopower enhancement in lead telluride nanostructures. Phys. Rev. B **70**(11) (2004)
46. Suryanarayana, C.: Mechanical alloying and milling. Progr. Mater. Sci. **46**(1–2), 1–184 (2001)
47. Recknagel, C., Reinfried, N., Hohn, P., Schnelle, W., Rosner, H., Grin, Y., Leithe-Jasper, A.: Application of spark plasma sintering to the fabrication of binary and ternary skutterudites. Sci. Tech. Adv. Mater. **8**(5), 357–363 (2007)
48. Liu, W.S., Zhang, B.P., Li, J.F., Zhao, L.D.: Thermoelectric property of fine-grained CoSb3 skutterudite compound fabricated by mechanical alloying and spark plasma sintering. J. Phys. Appl. Phys. **40**(2), 566–572 (2007)
49. Bao, S.Q., Yang, J.Y., Song, X.L., Peng, J.Y., Zhu, W., Fan, X.A., Duan, X.K.: Preparation of La-filled skutterudites by mechanical alloying and hot pressing and their thermal conductivities. Mater. Sci. Eng. **438**, 186–189 (2006)
50. Yang, J.Y., Chen, Y.H., Zhu, W., Bao, S.Q., Peng, J.Y., Fan, X.: Effect of sintering temperature on formation and thermoelectric properties of La0.4Ni0.4Co3.6Sb12 skutterudite by mechanical alloying and hot pressing. J. Phys. Appl. Phys. **38**(21), 3966–3969 (2005)
51. Liu, K.G., Xiang, D., Zhang, J.X.: Rapid synthesis of CoSb3 by MA-SPS and its thermoelectric properties. Rare Metals **24**(3), 257–260 (2005)
52. Yang, L., Wu, J.S., Zhang, L.T.: Thermoelectric properties of some skutterudite compounds with different grain size. J. Alloys Compd. **375**(1–2), 114–119 (2004)
53. Nakagawa, H., Tanaka, H., Kasama, A., Anno, H., Matsubara, K.: Grain size effects on thermoelectric properties of hot-pressed CoSb3. In: Proceedings of the 1997 16th International Conference on Thermoelectrics, ICT'97, August 26, 1997–August 29, 1997, Dresden, Ger 1997. International Conference on Thermoelectrics, ICT, Proceedings, pp. 351–355. IEEE
54. Mi, J.L., Zhao, X.B., Zhu, T.J., Tu, J.P.: Thermoelectric properties of Yb(0.15)Co(4)Sb (12) based nanocomposites with CoSb(3) nano-inclusion. J. Phys. Appl. Phys. **41**(20) (2008)
55. Alboni, P.N., Ji, X., He, J., Gothard, N., Tritt, T.M.: Thermoelectric properties of La(0.9)CoFe (3)Sb(12)-CoSb(3) skutterudite nanocomposites. J. Appl. Phys. **103**(11) (2008)
56. Shi, X., Chen, L.D., Bai, S.Q., Huang, X.Y., Zhao, X.Y., Yao, Q., Uher, C.: Influence of fullerene dispersion on high temperature thermoelectric properties of Ba(y)Co(4)Sb(12)-based composites. J. Appl. Phys. **102**(10) (2007)
57. Itoh, T., Ishikawa, K., Okada, A.: Effect of fullerene addition on thermoelectric properties of n-type skutterudite compound. J. Mater. Res. **22**(1), 249–253 (2007)
58. He, Z.M., Stiewe, C., Platzek, D., Karpinski, G., Muller, E., Li, S.H., Toprak, M., Muhammed, M.: Effect of ceramic dispersion on thermoelectric properties of nano-ZrO2/CoSb3 composites. J. Appl. Phys. **101**(4) (2007)
59. Shi, X., Chen, L., Yang, J., Meisner, G.P.: Enhanced thermoelectric figure of merit of CoSb3 via large-defect scattering. Appl. Phys. Lett. **84**(13), 2301–2303 (2004)
60. Katsuyama, S., Kanayama, Y., Ito, M., Majima, K., Nagai, H.: Thermoelectric properties of CoSb3 with dispersed FeSb2 particles. J. Appl. Phys. **88**(6), 3484–3489 (2000)
61. Zhang, L., Grytsiv, A., Kerber, M., Rogl, P., Bauer, E., Zehetbauer, M.J., Wosik, J., Nauer, G. E.: MmFe(4)Sb(12)- and CoSb3-based nano-skutterudites prepared by ball milling: kinetics of formation and transport properties. J. Alloys Compd. **481**(1–2), 106–115 (2009)
62. Abdellaoui, M., Gaffet, E.: The physics of mechanical alloying in a planetary ball mill—mathematical treatment. Acta Metall. Mater. **43**(3), 1087–1098 (1995)
63. Gerda Rogl, M.Z., Kerber, M., Rogl, P., Bauer, E.: Impact of ball milling and high-pressure torsion on the microstructure and thermoelectric properties of p- and n-type Sb-based skutterudites. Mater. Sci. Forum **667–669**, 1089–1094 (2011)

64. Herbst, J.F., Meyer, M.S., Pinkerton, F.E.: Magnetic hardening of Ce2Fe14B. J. Appl. Phys. **111**(7) (2012)
65. Croat, J.J., Herbst, J.F., Lee, R.W., Pinkerton, F.E.: High-energy product ND-FE-B permanent-magnets. Appl. Phys. Lett. **44**(1), 148–149 (1984)
66. Cahn, R.W.: Physical metallurgy, 3rd edn. Elsevier Science Publishers B.V. (1983)
67. Li, H., Tang, X., Su, X., Zhang, Q., Uher, C.: Nanostructured bulk YbxCo4Sb12 with high thermoelectric performance prepared by the rapid solidification method. J. Phys. Appl. Phys. **42**(14) (2009)
68. Li, H., Tang, X., Su, X., Zhang, Q.: Preparation and thermoelectric properties of high-performance Sb additional Yb(0.2)Co(4)Sb(12+y) bulk materials with nanostructure. Appl. Phys. Lett. **92**(20) (2008)
69. Zhou, C., Sakamoto, J., Morelli, D., Zhou, X., Wang, G., Uher, C.: Thermoelectric properties of Co[sub 0.9]Fe[sub 0.1]Sb[sub 3]-based skutterudite nanocomposites with FeSb[sub 2] nanoinclusions. J. Appl. Phys. **109**(6), 063722 (2011)
70. Zhao, X.Y., Shi, X., Chen, L.D., Zhang, W.Q., Bai, S.Q., Pei, Y.Z., Li, X.Y., Goto, T.: Synthesis of YbyCo4Sb12/Yb2O3 composites and their thermoelectric properties. Appl. Phys. Lett. **89**(9), 092121 (2006)
71. Zhou, C., Sakamoto, J., Morelli, D.: High-temperature thermoelectric properties of p-Type Yb-filled skutterudite nanocomposites with FeSb2 nanoinclusions. J. Electron. Mater. **41**(6), 1030–1035 (2012)
72. Rogl, G., Setman, D., Schafler, E., Horky, J., Kerber, M., Zehetbauer, M., Falmbigl, M., Rogl, P., Royanian, E., Bauer, E.: High-pressure torsion, a new processing route for thermoelectrics of high ZTs by means of severe plastic deformation. Acta Mater. **60**(5), 2146–2157 (2012)
73. Zhang, L., Grytsiv, A., Bonarski, B., Kerber, M., Setman, D., Schafler, E., Rogl, P., Bauer, E., Hilscher, G., Zehetbauer, M.: Impact of high pressure torsion on the microstructure and physical properties of Pr0.67Fe3CoSb12, Pr0.71Fe3.5Ni0.5Sb12, and Ba0.06Co4Sb12. J. Alloys Compd. **494**(1–2), 78–83 (2010)
74. Valiev, R.Z., Kaibyshev, O.A., Kuznetsov, R.I., Musalimov, R.S., Tsenev, N.K.: The low-temperature superplasticity of metallic materials. Doklady Akademii Nauk Sssr **301**(4), 864 (1988)
75. Zehetbauer, M.J., Kohout, J., Schafler, E., Sachslehner, F., Dubravina, A.: Plastic deformation of nickel under high hydrostatic pressure. J. Alloys Compd. **378**(1–2), 329–334 (2004)
76. Zehetbauer, M.J., Stuwe, H.P., Vorhauer, A., Schafler, E., Kohout, J.: The role of hydrostatic pressure in severe plastic deformation. Adv. Eng. Mater. **5**(5), 330–337 (2003)
77. Doherty, R.D., Hughes, D.A., Humphreys, F.J., Jonas, J.J., Jensen, D.J., Kassner, M.E., King, W.E., McNelley, T.R., McQueen, H.J., Rollett, A.D.: Current issues in recrystallization: a review. Mater. Sci. Eng. **238**(2), 219–274 (1997)
78. Wojciech, L., Suchanek, R.E.R.: Hydrothermal synthesis of advanced ceramic powders. Adv. Sci. Technol. **45**, 184–193 (2006)
79. Demazeau, G.: Solvothermal reactions: an original route for the synthesis of novel materials. J. Mater. Sci. **43**(7), 2104–2114 (2008)
80. Wang, Q., Pan, D.C., Jiang, S.C., Ji, X.L., An, L.J., Jiang, B.Z.: A solvothermal route to size- and shape-controlled CdSe and CdTe nanocrystals. J. Cryst. Growth **286**(1), 83–90 (2006)
81. Li, J.Q., Feng, X.W., Sun, W.A., Ao, W.Q., Liu, F.S., Du, Y.: Solvothermal synthesis of nano-sized skutterudite Co4-xFexSb12 powders. Mater. Chem. Phys. **112**(1), 57–62 (2008)
82. Lu, P.X., Wu, F., Han, H.L., Wang, Q.A., Shen, Z.G., Hu, X.: Thermoelectric properties of rare earths filled CoSb3 based nanostructure skutterudite. J. Alloys Compd. **505**(1), 255–258 (2010)
83. Tritt, T.M.: Thermal Conductivity, Theory, Properties and Applications. Kluwer Academic/Plenum Publishers, New York (2004)
84. Zhang, L., Rogl, G., Grytsiv, A., Puchegger, S., Koppensteiner, J., Spieckermann, F., Kabelka, H., Reinecker, M., Rogl, P., Schranz, W., Zehetbauer, M., Carpenter, M.A.: Mechanical properties of filled antimonide skutterudites. Mater. Sci. Eng. B **170**(1–3), 26–31 (2010)

85. Toprak, M.S., Stiewe, C., Platzek, D., Williams, S., Bertini, L., Muller, E.C., Gatti, C., Zhang, Y., Rowe, M., Muhammed, M.: The impact of nanostructuring on the thermal conductivity of thermoelectric CoSb3. Adv. Funct. Mater. **14**(12), 1189–1196 (2004)
86. Salvador, J.R., Yang, J., Shi, X., Wang, H., Wereszczak, A.A., Kong, H., Uher, C.: Transport and mechanical properties of Yb-filled skutterudites. Philosophical Magazine **89**(19), 1517–1534 (2009)
87. Ioffe, A.F.: Semiconductor Thermoelements and Thermoelectric Cooling. Infosearch Limited, London (1957)
88. Chernik, I.A., Kaidanov, V.I., Vinograd, M.I., Kolomoet, N.V.: Investigation of valence band of lead telluride using transport phenomena. Sov. Phys. Semiconduct. **2**(6), 645 (1968)
89. Jovovic, V., Thiagarajan, S.J., Heremans, J.P., Komissarova, T., Khokhlov, D., Nicorici, A.: Low temperature thermal, thermoelectric, and thermomagnetic transport in indium rich Pb[sub 1 - x]Sn[sub x]Te alloys. J. Appl. Phys. **103**(5), 053710 (2008)
90. Jovovic, V., Thiagarajan, S.J., West, J., Heremans, J.P., Story, T., Golacki, Z., Paszkowicz, W., Osinniy, V.: Transport and magnetic properties of dilute rare-earth-PbSe alloys. J. Appl. Phys. **102**(4), 043707 (2007)
91. Singh, D.J., Pickett, W.E.: Skutterudite antimonides—quasi-linear bands and unusual transport. Phys. Rev. B **50**(15), 11235–11238 (1994)
92. Sofo, J.O., Mahan, G.D.: Electronic structure and transport properties of CoSb3: a narrow band-gap semiconductor. Mater. Res. Soc. Symp. Proc. **545**, 315–320 (1999)
93. Koga, K., Akai, K., Oshiro, K., Matsuura, M.: Electronic structure and thermoelectric property of skutterudite CoSb3. Thermoelectric Materials 2001-Research and Applications, November 26, 2001–November 29, 2001 **691**, 339–344 (2002)
94. Dedkov, Y.S., Molodtsov, S.L., Rosner, H., Leithe-Jasper, A., Schnelle, W., Schmidt, M., Grin, Y.: Divalent state of ytterbium in YbFe4Sb12 filled skutterudite. Phys. C Supercond. **460–462**, 698–699 (2007)
95. Takegahara, K., Harima, H.: Electronic band structure of the filled skutterudite YbFe4Sb12. J. Phys. Soc. Jpn. **71**, 240–242 (2002)

Chapter 10
Thermoelectric Properties of $CoSb_3$ Based Skutterudites Filled by Group 13 Elements

Ken Kurosaki, Adul Harnwunggmoung, and Shinsuke Yamanaka

Abstract Thermoelectric (TE) generators can directly generate electrical power from waste heat, and thus could be an important part of the solution to future power supply and sustainable energy management. The main obstacle to the widespread use of TEs in diverse industries, e.g., for exhaust heat recovery in automobiles, is the low efficiency of materials in converting heat to electricity. The conversion efficiency of TE materials is quantified by the dimensionless figure of merit, *ZT*, and the way to enhance *ZT* is to decrease the lattice thermal conductivity (κ_{lat}) of the material, while maintaining a high electrical conductivity, i.e., to create a situation in which phonons are scattered but electrons are unaffected. Various concepts have been used in the search for this situation, e.g., the use of rattling of atoms weakly bonded in crystals and nanostructuring of materials. Here we report TE properties of skutterudites filled by group 13 elements, i.e., Ga, In, and Tl. Our group has examined the high-temperature TE properties of various skutterudites filed by group 13 elements, viz., Ga-filled $CoSb_3$, Tl-filled $CoSb_3$, and In/Tl double-filled $CoSb_3$. All systems exhibit relatively high TE figure of merit, especially, $Tl_{0.1}In_xCo_4Sb_{12}$ achieves a dramatic reduction of κ_{lat}, resulting in the $ZT = 1.20$ at 700 K—very high for a bulk material. We have demonstrated that the reduction of κ_{lat} in $Tl_{0.1}In_xCo_4Sb_{12}$ is due to the effective phonon scattering both by rattling of two atoms: Tl and In and by naturally formed nano-sized In_2O_3 particles (<50 nm).

K. Kurosaki (✉) • S. Yamanaka
Division of Sustainable Energy and Environmental Engineering, Graduate School of Engineering, Osaka University, 2-1 Yamadaoka, Suita, Osaka 565-0871, Japan
e-mail: kurosaki@see.eng.osaka-u.ac.jp; yamanaka@see.eng.osaka-u.ac.jp

A. Harnwunggmoung
Thermoelectric and Nanotechnology Research Center, Faculty of Science and Technology, Rajamangala University of Technology Suvarnabhumi, Huntra, Phranakhon Si Ayutthaya 13000, Thailand
e-mail: adul_harn@yahoo.com

X. Wang and Z.M. Wang (eds.), *Nanoscale Thermoelectrics*, Lecture Notes in Nanoscale Science and Technology 16, DOI 10.1007/978-3-319-02012-9_10,
© Springer International Publishing Switzerland 2014

Since the combined approach of double filling and self-formed nanostructures could be applicable to various clathrate compounds, our results suggest a new strategy in the improvement of bulk TE materials.

10.1 Introduction

Thermoelectric (TE) materials can convert waste heat into electrical power, which is an effective way to reduce greenhouse gas emissions and contribute substantially to future power supply and sustainable energy management [1–6]. The main obstacle to the widespread use of TEs in diverse industries, e.g., for exhaust heat recovery in automobiles, is the low efficiency of materials in converting heat to electricity. The efficiency of a material used in TE devices is determined by the dimensionless figure of merit, $ZT = S^2T\rho^{-1}\kappa^{-1}$, where S is the Seebeck coefficient, T is the absolute temperature, ρ is the electrical resistivity, and κ is the total thermal conductivity ($\kappa = \kappa_{lat} + \kappa_{el}$, where κ_{lat} and κ_{el} are the lattice and electronic contributions, respectively). Since the S, ρ, and κ_{el} in bulk materials are interrelated, it is very difficult to control them independently. Therefore, the reduction of κ_{lat} is essential to enhancing ZT. The ZT value of the materials currently used in commercial cooling devices is still limited to about 1 or less over the entire operating temperature range, corresponding to a device efficiency of several percent. Recent improvements in TE materials have led to many advances, and enhanced ZT values have been reported for several classes of bulk materials, including filled skutterudites.

The name of skutterudite is derived from a naturally occurring mineral with $CoAs_3$ structure, which was firstly discovered in Skutterud (Norway). The general formula of skutterudite compounds is MX_3, where M is one of the group 9 transition metals such as Co, Rh, or Ir and X is a pnictogen atom such as P, As, and Sb. These compounds are body-centered-cubic structure that contains 32 atoms in the unit cell with space group Im3. The most important point of the skutterudite structure is that there are two voids in the unit cell which can be filled by filler atoms with an ionic radius lower than the cage radius. This generates a so-called filled skutterudite with formula RM_4X_{12}, where R is electropositive element like rare earth or alkaline earth. Figure 10.1 displays the filled skutterudite structure where the R, M, and X are shown in red, blue, and green spheres, respectively.

Early investigations on unfilled skutterudites dates back to the mid-1950s. Among skutterudites, $CoSb_3$ has attracted the greatest interest in waste heat to electricity conversion applications due to its reasonable band gap of ~0.2 eV, high carrier mobility, and the fact that it is composed of inexpensive and environmentally benign constituent elements as compared to other skutterudites such as $CoAs_3$. However, the κ_{lat} of the pure binary $CoSb_3$ is too high, which leads to low ZT and thus poor conversion efficiency for TE applications.

In 1977 La-filled [7] and in 1991 Ba-filled [8] skutterudites were synthesized. However, it has not become popular. In 1994, Slack [9] proposed the concept of "phonon–glass electron–crystal" (PGEC) as one of the desirable features a material

Fig. 10.1 Filled-skutterudite structure of RM_4X_{12}. *R*, *M*, and *X* are shown in *red*, *blue*, and *green* spheres, respectively

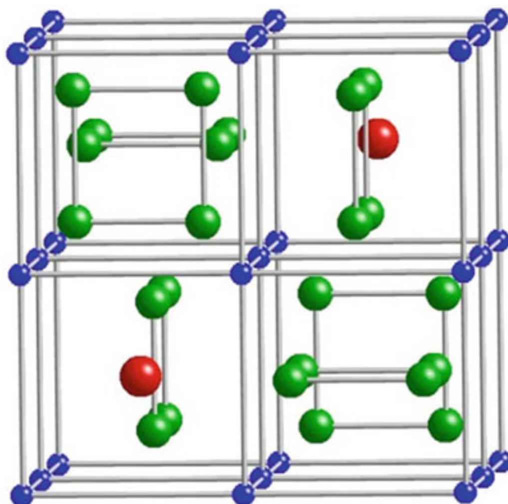

should possess to maximize the *ZT*, in which a material conducts heat like a glass but behaves like a good crystal for the electronic properties. The typical example of the PGEC concept is filled skutterudites, such as $CeFe_4Sb_{12}$ [10]. Filled skutterudites realize the PGEC concept through the following strategies: a semiconductor-like behavior may lead to large *S* and low ρ; in addition, the loosely bound filler atoms in the skutterudite cages act as rattlers and thereby reduce the κ_{lat} [11].

It has been reported that a large variety of guest atoms can be filled, such as rare earth elements [12–16], alkaline earth elements [17–19], alkali metals [20, 21], and others [22–26]. The filling atoms are loosely bound to the other atoms in the intrinsic cages, leading to strong phonon scattering and significant reduction of the κ_{lat} [27, 28]. In addition to the single-filled system, a double-filling approach has recently been attracting increasing attention. Introducing two filler types from different chemical groups into the cages of $CoSb_3$ could introduce two distinctive filler vibrational frequencies for a broader range lattice phonon scattering, leading to a further reduction of κ_{lat} [29, 30]. As the results, the maximum *ZT* values were improved to 1.3–1.4 in double-filled skutterudites as shown in Fig. 10.2 [12, 14, 16–21, 30–34].

As described above, it has been widely reported that the voids in $CoSb_3$ can be fully or partially filled with a variety of different atoms. However, reports on the TE properties of skutterudites filled by group 13 elements, such as Ga, In, and Tl, have been limited. Here we review the TE properties of $CoSb_3$-based skutterudites filled by group 13 elements, which are mainly obtained in our group. In particular, the TE properties of the single-filled system: $Tl_xCo_4Sb_{12}$ and $Ga_xCo_4Sb_{12}$ and the double-filled system: $Tl_{0.1}In_xCo_4Sb_{12}$ will be discussed.

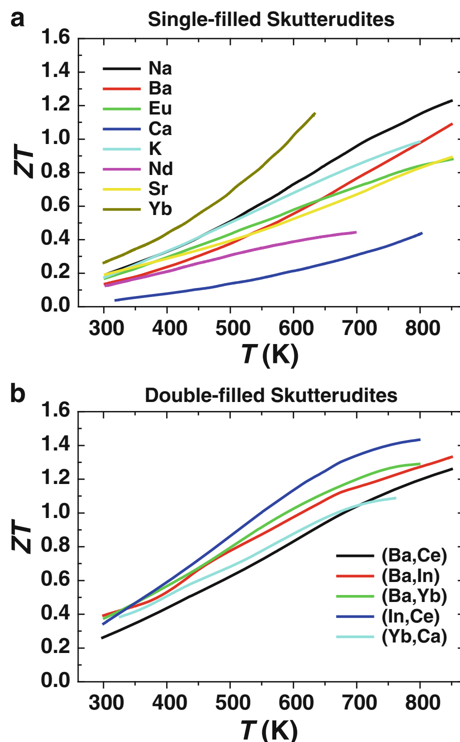

Fig. 10.2 Temperature dependence of dimensionless figure of merit, *ZT* of various filled-skutterudites reported so far; (**a**) single-filled system and (**b**) double-filled system

10.2 Thermoelectric Properties of Tl-filled skutterudite: $Tl_xCo_4Sb_{12}$ [26]

Among $CoSb_3$-based skutterudites filled by group 13 elements, the authors have focused on Tl-filled skutterudites: $Tl_xCo_4Sb_{12}$, because of the following reasons. First, the electronegativity of Tl is close to that of Sb, which suggests that it may have a small effect on the electrical transport properties of $CoSb_3$. Second, the radius of the void in a 12-coordinated site is close to the radius of Tl^{1+}. Finally, Tl is heavier than other elements that have been recognized as compatible R atoms in RCo_4Sb_{12}. However, there is only one report [22], of Tl-filled skutterudites in which the TE properties below room temperature have been systematically investigated. In addition, in [22], it has been reported that Tl-filled skutterudites readily formed and up to around 22 % of the voids in $CoSb_3$ could be filled with Tl. Therefore, the authors prepared the polycrystalline samples of $Tl_xCo_4Sb_{12}$ ($x = 0$, 0.05, 0.10, 0.15, 0.20, and 0.25) and examined their high-temperature TE properties from room temperature to 750 K [26].

Figure 10.3 shows powder x-ray diffraction (XRD) patterns of the polycrystalline samples of $Tl_xCo_4Sb_{12}$ ($x = 0$, 0.05, 0.10, 0.15, 0.20, and 0.25) prepared in our group, together with the peak positions calculated from the crystal structure of $CoSb_3$.

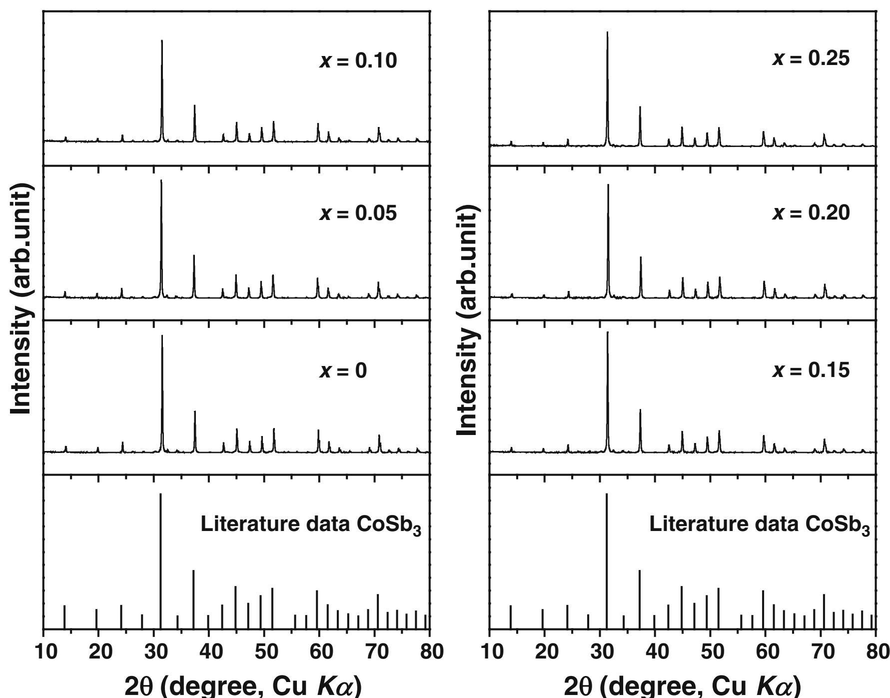

Fig. 10.3 Powder XRD patterns of polycrystalline samples of $Tl_xCo_4Sb_{12}$ ($x = 0$, 0.05, 0.10, 0.15, 0.20, and 0.25), together with the peak positions calculated from the crystal structure of $CoSb_3$

Basically, all samples are identified as skutterudite compounds, although they contain negligible amounts of $CoSb_2$ as an impurity phase. The lattice parameters of $Tl_xCo_4Sb_{12}$ increase almost linearly with the increase in the Tl content up to $x = 0.20$ and the lattice parameter of $Tl_{0.25}Co_4Sb_{12}$ is almost identical with that of $Tl_{0.20}Co_4Sb_{12}$, as shown in Fig. 10.4. Therefore, it can be concluded that the Tl-filling limit in $CoSb_3$ is between 20 and 25 at.%, which is consistent with the literature data [22].

Figure 10.5 shows the temperature dependence of (a) the electrical resistivity, ρ and (b) Seebeck coefficient, S for polycrystalline samples of $Tl_xCo_4Sb_{12}$. The magnitude of ρ for $CoSb_3$ is approximately 11×10^{-5} Ω m at 330 K and decreases with increasing temperature. On the other hand, the ρ values of $Tl_xCo_4Sb_{12}$ are rather low (1–3 $\times$ 10^{-5} Ω m at 330 K) and indicate slight-positive temperature dependency. The magnitude of ρ for $Tl_xCo_4Sb_{12}$ decreases with increase in the Tl content x. S for all samples is negative, which indicates that a majority of charge carriers are electrons. The absolute S of $CoSb_3$ is 330 μV K^{-1} at 330 K and remains constant up to around 450 K, then decreases gradually with increasing temperature. The absolute S of $Tl_xCo_4Sb_{12}$ decreases with increase in the Tl content x. The results for both ρ and S imply that Tl-filling leads to an increase of the electron

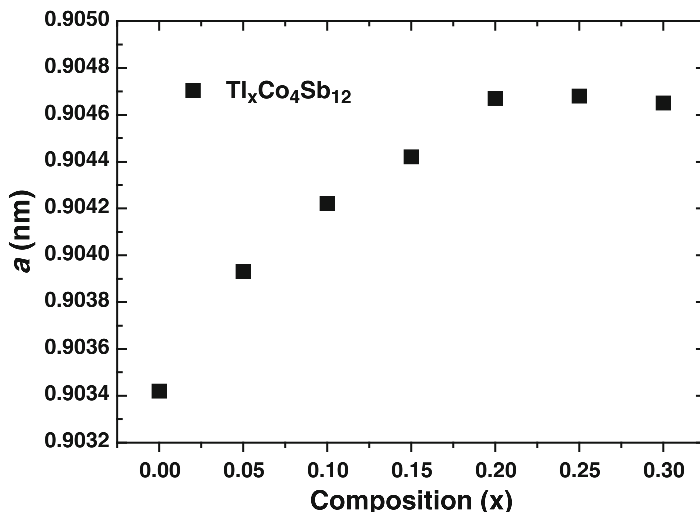

Fig. 10.4 Lattice parameters of polycrystalline samples of $Tl_xCo_4Sb_{12}$ ($x = 0$, 0.05, 0.10, 0.15, 0.20, and 0.25)

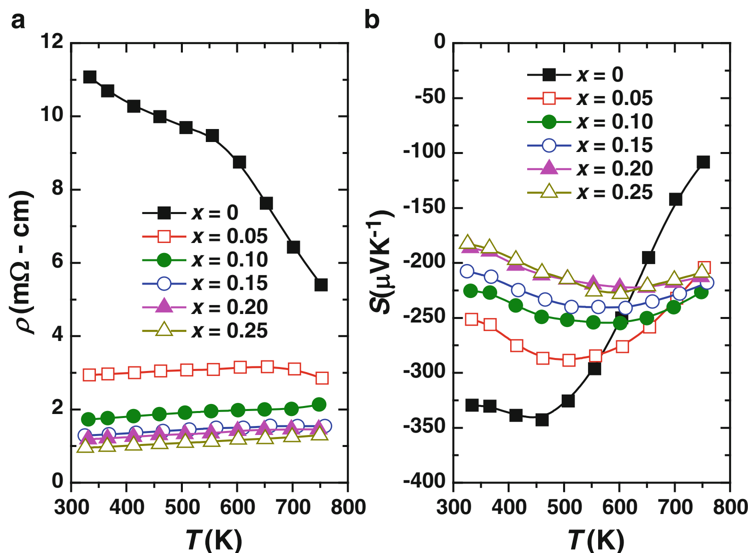

Fig. 10.5 Temperature dependences of (**a**) the electrical resistivity, ρ and (**b**) the Seebeck coefficient, S of polycrystalline samples of $Tl_xCo_4Sb_{12}$ ($x = 0$, 0.05, 0.10, 0.15, 0.20, and 0.25)

carrier concentration. Room temperature values of Hall carrier concentration (n_H) and Hall mobility (μ_H) for $Tl_xCo_4Sb_{12}$ are summarized in Table 10.1 and plotted in Fig. 10.6, as a function of the Tl content x. n_H for $Tl_xCo_4Sb_{12}$ increases with increasing Tl content, viz. n_H for $Tl_{0.25}Co_4Sb_{12}$ (23.9×10^{-19} cm^{-3}) is more than

Table 10.1 Lattice parameter a, density d, Seebeck coefficient S (300 K), electrical resistivity ρ (300 K), Hall carrier concentration n_H (300 K), Hall mobility μ_H (300 K), average sound velocity v_{ave}, Young's modulus E, and Debye temperature θ_D for polycrystalline samples of $Tl_xCo_4Sb_{12}$ ($x = 0, 0.05, 0.10, 0.15, 0.20$, and 0.25)

x	a (nm)	d (g cm^{-3})	% T.D.	S (μV K^{-1})	ρ (mΩ cm)	n_H (10^{19} cm^{-3})	μ_H (cm^2 V^{-1} s^{-1})	v_{ave} (m s^{-1})	E (GPa)	θ_D (K)
0	0.90342	7.55	98	−333	13.76	1.56	29.02	3,684	142	320
0.05	0.90393	7.62	99	−241	2.98	5.89	35.50	3,710	146	321
0.10	0.90422	7.59	98	−221	1.80	10.60	32.73	3,695	144	320
0.15	0.90442	7.71	99	−205	1.25	18.10	27.50	3,666	143	318
0.20	0.90467	7.69	98	−180	1.11	21.10	26.65	3,637	140	315
0.25	0.90468	7.69	98	−184	1.00	23.90	26.10	3,613	139	313

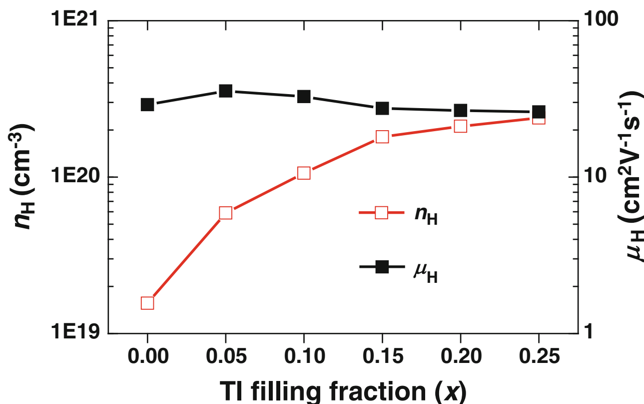

Fig. 10.6 The Hall carrier concentration, n_H and Hall mobility, μ_H at 300 K of polycrystalline samples of $Tl_xCo_4Sb_{12}$, as a function of the Tl filling fraction, x

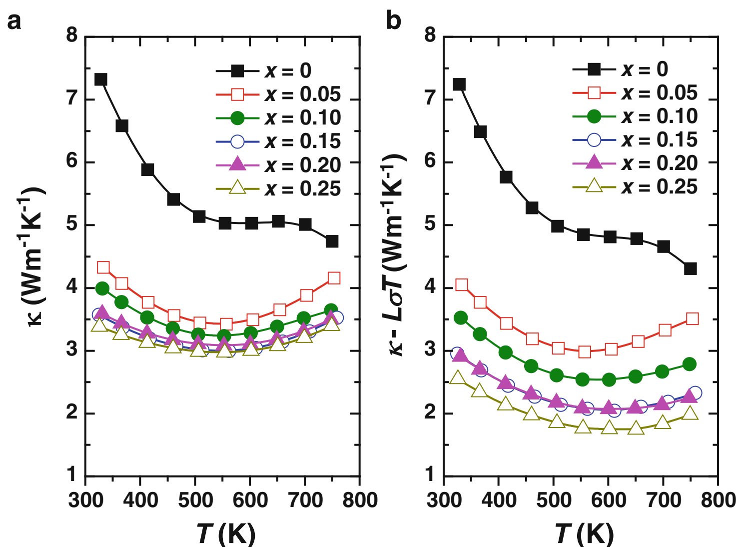

Fig. 10.7 Temperature dependences of the thermal conductivity of polycrystalline samples of $Tl_xCo_4Sb_{12}$ ($x = 0$, 0.05, 0.10, 0.15, 0.20, and 0.25); (**a**) total thermal conductivity, κ and (**b**) lattice thermal conductivity, κ_{lat}

ten times that of $CoSb_3$ (1.56×10^{-19} cm^{-3}). On the other hand, the $Tl_xCo_4Sb_{12}$ samples exhibits similar μ_H values at all Tl-filling contents. These results indicate that the Tl-filling increases the n_H, but has no significant influence on μ_H.

The thermal conductivity (κ) for $Tl_xCo_4Sb_{12}$ are significantly reduced by Tl-filling, as shown in Fig. 10.7a. $Tl_{0.25}Co_4Sb_{12}$ exhibits the lowest κ over the entire temperature range; at room temperature, κ for $Tl_{0.25}Co_4Sb_{12}$ is 3.4 W m^{-1} K^{-1}, which is less than

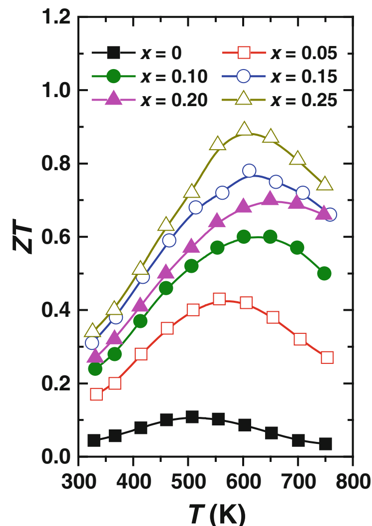

Fig. 10.8 Temperature dependences of the dimensionless figure of merit, *ZT* of polycrystalline samples of $Tl_xCo_4Sb_{12}$ ($x = 0$, 0.05, 0.10, 0.15, 0.20, and 0.25)

half that of $CoSb_3$. Figure 10.7b shows the temperature dependence of the lattice thermal conductivity (κ_{lat}) for $Tl_xCo_4Sb_{12}$. κ_{lat} was obtained by subtracting the electronic thermal conductivity ($\kappa_{el} = L\sigma T$, $L = 2.45 \times 10^{-8}$ W Ω K^{-2}) from the total (measured) thermal conductivity κ. κ_{lat} for $Tl_xCo_4Sb_{12}$ significantly decreases with increase in the Tl content. However, as summarized in Table 10.1, the experimental results for average sound velocity (v_{ave}), Young's modulus (E), and Debye temperature (θ_D) obtained from the sound velocity measurements are similar at all Tl-filling contents, despite κ_{lat} being significantly reduced by Tl-filling. These results imply that Tl in $CoSb_3$ has no direct effect on the strength of the interatomic bonding, but that Tl is weakly bonded with the other atoms, which results in a reduction of κ_{lat} by rattling within the cage.

The low κ, compared with $CoSb_3$, results in large TE figure of merit (*ZT*) for Tl-filled $CoSb_3$, as shown in Fig. 10.8. In particular, $Tl_{0.25}Co_4Sb_{12}$ exhibits the best *ZT* values; the maximum value of 0.90 is obtained at 600 K.

10.3 Thermoelectric Properties of Ga-Filled Skutterudite: $Ga_xCo_4Sb_{12}$ [35]

There have been various reports on the TE properties of skutterudites filled by various elements, such as Ba-, K-, Na-, Ca-, Nd-, Sr-, Eu-, Yb-, In-, and Tl-filled skutterudites [12, 14, 16–22, 26, 36–38]. Although the TE properties of In-, and Tl-filled skutterudites have been investigated, the Ga-$CoSb_3$ system has been scarcely investigated. Recently, Xiong et al. [39] has reported the TE properties of the $Yb_{0.26}Co_4Sb_{12}$/yGaSb system, where only very small amount of Ga can fill

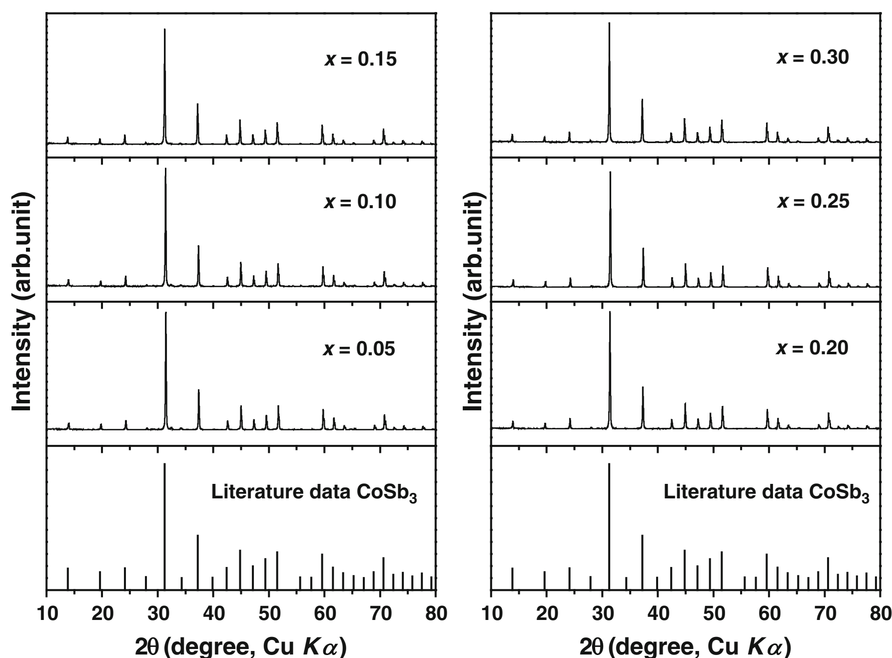

Fig. 10.9 Powder XRD patterns of polycrystalline samples of $Ga_xCo_4Sb_{12}$ ($x = 0.05, 0.10, 0.15, 0.20, 0.25$, and 0.30), together with the peak positions calculated from the crystal structure of $CoSb_3$

into the crystal voids of $CoSb_3$. Additionally, very recently, Qiu has reported that Ga atoms occupy both the void and Sb sites in $CoSb_3$ and couple with each other and the *ZT* quickly increases to 0.7 at a Ga doping content as low as 0.1 per Co_4Sb_{12} [40]. Here, the authors show the TE properties of polycrystalline samples of $Ga_xCo_4Sb_{12}$ ($x = 0.05, 0.10, 0.15, 0.20, 0.25$, and 0.30) in the temperature range from room temperature to 750 K, which are obtained in the author's group [35].

The powder XRD patterns of the polycrystalline samples of $Ga_xCo_4Sb_{12}$ ($x = 0.05, 0.10, 0.15, 0.20, 0.25$, and 0.30) are shown in Fig. 10.9. All the peaks in the XRD patterns are identified as the peaks derived from the skutterudite phase. However, in the XRD patterns of the samples of $x = 0.05$, 0.10, and 0.15, negligible peaks of $CoSb_2$ as the impurity phase can be observed. The lattice parameters calculated from the XRD patterns are plotted in Fig. 10.10, together with the data for Tl-filled $CoSb_3$ [26]. The lattice parameters of the Ga-$CoSb_3$ samples slightly increase with Ga-addition up to around $x = 0.05$, and after that keep a constant. In contrast, the lattice parameters of the Tl-$CoSb_3$ samples increase almost linearly with increasing Tl-addition up to $x = 0.20$ and after that keep a constant. These results imply that Tl can be filled up to around $x = 0.20$ in $Tl_xCo_4Sb_{12}$ but the maximum filling ratio of Ga in $CoSb_3$ is lower than $x = 0.05$ in $Ga_xCo_4Sb_{12}$. This result is well consistent with the other Ga-filled skutterudite reported by Xiong et al. [39], in which

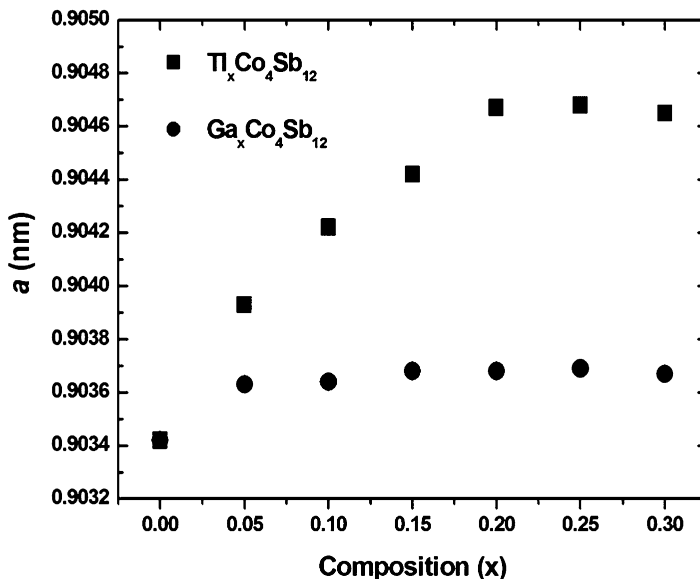

Fig. 10.10 Lattice parameters of polycrystalline samples of $Ga_xCo_4Sb_{12}$ ($x = 0.05, 0.10, 0.15, 0.20, 0.25$, and 0.30), together with the data of polycrystalline samples of $Tl_xCo_4Sb_{12}$

only very small amount of Ga can fill into the crystal voids of $CoSb_3$. In addition, in [40], it has been reported that the maximum filling fraction of Ga in the voids of $CoSb_3$ is around 8 %.

In order to confirm the filling limit of Ga into $CoSb_3$, the field emission scanning electron microscopy (FE-SEM) and energy dispersive x-ray (EDX) analysis was performed on the surface of the hot-pressed samples. The XRD pattern, FE-SEM image, and EDX mapping images of $Ga_{0.30}Co_4Sb_{12}$ are shown in Fig. 10.11. As shown in Fig. 10.11a, no peaks corresponding to GaSb are observed in the XRD pattern. Since the main peak position of Ga metal is close to a peak of $CoSb_3$, it is unclear that whether Ga metal exists or not in the sample. On the other hand, as shown in Fig. 10.11b, the area that Ga concentrated in small pores is observed in the FE-SEM image and the EDX mapping images. Therefore, it can be concluded that most of Ga exists as metal state in the $Ga_{0.30}Co_4Sb_{12}$ sample. This result is not consistent with the other Ga-filled skutterudite reported by Xiong et al. [39], in which some evidence of impurity phase of GaSb but not metallic Ga has been shown. At this point, the reason of the differences between our data and the literature data has not been clearly understood. From the quantitative EDX analysis, the amount of Ga in the matrix phase is confirmed to be approximately 0.1 at.%, i.e., $x = \sim 0.02$ in $Ga_xCo_4Sb_{12}$. Therefore, it can be said that the maximum filling ratio of Ga into $CoSb_3$ is $x = 0.02$ in $Ga_xCo_4Sb_{12}$, and when exceeding the filling limit, Ga exists as metal state. This is clearly different from the cases of In- and Tl-filled $CoSb_3$, in which both In and Tl can be filled up to approximately $0.05 < x < 0.1$ in

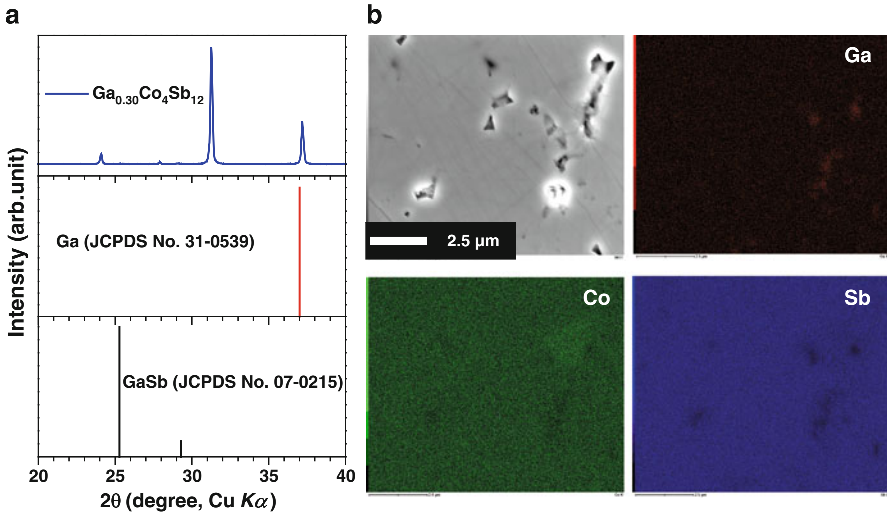

Fig. 10.11 (**a**) Powder XRD pattern of polycrystalline sample of $Ga_{0.30}Co_4Sb_{12}$, together with the peak positions of Ga and GaSb. (**b**) SEM and EDX mapping images of polycrystalline sample of $Ga_{0.30}Co_4Sb_{12}$

$In_xCo_4Sb_{12}$ [41] and $x = 0.2$ in $Tl_xCo_4Sb_{12}$ [26], respectively. The Ga metal may exist as liquid phase during high-temperature TE properties measurements.

In order to verify the maximum filling limit of Ga and Tl into $CoSb_3$, we performed low-temperature heat capacity analyses on the Co_4Sb_{12}, $Ga_{0.2}Co_4Sb_{12}$, and $Tl_{0.2}Co_4Sb_{12}$ samples. At low temperature (below 7 K), standard plots of C_P/T versus T^2 was linear for Co_4Sb_{12} sample and yielded Debye temperature of 306 K. This result is well consistent with the literature value (307 K for single crystals of Co_4Sb_{12} reported by Caillat et al. [42]). The contribution of the filling atoms to the heat capacity would emerge as a form of excess heat capacity (ΔC). In the present case, we considered the following two values of ΔC: $\Delta C_1 = C$ of $Ga_{0.2}Co_4Sb_{12}$ $-$ C of Co_4Sb_{12}, and $\Delta C_2 = C$ of $Tl_{0.2}Co_4Sb_{12}$ $-$ C of Co_4Sb_{12}. Figures 10.12 and 10.13 plot ΔC_1 and ΔC_2 as a function of temperature, respectively. ΔC is well approximated by an Einstein contribution:

$$\Delta C = C_E(T) = 3Ry\left(\frac{\theta_E}{T}\right)^2 \frac{\exp(\theta_E/T)}{(\exp(\theta_E/T) - 1)^2}, \tag{10.1}$$

where R is the gas constant, y is the content of the filling atom in the formula of $Ga_yCo_4Sb_{12}$ or $Tl_yCo_4Sb_{12}$, and θ_E is the Einstein temperature. Below 20 K, both ΔC_1 and ΔC_2 are well described by (10.1), in which we set two unknown parameters: y and θ_E. In the case of ΔC_1, y and θ_E were found to be 0.02 and 35 K, respectively. On the other hand, in the case of ΔC_2, y and θ_E were found to be 0.15 and 56 K, respectively. Thus, it can be said that Ga or Tl can be filled up to $y = 0.02$

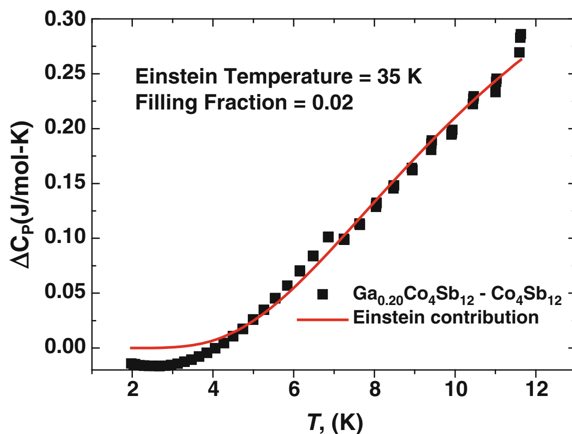

Fig. 10.12 The difference in the heat capacities between $Ga_{0.2}Co_4Sb_{12}$ and Co_4Sb_{12}, together with a line fitted by using the Einstein model

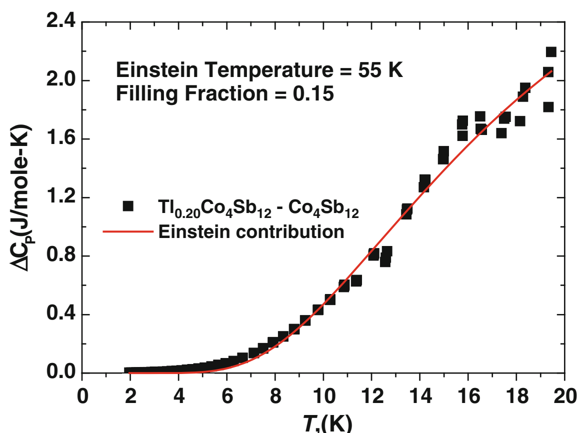

Fig. 10.13 The difference in the heat capacities between $Tl_{0.2}Co_4Sb_{12}$ and Co_4Sb_{12}, together with a line fitted by using the Einstein model

in $Ga_yCo_4Sb_{12}$ and $y = 0.15$ in $Tl_yCo_4Sb_{12}$, respectively. Note that the obtained Einstein temperature of 56 K is close to the value of 52 K estimated from the atomic displacement parameters for $Tl_{0.22}Co_4Sb_{12}$ [22] indicating the substantial rattling of Tl in the skutterudite structure. Similarly, in the case of Ga-$CoSb_3$ system, the maximum filling limit was calculated to be $y = 0.02$ in $Ga_yCo_4Sb_{12}$, well consistent with the XRD and FE-SEM/EDX results as described above.

Temperature dependences of the electrical resistivity (ρ) and the Seebeck coefficient (S) of the polycrystalline samples of $Ga_xCo_4Sb_{12}$ ($x = 0.05, 0.10, 0.15, 0.20, 0.25$, and 0.30) are shown in Fig. 10.14a, b, respectively. The ρ of all the samples decrease with temperature, showing semiconductor behavior. By adding Ga to $CoSb_3$, the ρ values increase with increasing x up to $x = 0.15$, and then decrease. The S values are negative for all the samples, indicating that the majority of charge carriers are electrons. The absolute S of all the samples are almost constant up to

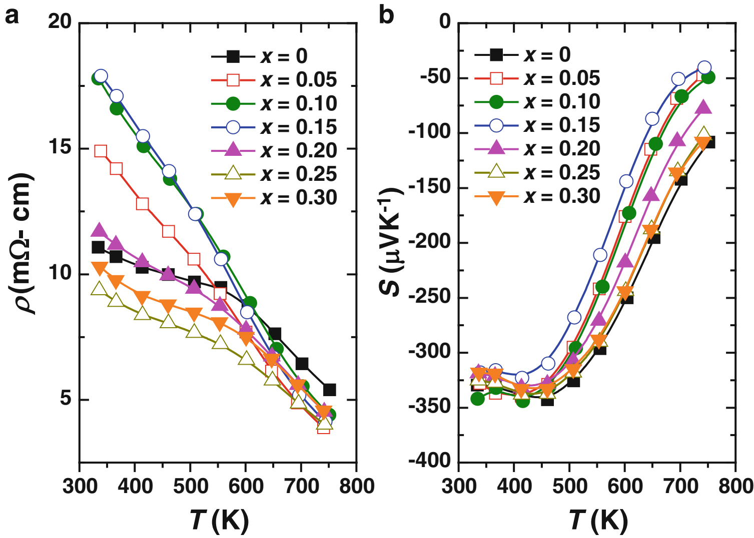

Fig. 10.14 Temperature dependences of (**a**) the electrical resistivity, ρ and (**b**) the Seebeck coefficient, S of polycrystalline samples of $Ga_xCo_4Sb_{12}$ ($x = 0.05, 0.10, 0.15, 0.20, 0.25$, and 0.30)

Table 10.2 Lattice parameter a, sample bulk density d, Hall carrier concentration n_H (300 K), and Hall mobility μ_H (300 K) for polycrystalline samples of $Ga_xCo_4Sb_{12}$ ($x = 0.05, 0.10, 0.15, 0.20, 0.25$, and 0.30)

x	a (nm)	d (g cm^{-3})	n_H (10^{19} cm^{-3})	μ_H (cm^2 V^{-1} s^{-1})
0.05	0.90363	7.65	1.51	27.8
0.10	0.90364	7.65	1.07	31.9
0.15	0.90368	7.64	2.06	24.5
0.20	0.90368	7.66	2.67	19.9
0.25	0.90369	7.63	3.42	15.9
0.30	0.90367	7.64	3.33	15.0

around 500 K, and decrease rapidly with increasing temperature, which is due to the thermal excitation of the charge carriers. At around room temperature, all the samples show the similar S values. However, at high temperatures, the absolute S decrease with increasing x in $Ga_xCo_4Sb_{12}$ up to $x = 0.15$, and then increase. As summarized in Table 10.2, the n_H slightly increases with increasing the amount of Ga, while the μ_H decreases, which is due to the combination of the Ga-filling into the voids in the $CoSb_3$ crystal and precipitation of Ga metal. In contrast to the Tl-filled $CoSb_3$, the n_H of the Ga-added $CoSb_3$ is not sufficiently increased because only a few Ga is filled into $CoSb_3$. The n_H of $Tl_{0.25}Co_4Sb_{12}$ is 23.90×10^{19} cm^{-3} [26], which is almost ten times larger than that of $Ga_{0.25}Co_4Sb_{12}$ (3.42×10^{19} cm^{-3}).

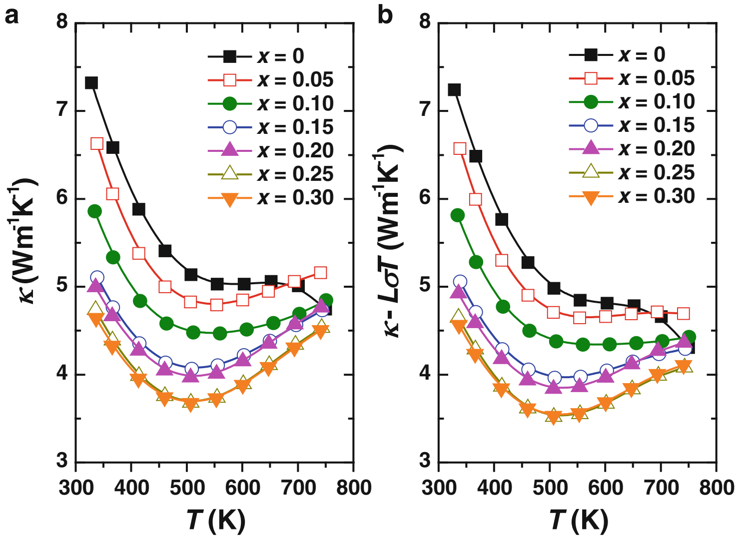

Fig. 10.15 Temperature dependences of the thermal conductivity of polycrystalline samples of $Ga_xCo_4Sb_{12}$ ($x = 0.05, 0.10, 0.15, 0.20, 0.25$, and 0.30); (**a**) total thermal conductivity, κ and (**b**) lattice thermal conductivity, κ_{lat}

Temperature dependences of the κ and the κ_{lat} for polycrystalline samples of $Ga_xCo_4Sb_{12}$ ($x = 0.05, 0.10, 0.15, 0.20, 0.25$, and 0.30) are shown in Fig. 10.15a, b, respectively. The κ decreases with increasing temperature first and then increases from around 550 K. This temperature dependence can be attributed to a bipolar conduction in semiconductors. The κ_{lat} of $Ga_xCo_4Sb_{12}$ drastically decreases with Ga-addition. $Ga_{0.25}Co_4Sb_{12}$ exhibits the lowest κ_{lat} (3.52 W m^{-1} K^{-1} at 500 K). These results imply that not only the filled Ga but also the precipitated Ga lead to the effective reduction of κ_{lat}.

Temperature dependence of the ZT for polycrystalline samples of $Ga_xCo_4Sb_{12}$ ($x = 0.05, 0.10, 0.15, 0.20, 0.25$, and 0.30) is shown in Fig. 10.16. Although Ga can be filled only up to $x = \sim 0.02$ in $Ga_xCo_4Sb_{12}$, significant reduction of κ_{lat} is achieved, leading to enhancement of ZT. In particular, $Ga_{0.25}Co_4Sb_{12}$ exhibits the maximum ZT value of 0.18 at around 500 K. This value is lower than those of In- and Tl-filled skutterudites [22, 26, 37, 38]. This low ZT of the Ga-$CoSb_3$ system is likely due to the unoptimized carrier concentration. In case of the Tl-$CoSb_3$ system, the Tl-filling into $CoSb_3$ increases carrier concentration [26]. However, in case of the Ga-$CoSb_3$ system, the carriers are not sufficiently doped because only a few Ga is filled into $CoSb_3$. Nonetheless, since Ga-adding to $CoSb_3$ is effective method for reduction of κ_{lat}.

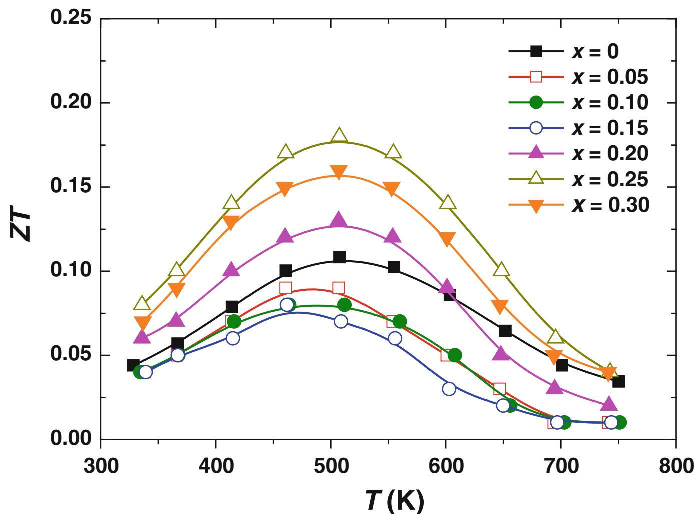

Fig. 10.16 Temperature dependences of the dimensionless figure of merit, *ZT* of polycrystalline samples of $Ga_xCo_4Sb_{12}$ ($x = 0.05$, 0.10, 0.15, 0.20, 0.25, and 0.30)

10.4 Thermoelectric Properties of Tl- and In Double-Filled Skutterudite: $Tl_{0.1}In_xCo_4Sb_{12}$ [43]

Skutterudites filled by group 13 elements, of Ga-, In-, and Tl-filled systems, have attracted much attention recently as high-performance TE materials. Among the compounds in the Tl-filled system, our group has examined the high-temperature TE properties of $Tl_yCo_4Sb_{12}$ and obtained a maximum *ZT* of 0.90 at 600 K for $Tl_{0.25}Co_4Sb_{12}$ [26]. The maximum *ZT* values for In- and Tl-filled skutterudites have been obtained at the compositions of the maximum filling limit [26, 37]. Thus, the enhancement of the *ZT* of these filled skutterudites is restricted by the filling limit of atoms into the voids of the skutterudite structure. In the case of In-filled skutterudites, there are a few reports in which In naturally forms nano-sized InSb inclusions when it exceeds the filling limit, and these nano-inclusions appear to play an important role in significantly reducing κ_{lat} [34, 44]. However, there have been a number of reports where no such nano-inclusions were observed in the same In-filled system [38, 45]. Thus, it remains unclear whether any nanostructures form in In-filled skutterudites.

Here, we review the results on the dramatically reduced κ_{lat}, and thus enhanced *ZT*, for $CoSb_3$-based skutterudites by a combined approach of double filling of group 13 elements (Tl and In) and self-forming of nanostructures [43].

In the XRD patterns of polycrystalline samples of $Tl_{0.1}In_xCo_4Sb_{12}$ ($x = 0.1, 0.2,$ and 0.3), all the peaks indicate a skutterudite structure with the space group *Im*3, and there are no notable peaks corresponding to impurities as shown in Fig. 10.17. The XRD patterns confirm that all samples have nearly the same lattice parameter

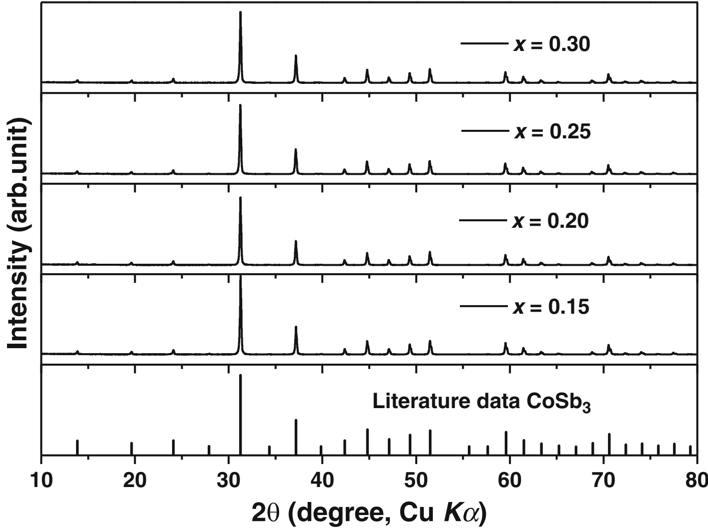

Fig. 10.17 Powder XRD patterns of polycrystalline samples of $Tl_{0.1}In_xCo_4Sb_{12}$ ($x = 0.15$, 0.20, 0.25, and 0.30), together with the peak positions calculated from the crystal structure of $CoSb_3$

Table 10.3 Lattice parameter a, sample bulk density d, Hall carrier concentration n_H (300 K), and Hall mobility μ_H (300 K) for polycrystalline samples of $Tl_{0.1}In_xCo_4Sb_{12}$ ($x = 0.15, 0.20, 0.25$, and 0.30)

x	a (nm)	d (g cm^{-3})	n_H (10^{19} cm^{-3})	μ_H (cm^2 V^{-1} s^{-1})
0.15	0.9047	7.75	23.61	35.21
0.20	0.9048	7.76	34.17	28.01
0.25	0.9048	7.78	34.13	27.43
0.30	0.9049	7.76	40.00	25.03

values, as summarized in Table 10.3. According to Vegard's rule, under the assumption that Tl is fully filled while In is partly filled, the lattice parameter a of $Tl_{0.1}In_xCo_4Sb_{12}$ can be written as:

$$a \text{ of } Tl_{0.1}In_xCo_4Sb_{12} = a \text{ of } Co_4Sb_{12} + \Delta a_1 + \Delta a_2, \quad (10.2)$$

where a of Co_4Sb_{12} is 0.9034 nm [26], $\Delta a_1 = a$ of $Tl_{0.1}Co_4Sb_{12} - a$ of Co_4Sb_{12}, and $\Delta a_2 = a$ of $In_xCo_4Sb_{12} - a$ of Co_4Sb_{12}. The values of Δa_1 and Δa_2 can be calculated from the changes in the lattice parameters of Tl- and In-filled $CoSb_3$ using the filling ratio obtained by the present authors' group. By fitting the calculated lattice parameter to the experimental one, we obtained $x = 0.09$. This indicates that the maximum filling limits of Tl and In in $Tl_{0.1}In_xCo_4Sb_{12}$ are 0.1 and 0.09, respectively. Therefore, it is believed that a secondary phase composed mainly of In may exist in addition to the skutterudite phase after exceeding the maximum filling limit of In.

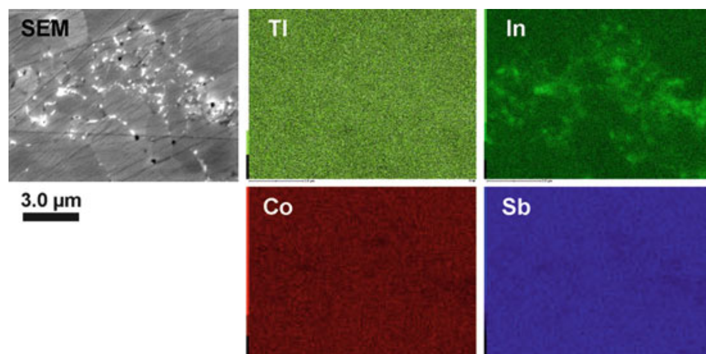

Fig. 10.18 FE-SEM and EDX mapping images of the polycrystalline sample of $Tl_{0.1}In_{0.3}Co_4Sb_{12}$

The FE-SEM and EDX mapping images of the hot-pressed $Tl_{0.1}In_{0.3}Co_4Sb_{12}$ sample are shown in Fig. 10.18. In these images, an In-rich region can be clearly observed mainly at the grain boundaries, implying that In added after exceeding the maximum filling limit precipitates as a secondary phase. Since the particle size of the secondary phase is too small, the peaks of this impurity phase cannot be observed in the XRD patterns.

In order to identify the chemical state of the In-based secondary phase, we performed transmission electron microscopy (TEM) and X-ray absorption fine structure (XAFS) analyses on the $Tl_{0.1}In_{0.3}Co_4Sb_{12}$ sample. TEM image taken from a single grain of a sintered pellet of $Tl_{0.1}In_{0.3}Co_4Sb_{12}$ is shown in Fig. 10.19a. Nanoparticles (<50 nm) can be clearly observed. They have mostly formed along the grain boundaries. It is thought that they are composed mainly of In present in excess of its filling limit. The nanoparticles were analyzed by electron diffraction techniques. The electron diffraction patterns obtained are shown in Fig. 10.19b, c. The incident beam was focused to a diameter of ~10 nm. The electron diffraction patterns are entirely consistent with In_2O_3 (space group: Ia-3) viewed along the [110] and [112] directions.

To identify the chemical state of In within the sample, In L_3-edge x-ray absorption near edge structure (XANES) measurements were performed on a $Tl_{0.1}In_{0.3}Co_4Sb_{12}$ bulk sample at the Synchrotron Light Research Institute, Thailand. Figure 10.19d compares the measured In L_3-edge spectra of this $Tl_{0.1}In_{0.3}Co_4Sb_{12}$ bulk sample and the reference In metal and In_2O_3 powder. Clearly, all the features of the XANES In L_3-edge spectrum of the $Tl_{0.1}In_{0.3}Co_4Sb_{12}$ bulk sample agree very well with those of the reference In_2O_3 powder. This indicates that the In added in excess of the filling limit within the sample is in the form of In_2O_3. Thus, the XANES measurements confirm that the $Tl_{0.1}In_{0.3}Co_4Sb_{12}$ sample contains In_2O_3.

Temperature dependences of the electrical resistivity (ρ) and the Seebeck coefficient (S) of the polycrystalline samples of $Tl_{0.1}In_xCo_4Sb_{12}$ ($x = 0.15, 0.20, 0.25$, and 0.30) are shown in Fig. 10.20a, b, respectively. The ρ of all the samples decrease dramatically with In-addition. By adding Tl and In to $CoSb_3$, the ρ values

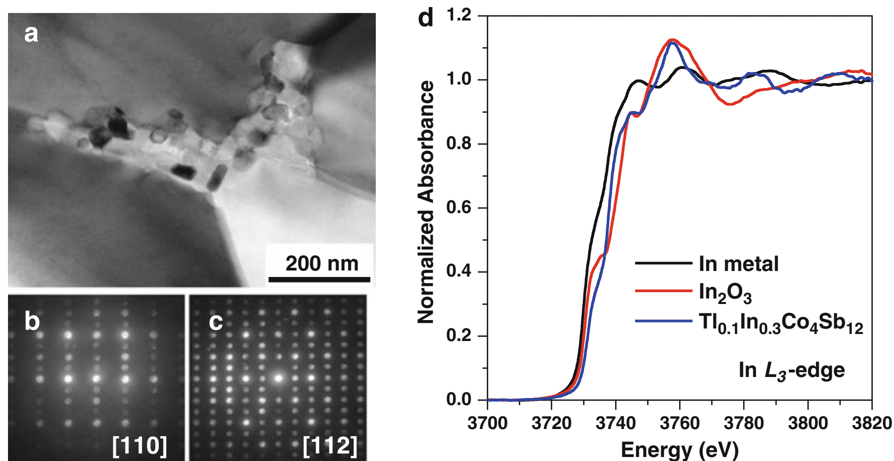

Fig. 10.19 (**a**) TEM image taken from a single grain of the sintered pellet of $Tl_{0.1}In_{0.3}Co_4Sb_{12}$; (**b**) and (**c**) electron diffraction patterns obtained with the electron beam aligned along the [110] and [112] directions, respectively; (**d**) comparison of the measured In L3-edge normalized spectra of a $Tl_{0.1}In_{0.3}Co_4Sb_{12}$ bulk sample with the reference In metal and In_2O_3 powder

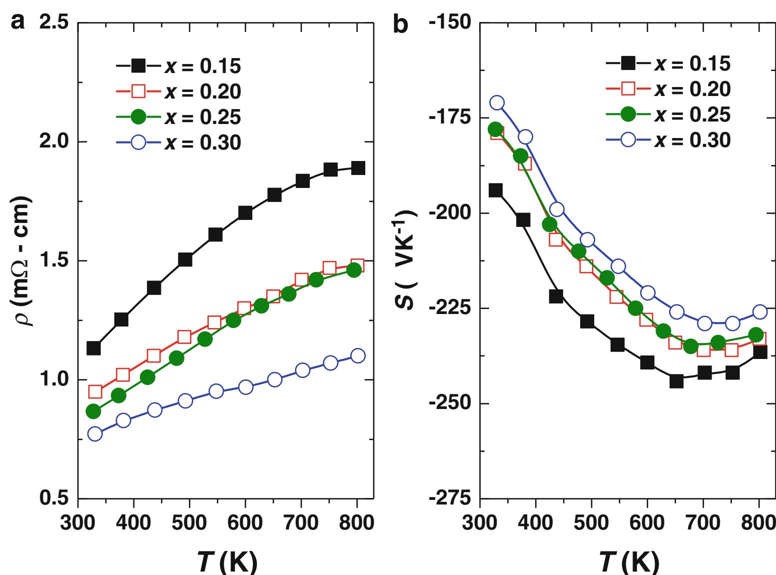

Fig. 10.20 Temperature dependences of (**a**) the electrical resistivity, ρ and (**b**) the Seebeck coefficient, S of polycrystalline samples of $Tl_{0.1}In_xCo_4Sb_{12}$ ($x = 0.15, 0.20, 0.25$, and 0.30)

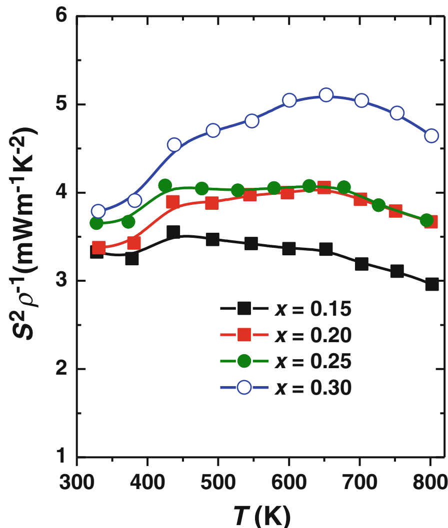

Fig. 10.21 Temperature dependences of the power factor, $S^2\rho^{-1}$ of polycrystalline samples of $Tl_{0.1}Tl_xCo_4Sb_{12}$ ($x = 0.15$, 0.20, 0.25, and 0.30)

of all the samples are below $1.25 \times 10^{-5}\ \Omega$ m at room temperature and increase with elevated temperature, typical of heavily doped semiconductors. The $Tl_{0.1}In_{0.3}Co_4Sb_{12}$ sample exhibits the lowest ρ value, $7.5 \times 10^{-6}\ \Omega$ m at room temperature. The S values are negative for all the samples, indicating that the majority of charge carriers are electrons. The absolute S of all the samples increases up to around 700 K, and decreases with increasing temperature. As summarized in Table 10.3, there is a large increase in n_H, while μ_H shows a minimal increase with increasing total filling fraction, which means that Tl/In addition leads to a net increase in conduction electrons but has no significant influence on the scattering of carriers. As shown in Fig. 10.21, all the samples show the constant and large values of the power factor ($S^2\rho^{-1}$) in the whole temperature range investigated in the present study. The $Tl_{0.1}In_{0.3}Co_4Sb_{12}$ sample exhibits the highest power factor, around 5.0 mW m^{-1} K^{-2} in relatively wide temperature range from 600 to 750 K.

Temperature dependences of the κ and the κ_{lat} for polycrystalline samples of $Tl_{0.1}In_xCo_4Sb_{12}$ ($x = 0.15$, 0.20, 0.25, and 0.30) are shown in Fig. 10.22a, b, respectively. The κ decreases with increasing temperature first and then increases from around 600 to 700 K. This temperature dependence can be attributed to a bipolar conduction in semiconductors. The κ_{lat} of $Tl_{0.1}In_xCo_4Sb_{12}$ drastically decreases with In-addition due to the phonon scattering by Tl- and In-rattling and nano-sized In_2O_3 precipitated at grain boundaries.

The temperature dependences of the κ_{lat} of polycrystalline samples of $CoSb_3$, $Tl_{0.1}Co_4Sb_{12}$, $Tl_{0.1}In_{0.1}Co_4Sb_{12}$, and $Tl_{0.1}In_{0.3}Co_4Sb_{12}$ are shown in Fig. 10.23. A comparison between the κ_{lat} values of $CoSb_3$ and $Tl_{0.1}Co_4Sb_{12}$ reveals a significant reduction of κ_{lat}. This is due to the effective phonon scattering by the rattling of Tl. Moreover, filling with In in addition to Tl yields a further reduction of κ_{lat} in the $Tl_{0.1}In_{0.1}Co_4Sb_{12}$ sample, suggesting that the double-filling approach is effective

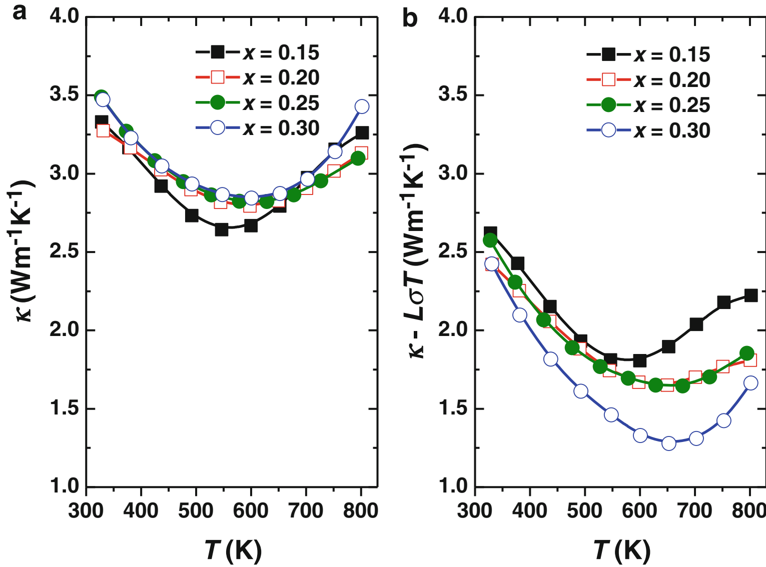

Fig. 10.22 Temperature dependences of the thermal conductivity of polycrystalline samples of $Tl_{0.1}In_xCo_4Sb_{12}$ ($x = 0.15, 0.20, 0.25$, and 0.30); (**a**) total thermal conductivity, κ and (**b**) lattice thermal conductivity, κ_{lat}

Fig. 10.23 Temperature dependences of the dimensionless figure of merit, *ZT* of polycrystalline samples of $Tl_{0.1}In_xCo_4Sb_{12}$ ($x = 0.15, 0.20, 0.25$, and 0.30)

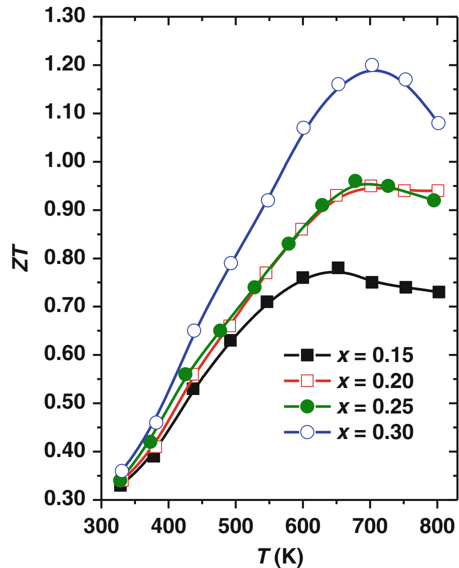

for phonon scattering, and hence in reducing κ_{lat}. Furthermore, it can be confirmed that the κ_{lat} of the $Tl_{0.1}In_{0.3}Co_4Sb_{12}$ sample is much lower than those of the other samples. This implies that the rattling of Tl/In, as well as the In_2O_3 nanoparticles formed at the grain boundaries, scatter heat-carrying phonons, leading to the

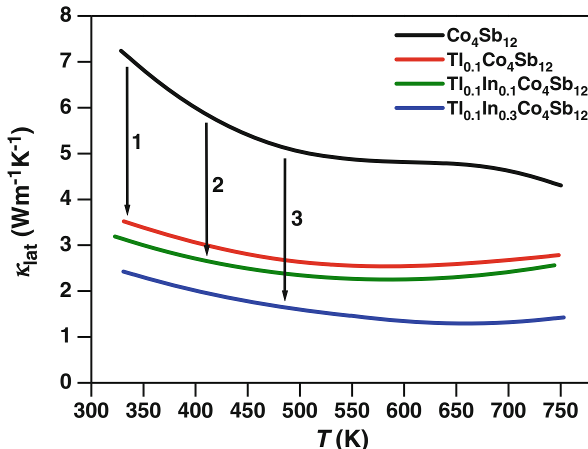

Fig. 10.24 Temperature dependence of the lattice thermal conductivity, κ_{lat} of polycrystalline samples of $CoSb_3$, $Tl_{0.1}Co_4Sb_{12}$, $Tl_{0.1}In_{0.1}Co_4Sb_{12}$, and $Tl_{0.1}In_{0.3}Co_4Sb_{12}$. The numbers *1*, *2*, and *3* in the figure represent phonon scattering by Tl-rattling, Tl- and In-rattling, and Tl- and In-rattling plus In_2O_3 nanoparticles, respectively

dramatic reduction of κ_{lat}. Owing to the very low κ_{lat}, the $Tl_{0.1}In_{0.3}Co_4Sb_{12}$ sample exhibits an excellent *ZT*; its maximum value is 1.20 at around 700 K, as shown in Fig. 10.24.

We can conclude that the Tl/In-double-filled skutterudite exhibits the excellent TE properties. Tl and In are filled up to x = ~0.09 in $Tl_{0.1}Tl_xCo_4Sb_{12}$ when exceeding the filling limit, In existed as nano-sized In_2O_3 (<50 nm) at grain boundaries. By investigating the TE properties of Tl- and In-double-filled $CoSb_3$-based skutterudites, we demonstrate that the reduction of κ_{lat} is due to the effective phonon scattering induced both by the rattling of Tl and In and by the naturally formed In_2O_3 nanoparticles (<50 nm). This yields a dramatic enhancement of *ZT* to be 1.20 at 700 K. The combined approach of double filling and self-formed nanostructures might be applicable to various clathrate compounds. Thus, these results point to a new strategy in the improvement of bulk TE materials.

10.5 Summary

In this chapter, we reviewed the TE properties of $CoSb_3$-based skutterudites filled by group 13 elements, i.e., the systems of $Tl_xCo_4Sb_{12}$, $Ga_xCo_4Sb_{12}$, and $Tl_{0.1}In_xCo_4Sb_{12}$. The temperature dependence of *ZT* of the best materials in the individual system is summarized in Fig. 10.25.

Tl can be filled in $CoSb_3$ up to around x = 0.2 in $Tl_xCo_4Sb_{12}$. Since the valence state of Tl in $CoSb_3$ can be considered to be Tl^{1+}, the Tl-filling yields net increase in electron carriers. Therefore, the carrier concentration of $CoSb_3$ can be controlled by Tl-filling. On the other hand, Tl filled in $CoSb_3$ can act as rattlers and scatter heat carrying phonons efficiently. Therefore, Tl-filled $CoSb_3$ exhibits low κ_{lat} with optimized carrier concentration, and hence high *ZT* value; the maximum *ZT* value is 0.90 at 600 K obtained for $Tl_{0.25}Co_4Sb_{12}$.

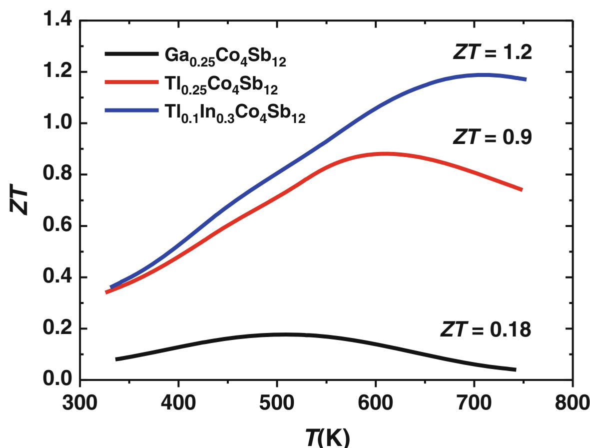

Fig. 10.25 The dimensionless figure of merit, *ZT* of polycrystalline samples of $Tl_{0.25}Co_4Sb_{12}$, $Ga_{0.25}Co_4Sb_{12}$, and $Tl_{0.1}In_{0.3}Co_4Sb_{12}$

In contrast to Tl-filled $CoSb_3$, Ga can be filled in $CoSb_3$ up to only $x = 0.02$ in $Ga_xCo_4Sb_{12}$, and when exceeding the filling limit, Ga exists as metal states mainly at grain boundaries in the polycrystalline samples of $Ga_xCo_4Sb_{12}$. Due to this low filling limit of Ga in $CoSb_3$, carriers are not sufficiently doped by Ga-filling. Nonetheless, not only very small amount of filled Ga but also precipitated Ga metals may scatter heat carrying phonons, leading to the reduction of κ_{lat}. Mainly due to the reduced κ_{lat}, the *ZT* is slightly enhanced by Ga-adding to $CoSb_3$; the maximum *ZT* value is 0.18 at 500 K obtained for $Ga_{0.25}Co_4Sb_{12}$.

In case of the double-filling system, i.e., $Tl_{0.1}In_xCo_4Sb_{12}$, all Tl is filled but In can be filled up to around $x = 0.09$ in $Tl_{0.1}In_xCo_4Sb_{12}$. In added in excess of the filling limit within the samples is in the form of In_2O_3 which is naturally formed as nanoparticles (<50 nm) mainly at the grain boundaries of the polycrystalline samples. Effective phonon scattering occurred both by the rattling of Tl and In and by the naturally formed In_2O_3 nanoparticles yield significant reduction of κ_{lat} and thereby dramatic enhancement of *ZT*. $Tl_{0.1}In_{0.3}Co_4Sb_{12}$ exhibits the maximum *ZT* of 1.20 at around 700 K, which is very high for bulk materials.

We consider the following two studies are important in this research for future. The first one is further enhancement of *ZT* by nanostructuring. Recently, various nanocrystalline bulk materials have been prepared by ball-milling followed by hot-pressing or spark plasma sintering and the enhancement of *ZT* have been achieved [46, 47]. The method is considered to be applied to the $CoSb_3$-based skutterudites. The second one is to develop p-type $CoSb_3$-based skutterudites filled by group 13 elements. Although the $CoSb_3$-based skutterudites filled by group 13 elements reported here have high *ZT* values, all the samples are n-type, i.e., they indicate negative *S* values. However, for a powerful TE module, the similar performances in both n-type and p-type TE materials is required. Therefore, the p-type $CoSb_3$-based skutterudites filled by group 13 elements should be developed. Very recently, our group has demonstrated that $Tl_xFe_yCo_{1-y}Sb_{12}$ exhibit p-type characteristics and relatively high *ZT* values. The details of the results will be reported in near future.

Acknowledgments This work was supported in part by a Grant-in-Aid for Scientific Research (No. 23686091) from the Ministry of Education, Culture, Sports, Science, and Technology, Japan. Additional support was kindly provided by the Rajamangala University of Technology Suvarnabhumi, Thailand, and the Government of Thailand.

References

1. Rowe, D.M.: CRC Handbook of Thermoelectrics. CRC Press, New York (1995)
2. Nolas, G.S., Sharp, J., Goldsmid, H.J.: Thermoelectrics: Basic Principles and New Materials Developments. Springer, New York (2001)
3. Bell, L.E.: Science **321**, 1457 (2008)
4. Ioffe, A.F.: Semiconductor Thermoelements and Thermoelectric Cooling. Infosearch, London (1957)
5. Snyder, G.J., Toberer, E.S.: Nat. Mater. **7**, 105 (2008)
6. Uher, C. In: Tritt, T.M. (ed.) Recent Trends in Thermoelectric Materials Research I, Semiconductors and Semimetals, vol. 69, p. 139. Academic Press, San Diego (2001)
7. Jeitschko, W., Braun, D.: Acta Cryst. **33**, 3401 (1977)
8. Stetson, N.T., Kauzlarich, S.M., Hope, H.: J. Solid State Chem. **91**, 140 (1991)
9. Slack, G.A. In: Rowe, D.M. (ed.) CRC Handbook of Thermoelectrics. CRC Press, New York (1995)
10. Morelli, D.T., Meisner, G.P.: J. Appl. Phys. **77**, 3777 (1995)
11. Sales, B.C., Mandrus, D.G., Chakoumakos, B.C. In: Tritt, T.M. (ed.) Recent Trends in Thermoelectric Materials Research I, Semiconductors and Semimetals, vol. 69. Academic Press, San Diego (2001)
12. Kuznetsov, V.L., Kuznetsova, L.A., Rowe, D.M.: J. Phys. Condens. Matter **15**, 5035 (2003)
13. Nolas, G.S., Cohn, J.L., Slack, G.A.: Phys. Rev. B **58**, 164 (1998)
14. Nolas, G.S., Kaeser, M., Littleton, R.T., Tritt, T.M.: Appl. Phys. Lett. **77**, 1855 (2000)
15. Morelli, D.T., Meisner, G.P., Chen, B.X., Hu, S.Q., Uher, C.: Phys. Rev. B **56**, 7376 (1997)
16. Pei, Y.Z., Bai, S.Q., Zhao, X.Y., Zhang, W., Chen, L.D.: Solid State Sci. **10**, 1422 (2008)
17. Chen, L.D., Kawahara, T., Tang, X.F., Goto, T., Hirai, T., Dyck, J.S., Chen, W., Uher, C.: J. Appl. Phys. **90**, 1864 (2001)
18. Puyet, M., Lenoir, B., Dauscher, A., Dehmas, M., Stiewe, C., Muller, E.: J. Appl. Phys. **95**, 4852 (2004)
19. Zhao, X.Y., Shi, X., Chen, L.D., Zhang, W.Q., Zhang, W.B., Pei, Y.Z.: J. Appl. Phys. **99**, 053711 (2006)
20. Pei, Y.Z., Chen, L.D., Zhang, W., Shi, X., Bai, S.Q., Zhao, X.Y., Mei, Z.G., Li, X.Y.: Appl. Phys. Lett. **89**, 221107 (2006)
21. Pei, Y.Z., Yang, J., Chen, L.D., Zhang, W., Salvador, J.R., Yang, J.H.: Appl. Phys. Lett. **95**, 042101 (2009)
22. Sales, B.C., Chakoumakos, B.C., Mandrus, D.: Phys. Rev. B **61**, 2475 (2000)
23. Nolas, G.S., Takizawa, H., Endo, T., Sellinschegg, H., Johnson, D.C.: Appl. Phys. Lett. **77**, 52 (2000)
24. Nolas, G.S., Yang, J., Takizawa, H.: Appl. Phys. Lett. **84**, 5210 (2004)
25. Fukuoka, H., Yamanaka, S.: Chem. Mater. **22**, 47 (2010)
26. Harnwunggmoung, A., Kurosaki, K., Muta, H., Yamanaka, S.: Appl. Phys. Lett. **96**, 202107 (2010)
27. Keppens, V., Mandrus, D., Sales, B.C., Chakoumakos, B.C., Dai, P., Coldea, R., Maple, M.B., Gajewski, D.A., Freeman, E.J., Bennington, S.: Nature **395**, 876 (1998)
28. Hermann, R.P., Jin, R.J., Schweika, W., Grandjean, F., Mandrus, D., Sales, B.C., Long, G.: Phys. Rev. Lett. **90**, 135505 (2003)

29. Yang, J., Zhang, W., Bai, S.Q., Mei, Z., Chen, L.D.: Appl. Phys. Lett. **90**, 192111 (2007)
30. Shi, X., Kong, H., Li, C.P., Uher, C., Yang, J., Salvador, J.R., Wang, H., Chen, L., Zhang, W.: Appl. Phys. Lett. **92**, 182101 (2008)
31. Bai, S.Q., Pei, Y.Z., Chen, L.D., Zhang, W.Q., Zhao, X.Y., Yang, J.: Acta Mater. **57**, 3135 (2009)
32. Salvador, J.R., Yang, J., Wang, H., Shi, X.: J. Appl. Phys. **107**, 043705 (2010)
33. Zhao, W.Y., Wei, P., Zhang, Q.J., Dong, C.L., Liu, L.S., Tang, X.F.: J. Am. Chem. Soc. **131**, 3713 (2009)
34. Li, H., Tang, X.F., Zhang, Q.J., Uher, C.: Appl. Phys. Lett. **94**, 102114 (2009)
35. Harnwunggmoung, A., Kurosaki, K., Plirdpring, T., Sugahara, T., Ohishi, Y., Muta, H., Yamanaka, S.: J. Appl. Phys. **110**, 013521 (2011)
36. Yang, J., Hao, Q., Wang, H., Lan, Y.C., He, Q.Y., Minnich, A., Wang, D.Z., Harriman, J.A., Varki, V.M., Dresselhaus, M.S., Chen, G., Ren, Z.F.: Phys. Rev. B **80**, 115329 (2009)
37. He, T., Chen, J., Rosenfeld, H.D., Subramanian, M.A.: Chem. Mater. **18**, 759 (2006)
38. Mallik, R.C., Stiewe, C., Karpinski, G., Hassdorf, R., Muller, E.: J. Electron. Mater. **38**, 1337 (2009)
39. Xiong, Z., Chen, X., Huang, X., Bai, S., Chen, L.: Acta Mater. **58**, 3995 (2010)
40. Qiu, Y., Xi, L., Shi, X., Qiu, P., Zhang, W., Chen, L., Salvador, J.R., Cho, J.Y., Yang, J., Chien, Y., Chen, S., Tang, Y., Snyder, G.J.: Adv. Funct. Mater. **23**, 3194 (2013)
41. Li, G., Kurosaki, K., Ohishi, Y., Muta, H., Yamanaka, S.J.: J. Electron. Mater. **42**, 1463 (2013). doi:10.1007/s11664-012-2290-4
42. Caillat, T., Borshchevsky, A., Fleurial, J.-P.: J. Appl. Phys. **80**, 4442 (1996)
43. Harnwunggmoung, A., Kurosaki, K., Kosuga, A., Ishimaru, M., Plirdpring, T., Yimnirun, R., Jutimoosik, J., Rujirawat, S., Ohishi, Y., Muta, H., Yamanaka, S.: J. Appl. Phys. **112**, 043509 (2012)
44. Ballikaya, S., Wang, G., Sun, K., Uher, C.: J. Electron. Mater. **40**, 570 (2011)
45. Deng, L., Jia, X.P., Su, T.C., Zheng, S.Z., Guo, X., Jie, K., Ma, H.A.: Mater. Lett. **65**, 2927 (2011)
46. Poudel, B., Hao, Q., Ma, Y., Lan, Y., Minnich, A., Yu, B., Yan, X., Wang, D., Muto, A., Vashaee, D., Chen, X., Liu, J., Dresselhaus, M.S., Chen, G., Ren, Z.: Science **320**, 634 (2008)
47. Joshi, G., Lee, H., Lan, Y., Wang, X., Zhu, G., Wang, D., Gould, R.W., Cuff, D.C., Tang, M.Y., Dresselhaus, M.S., Chen, G., Ren, Z.: Nano Lett. **8**, 4670 (2008)

Chapter 11
Nanoscale Self-assembled Oxide Bulk Thermoelectrics

Yu Zhao, Ashok Kumar, Céline Hin, and Shashank Priya

Abstract Thermoelectric materials directly convert thermal energy into electric energy through Seebeck effect. The nanostructured approach for these materials has led to significant improvements in the figure of merit mainly by tailoring the lattice thermal conductivity. In this chapter, we provide an overview of the strategies adopted for phonon scattering and its confinement in the nanostructures with the goal of reducing the thermal conductivity. We discuss the approaches that are being adopted for developing cost-effective thermoelectrics and identify the promise offered by oxide materials. Compared with the alloy-based thermoelectric materials, oxide thermoelectrics have many advantages including abundance of raw materials, low cost, non-toxicity, and thermal stability. Several important oxide thermoelectric candidates are introduced with specific focus on ZnO. Self-assembled nano-composites of ZnO have been shown to exhibit reduction in thermal conductivity by a factor of about three mainly due to the phonon scattering by uniformly distributed nanoprecipitates ($ZnAl_2O_4$) and large grain boundary area. The effects of nanoscale inclusion in Ca-Co-O system ($Ca_3Co_4O_9$) and natural superlattices in $SrO/SrTiO_3$ are also discussed. Several self-assembly techniques are discussed which are promising for fabrication of oxide thermoelectrics.

Y. Zhao (✉) • A. Kumar • S. Priya
Center for Energy Harvesting Materials and Systems (CEHMS), Virginia Tech,
Blacksburg, VA 24061, USA
e-mail: zhaoyu@vt.edu; ashokku@vt.edu; spriya@vt.edu

C. Hin
Materials Science and Engineering and Mechanical Engineering, Virginia Tech,
Blacksburg, VA 24061, USA
e-mail: celhin@vt.edu

X. Wang and Z.M. Wang (eds.), *Nanoscale Thermoelectrics*, Lecture Notes
in Nanoscale Science and Technology 16, DOI 10.1007/978-3-319-02012-9_11,
© Springer International Publishing Switzerland 2014

11.1 Introduction

Thermoelectric devices can be used as heat and electricity exchangers. Basic understanding of these devices has been developed over several decades since the discovery of Seebeck effect in 1821. These devices offer several distinct advantages over other alternatives such as silent operation, long lifetime, no harmful gaseous components or other materials that may require periodic replenishment, reversible heat-pumping direction, precise control of temperature (±0.1 °C) and capable of working in high temperature, radioactive, or constrained environments [1]. As a result thermoelectric devices have found wide-ranging applications in military, aerospace, and industrial or commercial products, which can be classified into three categories, e.g., coolers (or heaters), power generators, and thermal sensors [2]. Recently, interest has surged in applications of thermoelectrics for energy harvesting from wasted heat available in the environment such as transportation, manufacturing plants and human body. A wristwatch using thermoelectric generator was reported in late 1990s that extracted the temperature gradient between human body heat and environment. In automobiles, the thermoelectrics could replace belt-driven alternators, air conditioning units, seat cooling, and harvest energy from exhaust gases [3]. The role of thermoelectrics in powering the distributed wireless sensor networks (WSNs) has gained significant attention as well. These nodes are highly desired for the powering the sensors in structural health monitoring (SHM) tasks on variety of platforms such as engine, industrial process monitoring, and gas exploration. The use of thermoelectrics to power aerospace sensors has been demonstrated by European Aeronautic Defense and Space Company N.V. (EADS) [4]. Figure 11.1 provides the description of some commercially reported low power thermoelectric energy harvesters.

11.1.1 Materials Review

Thermoelectric (TE) materials for high temperature applications should have good reliability and exhibit high figure of merit (zT) in the desired operating regime. One composition will not fit for all the applications as zT varies with the temperature. Table 11.1 lists the thermoelectric materials extensively investigated in literature exhibiting reasonable figure of merit. The commonly used TE materials, such as chalcogenide compounds represented as Bi(Sb)Te [5, 6], PbTe [7] and related alloys, show good figure of merit at low and medium temperature range (room temperature to 800 K). Skutterudites represented by general formulation Co_4Sb_{12} [8] and SiGe [9] compounds have shown good performance in the medium-to-high temperature range (800–1,200 K). Recently, metal oxides, such as $NaCoO_2$ [10], $Ca_3Co_4O_9$ [11], ZnO [12], and $SrTiO_3$ [13], have been investigated mainly as a cost-effective rare-earth free substitute. Oxides have inherent

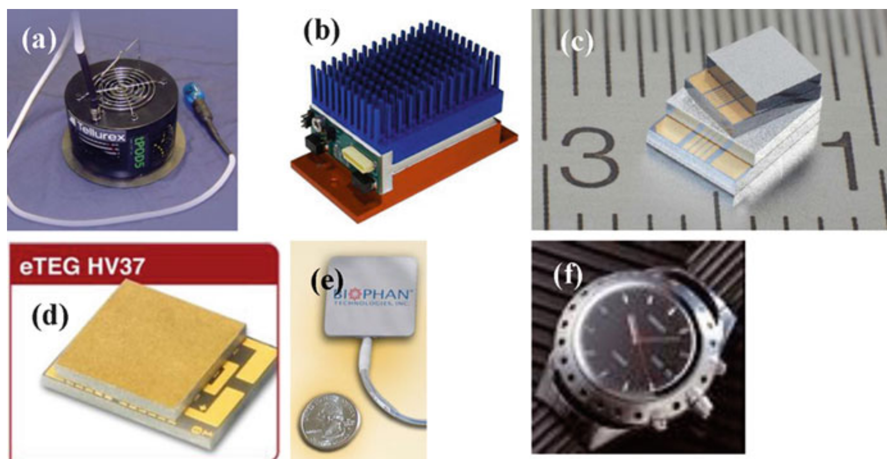

Fig. 11.1 (**a**) Tellurex Corporation, tPOD5 (http://www.buytpod.com/) 5 V DC, 500 mA, Diameter: 178 mm, Height: 95 mm; 2 lbs 14 oz; (**b**) Marlow, EHA-PA1AN1-R02-L1 (http://www.marlow.com/), Dimension—74 × 36 × 38 mm, Weight—1 g, Power at $\Delta T = 60$ °C: 2.3 mW; Power at $\Delta T = 10$ °C: 0.3 mW; (**c**) Micropelt, MPG-D651 (http://www.micropelt.com), Dimensions top side—2.5 × 2.5 mm, bottom side—3.375 × 2.5 mm; Seebeck voltage at 23 °C—75 mV $\mathrm{K}^{-}1$, thickness—1.09 mm; (**d**) Nextreme, eTEG™ HV37 (http://www.nextreme.com/), Output power levels of 1.0 mW and an open circuit voltage of 170 mV at a ΔT of 10 K, and 24 mW and 850 mV respectively at a ΔT of 50 K, Dimension: 2.1 mm × 2.9 mm × 0.6 mm; (**e**) Biothermal power source: (www.biophan.com/); (**f**) Seiko Thermic: (http://www.seikowatches.com/)

advantage of high temperature oxidation resistance and exhibit promising figure of merit in the high temperature range.

In past decades, significant interest has been placed on investigation of nanostructures in semiconducting thermoelectric alloys. Both low-dimension nanostructured alloys (e.g., superlattice structures, quantum dots superlattice, and nanowire) and bulk alloys with nanoscale features in the microstructure (e.g., nanodots and nanograins) have been designed and studied as summarized in Table 11.1 and further discussed in Sects. 11.2.2 and 11.2.3. However, scarcity of elements (Te), complex synthesis techniques (thin film deposition processes, such as MBE; spark plasma sintering, hot press), and poor durability at elevated temperatures (oxidation) limits the potential of many of these alloy compositions. Figure 11.2 provides the summary on the availability of the raw materials in the near future. The main element "Te" used in both Bi_2Te_3 and PbTe based alloys belongs to the critical material category that is in short supply. Silver, which is used for inducing nanoprecipitates in PbTe is precious metal. Some other rare earth elements, such as Yb, La, Ce, are also in short supply. Further certain elements are harmful for both human body and environment, such as Pb and Tl. These considerations and restrictions imposed upon the design of TE materials limit the options severely.

Table 11.1 Thermoelectric properties and synthesis method for common TE materials (based upon the reported experimental results in literature)

Composition and structure	zT	T (K)	κ (W m^{-1} K^{-1})	α (μV K^{-1})	σ (S cm^{-1})	Preparation method	Ref.
Alloy based-low dimensional structure							
Bi_2Te_3/Sb_2Te_3 superlattice	2.4	300	0.22 (⊥)			Low temperature growth	[5]
$(Bi,Sb)_2(Te,Se)_3$ QDSL	1.6	300		−219		MBE	[45]
$PbTe/Pb_{1-x}Eu_xTe$ thin-film quantum well	1.23 (2D)					MBE	[81]
Si nanowire	1	200	~0.8			SNAP process	[46, 47]
SiGe QDSL			0.9			MBE	[48]
Alloy based-bulk, crystal							
Bi_2Te_3 bulk with nanograin	1.4	372	1	220	500	BM, HP	[61, 77]
$Bi_{0.52}$ $Sb_{1.48}Te_3$ bulk with nanograin	1.56	300	0.7	230	700	Melt spinning SPS	[62]
$CsBi_4Te_6$ (SbI_3 doping) single crystal	0.82	225	~2	~170	~2,520	Single crystal growth	[122]
$AgPb_mSbTe_{m+2}$ ($m = 18$) bulk with nanodots	2.2	800	~1	−335	~200	Ingot synthesis, annealing	[63]
PbTe-2 %Sb, 0.5 %Pb bulk with nanodots	1.4	700	~1.4	−200	750	Melt-rapid cooling	[64–66]
$(GeTe)_{0.8}[(Ag_2Te)_{0.4}(Sb_2Te_3)_{0.6}]_{0.2}$ bulk	1.68	700				HP	[84]
$Na_{0.95}Pb_mSbTe_{m+2}$ ($m = 22$) bulk with nanodots	~1.7	650	1	339	165	Ingot synthesis	[85]
PbTe-12 %PbS-2 %Na bulk with nanodots	1.8	800	~1.2	~280	~300	Melt-rapid cooling	[67–69]
PbTe-2 %Tl	1.5	773	1	320	~100	Ingot synthesis	[15]
PbTe-6 % CaTe nanodots in bulk	1.5	765	~1.1	~250	~265	Ingot synthesis, annealing	[86]
PbTe-1 %CdTe-0.055 % PbI_2 bulk with nanodots	1.2	720	~1.1	−225	~400	Ingot synthesis, annealing	[87]
PbTe-2 % SrTe bulk with nanodots	2.2	900	0.96	280	~300	Ingot synthesis, annealing	[70, 78]

Ag_9TlTe_5 bulk	1.23	700	0.22	319	38	Ingot synthesis, sintering	[123]
$Ba_{0.08}La_{0.05}Yb_{0.04}Co_4Sb_{12}$ Skutterudites bulk	1.7	850	2.6	−195	1,300	Ingot synthesis, SPS	[124]
$Ba_{0.14}In_{0.23}Co_4Sb_{11.84}$ Skutterudites bulk	1.34	850	~2.5	−200	900	Ingot synthesis, SPS	[125]
$Yb_{14}MnSb_{11}$ single crystal	1	1,223	7.5	190	180	Single crystal growth	[126]
SiGe Bulk with nanograin	1.3	1,172	~2.5	−240	~600	HP	[80]
Zn_4Sb_3 bulk	1.3	670	6.5	190	500	Ingot synthesis, HP	[127]
BaGaGe crystal	1.35	900	~1.3	−170	600	Czochralski	[128]
$(Zr_{0.5}Hf_{0.5})_{0.5}Ti_{0.5}NiSn_{1-y}Sb_y$ bulk	1.5	700	~2.6	−310	~660	Arc melting, HP	[129]
$Cu_{2-x}Se$ bulk with liquid-like structure	1.5	1,000	~0.8	300	125	Ingot synthesis	[130]
Oxide based							
$Na_xCoO_{2-\delta}$ single crystal	1.2	800	5.1	200	1,900	Flux grow method	[10]
$(Ca_2CoO_3)_{0.7}CoO_2$ single crystal	0.87	973	3	240	430	Single crystal growth	[11]
$(Ca_{2.8}Ag_{0.05}Lu_{0.15})$ Co_4O_9 lamella-like grain with nano-inclusion	0.6	1,100	1.4	230	~140	BM, SPS	[71]
$Zn_{0.96}Al_{0.02}Ga_{0.02}O$ bulk	0.65	1,247	~5	~−250	~417	Solid reaction	[102]
ZnO–2 % Al bulk with nano inclusion	0.44	1,000	1.8	−310	~85	Chemical synthesis, Solid reaction	[72]

k is the thermal conductivity measured in watts per kelvin per meter; α is the Seebeck coefficient measured in volt per kelvin; σ is the electrical conductivity measured in siemens per meter; *T* is the absolute temperature measured in kelvin

MBE molecular beam epitaxy, *BM* ball milling, *SPS* spark plasma sintering, *SNAP* superlattice nanowire pattern transfer, *QDSL* quantum dots superlattice

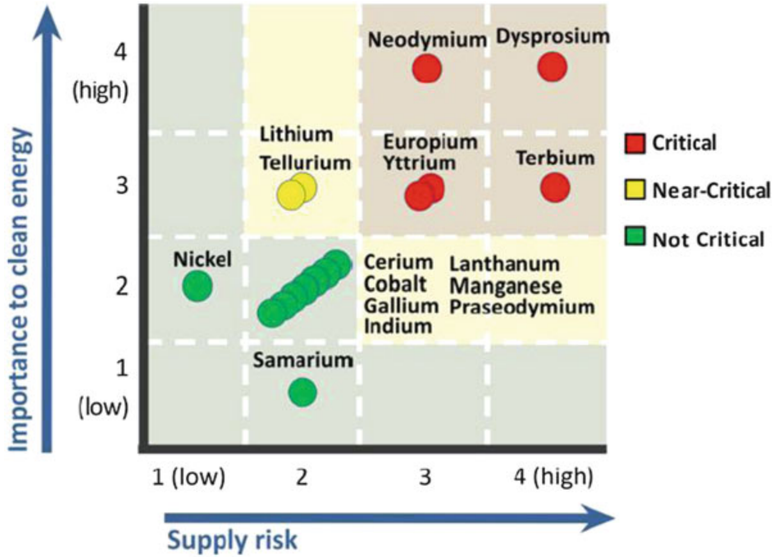

Fig. 11.2 Medium-Term (2015–2025) criticality matrix. Taken from: DOE's 2011 Critical Materials Strategy [112]

Combined with the requirement of high temperature operation, we can see that the choices become severely restricted and only simple oxides such as ZnO, $NaCoO_2$, $Ca_3Co_4O_9$, etc. emerge as the potential candidates. These materials employ cheap nontoxic elements that are available abundantly. Further, they have excellent high temperature durability in air. The oxide thermoelectrics could provide cheaper and environmentally friendly alternative to the tellurides and other alloy compositions. Comparing thermal and electrical transport properties of alloy and oxide based TE materials (Table 11.1), the main challenges for polycrystalline oxides are their relatively high thermal conductivity and low electrical conductivity, and therefore they exhibit performances half or one-third of the efficiency of alloys. Nanostructured approach promises to address these challenges and offers the opportunity to improve the performance of these cost-effective materials.

11.1.2 Strategies for Improving the Figure of Merit

In order to obtain high conversion efficiency, TE materials are required to exhibit good thermopower (Seebeck coefficient α) and electrical conductivity (σ), and low thermal conductivity ($\kappa = \kappa_{ph} + \kappa_{el}$). But it is difficult to control these parameters individually (α and σ; σ and κ). Semiconductors are considered as good

thermoelectrics due to their excess electron or hole density and carrier density alterability, and therefore exhibit larger thermopower than conductors. In addition, their moderate carrier concentration leads to relatively low κ values (larger κ_{ph} compared to κ_{el}). Generally low thermal conductivity is related to the complex structure or heavy elements [14], which is one guideline for finding and designing new TE materials. For example, skutterudites and clathrates have crystal framework with cages, which are filled by heavy elements, resulting in reduced thermal conductivity [14]. Another scheme for achieving high figure of merit relies on modification of power factor ($\alpha^2\sigma$) by using band structure engineering. The power factor is the product of Seebeck coefficient and electrical conductivity, both of which are determined by carrier density, but the dependence on carrier density is opposite. There is a maximum in power factor in the carrier concentration range of 10^{19} to 10^{21} cm^{-3}. Heremans had predicted and proved that a distortion (resonant levels close to the Fermi level) of the electronic density of states by Tl doping enhances the Seebeck coefficient [15]. Although calculations on presence of resonant levels using other doping elements have been published as well, few experimental results are available to validate these predictions.

In the 1990s, theoretical predictions [16] were made that zT could be enhanced by formation of nanostructures. In the optimum range of carrier density, the contribution of electrical thermal conductivity is only about 10 % of the total thermal conductivity. Hence large fraction of the heat is carried by phonons through the lattice; as a result phonon scattering from interfaces could be an effective method to lower the lattice thermal conductivity. When the scale of structure is close to the phonon mean free path (which is a function of the phonon velocity and phonon wavelength), phonon confinement is possible to be obtained resulting in significantly reduced lattice thermal conductivity. Based upon this underlying concept, the thermal conductivity was successfully decreased and zT larger than 1 was achieved [17]. The high density of interfaces and boundaries could be barriers for the electrons. The electron mean free path is usually shorter than that of phonon, so that the negative influence on electrical conductivity is not severe. Further quantum-confinement phenomenon enhances Seebeck effect and controls S and σ somewhat independently. In nanostructures, Seebeck coefficient is enhanced mainly due to preferential scattering of low-energy electrons at grain boundaries [18].

In Sect. 11.2, we will provide an overview of the recent developments on nanoscale structures and discuss its fundamental role towards controlling phonon transport. Several technologies utilized for the formation of nanostructures and self-assembled methods will be introduced. We will mainly focus on self-assembled oxide nanostructures and discuss their function in reducing the thermal conductivity, especially with respect to ZnO.

11.1.3 Modeling of Thermoelectric Materials

In thermoelectric materials, the figure of merit is calculated using a multiscale approach, combining the investigation of phonon and electron transport. Different theoretical approaches are used to study the phonon transport in thermoelectric materials: the Boltzmann transport equation [19, 20], the lattice dynamic theory, and the molecular dynamic combined with the Green–Kubo autocorrelation decay method. The Boltzmann transport equation is primarily used to study large system, but the input parameters depends on the experiment data. Consequently, molecular dynamic is preferred to determine the thermal conductivity in thermoelectric materials. The electron transport is calculated using first-principles calculation coupled with the Boltzmann transport theory [21–23].

11.1.3.1 Phonon Transport in Thermoelectric Materials

Equilibrium molecular dynamics method is commonly used to determine the thermal conductivity. The thermoelectric material system evolving without constraint will ultimately reach thermodynamic equilibrium after a certain number of steps. Consequently, the thermal conductivity can be derived from the fluctuation-dissipation theorem of the linear response theory, which links the transport properties to instantaneous fluctuations in the system. The thermal conductivity can be deduced from the variations of the instantaneous heat flux density of the system at equilibrium using the Green–Kubo relation [24–28]:

$$\kappa = \frac{V}{3k_{\mathrm{B}}T^2}\int_0^{\infty}\langle w(0)\cdot w(t)\rangle \mathrm{d}t \tag{11.1}$$

where T is the temperature, V is the volume of the system, and w is the instantaneous flux density in the system that is given by:

$$w(t) = \sum_{i=1}^{N} v_i E_i - \frac{1}{2}\sum_{i,j=1}^{N} r_{ij} v_i F_{ij} \tag{11.2}$$

The first and the second terms are the kinetic energy and the potential energy carried by each atom having a velocity v_i, respectively. In thermoelectric materials, the first term is generally negligible compared to the second term, which represents the potential energy of the lattice. r_{ij} is the distance between atom i and atom j, E_i is the total energy of one atom, and F_{ij} is the force of interaction between two atoms. Suitable interatomic potentials are the key to reproduce correctly the experimental thermal conductivity. For example, some potentials for the Bi_2Te_3 system fit to experimental data does not reproduce the lattice conductivity because of the anharmonic terms that have not been taken into account in the development of

the potentials [29, 30]. Alternative approaches such as the lattice dynamics theory have been successfully applied to determine the lattice conductivity in PbTe [31], Si [32], and half-Heuslers [33] thermoelectric materials.

11.1.3.2 Electron Transport in Thermoelectric Materials

In order to improve the power factor using band structure engineering, structure optimizations, total energies, and electronic structures are calculated using first-principles calculations. To determine the Seebeck coefficients, and the electrical conductivities, the density of states are used as an input of the Boltzmann transport theory [21–23]. A code, for calculating semi-classical transport coefficients, has even been developed, enabling systematic calculations of electrical conductivities and Seebeck coefficients. This code relies on the assumption that the scattering time is constant since it does not vary a lot with energy on the range of kT. It is however possible in certain cases to determine scattering relaxation time using the Kane model [34] to determine all the scattering mechanisms that include the scattering by deformation potential of acoustic phonons, scattering by polar-optical phonons, scattering by deformation potential of optical phonons, scattering by Coulomb potential of vacancies, and scattering by short-range deformation potential of vacancies. Using the BoltzTrap code and the calculated scattering relaxation time, studies in PbTe, and BiSbTe alloys give a general good accuracy between the theoretical power factor and the experiments [35, 36]. Theoretical approaches can also bring new concepts, such as demonstrated by Parker where he stated that low dimensional electronic structure can appear in bulk materials PbTe, PbSe, PbS, and SnTe [37]. More studies highlight that the doping levels seems to play a major role in the enhancement of the thermopowers in many different thermoelectric materials [36, 38, 39].

11.2 Role of Nanostructure in Improving Thermoelectric Properties

11.2.1 Fundamental Understanding of Influence of Nanostructure on Thermal Conductivity Through Phonon Transport

The phonons are the quanta of excitations of the normal modes of lattice vibrational motion, which transport the heat through the materials (depending on the polarization they are termed as acoustic and optical phonons). In long wave approximation, acoustic phonons display linear dispersion unlike the optical phonons, which are almost dispersion-less with a small group velocity. Therefore, acoustic phonons mainly contribute towards thermal conductivity. At low temperatures, contribution

from transverse acoustic (TA) phonons is dominant, while longitudinal acoustic (LA) phonons prevail at higher temperatures [40]. A bulk material containing n atoms per unit cell exhibits $3n$ phonon dispersion modes corresponding to each value of wave vector; three acoustic and $3(n - 1)$ optical. One can easily calculate the total number of acoustic and optical branches. For example, the GaAs has two atoms in their basis, and therefore, displays total of six phonon branches with three acoustic and three optical.

Thermal conductivity (κ) describes the property of a material to conduct heat, which is essentially determined by the phonon distribution. Phonons have a spectrum of wavelengths, which contribute to the total κ. Phonons encounter the resistance due to various scattering processes, such as scattering by other phonons, lattice disorders (vacancies, interstitials, and dopants), boundaries, and charge carriers, which restricts the phonon mean free path and leads to a finite thermal conductivity. Phonons with short wavelength are scattered by impurity atoms while interfaces scatter mid-to-long- wavelength phonons. According to specific heat of solids, the κ can be expressed by the following relation [41]:

$$\kappa = Cv^2\tau \tag{11.3}$$

where C and v denote the specific heat and velocity of sound at macroscopic level. Phonon relaxation time τ, which results from various scattering processes, can be expressed by Matthiessen's rule:

$$\tau_c^{-1} = \sum\nolimits_i \tau_i^{-1} \tag{11.4}$$

As atoms vibrate around their equilibrium positions and interact with neighboring atoms, it is easy to find the wavelength and amplitude of such vibrations. Further, the phonon mean free path is an important variable to understand the thermal conductivity. Considering the boundary scattering of phonons, Casimir obtained the following equation for κ [41]:

$$\kappa = \frac{1}{3}Cvl; \quad l_c^{-1} = \sum\nolimits_i l_i^{-1} \tag{11.5}$$

which defines the mean free path l that represents the distance between "collisions" through which phonons are randomly scattered. Phonon scattering through various processes govern the phonon mean free path (l) and the relaxation time (τ), which, in turn, modifies the phonon group velocity ($v_g = l/\tau$) and their propagation direction. Both the parameters l and τ are closely related to microscopic properties. For electron, the mean free path is shorter than phonon. Therefore, suitable strategies are possible, where we can selectively scatter phonons without strongly affecting electrons. Below, we will discuss the phonon scattering in nanostructure (low dimension) systems.

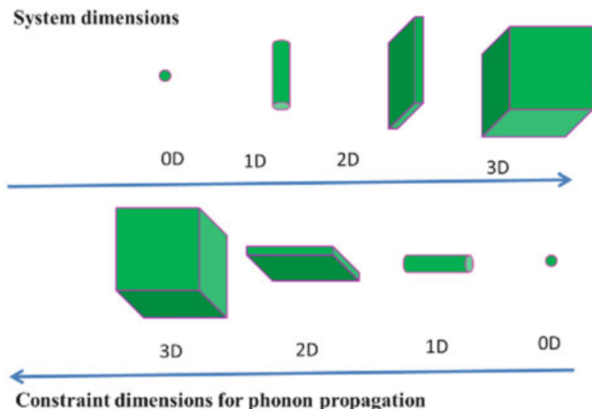

Fig. 11.3 0D, 1D, 2D, and 3D systems showing the directional constraints for phonon propagation

The nanostructuring in thermoelectrics can lead to the spatial confinement of phonons, and in turn, influence the phonon dispersion. The structures larger than the mean free path of phonons do not influence their movement. However, if feature size is around the mean free path of the phonons, the acoustic phonons can be scattered. Nanostructures (the high density of interfaces) modify the phonon–electron, phonon–defects (vacancies, interstitials, and dopants), and phonon–phonon interaction which results in restriction of the phonon mean free path. Thereby mid-to-long- wavelength phonons (low-frequency) would be inhibited from transport, and only high-frequency phonons would be allowed to propagate. Nanoscale systems have length-scale-directional limitations, e.g., as in 0D systems all longitudinal and transverse phonons are confined, phonon movement in 1D systems is restricted in two directions, and in 2D systems one of the dimensions acts as constraint for phonon movement. This directional constraint can significantly reduce the phonon transport in the constrained direction, if the constrained length scale is less than the mean free path (which is nanoscale) of the phonons (3D structures). The dimensional constraints for phonon propagation are shown in Fig. 11.3.

The surface roughness (δ) of nanostructure boundary also plays a critical role in reducing the thermal conductivity. For a nanowire of diameter "d" with specular scattering parameter (p), the mean free path due to the boundary scattering is expressed as [42]:

$$l_b = (1 + p)d/(1 - p) \tag{11.6}$$

where, p is given by Ziman's relation $p = \exp(-16\pi^3\delta^2/\lambda^2)$ in which δ is the surface roughness and λ is the phonon wavelength [42]. It is obvious that the thermal conductivity values are reduced with the reduced dimensions and increased surface roughness; however, the definite understanding behind this phenomenon has not been achieved. The thermal conductivity values investigated by

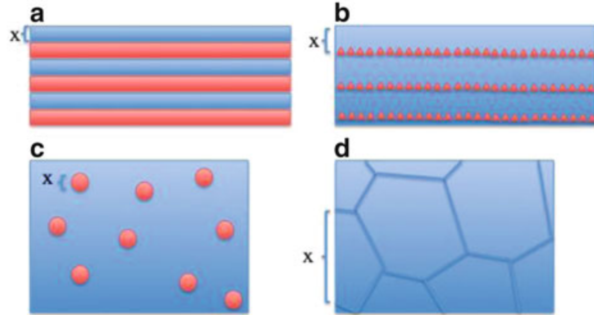

Fig. 11.4 Types of nanostructures: (**a**) superlattice, (**b**) quantum dots superlattice, (**c**) bulk with nanodots, (**d**) bulk with nanograins (the sizes of x are all in nanoscale)

Martin et al. [43] were found to have $(d/\delta)^2$ dependence. The strong phonon confinement could be achieved in the nanostructures coated with elastically dissimilar materials [21].

Several studies have been conducted to examine the influence of nanostructures on electron scattering [40]. At macroscopic level the electronic contribution to heat capacity can be given by following relation [44]:

$$\kappa_{\mathrm{el}} = \pi^2 k_{\mathrm{b}}^2 \frac{N_{\mathrm{f}}}{E_{\mathrm{f}} T} \tag{11.7}$$

where N_{f} is the number of free electrons, k_{b} is the Boltzmann constant, E_{f} is the Fermi energy level and T is the absolute temperature. The ratio of electronic thermal conductivity to phonon thermal conductivity can be expressed as [44]:

$$\kappa_{\mathrm{el}}/\kappa_{\mathrm{ph}} = 5N_{\mathrm{f}}\Theta_{\mathrm{D}}^3/24\pi^2 NT^2 T_{\mathrm{f}} \tag{11.8}$$

where N_{f}/N is the average number of free electrons contributed by each atom, T_{f} is Fermi temperature, and Θ_{D} is Debye temperature. As the temperature increases, the contribution of lattice to thermal conductivity increases. If one examines the temperature ($T_{\mathrm{o}} = \surd\ (5N_{\mathrm{f}}\ \Theta_{\mathrm{D}}^3/24\ \pi^2 NT^2 T_{\mathrm{f}})$), when the electrons have significant effect on thermal conductivity say $\kappa_{\mathrm{el}} = \kappa_{\mathrm{ph}}$, the temperature value is only a few percent of Debye temperature. This indicates that electron contribution to thermal conductivity can only be realized at very low temperatures.

Therefore, lattice thermal conductivity, which accounts for the major part of the overall thermal conductivity, can be reduced by strong phonon scattering resulting from the presence of high density of interfaces in nanostructure materials. The first experimental evidence confirming this effect resulted from the studies on low-dimensional materials. The breakthroughs in zT values (larger than 2) have been mostly realized through the study of low-dimensional (2D superlattice—Fig. 11.4a, 0D + 2D quantum dots superlattice—Fig. 11.4b and 1D nanowire) TE materials [5, 45–59], well summarized in a recent review paper [60]. These studies have provided fundamental understanding of the effect of

nanostructure on TE properties. Nevertheless, most low-dimensional TE materials are fabricated by slow and complex thin film deposition techniques (such as chemical and physical vapor deposition, molecular beam epitaxy), which prevent them from being implemented in mass applications. One of the important outcomes of the above studies has been a push towards developing the strategies for achieving nanostructured bulk materials. There are two types of bulk nanostructures (nanodots—Fig. 11.4c and nanograins—Fig. 11.4d) and both have been extensively investigated in recent years [61–78].

11.2.2 Nanostructures in Low Dimensional Materials: Superlattice, Quantum Dots Superlattice and Nanowire

As early as 1990s, theoretical calculations were made on Bi_2Te_3 quantum-well superlattice structures (Fig. 11.4a ultrathin multilayers) predicting significant enhancement in zT due to the highly anisotropic effective-mass tensor [79]. In order to achieve this enhancement in practice, the current must flow along the high in-plate (carrier mobility axis) and it was assumed that the lattice thermal conductivity would be unaffected when the thickness is larger than 1 nm. No direct experimental results are available to confirm these calculations, nevertheless, a significant reduction in lattice thermal conductivity (κ_{ph}) of cross-plane in superlattice structure was observed for several TE materials. The coherent back-scattering of phonons at superlattice interfaces had been invoked and lowest cutoff wavelength was achieved by superlattice period of 50 Å [5]. As discussed in previous section, the lattice thermal conductivity is related to the phonon mean free path l, which is restricted in superlattice structure leading to lower thermal diffusivity. In other words, phonons with frequency lower than $\omega_{coutoff}$ (equals to $2v/3l$) would be inhibited from transport by the superlattice structure. The superlattice period around 50 Å is desirable for minimizing κ_{ph}, which is consistent with the calculation. The lattice thermal conductivity of 0.22 W m^{-1} K^{-1} was achieved in p-type Bi_2Te_3/Sb_2Te_3 superlattice TE device, which is much lower than the normal bulk Bi_2Te_3 alloy and even lower than the minimum predicted thermal conductivity for bulk Bi_2Te_3 [5]. When the multilayer size was controlled between 10 and 40 nm by combining melt spinning and spark plasma sintering, the κ_{ph} was 0.6 W m^{-1} K^{-1}, and thus zT did not achieve similar high value of 2.4 [5] as thin-film device with superlattice structure [49].

The phonon blocking by 2D superlattice nanostructure has been demonstrated in SiGe alloy as well. Lee et al. [50] have shown that for 30–70 Å superlattice period, the cross-plane κ_{ph} decreases with the period thickness. The suppression of perpendicular thermal transport by internal reflection and acoustic mismatch was confirmed by calculation [51] and further experiment work on $Si/Si_{0.7}Ge_{0.3}$ and $Si_{0.84}Ge_{0.16}/Si_{0.76}Ge_{0.24}$ superlattices [52]. As the interfacial acoustic impedance

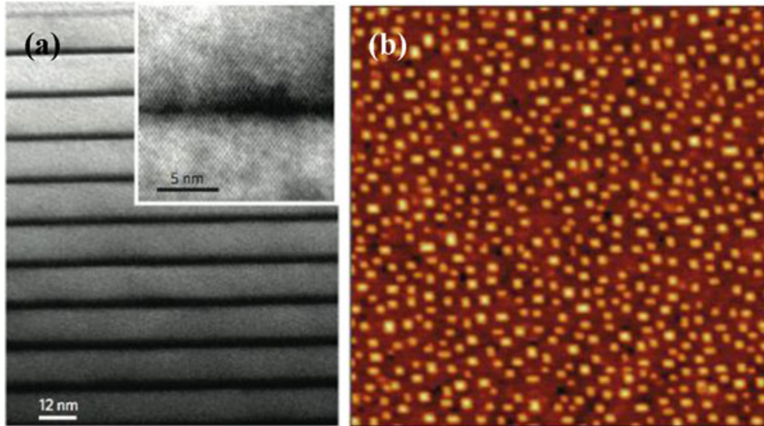

Fig. 11.5 (**a**) Bright-field TEM image of a sample with superlattice period of 12 nm. The *dark areas* correspond to the Ge layers. The *inset* shows a high resolution TEM of a nanodot; (**b**) AFM image of a single Ge/Si (001) dot layer before overgrowth with Si [48]

mismatch/roughness (equals to $(\rho \upsilon)_1/(\rho \upsilon)_2$, where ρ is the material density and υ is the speed of in material) of $Si/Si_{0.7}Ge_{0.3}$ is much larger than $Si_{0.84}Ge_{0.16}/Si_{0.76}Ge_{0.24}$, an obvious κ_{ph} reduction with decrease in period thickness was noticed in $Si/Si_{0.7}Ge_{0.3}$, but not in the second material, since acoustic impedance mismatch at interface plays a determining role of phonon reflection. Other examples of significantly reduced lattice thermal conductivity for superlattice systems include $PbTe/PbTe_xSe_{1-x}$ [53], $GaAs/Al_xGa_{1-x}As$ [54], and $In_xGa_{1-x}As/Al_yIn_zGa_{1-z}As$ [55].

Similar to the superlattice structure, quantum dot superlattice structure (QDSL) also has ultrathin multilayers (Figs. 11.4b and 11.5). In QSDL, one type of layers consists of randomly distributed nanodots of a second phase (Fig. 11.5b) (for some cases the nanodot is sufficient to create carrier confinement so that it is also named as nanodot superlattice NDSL). QDSL structure has a delta-function distribution of (phonon or electronic) density of states and discrete energy level due to three-dimensional quantum confinement [45]. Further compared with the superlattice structure with flat multilayer, QDSL has larger size roughness feature. So the nanoparticle layer was effective for scattering mid-to-long-wavelength phonons, and atomic defects on the other hand scattered the Brillouin zone edge phonons. The PbSeTe/PbTe QDSL material has been shown to provide improved TE device performance due to the presence of PbSe quantum nanodots embedded in PbTe matrix [45]. According to the Debye–Callaway model, half of the heat is carried by phonons with mean free path less than 19 nm in PbTe alloys. The κ_{ph} minimization has been attributed to short mean free paths of phonons in PbTe [56]. The mean free path l is larger than 100 nm in Si [48], which exhibits larger lattice thermal conductivity than PbTe-based alloys and mid-long mean free path phonons carry a large fraction of heat. Therefore, the QDSL structure could have more effective

phonon scattering performance in Si-based TE materials. When island dots with nano-size height are randomly distributed perpendicular to the transport direction and the film is dislocation free, the mean free path l is mainly determined by scattering from the nanodots so that the lattice thermal conductivity can be designed by superlattice period [48]. A minimum κ_{ph} 0.9 W m^{-1} K^{-1} is achieved from nanodot layer with 1.2 nm height and 70 % relative surface density, with the period of 3.6 nm [48], which is well below the amorphous Si limit of 2.5 W m^{-1} K^{-1}. The comparison of NDSL structure and matrix with randomly distributed nanoparticle has been conducted for InGaAs thin film materials [57].

The nanowire structure also influences the phonon motion and drastically reduces the thermal conductivity [46, 47, 58, 59]. For Si nanowires, the mean free path length is 110 nm for electrons and 300 nm for phonons. The nanowire maintains similar thermal power and electrical conductivity value as bulk Si while exhibiting 100-fold reduction in κ. This provides enhanced zT of 0.6 at room temperature (50 nm, wafer-scale arrays) [46] and about 1 at 200 K (20 nm) [47]. The decrease of κ depends on the nanowire diameter [46, 47] and roughness [46]. Lead chalcogenide (PbS, PbSe, PbTe) nanowires have been investigated for the phonon confinement effects and were found to exhibit similar reduction in κ with decrease in the nanowire diameter [58].

11.2.3 Nanostructures in Bulk Materials

In fact, the bulk structure does not require exact low dimensional geometry or perfect nanodots and interface. As long as high density of nanodots or interfaces exists, strong phonon scattering happens and the reduction of lattice thermal conductivity can be realized. Not only thin film and nanowire, but nanostructures (like nanoprecipitates, Fig. 11.4c) in bulk materials could shorten the phonon mean free path. PbTe-based material systems such as $AgPb_mSbTe_{2+m}$ with nanoprecipitate structure provide a good example for illustrating this principle [63]. In this system, Ag^+-Sb^{3+}-rich nanocrystals embedded uniformly in PbTe matrix to keep the charge balance of Ag^+ and Sb^{3+} pairs provide low thermal conductivity of less than 1 W m^{-1} K^{-1} (when $m = 10$ in chemical formulation). Another commonly studied system, PbTe-PbS, undergoes spinodal decomposition during annealing around 500 °C resulting in nanoscale coherent heterogeneities in PbTe matrix, as shown in Fig. 11.6 [67–69]. The size of the nanoprecipitates, which in general is less than 50 nm, varies with composition and annealing temperature. When the amount of PbS is relatively high (16 % atomic percent), spinodal-laminated structures with the period of about 2 nm are formed. Results show that the nanodots are more effective in scattering phonons than laminate structure, resulting from spinodal decomposition [68]. Nanoprecipitate formation in PbTe matrix has been extensively investigated in recent years with modifiers such as Sb [64–66, 73] Bi (BiSb) [64, 66, 73], Pb [65, 73], SnTe [74], and Ag_2Te [75]. Nearly all the nanoprecipitates in PbTe-based alloys are self-assembled nanocrystals

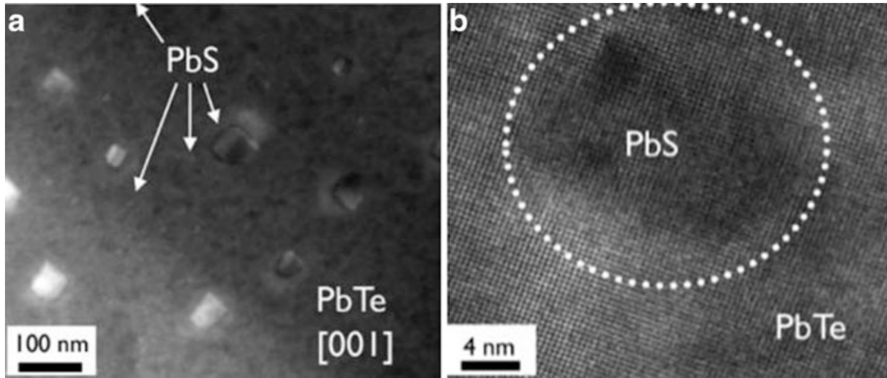

Fig. 11.6 (**a**) STEM image of PbTe-PbS 8 % showing two PbS particle sizes in PbTe matrix: larger about 100 nm and smaller 2–10 nm; (**b**) HRTEM image of nanoscale precipitates (smaller particles in (**a**)) located within the PbTe matrix [68]

that result in lattice misfit dislocations or large stain (large acoustic impedance mismatch/roughness). These nanoscale inclusions block the propagation of mid-to-long-wavelength phonons hence intensely reducing the κ_{ph}. In most cases, the charge carriers are also somewhat scattered leading to slight decrease of the electrical conductivity. Recently SrTe nanocrystals have been found to provide phonon blocking and charge transmitting functions [70, 78]. Due to very small valence band offset, there is no negative influence on the electrical conductivity by nanoprecipitates.

In comparison to the quantum dots superlattice, the nandots in bulk TE materials have two advantages: (1) the synthesis process is simple and easily controlled which is suitable for large scale fabrication, and (2) the structure is stable due to the self-assembly formation of nanoprecipitates. After the successful demonstration in bulk TE alloys, the nanostructuring concepts have been applied in oxide TE materials for obtaining low thermal conductivity. Nano-inclusion together with heavy doping and layered grain in $Ca_3Co_4O_{9+\delta}$ has been shown to result in 40 % decrease in thermal conductivity [71]. The minimum thermal conductivity of ZnO of the order of 1.5 W m^{-1} K^{-1} at 1,000 K was achieved through uniformly distributed nanoprecipitates in ZnO matrix [72].

The second method to create bulk nano-composite is to develop nanoscale grain sizes in polycrystalline material (Fig. 11.4d). It has been shown that the nano-size grains with sharp grain boundaries (Fig. 11.7a) in BiSbTe [77] exhibit strong phonon scattering thereby reducing the thermal conductivity by a factor of 2. Another interesting experiment worth discussing here is related to $Bi_{0.52}Sb_{1.48}Te_3$ ribbons synthesized from melt spinning having nanocrystals of dimension 5–10 nm, amorphous structures on contact surface and dendritic structure on free surface. After SPS, the bulk alloy preserved all the structures of ribbons, which achieved low thermal conductivity about 0.67 W m^{-1} K^{-1} with the lattice contribution of 0.26 W m^{-1} K^{-1} [62]. In SiGe system, the phonon long mean free path is larger to

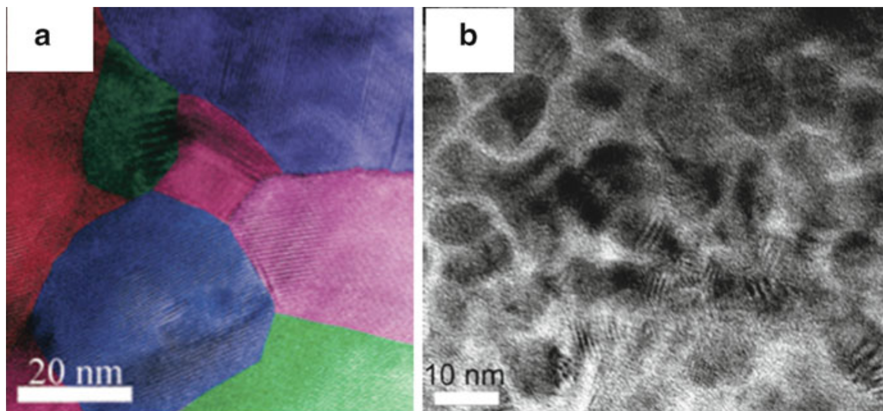

Fig. 11.7 TEM images showing (**a**) the nano size, high crystallinity, random orientation, and clean grain boundaries of BiSbTe bulk alloy [77]; (**b**) nanograins of SiGe bulk alloy [80]

300 nm [80], and thus the thermal conductivity can be easily deceased by forming nanocrystalline structure (Fig. 11.7b). The electrical conductivity was found not to have any significant change from the nanocrystalline structure as the mean free path length for electrons is in the order of 5 nm. A fraction of the heat is carried by the phonon with long mean free path and even the micron scale grain boundaries have phonon scattering effect. Investigations in Si-Ge system with samples having three different grain sizes (10–25 μm, 5–10 μm, and less than 5 μm) [76] have shown that the decrease of grain size results in reduction of thermal conductivity.

11.2.4 Synthesis Techniques

The selection of proper synthesis technique is crucial towards the fabrication of low-dimension and nanoscale structures in bulk TE. For low-dimensional (0D structure in QDSL, 1D nanowire, and 2D superlattice in thin film) systems, the fabrication methods are mostly based upon complex thin film deposition processes (such as molecular beam epitaxy and pulsed laser deposition). For example, molecular beam epitaxy (MBE) has been applied in fabrication of several thermoelectric alloys [45, 48, 81] and pulsed laser flash evaporation, ion-beam sputtering, metal organic chemical vapor deposition, molecular beam epitaxy, and electrodeposition techniques have been utilized for the synthesis of bismuth telluride thin films [82]. However, these materials are not practical for large-scale commercial use because atomic layer deposition processes are slow and expensive.

Large-scale fabrication of bulk nanostructured materials with compatible geometry is possible by using simple and mature technologies such as precipitation. The nano-size precipitates form by spontaneous decomposition processes, the

detailed discussion of which is provided in Sect. 11.2.5. For fabrication of bulk materials with nanoscale grain size, the process consists of two steps: (1) synthesis of nanoparticles and (2) consolidation of the particles to form dense body. Nanoparticles have been fabricated using mechanical alloying (ball-milling), hydrothermal method, chemical reaction, and melt spinning. High-energy ball-milling method has been applied for the synthesis of BiSbTe and SiGe nanopowders [61, 80]. While the composition and particle size obtained from ball-milling are usually not as uniform as powders obtained from chemical reaction or hydrothermal method. After the fabrication, the nanopowders need to be compacted into dense bulk maintaining the nanoscale grain size. In the conventional solid-state reaction method, first powders are compacted into green body and then sintering is conducted at high temperature to form the dense body. In order to prevent the rapid grain growth and maintain the nanoscale grain size, the high sintering temperature and long sintering time should be avoided. Hot-pressing has been used to prepare PbSe composites and the process has also been employed to produce SiGe polycrystalline materials [80, 83]. Hot-pressing is a pressure-assisted sintering process. With the applied pressure, much lower sintering temperature and shorter time are needed, during which the nanopowders grow together into a bulk material but the grains are still of nanoscale dimension. Spark plasma sintering is another modification of pressure-assisted sintering process, in which a spark discharges to heat the samples under high pressure.

Although the nanopowder fabrication, hot-pressing, and spark plasma sintering are quite mature techniques, there are still some challenges for deploying them in the synthesis of nano-composites. Firstly, most of the good TE materials are alloys, which need to be protected from the oxidation (especially for nano alloy particles with very high surface ratio). Thus, during mechanical alloying, hot-pressing or SPS, inert gas is required which increases the difficulty and cost of production. The density of bulk alloy should be high to prevent it from oxidation and environmental degradation. To achieve the high density, the high magnitude of pressure during hot-pressing or SPS is required which enhances the complexity of the equipment. Lastly, the nanograin structure is usually not stable at high temperature. $Bi_{0.52}Sb_{1.48}Te_3$ bulk alloy with nano grain sizes have been found to exhibit good thermal stability in the temperature range of 300–400 K [62]; however, SiGe that shows good figure of merit at relatively high temperature may deteriorate under continuous operation.

Here we are discussing about the nanostructured bulk materials where the kinetic and the thermodynamic of the system change. Because of the ball milling, there are more point defects that increase the diffusion coefficients of the different elements, and there is a large concentration of extended defects such as grain boundaries and dislocations. Phase diagram can change in presence of these extended defects. It is more difficult to predict the phase transformation during the thermal aging process.

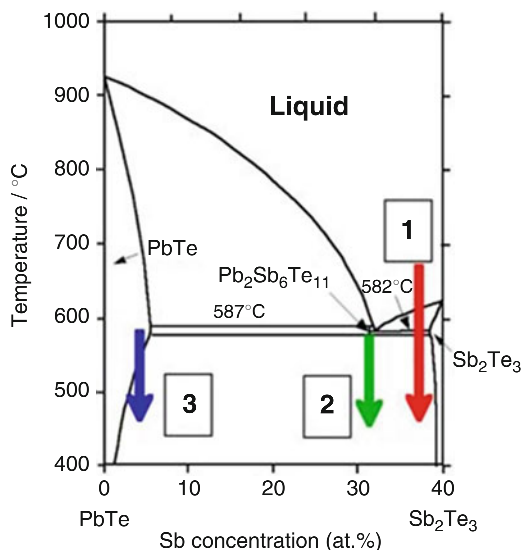

Fig. 11.8 Phase diagram of PbTe-Sb_2Te_3 [88]

11.2.5 Self-assembly Synthesis Techniques

The improvement in thermoelectric properties by formation of nanostructures can be achieved by adopting various strategies as discussed earlier and briefly summarized in Fig. 11.4. The self-assembly technique can provide a solution for the costly and time-consuming process generally used for the realization of nanostructured materials. In most of the self-assembly processes, the entropic effect is driven by the thermodynamic potentials (Gibbs or Helmholtz free energies), resulting from the entire system's statistical tendency to increase its entropy. Some material compositions are homogenous and stable in liquid state but metastable in the solid state. Thus, rapidly cooling the liquid through the solidus temperature could freeze and the entropic force will drive the precipitation of insoluble phases from the matrix under subsequent annealing. By controlling the annealing process, nanoscale precipitates can be formed with uniform distribution in the matrix. The composition selection and annealing process is critical for achieving the homogeneous precipitate structure. Since, the precipitates (or "nanodots") are self-assembled, the process is easy and simple, and these materials are stable at relatively high temperature. This approach has been utilized for achieving high thermoelectric performance in PbTe-based alloys [63–70, 73, 74, 78, 84–87] and ZnO [72]. For example, using the different regimes of the phase diagram and varying the solidification curve of PbTe-Sb_2Te_3 alloy, the bulk material with nanoprecipitates (blue arrow), lamella structure (green arrow), oriented epitaxial like interfaces and semi-coherent interfaces can be obtained (Fig. 11.8) [88]. Along the blue line with continuous cooling, Sb_2Te_3 solubility in PbTe decreases, and it

begins to precipitate. The size of the precipitates is small as the diffusion process in solid state is much more difficult than in liquid state. For the critical composition (shown by green arrow), annealing below the eutectoid temperature allows metastable phase $Pb_2Sb_6Te_{11}$ to decompose into PbTe and Sb_2Te_3 which assemble in lamellar bulk structure [88, 89]. The formation of lamellar structure is quite similar to the formation of the pearlitic steel. The temperature and decomposition time can be used to tune the interlamellar spacing.

Using chemical bonding and van der Waals force, several low-dimensional thermoelectric materials have been recently synthesized. Facile solvothermal method was utilized to obtain the bundles of Bi_2Te_3 nanorods [90] and a high ZT value of ~0.43 at 473 K was reported. In this process, the K_2TeO_3 was dissolved separately in the water solution of ethylenediamine and hydrazine hydrate $N_2H_4{\cdot}H_2O$ and then mixed, following the heat treatment processes. In another case of Bi_2Te_3, nanoplates of thickness 15–20 nm and self-assembled nanoflowers (which exhibited good value of power factor 8.6×10^{-6} W m^{-1} K^{-2} at 160) using nanoplates have been synthesized through hydrothermal synthesis technique [91]. Silver telluride-based hollow microspheres and dendritic nanostructures have been formed by the self-assembly of nanoparticles and nanosheets using solution based room temperature process [92]. The $[Ag(en)_2]^+$ particles assembled on the surface of tiny bubbles generated by the volatilization of anhydrous ethylenediamine and resulted in the formation of Ag hollow microspheres after chemical reaction. Ag_2Te hollow microspheres or dendritic nanostructures have been achieved through reaction of Ag and Te. Also, Si/SiGe superlattice nanowires consisting of interlaced nanodots have been successfully deposited by hybrid pulsed laser ablation–chemical vapor deposition (PLA-CVD) process [93]. Theoretical studies have predicted [94] the zT values of 4 and 6 for the PbSe/PbS and PbTe/PbSe superlattice nanowires of 5 nm diameter at 77 K respectively if the PLA-CVD process can be able to apply in these two materials. Hierarchical assembly of nanowires has been utilized through the microfluidic-assisted integration process for ZnO. The variables of the nanowires such as composition, diameter, growth direction, etc. were controlled via vapor–solid–liquid crystal growth mechanism [95].

11.3 Thermal Conductivity of Oxide Bulk Thermoelectrics with Self-assembled Structure

For expanding the range of application of thermoelectrics, both quality and cost of thermoelectric materials are important. Bulk alloys such as BiTe, PbTe have been shown to provide improved figure of merit higher than 1.5 (Table 11.1). However, as discussed earlier, high cost of raw materials or complex and costly fabrication processes together with oxidation issue prevent their commercialization in high

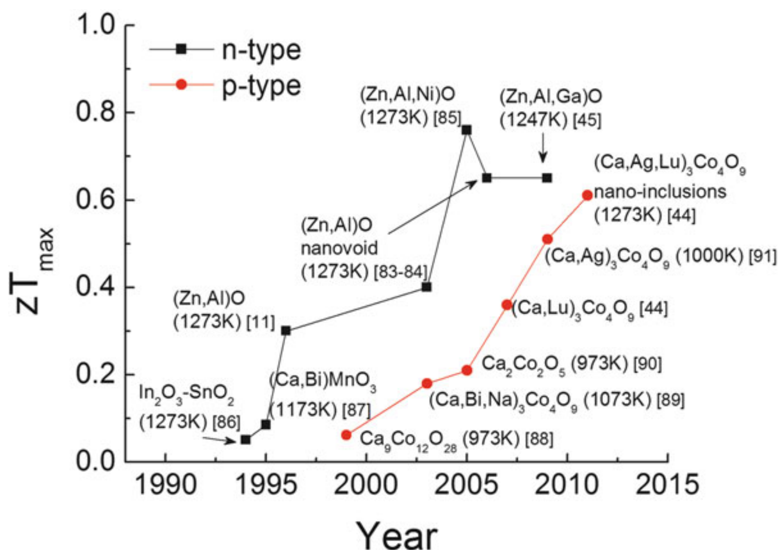

Fig. 11.9 History of the development of n- and p-type polycrystalline oxide TE materials [12, 71, 96–98, 102, 113–118]

temperature platforms. For thermoelectric oxides, although the figure of merit is still low compared to that of alloys due to their relatively high thermal conductivity and low electrical conductivity, these materials have the commercial advantage of cost, environmental friendliness, and stability at high temperature in air atmosphere. Also, in the past decade, there has been a great progress for n- and p-type polycrystalline oxides, as shown in Fig. 11.9. The zT enhancement of thermoelectric alloys by developing nanostructures has been predicted and experimentally validated (Sect. 11.2). Low dimension nanostructures provide a good opportunity for research but are difficult to implement at mass scale because of the complex synthesis techniques (thin film deposition). Large scale fabrication of bulk nanostructured materials with compatible geometry is possible by using mature sintering technologies. Bulk materials with self-assembled nanoprecipitate structure are promising because the process is driven by thermodynamic force. Therefore, precipitation is more stable at high temperature and method for achieving nanostructured materials is simple as compared to nanograin structure formed by SPS or hot-pressing. Few studies on nanostructuring in oxides have been conducted but these studies show promising results towards reducing the thermal conductivity. This section will discuss in detail the role of nanostructures in reduction of thermal conductivity in thermoelectric oxides, with specific focus on self-assembled nanoprecipitates in ZnO.

11.3.1 Self-assembled Nanostructure and Effect of Dimension on Thermal Conductivity of ZnO Bulk Thermoelectrics

Doped ZnO has good Seebeck coefficient (around 200 μV K^{-1}) and large variation in electrical property [12]. Moreover, it exhibits substantial stability at high temperatures and therefore it is considered as a promising thermoelectric material [12, 72, 96–98]. The decrease of κ is an essential strategy towards improving its figure of merit. Because ZnO consists of light elements (with moderate Al doping) arranged in simple wurtzite crystal structure, it exhibits high thermal conductivity of 100 W m^{-1} K^{-1} at room temperature [99].

Various techniques have been investigated to reduce the thermal conductivity of ZnO in literature. Voids were introduced in ZnO matrix by foaming technique that employs polystyrene in order to block the phonon transport. The size of inclusion is critical for κ decrease, for example, when the voids were in nanoscale size range, the ZnO matrix revealed ~16–25 % reduced κ values [96], and the micron size pores have little effect on the κ reduction [97]. The thermal conductivity of ZnO has been noticed to decrease by doping as well [98, 100, 101]. The value of κ diminished to ~5 W m^{-1} K^{-1} [102] in Ga and Al co-doped ZnO, because of the granular texture from Ga impurity, but ZnO ceramics with Ga doping were highly porous, and therefore had adverse effect on electrical conductivity.

Similar to that of PbTe-based alloys with nanodot structure, precipitates can be formed spontaneously in ZnO with Al addition due to the limited solubility of Al in ZnO [103]. As the extra amount of Al atoms is metastable in the solid solution, the secondary phase is spontaneously precipitated in ZnO with Al addition during high temperature sintering process. ZnO–Al composites with nanosize (Fig. 11.10a–d) and micro-size (Fig. 11.10e–f) precipitates can be fabricated by same solid-state reaction of mixture of ZnO and Al_2O_3 powders using different annealing temperatures in air. When Al concentration is below 2 mol%, the size of precipitates is uniform and in the vicinity of 50 nm (Fig. 11.10b, c). The $Zn_{0.97}Al_{0.03}O$ samples possess both 50 and 400 nm precipitates (Fig. 11.10d). Typical values of micron-size precipitates are in the range of 1–3 μm as shown in the magnified view in Fig. 11.10f. Elemental mapping performed using energy-dispersive spectroscopy (EDS) on a typical $Zn_{0.96}Al_{0.04}O$ sample revealed that precipitates with $ZnAl_2O_4$ phase composition distributed uniformly throughout the sample, both inside and at the grain boundaries (Fig. 11.10g). The grain sizes are in the range of 1–5 μm for ZnO–Al nano-composites, while 20–50 μm for ZnO–Al micro-composites.

The phonon scattering behavior depends on several mechanisms: Umklapp phonon–phonon scattering, phonon–impurity scattering, and phonon–boundary scattering. So the combined relaxation time can be given from (11.4) as [104]:

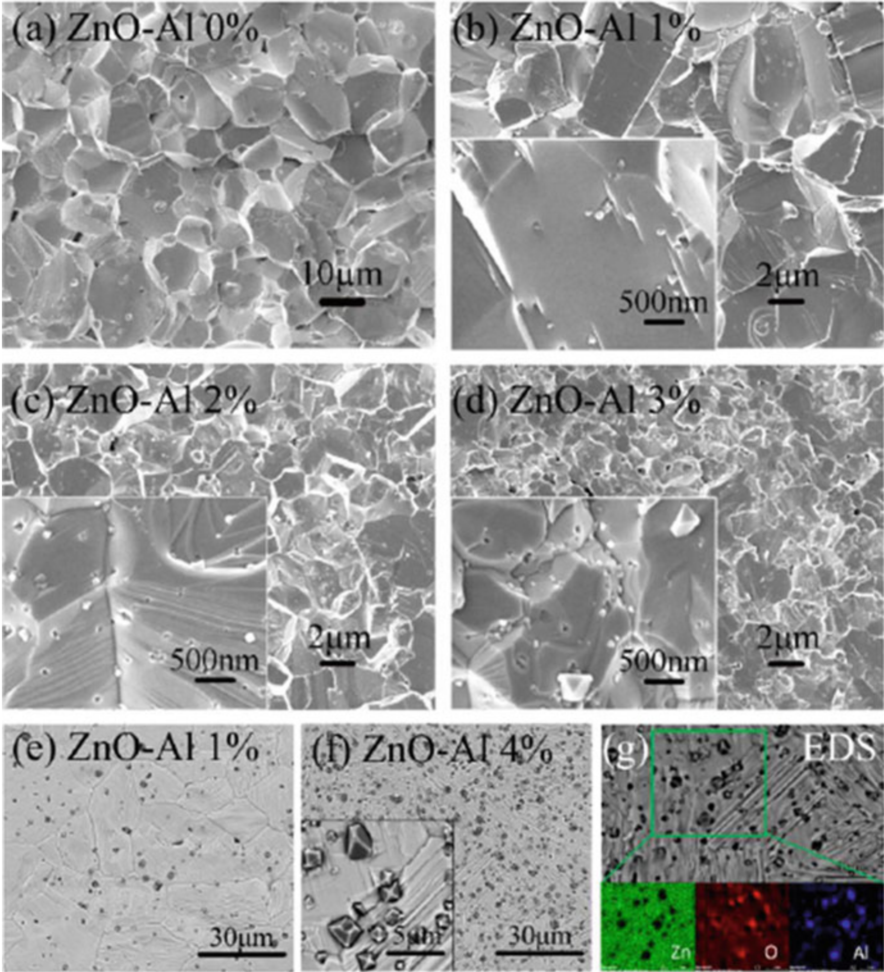

Fig. 11.10 (**a**–**d**) SEM images of ZnO–Al nano-composites (*brighter particles* are $ZnAl_2O_4$ nanoprecipitates and insets are higher magnification SEM); (**e** and **f**) contrast SEM images using back-scattered electron of ZnO–Al micro-composites (*darker particles* are $ZnAl_2O_4$ precipitates); (**g**) EDS elemental mapping of $(Zn_{0.96}Al_{0.04})O$ sample on element Zn (*green*), O (*red*) and Al (*blue*) [119]

$$\frac{1}{\tau_{\mathrm{C}}} = \frac{1}{\tau_{\mathrm{U}}} + \frac{1}{\tau_{\mathrm{M}}} + \frac{1}{\tau_{\mathrm{B}}} + \frac{1}{\tau_{\text{ph-e}}} \tag{11.9}$$

where τ_{C}, τ_{U}, τ_{M}, τ_{B}, and $\tau_{\text{ph-e}}$ denote total, Umklapp phonon–phonon scattering, phonon–impurity scattering, phonon–boundary scattering, and phonon–electron scattering relaxation times, respectively. Assuming additional Al^{3+} ions stay in precipitates, the Umklapp phonon–phonon scattering, phonon–impurity scattering,

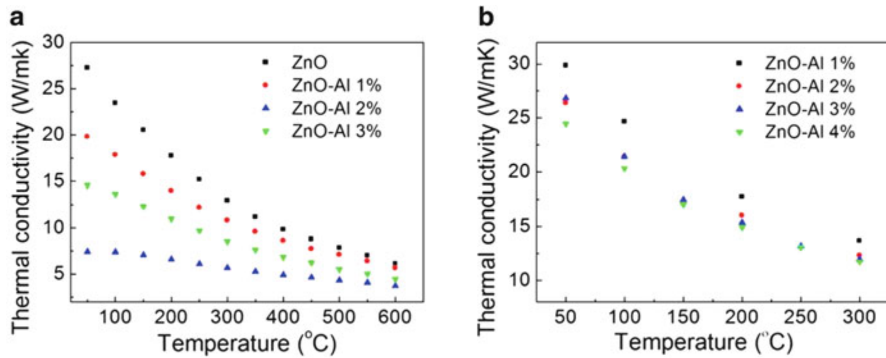

Fig. 11.11 Temperature dependence of thermal conductivities of ZnO–Al (**a**) nano-composites; (**b**) micro-composites [119]

and phonon–electron scattering in ZnO–Al nano-composites can be considered to be comparable, so cannot lead to large κ difference. Because of the formation of nanoprecipitates and grain size reduction, phonon–boundary scattering (interface scattering) is the key factor for κ variation, which can be expressed as [104]:

$$\frac{1}{\tau_{\mathrm{B}}} = \frac{V}{D}(1 - p) \tag{11.10}$$

where V is the phonon group velocity, D is the dimension of the system, and p is the surface roughness factor. The value of p close to 1 means a smooth surface where the scattering is purely specular and the relaxation time goes to ∞.

Since nano-composites have nanoscale precipitates and smaller grains, the phonon relaxation time (in other way the phonon mean free path) is shorter in nano-composites than in micro-composites. These nanoscale inclusions block the propagation of mid-to-long-wavelength phonons, resulting in the reduction of κ especially in relative low temperature ranges shown in Fig. 11.11. With increase in Al content, nano-composites were found to display much larger decrease in the value of κ. For nano-composites, with increase of Al addition to 2 mol%, the amount of precipitates formed increases but the size was still below 50 nm. Thereby the samples containing 2 mol% Al displayed the minimum thermal conductivity for the whole range of measurement temperature; values being 7.5 W m^{-1} K^{-1} at room temperature and 3.7 W m^{-1} K^{-1} at 600 °C. These values are 73 and 40 % lower than that of pure ZnO samples synthesized under the same conditions. When Al concentration increases to 3 mol%, part of the precipitates increase the size to about 400 nm, so that the reduction of κ is not as efficient as that with 2 mol% Al. This indicates the significance of the size of precipitates. While ZnO–Al micro-composites exhibited progressive decrease in the values of κ with increase in Al content; the relative decrease in value of κ was only ~15 % for the samples containing 4 mol% Al than those containing 1 mol% Al in all temperatures ranges mainly because of micron size precipitates.

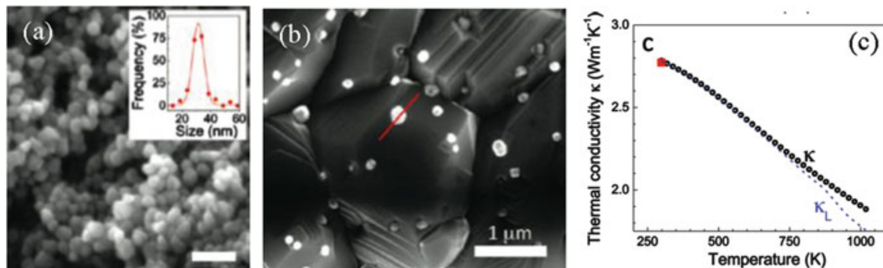

Fig. 11.12 SEM micrograph of (**a**) ZnO nanocrystals synthesized with microwave doses of 16 48 kJ g^{-1} and (**b**) bulk ZnO nano-composite with 1 at.% Al; (**c**) thermal conductivity for ZnO nano-composite pellets with 0.25 at.% Al [72]

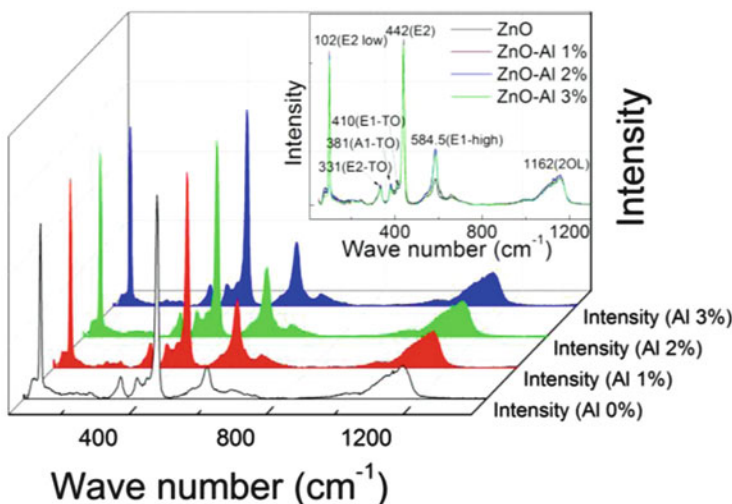

Fig. 11.13 Raman spectra of ZnO–Al nano-composites [119]

ZnO with nano inclusions were also synthesized by sintering ZnO from thermal decomposition method [72]. The nanopowders with single phase and average size of 30 nm (Fig. 11.12a) can be synthesized by thermal decomposition of zinc and aluminum acetates in pentanediol with oleylamine as a surfactant. Self-assembled nanoprecipitates with the size of 30–200 nm were formed during sintering and uniformly distributed in ZnO matrix (Fig. 11.12b). Low thermal conductivity (Fig. 11.12c) of ZnO was measured at room temperature and calculated at higher temperatures and the reduction of κ was attributed to ZnO grain boundary, $ZnAl_2O_4$ nanosize precipitates, point defects and porosity (~90 % relative density) [72].

Raman spectroscopy (Fig. 11.13) has been utilized to confirm the phonon scattering mechanism of phonon scattering in ZnO with nanoprecipitates structure.

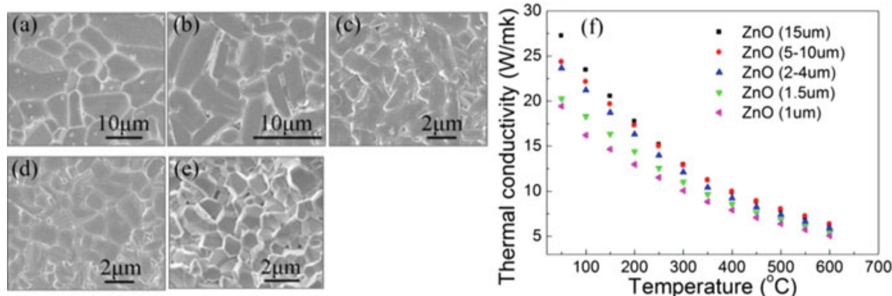

Fig. 11.14 SEM images of ZnO with different grain size (**a**–**e**); and temperature dependence of thermal conductivity of ZnO with different grain size (**f**) [119]

The ZnO with wurtzite structure belongs to the C^4_{6v} space group ($P6_3mc$), and exhibits 12 possible vibrational modes, among which the A_1, E_1, and E_2 are Raman-active optical modes [99]. The Raman active optical phonon E_2 mode of the ZnO around 440 cm^{-1} has high intensity displaying a sharp and strong peak. Because of ionic character of Zn–O bonds, polar modes (A_1 and E_1) exhibit large splitting as longitudinal optical (LO) and transverse optical (TO) modes. The mode "E_1-high" is much stronger in the ZnO–Al samples in comparison to pure ZnO samples. Theoretical prediction reported that confined LO phonon wavenumber to be between A_1 (LO) (574 cm^{-1}) and E_1 (LO) (590 cm^{-1}) [105] in ZnO nanostructure. Experimental studies confirmed the phenomena that confined LO phonon modes to appear at 588 cm^{-1} (for 8.5 nm) and 584 cm^{-1} (for 4.0 nm) [106, 107]. So the higher intensity at 584.5 cm^{-1} in Fig. 11.13 is attributed to phonon confinement by nano-size precipitated phase in ZnO–Al nano-composites. Further, no peak shift and broadening of the Raman peaks is observed which can only happen when quantum dot size approaches to exciton Bohr radius [108]. Phonon scattering at ZnO–$ZnAl_2O_4$ interface can occur in both ZnO–Al micron- and nano-composites, however phonon confinement in the homogeneously distributed nanoprecipitates leads to larger decrease in the value of κ.

As mentioned before, ZnO grain boundary is another potential phonon–boundary scattering center. Smaller grain size reveals the higher density of interfaces and therefore exhibits lower value of κ (Fig. 11.14). The values of κ for ZnO with grain sizes of 5–10 μm, 2–4 μm, 1.5 μm and 1 μm have shown the decrement by 10 %, 13 %, 25 % and 28 % respectively at room temperature in comparison to the value of κ for the largest grain size of 10–15 μm. The grain size dependent κ reduction is more evident at lower temperatures (<200 °C). At relative higher temperatures (>400 °C), ZnO with grain sizes of 10–15, 5–10, and 2–4 μm has almost the same κ (the difference is less than 5 %). ZnO with smaller grains, 1.5 μm and 1 μm revealed reduction in the value of κ by ~13 % and 18 % respectively at 600 °C. All the samples revealed relative density higher than 96 % indicating that the porosity is not the main factor contributing to the phonon scattering. The results confirm that grain (micron scale) boundary area has

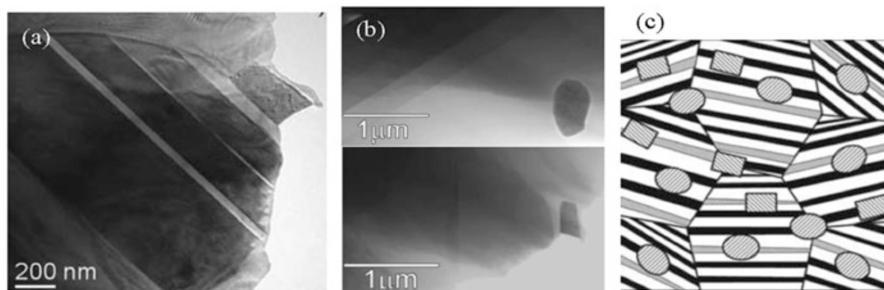

Fig. 11.15 (**a**) BF-TEM images of $Co_3Co_4O_9$ with heavy doping of Ag and Eu; (**b**) STEM of Ag precipitates in $Co_3Co_4O_{9\delta}$; (**c**) heavily doped aligned lamellar nanostructures with embedded nano-size inclusions [71]

significant contribution towards the blocking of long-wavelength phonons (with free path in mesoscale) but the degree of reduction is smaller than the contribution of nanoprecipitates, which block the main heat carrier, phonon with mid-to-long free path.

11.3.2 Nanostructure of p-Type Ca-Co-O and n-Type $SrTiO_3$ Bulk Thermoelectrics

The compounds $Ca_3Co_4O_9$ and $NaCo_2O_4$ exhibit large thermopower and metal-like conductivity. They both belong to A_xCoO_2 (A = Na, Ca, Sr, Ba; x is varying for different A) family with similar alternating layer structure, CdI_2-type CoO_2^- and $Ca_2CoO_3^+$ or A^+ layer, resulting in phonon blocking and therefore relatively low thermal conductivity along *c*-axis direction as compared to other oxide TE materials [109]. For $NaCo_2O_4$, the application in power generation has challenges because of the volatility of Na and the instability in the humid conditions [71]. Ca-Co-O ceramic system with textured microstructure have been obtained by using SPS which has the promise of providing lower thermal conductivity along *c*-axis [109]. During ball-milling process and SPS, spontaneously oriented lamellar nanostructure (Fig. 11.15a) was formed in the presence of Ag inclusions (Fig. 11.15b). The grains with multilayer structure were randomly oriented with high angle boundary [71]. The Ag inclusions with the diameter of 350 nm consisted of spherical and cubical shape particles. The lamellar nanostructure together with Ag nano inclusion and heavy doping element Eu was found to provide a lower thermal conductivity [71]. With high concentration of Ag, the inclusion aggregated and thermal conductivity was found to increase as compared to the sample without Ag and Eu.

$SrTiO_3$ is another n-type thermoelectric candidate with large Seebeck coefficient (−100 to −300) and its electrical conductivity can be controlled by Nb^{5+} and La^{3+} doping. With the perovskite structure, the thermal conductivity of $SrTiO_3$ is lower

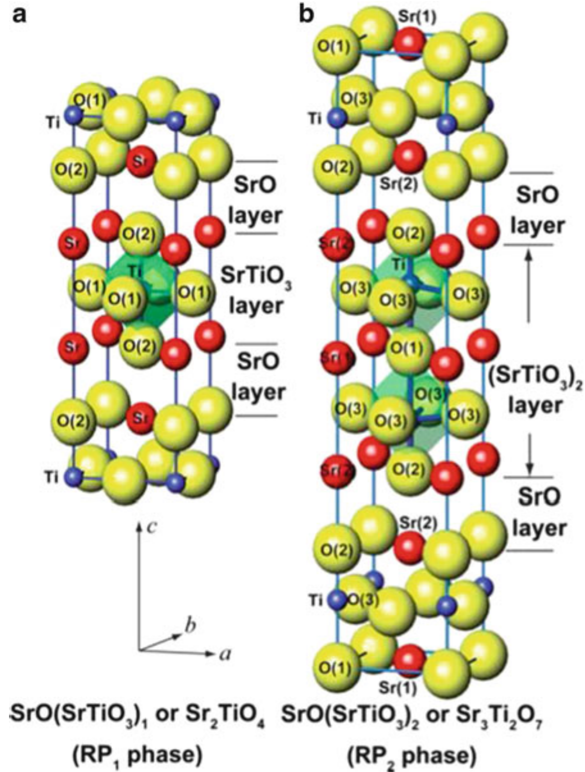

Fig. 11.16 Schematic crystal structures of Ruddlesden–Popper phase, $SrO/(SrTiO_3)_n$ with (**a**) $n = 1$ and (**b**) $n = 2$ [120, 121]

than that of ZnO but higher than layered $Co_3Co_4O_9$, having magnitude of 11–3.2 W m^{-1} K^{-1} in the range of 300–1,000 K [110]. Thermal conductivity reduction was found to vary with different doping elements and Dy has been found to show good phonon blocking as compared to Nb, La, Y, Sm, and Gd [111]. The natural superlattice Ruddlesden–Popper (RP) phase is good for phonon blocking. Consisting of alternating SrO and $SrTiO_3$ layers (Fig. 11.16), rare earth elements doped RP phase exhibits much lower thermal conductivity than $SrTiO_3$. Similar to the layered Ca-Co-O system, there is phonon scattering at SrO–$SrTiO_3$ interface.

11.4 Conclusions

Thermoelectric generator can efficiently convert unused heat into electricity, and nanostructure based bulk thermoelectric devices can be promising due to the enhanced figure of merit (zT). Low-dimensional systems (2D superlattice, 0D + 2D quantum dots superlattice and 1D nanowire), and nanostructures

synthesized in bulk (nanodots and nanograins) have been studied in recent decades and proven to be good phonon scattering centers for low thermal conductivity. Oxides thermoelectrics synthesized from abundant and low cost raw materials offer the high temperature stability due to their high oxidation resistance. Self-assembly techniques have been successfully applied for the fabrication of bulk oxide thermoelectrics with nanostructure. The self-assembled nanostructures in n-type ZnO were introduced which resulted in large reduction in thermal conductivity, by a factor of about three. The thermal conductivity reduction was attributed to the phonon scattering and confinement by uniformly distributed nanoprecipitates ($ZnAl_2O_4$) and large grain boundary area. Nano lamellar and inclusion structure in p-type Ca-Co-O system ($Ca_3Co_4O_9$), and natural superlattices structure in n-type $SrO/SrTiO_3$ result in thermal conductivity reduction as well. In the near future thermoelectric waste heat recovery by using oxides will make a significant contribution, over a wide range of applications, in power generator and cooling system.

Acknowledgments The authors (Y. Z. and S. P.) gratefully acknowledge the financial support provided by NSF/DOE Thermoelectrics Partnership. The author (A. K.) would also like to acknowledge the support from the CEHMS seed program.

References

1. Laird Technologies, Thermoelectric Handbook. www.lairdtech.com
2. Zebarjadi, M., Esfarjani, K., Dresselhaus, M.S., Ren, Z.F., Chen, G.: Perspectives on thermoelectrics: from fundamentals to device applications. Energy Environ. Sci. **5**, 5147–5162 (2012)
3. Stabler, F.: Benefits of thermoelectric technology for the automobile. Presented at DOE thermoelectric applications workshop, San Diego, CA, 2011
4. Samson, D., Kluge, M., Fuss, T., Schmid, U., Becker, T.: Flight test results of a thermoelectric energy harvester for aircraft. J. Electron. Mater. **41**(6), 1134–1137 (2012)
5. Venkatasubramanian, R., Siivola, E., Colpitts, T., O'Quinn, B.: Thin-film thermoelectric devices with high room-temperature figures of merit. Nature **413**, 597–602 (2001)
6. Wright, D.A.: Thermoelectric properties of bismuth telluride and its alloys. Nat. Mater. **181**, 834 (1958)
7. Fano, V.: Lead telluride and its alloys, Chapter 21. In: Rowe, D.M. (ed.) CRC handbook of thermoelectrics. CRC Press LLC, Boca Raton, FL (1995)
8. Nolas, G.S., Morelli, D.T., Tritt, T.M.: SKUTTERUDITES-a phonon-glass-electron crystal approach to advanced thermoelectric energy conversion applications. Annu. Rev. Mater. Sci. **29**, 89–116 (1999)
9. Vining, C.B.: Silicon germanium, Chapter 28. In: Rowe, D.M. (ed.) CRC handbook of thermoelectrics. CRC Press LLC, Boca Raton, FL (1995)
10. Terasaki, I., Sasago, Y., Uchinokura, K.:Large thermoelectric power in $NaCo_2O_4$ single crystals. Phys. Rev. B **56**, R12685–R12687 (1997)
11. Shikano, M., Funahashi, R.: Electrical and thermal properties of single-crystalline $(Ca_2CoO_3)_{0.7}CoO_2$ with a $Ca_3Co_4O_9$ structure. Appl. Phys. Lett. **82**, 1851–1853 (2003)
12. Ohtaki, M., Tsubota, T., Eguchi, K., Arai, H.: High temperature thermoelectric properties of $(Zn_{1-x}Al_x)O$. J. Appl. Phys. **79**, 1816–1818 (1996)

13. Okuda, T., Nakanishi, K., Miyasaka, S., Tokura, Y.: Large thermoelectric response of metallic perovskites: $Sr_{1-x}La_xTiO_3$. Phys. Rev. B **63**, 113104 (2001)
14. Snyder, G.J., Toberer, E.S.: Complex thermoelectric materials. Nat. Mater. **7**, 105–114 (2008)
15. Heremans, J.P., Jovovic, V., Toberer, E.S., Saramat, A., Kurosaki, K., Charoenphakdee, A., Yamanaka, S., Snyder, G.J.: Enhancement of thermoelectric efficiency in PbTe by distortion of the electronic density of states. Science **321**, 554–557 (2008)
16. Hicks, L.D., Dresselhaus, M.S.: Thermoelectric figure of merit of a one-dimensional conductor. Phys. Rev. B **47**, 16631–16634 (1993)
17. Li, J.F., Liu, W.S., Zhao, L.D., Zhou, M.: High-performance nanostructured thermoelectric materials. NPG Asia Mater. **2**(4), 152–158 (2010)
18. Mahan, G.D., Sofo, J.O.: The best thermoelectrics. Proc. Natl. Acad. Sci. U. S. A. **93**, 7436–7439 (1996)
19. Callaway, J.: Model for lattice thermal conductivity at low temperatures. Phys Rev **113**, 1046–1051 (1959)
20. Holland, M.G.: Analysis of lattice thermal conductivity. Phys. Rev. **132**, 2461–2471 (1963)
21. Ziman, J.M.: Electrons and Phonons. University Press, Oxford (1979)
22. Jones, W., March, N.H.: Theoretical Solid State Physics. Courier Dover, New York (1985)
23. Madsen, G.K.H., Schwarz, K., Blaha, P., Singh, D.J.: Electronic structure and transport in type-I and type-VIII clathrates containing strontium, barium and europium. Phys. Rev. B **68**, 125212 (2003)
24. Allen, M.P., Tildesley, D.J.: Computer simulation of liquids. Oxford University Press, New York (1997)
25. Frenkel, D., Berend, S.: Understanding Molecular Simulation. Academic, San Diego (1996)
26. Votano, J.R., Parham, M., Hall, L.H., Kier, L.B., Hall, L.M.: Prediction of aqueous solubility based on large datasets using several QSPR models utilizing topological structure representation. Chem. Biodivers. **1**, 1829–1841 (2004)
27. Zwanzig, R.: Time—correlation functions and transport coefficients in statistical mechanics. Annu. Rev. Phys. Chem. **16**, 67–102 (1965)
28. Ladd, A.J.C., Moran, B.: Lattice thermal conductivity: a comparison of molecular dynamics and anharmonic lattice dynamics. Phys. Rev. B **34**, 5058–5064 (1986)
29. Jenkins, J.O., Rayne, J.A., Ure, R.W.: Elastic moduli and phonon properties of Bi_2Te_3. Phys. Rev. B **5**, 3171–3184 (1972)
30. Kullmann, W., Eichhorn, G., Rauh, H., Geick, R., Eckold, G., Steigenberger, U.: Lattice dynamics and phonon dispersion in the narrow gap semiconductor Bi_2Te_3 with sandwich structure. Phys. Status Solidi B **162**, 125–140 (1990)
31. Shiga, T., Shiomi, J., Esfarjani, K., Delaire, O., Chen, G.: Unpublished
32. Esfarjani, K., Chen, G., Stokes, H.T.: Heat transport in silicon from first principles calculations. Phys. Rev. B **84**, 085204 (2011)
33. Shiomi, J., Esfarjani, K., Chen, G.: Thermal conductivity of half—Heusler compounds from first—principles calculations. Phys. Rev. B **84**, 104302 (2011)
34. Kane, E.O.: Semiconductors and Semimetals, vol. 1. Academic, New York (1966). pp. 75–100
35. Huang, B.L., Kaviany, M.: Ab initio and molecular dynamics predictions for electron and phonon transport in bismuth telluride. Phys. Rev. B **77**, 125209 (2008)
36. Singh, D.J.: Doping—dependent thermopower of PbTe from Boltzmann transport calculations. Phys. Rev. B **81**, 195217 (2010)
37. Parker, D., Chen, X., Singh, D.J.: High three dimensional thermoelectric performance from low dimensional bands. arXiv: 1211.4006. Cond. Mat. Mtrl. Sci. (2012)
38. Zhang, L., Singh, D.J.: Electronic structure and thermoelectric properties of layered PbSe-WSe_2 materials. Phys. Rev. B **80**, 075117 (2009)
39. Parker, D., Singh, D.J.: Potential thermoelectric performance from optimization of hole—doped Bi_2Se_3. Phys. Rev. X **1**, 021005 (2011)

40. Balandin, A.A.: Nanophononics: phonon engineering in nanostructures and nanodevices. Nanosci. Nanotechnol. **5**, 1015–1022 (2005)
41. Bhandari, C.M., Rowe, D.M.: Lattice Thermal Conductivity. Thermal Conduction in Semiconductors. University Press, Oxford (1979)
42. Saha, S.K.: Theoretical Study of Thermal Transport at Nano Constrictions and Nanowires with Sawtooth Surface Roughness, Ph.D. Thesis, University of Texas at Austin (2007)
43. Martin, P., Aksamija, Z., Pop, E., Ravaioli, U.: Impact of phonon surface roughness scattering on thermal conductivity of thin Si nanowires. Phys. Rev. Lett. **102**, 125503 (2009)
44. Razeghi, M.: Fundamentals of Solid State Engineering. Springer, New York (2009)
45. Harman, T.C., Taylor, P.J., Walsh, M.P., LaForge, B.E.: Quantum dot superlattice thermoelectric materials and devices. Science **297**, 2229–2232 (2002)
46. Hochbaum, A.I., Chen, R.K., Delgado, R.D., Liang, W.J., Garnett, E.C., Najarian, M., Majumdar, A., Yang, P.D.: Enhanced thermoelectric performance of rough silicon nanowires. Nature **451**, 163–168 (2008)
47. Boukai, A.I., Bunimovich, Y., Tahir-Kheli, J., Yu, J.K., Goddard, W.A., Heath, J.R.: Silicon nanowires as efficient thermoelectric materials. Nature **451**, 168–171 (2008)
48. Pernot, G., Stoffel, M., Savic, I., Pezzoli, F., Chen, P., et al.: Precise control of thermal conductivity at the nanoscale through individual phonon-scattering barriers. Nat. Mater. **9**, 491–495 (2010)
49. Tang, X.F., Xie, W.J., Li, H., Zhao, W.Y., Zhang, Q.J.: Preparation and thermoelectric transport properties of high-performance p-type Bi_2Te_3 with layered nanostructure. Appl. Phys. Lett. **90**, 012102 (2007)
50. Lee, S.-M., Cahill, D.G.: Thermal conductivity of Si–Ge superlattices. Appl. Phys. Lett. **70**, 2957 (1997)
51. Hyldgaard, P., Mahan, G.D.: Phonon superlattice transportation. Phys. Rev. B **56**, 10754–10757 (2000)
52. Huxtable, S.T., Abramson, A.R., Tien, C.-L., Majumdar, A.: Thermal conductivity of Si/Si/Ge and SiGe/SiGe superlattices. Appl. Phys. Lett. **80**, 1737 (2002)
53. Caylor, J.C., Coonley, K., Stuart, J., Colpitts, T., Venkatasubramanian, R.: Enhanced thermoelectric performance in PbTe-based superlattice structures from reduction of lattice thermal conductivity. Appl. Phys. Lett. **87**, 023105 (2005)
54. Capinski, W.S., Maris, H.J.: Thermal conductivity of GaAs/AlAs superlattices. Phys. B **219–220**, 699–701 (1996)
55. Kim, W., Singer, S.L., Majumdar, A., Vashaee, D., Bian, Z., et al.: Cross-plane lattice and electronic thermal conductivities of ErAs-InGaAs/InGaAlAs superlattices. Appl. Phys. Lett. **88**(242107) (2006)
56. Koh, Y.K., Vineis, C.J., Calawa, S.D., Walsh, M.P., Cahill, D.G.: Lattice thermal conductivity of nanostructured thermoelectric materials based on PbTe. Appl. Phys. Lett. **94**, 153101 (2009)
57. Kim, W., Zide, J., Gossard, A., Klenov, D., Stemmer, S., Shakouri, A., Majumdar, A.: Thermal conductivity reduction and thermoelectric figure of merit increase by embedding nanoparticles in crystalline semiconductors. Phys. Rev. Lett. **96**, 045901 (2006)
58. Fardy, M., Hochbaum, A.L., Goldberger, J., Zhang, M.M., Yang, P.: Synthesis and thermoelectrical characterization of lead chalcogenide nanowires. Adv. Mater. **19**, 3047–3051 (2007)
59. Zhao, X.B., Ji, X.H., Zhang, Y.H., Zhu, T.J., Tu, J.P., et al.: Bismuth telluride nanotubes and the effects on the thermoelectric properties of nanotube-containing nanocomposites. Appl. Phys. Lett. **86**, 062111 (2005)
60. Vineis, C.J., Shakouri, A., Majumdar, A., Kanatzidis, M.G.: Nanostructured thermoelectrics—big efficiency gains from small features. Adv. Mater. **22**, 3970 (2010)
61. Poudel, B., et al.: High-thermoelectric performance of nanostructured bismuth antimony telluride bulk alloys. Science **320**, 634–638 (2008)

62. Xie, W.J., Tang, X.F., Yan, Y.G., Zhang, Q.J., Tritt, T.M.: High thermoelectric performance BiSbTe alloy with unique low-dimensional structure. J. Appl. Phys. **105**, 113713 (2009)
63. Hsu, K.F., et al.: Cubic $AgPb_mSbTe_{2+m}$: bulk thermoelectric materials with high figure of merit. Science **303**, 818–821 (2004)
64. Androulakis, J., et al.: Nanostructuring and high thermoelectric efficiency in p-type Ag $(Pb_{1-y}Sn_y)_mSbTe_{2+m}$. Adv. Mater. **18**, 1170–1173 (2006)
65. Sootsman, J.R., Kong, H., Uher, C., D'Angelo, J.J., Wu, C.-I., Hogan, T.P., Caillat, T., Kanatzidis, M.G.: Large enhancements in the thermoelectric power factor of bulk pbTe at high temperature by synergistic nanostructuring. Angew. Chem. Int. Ed. **120**, 8746–8750 (2008)
66. Gueguen, A., Poudeu, P.F.P., Li, C.P., Moses, S., Uher, C., He, J.Q., Dravid, V., Paraskevopoulos, K.A., Kanatzidis, M.G.: Thermoelectric properties and nanostructuring in the p-type materials $NaPb_{18-x}Sn_xMTe_{20}$ (M = Sb, Bi). Chem. Mater. **21**, 1683–1694 (2009)
67. Androulakis, J., Lin, C.-H., Kong, H.-J., Uher, C., Wu, C.-I., Hogan, T., Cook, B.A., Caillat, T., Paraskevopoulos, K.M., Kanatzidis, M.G.: Spinodal decomposition and nucleation and growth as a means to bulk nanostructured thermoelectrics, enhanced performance in $Pb_{1-x}Sn_xTe$-PbS. J. Am. Chem. Soc. **129**, 9780–9788 (2007)
68. Girard, S.N., He, J., Li, C., Moses, S., Wang, G., Uher, C., Dravid, V.P., Kanatzidis, M.G.: In situ nanostructure generation and evolution within a bulk thermoelectric material to reduce lattice thermal conductivity. Nano Lett. **10**, 2825–2830 (2010)
69. Girard, S.N., He, J.Q., Zhou, X., Shoemaker, D., Jaworski, C., Uher, C., Dravid, V.P., Heremans, J.P., Kanatzidis, M.G.: High performance Na-doped PbTe_PbS thermoelectric materials: electronic density of states modification and shape-controlled nanostructures. J. Am. Chem. Soc. **133**, 16588–16597 (2011)
70. Biswas, K., He, J., Blum, I.D., Wu, C.-I., Hogan, T.P., Seidman, D.N., Dravid, V.P., Kanatzidis, M.G.: High-performance bulk thermoelectrics with all-scale hierarchical architectures. Nature **489**, 414–418 (2012)
71. Van Nong, N., Pryds, N., Linderoth, S., Ohtaki, M.: Enhancement of the thermoelectric performance of p-type layered oxide $Ca_3Co_4O_{9+\delta}$ through heavy doping and metallic nanoinclusions. Adv. Mater. **23**, 2484–2490 (2011)
72. Jood, P., Mehta, R.J., Zhang, Y., Peleckis, G., Wang, X., Siegel, R.W., Borca-Tasciuc, T., Dou, S.X., Ramanath, G.: Al-doped zinc oxide nanocomposites with enhanced thermoelectric properties. Nano Lett. **11**, 4337–4342 (2011)
73. He, J.Q., Sootsman, J.R., Girard, S.N., Zheng, J.C., Wen, J.G., Zhu, Y., Kanatzidis, M.G., Dravid, V.P.: On the origin of increased phonon scattering in nanostructured PbTe based thermoelectric materials. J. Am. Chem. Soc. **132**, 8669–8675 (2010)
74. He, J.Q., Gueguen, A., Sootsman, J., Zheng, J.C., Wu, L., Zhu, Y., Kanatzidis, M.G., Dravid, V.P.: Role of self-organization, nanostructuring, and lattice strain on phonon transport in $NaPb_{18-x}Sn_xBiTe_{20}$ thermoelectric materials. J. Am. Chem. Soc. **131**, 17828–17835 (2009)
75. Pei, Y., Heinz, N.A., LaLonde, A.D., Jeffrey Snyder, G.: Combination of large nanostructures and complex band structure for high performance thermoelectric lead telluride. Energy Environ. Sci. **4**, 3640–3645 (2011)
76. Rowe, D.M., Shukla, V.S., Savvides, N.: Phonon scattering at grain boundaries in heavily doped fine-grained silicon–germanium alloys. Nature **290**, 765–766 (1981)
77. Lan, Y.C., et al.: Structure study of bulk nanograined thermoelectric bismuth antimony telluride. Nano Lett. **9**, 1419–1422 (2009)
78. Biswas, K., He, J., Zhang, Q., Wang, G., Uher, C., Dravid, V.P., Kanatzidis, M.G.: Strained endotaxial nanostructures with high thermoelectric figure of merit. Nat. Chem. **3**, 160–166 (2011)
79. Hicks, L.D., Dresselhaus, M.S.: Effect of quantum-well structures on the thermoelectric figure of merit. Phys. Rev. B **47**, 12727–12731 (1993)
80. Wang, X.W., Lee, H., Lan, Y.C., Zhu, G.H., Joshi, G., Wang, D.Z., Yang, J., Muto, A.J., Tang, M.Y., Klatsky, J., Song, S., Dresselhaus, M.S., Chen, G., Ren, Z.F.: Enhanced

thermoelectric figure of merit in nanostructured n-type silicon germanium bulk alloy. Appl. Phys. Lett. **93**, 193121 (2008)

81. Harman, T.C., Spears, D.L., Manfra, M.J.: High thermoelectric figures of merit in PbTe quantum wells. J. Electron. Mater. **25**, 1121–1127 (1996)
82. Liao, C.N., She, T.H.: Preparation of bismuth telluride thin films through interfacial reaction. Thin Solid Films **515**, 8059–8064 (2007)
83. Miller, J.F., Himes, R.C.: Properties of PbSe prepared by powder-metallurgy techniques. J. Electrochem. Soc. **107**, 915–919 (1960)
84. Christakudis, G.C., Plachkova, S.K., Shelimova, L.E., Avilov, E.S.: Thermoelectric figure of merit of some compositions in the system $(GeTe)_{1-x}[(Ag_2Te)_{1-y}(Sb_2Te_3)_y]_x$. Phys. Status Solidi A **128**, 465 (1991)
85. Poudeu, P.F.P., D'Angelo, J., Downey, A.D., Short, J.L., Hogan, T.P., Kanatzidis, M.G.: High thermoelectric figure of merit and nanostructuring in bulk p-type $Na_{1-x}Pb_mSb_yTe_{m+2}$. Angew. Chem. Int. Ed. **45**, 3835–3839 (2006)
86. Biswas, K., He, J., Wang, G., Lo, S.-H., Uher, C., Dravid, V.P., Kanatzidis, M.G.: High thermoelectric figure of merit in nanostructured p-type PbTe–MTe (M = Ca, Ba). Energy Environ. Sci. **4**, 4675–4684 (2011)
87. Ahn, K., Han, M.K., He, J., Androulakis, J., Balikaya, S., Uher, C., Dravid, V.K., Kanatzidis, M.G.: Exploring resonance levels and nanostructuring in the PbTe − CdTe system and enhancement of the thermoelectric figure of merit. J. Am. Chem. Soc. **132**, 5227 (2010)
88. Ikeda, T., Ravi, V.A., Snyder, G.J.: Formation of Sb_2Te_3 Widmanstätten precipitates in thermoelectric PbTe. Acta Mater. **57**, 666 (2009)
89. Ikeda, T., Collins, L., Ravi, V.A., Gascoin, F., Haile, S.M., Snyder, G.J.: Self-assembled nanometer lamellae of thermoelectric PbTe and Sb2Te3 with epitaxy-like interfaces. Chem. Mater. **19**(4), 763–767 (2007)
90. Song, S., Jipeng, F., Li, X., Gao, W., Zhang, H.: Facile synthesis and thermoelectric properties of self-assembled Bi_2Te_3 one-dimensional nanorod bundles. Chem. Eur. J. **19**, 2889–2894 (2013)
91. Jipeng, F., Song, S., Zhang, X., Cao, F., Zhou, L., Li, X., Zhang, H.: Bi_2Te_3 nanoplates and nanoflowers: synthesized by hydrothermal process and their enhanced thermoelectric properties. CrystEngComm **14**, 2159–2165 (2012)
92. Dong, G.-H., Zhu, Y.-J.: Room-temperature solution synthesis of Ag_2Te hollow microspheres and dendritic nanostructures, and morphology dependent thermoelectric properties. CrystEngComm **14**(1805) (2012)
93. Li, D.Y., Wu, Y.Y., Fan, R., Yang, P.D., Majumdar, A.: Thermal conductivity of Si/SiGe superlattice nanowires. Appl. Phys. Lett. **83**, 3186 (2003)
94. Lin, Y.M., Dresselhaus, M.S.: Thermoelectric properties of superlattice nanowires. Phys. Rev. B **68**, 075304 (2003)
95. Wu, Y., Yan, H., Huang, M., Messer, B., Song, J.H., Yang, P.: Inorganic semiconductor nanowires: rational growth, assembly, and novel properties. Chem. Eur. J. **8**, 1261–1268 (2002)
96. Ohtakil, M., Hayashi, R.: Enhanced thermoelectric performance of nanostructured zno: a possibility of selective phonon scattering and carrier energy filtering by nanovoid structure. Paper presented at 25th international conference on thermoelectrics, Vienna, Austria, 6–10 Aug 2006
97. Ohtaki, M., Maehara, S. Shige, S.: Thermoelectric properties of Al-doped ZnO sintered with nanosized void forming agents. In: Twenty-second international conference on thermoelectrics, proceedings Ict '03, pp 171–174 (2003)
98. Kim, K.H., Shim, S.H., Shim, K.B., Niihara, K., Hojo, J.: Microstructural and thermoelectric characteristics of zinc oxide-based thermoelectric materials fabricated using a spark plasma sintering process. J. Am. Ceram. Soc. **88**, 628–632 (2005)

99. Özgür, Ü., Alivov, Y.I., Liu, C., Teke, A., Reshchikov, M.A., Doğan, S., Avrutin, V., Cho, S.-J., Morkoç, H.: A comprehensive review of ZnO materials and devices. J. Appl. Phys. **98**, 041301 (2005)
100. Tsubota, T., Ohtaki, M., Eguchi, K., Arai, H.: Thermoelectric properties of Al-doped ZnO as a promising oxide material for high-temperature thermoelectric conversion copy. J. Mater. Chem. **7**, 85–90 (1997)
101. Cai, K.F., Müller, E., Drašar, C., Mrotzek, A.: Preparation and thermoelectric properties of Al-doped ZnO ceramics. Mater. Sci. Eng. B **104**, 45–48 (2003)
102. Ohtaki, M., Araki, K., Yamamoto, K.: High thermoelectric performance of dually doped ZnO ceramics. J. Electron. Mater. **38**, 1234–1238 (2009)
103. Shirouzu, K., Ohkusa, T., Hotta, M., Enomoto, N., Hojo, J.: Distribution and solubility limit of Al in Al_2O_3-doped ZnO sintered body. J. Ceram. Soc. Jpn. **115**, 254–258 (2007)
104. Zou, J., Balandin, A.: Phonon heat conduction in a semiconductor nanowire. J. Appl. Phys. **89**, 2932–2938 (2001)
105. Kulkarni, A.J., Zhou, M.: Size-dependent thermal conductivity of zinc oxide nanobelts. Appl. Phys. Lett. **88**, 141921 (2006)
106. Rajalakshmi, M., Arora, A.K., Bendre, B.S., Mahamuni, S.: Optical phonon confinement in zinc oxide nanoparticles. J. Appl. Phys. **87**, 2445–2448 (2000)
107. Fonoberov, V.A., Balandin, A.A.: Interface and confined polar optical phonons in spherical ZnO quantum dots with wurtzite crystal structure. Phys. Status Solidi C **1**, 2650–2653 (2004)
108. Fonoberov, V.A., Balandin, A.A.: Interface and confined optical phonons in wurtzite nanocrystals. Phys. Rev. B **70**, 233205 (2004)
109. Itahara, H., Seo, W.S., Lee, S., Nozaki, H., Tani, T., Koumoto, K.: The formation mechanism of a textured ceramic of thermoelectric [Ca2CoO3]0.62[CoO2] on β-Co(OH)2 templates through in situ topotactic conversion. J. Am. Chem. Soc. **127**, 6367–6373 (2005)
110. Koumoto, K., Wang, Y.F., Zhang, R.Z., Kosuga, A., Funahashi, R.: Oxide thermoelectric materials—a nanostructuring approach. Annu. Rev. Mater. Res. **40**, 363–396 (2010)
111. Muta, H., Kurosaki, K., Yamanaka, S.: Thermoelectric properties of rare earth doped $SrTiO_3$. J. Alloys Compd. **350**, 292–295 (2003)
112. U.S. Department of Energy: Critical materials strategy. http://energy.gov/sites/prod/files/DOE_CMS2011_FINAL_Full.pdf(2011). Accessed 23 Dec 2011
113. Ohtaki, M., Ogura, D., Eguchi, K., Arai, H.: High-temperature thermoelectric properties of In_2O_3-based mixed oxides and their applicability to thermoelectric power generation. J. Mater. Chem. **4**, 653–656 (1994)
114. Ohtaki, M., Koga, H., Tokunaga, T., Eguchi, K., Arai, H.: Electrical transport properties and high-temperature thermoelectric performance of $(Ca_{0.9}M_{0.1})MnO_3$ (M = Y, La, Ce, Sm, In, Sn, Sb, Pb, Bi). J. Solid State Chem. **120**, 105–111 (1995)
115. Li, S., Funahashi, R., Matsubara, I., Ueno, K., Yamada, H.: High temperature thermoelectric properties of oxide $Ca_9Co_{12}O_{28}$. J. Mater. Chem. **9**, 1659–1660 (1999)
116. Masuda, Y., Nagahama, D., Itahara, H., Tani, T., Seo, W.S., Koumoto, K.: Thermoelectric performance of Bi- and Na-substituted $Ca_3Co_4O_9$ improved through ceramic texturing. J. Mater. Chem. **13**, 1094–1099 (2003)
117. Zhang, Y.F., Zhang, J.X., Liu, Q.M.: Rapid synthesis of $Ca_2Co_2O_5$ textured ceramics by coprecipitation method and spark plasma sintering. J. Alloys Compd. **399**, 64–68 (2005)
118. Wang, Y., Sui, Y., Cheng, J., Wang, X., Su, W.: Comparison of the high temperature thermoelectric properties for Ag-doped and Ag-added $Ca_3Co_4O_9$. J. Alloys Compd. **477**, 817–821 (2009)
119. Zhao, Y., et al.: Thermal conductivity of self-assembled nano-structured ZnO bulk ceramics. J. Appl. Phys. **112**, 034313 (2012)
120. Lee, K.H., Kim, S.W., Ohta, H., Koumoto, K.: Ruddlesden-Popper phases as thermoelectric oxides—Nb-doped $SrO(SrTiO_3)_n$ (n = 1,2). J. Appl. Phys. **100**, 063717 (2006)
121. Wang, Y., Lee, K., Ohta, H., Koumoto, K.: 103-Thermoelectric properties of electron doped $SrO(SrTiO_3)_n$ (n = 1,2) ceramics. J. Appl. Phys. **105**, 103701 (2009)

122. Chung, D.Y., et al.: A new thermoelectric material: $CsBi_4Te_6$. J. Am. Chem. Soc. **126**, 6414–6428 (2004)
123. Kurosaki, K., Kosuga, A., Muta, H., Uno, M., Yamanaka, S.: Ag_9TlTe_5-a high-performance thermoelectric bulk material with extremely low thermal conductivity. Appl. Phys. Lett. **87**, 061919 (2005)
124. Shi, X., Yang, J., Salvador, J.R., Chi, M., Cho, J.Y., Wang, H., Bai, S., Yang, J., Zhang, W., Chen, L.D.: Multiple-filled skutterudites high thermoelectric figure of merit through separately optimizing electrical and thermal transports. J. Am. Chem. Soc. **133**, 7837–7846 (2011)
125. Zhao, W.Y., Wei, P., Zhang, Q.J., Dong, C.L., Liu, L.S., Tang, X.F.: Enhanced thermoelectric performance in barium and indium double-filled skutterudite bulk materials via orbital hybridization inducted by indium filler. J. Am. Chem. Soc. **131**, 3713–3720 (2009)
126. Brown, S.R., Kauzlarich, S.M., Gascoin, F., Snyder, G.J.: $Yb_{14}MnSb_{11}$-new high efficiency thermoelectric material for power generation. Chem. Mater. **18**, 1873–1877 (2006)
127. Caillat, T., Fleurial, J.-P., Borshchevsky, A.: Preparation and thermoelectric properties of semiconducting Zn_4Sb_3. J. Phys. Chem. Solids **58**, 1119–1125 (1997)
128. Saramat, A., Svensson, G., Palmqvist, A.E.C., Stiewe, C., Mueller, E., Platzek, D., Williams, S.G.K., Rowe, D.M., Bryan, J.D., Stucky, G.D.: Large thermoelectric figure of merit at high temperature in Czochralski-grown clathrate $Ba_8Ga_{16}Ge_{30}$. J. Appl. Phys. **99**, 023708 (2006)
129. Sakurada, S., Shutoh, N.: Effect of Ti substitution on the thermoelectric properties of (Zr, Hf) NiSn half-Heusler compounds. Appl. Phys. Lett. **86**, 082105 (2005)
130. Liu, H.L., Shi, X., Xu, F.F., Zhang, L.L., Zhang, W.Q., Chen, L.D., Li, Q., Uher, C., Day, T., Snyder, G.J.: Copper ion liquid-like thermoelectrics. Nat. Mater. **11**, 422 (2012)

Chapter 12
Thermoelectric Properties of Carbon Nanotubes and Related One-Dimensional Structures

H.J. Liu

Abstract Using nonequilibrium molecular dynamics simulations and nonequilibrium Green's function method, we investigate the thermoelectric properties of carbon nanotubes and related one-dimensional structures, which include ultrasmall and larger diameter carbon nanotubes, as well as graphene nanoribbons (GNRs) and carbon nanowires (CNWs). It is found that the transmission function of these one-dimensional carbon nanostructures display a clear stepwise structure that gives the number of electron channels. By optimizing the carrier concentration, characteristic size, and/or operating temperature, these systems could exhibit very high figure of merit. Moreover, their thermoelectric performance can be significantly enhanced via man approaches such as surface design, isotope substitution, isoelectronic impurities, and hydrogen adsorption. It is thus reasonable to expect that carbon nanotubes and related one-dimensional carbon nanostructures may be promising candidates for high-performance thermoelectric materials.

12.1 Introduction

Thermoelectric materials have attracted a lot of attention from the science community due to their interesting transport properties and potential applications in cooling and power generation. The efficiency of a thermoelectric material is given by the dimensionless figure of merit (*ZT* value)

$$ZT = S^2\sigma T/\left(\kappa_e + \kappa_p\right) \qquad (12.1)$$

In this formula, S is the Seebeck coefficient, σ is the electrical conductivity, T is the absolute temperature, κ_e and κ_p are the electron and phonon contributions to the

H.J. Liu (✉)
Key Laboratory of Artificial Micro- and Nano-structures of Ministry of Education and School of Physics and Technology, Wuhan University, Wuhan 430072, China
e-mail: phlhj@whu.edu.cn

X. Wang and Z.M. Wang (eds.), *Nanoscale Thermoelectrics*, Lecture Notes in Nanoscale Science and Technology 16, DOI 10.1007/978-3-319-02012-9_12,
© Springer International Publishing Switzerland 2014

thermal conductivity, respectively. Good thermoelectric materials behave as glass for phonons and crystal for electrons [1], and one therefore must try to maximize the power factor ($S^2\sigma$) and/or minimize the thermal conductivity ($\kappa = \kappa_e + \kappa_p$). As these transport coefficients (S, σ, and κ) are coupled with each other and related to the crystal structure and carrier concentration, it is very difficult to significantly improve the thermoelectric performance of conventional materials, which has a highest *ZT* value of about 1.0 [2, 3]. Since the pioneering works of Hicks and Dresselhaus [4, 5], much effort has been devoted to the studies of low-dimensional or nano-thermoelectric materials, which are believed to exhibit much higher *ZT* values on account of enhanced power factor caused by quantum confinement and energy filtering effects as well as reduced thermal conductivity due to enhanced phonon boundary scattering. However, the experimental realization of such systems remains a big challenging for the best thermoelectric materials which usually contains one or more elements of Bi, Sb, Te, Co, Ag, and Pb. Moreover, these elements are either toxic or expensive. The environmental problems they cause and the high economic cost therefore restrict their practical applications.

As an interesting quasi-one-dimensional nanostructure with many unusual properties, carbon nanotubes (CNTs) have attracted a lot of attention from the science community since their discovery [6]. However, few people believe that CNTs could be promising thermoelectric materials. This is probably due to the fact that although CNTs can have much higher electrical conductivity, their thermal conductivity are also found to be very high [7–12]. As a result, the *ZT* values of CNTs predicated from previous works [11, 13] are rather small (~0.0047). Prasher et al. [14] found the so-called “CNT bed” structure could reduce the thermal conductivity of CNTs. However, the random network of the samples may weaken the electronic transport and the room temperature *ZT* value is estimated to be 0.2. Jiang et al. [15] investigated the thermoelectric properties of single-walled CNTs using a nonequilibrium Green’s function approach. They found that CNTs exhibit very favorable electronic transport properties but the maximum *ZT* value is only 0.2 at 300 K. The possible reason is the neglect of nonlinear effect [16] in the phonon transport and the corresponding thermal conductivity was overestimated. If the thermal conductivity can be significantly reduced without much change to their electronic transport, CNTs may have very favorable thermoelectric properties. In this work, we use a combination of nonequilibrium Green’s function and nonequilibrium molecular dynamics simulations to study the thermoelectric properties of a series of CNTs with different diameters and chiralities. We will first focus on three kinds of ultrasmall single-wall carbon nanotubes, namely, the zigzag (5,0), the chiral (4,2), and the armchair (3,3). These nanotubes were fabricated by a templating method and have a diameter of about 0.4 nm [17], probably at or close to the theoretical limit. We will then deal with carbon nanotubes having relatively larger diameter. They are the zigzag (7,0), (8,0), (10,0), (11,0), (13,0), (14,0), and the chiral (4,2), (5,1), (6,2), (6,4), (8,4), (10,5), and all are semiconducting in their pristine form. To be complete, our theoretical calculations are extended to the related one-dimensional carbon nanostructures, which include graphene nanoribbons (GNRs) and carbon nanowires (CNWs). By cooperatively manipulate the electronic and phonon transports, we shall

see these carbon nanostructures could be optimized to exhibit much higher ZT value. Moreover, their thermoelectric performance can be significantly enhanced via man means such as surface design, isotope substitution, isoelectronic impurities, and hydrogen adsorption. Our theoretical investigations suggest that carbon nanotubes and related one-dimensional structures could be very promising candidates for future thermoelectric applications.

12.2 Computational Details

The electronic transport has been studied using the nonequilibrium Green's function (NEGF) method as implemented in the Atomistix ToolKit (ATK) software package [18, 19]. As usual in the NEGF model, the carbon nanotube (and related one-dimensional structures) is divided into a central part connected by the left and right semi-infinite ones. We focus on the ballistic transport and the weak electron–phonon scattering is ignored. During the self-consistent calculations, we use the Troullier–Martins non-local pseudopotentials [20] to describe the electron–ion interactions. The exchange-correlation energy is in the form of PW91 [21] and the Brillouin zone is sampled with $1 \times 1 \times 100$ Monkhorst–Pack $\boldsymbol{k}$-mesh [22]. The mixing rate of electronic Hamiltonian is set to be 0.1, and the convergent criterion for the total energy is 4×10^{-5} eV. We use a double ζ basis set plus polarization for the carbon atoms and the cutoff energy is set as 150 Ry. On the other hand, the thermal transport is calculated using the reverse nonequilibrium molecular dynamics (NEMD) simulations implemented in the LAMMPS software package [23]. We adopt the Tersoff potential [24] and solve Newtonian equations of motion according to the Müller-Plathe algorithm [25] with a fixed time step of ~0.5 fs. To make sure that the system has reached steady state, a constant temperature simulation of seven million steps and a constant energy simulation of three million steps are carried out. The nanotubes (and related one-dimensional structures) are then divided into N equal segments with periodic boundary condition, and the segments at $N/4$ and $3N/4$ are defined as hot and cold regions, respectively. The kinetic energies are swapped between the coldest atom(s) in the hot region and the hottest one(s) in the cold region, then a temperature gradient responses and thermal flux maintains via atoms interactions in neighboring segments [26, 27]. Our calculated results are carefully tested with respect to the number of divisions and time steps.

12.3 Ultrasmall Carbon Nanotubes

We begin with the electronic transport of the ultrasmall carbon nanotubes having a diameter of about 0.4 nm. As mentioned before, we use a standard model where the central scattering region is connected by two semi-infinite electrodes which are also carbon nanotubes in the present study. To get reliable results, the length of the

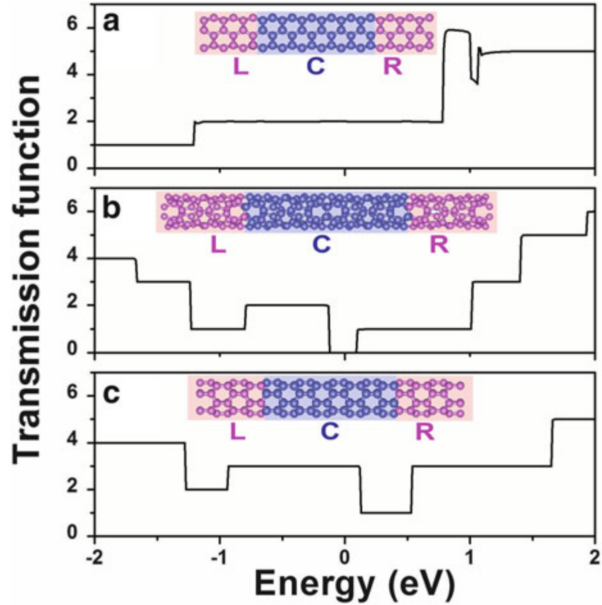

Fig. 12.1 (*Color online*) Transmission function of 0.4 nm carbon nanotubes: (**a**) armchair (3,3), (**b**) chiral (4,2), and (**c**) zigzag (5,0) under zero bias voltage. The *inset* are ball-and-stick models of these nanotubes which are divided into a central part connected by the *left* and *right* semi-infinite ones as usually done in the NEGF approach

central part is carefully tested which contain 10, 2, and 6 unit cells for the (3,3), (4,2), and (5,0) tubes, respectively. Figure 12.1 shows the calculated transmission function $T(E)$ of these nanotubes under zero bias voltage. We see that all of them display a clear stepwise structure that gives the number of electron channels. The quantized transmission indicates ballistic transport of electron in the carbon nanotubes as suggested by previous studies. It should be mentioned that the transmission function of (4,2) tube vanishes around the Fermi level, which is consistent with the fact that among the 0.4 nm nanotubes, the (4,2) tube is the only semiconductor with a band gap of ~0.2 eV [28].

Based on the calculated transmission function, the electronic transport coefficients can be readily obtained [29]. As the cross-sectional area is not well defined for quasi-one-dimensional systems such as CNTs, we will discuss the conductance (G, λ_e, or λ_p) [30] instead of the conductivity (σ, κ_e, or κ_p) mentioned before. The dimensionless figure of merit is therefore rewritten as

$$ZT = S^2 GT / \left(\lambda_e + \lambda_p\right) \tag{12.2}$$

Let

$$L_m(\mu) = \frac{2}{h} \int_{-\infty}^{\infty} dE\, T(E)(E-\mu)^m \left(-\frac{\partial f(E,\mu)}{\partial E}\right) \tag{12.3}$$

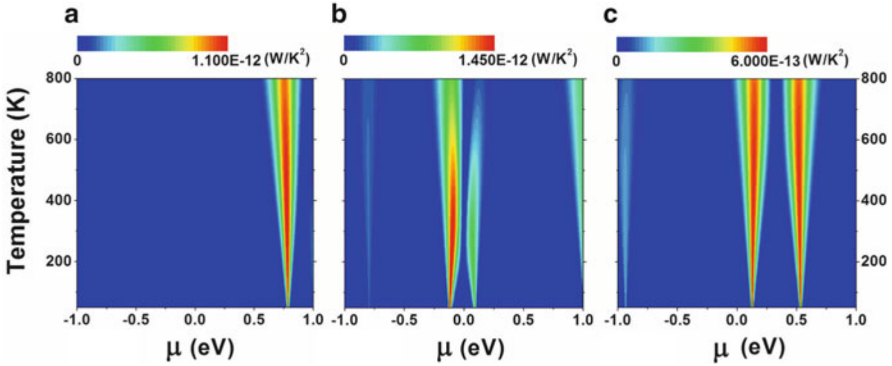

Fig. 12.2 (*Color online*) Calculated power factor S^2G of 0.4 nm carbon nanotubes: (**a**) (3,3), (**b**) (4,2), and (**c**) (5,0) as a function of chemical potential μ and temperature T

where $f(E,\mu)$ is the Fermi–Dirac distribution function, we can then respectively write the Seebeck coefficient, the electrical conductance, and the electronic thermal conductance as

$$S(\mu,T) = \frac{1}{eT}\frac{L_1(\mu)}{L_0(\mu)} \tag{12.4}$$

$$G(\mu,T) = e^2 L_0(\mu) \tag{12.5}$$

$$\lambda_e(\mu,T) = \frac{1}{T}\left\{L_2(\mu) - \frac{[L_1(\mu)]^2}{L_0(\mu)}\right\} \tag{12.6}$$

Figure 12.2 plots the redefined power factor (S^2G) as a function of chemical potential μ and temperature T for the (3,3), (4,2), and (5,0) tubes. As indicated in the color scale, the red and blue stand for large and small calculated values of S^2G, respectively. Note here the chemical potential determines the doping level of the system, and the positive and negative μ correspond to n-type and p-type doping, respectively. As can be seen from Fig. 12.2, the calculated power factor exhibit one or two highlight areas with obviously large values in a wide temperature range. This observation suggests that one can always enhance the thermoelectric performance of these nanotubes by appropriate n-type and/or p-type doping. If we focus on the room temperature, we find from Table 12.1 that the (4,2) and (3,3) tubes have relatively large value of S^2G compared with that of the (5,0) tube. However, the much higher electronic thermal conductance λ_e makes the pristine (3,3) tube less possible for the thermoelectric applications. The most favorable candidate should be (4,2) tube which has a very small λ_e but larger S^2G with chemical potential close to the Fermi level.

We now move to the discussion of phonon transport by using the NEMD simulation, which can handle anharmonicity and turns out to be an efficient approach

Table 12.1 Optimized ZT value at 300 K for the 0.4 nm carbon nanotubes (3,3), (4,2), and (5,0). The tube length is assumed to be 1 μm. The corresponding chemical potential μ, the power factor S^2G, the electronic thermal conductance λ_e, and the lattice thermal conductance λ_p and conductivity κ_p are also indicated

Tube	μ (eV)	S^2G (W/K^2)	λ_e (nW/K)	λ_p (nW/K)	κ_p (W/m·K)	ZT
(3,3)	0.78	1.11×10^{-12}	1.89	0.21	1,615	0.16
(4,2)	−0.09	1.39×10^{-12}	0.08	0.18	1,330	1.6
(5,0)	0.53	5.81×10^{-13}	0.96	0.30	2,073	0.14

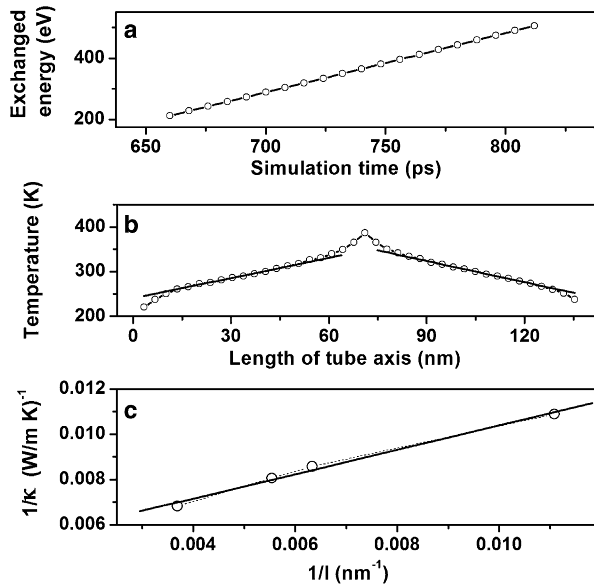

Fig. 12.3 (**a**) Typical time variation of the exchanged kinetic energy for the (4,2) tube; (**b**) Typical temperature profile for the (4,2) tube at an average temperature of 300 K; (**c**) The inverse thermal conductivity $1/\kappa_p$ as a function of inverse tube length $1/l$, where the *open circles* represent explicit MD results and the *solid line* indicates a linear fit

to calculate thermal conductivity as long as the temperature is not very low. In the present work, the nanotubes are divided into 40 equal segments, and the 1st (21th) one is set as cold (hot) region. One atom in each region exchange their kinetic energy every 80 time steps and others interact to reach a quasi-equilibrium state until the next exchange happens. Figure 12.3a shows the exchanged kinetic energy as a function of simulation time for the (4,2) tube at 300 K. The simulation cell is about 135 nm in length. We see that the exchanged energy increases linearly in the whole simulation time, which suggests a stable heat flux J from the hot to cold region. As shown in Fig. 12.3b, there is a linear temperature response along the tube axis except for the middle hot region and outer cold region. The temperature gradient ∇T is thus obtained by averaging the slope values of two linearly fitted lines shown in Fig. 12.3b. Inserting these values into the Fourier's law

$$\kappa_p = J/(A \cdot \nabla T) \tag{12.7}$$

the phonon-derived thermal conductivity κ_p can be calculated. Here A is the cross-sectional area which has certain arbitrariness for low-dimensional systems such as CNTs. A proper treatment is using the thermal conductance λ_p [30] which is related to the thermal conductivity by

$$\lambda_p = \kappa_p A/l \tag{12.8}$$

where l is the length of CNTs and in the order of micron size for most carbon nanotubes samples.

It is well known that the thermal conductivity κ_p of bulk materials is only determined by their composite and is size independent. This is however not the case for low-dimensional systems. Both experiment measurement [31] and MD simulations [32, 33] indicate that the thermal conductivity of CNTs are related to their length. As most thermal energy is transported by acoustic phonons which scatter at the boundary of the tubes and the phonon mean free path is limited by the size of the simulation cell, the thermal conductivity increases with increasing tube length within the ballistic transport regime. When the transport extends to the diffusive regime, the thermal conductivity diverges as $\kappa_p \sim l^{\beta}$, where the exponent β depends on the temperature and tube length l. In order to obtain a fully diffusive thermal conductivity of our systems, the κ_p with different tube lengths are calculated and extrapolated to obtain a good estimate at infinite length. A simple approach of effective phonon travel path l_{eff} is given by

$$1/l_{\text{eff}} = 1/l_{\infty} + 4/l \tag{12.9}$$

where l is the length of simulated CNTs, l_{∞} is the phonon mean free path for infinite system, and the factor 4 means that phonons will be at an average distance $l/4$ from either the cold region or the hot one where the last anharmonic scattering event occurred [27]. This formula suggests that a plot of $1/\kappa_p$ vs. $1/l$ should be linear, and that the thermal conductivity of CNTs at any length can thus be calculated. Figure 12.3c gives the results for the (4,2) tube, where the solid line is fitted from the $1/\kappa_p$ at a series of tube length. If the tube has a typical length of 1 μm, the thermal conductivity can be readily obtained by extrapolating to $1/l = 0.001\ \text{nm}^{-1}$.

It should be mentioned that in our MD simulation, the temperature is defined by the formula

$$\langle E \rangle = \sum_{i=1}^{N} \frac{1}{2} m v_i^2 = \frac{3}{2} N k_B T_{\text{MD}} \tag{12.10}$$

where $\langle E \rangle$ is the mean kinetic energy, N is the number of atoms in the simulation cell, m is the atomic mass, v_i is the velocity of atom i, and k_B is the Boltzmann constant. However, this formula is valid only when the temperature is higher than the Debye temperature Θ_D. If we are interested in the room or intermediate

temperature region which is lower than the Θ_D of CNTs (usually 500–1,000 K), a quantum correction to both the MD temperature and the thermal conductivity must be carried out. This is done by redefining the MD temperature as [34]:

$$3Nk_BT_{MD} = \int_0^{\omega_\Theta} D(\omega)n(\omega, T)\hbar\omega d\omega \tag{12.11}$$

where $D(\omega)$ is the phonon density of states obtained from density functional perturbation theory, $n(\omega,T)$ is the Bose–Einstein distribution, and ω_Θ is the Debye frequency. The quantum corrected thermal conductivity κ_p as well as the thermal conductance λ_p for the 0.4 nm nanotubes at 300 K are summarized in Table 12.1, where the tube length is assumed to be 1 μm. We find these three kinds of nanotubes have quite different thermal conductivity although they are nearly of the same diameter. It is generally accepted that the acoustic branches play a significant role in the thermal conductivity of carbon nanotubes [35]. As the calculated heat capacity and the phonon group velocity of those 0.4 nm nanotubes are more or less similar to each other, we believe that the large difference in the thermal conductivity (or thermal conductance) is mainly due to their different phonon mean free path.

Based on the calculated power factor S^2G, the electronic thermal conductance λ_e, and the phonon-induced thermal conductance λ_p, we are able to evaluate the figure of merit according to (12.2). Due to relatively larger S^2G and smaller λ_e and λ_p (see Table 12.1), we find that the (4,2) tube has the highest *ZT* value among the three kinds of 0.4 nm tubes, which is 1.6 (at length of 1 μm) at room temperature. This value is already larger than those reported previously for larger diameter carbon nanotubes or their composites [14, 15, 36]. We further find that, chemisorptions of hydrogen on the (4,2) tube could result in a significant reduction of both the λ_p and λ_e while maintaining good power factor S^2G. For the optimized product where two hydrogen atoms chemisorbed on top of the C–C bond that has the lowest angle with the tube axis (see Fig. 12.4a), we see from Table 12.2 that the calculated λ_p (λ_e) is only 0.067 nW/K (0.038 nW/K) compared with 0.18 nW/K (0.08 nW/K) of the pristine (4,2) tube. The maximum *ZT* value of the chemisorbed (4,2) tube is thus increased to 3.5, which is comparable to that of the best commercial materials.

In addition to the surface design mentioned above, we find that formation of carbon nanotube bundles could also give an improved *ZT* value. Here we consider two examples, namely, the doublet (3,3) and the triplet (5,0). In contrast to the weak tube–tube interactions found in bundle of large diameter nanotubes, the ultrasmall tubes within the doublet and triplet bundles are covalently connected [37] as shown in Fig. 12.4b, c. Our MD simulations indicate that such new forms of bundle are energetically favorable and kinetically stable around room temperature. Due to very strong tube–tube interactions, we see from Tables 12.1 and 12.2 that the electronic thermal conductance λ_e is lowered by 93 % for the doublet (3,3), and 85 % for the triplet (5,0). Moreover, there is an obvious increase of the corresponding power factor S^2G and a decrease of the phonon-derived thermal conductivity κ_p. As a result, the calculated *ZT* value increases significantly from 0.14 to 1.8 for the triplet (5,0), and from 0.16 to 2.7 for the doublet (3,3).

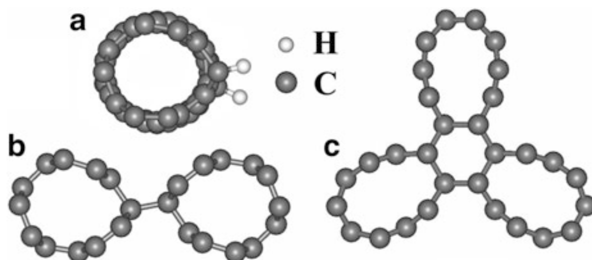

Fig. 12.4 Top-view of the fully relaxed structures for (**a**) the (4,2) tube chemisorbed with two hydrogen atoms, (**b**) the doublet bundle of (3,3) tube, and (**c**) the triplet bundle of (5,0) tube

Table 12.2 Optimized *ZT* value at 300 K for the chemisorbed (4,2) tube, the doublet bundle of (3,3) tube, and the triplet bundle of (5,0) tube. The tube length is assumed to be 1 μm. The corresponding chemical potential μ, the power factor S^2G, the electronic thermal conductance λ_e, and the lattice thermal conductance λ_p and conductivity κ_p are also indicated

Structure	μ (eV)	S^2G (W/K^2)	λ_e (nW/K)	λ_p (nW/K)	κ_p (W/m·K)	*ZT*
Tube (4,2) + H_2	0.81	1.24×10^{-12}	0.038	0.067	281	3.5
Doublet (3,3)	0.79	3.22×10^{-12}	0.13	0.23	885	2.7
Triplet (5,0)	0.24	2.49×10^{-12}	0.14	0.27	622	1.8

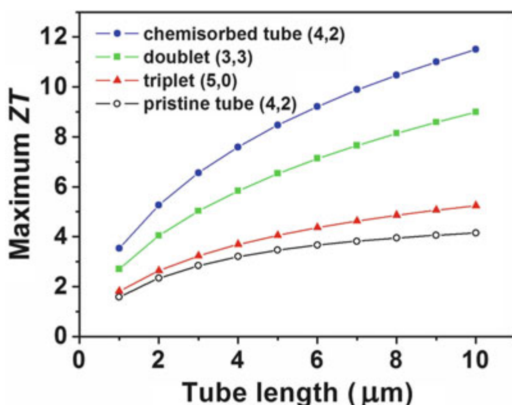

Fig. 12.5 (*Color online*) The optimized *ZT* value at 300 K as a function of tube length for the pristine (4,2) tube, the (4,2) tube with chemisorbed hydrogen, the triplet bundle of (5,0) tube, and the doublet bundle of (3,3) tube

It should be emphasized that we have assumed that the tube length is 1 μm in the above discussions. This is not necessarily the case for real system where the tube length varies from sample to sample. As the thermal conductance λ_p will decrease with increasing tube length, our calculated *ZT* values may further increase as obviously shown in Fig. 12.5. For example, the *ZT* value of pristine and hydrogen adsorbed (4,2) tube with length of 3 μm can be respectively enhanced to 2.8 and 6.6 at optimized chemical potential. Similar trends can be found for the carbon nanotube bundles, which has a *ZT* value of 4.1 for the triplet (5,0), and 6.5 for the doublet (3,3) when the bundle length is 5 μm. If the sample length is further increased to 10 μm, we see from Fig. 12.5 that the predicated *ZT* value can be as high as 11.5 for the (4,2) tube chemisorbed with hydrogen. The significantly enhanced *ZT* values suggest very favorable thermoelectric applications of these 0.4 nm carbon nanotubes.

12.4 Larger Diameter Carbon Nanotubes

We now consider carbon nanotubes with relatively larger diameter. As mentioned in Sect. 12.1, they are the zigzag series (7,0), (8,0), (10,0), (11,0), (13,0), (14,0), and the chiral series (4,2), (5,1), (6,2), (6,4), (8,4), (10,5). We first investigate the phonon transport of these CNTs by using the NEMD simulations, where the phonon-induced thermal conductivity κ_p is calculated according to (12.7). Table 12.3 summarizes the NEMD calculated room temperature thermal conductivity κ_p of a series of zigzag and chiral nanotubes. We see that κ_p of these carbon nanotubes are indeed very high which range from several hundreds to more than one thousand of W/m·K. If we focus on the zigzag series, we find that the thermal conductivity decreases as the tube diameter is increased. This is also the case for the chiral series with the same chiral angle (e.g., the (4,2), (8,4), and (10,5) tubes). The reason is that larger diameter CNTs have smaller average group velocity and the probability of the umklapp process is higher [38, 39]. On the other hand, if we focus on those CNTs with roughly similar diameters (e.g., (7,0) vs. (6,2), (11,0) vs. (8,4), (13,0) vs. (10,5)), it is interesting to find that the thermal conductivity of chiral tube is always lower than that of zigzag one. As these CNTs have similar average group velocity, we believe the more frequent phonon umklapp scattering in the chiral tubes makes a significant contribution to the reduced thermal conductivity.

We now move to the discussions of electronic transport by using the NEGF approach. Figure 12.6 shows the calculated electronic transmission function $T(E)$ for the above mentioned zigzag and chiral series. Within the rigid-band picture, $E > 0$ corresponds to the n-type doping while $E < 0$ corresponds to the p-type doping. Here we focus on the electron ballistic transport and ignore the weak electron–phonon scattering. We see that all the investigated CNTs exhibit quantized transmission which can be essentially derived from their energy band structures. The vanishing transmission function around the Fermi level is consistent with the fact that all of them are semiconducting. It is interesting to find those CNTs with larger diameter have symmetrically distributed transmission function near the

Table 12.3 Calculated phonon-derived thermal conductivity κ_p at 300 K for the zigzag (7,0), (8,0), (10,0), (11,0), (13,0), (14,0) tubes and chiral (4,2), (5,1), (6,2), (6,4), (8,4), (10,5) tubes. The corresponding tube diameter d and chiral angle θ are also given

Tubes		d (nm)	θ (°)	κ_p (W/m·K)
Zigzag series	(7,0)	0.548	0	1,270
	(8,0)	0.627	0	955
	(10,0)	0.783	0	809
	(11,0)	0.862	0	778
	(13,0)	1.019	0	613
	(14,0)	1.097	0	599
Chiral series	(4,2)	0.414	19.2	1,337
	(5,1)	0.436	8.9	1,413
	(6,2)	0.565	13.9	1,009
	(6,4)	0.683	23.4	829
	(8,4)	0.829	19.2	721
	(10,5)	1.036	19.2	564

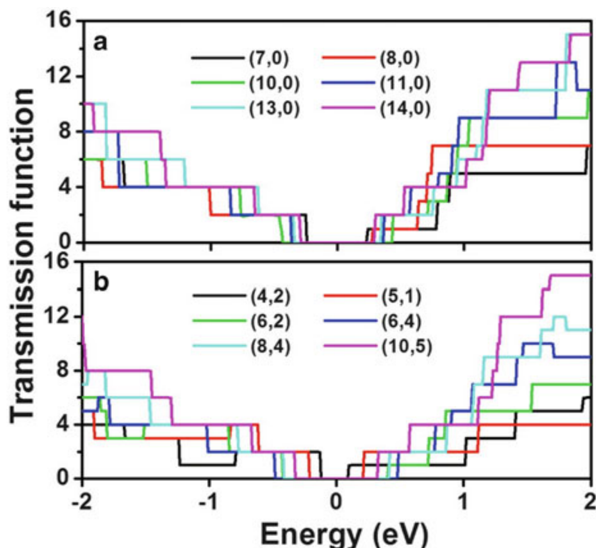

Fig. 12.6 (*Color online*) Calculated electron transmission function for a series of (**a**) zigzag tubes and (**b**) chiral tubes

Fermi level. However, this is not the case for the smaller diameter CNTs such as (7,0), (8,0), and (4,2), where we see the number of first conduction channel is 2 for the *p*-type doping and 1 for the *n*-type doping. By integrating [29] the calculated transmission function $T(E)$, one can easily obtain the Seebeck coefficient S, the electrical conductance G, and the electronic thermal conductance λ_e within the linear response limit. Here we choose the zigzag (10,0) and chiral (6,4) as two typical examples and plot in Fig. 12.7 the corresponding transport coefficients at 300 K as a function of chemical potential μ. Note the chemical potential indicates the doping level or carrier concentration of the system, and the *n*-type doping corresponds to $\mu > 0$ while *p*-type corresponds to $\mu < 0$. As can be seen from Fig. 12.7a, b, both the electrical conductance G and the electronic thermal conductance λ_e of these two CNTs vanish around the Fermi level ($\mu = 0$) since this area corresponds to the band gap of the systems. When the chemical potential moves to the edge of the first conduction channels, there is a sharp increase of the electrical conductance G and the electronic thermal conductance λ_e. For both the (10,0) and (6,4) tubes, the Seebeck coefficient S shown in Fig. 12.7c is rather symmetric about the Fermi level, which can be attributed to the symmetrically distributed first conduction channels (see Fig. 12.6). The absolute value of Seebeck coefficient reaches the maximum value at $\mu \approx \pm k_B T$ and then decreases until vanish near the edge of band gap.

Figure 12.7d shows the chemical potential dependent ZT value at 300 K for the (10,0) and (6,4) tubes. We see that both of them exhibit two peak values around the Fermi level, which suggest that by appropriate *p*-type and *n*-type doping, one can significantly enhanced the thermoelectric performance of CNTs. For the (10,0) tube, the maximum ZT value is found to be 0.9 and appears at $\mu = \pm 0.40$ eV. In the

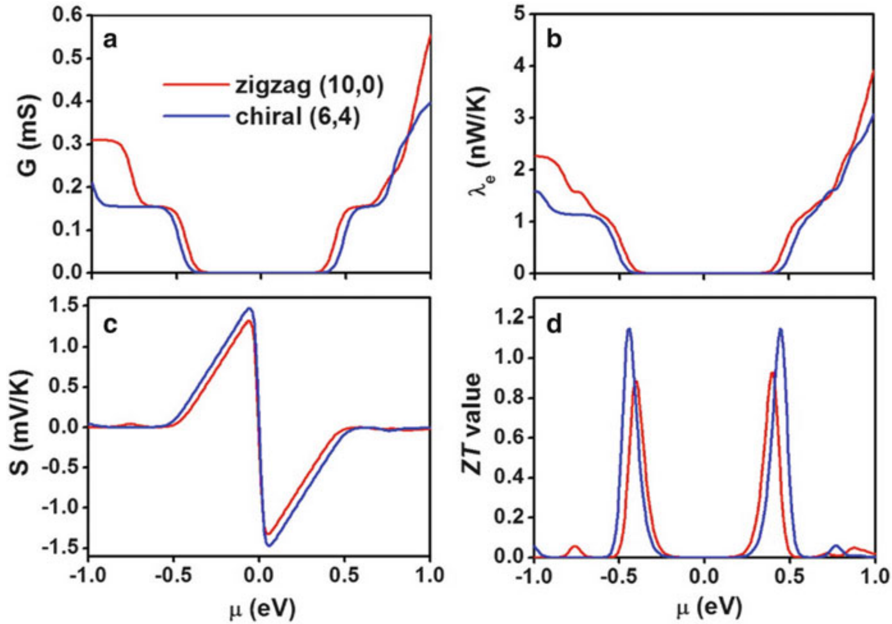

Fig. 12.7 (*Color online*) Calculated transport coefficients at 300 K as a function of chemical potential for the zigzag (10,0) and chiral (6,4): (**a**) electric conductance, (**b**) electronic thermal conductance, and (**c**) Seebeck coefficient. The corresponding *ZT* values are shown in (**d**)

case of (6,4) tube, the *ZT* value can be optimized to 1.1 at $\mu = \pm 0.44$ eV. The same doping level for the *p*-type and *n*-type doping in the (10,0) or (6,4) tubes is very beneficial for their applications in real thermoelectric devices.

Up to now we are dealing with room temperature and the corresponding *ZT* values are still not comparable to that of the best commercial materials. Moreover, a thermoelectric material may be needed to operate at different temperatures for different applications. We thus perform additional transport calculations where the temperature ranges from 250 K to 1,000 K. Figure 12.8 plots the calculated *ZT* values as a function of temperature for the above mentioned zigzag and chiral series. At each temperature, two *ZT* values are shown which correspond to the optimized *p*-type and *n*-type doping in each tube. Except for the small (4,2) tube with a maximum *ZT* value at 300 K, we see from Fig. 12.8 that the thermoelectric performance of other CNTs can be significantly enhanced at relatively higher temperature. The maximum *ZT* value that achieved is 3.5 for the zigzag (10,0) at 800 K, and 4.5 for the chiral (6,4) at 900 K. These values are very competitive with that of conventional refrigerators or generators. It is interesting to note that among the investigated CNTs, both the (10,0) and (6,4) tubes have an intermediate diameter (0.7–0.8 nm), and those with larger or smaller diameters have relatively less favorable thermoelectric performance. On the other hand, we see that almost all the zigzag tubes exhibit a peak *ZT* value at intermediate temperature (700–800 K).

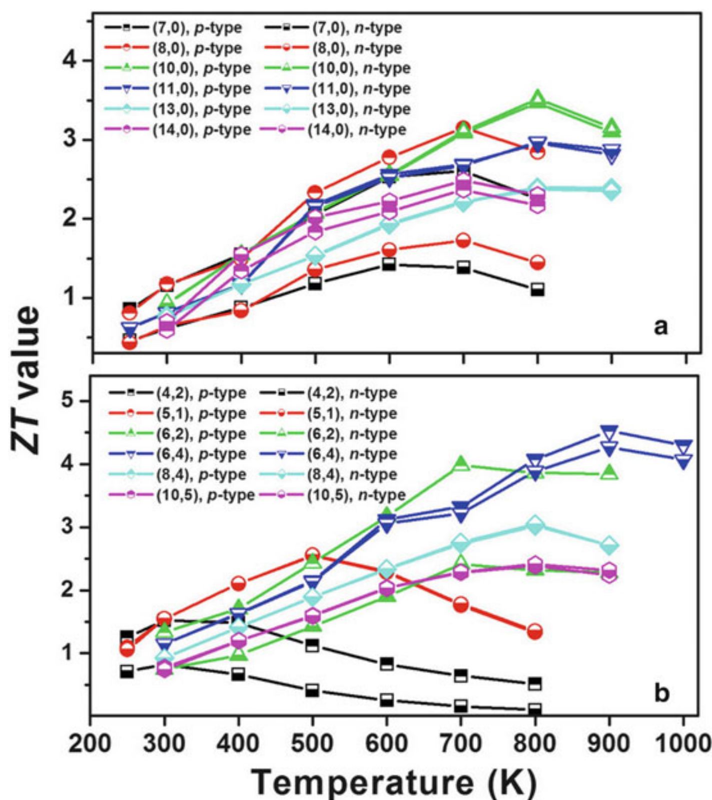

Fig. 12.8 (*Color online*) Optimized *ZT* values as a function of temperature for a series of (**a**) zigzag tubes and (**b**) chiral tubes. The results for the *p*-type and *n*-type doping are both shown

In contrast, the peak for chiral series moves roughly from 300 K to 900 K as the tube diameter is increased. Our calculated results thus provide a simple map by which one can efficiently find the best CNT for the thermoelectric applications at different operating temperatures.

To further improve the thermoelectric performance of these CNTs, we have considered isotope substitution which is believed to reduce the phonon-induced thermal conductance without changing the electronic transport properties [40–42]. Here we choose (10,0) as an example since it has the highest *ZT* value among those zigzag series, and the zigzag tubes are usually more easily to be fabricated in or selected from the experiments than the chiral ones. In our calculations, the ^{12}C atoms in the (10,0) tube are randomly substituted by ^{13}C atoms at different concentrations. The corresponding lattice thermal conductance as well as the *ZT* value at 800 K is shown in Fig. 12.9 with respect to the pristine values. Due to the mass difference between ^{12}C and ^{13}C, we see that the calculated thermal conductance of (10,0) tube decreases with increasing concentration of ^{13}C atoms.

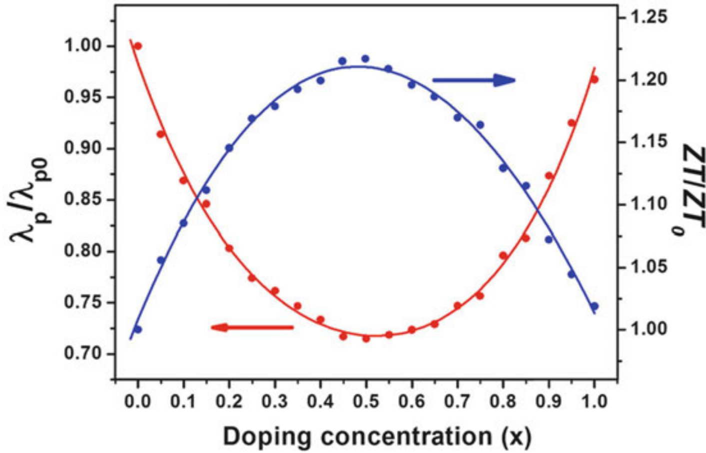

Fig. 12.9 (*Color online*) Calculated lattice thermal conductance (*red*) and optimized *ZT* value (*blue*) at 800 K for the (10,0) tube, where the ^{12}C atoms are substituted by ^{13}C atoms with different concentrations. Note that the results are given with respect to those of the pure ^{12}C tube

Of course, if half or more ^{12}C atoms are substituted, the situation is reversed. The thermal conductance can be well fitted by a double exponential function:

$$\lambda_p/\lambda_{p_0} = 0.36\,e^{-x/0.28} + 0.35\,e^{-(1-x)/0.24} + 0.62 \tag{12.12}$$

where x is the concentration of ^{13}C atoms. For a light isotope substitution ($^{12}C_{0.95}{}^{13}C_{0.05}$), the thermal conductance is already reduced by about 9 % and the *ZT* value can be increased to 3.7 from the pristine value of 3.5. If half ^{12}C atoms are replaced ($^{12}C_{0.5}{}^{13}C_{0.5}$), the corresponding thermal conductance reaches the minimum and the *ZT* value can be as high as 4.2, which suggest its appealing thermoelectric applications.

Introducing isoelectronic impurities is another effective way to localize phonon and reduce lattice thermal conductance due to impurity scattering [43]. Here we choose Si as an example and consider a very low concentration where one C atom in a (10,0) supercell containing three primitive cells is replaced by Si atom. The resulting product has a nominal formula of $C_{119}Si$ and is schematically shown in Fig. 12.10a. As the mass difference between C and Si is even larger, we find that the phonon-derived thermal conductance of $C_{119}Si$ is significantly reduced by 45–60 % compared with that of pristine (10,0) tube in the temperature range from 300 K to 900 K. On the other hand, since C and Si atoms have the same electron configuration, one may expect that Si doping will not change much to the electronic transport properties. Indeed, our calculations only find a small weakening of the power factor S^2G. As a result, we see from Fig. 12.10c there is an overall increase of the *ZT* value at temperature range from 300 K to 700 K. The Si-doped product has a maximum $ZT = 4.0$ at $T = 600$ K compared with the pristine value of 3.5 at $T = 800$ K. It is

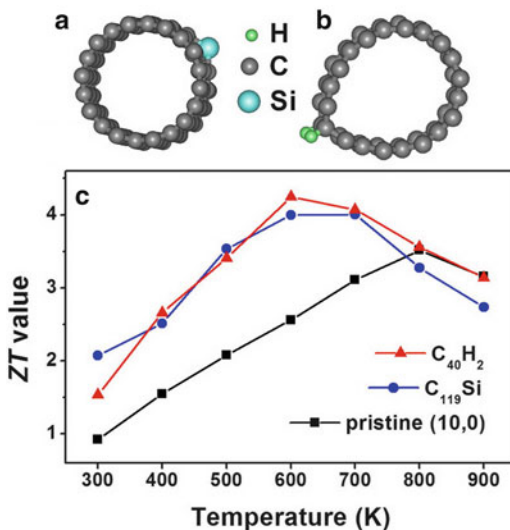

Fig. 12.10 (*Color online*) Top-view of the fully relaxed structures for (**a**) Si doped (10,0) tube with nominal formula of $C_{119}Si$, and (**b**) the (10,0) tube chemisorbed with hydrogen atoms having nominal formula of $C_{40}H_2$. (**c**) plots the optimized *ZT* value as a function of temperature for the $C_{119}Si$ and $C_{40}H_2$ products, and the results for the pristine (10,0) tube is also shown for comparison

worth to mention that in a wide temperature range (450–850 K), the *ZT* values of the Si-doped product are all higher than 3.0 which is very beneficial for their thermoelectric applications.

A similar improvement of the thermoelectric performance can be achieved by hydrogen adsorption on the (10,0) tube. As shown in Fig. 12.10b, two hydrogen atoms are chemisorbed on top of a C–C bond along the tube axis and the product has a concentration of $C_{40}H_2$. Our calculated results indicate that such hydrogen adsorption causes deformation of the (10,0) tube, and reduces both the phonon and electron induced thermal conductance while keep the power factor S^2G less affected. For example, the calculated λ_p at 600 K is 0.072 nW/K, which is much lower than that found for the pristine (10,0) tube (0.21 nW/K). The calculated λ_e also decreases from 0.089 nW/K to 0.062 nW/K. At the same time, we find that the power factor S^2G of chemisorbed product (9.47×10^{-13} W/K^2) is slightly lower than that of the pristine (10,0) tube (1.28×10^{-12} W/K^2). As a result, the calculated *ZT* value at 600 K increases significantly from 2.6 to 4.2 which is even higher than the highest value of pristine (10,0). The chemisorptions of hydrogen also increases the *ZT* value at other temperatures, as indicated in Fig. 12.10c. It is interesting to note that the temperature dependent behavior almost coincide with that from Si doping, especially in the temperature region from 400 K to 700 K.

12.5 Graphene Nanoribbons

The GNRs can be visualized as unfolding carbon nanotubes and are usually classified into armchair graphene nanoribbons (AGNRs) and zigzag graphene nanoribbons (ZGNRs) according to their edge shape. Following the conventional

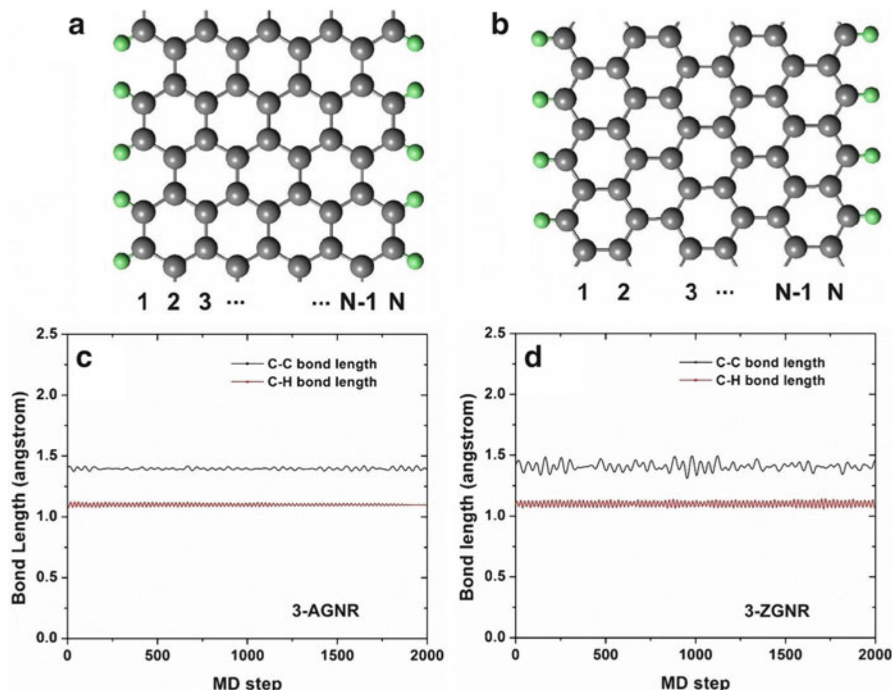

Fig. 12.11 (*Color online*) Ball-and-stick model of (**a**) *N*-AGNRs and (**b**) *N*-ZGNRs, where the *black ball* stands for carbon atom and the *green* for hydrogen atom. The first-principles molecular dynamics results of the C–C and C–H distance at the edges are plotted in (**c**) and (**d**) for the 3-AGNR and 3-ZGNR, respectively

notation [44, 45], the AGNRs (ZGNRs) can be identified by the number of dimer lines (zigzag chains) across the ribbon width and are labeled as *N*-AGNRs (*N*-ZGNRs). Figure 12.11a, b is a ball-and-stick model of *N*-AGNRs and *N*-ZGNRs, respectively. Note all the carbon atoms at the edges are passivated by hydrogen atoms. Here we consider a series of narrow GNRs with $N = 3$, 4, 5, and 6 for both the AGNRs and ZGNRs, where the width varies from 4 to 14 Å. As the widths of these GNRs are quite small, it is nature to ask whether they are stable as standalone entities. We thus perform first-principles molecular dynamics (MD) for the narrowest 3-AGNR and 3-ZGNR. The MD starts at 300 K and runs for 2,000 steps with a time step of 0.5 fs. Figure 12.11c, d plot the corresponding C–C and C–H distance at the edges in the whole MD running time. We see there are only slight fluctuations around the C–C bond length of 1.40 Å and C–H bond length of 1.10 Å, which indicates that the narrow AGNRs and ZGNRs considered in our work are rather stable. It should be mentioned that the stability of hydrogen-passivated products have also been confirmed previously [44] and can be comparable to that of a graphene sheet.

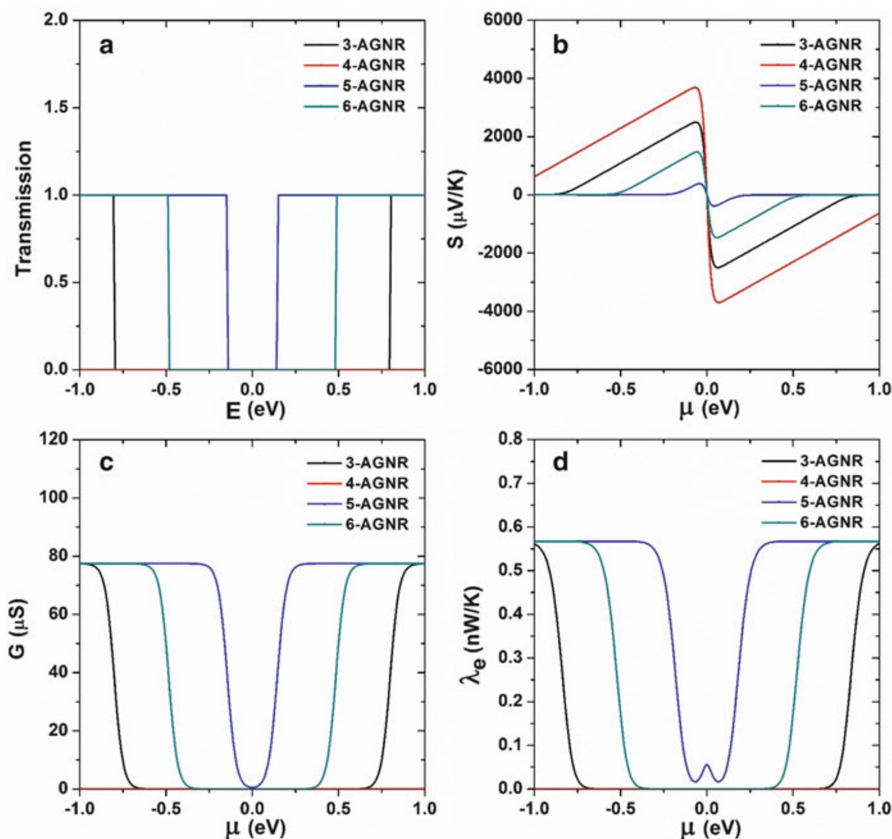

Fig. 12.12 (*Color online*) Calculated transport coefficients for the AGNRs series as a function of chemical potential: (**a**) transmission function, (**b**) Seebeck coefficient, (**c**) electrical conductance, and (**d**) electronic thermal conductance

We have calculated the energy band structures of these GNRs and all of them are found semiconducting with direct band gaps. In the case of AGNRs, we find that the variations of gap as a function of ribbon width exhibit three distinct family behaviors [44, 46, 47], which is the largest for $N = 3n + 1$, the smallest for $N = 3n + 2$, with $N = 3n$ in between (Here n is a positive integer). For the ZGNRs, however, such oscillation of band gap disappears and the spins of two edges are antiferromagnetically ordered, which agree well with previous studies [44]. To investigate the electronic transport properties, we firstly calculate the transmission function $T(E)$ of these GNRs using the NEGF approach. As shown in Fig. 12.12a, the transmissions of all the AGNRs display clear stepwise structures that are symmetrical about the Fermi level ($E = 0$). The number of the first conduction channel is 1 for both the n-type ($E > 0$) and p-type doping ($E < 0$), which can be essentially obtained by counting the number of energy bands at a certain energy. The transmission function vanishes around the Fermi level, which is consistent with

the fact that all the investigated AGNRs are semiconducting with family behavior of their band gaps. By integrating the calculated transmission function $T(E)$, the Seebeck coefficient S, the electrical conductance G, and the electronic thermal conductance λ_e can be readily obtained [15, 29, 48]. Figure 12.12b–d plot these transport coefficients at 300 K as a function of chemical potential μ. Within the rigid-band picture [49], the chemical potential indicates the doping level (or carrier concentration) of the system. For n-type doping the chemical potential is positive, while it is negative for p-type doping. We see that close to the Fermi level ($\mu = 0$), the Seebeck coefficients of these AGNRs exhibit much larger absolute values, which increase with increasing band gap. For the 4-AGNR having the largest gap, the Seebeck coefficient can be as high as 3,690 μV/K. Such large value indicates that GNRs may have very favorable thermoelectric properties. On the other hand, the calculated electrical conductance and electronic thermal conductance are very small around the Fermi level. At the edge of the first conduction channel, there is a sharp increase of both of them. These observations suggest that by choosing a proper chemical potential, one may find a trade-off between S, G, and λ_e of AGNRs thus significantly enhance their thermoelectric performance. We will come back to this point later.

Figure 12.13 shows the calculated electronic transport coefficients of the ZGNRs series. Unlike that found in the AGNRs, we see from Fig. 12.13a that the transmission spectrum is no longer symmetrical about the Fermi level. Moreover, the difference between each ZGNR is rather small, especially for the n-type doping. This is reasonable since all the investigated ZGNRs have very similar energy band structures. The Seebeck coefficient shown in Fig. 12.13b also coincides with each other and the maximum value is found to be 554 μV/K. This value is much smaller than that of the AGNRs series and suggests that ZGNRs may be less favorable for the thermoelectric applications. Close to the Fermi level, we see from Fig. 12.13c, d that the electrical conductance and the electronic thermal conductance are very small as observed in the AGNR series. However, there is a peak both below and above the Fermi level which is consistent with the abrupt change of their transmission function around the first conduction channel.

To investigate the thermal transport of GNRs, we have calculated the phonon-derived thermal conductance (λ_p) using the NEMD method. We choose the molecular dynamics simulation since it is much faster than other approaches and can handle nonlinearity when dealing with heat transport. Indeed, it has previously been shown [27] that NEMD is an efficient approach to calculate thermal conductance which includes both ballistic and diffusive transport for a wide temperature range. Our calculated results at 300 K are shown in Fig. 12.14a. Note the thermal conductance of low-dimensional systems such as GNRs are related to their length and is assumed to be 1 μm in the present calculations [50]. We see that the thermal conductance of both AGNRs and ZGNRs increase with the ribbon width. This is reasonable since increasing N of GNRs can increase the number of phonon modes [51]. Moreover, the calculated thermal conductance of AGNRs are nearly one order of magnitude smaller than that of ZGNRs. Similar results [52, 53] were found using a NEGF approach for phonon transport. Such strong anisotropy of thermal conductance is mainly

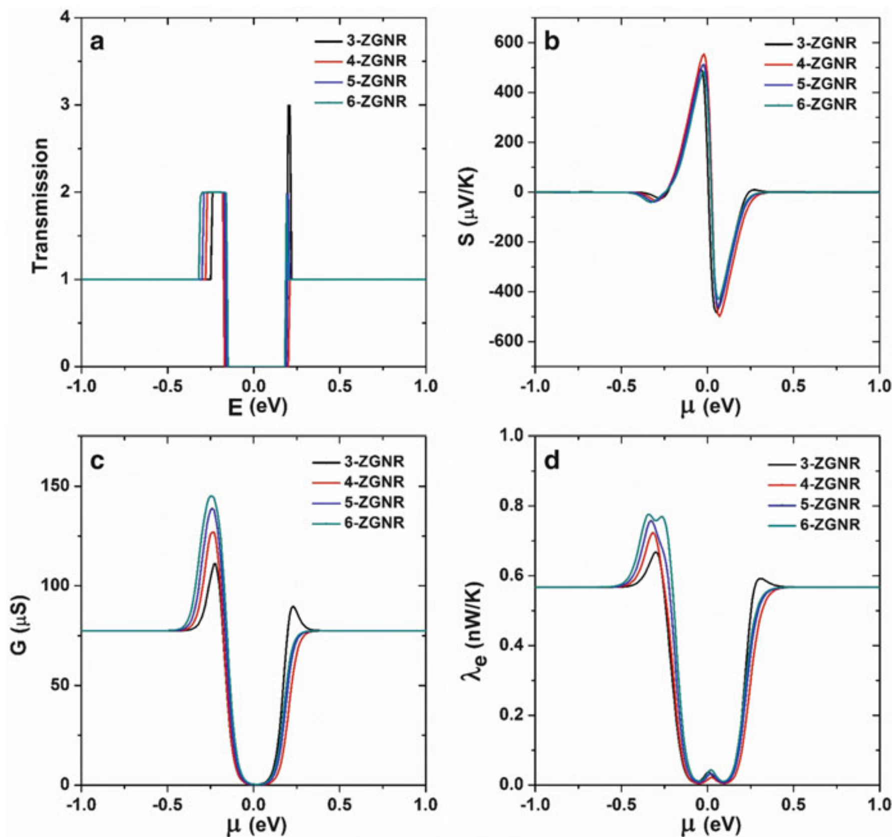

Fig. 12.13 (*Color online*) Calculated transport coefficients for the ZGNRs series as a function of chemical potential: (**a**) transmission function, (**b**) Seebeck coefficients, (**c**) electrical conductance, and (**d**) electronic thermal conductance

caused by different phonon scattering rates at the zigzag and armchair edges [54], and that low-frequency phonon bands of ZGNRs are more dispersive than those of the AGNRs [53]. All these observations suggest that narrow AGNRs could have very favorable thermoelectric properties. On the other hand, we find that in the AGNRs the phonon contribution to the thermal conductance is comparable to that from electron (see Table 12.4). This is however not the case for the ZGNRs where the phonon part plays a major role. It is therefore reasonable to expect that by reducing the phonon-induced thermal conductance, one could efficiently enhance the thermoelectric performance of ZGNRs.

With all the transport coefficients calculated, we are now able to evaluate the figure of merit. Figure 12.14b plots the room temperature *ZT* value as a function of chemical potential for the above-mentioned AGNRs series. We see the overall topology is rather symmetric and each of them exhibit two identical peaks around the Fermi level. This indicates that by appropriate *p*-type or *n*-type doping in

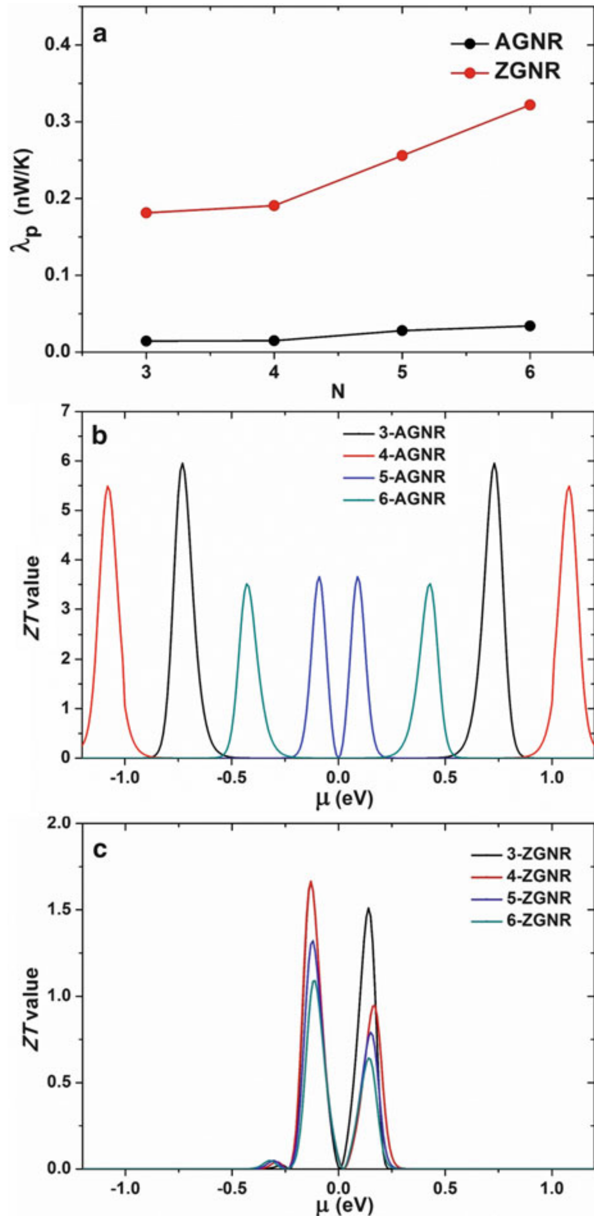

Fig. 12.14 (*Color online*) (**a**) Calculated phonon-derived thermal conductance at 300 K for the AGNRs and ZGNRs series. (**b**) and (**c**) are the calculated room temperature *ZT* value as a function of chemical potential for the AGNRs and ZGNRs series, respectively

the AGNRs, one could obtain much higher *ZT* values at room temperature. It should be emphasized that all the investigated AGNRs in our work exhibit *ZT* values larger than 3.0, which suggests that if used as thermoelectric materials they can compete with the conventional energy conversion method. Moreover, the maximum *ZT*

Table 12.4 Calculated room temperature *ZT* values and corresponding transport coefficients at optimized chemical potential for a series of armchair and zigzag nanoribbons. The ribbon width and the band gap of each structure are also shown

Structure	Width (Å)	Gap (eV)	μ (eV)	S (μV/K)	G (μS)	λ_e (nW/K)	λ_p (nW/K)	ZT
3-AGNR	4.19	1.59	±0.73	324	4.74	0.011	0.014	6.0
4-AGNR	5.42	2.32	±1.08	351	4.01	0.012	0.015	5.4
5-AGNR	6.65	0.27	±0.09	274	8.21	0.023	0.028	3.7
6-AGNR	7.88	0.99	±0.43	275	8.20	0.019	0.034	3.5
3-ZGNR	6.97	0.37	−0.13	235	22.07	0.039	0.18	1.7
4-ZGNR	9.10	0.39	−0.13	240	22.72	0.045	0.19	1.7
5-ZGNR	11.23	0.47	−0.12	243	22.92	0.050	0.26	1.3
6-ZGNR	13.36	0.44	−0.11	213	31.71	0.053	0.32	1.1

value increases with decreasing ribbon width. For the narrowest 3-AGNR, a maximum *ZT* value of 6.0 can be reached at $\mu = \pm 0.73$ eV. Compared with other low-dimensional carbon materials such as carbon nanotubes (See Sect. 12.3), the significantly enhanced thermoelectric performance of AGNRs can be attributed to very small thermal conductance from both the electrons and phonons. Our calculated *ZT* values are summarized in Table 12.4 where the corresponding chemical potential and transport coefficients are also given.

The picture for the ZGNRs series is however quite different. As shown in Fig. 12.14c, the peak *ZT* value at $\mu < 0$ is relatively larger than that at $\mu > 0$, which means that *p*-type doping are more favorable than *n*-type doping to enhance the thermoelectric performance. Compared with those of AGNRs, we see the *ZT* values of ZGNRs are much smaller. If we compare the calculated transport coefficients listed in Table 12.4, we find ZGNRs actually have relatively larger power factor (S^2G). The less favorable thermoelectric performance of ZGNRs is therefore caused by their larger thermal conductance (λ), and in particular, the phonon contribution to it. As the investigated ZGNRs show similar transport coefficients around the Fermi level, we see their maximum *ZT* values appear at almost the same chemical potential. The *ZT* values also increase with decreasing ribbon width, but with a less extent.

12.6 Carbon Nanowires

The CNWs can be visualized as a virtual cylinder cut from the bulk diamond along certain directions. Figure 12.15 shows the top and side view of CNWs with three typical orientations: [100], [110], and [111]. All of them have a lateral diameter of about 5.0 Å. We see that the nanowire surface is reconstructed with all the initial dangling bonds eliminated, which is consistent with previous observations [55]. The unit cell contains 21, 14, and 26 carbon atoms, for the [100], [110], and [111] CNWs, respectively. The length of translational vector along the wire axis is calculated to be 3.66, 2.54, and 6.25 Å, respectively. As the diameter of these

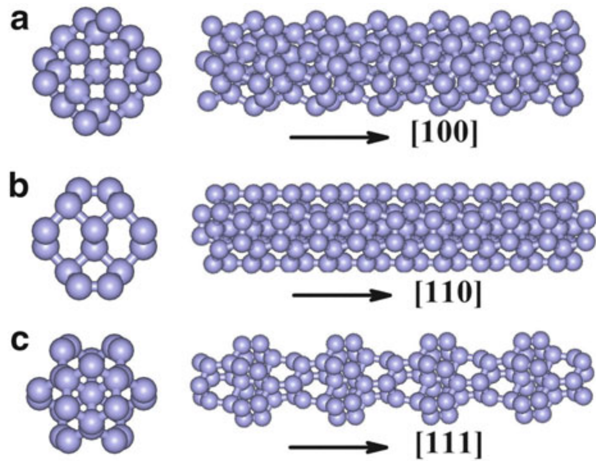

Fig. 12.15 Top (*left*) and side view (*right*) of three kinds of 5 Å carbon nanowires: (**a**) CNW [100], (**b**) CNW [110], and (**c**) CNW [111]

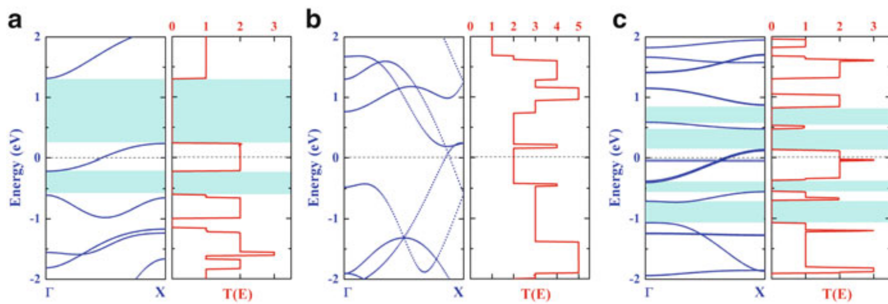

Fig. 12.16 (*Color online*) Energy band structure and electron transmission function for (**a**) CNW [100], (**b**) CNW [110], and (**c**) CNW [111]. The Fermi level is at 0 eV. The zero transmission windows near the Fermi level are *shaded*

CNWs is very small, it is natural to ask whether they are stable as standalone entities. We thus calculate the corresponding phonon dispersion relations (not shown here) using the density functional perturbation theory (DFPT) [56]. Our calculations find no imaginary frequency for any of the three kinds of CNWs, which indicates the structural stability of these ultrasmall systems. It should be mentioned that among these three kinds of CNWs, the surface roughness is the highest for the [111], the lowest for the [110], and the [100] is somehow in between. Such a structural characteristic may result in different phonon-derived thermal conductances, and we will come back to this point later.

In Fig. 12.16, we plot the energy band structure and the electronic transmission function for all the three kinds of 5 Å CNWs. We see that the transmissions display clear stepwise structures which indicate ballistic transport of electrons. The quantized transmission can be essentially derived from the number of energy bands at

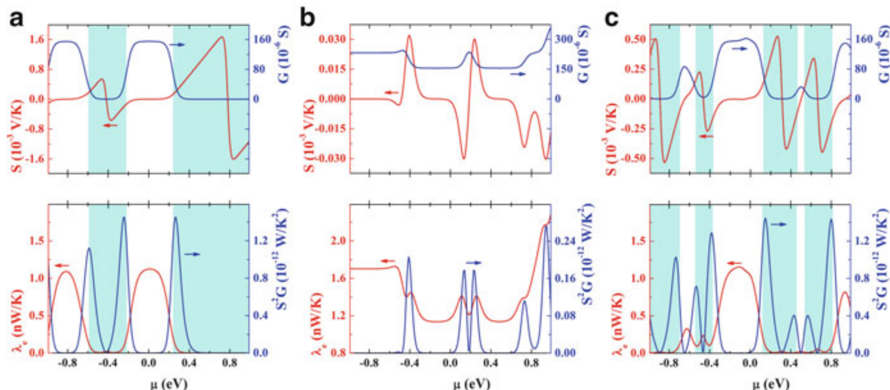

Fig. 12.17 (*Color online*) Calculated electronic transport coefficients: Seebeck coefficient, electrical conductance, electronic thermal conductivity, and power factor as a function of chemical potential at room temperature for three kinds of 5 Å CNWs: (**a**) [100], (**b**) [110], and (**c**) [111]. The zero transmission windows near the Fermi level are *shaded*

any given energy. Although all the three CNWs are found to be metallic, it is interesting to note that around the Fermi level, the [100] and [111] CNWs exhibit several zero transmission windows as indicated by shadows in Fig. 12.16a, c. By appropriate doping, one may be able to move the Fermi level to the edge of zero transmission windows thus the carrier concentration can be optimized to exhibit enhanced power factor. This is very similar to the case of semiconducting carbon nanotubes and GNRs discussed in previous sections. In the following discussions, we shall see that these metallic CNWs can be also optimized to exhibit high ZT values only if the zero transmission window is close to the Fermi level.

Based on the calculated transmission function $T(E)$, the Seebeck coefficient S, the electrical conductance G, the electronic thermal conductance λ_e as well as the power factor S^2G can be readily obtained [29]. Figure 12.17 plots these electronic transport coefficients at 300 K as a function of chemical potential μ for the 5 Å CNWs. Within the rigid-band picture [49], the chemical potential indicates the doping level (or carrier concentration) of the system. For p-type doping, the chemical potential is negative while it is positive for n-type doping. If we focus on the CNW [110], we see from Fig. 12.17b that the electrical conductance is high at the chemical potential where the Seebeck coefficient is almost vanishing. As a consequence, the electronic thermal conductance is high and the power factor is very low, which suggests that the CNW [110] is not suitable as a thermoelectric material. This is consistent with the fact that the transmission function of the CNW [110] is continuous without any zero transmission windows (see Fig. 12.16b). For the [100] and [111] CNWs, however, we see from the upper panel of Fig. 12.17a, c that near the edge of the zero transmission window the absolute value of the Seebeck coefficient is relatively large and the electrical conductance increases sharply, which tends to maximize the power factor as indicated in the lower panel of Fig. 12.17a, c. At the same time,

Table 12.5 Calculated room temperature *ZT* values at optimized chemical potential (both *p*-type and *n*-type doping) for three kinds of 5 Å CNWs and their partial hydrogen-passivated products. The corresponding electron and phonon transport coefficients are also listed. For better comparison, the phonon-derived thermal conductance and thermal conductivity are both shown

Structure	μ (eV)	S (μV/K)	G (μS)	S^2G (W/K^2)	λ_e (nW/K)	λ_p (nW/K)	κ_p (W/m·K)	*ZT*
CNW [100]	−0.28	−307.1	11.5	1.09×10^{-12}	0.027	0.044	224	4.62
	0.30	275.3	11.5	1.09×10^{-12}	0.026			4.64
CNW [110]	−0.41	319.6	20.2	0.21×10^{-12}	1.429	0.220	1,120	0.04
	0.94	−303.7	29.5	0.27×10^{-12}	2.173			0.03
CNW [111]	−0.76	−289.4	10.1	0.84×10^{-12}	0.014	0.021	107	7.19
	0.19	320.6	9.75	1.00×10^{-12}	0.024			6.72
PP-CNW [100]	−0.93	306.5	5.80	0.54×10^{-12}	0.013	0.023	117	4.55
	0.39	307.8	5.75	0.54×10^{-12}	0.014			4.51
PP-CNW [110]	−0.17	−277.3	16.5	1.27×10^{-12}	0.041	0.093	474	2.84
	0.12	269.1	24.0	1.74×10^{-12}	0.044			3.80
PP-CNW [111]	−0.11	320.0	7.02	0.72×10^{-12}	0.008	0.013	66	10.2
	0.15	344.5	4.16	0.49×10^{-12}	0.009			6.71

we see that the electronic thermal conductance is relatively low at the edge of the zero transmission window. Both of these aspects are very beneficial to achieving a high *ZT* value.

To evaluate the *ZT* value explicitly, we have to know the phonon-derived thermal conductance. As before, we use the NEMD since it is much faster than other approaches and can handle nonlinearity when dealing with phonon transport. Our calculated room temperature phonon transport coefficients are summarized in Table 12.5. For better comparison, the phonon-derived thermal conductance and thermal conductivity are both shown. Note that the phonon-derived thermal conductance of low-dimensional systems is related to their length and we consider the size effect as discussed in Sect. 12.3. In the present calculations, the length of these CNWs is assumed to be 1 μm. We see from Table 12.5 that the thermal conductance (λ_p) of these nanowires exhibits an obvious orientation dependence, where the λ_p of CNW [110] is about five and ten times larger than those of the [100] and [111] CNWs, respectively. This is believed to be caused mainly by their different group velocities for the acoustic phonon modes [57]. In addition, as we mentioned above, the [100] and [111] CNWs have a significant intrinsic surface roughness which will scatter phonons and reduce the thermal conductance. Indeed, Donadio et al. have taken advantage of the roughness by annealing to reduce the thermal conductivity of silicon nanowires [58]. It is worth mentioning that the orientation dependence of λ_p was also found in previous works for other diameter CNWs [57, 59, 60]. On the other hand, our calculated λ_p of [100] and [111] CNWs are about one order of magnitude smaller compared with those of CNTs having similar diameters (e.g., the calculated λ_p of (7,0) and (5,1) tubes are 0.359 and 0.269 nW/K, respectively). The significantly reduced thermal conductance of these two CNWs makes them very favorable candidates for thermoelectric applications. It should be emphasized that

although the calculated thermal conductivity are somewhat larger than those of conventional thermoelectric materials, the power factor of CNWs are three orders of magnitude larger than those of conventional thermoelectric materials, thus leading to a high *ZT* value.

With all the transport coefficients specified, we are now able to calculate *ZT* values of these 5 Å CNWs. As discussed above, one can obtain high power factor and low electronic thermal conductance at the edge of the zero transmission window. Within the rigid-band picture, this can be done by appropriate *p*-type or *n*-type doping which can move the Fermi level to the desired chemical potential (i.e., the edge of the zero transmission window). The optimized *ZT* values of 5 Å CNWs are summarized in Table 12.5 where the corresponding chemical potential (μ) and transport coefficients (S, G, S^2G, λ_e, and λ_p) are also given. Note the *ZT* values and all the transport coefficients are evaluated at 300 K. Compared with other carbon-based one-dimensional structures such as CNTs (see Table 12.1), the thermal conductance of CNWs from both electrons and phonons is nearly one order of magnitude smaller, which leads to their significantly improved thermoelectric performance in spite of the slightly lower power factor. We see that, indeed, the [100] and [111] CNWs exhibit much higher *ZT* values at optimized doping levels. The strong orientation dependence of *ZT* values can be attributed to the fact that among these three kinds of CNWs, the [100] and [111] CNWs have zero transmission windows around the Fermi level (see Fig. 12.16), and thus the carrier concentration can be optimized to exhibit relatively higher power factor S^2G and lower electronic thermal conductance λ_e. At the same time, the phonon-derived thermal conductance λ_p of [100] and [111] CNWs are much lower than that of [110] CNW. It should be mentioned that the *ZT* values of [100] and [111] CNWs are significantly larger than those of the current best thermoelectric materials. For example, the experimentally measured *ZT* value of Sb_2Te_3 is 1.1 at room temperature [61], while the $Mg_2Si_{1-x}Sn_x$ solid solutions [62] and multiple-filled skutterudites [63] have *ZT* of 1.3 and 1.7 at 700 K and 850 K, respectively. We want to emphasize that the *ZT* values of [100] and [111] CNWs are much larger than 3.0 which suggests that they are very competitive vis-à-vis the conventional energy conversion methods. Moreover, the *ZT* values of CNW [100] are almost identical for the *p*-type and *n*-type doping, which suggests that this CNW is particularly suitable for fabrication of both *p*-legs and *n*-legs of thermoelectric modules. We want to mention that in the present work we focus on the CNWs with very small diameters (~5 Å). If the diameter of CNW is increased, the *ZT* value may decrease since the thermal conductance will increase accordingly [59]. However, by means of hydrogen passivation, isotope doping or using core–shell structure, etc., one can reduce the thermal conductance thus larger diameter CNWs may still be possible thermoelectric materials.

As the CNWs are experimentally synthesized under hydrogen flow [64], it is quite possible that the surface of these CNWs contains hydrogen with certain coverage. Here we consider a general case where the surface carbon atoms are partially passivated (PP) by hydrogen atoms. The resulting systems have nominal formulas of $C_{21}H_{12}$, $C_{14}H_5$, and $C_{26}H_{13}$, for the [100], [110], and [111] CNWs,

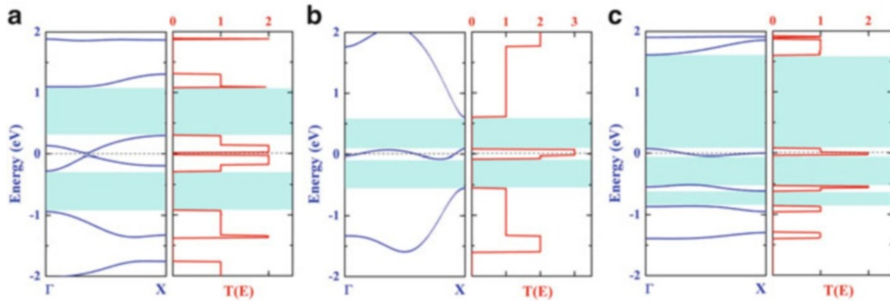

Fig. 12.18 (*Color online*) Energy band structure and electron transmission function for (**a**) PP-CNW [100], (**b**) PP-CNW [110], and (**c**) PP-CNW [111]. The Fermi level is at 0 eV. The zero transmission windows near the Fermi level are *shaded*

respectively. The corresponding energy band structure and electron transmission function are shown in Fig. 12.18. It can be seen that for all the three PP-CNWs, there are two or three zero transmission windows around the Fermi level, which is beneficial to their thermoelectric performance via proper doping as discussed above. Compared with those shown in Fig. 12.16, the PP-CNWs exhibit somewhat lower transmission, which is attributed to the fact that the energy bands of partially passivated products are usually singly degenerate. The optimized *ZT* values as well as the corresponding transport coefficients for these PP-CNWs are also summarized in Table 12.5. We see that the phonon-derived thermal conductance is significantly reduced (to about half the value) when the surface carbon atoms are partially passivated. This is due to the added disorder and the C/H mass difference scattering. On the other hand, we see from Table 12.5 that the reduced transmission coefficients somewhat decrease the power factor and the electronic thermal conductance for the [100] and [111] CNWs, while the additional zero transmission window significantly increases the power factor but greatly decreases the electronic thermal conductance for the [110] CNW. As a result, the *ZT* values of the CNW [110] are significantly enhanced to 2.84 and 3.80 for the *p*-type and *n*-type doping, respectively. In the case of the [111] CNW, we find that the thermal conductance is reduced more than the power factor upon partial passivation and therefore the maximum *ZT* value is further improved to 10.2 via proper *p*-type doping. For the [100] CNW, the partial passivation of hydrogen leads to a comparable reduction of the thermal conductance and the power factor, and the *ZT* value remains about 4.6 for both the *p*-type and *n*-type doping.

12.7 Summary

In summary, the thermoelectric properties of three kinds of ultrasmall diameter carbon nanotubes are studied by using nonequilibrium Green’s function method and nonequilibrium molecule dynamics simulations. Our calculated results indicate that

although these nanotubes do not have much higher *ZT* value in the pristine form, their thermoelectric performance can be significantly enhanced via surface design, formation of bundles, and increasing the tube length, etc. For carbon nanotubes with relatively larger diameter, our theoretical calculations indicate that by appropriate *n*-type and *p*-type doping, one can obtain much higher *ZT* value for both the zigzag and armchair CNTs, and those tubes with intermediate diameter (0.7–0.8 nm) seems have better thermoelectric properties than others. Taking the zigzag (10,0) as an example, we show that the phonon-induced thermal conductance can be effectively reduced by isotope substitution, isoelectronic impurities, and hydrogen adsorption, while the electronic transport is less affected. As a result, the *ZT* value can be further enhanced and is very competitive with that of the best commercial materials. To experimentally realize this goal, one need to fabricate CNTs with specific diameter and chirality, and the tube length should be at least 1 μm. This may be challenging but very possible considering the fact that (10,0) tube were successfully produced by many means such as direct laser vaporization [65], electric-arc technique [66], and chemical vapor deposition [67], and can be selected from mixed or disorder samples using DNA-based separation process [68].

In the case of graphene nanoribbons, our theoretical calculations indicate that the electronic transport coefficients of AGNRs exhibit obvious width dependence, which is closely related to their family behavior of the energy band gap. In contrast, all the investigated ZGNRs have similar band structures and the calculated transport coefficients almost coincide with each other. On the other hand, the phonon-induced thermal conductance of AGNRs is much smaller than those of ZGNRs, and both increase with increasing ribbon width. As for the CNWs, we show that ultrasmall diameter CNWs with particular orientations can exhibit large power factors and low electronic thermal conductances at the edge of the so-called zero transmission windows. The phonon-induced thermal conductance is nearly one order of magnitude smaller than those of CNTs according to the nonequilibrium molecular dynamics simulation. As a result, one obtains room temperature *ZT* values much higher than 3.0 by appropriate *p*-type and *n*-type doping. Moreover, it is found that partial hydrogen passivation can reduce the thermal conductance by about 50 % and further improve the maximum *ZT* to values in excess of 10 for the CNW [111].

In a word, our theoretical investigations suggest that carbon nanotubes and related one-dimensional carbon nanostructures possess outstanding thermoelectric properties that exceed those of current state-of-the-art thermoelectric materials and thus appear very prospective for thermoelectric applications. Major effort should be directed towards realization of these high-performance and environment friendly thermoelectric materials.

Acknowledgements This work was supported by the National Natural Science Foundation (Grant No. 51172167) and the "973 Program" of China (Grant No. 2013CB632502). We also acknowledge financial support from the China Scholarship Council.

References

1. Slack, G.A. In: Rowe, D.M. (ed.) CRC Handbook of Thermoelectrics, p. 407. CRC Press, Boca Raton (1995)
2. Tritt, T.: Science **283**, 804 (1999)
3. DiSalvo, F.J.: Science **285**, 703 (1999)
4. Hicks, L.D., Dresselhaus, M.S.: Phys. Rev. B **47**, 12727 (1993)
5. Hicks, L.D., Dresselhaus, M.S.: Phys. Rev. B **47**, 16631 (1993)
6. Iijima, S.: Nature (Lond.) **354**, 56 (1991)
7. Hone, J., Whitney, M., Piskoti, C., Zettl, A.: Phys. Rev. B **59**, R2514 (1999)
8. Hone, J., Llaguno, M.C., Nemes, N.M., Johnson, A.T., Fischer, J.E., Walters, D.A., Casavant, M.J., Schmidt, J., Smalley, R.E.: Appl. Phys. Lett. **77**, 666 (2000)
9. Berber, S., Kwon, Y.K., Tomanek, D.: Phys. Rev. Lett. **84**, 4613 (2000)
10. Kim, P., Shi, L., Majumdar, A., McEuen, P.L.: Phys. Rev. Lett. **87**, 215502 (2001)
11. Yu, C., Shi, L., Yao, Z., Li, D., Majumdar, A.: Nano Lett. **5**, 1842 (2005)
12. Pop, E., Mann, D., Cao, J., Wang, Q., Goodson, K., Dai, H.: Phys. Rev. Lett. **95**, 155505 (2005)
13. Purewal, M.S., Hong, B.H., Ravi, A., Chandra, B., Hone, J., Kim, P.: Phys. Rev. Lett. **98**, 186808 (2007)
14. Prasher, R.S., Hu, X.J., Chalopin, Y., Mingo, N., Lofgreen, K., Volz, S., Cleri, F., Keblinski, P.: Phys. Rev. Lett. **102**, 105901 (2009)
15. Jiang, J.W., Wang, J.S., Li, B.: J. Appl. Phys. **109**, 014326 (2011)
16. Wang, J.S., Wang, J., Zeng, N.: Phys. Rev. B **74**, 033408 (2006)
17. Wang, N., Tang, Z.K., Li, G.D., Chen, J.S.: Nature (Lond.) **408**, 50 (2000)
18. Brandbyge, M., Mozos, J.L., Ordejon, P., Taylor, J., Stokbro, K.: Phys. Rev. B **65**, 165401 (2002)
19. Soler, J.M., Artacho, E., Gale, J.D., Garcia, A., Junquera, J., Ordejon, P., Sanchez-Portal, D.: J. Phys.: Conders. Matter. **14**, 2745 (2002)
20. Troullier, N., Martins, J.L.: Phys. Rev. B **43**, 8861 (1991)
21. Perdew, J.P., Wang, Y.: Phys. Rev. B **45**, 13244 (1992)
22. Monkhorst, H.J., Pack, J.D.: Phys. Rev. B **13**, 5188 (1976)
23. Plimpton, S.: J. Comput. Phys. **117**, 1 (1995). Code available at: http://lammps.sandia.gov/download.html
24. Tersoff, J.: Phys. Rev. B **39**, 5566 (1989)
25. Muller-Plathe, F.: J. Chem. Phys. **106**, 6082 (1997)
26. Osman, M.A., Srivastava, D.: Nanotechnology **12**, 21 (2001)
27. Schelling, P.K., Phillpot, S.R., Keblinski, P.: Phys. Rev. B **65**, 144306 (2002)
28. Liu, H.J., Chan, C.T.: Phys. Rev. B **66**, 115416 (2002)
29. Esfarjani, K., Zebarjadi, M., Kawazoe, Y.: Phys. Rev. B **73**, 085406 (2006)
30. Alaghemandi, M., Algaer, E., Böhm, M.C., Müller-Plathe, F.: Nanotechnology **20**, 115704 (2009)
31. Chang, C.W., Okawa, D., Garcia, H., Majumdar, A., Zettl, A.: Phys. Rev. Lett. **101**, 075903 (2008)
32. Che, J., Cagin, T., Goddard III, W.A.: Nanotechnology **11**, 65 (2000)
33. Huang, Z.X., Tang, Z.A.: Physica B **373**, 291 (2006)
34. Maiti, A., Mahan, G.D., Pantelides, S.T.: Solid State Commun. **102**, 517 (1997)
35. Donadio, D., Galli, G.: Phys. Rev. Lett. **99**, 255502 (2007). Erratum *ibid.* **103**, 149901 (2009)
36. Kim, D., Kim, Y., Choi, K., Grunlan, J.C., Yu, C.: ACS Nano **4**, 513 (2010)
37. Wen, Y.W., Liu, H.J., Pan, L., Tan, X.J., Lv, H.Y., Shi, J., Tang, X.F.: J. Phys. Chem. C **115**, 9227 (2011)
38. Cao, J.X., Yan, X.H., Xiao, Y., Ding, J.W.: Phys. Rev. B **67**, 045413 (2003)
39. Cao, J.X., Yan, X.H., Xiao, Y., Ding, J.W.: Phys. Rev. B **69**, 073407 (2004)
40. Zhang, G., Li, B.: J. Chem. Phys. **123**, 114714 (2005)

41. Chang, C.W., Fennimore, A.M., Afanasiev, A., Okawa, D., Ikuno, T., Garcia, H., Li, D., Majumdar, A., Zettl, A.: Phys. Rev. Lett. **97**, 085901 (2006)
42. Balasubramanian, G., Puri, I.K., Böhm, M.C., Leroy, F.: Nanoscale **3**, 3714 (2011)
43. Chen, J., Zhang, G., Li, B.: Appl. Phys. Lett. **95**, 073117 (2009)
44. Son, Y.W., Cohen, M.L., Louie, S.G.: Phys. Rev. Lett. **97**, 216803 (2006)
45. Son, Y.W., Cohen, M.L., Louie, S.G.: Nature **444**, 347 (2006)
46. Barone, V., Hod, O., Scuseria, G.E.: Nano Lett. **6**, 2748 (2006)
47. Yang, L., Park, C.H., Son, Y.W., Cohen, M.L., Louie, S.G.: Phys. Rev. Lett. **99**, 186801 (2007)
48. Sivan, U., Imry, Y.: Phys. Rev. B **33**, 551 (1986)
49. Holland, M.G.: Phys. Rev. **132**, 2461 (1963)
50. The real length of GNRs varies from sample to sample and is usually in the order of 1 μm. Increasing the ribbon length will decrease the thermal conductance which can further enhance their thermoelectric performance.
51. Guo, Z., Zhang, D., Gong, X.G.: Appl. Phys. Lett. **95**, 163103 (2009)
52. Xu, Y., Chen, X., Gu, B.L., Duan, W.: Appl. Phys. Lett. **95**, 233116 (2009)
53. Tan, Z.W., Wang, J.S., Gan, C.K.: Nano Lett. **11**, 103508 (2011)
54. Hu, J., Ruan, X., Chen, Y.P.: Nano Lett. **7**, 2730 (2009)
55. Barnard, A.S., Russo, S.P., Snook, I.K.: Surf. Sci. **538**, 204 (2003)
56. Baroni, S., de Gironcoli, S., Dal Corso, A., Giannozzi, P.: Rev. Mod. Phys. **73**, 515 (2001)
57. Jiang, J.W., Wang, B.S., Wang, J.S.: Phys. Rev. B **83**, 235432 (2011)
58. Donadio, D., Galli, G.: Phys. Rev. Lett. **102**, 195901 (2009)
59. Li, W., Mingo, N., Lindsay, L., Broido, D.A., Stewart, D.A., Katcho, N.A.: Phys. Rev. B **85**, 195436 (2012)
60. Guo, J., Wen, B., Melnik, R., Yao, S., Li, T.J.: Physica E **43**, 155 (2010)
61. Mehta, R.J., Zhang, Y., Karthik, C., Singh, B., Siegel, R.W., Borca-Tasciuc, T., Ramanath, G.: Nat. Mater. **11**, 233 (2012)
62. Liu, W., Tan, X.J., Yin, K., Liu, H.J., Tang, X.F., Shi, J., Zhang, Q.J., Uher, C.: Phys. Rev. Lett. **108**, 166601 (2012)
63. Shi, X., Yang, J., Salvador, J.R., Chi, M., Cho, J.Y., Wang, H., Bai, S., Yang, J., Zhang, W., Chen, L.: J. Am. Chem. Soc. **133**, 7837 (2011)
64. Hsu, C.-H., Cloutier, S.G., Palefsky, S., Xu, J.: Nano Lett. **10**, 3272 (2010)
65. Guo, T., Nikolaev, P., Thess, A., Colbert, D.T., Smalley, R.E.: Chem. Phys. Lett. **243**, 49 (1995)
66. Journet, C., Maser, W.K., Bernier, P., Loiseau, A., Chapelle, M.L., Lefrant, S., Deniard, P., Leek, R., Fischer, J.E.: Nature **388**, 756 (1997)
67. Kong, J., Soh, H.T., Cassell, A.M., Quate, C.F., Dai, H.: Nature **395**, 878 (1998)
68. Zheng, M., Jagota, A., Semke, E.D., Diner, B.A., Mclean, R.S., Lustig, S.R., Richardson, R.E., Tassi, N.G.: Nat. Mater. **2**, 338 (2003)

Chapter 13
The Thermoelectric Properties in Graphene and Graphene Nanoribbons

Changning Pan, Zhongxiang Xie, and Keqiu Chen

Abstract The two-dimensional (2D) graphene with many remarkable physical properties, such as high mechanical robustness, excellent thermal conductivity, extremely high conductance, and giant Seebeck coefficient as well as particular electronic band structures, promises well for potential applications in nanoelectronics, spintronics, photonics, and optoelectronics. The quasi-one-dimensional (1D) graphene nanoribbons (GNRs) and graphene nanojunctions (GNJs), which can be precisely patterned from graphene, are the most elementary building blocks for future nanodevices and nanocircuits. In this chapter, we review the latest advances on graphene, GNRs and GNJs in both theoretical and experimental level, including thermal transport, electronic transport as well as thermoelectric properties. In particular, how to enhance the thermoelectric properties in the 1D graphene-based nanostructures through the geometry-decorated method (antidot lattices, nanopores, edge disorder, defect-engineering, and so on) is presented in detail and some novel results are elucidated clearly. It provides the reader a comprehensive understanding of the recent progress in realistic 1D graphene nanostructures, and will be helpful for designing nanodevices based on graphene in the future.

13.1 Introduction

Graphene is an infinite two-dimensional (2D) monolayer, which is composed of sp^2 hybridized carbon atom structures belonging to one of the five 2D Bravais lattices called the hexagonal lattice. It is the basic unit of carbon allotropes and can be wrapped up into 0D fullerenes, rolled into 1D nanotubes or stacked into 3D graphite. Since it was successfully fabricated in experiments [1] in 2004, the graphene has attracted great interest in their fundamental physical properties, such as thermal

C. Pan • Z. Xie • K. Chen (✉)
Department of Applied Physics, Hunan University, Changsha 410082, China
e-mail: panchangning2000@sina.com; xiezhongxiang@hnu.edu.cn; keqiuchen@hnu.edu.cn

X. Wang and Z.M. Wang (eds.), *Nanoscale Thermoelectrics*, Lecture Notes in Nanoscale Science and Technology 16, DOI 10.1007/978-3-319-02012-9_13,
© Springer International Publishing Switzerland 2014

properties, electronic properties, optical properties, and magnetic properties [2–12]. Owing to the unique physical properties, graphene is foreseen to have potential applications in nanoelectronics, spintronics, photonics, and optoelectronics and be a promising material to take place of semiconductor Si in some fields. Based on the existing well-controlled planar carve technologies [13–17], quasi-one-dimensional graphene nanoribbon (GNR) and graphene nanojunctions (GNJs) can be precisely patterned from two-dimensional graphene, which provides a new possibility of GNR-based devices and integrated-graphene circuits (IGCs). For instance, All-graphene circuits, which include semiconducting GNR channels connected by metallic GNR interconnects, could be achieved from a graphene sheet by using the electron- or ion-beam lithography or direct focused electron or ion-beam writing [18]. In terms of the edge orientation, the GNRs are classified to zigzag-edged (ZGNRs) and armchair-edged nanoribbons (AGNRs). The electronic properties of GNRs are highly dependent on their edge orientations and widths. In more detail, ZGNRs possess spin-polarized peculiar edge states and result in the half-metallic properties under transverse electric field. In contrast, the AGNRs can be either metallic or semiconducting properties which is dependent on their widths, i.e., AGNR with widths $N_a = 3k + 2$ has been shown to be metallic and otherwise to be semiconducting, where k is an integer. So far, the thermal transport properties, electron transport properties, and thermoelectric energy conversion of graphene and GNRs have been extensively investigated and some intriguing results have been obtained.

In this chapter, we provide a comprehensive review about the latest advance in the thermoelectric effect (TE) of the GNRs and GNJs, how to enhance the TE, for instance, antidot lattices, nanopores, defect-engineering, edge disorder, and so on, is introduced. The chapter is organized as following: the second part introduces the thermoelectric energy conversion mechanism and the nonequilibrium Green's function approach. The third part is devoted to the thermoelectric effect of the graphene and pristine GNRs. In the fourth part, we focus on the enhancement by using geometry-decorated engineering. A summery is given in the fifth part.

13.2 Model and Approach

13.2.1 The Energy Dispersion Relation of the 2D Graphene

Firstly, we introduce the crystal structure of the 2D graphene [19]. The unit cell, including two atoms A and B, are shown in Fig. 13.1a as the dotted rhombus, where $\vec{a}_1$ and $\vec{a}_2$ are unit vectors in real space, and can be expressed as $\vec{a}_1 = (\sqrt{3}a/2, a/2)$, $\vec{a}_2 = (\sqrt{3}a/2, -a/2)$, with $a = |\vec{a}_1| = |\vec{a}_2| = 2.46$ Å the lattice constant of the 2D graphene. The nearest-neighbor distance between two carbon atoms, $a_{c-c} = 1.42$ Å. The first Brillouin zones are shown as the shaded

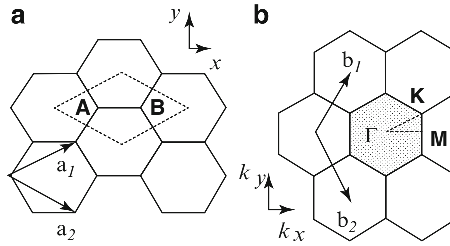

Fig. 13.1 (**a**) The unit cell and the unit vectors $\vec{a}_1$, $\vec{a}_2$ in the real space, (**b**) Brillouin zone and the reciprocal lattice vectors $\vec{b}_1$, $\vec{b}_2$ of two-dimensional graphene, three high symmetry points Γ, *M*, and *K* corresponding to the center, the corner, and the center of the edge, respectively [19]

hexagon in Fig. 13.1b, where $\vec{b}_1$ and $\vec{b}_2$ are the reciprocal lattice vectors, and $\vec{b}_1 = \left(2\pi/\sqrt{3}a, 2\pi/a\right)$, $\vec{b}_2 = \left(2\pi/\sqrt{3}a, -2\pi/a\right)$ corresponding to a lattice constant of $4\pi/\sqrt{3}a$ in reciprocal space. In general, the three high symmetry points, Γ, *K*, and *M* are defined as the center, the corner, and the center of the edge, respectively. Following these definitions and using the tight-binding (TB) model approach, the energy dispersion relations can be calculated throughout the whole Brillouin zone.

It is well known that there are σ bonds and π covalent bonds in sp^2 hybridized configuration for the 2D graphite. The π covalent bonds are made by the $2p_z$ orbital perpendicular to the graphene plane. It is very important for determining the solid state properties of graphite. In the TB calculation, the on-site energy $\varepsilon_c = 0$, hopping energies $t = -3.033$ eV and overlap integral $s = 0.129$ are used, it fully consists with the first principles calculation of the graphene energy bands [20, 21].

Besides the $2p_z$ atomic orbital, there are three other atomic orbitals of sp^2 covalent bonding per carbon atom, i.e., $2s$, $2p_x$, and $2p_y$. When we take the coupling parameters of carbon atoms in the Hamiltonian as [19], the energy dispersion relations for 2D graphene for π and σ bands, along the high symmetry axes $K \rightarrow \Gamma \rightarrow M \rightarrow K$, can be plotted as Fig. 13.2. The upper energy dispersion curve describes the antibonding π* band, and the lower energy curve describes the π band. The π band and the antibonding π* band are degenerate at the high symmetry points *K*. In addition, there exist three σ bands which display below the Fermi energy and three antibonding σ* bands above the Fermi energy. From the energy dispersion relations, it is found that the π bond and the two σ bonds cross each other, and the same behavior appear for the π* bond and the two σ* bonds. Moreover, there is no band separation at the crossing points. Hence, we can see that the 2D graphene is gapless. It doesn't like the GNRs in which the gap is opened and change with the chirality and width of nanoribbons.

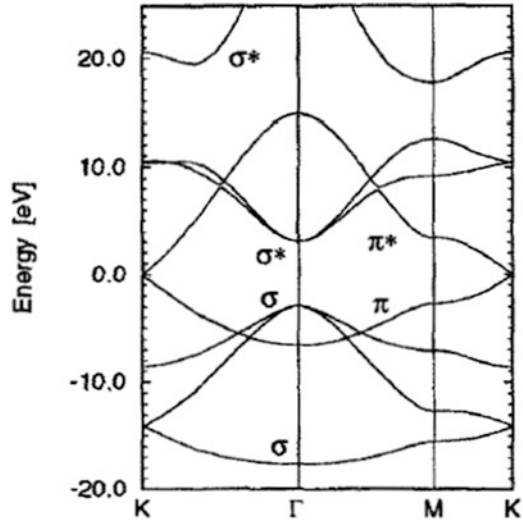

Fig. 13.2 The energy dispersion relations for the π bond and the two σ bonds of the 2D graphene along the high symmetry axes $K \rightarrow \Gamma \rightarrow M \rightarrow K$ [19]

13.2.2 The Phonon Dispersion Relation of Two-Dimensional Graphene

According to the force constant model, in which inter-atomic forces are represented by spring constants, the equation of motion for the displacement of the ith coordinate, $u_i = (x_i, y_i, z_i)$ for N atoms in the unit cell is given by

$$M_i \ddot{u}_i = \sum_j K^{ij}\left(u_j - u_i\right), \quad (i = 1, 2, \ldots, N),$$

where M_i is the mass of the ith atom and K^{ij} is the 3×3 force constant tensor which represents the interaction between ith and jth atoms. In general, if we take the more number of the force constants in the sum over j, the calculations are closer to the experimental results. For the sake of simplicity, we only take over a few neighbor distances interaction relative to the ith atom. But, at least the fourth nearest-neighbor interactions must be included to describe the twisted modes [22].

After considered the force constant of interaction atoms up to fourth neighbor, using the set of force constants in Table 13.1, the phonon dispersion relation of the graphene can be described as Fig. 13.3. There exist three dispersion curves originated from the high symmetry point Γ of the Brillouin zone, which correspond to three acoustic modes, i.e., the out-of-plane mode, the in-plane tangential mode, and the in-plane radial mode. However, the other three curves correspond to one out-of-plane optical mode and two in-plane optical modes, respectively.

Table 13.1 The fourth nearest-neighbor force constant parameters for graphene in units of 10^4 dyn/cm [22]

Radial	Tangential	
$\phi_{\mathrm{r}}^{(1)} = 36.50$	$\phi_{\mathrm{ti}}^{(1)} = 24.50$	$\phi_{\mathrm{to}}^{(1)} = 9.82$
$\phi_{\mathrm{r}}^{(2)} = 8.80$	$\phi_{\mathrm{ti}}^{(2)} = -3.23$	$\phi_{\mathrm{to}}^{(2)} = -0.40$
$\phi_{\mathrm{r}}^{(3)} = 3.00$	$\phi_{\mathrm{ti}}^{(3)} = -5.25$	$\phi_{to}^{(3)} = 0.15$
$\phi_{\mathrm{r}}^{(4)} = -1.92$	$\phi_{\mathrm{ti}}^{(4)} = 2.29$	$\phi_{\mathrm{to}}^{(4)} = -0.58$

Here $\phi_{\mathrm{r}}^{(n)}$, $\phi_{\mathrm{ti}}^{(n)}$, and $\phi_{\mathrm{to}}^{(n)}$ represent the force constant parameters in the radial (bond-stretching), in-plane, and out-of-plane tangential (bond-bending) direction, respectively

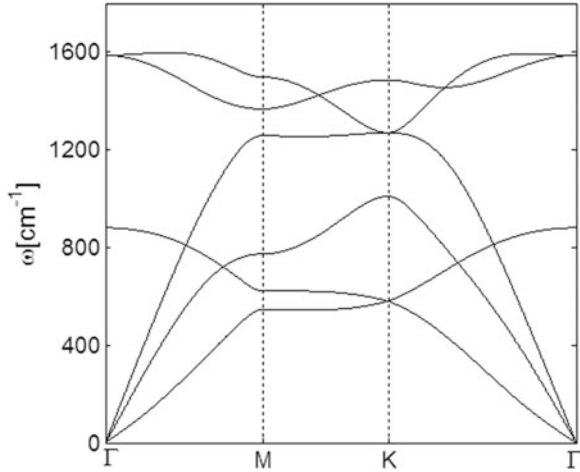

Fig. 13.3 The phonon dispersion curves plotted along the high symmetry directions for the 2D graphene

13.2.3 *The Definition of Thermoelectric Effect*

13.2.3.1 Phonon Thermal Transport

In general, we use the nonequilibrium Green's function (NEGF) approach [23–28] to calculate the phonon transport in graphene. The approach can be simply generalized as the following steps. The whole system is divided into three different parts: left lead (L), center region (C), and right lead (R). The left/right leads are semi-infinite periodic structures and are treated as the heat baths. In this geometry, the Hamiltonian of the whole system can be given by

$$H_{\mathrm{sys}} = \sum_{\alpha=\mathrm{L,C,R}} H_\alpha + \left(u^{\mathrm{L}}\right)^{\mathrm{T}} V^{\mathrm{LC}} U^{\mathrm{C}} + \left(u^{\mathrm{C}}\right)^{\mathrm{T}} V^{\mathrm{CR}} u^{\mathrm{R}} + V_{\mathrm{n}}.$$

Where $H_\alpha = \frac{1}{2}\left(\dot{u}^\alpha\right)^{\mathrm{T}} \dot{u}^\alpha + \frac{1}{2}\left(u^\alpha\right)^{\mathrm{T}} K^\alpha u^\alpha$ represents harmonic oscillators, and u^α is the row vector consisting of the vibrational displacement of each atom multiplied by its square root of mass in three different regions α(L,C,R), i.e., the mass normalized displacement variables. K^α is the force constant matrices in the corresponding

region, V^{LC} and V^{CR} are the coupling matrices between left/right leads and center. Here $V^{\mathrm{LC}} = (V^{\mathrm{CL}})^{\mathrm{T}}$ and $V^{\mathrm{RC}} = (V^{\mathrm{CR}})^{\mathrm{T}}$. V_{n} is the nonlinear interaction in the central region. It is ignored generally in many studies. The reason and effect will be discussed in the conclusion of the chapter. Using the Hamiltonian of the system, we can calculate the retarded surface Green's function for the center region and left/right leads:

$$g_{\alpha}^{\mathrm{r}} = \left[(\omega + i\eta)^2 I - K^{\alpha}\right]^{-1}, (\alpha = \mathrm{L, C, R})$$

i.e., the retarded Green's function of the isolated central region $g_{\mathrm{C}}^{\mathrm{r}}$, the surface Green's function of the two isolated leads $g_{\mathrm{L/R}}^{\mathrm{r}}$. Generally, the retarded Green's function $g_{\mathrm{C}}^{\mathrm{r}}$ can be directly computed by the formula. But, it is difficult to calculate the surface Green's function $g_{\mathrm{L/R}}^{\mathrm{r}}$ due to the semi-infinite leads; it will be computed by a recursive iteration technique [29]. So it is still a challenge to use the NEGF approach for many realistic systems.

After obtaining the surface Green's function of the leads, the retarded self-energy of the leads can be given by $\sum_{\alpha}^{\mathrm{r}} = V^{\mathrm{C}\alpha} g_{\alpha}^{\mathrm{r}} V^{\alpha\mathrm{C}}$, it contains the coupling information between leads and center region. Correspondingly, with the conjugate relation $\sum_{\alpha}^{\mathrm{a}} = (\sum_{\alpha}^{\mathrm{r}})^{\dagger}$, the Γ function is given by

$$\Gamma_{\alpha} = i\left(\sum\nolimits_{\alpha}^{\mathrm{r}} - \sum\nolimits_{\alpha}^{\mathrm{a}}\right) = -2\mathrm{Im} V^{\mathrm{C}\alpha} g_{\alpha}^{\mathrm{r}} V^{\alpha\mathrm{C}}.$$

Then the retarded Green's function can be expressed as

$$G^{\mathrm{r}} = \left[(\omega + i\eta)^2 I - K^{\mathrm{C}} - \sum\nolimits_{\mathrm{L}}^{\mathrm{r}} - \sum\nolimits_{\mathrm{R}}^{\mathrm{r}}\right]^{-1},$$

which describes the interaction between the center region and the leads. In terms of the so-called Caroli formula, the transmission coefficient can be calculated as

$$T[\omega] = \mathrm{Tr}(G^{\mathrm{r}} \Gamma_{\mathrm{L}} G^{\mathrm{a}} \Gamma_{\mathrm{R}}),$$

here $G^{\mathrm{r}} = (G^{\mathrm{a}})^{\dagger}$ is the retarded Green's function for the central region. Accordingly, we can express the phonon thermal conductance in a form similar to the Landauer formula [30] for the ballistic transport as,

$$\kappa_{\mathrm{ph}} = \frac{1}{2\pi} \int \mathrm{d}\omega \hbar\omega T_{\mathrm{ph}}[\omega] \left[\frac{\partial f(\omega, T)}{\partial T}\right],$$

where $f(\omega,T) = \{\exp[\hbar\omega/(k_{\mathrm{B}}T)] - 1\}^{-1}$ is the Bose–Einstein distribution for phonons at the frequency ω and absolute temperature T. The density of states for phonon is given by

$$\rho_i(\omega) = -\frac{2\omega}{\pi} \sum_{\beta=x,y,z} \mathrm{Im}\left[G_\mathrm{C}^\mathrm{r}(\omega)\right]_{i\beta,i\beta},$$

which describes the phonon distribution information at the ith atom-site in the central scattering region.

13.2.3.2 Electron Transport

For the electron transport, the procedure of the calculation is very similar to the phonon transport; only two physical quantities substitutions are needed to make as the following:

$$K_\mathrm{C} \to H_\mathrm{e}, \quad (\omega + i\eta)^2 \to E + i\eta,$$

i.e., the force constant matrix K_C is replaced by the electron Hamiltonian H_e, and the square of frequency ω^2 is replaced by the energy of the electron, E. After obtaining the electron transport function, the physical quantities, which are related to the thermoelectric conversion, can be derived as following, respectively.

At the first, the electronic conductance is given by:

$$G_\mathrm{e} = -\frac{I}{V}\bigg|_{\Delta T=0} = \frac{-1}{V} \times \Delta\mu \frac{2q}{h} \int_{-\infty}^{+\infty} \mathrm{d}E T(E) \frac{\partial f(E,\mu,T)}{\partial \mu} = q^2 L_0.$$

Then, the electron thermal conductance is given by:

$$\begin{aligned}
\kappa_\mathrm{el} &= -\frac{I_Q}{\Delta T}\bigg|_{I=0} \\
&= \frac{-1}{\Delta T} \times \left[\Delta\mu \frac{2}{h} \int_{-\infty}^{+\infty} \mathrm{d}E T(E) \frac{\partial f(E,\mu,T)}{\partial \mu} (E-\mu) \right. \\
&\quad \left. + \Delta T \frac{2}{h} \int_{-\infty}^{+\infty} \mathrm{d}E T(E) \frac{\partial f(E,\mu,T)}{\partial T} (E-\mu) \right] \\
&= \frac{1}{T} \times \left(L_2 - \frac{L_1^2}{L_0}\right),
\end{aligned}$$

here, $q = -e$ is the charge of the electron, h is the Plank constant, and μ is the chemical potential. $f(E,\mu,T)$ is the Fermi–Dirac distribution function.

The Peltier coefficient, which describes the amount of heat that is carried by an electrical current when it passes through a material [31], is

$$\Pi = \frac{I_Q}{I}\bigg|_{\Delta T=0} = \frac{\Delta\mu \frac{2}{h}\int_{-\infty}^{+\infty} \mathrm{d}ET(E)\frac{\partial f(E,\mu,T)}{\partial\mu}(E-\mu)}{\Delta\mu \frac{2q}{h}\int_{-\infty}^{+\infty} \mathrm{d}ET(E)\frac{\partial f(E,\mu,T)}{\partial\mu}} = \frac{L_1}{qL_0}.$$

On the contrary, the temperature gradient can generate the electric voltage; the thermoelectric efficiency is represented by the Seebeck coefficient and can be calculated as

$$S = -\frac{V}{\Delta T}\bigg|_{I=0} = \frac{1}{q}\left\{\frac{2q}{h}\int_{-\infty}^{+\infty} \mathrm{d}ET(E)\frac{\partial f}{\partial T}\bigg/\frac{2q}{h}\int_{-\infty}^{+\infty} \mathrm{d}ET(E)\frac{\partial f}{\partial\mu}\right\} = \frac{1}{qT}\times\frac{L_1}{L_0},$$

where I and I_Q are the electronic current and electron thermal current. In the ballistic transport region, they can be derived by the Landauer-Buttiker formulae:

$$I = \frac{2q}{h}\int_{-\infty}^{+\infty} \mathrm{d}ET_{\mathrm{e}}(E)[f(E,\mu_{\mathrm{L}}) - f(E,\mu_{\mathrm{R}})],$$
$$I_Q = \frac{2}{h}\int_{-\infty}^{+\infty} \mathrm{d}ET_{\mathrm{e}}(E)[f(E,\mu_{\mathrm{L}}) - f(E,\mu_{\mathrm{R}})](E-\mu).$$

Meanwhile, an intermediate function

$$L_n(\mu,T) = \frac{2}{h}\int \mathrm{d}ET_{\mathrm{e}}(E)(E-\mu)^n\left[-\frac{\partial f(E,\mu,T)}{\partial E}\right]$$

is introduced for simplifying the tedious formulae expression.

As the name indicates, thermoelectricity involves conversion of energy from thermal to electrical using charge and heat transport in solid materials. The performance of thermoelectric material is quantified by the dimensionless figure of merit, ZT [32–34], where Z means the measure of a material's thermoelectric properties and T is the absolute temperature. It can be calculated by the following formula:

$$ZT = \frac{G_{\mathrm{e}}S^2T}{\kappa_{\mathrm{el}} + \kappa_{\mathrm{ph}}}.$$

A large value of ZT should own the large value of Seebeck coefficient S, the large value of conductance G_{e}, and a low value of the thermal conductances ($\kappa_{\mathrm{el}} + \kappa_{\mathrm{ph}}$). But these quantities are unfavorable and closely interrelated to each other, the variation of the one value will inevitably influence the others. One needs to have a careful tradeoffs to obtain the maximum efficiency of a thermoelectric conversion.

In general, the maximum efficiency of the thermoelectric devices for electricity generation can be given by:

$$\eta_{\max} = \frac{T_{\mathrm{H}} - T_{\mathrm{L}}}{T_{\mathrm{H}}} \times \left(1 - \frac{1 + \frac{T_{\mathrm{L}}}{T_{\mathrm{H}}}}{\sqrt{1 + ZT} + \frac{T_{\mathrm{L}}}{T_{\mathrm{H}}}}\right),$$

here $T_{\mathrm{H/L}}$ are the high/low temperatures of the hot/cold baths. From the above formula, one can conclude that the larger temperature differences, $T_{\mathrm{H}} - T_{\mathrm{L}}$, will lead to higher efficiency. The upper limit of the value of $\eta_{\max}$ can be achieved at the limit $T_{\mathrm{L}}/T_{\mathrm{H}} = 0$. For the value $ZT = 1$, $\eta_{\max}$ can be exceed 0.29, so thermoelectric devices with $ZT \geq 1$ are regarded as good thermoelectrics performance, while value of $ZT \geq 3$, corresponding to $\eta_{\max} \geq 0.5$, is needed to compete with conventional power generators and refrigerators. More realistically, finding thermoelectric materials with $ZT \approx 2$–3, which are stable over a broad temperature range and with low parasitic losses, is expected presently for thermoelectric applications [35, 36].

13.3 Thermoelectric of 2D Graphene and Pristine GNRs

For 2D graphene monolayer, consisting of sp^2 hybridized carbon atom structures, its electrical conductance is as high as that of copper [37]. Meanwhile, graphene possesses extremely high thermal conductivity in the range ~(4.84 ± 0.44) × 10^3 to (5.30 ± 0.48) × 10^3 W/mK at the room temperature [38, 39], it is almost an order of magnitude higher than that of copper. In addition, due to the zero band gap, the pristine graphene has relatively smaller the Seebeck coefficient [39] than the GNRs. So the pristine graphene possesses lower thermoelectric performance, and can't be directly applied as a thermoelectric material. However, the band gaps can be opened up by appropriate cutting of the graphene sheets as the nanoribbons [40–42]. Moreover, the band gap is varied by the chirality of the edge and the width of graphene ribbon [43, 44], it has been verified experimentally in [45]. For the sake of the convenience in the following discussion, we denote the armchair edge ribbons which have N_{a} carbon dimmer lines across the ribbon width as N_{a}-AGNRs, it is shown in Fig. 13.4a. In the same approach, the zigzag edge ribbons which have N_{z} carbon dimmer lines across the ribbon width are names as N_{z}-ZGNRs [2], as it is shown in Fig. 13.4b. With the above-mentioned denotation, we can discuss specifically the electron transport properties of graphene ribbons. All of the graphene ribbons with zigzag edges (ZGNRs) possess spin-polarized edge states, which the charge density is strongly localized on the zigzag edge sites, and exhibit metallic behavior [43]. In order to further understand the physical reason, we plot the energy bands for different ribbon width $N_{\mathrm{z}} = 4$, 6, 8, in Fig. 13.5, we can see that the highest valence band state and the lowest conduction band state are always degenerate at $k = \pi$, and they are nearly flat near the Fermi level. Accordingly, the charge density of states gives rise to a sharp peak at the Fermi level due to the edge states.

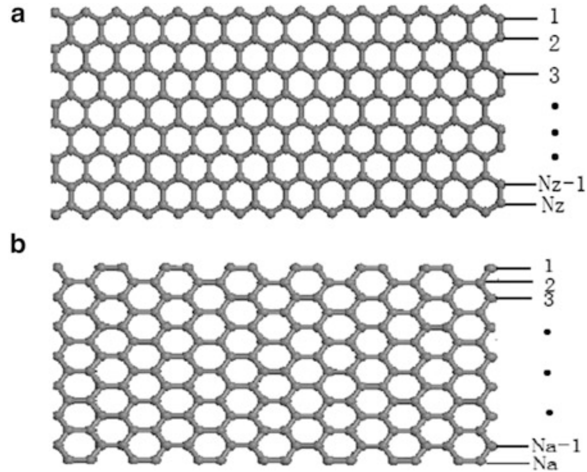

Fig. 13.4 (**a**) The pristine zigzag-edged graphene nanoribbon (N_z-ZGNR). (**b**) The pristine armchair-edged graphene nanoribbon (N_a-AGNR)

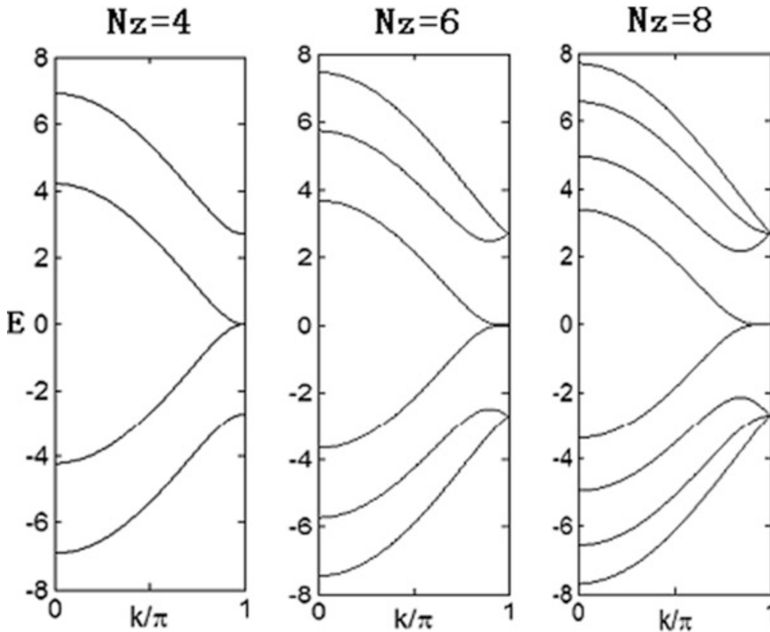

Fig. 13.5 The energy dispersion of the pristine zigzag-edged graphene nanoribbons: 4-ZGNR, 6-ZGNR, 8-ZGNR

Theses edge states are very important for the transport of electron and lead to a lot of novel physical phenomena. In contrast, the electronic properties of the armchair edges graphene ribbons (AGNRs) are dependent on their width, i.e., the N_a-AGNRs show metallic when the width $N_a = 3k + 2$ is satisfied, otherwise, the materials

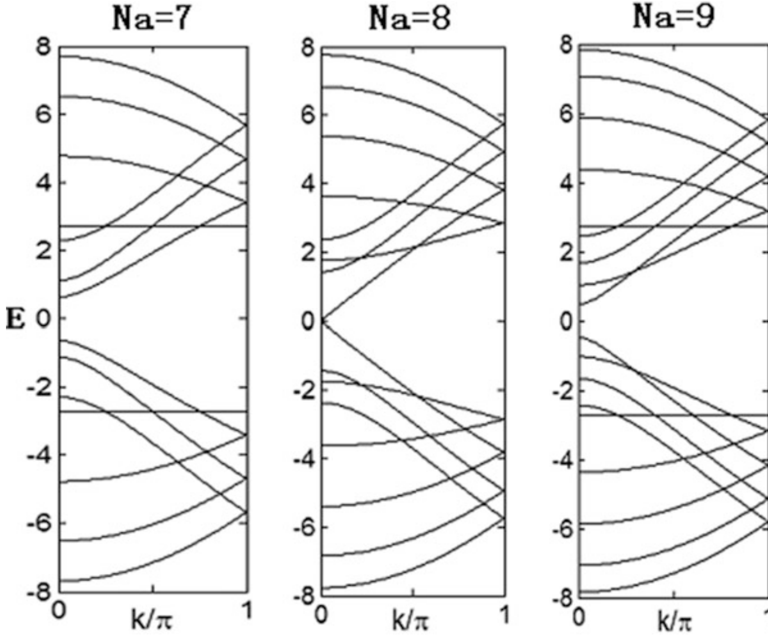

Fig. 13.6 The energy dispersion of the pristine armchair-edged graphene nanoribbons: 7-AGNR, 8-AGNR, 9-AGNR

exhibit semiconducting properties, and the band gaps have been opened in this way, where k is an integer. From the calculated band structures of three different armchair edges ribbons for $N_a = 7, 8, 9$ in Fig. 13.6, we find that the gaps are opened for 7-AGNR and 9-AGNR and become the semiconductor materials; however, the 8-AGNR always remains gapless and exhibits metallic as the pristine ZGNR. In addition, for the insulating armchair ribbons, the band gap degrades with increasing the ribbon width and tends to zero in the limit of very large N_a [43].

When the gap-band is opened, the Seebeck coefficient significantly increases at the subband edge. For the purpose of comparison, Ouyang et al. [46] studied a theoretical study on the thermoelectric properties of pristine graphene and perfect GNRs. As shown in Fig. 13.7, both of the simulated S versus μ curve have similarity at the different temperature, i.e., they are antisymmetric about the Dirac point [47] due to the symmetrical band structures, and the peaks grow near the Dirac point. However, the maximum magnitude of the thermopower of the GNR is significantly larger than that of graphene. For 2D graphene, the thermopower is less than 100 μV/K, the perfect 15-AGNR, however, is in the order of mV/K. The main reason is that S is determined by the electron transmission-weighted average value of the heat energy $E - \mu$. For the semiconducting GNR, the electrons at the conduction subband edge have much larger heat energy $E - \mu$ than the gapless 2D graphene and contribute for

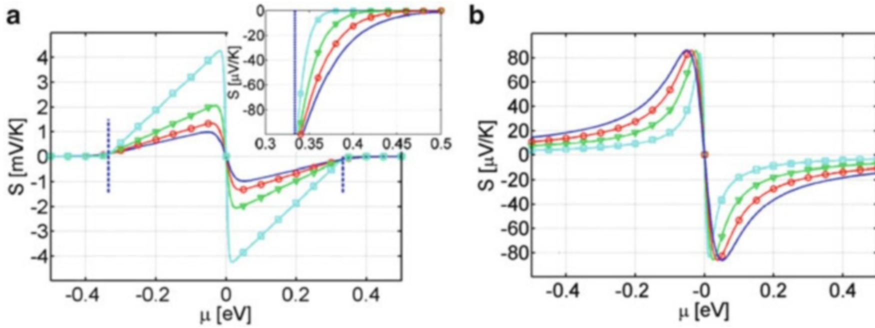

Fig. 13.7 The simulated thermopower S versus chemical potential μ curve for (**a**) a pristine 15-AGNR and (**b**) a 2D graphene at different temperatures: $T = 75$ K (*squares*), 150 K (*triangles*), 225 K (*circles*), and 300 K (*unmarked*) [46]

high thermopower. Thus, the peaks of |*S*| usually occur at the conduction subband edge, and the maximum magnitudes of |*S*| always appear at the first subband edge for pristine GNRs. Furthermore, the studies show that the Seebeck coefficient *S* can be increased by reducing the dimensionality of the system [48–50]. From the general principle, we can infer that the quasi-1D GNRs have larger *S* than the 2D graphene.

Although the high thermopower is reached, however, the pristine GNRs are always considered to be very inefficient thermoelectric materials with the figure of merit *ZT* range from 0.05 to 0.20, the reason is that the pristine GNRs posses the extremely high phonons thermal conductivity. In Figs. 13.8 and 13.9, the quantity *ZT* is plotted as a function of the chemical potential for zigzag edge 4-ZGNR, 6-ZGNR, 8-ZGNR and armchair edge 7-AGNR, 8-AGNR, 9-AGNR, respectively. The *ZT* peaks are strictly symmetric about the Dirac point for both ZGNRs and AGNRs. However, the metallic or semiconducting characters lead to very different thermoelectric properties. The metallic ZGNRs exhibits very small *ZT* factor of merit, while the semiconducting 7-AGNR and 9-AGNR have relatively high *ZT* values due to the presence of the band gap, more than several times higher than the ZGNRs. In addition, it is found that the quasimetallic AGNRs have still very low thermoelectric performance, for example, the 8-AGNR still leads to significantly low *ZT* ~0.03.

The *ZT*, which is much less than the unity, indicate the pristine GNRs is not intrinsically a good candidate for thermoelectric materials and cannot be directly utilized for thermoelectric devices without modifications. To optimize the thermoelectric properties, so that it can be achieved for thermoelectric applications, one need to largely reduce the thermal conductivity contributed by the phonons through modified approaches, but, on the other hand, the electronic conductance ideally should not be affected. Many approaches have already been examined, such as antidote lattices [51–53], point defects [46, 54, 55], edge disorder [56–58], edge

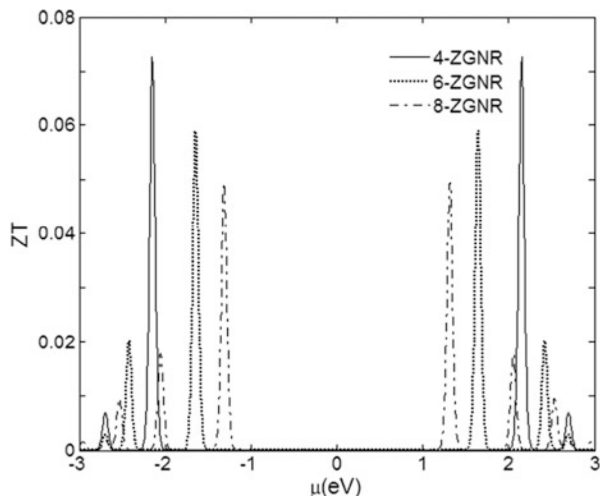

Fig. 13.8 The figure of merit *ZT* at the room temperature 300 K for the pristine zigzag-edged graphene nanoribbons: 4-ZGNR, 6-ZGNR, 8-ZGNR

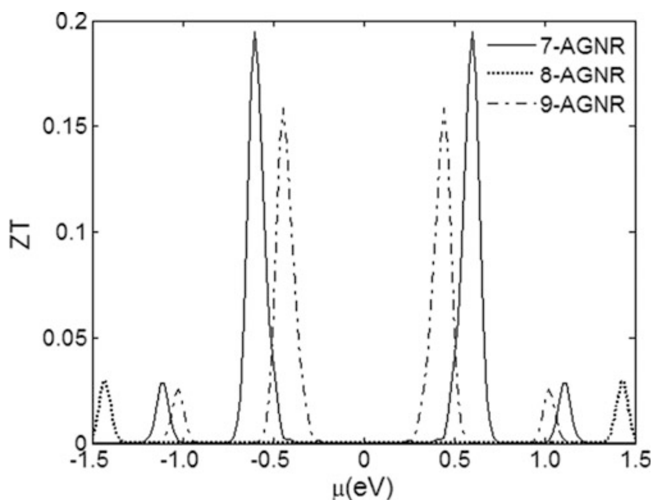

Fig. 13.9 The figure of merit *ZT* at the room temperature 300 K for the pristine armchair-edged graphene nanoribbons: 7-AGNR, 8-AGNR, 9-AGNR

passivation [59–61], random hydrogen vacancies of GNRs [62], doping of carbon isotopes [63, 64], mechanical strain [65], superlattices [66], GNRs junctions [67–71], molecular junctions [72], nanopores GNRs [73], and so on. And the high figure of merit *ZT*s have been obtained. In what following, we review the latest advances on the enhancement of thermoelectric properties and discuss how the geometry effects the *ZT* of GNRs.

13.4 Enhancement of Thermoelectric in Graphene Nanoribbons (GNRs) and Nanojunctions (GNJs)

13.4.1 Enhancement of Thermoelectric by Graphene Antidot Lattices

Antidot lattices, which were defined on a 2D electron gas at semiconductor heterostructures, can be fully fabricated on the graphene sheets by electron beam lithography [74, 75], block copolymer lithography [76, 77], nanorod photocatalysis [78], and anisotropic etching [79] with any size and shape. The class of man-made structures displays many intricate transport properties. In [41], Pedersen et al. reported that graphene antidot lattices (GALs), i.e., graphene sheets with regularly spaced holes, can controllably manipulate the electronic properties of graphene sheets. The zero band gap material can be converted into the semiconductor by introducing the antidots and the magnitude of the band gap can be tuned by the scale, edge shape, and arrangement of the antidot [42]. When the gap is opened, the thermoelectric properties of the material will keep a change accordingly. Based on the π-tight-binding model ($V_{pp\pi} = 2.7$ eV) and the Brenner potential [80], Gunst's group [52] computed the electronic and thermal transport properties of finite graphene antidot lattices and investigated how different antidot edge shapes and sizes affect the thermoelectric properties. The studied system is plotted as Fig. 13.10: an antidot lattice of finite length, with simply triangular array of hexagonal unit cells, connected by two pristine graphene leads. The results, as shown in Fig. 13.11, show that the transport gap of finite antidot lattice structures is fast converged to the gap of the infinite after six to seven unit cell repetitions. The maximal thermoelectric figure of merit *ZT* can be obtained after length convergence has been achieved. It is achieved as high as 0.25 for the armchair edge antidot at room temperature. By contrast, the *ZT* [in Fig. 13.12] is significantly lower for the GALs with zigzag edge due to the formation of edge localization states at zigzag edges. Furthermore, there is also a week increasing trend with the increasing of the hole dimension and higher *ZT* could be reached by increasing the hole dimension.

Focus on the influence of the antidot shapes, the authors, in [53], reported the thermoelectric properties of the different unit cell antidot: including the circular, rectangular, hexagonal, and triangular antidot shapes (as shown in Fig. 13.13). A third nearest-neighbor tight-binding (NNTB) model [81] and a fourth nearest-neighbor force constant model [19, 82] are considered. In more detail, the systems Cir(10,108), Rect(10,120), Hex(10,120), IsoTri(10,126), and RightTri(10,126) (Following the nomenclature introduced in [53]) have been investigated contrastively when keep nearly the same area for GALs. As shown in Fig. 13.14, iso-triangular antidot lattices have the highest thermoelectric figure of merit *ZT* due to the smallest thermal conductance resulted by longer boundaries and one of the largest Seebeck coefficient. All of these results can give us an insight into how these new materials can be utilized in the future for the thermoelectric applications.

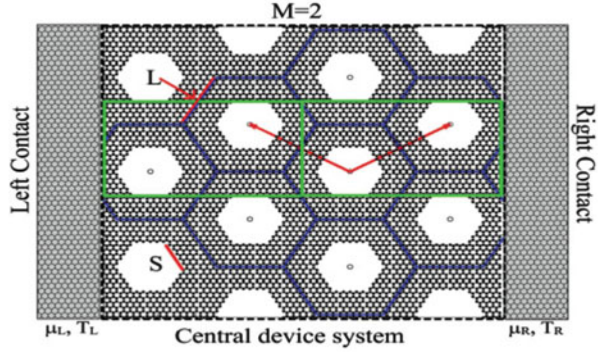

Fig. 13.10 The simulated structures of triangular graphene antidot lattices with rectangular unit cell and zigzag edge shapes. The length of $M = 2$ corresponds to four holes in the transport direction for {10, 5zz} GAL [52]

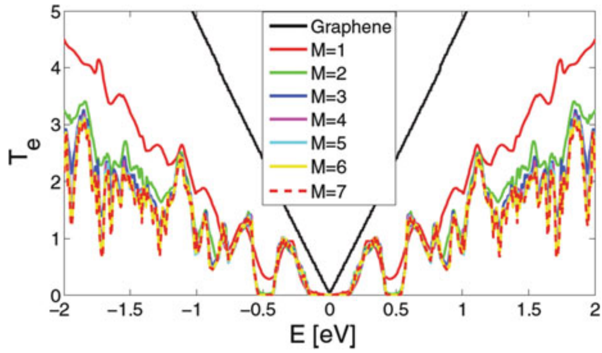

Fig. 13.11 The electronic transmission T_e of a {10, 3arm} antidot lattice as a function of energy E (eV) for different length M [52]

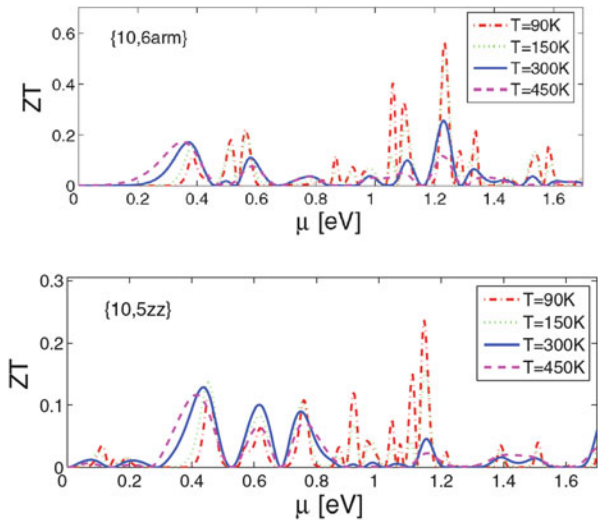

Fig. 13.12 *ZT* of {10, 6arm} and {10, 5zz} antidot lattices as a function of chemical potential μ at four temperatures [90, 150, 300, 450] K [52]

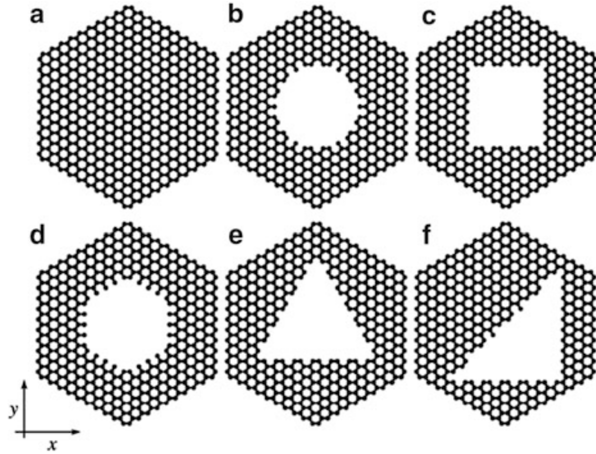

Fig. 13.13 The schematic geometrical structures for different GALs: (**a**) pristine graphene, (**b**) Circ(10,108), (**c**) Rect(10,120), (**d**) Hex (10,120), (**e**) IsoTri (10,126), (**f**) RightTRi (10,126), respectively [53]

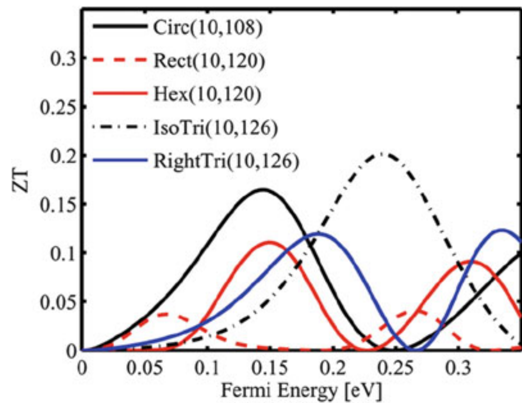

Fig. 13.14 The figure of merit *ZT* versus the Fermi energy for different GALs: Circ(10,108), Rect (10,120), Hex(10,120), IsoTri(10,126), RightTRi (10,126), respectively [53]

13.4.2 Enhancement of Thermoelectric by Resonant Tunneling of Electrons

As mentioned in the above discussion, the electronic properties of GNRs strongly depend on their edge orientations and widths [44], while the thermal conductances have little effect about the edge shapes and mainly depend on the widths. Hence, one want to know what will happen if different edge shapes GNRs are alternatively connected. Recently, Mazzamuto' group reported the thermoelectric properties of the mixed edges GNRs [67], denoted by *n*-MGNRs, and it can be seen as a mixture of both zigzag and armchair edges in the transport direction, as shown in Fig. 13.15a. In their studies, the fifth nearest-neighbor force constant model (FCM) [71] in phonon Hamiltonian and a simple NNTB electron Hamiltonian [83, 84] is considered. In the considered system, the armchair edges have an opening band gap, while zigzag edges

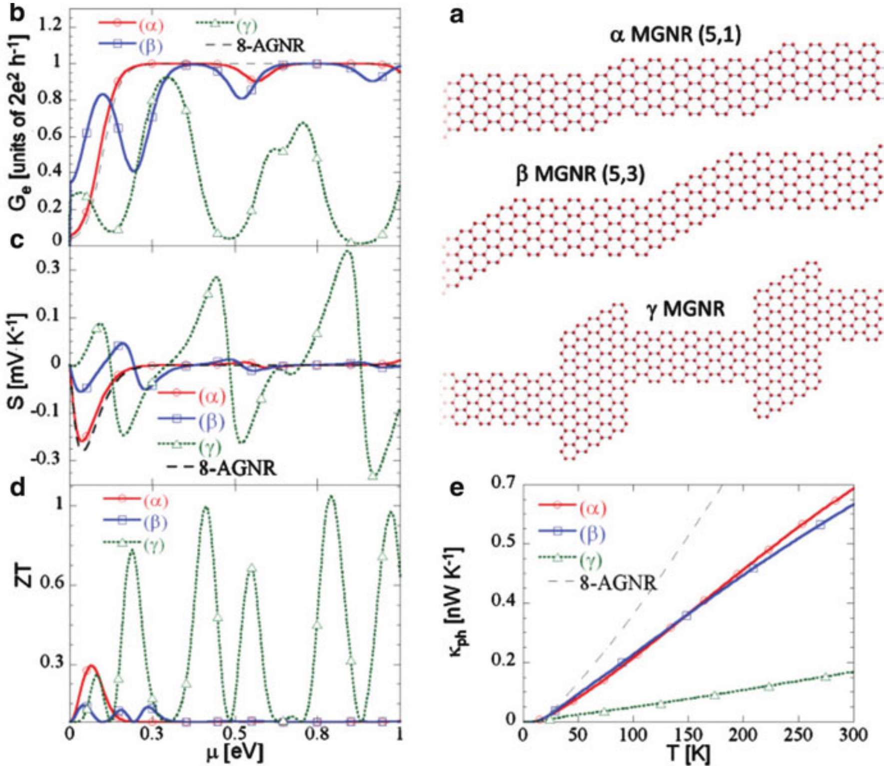

Fig. 13.15 (**a**) The schematic geometrical structures for different MGNRs: αMGNR(5,1), and βMGNR(5,3), and γMGNR. (**b**)–(**d**) The corresponding the electronic conductance G_e, Seebeck coefficient S, and thermoelectric factor of merit ZT versus the chemical potential μ, (**e**) phonon thermal conductance versus the temperature [67]

generate gapless edge localized states. For the electron transport, the armchair edges sections can be seen as barriers between localized zigzag edge states. The overall devices form the multibarrier systems. As a result, the electron strongly selectively transport through the systems. A resonant tunneling transport occurs and induces very strong oscillations of electronic conductance as predicted in [85, 86] for multibarrier systems. Since the barrier effects of the armchair edges sections, when this section becomes longer, the barrier effects become stronger. But, for a certain long of armchair edges section, the increasing of zigzag edges section can strengthen selective electron transports resulting in the larger amplitude of the conductance. As shown in Fig. 13.15b, the oscillations of the structure βMGNR(5,3) with chirality (5,3) are more pronounced than the structure αMGNR(5,1) with chirality (5,1) and give rise to several large peak value of the conductance. In terms of the Cutler–Mott theory $\{S \propto \mathrm{d}[\ln(G_e)]/\mathrm{d}E\}$, the thermopower is proportional to the logarithmic derivative of the electronic conductance, the numerical fluctuations lead to larger Seebeck coefficient S. As a consequence of the strong resonant tunneling effect, the

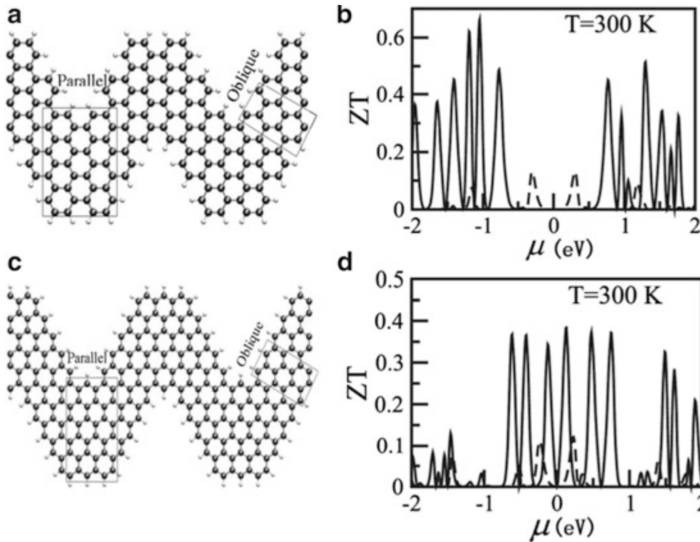

Fig. 13.16 The schematic geometrical structures for different GNWs: (**a**) AA-96, (**c**) ZZ-64; the thermoelectric figure of merit *ZT* of (**b**) AA-96 (*solid line*) and pristine 9-AGNR (*dashed line*), (**d**) the ZZ-64 (*solid line*) and 6-ZGNR (*dashed line*) as a function of the chemical potential μ at room temperature ($T = 300$ K) [87]

thermopower *S* is significantly enhanced, as seen in Fig. 13.15c, the γMGNR has larger thermopower *S* than the αMGNR(5,1) and βMGNR(5,3). In addition to the resonant tunneling effect of the electron, the thermal conductance of MGNRs is dramatically reduced due to the discrepancy between AGNR and ZGNR vibrational modes [57]. Combined with the optimized thermopower and significantly reduced phonon thermal conductance, the thermoelectric properties have been strongly enhanced in the patterned GNRs. *ZT* of the structure γMGNR can exceed unity at room temperature [in Fig. 13.15d]. It is very useful and helpful for designing high thermoelectric properties graphene nanodevices in the future.

More recently, Liang et al. [87] reported that another kinds of periodic GNR counterparts can also enhance the thermoelectric properties by using the electronic resonant tunneling effect. It is named as graphene nanowiggles (GNWs). The systems are the periodic repetitions of GNR junctions resulting in the quasi-1D wiggle-edged structures as Fig. 13.16a, b. Experimentally, using surface-assisted coupling of molecular precursors into linear poly phenylenes and their subsequent cyclodehydrogenation, these structures can be synthesized and observed by an atomically precise bottom-up approach [88] in the laboratory. Here, following the notations of GNWs introduced in [87, 89], we denote the structures with the width of the parallel and oblique sectors, i.e., AA-96 represents the GNW consisted of 9-AGNR and 6-AGNR in the parallel and oblique sectors [Fig. 13.16a], while the ZZ-64 GNW comprises 6-ZGNR and 4-ZGNR in the parallel and oblique sectors

[Fig. 13.16b], respectively. In their studies, a combination of density-functional theory and semiempirical approach were employed, the results showed that a large number of flat phonon bands existed for both AA-GNWs and ZZ-GNWs [87]. Compared to the perfect GNRs, these flat phonon bands give little contribute to thermal transports $T_{ph}(\omega)$. As a result, the thermal conductances of GNWs are significantly decreased to 0.54 nW/K (for AA-96 and ZZ-64) at the room temperature. They are much less than the thermal conductances of perfect 1.22 nW/K for 9-AGNR and 1.95 nW/K for 6-ZGNR. For electron transports, the parallel sectors can be acted as barriers between oblique sectors in the GNWs. Therefore, the GNWs can be also seen as multibarrier systems. The resonant tunneling transport may occur and induce strong oscillations of the conductance and thermopower [67, 85]. Such resonant tunneling effect preserves excellent electrical conductance. Combined with the excellent conductance and the degreasing thermal conductance, GNWs are found to have significantly enhanced thermoelectric performance, as shown in Fig. 13.16b, d, many ZT peaks value occur, and the value of maximum can reach 0.65 for AA-96, it is six to seven times larger than that of the perfect GNRs with the same width. The maximum can nearly reach 0.4 for ZZ-64 which is less than the AA-96. Among all GNWs structures studied in [87], AA-65 possesses the maximum $ZT = 0.79$ at room temperature. Most of the AA structures have ZT higher than 0.5. In contrast, the AA-GNWs are more promising candidates than ZZ-GNWs for thermoelectric applications.

13.4.3 Enhancement of Thermoelectric by Edge Currents

As mentioned above, the edge current, which results from the quasiparticles sufficiently close to the Dirac point (DP) and peaks around the edges for both ZGNRs and chiral graphene nanoribbons (CGNRs), plays an important role in electronic transport properties. Thus, drilling nanopores in the interior will not substantially effects the so-called edge current. Experimentally, the nanopore arrays in GRNs [77, 90] have been realized recently by a variety of advanced techniques. In [73], Chang et al. reported the thermoelectric of GNRs with an array of nanopores in transport direction for ZGNRs and CGNRs. The schematic view of 20-ZGNR and (8,1)-CGNR with a chiral angle $\theta = 5.8°$ are shown as Fig. 13.17a, c. The diameter of each nanopore and distance of nearest-neighbor nanopore are displayed, respectively. The length of GNRs is set to $L = 1.2$ μm in actual calculations, composed of 300 nanopores. In these models, on the one hand, the electron transports are not substantially modified due to the edge currents, which are reduced from $T_e = 3$ in infinite homogeneous GNRs to $T_e \approx 2$ near the DP, on the other hand, since the homogeneity are broken by introduced nanopores in nanowire, the propagation of phonons are substantially impeded due to the imperfect transports. Correspondingly, the lattice thermal conductance significantly reduced from the $\kappa_{ph} = 6.2$ nW/K for perfect 20-GNR to $\kappa_{ph} = 0.68$ nW/K for 20-GNRs with nanopores, and from $\kappa_{ph} = 3.5$ nW/K for (8,1)-CGNR to $\kappa_{ph} = 0.32$ nW/K for (8,1)-CGNR with nanopores at room temperature, which is an order of reducing for nanopores GNRs.

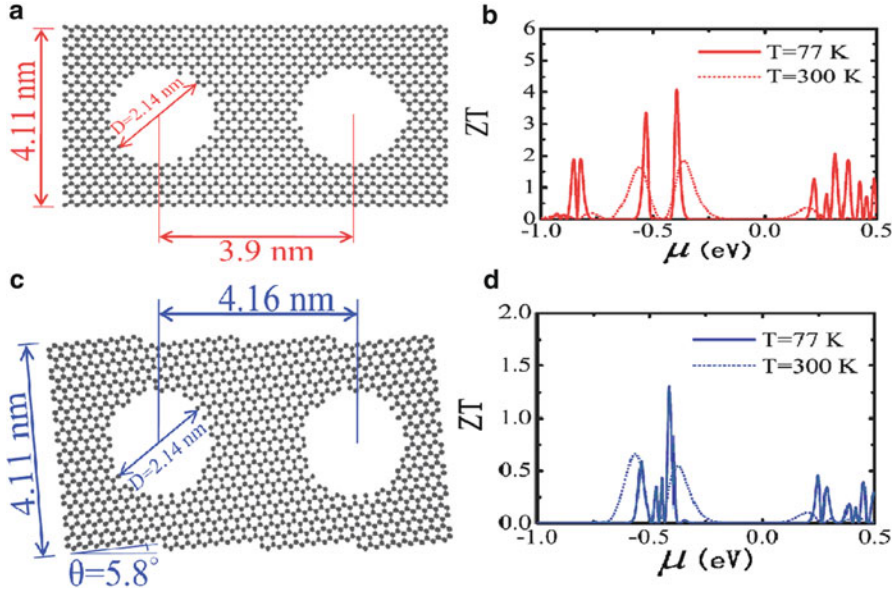

Fig. 13.17 The schematic geometrical structures: (**a**) 20-ZGNR and (**c**) (8,1)-CGNR with chiral angle $\theta = 5.8°$, the length of these GNRs is set to $L = 1.2$ μm and compose of 300 nanopores in real structure; the corresponding thermoelectric figure of merit *ZT*of (**b**) 20-ZGNR and (**d**) the (8,1)-CGNR as a function of the chemical potential μ at both room temperature 300 K (*dashed line*) and liquid nitrogen 77 K (*solid line*) [73]

Furthermore, the length of $L = 1.2$ μm is close to the limit of electron and thermal transports beyond which a further increase of L does not change significantly the conductance G_e and the thermal conductance κ_{ph}. Benefit from these two effects, the thermoelectric efficient can be boosted dramatically, the maximum $ZT \approx 4$ at liquid nitrogen temperature $T = 77$ K and $ZT \approx 2$ at room temperature $T = 300$ K can be obtained by introduced the periodic array of identical nanopores. In contrast, the CGNR with a periodic nanopores possess lower thermoelectric, but the values of ZT can still excess unity at $T = 77$ K. Hence, the ZGNRs and CGNRs with an array of nanopores in their interior could act as the building blocks of highly efficient thermoelectric devices.

13.4.4 Enhancement of Thermoelectric by Supercell Structures

In addition to the graphene, hexagonal boron nitride (h-BN) is also single-atomic-layer honeycomb materials [91–95]. Similarly, because of the quantum confinement effect, it exhibits a various novel physical phenomenon in electric and thermal

transports. Furthermore, the 2D hybrid sheet, which composed of graphene and h-BN, has been synthesized by the thermal catalytic chemical vapor deposition method [96] in experiment. Recently, Yang et al. [66] reported that the hybrid graphene/boron nitride nanoribbons (BCNNRs) can remarkably enhance the thermoelectric properties of nanomaterial. As shown in Fig. 13.18a, b, the central scattering region is composed of the hybrid graphene/boron nitride ribbons with the armchair and zigzag edges, named as A-BCNNR and Z-BCNNR, while the left/right lead is the pristine GNRs for all systems. The widths of ribbons are labeled by N_a and N_z for armchair and zigzag edges, respectively. L_{BN} (L'_{BN}) and L_C (L'_C) are the lengths of h-BN and graphene in the supercell. Accordingly, $L_S = (L_{BN} + L_C)$ and $L'_S = (L'_{BN} + L'_C)$ represent the lengths of the supercell in armchair- and zigzag-edged nanoribbons, respectively. Compared with the pristine armchair-edged ribbons, the figure of merit *ZT* can be boosted about 10–20 times for metallic AGNRs with width index $3k + 2$ (where k is the positive integer) as shown in Fig. 13.18c, e, but the *ZT* have small enhancement about 1.5–3 times for semiconductor AGNRs. In addition, for the zigzag edge structure, *ZT* is improved two to three times compared to that of pristine ZGNRs (shown in Fig. 13.18d, f). In fact, these hybrid structures have strong effects on the thermal and electronic conduction due to the destructive channels which block the carrier transmission. The decrease of electronic conductance is even stronger than the thermal conductance. But thanks to the destructive channels of electron transmission, the Seebeck coefficients have greatly improved in BCNNRs structures. Therefore, the increase of the Seebeck coefficient, together with the corresponding decrease of the thermal conductance, outweighs the decrease in the electrical conductance and leads to very high *ZT*. Furthermore, for a given width of BCNNRs, with the increase of the periodic number N, the *ZT* gradually increase firstly, but, when the periodic number is greater than 6, the *ZT* approaches almost a constant value.

The physical reason is that, when the number N is large enough, the whole central scattering region can be approximately seen as a superlattice structure composed of alternating h-BN and graphene, thus the electron and phonon transports approach the value of the superlattice and have small change for more periodic number. Hence, these hybrid nanostructures provide another route for building highly efficient thermoelectric devices.

13.4.5 Enhancement of Thermoelectric by Heterojunctions

The heterojunction is one of the most important structures in the nanomaterial. It can be used to control and regulate effectively the thermal and electric transport. As a result, the thermoelectric performance of nanomaterials will be changed drastically by the introduced heterojunction structures. In [68], we have investigated systematically the effect of the heterojunction to the thermoelectric properties for AGNRs and ZGNRs. How to improve the thermoelectric efficiency has also been presented.

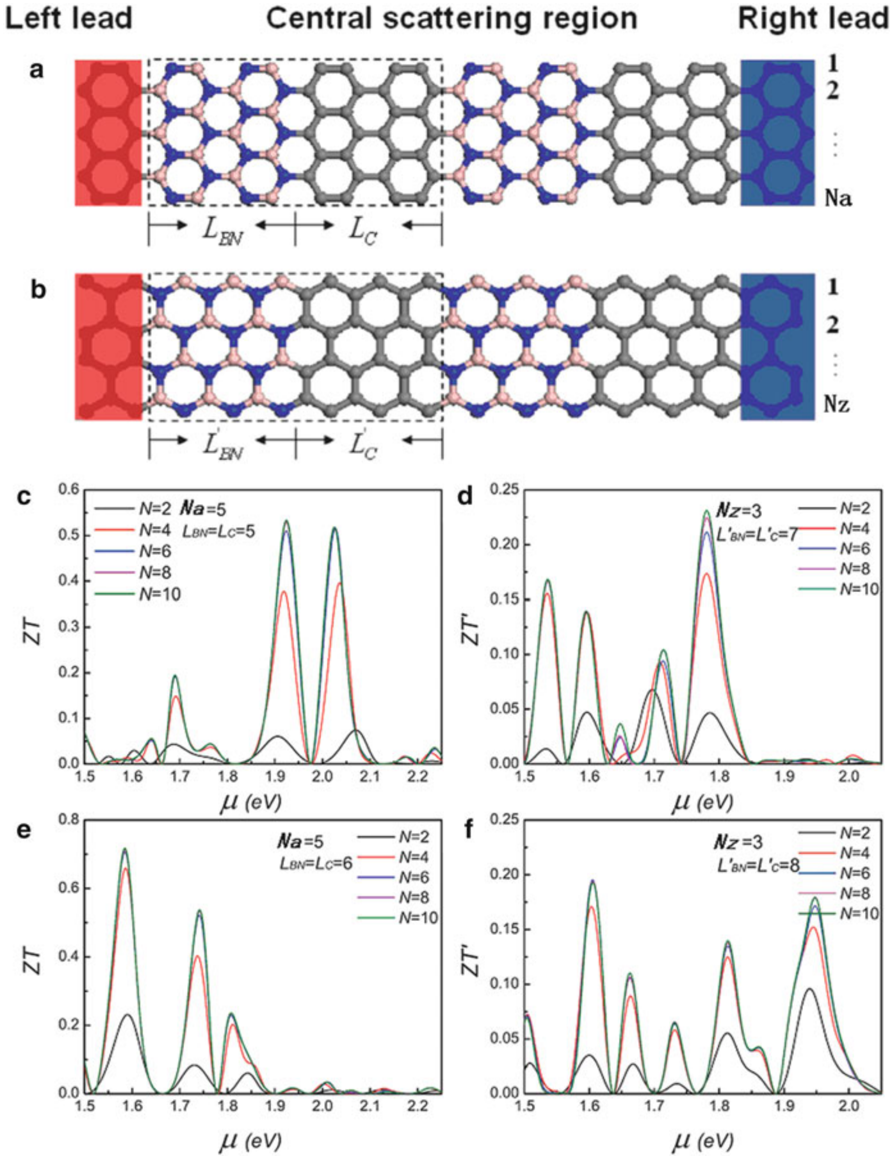

Fig. 13.18 The schematic geometrical structures: (**a**) A-BCNNR and (**b**) Z-BCNNR; the corresponding thermoelectric figure of merit ZT (ZT') with different width N_a(N_z), periodic number (N) and length of the superlattices L_S(L'_S) of BCNNRs as a function of the chemical potential μ at both room temperature 300 K: (**c**) and (**e**) for A-BCNNRs; (**d**) and (**f**) Z-BCNNRs [66]

The studied structures are simulated in Fig. 13.19a, b, two typical heterojunction structures with zigzag and armchair edges are considered. In the ballistic region, the phonon–phonon and electron–phonon interactions are neglected because they are very weak. In our calculation, we considered the nearest coupling for the electric

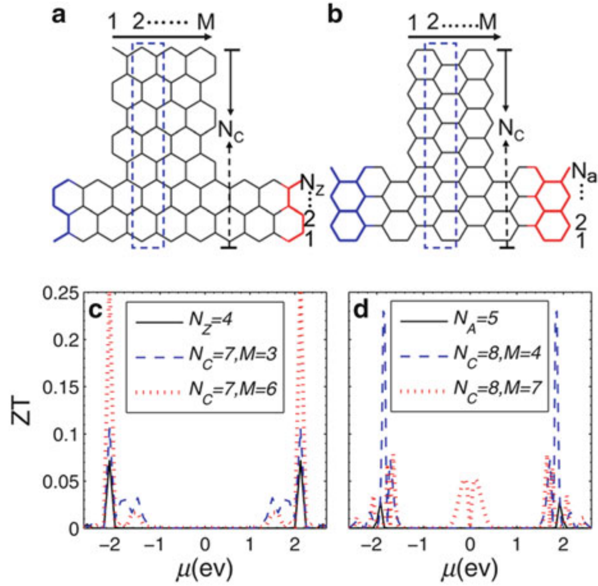

Fig. 13.19 Schematic structure of (**a**) zigzag- and (**b**) armchair-edge heterojunctions. Thermoelectric figure of merit *ZT* as a function of the chemical potential μ at room temperatures $T = 300$ K for (**c**) ZGNRs and (**d**) ZGNRs

transport and the fourth nearest-neighbor FCM for the thermal transport in the tight-binding model, some interesting result has been found. When the heterojunctions are introduced in GNRs, the electronic transports $T_e(E)$ are decreased by the interface elastic scattering for both AGNRs and ZGNRs. But, there are distinctly different between these two transports due to the different electronic band structures. The electric transport keeps the quasi-ballistic behavior within the first conductance band. Whereas the quasi-ballistic transport is destroyed strongly by the interface mismatching. So, it is more sensitive to the structural parameters of the structures. On the other hand, the phonon thermal conductances are also dramatically decreased due to the phonon-interface scatting. Compared to the AGNRS, ZGNRs have more available phonon channels to conduct heat. Moreover, the dispersive phonon bands are generally dominated at the low frequency, which are always less scattered by the interface mismatching. As a result, the reduction of ZGNRs is less than AGNRs. It is similar to the electronic case. In addition, the dips of electric transmission $T_e(E)$ rise near the subband edge due to the interface elastic scattering. These rapid variations of $T_e(E)$ greatly enhance the Seebeck coefficient (thermopower) which fully consists with the Cutler–Mott theory mentioned above. Together with the depressed phonon thermal conductances, the enhanced thermopowers lead to high thermoelectric properties in the systems. As shown in Fig. 13.19c, d, the maximum *ZT* is improved nearly an order of magnitude for the 5-AGNR with $N_c = 8$, $M = 4$ and five times for the 4-ZGNR with $N_c = 7$, $M = 6$. These results provide an efficient way to improve the thermoelectric performance of GNRs by the heterojunctions.

13.4.6 Enhancement of Thermoelectric by Defects

In the process of patterning epitaxially grown graphene, GNRs may have several kinds of defects such as pentagon/heptagon defects, vacancies, adatoms, substitution, disorder, and even combinations of some of them. Defects can lead to the localized states in the vicinity of defects at particular energies in GNRs, which can significantly affect both the electronic and thermal transport properties. For example, it has been known that defects can induce the form of additional gaps of the electronic transmission, which benefit to enhance the peaks of the Seebeck coefficient. On the other hand, defects also can significantly decrease the phonon thermal conductance. Here, we introduce the defective disorder on the thermoelectric performances of GNRs. The defective disorders are treated by randomly removing the atoms (carbon or hydrogen) out of the channel. Based on the distributed positions of defects, two representative defective disorders such as edge disorder (namely edge roughness) and lattice vacancy with random distribution in bulk region are considered. Some interesting properties are revealed.

1. The edge disorder effects in zigzag GNRs

It has been demonstrated in [97] that how the edge disorder affect the electronic and phononic transport properties of zigzag GNRs. The modeled structure is shown in Fig. 13.20a. The central region includes the disorder part, whereas the left and right are taken as semi-infinite perfect GNRs of given width. For different lengths L, an ensemble of edge disordered ZGNRs is generated. After performing the electronic and phononic calculations for each configuration, the transmission coefficients are obtained by averaging the transmission spectra over the ensembles of 100 disordered edge profiles. From the results in [97], it is found that, compared to the perfect case, the transmission coefficient reduce significantly even for samples as short as 50 nm, and the reduction is more evident for longer samples. At the same time, by comparing the reduction in transmission values for two different widths, one can see that the phonon transmission coefficient is lower for the higher disorder degree. It is also seen that the edge disorder reduces the phonon transport effectively for all energy values except very low energies, which is very different from the results that isotopic disorder or Anderson-like disorder in nanotubes suppress highest-energy modes more strongly than other modes. This is because that the edge disorder not only modifies the vibrational frequencies but also changes the number of modes throughout the ribbon except the mode $\omega = 0$. On the other hand, the influence of the edge disorder on the electronic transport is not parallel to the phonon case. When the edge disorder is introduced, the electronic transmission coefficient drops shapely and even a transport gap opens at the charge neutrality point (CNP). Such the gap is attributed to the fact that the electronic states are fully localized at the edge at the CNP. When the relative amount of disorder or the length of the system is increased, the width of the gap, which is opened by edge disorder, is also increased. But close to the subband edges, the transmission coefficient T_e is abruptly increased by the edge disorder. Hence, the large derivatives of T_e can be

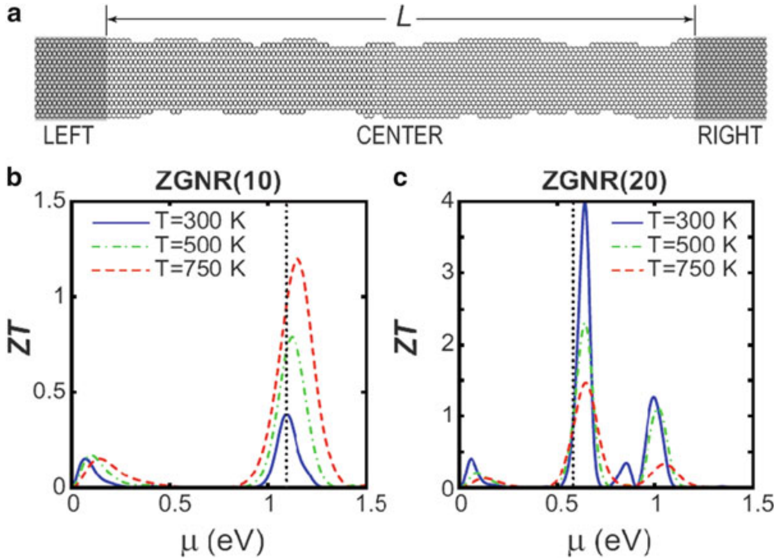

Fig. 13.20 (**a**) Schematic structure of the ZGNR with the edge disorder. Thermoelectric figure of merit *ZT* as a function of the chemical potential μ at different temperatures $T = 300, 500, 750$ K for (**b**) 10-ZGNR and (**c**) 20-ZGNR [97]

obtained in this system, which is useful to enhance the thermoelectric properties of GNRs. The calculated *ZT* value is shown in Fig. 13.20b, c. As expected, the maximum of *ZT* is enhanced strongly compared to the perfect case. At room temperature, *ZT* reaches 0.39 and 4 for 10-ZGNR and 20-ZGNR, respectively. For 10-ZGNR, the *ZT* increases with the temperature up to 1.2 at 750 K, while for the wider ribbon it decreases with the temperature. These indicate that high *ZT* can be achieved sensitively depending on the ribbon width and the relative amount of edge disorder.

2. The edge disorder effects in armchair GNRs

Figure 13.21a shows the 16-AGNR structure with different values of roughness index: 5 %, 10 %, 15 %, respectively. The roughness index is defined as the probability for each edge dimer to be removed. The phonon thermal conductance as a function of temperature is shown in Fig. 13.21b, while the electronic conductance G_e, the Seebeck coefficient S and the figure of merit *ZT* as a function of the chemical potential μ at room temperature are plotted in Fig. 13.21c–e, respectively. Here, to make a comparison, the perfect case is also given. From Fig. 13.21b, it is seen that the edge disorder decreases strongly the phonon thermal conductance which decays from 2.4 nW/K for the pristine case to about 1.6 nW/K for the disordered armchair GNRs at room temperature. These results for roughness indices of 5 and 10 % seem to be similar but it is actually fortuitous. In principle, the decrease of the thermal conductance induced by the edge disorder is useful to enhance the *ZT*. However, the *ZT* value

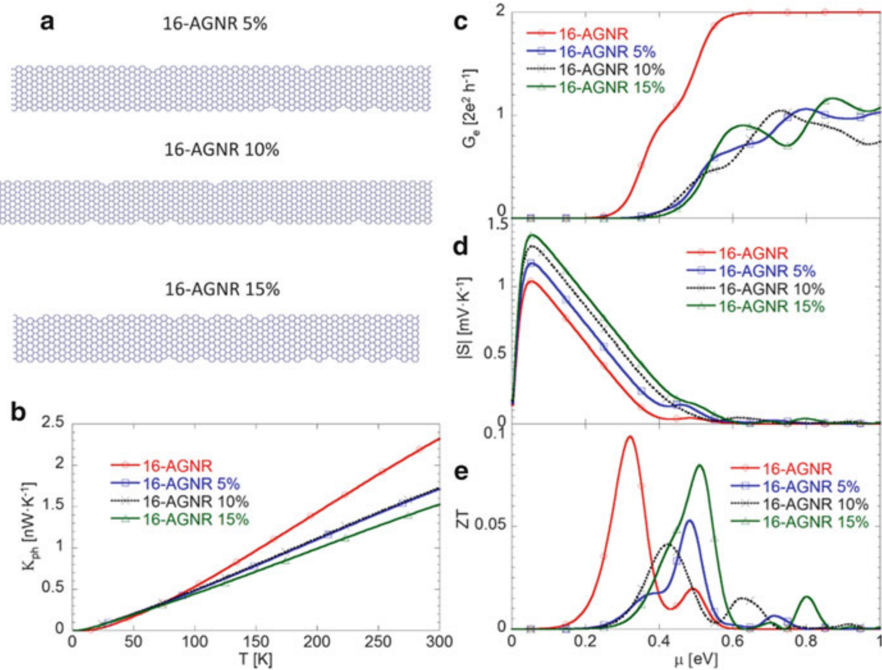

Fig. 13.21 (**a**) 16-AGNR structure with different values of roughness index: 5, 10, and 15 %. (**b**) Phonon thermal conductance as a function of the temperature *T*, (**c**) electronic conductance, (**d**) Seebeck coefficient, and (**e**) figure of merit *ZT* as a function of the chemical potential μ for the perfect 16-AGNRand 16-AGNRs with edge disorders [98]

for the edge disordered armchair GNRs is lower than that for the perfect case, since the edge disorder also affects the electronic transport properties with negative overall effects on the *ZT*. As shown in Fig. 13.21c, the electric conductance is decreased for all roughness indexes. Additionally, the random edge profiles produce random oscillations of electronic conductance at high energy. As a result, the *ZT* peaks of rough GNRs are all smaller than that of the perfect AGNR. The peak values of the *ZT* and their energy position strongly depend on the random edge profile which is impossible to control. Thus, the edge roughness cannot be considered as an efficient way to improve the thermoelectric properties of armchair GNRs, very different from that for the zigzag case.

3. Lattice vacancies in bulk region

Similar to the case with the edge disorder, the phonon thermal conductance is decreased by the lattice vacancy inside the ribbon (as shown in Fig. 13.22a). Figure 13.22b shows the phonon thermal conductance of the 16-AGNR with lattice vacancy distributed randomly is almost two times smaller than the perfect 16-AGNR. This decrease is slightly less pronounced for the 16-AGNR with lattice vacancies

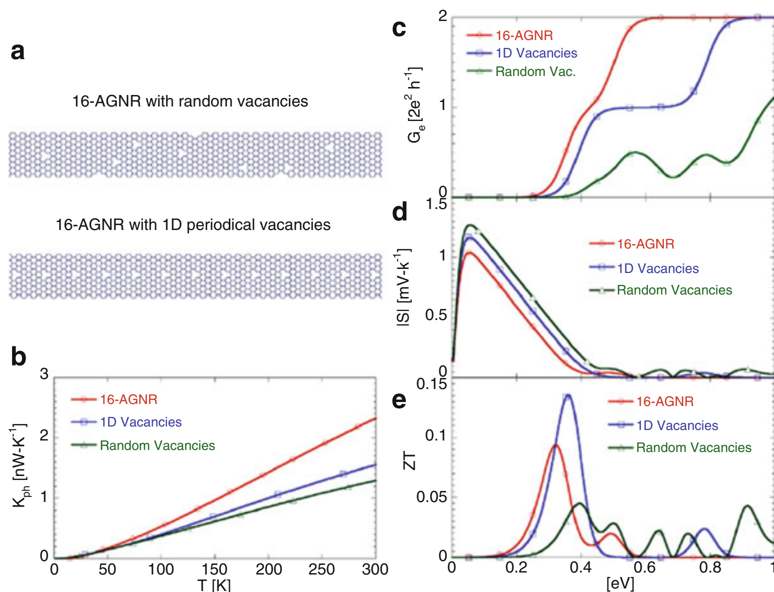

Fig. 13.22 (**a**) 16-AGNR structure with random vacancies and with periodic distribution of vacancies. (**b**) Phonon thermal conductance as a function of the temperature T, (**c**) electronic conductance, (**d**) Seebeck coefficient, and (**e**) figure of merit ZT as a function of the chemical potential μ [98]

distributed periodically. Due to the introduction of lattice defect, the band gap is enhanced and the electronic conductance tends to be reduced (Fig. 13.22c).

Meanwhile, the enhancement of the Seebeck coefficient is observed in Fig. 13.22d. Similar to the armchair case with the edge disorders, the lattice vacancies with random distribution have a negative influence on the thermoelectric properties in armchair GNRs. Figure 13.22e shows that the peak of the ZT in the case with random vacancies decreases from 0.08 (the perfect value) to 0.03. On the contrary, when the lattice vacancies are distributed periodically, the peak of the ZT increases to 0.13 due to the effective width reduction.

13.5 Concluding Remarks

This chapter has reviewed comprehensively the thermoelectric properties of the 2D graphene, 1D GNRs, and quasi-1D graphene nanoribbon-based heterojunctions. How to enhance the thermoelectric of these nanostructures by artificially decorated approaches, for instance, edge disorder, defect-engineering, antidot lattices, nanopores, and so on, has also been discussed in detail. In the most of the case, the thermoelectric figure of merit ZT can be significantly enhanced and exceed the unit. So the artificially structured graphene can be regarded as the good thermoelectric

materials and can become the promising candidates for taking place of the semiconductor Si in nanodevices and nanocomposites.

However, from the published literature on the thermoelectric properties of these structures, it can be found easily that most previous researches mainly focus on the theoretical level, the measurement of experiment is scarcely reported [99–102], it is a very important for further understanding the real thermoelectric properties of the graphene. Hence, intensive work would be attempted to investigate the thermoelectric of the material on the experimental level.

In addition, there exist some imperfections in the previous theoretical investigations. (1) Most of the discussions are limited in the ballistic region for the thermal transport. The nonlinear interaction of the system Hamiltonian in the center has been ignored in the calculation of thermal conductance contributed by phonon. But for real systems, the nonlinear interaction describes the resistive Umklapp phonon–phonon scattering which plays an important role in the interpretation of experiments; it may change the transmission spectrum and will lead to decrease in the phonon thermal conductance, especially for high temperature region. (2) Compared with the phonon–phonon scattering, the electron–phonon scattering [46, 63] is relatively weak in thermal transport, it is also neglected due to the difficult of the approach. (3) Mean-field approximation has been utilized in the NEGF method, which only works well for relatively weak nonlinear interaction [27]. Furthermore, the self-consistent iteration fails to converge for complex structures. When taking account of relatively strong nonlinear interaction in high temperature, another good approximation must be found to adapt for the complex case. (4) Under a weak magnetic field, the phonon Hall effect [12, 103] will appear, meanwhile, the spin of the electron in the graphene will be influenced. Therefore, the transport of thermal and electron will be change by the magnetic field. Moreover, it gives rise to Hall effect of electron under the electric field. The conductance will be affected inevitably. All of these case, the thermoelectric properties will be largely changed by the extra field energy. But it has little been reported in these aspects. So it is still a challenge to understand thoroughly the thermoelectric properties of graphene, even a lot of significant research progresses have been achieved.

Acknowledgements This work was supported by the National Natural Science Foundation of China (Nos. 91227125 and 11274105), by the National Basic Research Program of China (Nos. 2012CB932703 and 2011CB606405), by Hunan Provincial Natural Science Foundation of China (No. 12JJ2002). The authors are grateful to all the other authors of related papers and some cited Figures.

References

1. Novoselov, K.S., Geim, A.K., Morozov, S.V., Jiang, D., Zhang, Y., Dubonos, S.V., Grigorieva, I.V., Firsov, A.A.: Electric field effect in atomically thin carbon films. Science **306**, 666 (2004)
2. Xu, Y., Chen, X.B., Gu, B.L., Duan, W.H.: Intrinsic anisotropy of thermal conductance in graphene nanoribbons. Appl. Phys. Lett. **95**, 233116 (2009)

3. Xu, Y., Chen, X.B., Wang, J.S., Gu, B.L., Duan, W.H.: Thermal transport in graphene junctions and quantum dots. Phys. Rev. B **81**, 195425 (2010)
4. Masahiro, M., Takahiro, Y., Kazuyuki, W.: Defect-induced circulating thermal current in graphene with nanosized width. Phys. Rev. B **77**, 033412 (2008)
5. Takahiro, Y., Kazuyuki, W., Kazuaki, M.: Empirical-potential study of phonon transport in graphitic ribbons. Phys. Rev. B **70**, 245402 (2004)
6. Lan, J.H., Wang, J.S., Gan, K.G., Chin, S.K.: Edge effects on quantum thermal transport in graphene nanoribbons: tight-binding calculations. Phys. Rev. B **79**, 115401 (2009)
7. Xu, Z.P., Zheng, Q.S., Chen, G.H.: Elementary building blocks of graphene-nanoribbon-based electric devices. Appl. Phys. Lett. **90**, 223115 (2007)
8. Mak, K.F., Sfeir, M.Y., Wu, Y., Lui, C.H., Misewich, J.A., Heinz, T.F.: Measurement of the optical conductivity of graphene. Phys. Rev. Lett. **101**, 196405 (2008)
9. Abergel, D.S.L., Fal'ko, V.I.: Optical and magneto-optical far-infrared properties of bilayer graphene. Phys. Rev. B **75**, 155430 (2007)
10. Gusynin, V.P., Sharapov, S.G.: Transport of Dirac quasiparticles in graphene: Hall and optical conductivities. Phys. Rev. B **73**, 245411 (2006)
11. Xing, Y.X., Sun, Q.F., Wang, J.: Nernst and Seebeck effects in a graphene nanoribbon. Phys. Rev. B **80**, 235411 (2009)
12. Peng, F.: Magnetic field induced thermal effect of phonons in graphene. Physica Status Solidi (b) **248**(6), 1388–1391 (2011)
13. Baek, I.B., Yang, J.H., Cho, W.J., Ahn, C.G., Im, K., Lee, S.: Electron beam lithography patterning of sub-10 nm line using hydrogen silsesquioxane for nanoscale device applications. J. Vac. Sci. Technol. B **23**, 3120 (2005)
14. Bilenberg, B., Schøler, M., Shi, P., Schmidt, M.S., Bøggild, P., Fink, M., Schuster, C., Reuther, F., Gruetzner, C., Kristensen, A.: Comparison of high resolution negative electron beam resists. J. Vac. Sci. Technol. B **24**, 1776 (2006)
15. van Kan, J.A., Bettiol, A.A., Watt, F.: Proton beam writing of three-dimensional nanostructures in hydrogen silsesquioxane. Nano Lett. **6**(3), 579–582 (2006)
16. Remeika, M., Bezryadin, A.: Sub-10 nanometre fabrication: molecular templating, electron-beam sculpting and crystallization of metallic nanowires. Nanotechnology **16**(1172) (2005)
17. Nagase, T., Gamo, K., Kubota, T., Mashiko, S.: Maskless fabrication of nanoelectrode structures with nanogaps by using Ga focused ion beam. Microelectron. Eng. **78–79**(Special Issue), 253–259 (2005)
18. Areshkin, D.A., White, C.T.: Building blocks for integrated graphene circuits. Nano Lett. **7**(11), 3253–3259 (2007)
19. Saito, R., Dresselhaus, G., Dresselhaus, M.: Physical Properties of Carbon Nanotubes. Imperial College Press, London (1998)
20. Dresselhaus, M.S., Dresselhaus, G., Sugihara, K., Spain, I.L., Goldberg, H.A.: Graphile Fibers and Filaments. Springer Series in Materials Science, vol. 5. Springer, Berlin (1988)
21. Painter, G.S., Ellis, D.E.: Electronic band structure and optical properties of graphite from a variational approach. Phys. Rev. B **1**(4747) (1970)
22. Jishi, R.A., Venkataraman, L., Dresselhaus, M.S., Dresselhaus, G.: Phonon modes in carbon nanotubules. Chem. Phys. Lett. **209**, 77–82 (1993)
23. Wang, J.S., Wang, J., Zeng, N.: Nonequilibrium Green's function approach to mesoscopic thermal transport. Phys. Rev. B **74**, 033408 (2006)
24. Wang, J.S., Zeng, N., Wang, J., Gan, C.K.: Nonequilibrium Green's function method for thermal transport in junctions. Phys. Rev. E. **75**, 061128 (2007)
25. Mingo, N.: Anharmonic phonon flow through molecular-sized junctions. Phys. Rev. B **74**, 125402 (2006)
26. Yamamoto, T., Watanabe, K.: Nonequilibrium Green's function approach to phonon transport in defective carbon nanotubes. Phys. Rev. Lett. **96**(255503) (2006)
27. Wang, J.S., Wang, J., Lü, J.T.: Quantum thermal transport in nanostructures. Eur. Phys. J. B **62**, 381 (2008)

28. Jiang, J.W., Wang, J.S., Li, B.W.: A nonequilibrium Green's function study of thermoelectric properties in single-walled carbon nanotubes. J. Appl. Phys. **109**, 014326 (2011)
29. Sancho, M.P.L., Sancho, J.M.L., Rubio, J.: Highly convergent schemes for the calculation of bulk and surface Green functions. J. Phys. F Met. Phys. **15**, 851 (1985)
30. Landauer, R.: Spatial variation of currents and fields due to localized scatterers in metallic conduction. IBM J. Res. Dev. **1**(3), 223–231 (1957)
31. MacDonald, D.K.C.: Thermoelectricity, An introduction to the Principles. Dover, Mineola, NY (2006)
32. Goldsmid, H.J.: Thermoelectric Refrigeration. Plenum, New York (1964)
33. Goldsmid, H.J.: Electronic Refrigeration. Pion, London (1986)
34. Nolas, G.S., Sharp, J., Goldsmid, J.: Thermoelectrics: Basic Principles and New Materials Developments. Springer, New York (2001)
35. Vining, C.B.: An inconvenient truth about thermoelectrics. Nat. Mater. **8**, 83 (2009)
36. Tritt, T.M.: Thermoelectric phenomena, materials, and applications. Annu. Rev. Mater. Res. **41**, 433 (2011)
37. Chen, J.H., Jang, C., Xiao, S., Ishighami, M., Fuhrer, M.: Intrinsic and extrinsic performance limits of graphene devices on SiO2. Nat. Nanotechnol. **3**, 206 (2008)
38. Balandin, A.A., Ghosh, S., Bao, W., Calizo, I., Teweldebrhan, D., Miao, F., Lau, C.N.: Superior thermal conductivity of single-layer graphene. Nano Lett. **8**, 902 (2008)
39. Seol, J.H., Jo, I., Moore, A.L., Lindsay, L., Aitken, Z.H., Pettes, M.T., Li, X., Yao, Z., Huang, R., Broido, D., Mingo, N., Ruoff, R.S., Shi, L.: Two-dimensional phonon transport in supported graphene. Science **328**, 213 (2010)
40. Han, M.Y., Özyilmaz, B., Zhang, Y., Kim, P.: Energy band-gap engineering of graphene nanoribbons. Phys. Rev. Lett. **98**, 206805 (2007)
41. Pedersen, T.G., Flindt, C., Pedersen, J., Jauho, A.P., Mortensen, N.A., Pedersen, K.: Optical properties of graphene antidot lattices. Phys. Rev. B **77**, 245431 (2008)
42. Zhang, A., Teoh, H.F., Dai, Z., Feng, Y.P., Zhang, C.: Band gap engineering in graphene and hexagonal BN antidot lattices: a first principles study. Appl. Phys. Lett. **98**, 023105 (2011)
43. Nakada, K., Fujita, M., Dresselhaus, G., Dresselhaus, M.S.: Edge state in graphene ribbons: nanometer size effect and edge shape dependence. Phys. Rev. B **54**(17954) (1996)
44. Li, T.C., Lu, S.P.: Quantum conductance of graphene nanoribbons with edge defects. Phys. Rev. B **77**, 085408 (2008)
45. Ritter, K.A., Lyding, J.W.: The influence of edge structure on the electronic properties of graphene quantum dots and nanoribbons. Nat. Mater. **8**, 235 (2009)
46. Ouyang, Y., Guo, J.: A theoretical study on thermoelectric properties of graphene nanoribbons. Appl. Phys. Lett. **94**, 263107 (2009)
47. Zuev, Y.M., Chang, W., Kim, P.: Thermoelectric and magnetothermoelectric transport measurements of graphene. Phys. Rev. Lett. **102**, 096807 (2009)
48. Dresselhaus, M., Chen, G., Tang, M., Yang, R., Lee, H., Wang, D., Ren, Z., Fleurial, J., Gogna, P.: New directions for low-dimensional thermoelectric materials. Adv. Mater. **19**, 1043 (2007)
49. Pichanusakorn, P., Bandaru, P.: Nanostructured thermoelectrics. Mater. Sci. Eng. R **67**, 19 (2010)
50. Kim, R., Datta, S., Lundstrom, M.S.: Influence of dimensionality on thermoelectric device performance. J. Appl. Phys. **105**, 034506 (2009)
51. Pedersen, T.G., Flindt, C., Pedersen, J., Mortensen, N.A., Jauho, A.P., Pedersen, K.: Graphene antidot lattices: designed defects and spin qubits. Phys. Rev. Lett. **100**, 136804 (2008)
52. Gunst, T., Markussen, T., Jauho, A.P., Brandbyge, M.: Thermoelectric properties of finite graphene antidot lattices. Phys. Rev. B **84**, 155449 (2011)
53. Karamitaheri, H., Pourfath, M., Faez, R., Kosina, H.: Geometrical effects on the thermoelectric properties of ballistic graphene antidot lattices. J. Appl. Phys. **110**, 054506 (2011)

54. Haskins, J.B., Kinaci, A., Sevik, C., Sevincli, H., Cuniberti, G., Cagin, T.: Substantial reduction of thermal conductivity of defected carbon nanotubes. ACS Nano **5**, 3779 (2011)
55. Adamyan, V., Zavalniuk, V.: Phonons in graphene with point defects. J. Phys. Condens. Matter **23**, 015402 (2011)
56. Li, W., Sevincli, H., Cuniberti, G., Roche, S.: Phonon transport in large scale carbon-based disordered materials: implementation of an efficient order-N and real-space Kubo methodology. Phys. Rev. B **82**, 041410 (2010)
57. Savin, A.V., Kivshar, Y.S., Hu, B.: Suppression of thermal conductivity in graphene nanoribbons with rough edges. Phys. Rev. B **82**, 195422 (2010)
58. Li, W., Sevincli, H., Roche, S., Cuniberti, G.: Efficient linear scaling method for computing the thermal conductivity of disordered materials. Phys. Rev. B **83**, 155416 (2011)
59. Schiffli, J., Hu, S., Vallabhaneni, A., Ruan, X., Chen, Y.: Tuning the thermal conductivity of graphene nanoribbons by edge passivation and isotope engineering: a molecular dynamics study. Appl. Phys. Lett. **97**, 133107 (2010)
60. Tan, Z.W., Wang, J.S., Gan, C.K.: First-principles study of heat transport properties of graphene nanoribbons. Nano Lett. **11**(1), 214 (2011)
61. Zheng, H., Liu, J.H., Tan, X.J., Lv, H.Y., Pan, L., Shi, J., Tang, X.F.: Enhanced thermoelectric performance of graphene nanoribbons. Appl. Phys. Lett. **100**, 093104 (2012)
62. Ni, X.X., Liang, G.C., Wang, J.S., Li, B.W.: Disorder enhances thermoelectric figure of merit in armchair graphane nanoribbons. Appl. Phys. Lett. **95**, 192114 (2009)
63. Mingo, N., Esfarjani, K., Broido, D.A., Stewart, D.A.: Cluster scattering effects on phonon conduction in graphene. Phys. Rev. B **81**, 045408 (2010)
64. Zhang, H., Lee, G., Fonseca, A.F., Borders, T.L., Cho, K.: Isotope effect on the thermal conductivity of graphene. J. Nanomater. **2010**, 537657 (2010)
65. Wei, N., Xu, L., Wang, H., Zheng, J.: Strain engineering of thermal conduction electric figure of merit in armchair graphane nanoribbons. Nanotechnology **22**, 105705 (2011)
66. Yang, K.K., Chen, Y.P., D'Agosta, R., Xie, Y., Zhong, J.X., Rubio, A.: Enhanced thermoelectric properties in hybrid graphene/boron nitride nanoribbons. Phys. Rev. B **86**, 045425 (2012)
67. Mazzamuto, F., HungNguyen, V., Apertet, Y., Caër, C., Chassat, C., Saint-Martin, J., Dollfus, P.: Enhanced thermoelectric properties in graphene nanoribbons by resonant tunneling of electrons. Phys. Rev. B **83**, 235426 (2011)
68. Xie, Z.X., Tang, L.M., Pan, C.N., Li, K.M., Chen, K.Q.: Enhancement of thermoelectric properties in graphene nanoribbons modulated with stub structures. Appl. Phys. Lett. **100**, 073105 (2012)
69. Pan, C.N., Xie, Z.X., Tang, L.M., Chen, K.Q.: Ballistic thermoelectric properties in graphene-nanoribbon-based heterojunctions. Appl. Phys. Lett. **101**, 103115 (2012)
70. Huang, W., Wang, J.S., Liang, G.: Theoretical study on thermoelectric properties of kinked graphene nanoribbons. Phys. Rev. B **84**, 045410 (2011)
71. Chen, Y., Jayasekera, T., Calzolari, A., Kim, K., Nardelli, M.B.: Thermoelectric properties of graphene nanoribbons, junctions and superlattices. J. Phys. Condens. Matter **22**, 372202 (2010)
72. Saha, K.K., Markussen, T., Thygesen, K.S., Nikolić, B.K.: Multiterminal single-molecule–graphene-nanoribbon junctions with the thermoelectric figure of merit optimized via evanescent mode transport and gate voltage. Phys. Rev. B **84**, 041412(R) (2011)
73. Chang, P.H., Nikolić, B.K.: Edge currents and nanopore arrays in zigzag and chiral graphene nanoribbons as a route toward high-ZT thermoelectrics. Phys. Rev. B **86**, 041406(R) (2012)
74. Eroms, J., Weiss, D.: Weak localization and transport gap in graphene antidot lattices. New J. Phys. **11**, 095021 (2009)
75. Begliarbekov, M., Sul, O., Santanello, J., Ai, N., Zhang, X., Yang, E.H., Strauf, S.: Optical control of edge chirality in graphene. Nano Lett. **11**, 1254 (2011)
76. Kim, M., Safron, S.N., Han, E., Arnold, M.S., Gopalan, P.: Fabrication and characterization of large-area. Semiconducting nanoperforated graphene materials. Nano Lett. **10**, 1125 (2010)

77. Bai, J., Zhong, X., Jiang, S., Huang, Y., Duan, X.: Graphene nanomesh. Nat. Nanotechnol. **5**, 190–194 (2010)
78. Akhavan, O.: Graphene nanomesh by ZnO nanorod photocatalysts. ACS Nano **4**, 4174 (2010)
79. Krauss, B., Nemes-Incz, P., Skakalova, V., Biro, L.P., von Klitzing, K., Smet, J.H.: Raman scattering at pure graphene zigzag edges. Nano Lett. **10**, 4544 (2010)
80. Brenner, D.W.: Empirical potential for hydrocarbons for use in simulating the chemical vapor deposition of diamond films. Phys. Rev. B **42**, 9458 (1990)
81. Gunlycke, D., White, C.T.: Tight-binding energy dispersions of armchair-edge graphene nanostrips. Phys. Rev. B **77**, 115116 (2008)
82. Xie, Z.X., Li, K.M., Tang, L.M., Pan, C.N., Chen, K.Q.: Nonlinear phonon transport and ballistic thermal rectification in asymmetric graphene-based three terminal junctions. Appl. Phys. Lett. **100**, 183110 (2012)
83. Zhao, P., Chauhan, J., Guo, J.: Computational study of tunneling transistor based on graphene nanoribbon. Nano Lett. **9**(2), 684 (2009)
84. Mazzamuto, F., Saint-Martin, J., Valentin, A., Chassat, C., Dollfus, P.: Edge shape effect on vibrational modes in graphene nanoribbons: a numerical study. J. Appl. Phys. **109**, 064516 (2011)
85. Guttman, G.D., Ben-Jacob, E., Bergman, D.J.: Thermopower of mesoscopic and disordered systems. Phys. Rev. B **51**, 17758 (1995)
86. Larsson, M., Antonyuk, V.B., Malshukov, A.G., Chao, K.A.: Thermopower anomaly in multiple barrier structures. Phys. Rev. B **68**, 233302 (2003)
87. Liang, L.B., Cruz-Silva, E., Girão, E.C., Meunier, V.: Enhanced thermoelectric figure of merit in assembled graphene nanoribbons. Phys. Rev. B **86**, 115438 (2012)
88. Cai, J., Ruffieux, P., Jaafar, R., Bieri, M., Braun, T., Blankenburg, S., Muoth, M., Seitsonen, A.P., Saleh, M., Feng, X., Müllen, K., Fasel, R.: Atomically precise bottom-up fabrication of graphene nanoribbons. Nature (London) **466**(470) (2010)
89. Girao, E.C., Liang, L., Cruz-Silva, E., Filho, A., Meunier, V.: Emergence of atypical properties in assembled graphene nanoribbons. Phys. Rev. Lett. **107**, 135501 (2011)
90. Tada, K., Haruyama, J., Yang, H.X., Chshiev, M., Matsui, T., Fukuyama, H.: Ferromagnetism in hydrogenated graphene nanopore arrays. Phys. Rev. Lett. **107**, 217203 (2011)
91. Wirtz, L., Marini, A., Gruning, M., Attaccalite, C., Kresse, G., Rubio, A.: Comment on "huge excitonic effects in layered hexagonal boron nitride". Phys. Rev. Lett. **100**, 189701 (2008)
92. Serrano, J., Bosak, A., Arenal, R., Krisch, M., Watanabe, K., Taniguchi, T., Kanda, H., Rubio, A., Wirtz, L.: Vibrational properties of hexagonal boron nitride: inelastic X-ray scattering and ab initio calculations. Phys. Rev. Lett. **98**, 095503 (2007)
93. Gruneis, A., Serrano, J., Bosak, A., Lazzeri, M., Molodtsov, S.L., Wirtz, L., Attaccalite, C., Krisch, M., Rubio, A., Mauri, F., Pichler, T.A.: Phonon surface mapping of graphite: disentangling quasi-degenerate phonon dispersions. Phys. Rev. B **80**, 085423 (2009)
94. Rubio, A., Corkill, J.L., Cohen, M.L.: Theory of graphitic boron nitride nanotubes. Phys. Rev. B **49**, 5081 (1994)
95. Blase, X., Rubio, A., Louie, S.G., Cohen, M.L.: Stability and band gap constancy of boron nitride nanotubes. Euro Phys. Lett. **28**, 335 (1994)
96. Ci, L., Song, L., Jin, C., Jariwala, D., Wu, D., Li, Y., Srivastava, A., Wang, Z.F., Storr, K., Balicas, L., Liu, F., Ajayan, M.: Atomic layers of hybridized boron nitride and graphene domains. Nat. Mater. **9**, 430 (2010)
97. Sevincli, H., Cuniberti, G.: Enhanced thermoelectric figure of merit in edge-disordered zigzag graphene nanoribbons. Phys. Rev. B **81**, 113401 (2010)
98. Mazzamuto, F., Saint-Martin, J., Nguyen, V.H., Chassat, C., Dollfus, P.: Thermoelectric performance of disordered and nanostructured graphene ribbons using Green's function method. J. Comput. Electron. **11**, 67–77 (2012)
99. Wei, P., Bao, W.Z.Y., Lau, C.N., Shi, J.: Anomalous thermoelectric transport of Dirac particles in graphene. Phys. Rev. Lett. **102**, 166808 (2009)

100. Lee, J.U., Yoon, D., Kim, H., Lee, S.W., Cheong, H.: Thermal conductivity of suspended pristine graphene measured by Raman spectroscopy. Phys. Rev. B **83**, 081419(R) (2011)
101. Checkelsky, J.G., Ong, N.P.: Thermopower and Nernst effect in graphene in a magnetic field. Phys. Rev. B **80**, 081413(R) (2009)
102. Wang, D.Q., Shi, J.: Effect of charged impurities on the thermoelectric power of graphene near the Dirac point. Phys. Rev. B **83**, 113403 (2011)
103. Strohm, C., Rikken, G.L.J.A., Wyder, P.: Phenomenological evidence for the phonon Hall effect. Phys. Rev. Lett. **95**, 155901 (2005)

Chapter 14
Silicon Nanostructures for Thermoelectric Applications

Massimo Totaro and Giovanni Pennelli

Abstract In this chapter, an overview on silicon nanostructures for thermoelectric applications is presented. After an introduction on the key concepts of thermoelectricity, we show that nanostructuring is one of the most promising solutions for making high efficient thermoelectric devices. In particular, we discuss the use of nanostructured silicon as a good thermoelectric material, due to its abundance, its nontoxicity, and its technological pervasiveness in the society, compared to other materials often proposed in the literature. Furthermore, a top-down process for the reliable fabrication of very complex and large area arrays of silicon nanowires (SiNWs) is shown and discussed. Finally, we show that these networks can be employed for the fabrication of high efficiency thermoelectric generators, and the high reliability and the high tolerance with respect to SiNW width dispersion are demonstrated by means of numerical simulations.

14.1 Introduction

Increasing energy demand and global warming have in recent years generated a burgeoning activity dedicated to the development of low-CO_2 and sustainable energy production technologies [1–3]. Nowadays, electrical power is mainly

M. Totaro (✉)
Center for Micro-BioRobotics @SSSA, Istituto Italiano di Tecnologia,
Viale Rinaldo Piaggio 34, I-56025 Pontedera (PI), Italy

Dipartimento di Ingegneria dell'Informazione, Università di Pisa, Via Caruso 16,
I-56122 Pisa, Italy
e-mail: massimo.totaro@iit.it

G. Pennelli
Dipartimento di Ingegneria dell'Informazione, Università di Pisa, Via Caruso 16,
I-56122 Pisa, Italy
e-mail: g.pennelli@iet.unipi.it

X. Wang and Z.M. Wang (eds.), *Nanoscale Thermoelectrics*, Lecture Notes in Nanoscale Science and Technology 16, DOI 10.1007/978-3-319-02012-9_14,
© Springer International Publishing Switzerland 2014

obtained from fossil fuels and nuclear energy, while the electricity produced by renewable sources (sun, wind, etc.) is only a very small fraction. The transformation of almost all energy sources into mechanical or electrical energy, such as means of transport, industrial processes, or electric power transmission lines, produces always a substantial waste heat, which is in average about the 60 % of the input energy.

Moreover, a significant portion of this waste heat is produced by relatively low energy heat sources ($T < 300\ ^{\circ}\mathrm{C}$) [4], and there is not yet a technology available to convert this energy into electricity with high efficiency. In the last 10 years, thermoelectric (TE) generation is being more and more considered one of the most promising solutions. The thermoelectric conversion is based on the Seebeck effect [5]. Carriers in metals and in semiconductors transport electrical charge as well as heat. When a temperature gradient is applied to the extremities of a conductor, the mobile charge carriers at the HOT side flow through the device to the COLD contact. At the equilibrium, this temperature gradient generates an electrostatic voltage difference V, and this effect is the basis of thermoelectric energy conversion. Thermoelectrics has several advantages even over photovoltaics [6, 7], always indicated as the best and leading sustainable energy source, because of the endless possibilities to recover waste heat from a huge variety of industrial processes [8–10], and because of the potentially higher efficiency, both vs.conventional Si-based cells and vs. thin-film large-area devices. Furthermore, waste heat can also be recovered from several distributed sources, such as residential heating and automotive exhaust, making TE conversion the ideal solution for localized energy harvesting, without any need of centralized systems and energy transport lines, usually expensive and with several maintenance required.

One of the most limiting factors of thermoelectric generators is the significant portion of the thermal energy lost by Joule effect, due to the finite electrical conductivity of the material, and by direct heat conduction from the hot to the cold region of the device, due to the thermal conductivity of the materials. For this reason, a device with high electrical but low thermal conductivity should be developed. Regrettably, this is hard to achieve with metals, since the two parameters are directly correlated, thus giving very poor TE performances.

As far as now, lead and bismuth telluride compounds present the best TE properties [11], being the most widely used material for TE energy conversion, with an efficiency about 6–8 %. However, such compounds as material for energy generation in very large-scale applications have several disadvantages. First of all, some of these materials are unstable above 1,000 K, due to melting or vaporization, thus they are not suitable for high temperature processes. In addition, the abundance on the Earth's surface of these materials is another factor which limits the development of large-scale applications. Indeed, in an industrial context, the price of a material, due to market request and to its extraction and transformation costs, influences largely the whole device cost, making very unlikely the widespread

use of current thermoelectric systems for waste energy harvesting. Furthermore, low natural abundance is often accompanied by a certain level of toxicity for the environment, and health hazard for people. In particular, tellurium and thallium, which appears in a large number of the high performance thermoelectric compounds presently used, are considered to be highly toxic metals, and this also affects the cost of material packaging and recycling to minimize the environmental contamination. In addition, these materials should particularly be avoided for high temperature processes since they tend to vaporize and release harmful pollutants to the environment.

Finally, in last years the sustainability is commanding ever-increasing attention. It can be viewed as the use of a material in the future without worrying about its availability or its degradation. Sustainability mainly depends on the resource availability, which is the total amount of the material on the Earth's crust, and on the reserve availability, defined as the quantity of the element that is currently possible to extract. From both these points of view, high performance thermoelectric alloys present critical concerns.

On the other hand, silicon would satisfy all the above requirements, since, after oxygen, it is the most abundant element on the Earth's surface, it is not toxic, it is stable even at very high temperatures, and it is sustainable for very large-scale applications [11], as demonstrated by its pervasiveness in the society. Moreover, due to its large employment as leading element in modern microelectronics, and to the impressive technological development of microchip fabrication, the costs related to the material processing, to the system fabrication, and to the distribution into the market are much lower if compared to any other material or compound. Finally, silicon-based thermoelectric modules can be easily integrated in existing electronic systems, giving a significant breakthrough to energy harvesting applications.

Unfortunately, bulk silicon, due to its quite high thermal conductivity, presents very poor thermoelectric performances [12]. Interestingly, in recent years, it has been demonstrated, as we discuss below, that in silicon nanostructures, and in particular in silicon nanowires, nanoscale dimensions can enhance the surface scattering of phonons that can be viewed as lattice vibrations which act as heat carriers, without degrading electronic transport. In this way, the conversion efficiency of silicon-based thermoelectric generators (TEGs) can become competitive with now available commercial thermal engines.

In this chapter, after a description of thermoelectric effects in bulk materials, we discuss which are the key parameters to optimize the thermoelectric efficiency, and we clarify the proper use of different thermoelectric figures of merit commonly found in the literature. Then, we show how nanostructuring can allow silicon to be used as high efficiency thermoelectric material, and we present a top-down process for the fabrication of large area silicon nanowire arrays for thermoelectric applications. Finally, we discuss their reliability with respect to the random nanowire breakdown, and we demonstrate by means of numerical simulation their high tolerance with respect to the nanowire width dispersion.

14.2 Thermoelectric Effect in Bulk Materials

In the case of thermoelectric systems, we have a device, as shown in Fig. 14.1, with a temperature gradient $\Delta T = T_H - T_C$ at its extremities where T_H are T_C are HOT and COLD side temperatures, respectively. This gradient induces a voltage drop V, related to ΔT through the Seebeck coefficient, defined as the ratio of the voltage drop and the temperature difference at the extremities of the device:

$$S = \frac{V}{\Delta T}, \tag{14.1}$$

However, in the case of the device depicted in Fig. 14.1, if we suppose to measure the voltage drop V by means of a voltmeter, the result will be zero. Indeed, in a closed circuit the total temperature gradient is zero, and the only way to obtain a non-null V is to put two materials with different Seebeck coefficients S_1 and S_2 between T_H and T_C, as sketched in the upper panel of Fig. 14.2. In this way, we obtain

$$V = (S_2 - S_1)(T_H - T_C). \tag{14.2}$$

Thus, the output voltage depends on the product of the Seebeck coefficient difference and the temperature gradient. If the two materials are metals, both Seebeck coefficients will have the same sign, since carriers are always electron which diffuses from the HOT to the COLD side, and the total $S = S_2 - S_1$ coefficient will be very low, with a consequent low voltage V. On the other hand, if we have

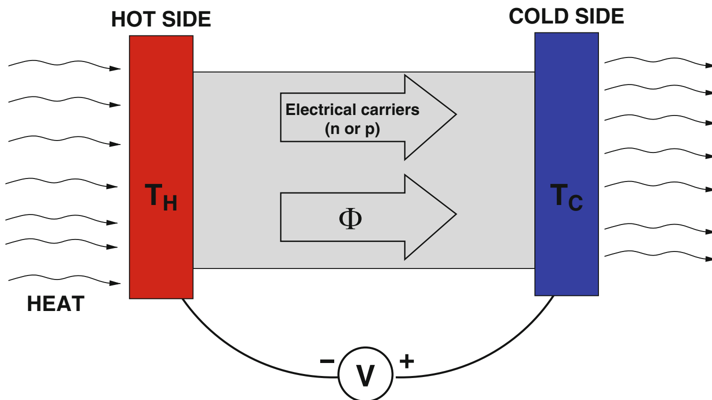

Fig. 14.1 Sketch of a thermoelectric device, where a temperature gradient $\Delta T = T_H - T_C$ between the HOT and the COLD side induces a voltage drop V at its extremities

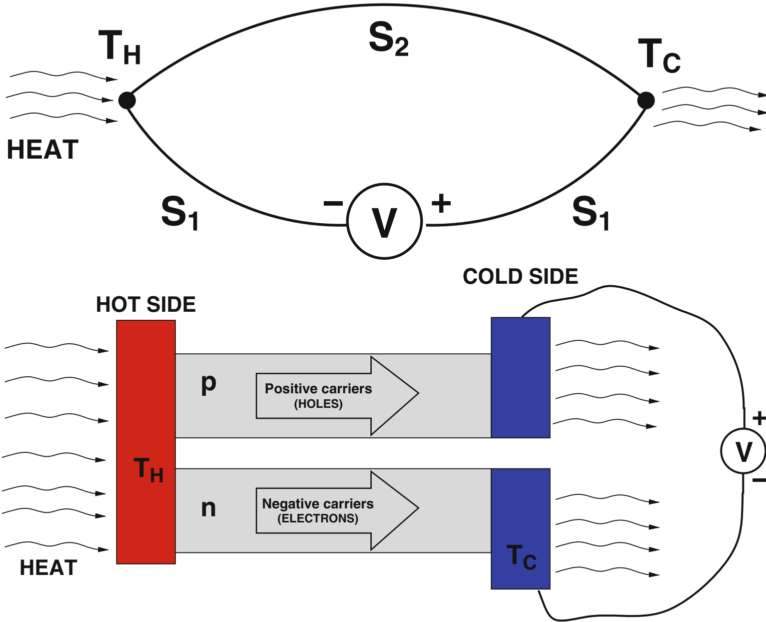

Fig. 14.2 *Upper panel*: Schematic sketch of a thermocouple, composed of two materials with different Seebeck coefficient. When a temperature gradient T_H–T_C occurs at the contacts between the two materials, a non-null voltage V can be observed. *Lower panel*: schematic sketch of a thermoelectric generator, composed of two n and p-type semiconductors, connected thermally in parallel and electrically in series

semiconductors, since charge carriers will always diffuse from the hot side to the cold one, in the case of n doped materials electrons will charge the cold side *negatively*, with $S_n < O$, meanwhile in the case of p doped the cold side will be charged *positively* by holes, with $S_p > 0$. Thus, if we connect n-type and p-type modules thermally in parallel and electrically in series, as shown schematically in the lower panel of Fig. 14.2, we obtain

$$V = (S_p - S_n)(T_H - T_C) \tag{14.3}$$

$$V = (S_p + |S_n|)(T_H - T_C) \tag{14.4}$$

In this way, the total Seebeck coefficient is the sum of absolute values of the two Seebeck coefficients, giving a higher output voltage V.

14.3 Thermoelectric Power Factor and Efficiency

The aim of any energy conversion system is to have the highest efficiency, that is defined as

$$\eta = \frac{P_L}{P_{IN}}, \tag{14.5}$$

where P_L and P_{IN} are the power supplied to the load and the input power, respectively.

In this context, we should identify which quantities are involved in the thermoelectric power conversion picture.

First of all, let us suppose that the device extremities can be maintained at fixed temperatures T_H and T_C. This means that the HOT side can be considered as an infinite heat source, while the COLD side an infinite heat sink. In this case, we can ignore the heat flux Φ through the device, and it is sufficient to optimize the maximum output electrical power

$$P_{el} = \frac{V^2}{4R} = S^2 \Delta T^2 \sigma \frac{A}{4L}, \tag{14.6}$$

where

$$R = \frac{L}{\sigma A} \tag{14.7}$$

is the internal device resistance (remembering that the maximum power transfer is obtained if the load and the internal resistances are equal), σ its electrical conductivity, L and A the length and the cross-section surface of the conductor, respectively. Considering that L and A are two geometrical factors, so not related to material properties, and the temperature gradient ΔT is kept constant, to maximize the output power, we should optimize the factor $S^2\sigma$, which for this reason is commonly known as *thermoelectric power factor*. In this context, we should find a material with S and σ as high as possible. For this kind of applications, due to its properties (both huge electrical conductance and Seebeck coefficient), graphene seems to be the ideal material, which lead to predict a *giant thermoelectric effect in graphene* [13].

Unfortunately, in almost all real applications, the assumption of infinite heat source and/or sink is not satisfied. Indeed, the heat flux through the device, due to its finite thermal conductivity k, reduces ΔT unavoidably, or by raising T_C up if the heat flux from the HOT side is larger than the heat that the COLD side can dissipate, or by lowering T_H down when the heat source is not able to supply enough thermal energy to balance the heat flowing to the COLD side. In many cases, both phenomena can occur simultaneously. Then, a new dynamic thermal equilibrium, with lower ΔT and with a significant efficiency loss, can be obtained, or both sides will

reach the same temperature, with a consequent null thermoelectric conversion. Thus, we should take into account also the thermal conductivity k, and, in particular, to optimize thermoelectric performances we would like to have a material with the highest σ and the lowest k. Briefly, our aim is to find an unusual phonon-glass and electron-crystal material [14]. The phonon-glass behavior is needed for as low a thermal conductivity as possible, while the electron-crystal requirement hails from the fact that crystalline materials (in particular semiconductors) are the best compromise for the electronic properties (Seebeck coefficient and electrical conductivity).

To evaluate the quality of a thermoelectric material we can introduce the factor of merit [5]

$$Z = \frac{S^2 \sigma}{k}. \tag{14.8}$$

This factor, which depends only on the physical properties of a material, is useful since it appears in the thermoelectric maximum efficiency expression [5]:

$$\eta_{\mathrm{TOT}} = \eta_C \cdot \eta_{\mathrm{TH}} = \frac{T_H - T_C}{T_H} \frac{\sqrt{1 + Z\overline{T}} - 1}{\sqrt{1 + Z\overline{T}} + T_C/T_H}, \tag{14.9}$$

where $\overline{T} = (T_H + T_C)/2$ is the average absolute temperature. We have to note that this expression is only a first order approximation and, while it is almost always used in the literature for evaluating thermoelectric performances, it is strictly correct only if S, σ and k, and therefore Z, can be considered constant with respect to the temperature between T_C and T_H [15]. Of course, this is only a rough approximation, since, as well known, all the above parameters vary with the temperature, both in metals and in semiconductors. In this case, an averaged Z is often used [15].

Moreover, we can observe that η_{TOT} is composed of two terms. The first one, $\eta_C = (T_H - T_C)/T_C$ is the Carnot efficiency, which is the maximum efficiency for any thermal cycle operating between T_C and T_H [5]. The second term, η_{TH}, can be ascribed to the thermoelectric conversion process, and it depends only on the material chosen for the device.

As well known, due to the second law of thermodynamics, the Carnot limit is unavoidable. Thus, for example, any thermal machine working between room temperature (300 K) and 800 K cannot reach a total efficiency over than 62.5 %. However, commonly available internal combustion engines (such as diesel or gasoline-based ones) have a typical efficiency around 20 %. Aware of this fact, thermoelectrics can be a valid option for competitive energy conversion if a total efficiency approaching the 20 % can be reached. In Fig. 14.3, we can see the theoretical maximum efficiency of a thermoelectric device, as a function of T_H and assuming the COLD side at room temperature (300 K), for different values of the Z factor. While for Z less than 10^{-3} the efficiency is well below the 20 % target

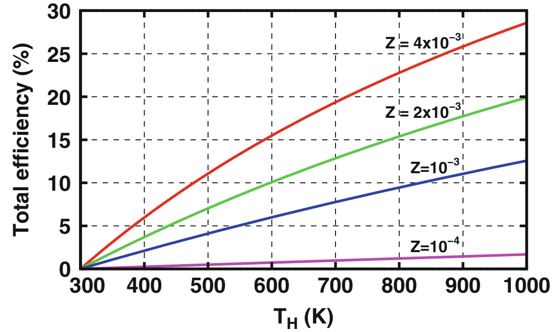

Fig. 14.3 Maximum thermoelectric total efficiency as a function of T_H, assuming $T_C = 300$ K, for different values of Z

even at quite high temperatures, we can see that an increase to $Z = 4{\times}10^{-3}$ rises the efficiency up to more than the 20 % for temperatures above 700 K. Furthermore, even for $Z = 2{\times}10^{-3}$ the efficiency starts to be competitive, with a value of 15 % at 800 K, easily obtainable, for example, with solar concentration systems, and 20 % at 1,000 K, that can be reached in several industrial processes. Thus, it is apparent to understand the big effort in the scientific community to improve thermoelectric performances by fabricating complex alloys [16] or, in recent years, by nanostructuring [17], and the significant interest of the industrial sector in these kinds of applications.

Thermoelectric efficiency and figure of merit, which is the right factor?

Instead of Z, in the literature, we can often find as figure of merit the parameter ZT, with T the *average* absolute temperature. The product ZT appears explicitly in Eq. (14.9); moreover, it is a dimensionless parameter, with typical values around 1. Thus, it is "easy" to remember, to cite, and to compare. Also for these reasons, it is often used as the "unit of measurement" for thermoelectric performances. However, as we explain below, this factor should be handled carefully, and, unfortunately, sometimes its misuse can give incomplete or even incorrect indications on thermoelectric materials. From this point of view, we could state, as often found in the literature, that a material whose ZT is higher than 1 can be considered a good thermoelectric material. However, this statement is incomplete if we do not specify the operating temperatures (T_H and T_C) of the thermoelectric device.

First of all, the T value in ZT is the *average* absolute temperature, and according to Eq. (14.9) we should write $\overline{T}$. Observing again the curves of Fig. 14.3, we can obtain a 20 % total efficiency (which is, more or less, our goal) with a material whose $ZT = 2$ at $T_H = 700$ K ($Z = 0.004$ K^{-1} and $\overline{T} = 500$ K), and, for such a material, we can often find $ZT = 1.2$ at room temperature (300 K). The latter value is often cited as the threshold for a good thermoelectric material. Unfortunately, this statement, if incomplete, could

(continued)

(continued)

have some critical points. First of all, saying $ZT = 1.2$ at 300 K should mean that $\overline{T} = 300$ K. For this reason, it is an indicative factor if we suppose that the conversion process is operating with $\overline{T}$ around the room temperature, as for example in domestic heating or air conditioning systems. In this case, if ΔT is less than 100 K, the variation of Z with respect to the temperature is not very relevant. Indeed, both S and σ do not vary too much, especially in heavily doped semiconductors, where the carrier mobility is limited by the scattering with lattice impurities. Thus, comparing different materials or compounds with ZT at room temperature is indicative only for quite low temperature processes. Otherwise, in applications where the conversion occurs between 300 K and T_H about 500 K or more, the approximation of constant Z in the whole temperature range is not satisfied, and the ZT parameter at room temperature could give incorrect information.

In addition, it is obvious that if $T_C = 300$ K is supposed, considering ZT at room temperature means that the device would operate between 300 K and. . .300 K, giving, for the Carnot law, an efficiency of 0! Briefly, without paying attention to previous facts, we could measure the thermoelectric performances with an almost fictitious value; in addition, we should be careful to avoid confusion between the average temperature $\overline{T}$ that should be considered in ZT and the absolute temperature T_H.

Another critical point is that giving a ZT value can be, sometimes, a bit misleading. Indeed, the same value can be obtained with another (worse) material just by varying the operating temperature, so it is not an absolute "unit of measurement," as Z alone could be. In this context, the main strategy to obtain the best thermoelectric efficiency is to maximize the ZT of a material. Even if we handle correctly this parameter, we could achieve incomplete results. If, for example, we find a material whose maximum ZT is 3 at 500 K (which means $T_H = 700$ K if $T_C = 300$ K), according to the ZT optimizing strategy, we will try to use the thermoelectric device at that temperature, with an efficiency, from expression (14.9) with $T_C = 300$ K, $\eta_{TOT} = 0.\ 1538$ (15.38 %). On the other hand, if the same material had $ZT = 2.5$ at 700 K ($T_H = 1,100$ K with $T_C = 300$ K), we would obtain $\eta_{TOT} = 0.2164$ (21.64 %), with a significant improvement, due to the much higher T_H, at a lower ZT.

Furthermore, the operating temperature T_H is often imposed by the process that we want to exploit, or it can be tuned only slightly. Thus, the strategy to optimize the ZT factor should consider in any case at which temperature we want to operate, and, if T_H cannot be varied, it actually means to optimize Z at a given temperature. For example, if our aim is to recover waste energy from domestic heating, it would be unlikely to exploit successfully a system which

(continued)

(continued)

has the best efficiency at 800 K (and, thus a commonly indicated ZT value around 1 *at room temperature*). This indicates that the best strategy should be to consider both Z and T, but separately, if we want to optimize the whole thermoelectric efficiency.

Finally, regarding the ZT misuse, in few cases, we can find graphics for the theoretical maximum efficiency where different curves, as a function of the temperature, equivalent to those in Fig. 14.3, are shown taking ZT as parameter, instead of Z. In this way, we impose implicitly that, for a certain curve, the whole factor ZT should be independent to the temperature $\overline{T}$, that would be true only if the factor Z was proportional to $1/\overline{T}$. Unfortunately, as already shown above, the expression is valid only if Z is constant with the temperature, and we run into an inconsistency.

In conclusion, the widespread use of ZT as thermoelectric figure of merit, without any wisdom, can lead to wrong conclusions about thermoelectric performances. Indeed, it should sound strange to use as 'unit of measurement' a parameter which does not give absolute indications and, most importantly, with values that, according to the application, can be fictitious. For these reasons, in our exposition we prefer to use Z as much as possible, and we will always keep in mind the previous considerations when referring to ZT.

14.4 Nanostructuring Strategy for Thermoelectric Applications

Nanostructuring is one of the most powerful strategies to increase the thermoelectric figure of merit of materials [18]

$$Z = \frac{S^2\sigma}{k}, \tag{14.10}$$

Through nanofabrication, the device active elements become comparable in size to the phonon mean free path (m.f.p.), and thus benefit from a reduced k via enhanced surface scattering of the acoustic phonons that provide the most significant contribution to the overall thermal conductivity. Electrical conductivity σ however, remains essentially unaltered owing to a much smaller electron m.f.p., thereby yielding a real advantage for thermoelectrics. To this end, current research concentrates on the search for novel nanostructured materials, characterized by high σ but low k to enhance the thermoelectric conversion figure of merit Z (or the alternative dimensionless parameter ZT, as discussed previously). As mentioned earlier, there

are encouraging prospects for limiting the value of the overall thermal conductivity k via nano-engineering of the materials. k can be expressed in general as the sum of two contributions due to the charge carriers (k_e), and the lattice (namely due to heat transmission by crystalline lattice vibrations or phonons) k_{ph} [19],

$$k = k_e + k_{\mathrm{ph}}. \tag{14.11}$$

For bulk elemental metals k_e provides a dominant contribution to k and is related to σ by the Wiedemann–Franz law [19]:

$$\frac{k_e}{\sigma} = \frac{\pi^2}{3}\left(\frac{k_B}{e}\right)^2 T, \tag{14.12}$$

where k_B is the Boltzmann constant, e the electron charge, and T the absolute temperature. This means that k_e cannot be decreased without altering σ, thereby making metals poor TE materials. Interestingly, however, there are significant deviations from these behaviors in both alloyed semiconductor superlattices, and nanostructured semiconductors.

14.5 The Choice of Silicon as Thermoelectric Material

The case of silicon is worth mentioning explicitly, given its nontoxic nature, versatility, abundance, and its pervasiveness in society as the elective semiconductor for microelectronics. In silicon the main contribution to k is given by $k_{\mathrm{ph}} = 148\mathrm{W/mK}$, whereas k_e, that depends on doping, is less than 1 W/mK. Most importantly, theoretical studies [20, 21] confirmed by experiments [22, 23] have shown the possibility to suppress k by up to 2 orders of magnitude, to 1 W/mK, thereby yielding $Z = 0.002\ \mathrm{K}^{-1}$ (with an equivalent $ZT = 0.6$ at 300 K). This is possible because the phonon mean free path (m.f.p.) is much longer than the electron m.f.p., i.e. of the order of 20–50 nm compared to 2–10 nm for electrons. When the lateral dimensions of the nanowires become comparable with the phonon m.f.p, conduction of the latter results limited by surface scattering, thus leading to a decrease in k, and determining an increase in Z. A further thermal conductivity reduction can be obtained by suitable surface treatments [18, 24, 25], aimed, for example, at increasing the surface roughness, and thus again the phonon m.f.p. owing to enhanced phonon scattering. Interestingly, this can be done in such a way that the electrical properties are almost perfectly preserved. Overall, by the combined effect of reduced dimensions and enhanced surface roughness, an increase of Z of more than 2 orders of magnitude can be expected. Obviously, once k_{ph} is minimized and reduced to values below or comparable to k_e, it is important again to consider the factors affecting both k_e and k_{ph} (such as effective mass, electronegativity and atomic weight of the component elements, charge mobility and energy gap) as already discussed a decade ago in the

excellent review by Disalvo [26]. While significant work has been done since then, especially in terms of materials nanostructuring [27], there are still ample margins for improvement in the engineering of TEGs with *ZT* at high temperatures (800–1,000 K) of 4 or greater, for example by seeking further reduction of the NWs diameter, their uniformity, density, and the control of their doping level. Importantly, in considering the best results obtained to date, it is also useful to distinguish, as already stated previously, between nontoxic, up-scalable, and essentially "sustainable" materials such as nanostructured-Si (for which *ZT* at room temperature is essentially still limited to 1 or less), and "high-*Z*" materials (e.g., based on Pb, Te, Sb, Bi, and their nanostructured alloys), which while attaining *ZT* values at 300 K of 3 or more [11, 26] raise significant concerns in terms of scalability, toxicity, and eventually sustainability, a property that is commanding ever increasing attention.

In any case, a single SiNW can convert into a negligible energy. For this reason, the research should be focused on the fabrication of large SiNW arrays [28], in order to exploit the TE nanoscale properties in macroscopic devices. By putting in parallel *n* and *p* doped SiNW arrays, high efficiency TEGs can be fabricated.

14.6 Fabrication of Silicon Nanowire Networks

The reduced SiNW thermal conductivity gives interesting possibilities for the fabrication of devices to be used for thermoelectric generation with high heat to electrical power conversion efficiency. These devices could be usefully employed for energy harvesting purposes. However, for the development of usable SiNW-based thermoelectric generators a technique for a massive and reliable production of well-organized, very long, SiNWs must be available. Such a technology could also be employed for the fabrication of several electronic devices, such as solid-state memories [29], or sensors based on large arrays of very sensitive nanowires [30].

Here we present a top-down technique for the fabrication of a well-organized and very reliable network based on a large amount (order of 10^5 SiNWs per mm^2) of narrow ($<$ 50 nm) silicon nanowires. In ideal conditions (i.e., no defects are present) these very large area SiNW arrays are equivalent to the parallel of many very long (order of millimeters) and small SiNW. On the other hand, the arrays are much more tolerant to unavoidable random defects of single, very long, nanowires.

Figure 14.4 shows SEM photos of a typical top down fabricated SiNW net. In the upper panel, a low magnification image showing the 1×0.6 mm^2 area of the SiNW network (dark zone of the image) is shown; clear areas are silicon, and a trench (dark) runs at the borders of the net to provide electrical insulation. Conduction is measured (see the next sections) between crystalline silicon areas (top and bottom terminals) which are accessed through aluminum contacts (not visible). In the lower panel, the texture of the net, made of SiNWs 3 μm long, is shown; the SEM image of the inset shows the 50 nm wide Si core, embedded in silicon dioxide. The implemented fabrication technique is an advancement of a previously

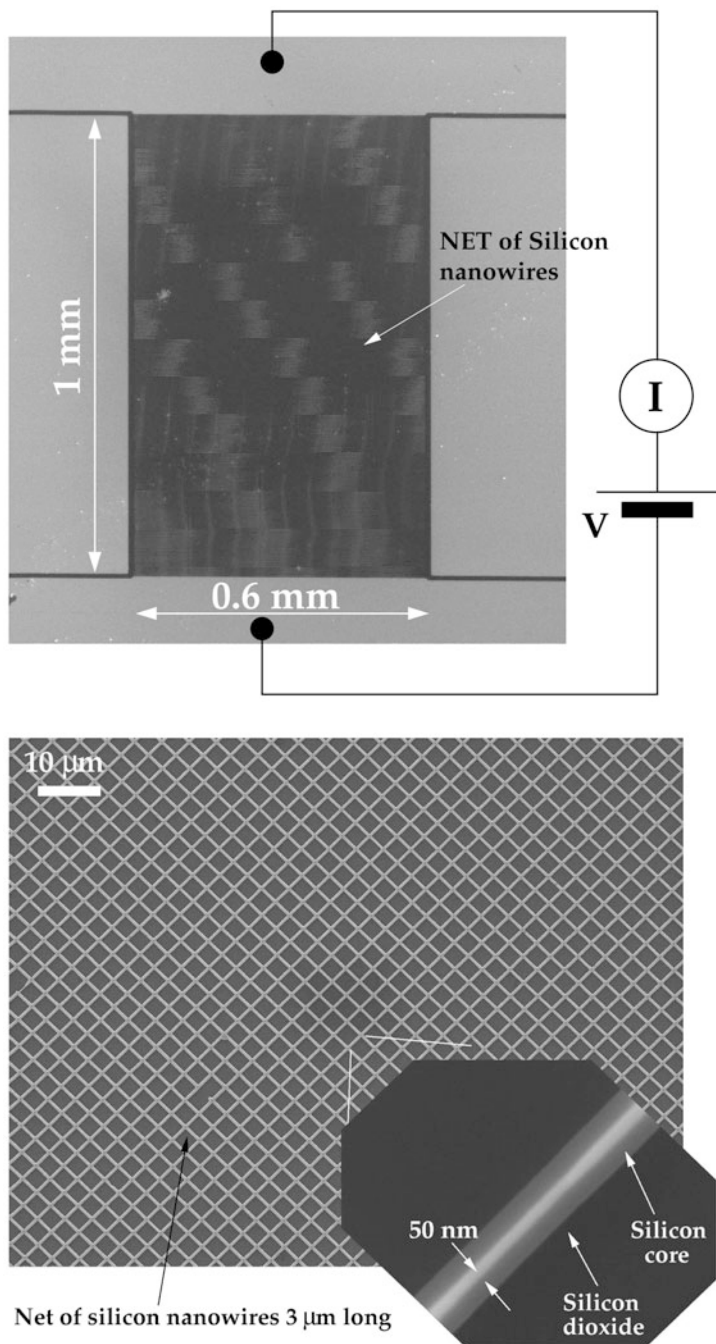

Fig. 14.4 SEM images of a silicon nanowire network. *Upper panel*: a low magnification image showing the overall dimension of the network. *Lower panel*: the texture made of 3 μm long SiNW is shown; the *inset* shows a detail of the SiNW with a core width of 50 nm. (Reprinted with permission of Elsevier, from [28])

developed top-down process [31, 32] that allows the reliable fabrication of devices based on narrow (down to 10 nm), micrometers long, single SiNWs, whose both mechanical [33] and electrical properties [34, 35] have been fully investigated in our recent works. The process is developed on Silicon On Insulator (SOI) substrates, with a top silicon layer 260 nm thick. The doping of the top silicon layer has been adjusted by means of a solid source doping technique based on Filmtronics ceramic wafer for phosphorus (*n*-type) or boron (*p*-type), already employed for the selective doping of a silicon nanowire [36]. The doping process consists in the pre-deposition and the drive-in steps. The ceramic wafer is brought into contact with the SOI substrate, and a rapid thermal annealing (RTA) cycle in N_2 atmosphere is performed. Varying the temperature and the time of pre-deposition process the top layer can be doped as needed. After the ceramic wafer removal, an RTA cycle at 1, 150 $^{\circ}$C for 10 min, with 1 min in O_2 atmosphere and 9 min in N_2 atmosphere, is applied to the SOI sample. Afterwards, a 50 nm thick top dioxide layer, used as a mask for the following silicon anisotropic etching, is grown by means of a dry oxidation step at 1, 150 $^{\circ}$C for 5 min. The final doping, and carrier mobility, of silicon nanowires is still and open problem, because they depend on many factors as interfacial states density, surface segregation of doping species, and so on.

A silicon dioxide layer is grown on top by dry thermal oxidation. A suitable SiO_2 mask is then obtained by a high resolution electron beam lithography step [37], through standard PMMA resist and calibrated chemical wet etching. It is important to underline that electron beam lithography is not mandatory for this step. Indeed, SiNWs with a cross-section smaller than 30 nm can be fabricated starting from 150 nm masks, easily obtainable with advanced optical lithography, making this process suitable for massive and very large-scale production.

The most critical point of the lithographic step is to optimize the electron beam process in order to achieve the lowest dispersion in the SiNW widths. As known, in a large structure defined by means of electron-beam lithography, the effective dose in different region of the device is not uniform, due to proximity effects. In fact, the forward and the back-scattering of electrons hitting the target broaden the exposed area of a single spot. The result is that highly dense patterned regions can be over exposed easily, while portions with very few surrounding patterns are often under exposed. In a very high-resolution process (with several thousands of dense different structures) this will affect the lithographic step with no chance to fabricate the desired device. In order to overcome this limitation, a very big effort has been made and several correction techniques have been developed. The common point of all techniques is to lower the dose in dense patterned regions, while at the boundaries it is raised. Unfortunately, the exact solution of the problem is computationally very demanding, since it has an exponential growth with the exposed area. For this reason, often only approximated techniques can be performed. Regarding the large area and high density of the devices here proposed, an ad hoc procedure for the correction of electron beam lithography intra proximity effects has been developed in order to obtain a more uniform exposure on large areas. As shown in Fig. 14.5 the SiNW network is defined by writing several rows of boxes, starting from the one

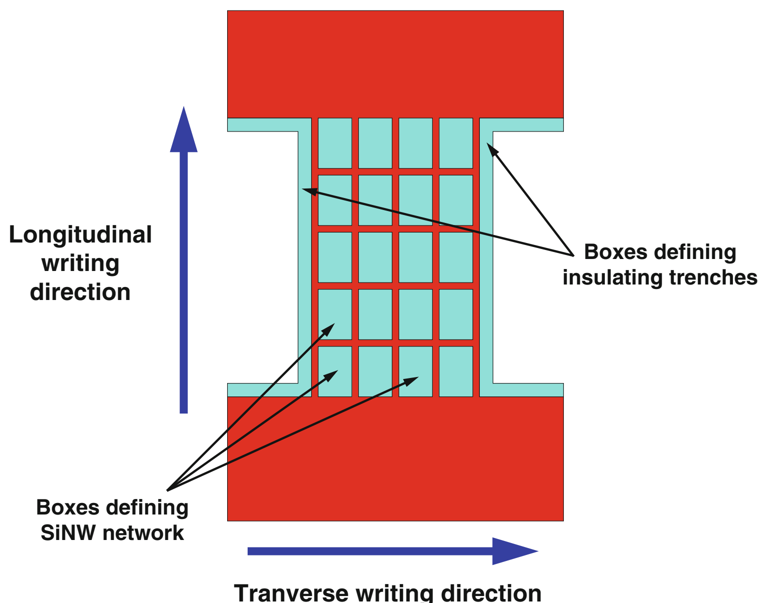

Fig. 14.5 A sketch of the adopted e-beam writing strategy and of the intra proximity effect correction. (Reprinted with permission of Elsevier, from [28])

corner of the structure that we want to fabricate. Moreover, the device is isolated from the whole Si chip by means of lateral trenches. The dose is partially compensated along the transverse writing direction by tuning the exposure dose of the insulating trenches. On the other hand, the compensation in the longitudinal writing direction is obtained by varying the exposure dose of each box, that is larger at the boundaries and it is reduced toward the center of the device. In Fig. 14.6 we show a comparison between the boundary regions of some arrays without (in a and b) and with the proximity effect correction applied. As we can note, in the first case we have under-exposition and poor pattern definition, while, if the correction is applied, we obtain very uniform and well-patterned networks.

Silicon anisotropic wet etching has been used in order to obtain very uniform wires with trapezoidal cross section, laterally delimited by [111] silicon crystalline planes. Stress controlled oxidation [32] is then used for defining the SiNWs and reducing their width in a well-controlled and reliable way. At the end of the oxidation-reduction process, each silicon nanowire has a triangular cross section. As it has been demonstrated [38], by using this technique it is possible to obtain very narrow SiNW even starting by not very small initial structures (over 100–150 nm of initial width) that could be obtained even with advanced optical lithography, in order to reduce fabrication costs. The initial width of the structures is limited only by the maximum nanowire density that has to be obtained in the final device.

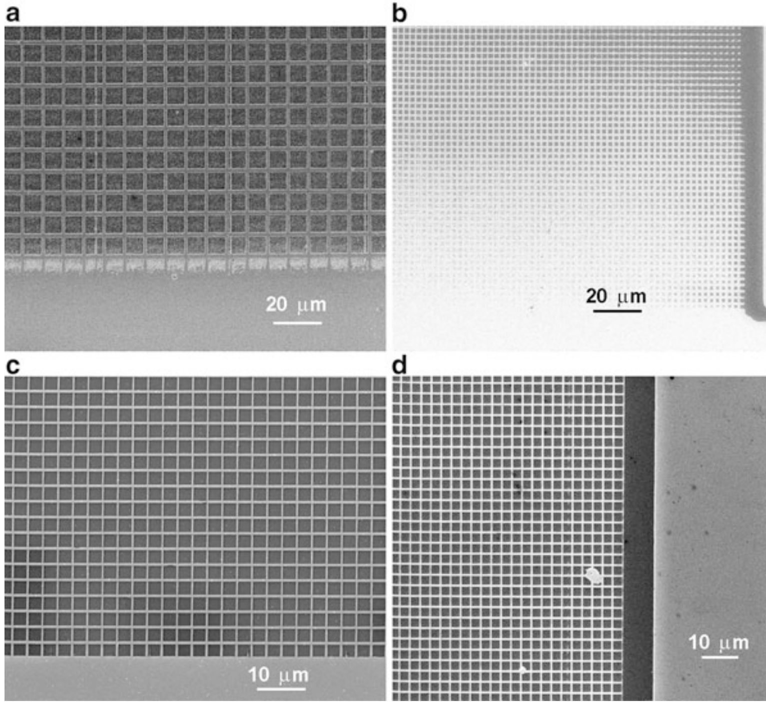

Fig. 14.6 (**a**) and (**b**) SEM images of SiNW array boundary regions without any proximity effect correction applied. (**c**) and (**d**) Similar boundary regions with the proximity effect correction

14.7 Random Failures in SiNW Networks

As schematically represented in the sketches of Fig. 14.7a and b, a silicon nanowire network is equivalent to many parallel silicon nanowires, each of the same width of the SiNWs forming the texture and of the same length of the whole net (1 mm in the case of the net shown in Fig. 14.4). In particular, important properties connected to the low nanowire width, such as large electrical to thermal conductivity ratio, are preserved; in Fig. 14.7c a sketch of the electrical equivalent resistor network is shown. Each of the $N \times M$ (row by column) resistors of the network models a SiNW of the net texture with a resistance value R_0 (conductance value $G_0 = 1/R_0$). It is trivial to demonstrate that this resistor network is equivalent to M parallel resistors, each given by the series of N elementary resistor of the network that are the vertical branches in the sketch of Fig. 14.7c. In the case of a perfect network, horizontal branches are ineffective both for the electrical and for the thermal conduction. The key point in using a silicon nanowire network is that this structure is much more tolerant to nanowire failures (as breaking) that can occur during the fabrication process for the presence of defects or other.

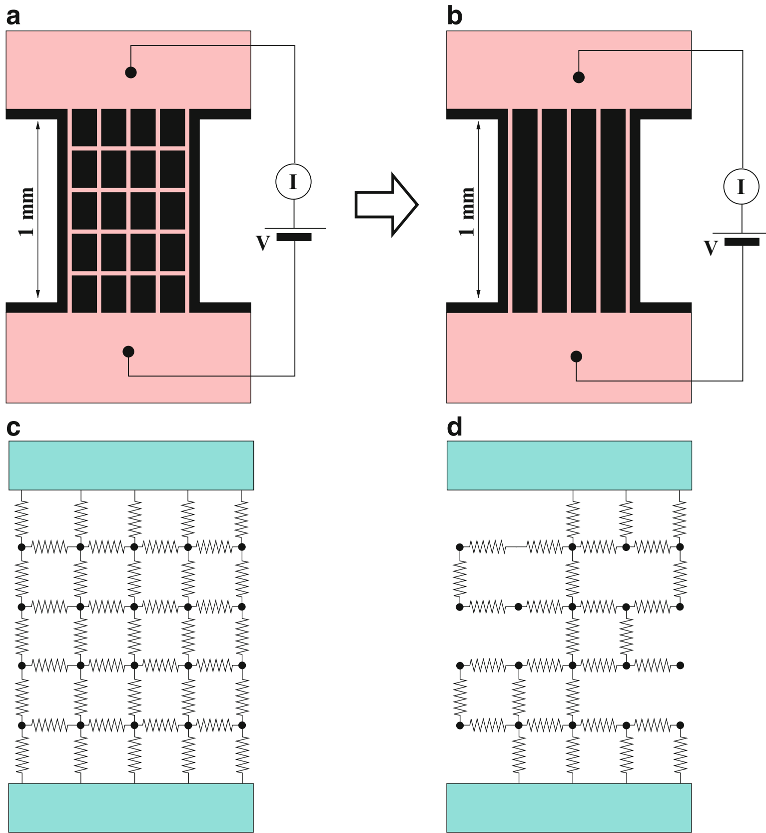

Fig. 14.7 Sketch of a SiNW network (**a**), electrically and thermally equivalent to many very long SiNWs in parallel (**b**). In (**c**) the equivalent electrical resistor network is shown and in (**d**) it is shown how random nanowire failures can be schematized by removing resistors from the net. (Reprinted with permission of Elsevier, from [28])

This allows the fabrication of very large areas SiNW networks (equivalent to millimeters long SiNWs in parallel) with high reliability and repeatability of the total thermal and electrical resistance of the net.

In order to give theoretical support to these considerations, a Monte Carlo technique has been implemented and applied to resistor networks. An ad hoc program for the resolution of electrical networks with a great number of resistance, based on a recursive optimized $Y{-}\Delta$ transformations [39], has been developed in order to optimize computational times. The program has been tested on a complete network of $N{\times}M$ resistors of resistivity R_0, confirming that it is equivalent to M parallel resistors, each of value $N{\times}R_0$. If, for example, $N{\times}M = 291{\times}190$ resistors with $R_0 = 1$ kΩ are considered, the total resistance of the net resulted exactly $1{\times}291/190 = 1.53$ kΩ. Nanowire failures, due to defects in the fabrication

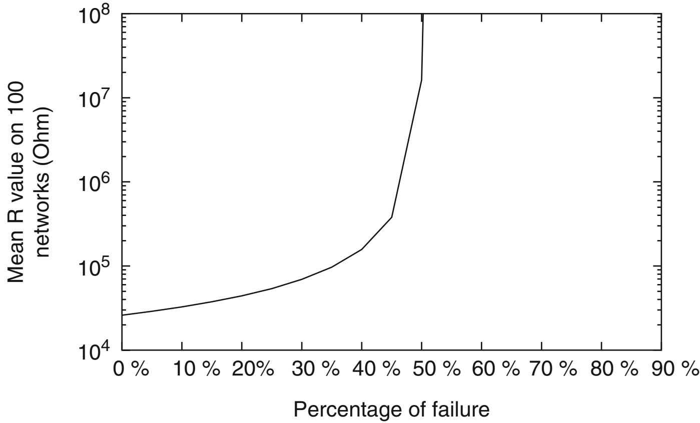

Fig. 14.8 The average value of resistance, evaluated on 100 networks with 291 $\times$190 initial number of resistors, is reported as a function of percentage of randomly removed resistors that simulated the nanowire failure. (Reprinted with permission of Elsevier, from [28])

process, have been modeled by randomly removing resistors from the net, as schematically shown in Fig. 14.7d. For each resistor a random number with an uniform distribution between 0 and 1 has been generated [40] and compared with a threshold P that established the probability (percentage) of failures: the resistor is removed if the random number is below the threshold P. The random removal of resistors has been repeated a suitable number n of times (population), stating from the same initial resistor network. Figure 14.8 shows the evaluated resistance of a network with $N \times M$ 291$\times$190 resistors, each with a resistance of 17 kΩ, as a function of percentage of failure. A population of $n = 100$ networks has been considered for each percentage, and the average value of resistance is reported as a function of percentage of randomly removed resistors (threshold value). It can be seen that the net total resistance value shows a reduced variation even for high percentage of failure (10–20 %). For example, the resistance increases from 26 kΩ (no failures) to 33 kΩ in the case of 10 % of failures. According to the bond percolation theory [41, 42], a full failure (disconnection between top and bottom contacts) occurs only for very high nanowire failure percentages; in the case of Fig. 14.8 only failure percentages greater than 40 % give a complete disconnection between the top and the bottom contacts of the network.

In the case of M parallel resistors, each representing a millimeter long nanowire (no horizontal branches), the reliability of the top to down connection with respect to nanowire failure is much more small. The same defect density can be considered by assuming that a millimeter long nanowire is outlined as the series of N elementary resistors R_0 (conductivity G_0), representing a nanowire of the texture 3 μm long, with a probability failure P. The failure of one elementary resistor of the series brings to the failure of the millimeter long nanowire. The probability that an

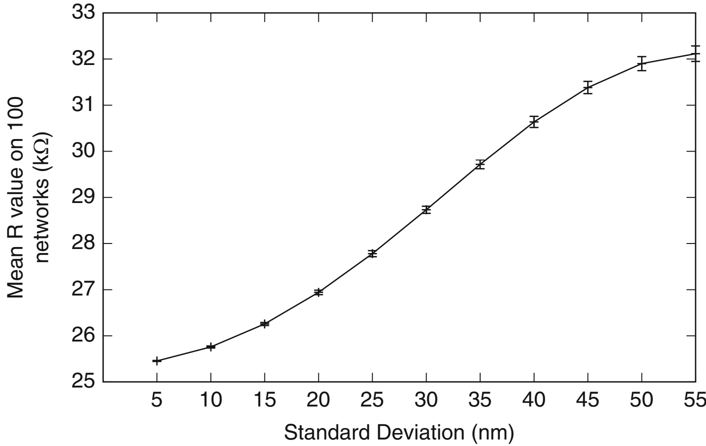

Fig. 14.9 The average value of resistance, evaluated on 100 networks with 291×190 random resistors, is reported as a function of the silicon nanowire width dispersion (standard deviation). (Reprinted with permission of Elsevier, from [28])

elementary resistor R_0 does not fail is $1-P$; making the reasonable hypothesis that failure events are uncorrelated, the probability that the series (the sum) of N resistors does not fail is the product of each single probability. This means that the probability of conduction for a millimeter long nanowire is $1-P^N$, and it results to be very small even with low P because it depends on N that in the case of long nanowires is of the order of several hundreds. If M long nanowires are placed in parallel, the total conductance can be evaluated as $G = M \times G_0/N$ in the case of no failures (no defects); in the case of failures with probability P, the expression for the total conductance can be evaluated as

$$G = M \times G_0 \frac{(1-P)^N}{N}. \tag{14.13}$$

For example, by considering again $R_0 = 17$ kΩ, ($G_0 = 5.88 \times 10^{-5}\ \Omega^{-1}$), the total conductance in the case of 10 % of failures ($P = 0.\ 1$) is $G = 1.2 \times 10^{-15}\ \Omega^{-1}$ and the total resistance is $1/G = 8.2\ \times 10^{14}$, i.e. top and bottom are practically disconnected.

Tolerance of the total net electrical resistance with respect to nanowire width dispersion has been investigated. Random resistance networks have been generated; each resistor has been evaluated by considering an ohmic behavior of nanowires. Each one has a length of 3 μm and a random width generated by means of a gaussian random generator [40] with a given average width of 80 μm and standard deviation σ. Figure 14.9 shows the average total network resistance, evaluated on 100 random nets (generated by different seeds), as a function of the nanowire width standard deviation σ. The errorbars show the standard deviations of

the total net resistance that resulted to be well reduced with respect to the dispersion of the nanowire width. For example, given a $\sigma = \pm\ 50$ nm (more than 60 % of the average width of 80 nm), the total average resistance is 31,900 Ω with a standard deviation of ±152 Ω that is less than 5 %. This demonstrates the robustness of the total electrical resistance of the net with respect to the nanowire width dispersion. However, as far as the thermal conductivity is concerned, its reduction seems not to be linear with the nanowire width [18, 22]; in this case the average nanowire width and dispersion must be low enough for maintaining the thermal conductivity below a suitable value.

14.8 Network Reliability and Electrical Characterization

An estimation of nanowire failure percentage in fabricated networks, as the one shown in Fig. 14.4, can be performed by means of SEM inspection. For example, SEM photo of Fig. 14.10a shows a portion of a typical SiNW network, and interruptions (broken nanowires) in the network are enlightened. By inspecting several samples of fabricated SiNW networks, we can conclude that the mean value of failures is between 10 and 15 %. This value is well below the threshold failure percentage for which the whole resistance grows up noticeably. Figure 14.10b shows a typical $I-V$ characteristic measured for an SiNW network. The dispersion of the SiNW width W in a very large portion of the device is between 50 and 90 nm, and the proximity effect correction strategy previously described has been applied. The ohmic behavior shows that nonlinear effects in the conduction are negligible, and the value of about 66.7 kΩ is consistent to the above considerations about the electrical equivalence of the whole network with a large number of 1 mm long single nanowires in parallel. Indeed, from previous electrical measurements of a single SiNW the conductivity can be estimated of $40\times10^3\ \Omega^{-1}\ \mathrm{m}^{-1}$ (heavily doped). The measured resistance value of the network is comparable to the one of 190 SiNWs in parallel, with a length of 1 mm and a width mean value $W \simeq 72$ nm, which is very close to the W mean value observed by SEM inspection in a very large region of the device. Moreover, as it has been previously demonstrated, even a large dispersion in the width at the boundaries of the device does not affect the electrical characteristics of the network significantly, since the whole behavior of such devices is dominated by the large number of SiNWs smaller than 90 nm observed inside the structure.

14.9 Conclusions

In this chapter, after an introduction on the key concepts of thermoelectricity and a discussion of the different figures of merit used in the literature, we showed which are, nowadays, the limiting factors of a widespread diffusion of thermoelectric

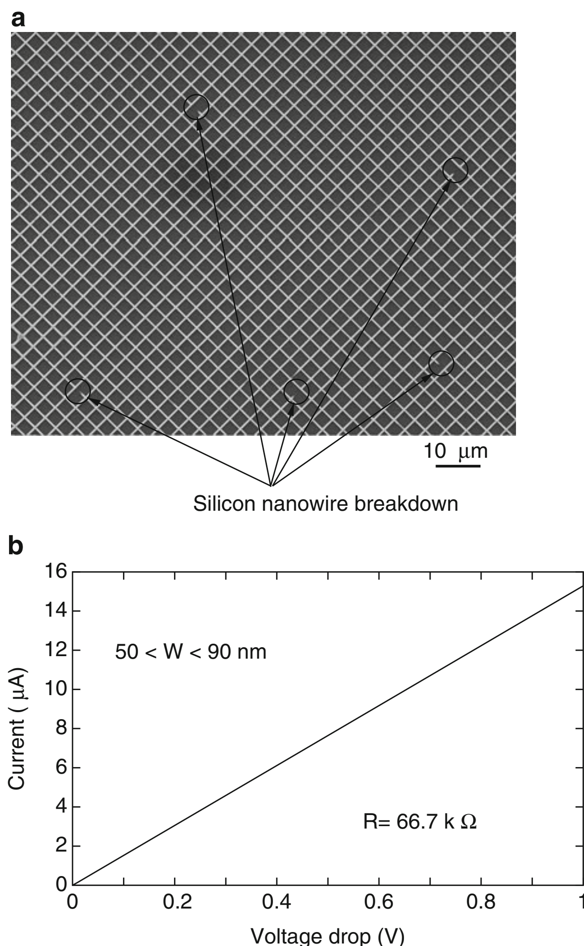

Fig. 14.10 In (**a**) an SEM image of a portion of SiNW network is shown; nanowire failures are enlightened. In (**b**) the $I-V$ characteristics of the SiNW network shown in (**a**), measured between the top and bottom contacts, are reported. The conduction is linear and the resistance is very similar to the one of many small and long silicon nanowires. (Reprinted with permission of Elsevier, from [28])

generators. In particular, currently available high efficient materials present several concerns in terms of abundance, toxicity, technological development, market distribution, and, ultimately, sustainability, which in last years is acquiring ever-increasing impact in the worldwide economy. Silicon could overcome all these aspects, since it is the most abundant element on the Earth's surface, it is not toxic, and, definitely, it is sustainable. Moreover, its technology and its market are impressively advanced, due to the leading role of silicon in the modern microelectronics. The main problem of bulk silicon for thermoelectric applications is its quite

high thermal conductivity *k* (about 148 W/mK), which does not allow relevant conversion efficiencies. We showed how nanostructuring can reduce *k* up to two order of magnitude, mainly due to the surface scattering of acoustic phonons, without any degradation of electrical properties, thus obtaining a significant improvement of thermoelectric performances.

Then, we presented a CMOS-compatible top-down process exploited for the fabrication of silicon nanowire arrays. We showed that these very large area networks are very reliable with respect to the failure of single SiNWs (the whole resistance variation is less than one order of magnitude up to 40 % of SiNW failures). Furthermore, the average value is very robust with respect to the SiNW width dispersion (even with a standard deviation about the 60 % of the average width value, the whole resistance standard deviation is less than 5 %).

These results are very promising for the fabrication of large area silicon nanowire networks that could allow practical applications of the interesting properties of SiNWs. In particular, the equivalence of reliable networks to the parallel of many, millimeters long, SiNWs makes this technique suitable for the fabrication of high efficiency thermoelectric devices. Finally, the possible implementation of this technique with advanced optical lithography is very promising for the fabrication of even larger area SiNW networks to be applied to energy harvesting.

References

1. Damen, K., Van Troost, M., Faaij, A., Turkenburg, W.: A comparison of electricity and hydrogen production systems with CO_2 capture and storage. Part A: Review and selection of promising conversion and capture technologies. Prog. Energy Combust. Sci. **32**, 215 (2006)
2. Lund, H.: Renewable energy strategies for sustainable development. Energy **32**, 912 (2007)
3. Jefferson, M.: Sustainable energy development: performance and prospects. Ren. Energy **31**, 571 (2006)
4. Bubnova, O., Crispin, X.: Towards polymer-based organic thermoelectric generators. Energy Environ. Sci. **5**, 9345 (2012)
5. Rowe, D.M.: Handbook of Thermoelectrics. CRC Press, Boca Raton (1995)
6. Xi, H., Luo, L., Fraisse, G.: Development and applications of solar-based thermoelectric technologies. Ren. Sust. Energy Rev. **11**, 923 (2007)
7. Fleurial, J.P.: Thermoelectric power generation materials: technology and application opportunities. JOM **61**, 79 (2009)
8. Yu, C., Chau, K.T.: Thermoelectric automotive waste heat energy recovery using maximum power point tracking. Energy Convers. Manag. **50**, 1506 (2009)
9. Bell, L.E.: Cooling, heating, generating power, and recovering waste heat with thermoelectric systems. Science **321**(5895), 145 (2008)
10. Stehlk, P.: Contribution to advances in waste-to-energy technologies. J. Clean. Prod. **17**(10), 919 (2009)
11. Yadav, G., Susoreny, J. A., Zhang, G., Yang, H., Wu, Y.: Nanostructure-based thermoelectric conversion: an insight into the feasibility and sustainability for large-scale deployment. Nanoscale **3**, 3555 (2011)
12. Heikes, R.R., Ure, R.W.: Thermoelectricity: Science and Engineering. Interscience, New York (1961)

13. Dragoman, D., Dragoman, M.: Giant thermoelectric effect in graphene. Appl. Phys. Lett. **91**, 203116 (2007)
14. Ishiwata, S., Shiomi, Y., Lee, J.S., Bahramy, M.S., Suzuki, T., Uchida, M., Arita, R., Taguchi, Y., Tokura, Y.: Extremely high electron mobility in a phonon-glass semimetal. Nat. Mater. **12**, 512 (2013)
15. Snyder, G.J., Ursell, T.S.: Thermoelectric efficiency and compatibility. Phys. Rev. Lett. **91** (14), 148031 (2003)
16. Snyder, G.J, Toberer, E.S.: Complex thermoelectric materials. Nat. Mater. **7**, 105 (2008)
17. Tritt, T.M., Subramian, M.A.: Thermoelectric materials, phenomena, and applications: A Bird's Eye View. Mrs Bull. **31**(3), 188 (2006)
18. Hochbaum, A.I., Chen, R., Delgado, R.D., Liang, W., Garnett, E.C., Najarian, M., Majumdar, A., Yang, P.: Enhanced thermoelectric performance of rough silicon nanowires. Nat. Lett.**451**, 163 (2008)
19. Jones, W., March, N.H.: Theoretical Solid State Physics. Courier Dover Publications, New York (1985)
20. Mingo, N.: Calculation of Si nanowire thermal conductivity using complete phonon dispersion relations. Phys. Rev. B **68**, 113308 (2003)
21. Liang, G., Huang, W., Koong, C.S., Wang, J-S., Lan, J.: Geometry effects on thermoelectric properties of silicon nanowires based on electronic band structures. J. Appl. Phys. **107**(1), 014317 (2010)
22. Li, D., Wu, Y., Kim, P., Shi, L., Yang, P., Majumdar, A.: Thermal conductivity of individual silicon nanowires. Appl. Phys. Lett. **83**, 2934 (2003)
23. Hippalgaonkar, B.H.K., Chen, R., Sawyer, K., Ercius, P., Majumdar, A.: Fabrication of microdevices with integrated nanowires for investigating low-dimensional phonon transport. Nano Lett. **10**(11), 4341 (2010)
24. Liu, L., Chen, X.: Effect of surface roughness on thermal conductivity of silicon nanowires. J. Appl. Phys. **107**(3), 033501 (2010)
25. Boukai, A.I., Bunimovich, Y., Tahir-Kheli, J., Goddar, W.A., Heat, J.R.: Silicon nanowires as efficient thermoelectric materials. Nat. Lett. **451**, 06458 (2008)
26. DiSalvo, F.J.: Thermoelectric cooling and power generation. Science **285**(5428), 703 (1999)
27. Koukharenko, E., Boden, S.A., Platzek, D., Bagnall, D.M., White, N.M.: Scalable silicon nanostructuring for thermoelectric applications. J. Electron. Mater. **42**, 2144 (2013)
28. Totaro, M., Pennelli, G., Bruschi, P.: Top down fabricated silicon nanowire networks for thermoelectric applications. Microelectron. Eng. **97**, 157 (2012)
29. Totaro, M., Pennelli, G., Piotto, M.: Investigation of silicon nanowire breakdown properties for the realization of one-time programmable memories. Microelectron. Eng. **88**, 2413 (2010)
30. Elibol, O.H., Morisette, D., Akin, D., Denton, J.P., Bashir, R.: Integrated nanoscale silicon sensors using top-down fabrication. Appl. Phys. Lett. **83**, 4613 (2003)
31. Pennelli, G., Piotto, M.: Fabrication and characterization of silicon nanowires with triangular cross section. J. Appl. Phys. **100**, 054507 (2006)
32. Pennelli, G., Pellegrini, B.: Fabrication of silicon nanostructures by geometry controlled oxidation. J. Appl. Phys. **101**, 10450 (2007)
33. Pennelli, G., Totaro, M., Nannini, A.: Correlation between surface stress and apparent young's modulus of top-down silicon nanowires. ACS Nano **6**, 10727 (2012)
34. Pennelli, G., Totaro, M., Bruschi, P.: Surface roughness and electron backscattering in high aspect ratio silicon nanowires. Microelectron. Eng. **88**, 2368 (2010)
35. Pennelli, G., Totaro, M., Piotto, M., Bruschi, P.: Seebeck coefficient of nanowires interconnected into large area networks. Nano Lett. **13**, 2592 (2013)
36. Pennelli, G., Totaro, M., Piotto, M.: Selective doping of silicon nanowires by means of electron beam stimulated oxide etching. Nano Lett. **12**, 1096 (2012)
37. Pennelli, G., D'Angelo, F., Piotto, M., Barillaro, G., Pellegrini, B.: A low cost high resolution pattern generator for electron-beam lithography. Rev. Sci. Instrum. **74**, 3579 (2003)

38. Pennelli, G.: Top down fabrication of long silicon nanowire devices by means of lateral oxidation. Microelectron. Eng. **89**, 2139 (2006)
39. Frank, D.J., Lobb, C.J.: Highly efficient algorithm for percolative transport studies in two dimensions. Phys. Rev. B **37**, 302 (1988)
40. Teukolsky, S.A., Vettering, W.T., Flannery, B.P., Press, W.H.: Numerical Recipes in C: The Art of Scientific Computing. Cambridge University Press, Cambridge (1992)
41. Stauffer, D., Aharony, A.: Introduction to Percolation Theory. CRC Press, London (1994)
42. Shklowskii, B.I., Efros, A.L.: Electronic Properties of Doped Semiconductors. Springer, New York (1984)

Chapter 15
Modeling and Analysis of Strain Effects on Thermoelectric Figure of Merit in Si/Ge Nanocomposites

Y. Xu and G. Li

Abstract In this chapter, strain effect on the thermoelectric figure of merit is investigated in *n*-type Si/Ge nanocomposite materials. Strain effect on phonon thermal conductivity in the nanocomposites is computed through a model combining the strain-dependent lattice dynamics and the ballistic phonon BTE. The Seebeck coefficient and electrical conductivity of the Si/Ge nanocomposites are calculated by an analytical model derived from the Boltzmann transport equation (BTE) under the relaxation-time approximation. The effect of strain is incorporated into the BTE through strain-induced energy shift and effective mass variation calculated from the deformation potential theory and a degenerate $\mathbf{k} \cdot \mathbf{p}$ method at the zone-boundary X point. Electronic thermal conductivity is computed from electrical conductivity by using the Wiedemann–Franz law. Various strains are applied in the transverse plane of the Si/Ge nanocomposites. Thermoelectric properties including thermal conductivity, electrical conductivity, Seebeck coefficient, and dimensionless figure of merit are computed for Si/Ge nanocomposites under these strain conditions.

15.1 Introduction

Thermoelectric materials and devices have promising applications in power generation, cooling systems, and waste heat recovery [6, 20, 42, 68, 77]. Driving these applications are several attractive properties, such as being pollution-free, silent, reliable, and scalable. However, presently they are only in limited use due to their relatively low energy conversion efficiency. They are not able to match the

Y. Xu • G. Li (✉)
College of Engineering and Science, Clemson University, Clemson, SC 29634, USA
e-mail: yxu@g.clemson.edu; gli@clemson.edu

X. Wang and Z.M. Wang (eds.), *Nanoscale Thermoelectrics*, Lecture Notes in Nanoscale Science and Technology 16, DOI 10.1007/978-3-319-02012-9_15,
© Springer International Publishing Switzerland 2014

performance of conventional refrigeration or efficiently generate power. The efficiency of thermoelectric materials is evaluated by the dimensionless figure of merit defined by ZT $= S^2\sigma T/k_t$, where S, σ, and T, respectively, denote the Seebeck coefficient, electrical conductivity, and absolute temperature, while k_t represents the thermal conductivity, including contributions from phonons and electrons [29]. The key goal in thermoelectrics research is to increase ZT, but this is a challenging process because adjustment of one parameter unavoidably involves variations of others [18]. In the past decade, synthesis and processing techniques have been developed to create nanostructured materials with highly controlled material composition, structures and related physical properties [2, 26, 30, 78]. Examples of the engineered nanostructures include nanotubes, quantum dots, superlattices, thin films, and nanocomposites. Recently, it has been reported that ZT values can be significantly improved in nanocomposites due to the largely increased material interfaces, which strongly scatter phonons but only slightly influence the charge carrier transport, leading to significantly reduced phonon thermal conductivity and maintained or improved power factor $S^2\sigma$ [71, 83]. Compared to one of the state-of-the-art thermoelectric power generation material, $Si_{0.8}Ge_{0.2}$ alloy, which has been used in space radioisotope thermoelectric power generators that operate at about 900° with a maximum efficiency of about 7 % [18], nanostructured Si/Ge bulk alloy leads to larger figure of merits due to the decreased phonon thermal conductivity [33, 76]. This method and others are being used to attempt to increase ZT values and create more universally viable thermoelectric nanocomposite materials.

Strain has long been serving as an important tool in enhancing the performance of modern CMOS devices [37, 58, 65, 69]. Crystal lattice deformation can induce band structure changes in semiconductor materials which commonly composed of band splitting and band warping [41, 69]. Band splitting may cause electron redistribution in the band valleys while band warping can result in conductivity effective mass change. The band splitting can reduce the inter-valley scattering and increase electron occupancy in the valleys with lower energies, and consequently influence the electron transport in the material. In addition, previous studies show that strain between two crystal lattices can also change the effective thermal conductivity [1, 5, 22, 51]. These results have motivated the authors to investigate the strain effects on the thermal and electrical transport properties of nanocomposite TE materials and explore the possibility to further increase the ZT by utilizing the strain effects through mechanical deformation. Investigating the strain effect on ZT of nanocomposites will not only help understanding the behavior of nanocomposite thermoelectric materials under strain but also introduce additional dimensions to the design space of nanocomposite thermoelectric materials.

In this work, we seek to investigate the effect of mechanical deformation on the thermal and electrical transport properties and the dimensionless figure of merit of Si/Ge nanocomposite thermoelectric materials. Strain can be introduced into nanocomposite materials under several conditions, such as phonon-induced lattice vibrations, lattice mismatch in nanocomposite growth, and applied external

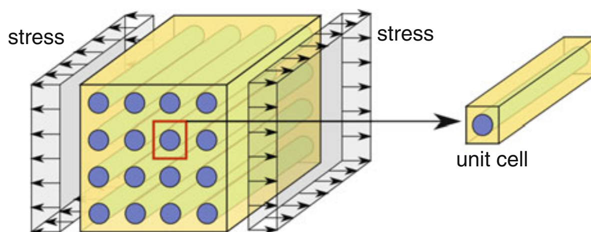

Fig. 15.1 $Si_{0.2}Ge_{0.8}$ nanocomposite material with applied strain

mechanical force. We focus on studying the effect of externally applied stresses on σ, S, k_t and ZT of n-type $Si_{1-x}Ge_x$ nanocomposites with Si (or Ge) nanowires embedded in Ge (or Si) host, as depicted in Fig. 15.1. The strain effect on phonon thermal conductivity in the nanocomposite material is simulated from a model [79] combining the lattice dynamics for phonon dispersion change (i.e., wave effects) due to strain with the ballistic phonon BTE for interface scattering of phonons (i.e., particle effects). In the model, several strain-dependent phonon scattering properties of the materials are used to link the lattice dynamics and the BTE. In this approach, there is no fitting parameter in the calculation. In addition, the finite volume solution of BTE over unstructured meshes allows thermal transport analysis of nanocomposites with complex geometries. The strain-dependent Seebeck coefficient and electrical conductivity of the Si/Ge nanocomposites are calculated from analytical models derived from the BTE under the relaxation-time approximation with strain-induced energy shift and effective mass variation, which are computed from the deformation potential theory and a two-band degenerate $\mathbf{k} \cdot \mathbf{p}$ method. In addition, electronic thermal conductivity is calculated from electrical conductivity by using the Wiedemann–Franz law. Then, by combining the strain effect models (phonon and electron), the strain effect on ZT of the nanocomposite materials is obtained [80].

The rest of the chapter is organized as follows. Section 15.2 describes the theoretical and computational models and calculated results depicting the strain effect on thermal transport in Si/Ge nanocomposite materials. Section 15.3 describes the theoretical model and a set of calculated electron transport properties of strained Si/Ge nanocomposites. The prediction of strain-dependent dimensionless figure of merit of $Si_{0.8}Ge_{0.2}$ nanocomposites is presented in Sect. 15.4. Section 15.5 gives conclusions.

15.2 Strain Effect on Thermal Transport in Si/Ge Nanocomposites

Thermal conductivity of doped semiconductors under uniaxial stress at low temperatures is relatively well understood [12, 34, 55, 61]. Recently, residual strain in nanocomposite materials has been studied by several groups. Borca-Tasciuc et al. measured thermal conductivity in the cross-plane direction of symmetrically

strained Si–Ge superlattices [7]. Abramson et al. studied interfacial strain on phonon transport and thermal conductivity of heterostructures around Debye temperature by Molecular Dynamics (MD) study [1]. Picu et al. have also employed Molecular Dynamics to study the residual strain effect on heat transport in nanostructures by using a Lennard–Jones solid at low temperatures and concluded that tensile (or compressive) strain led to a reduction (or enhancement) of the lattice thermal conductivity [51]. While these studies have shown the significance of strain on the nanoscale thermal transport, they are limited to single crystal materials or the residual strain effect at the interface of two different materials. Thermal conductivity variation of nanocomposite materials due to externally applied mechanical strain has not been studied. In addition, either analytical or pure atomistic methods such as Molecular Dynamics were employed in previous studies of strain effect. In strained nanocomposites, it is difficult to study the strain effect by using analytical approaches due to multiple material phases and complex geometry of the inclusion phase. Although lattice strain can be accommodated in MD calculations, the size of the system is limited due to the computational cost. For nanocomposites with characteristic length larger than a few nanometers, MD simulations would become very inefficient. Another nanoscale thermal transport analysis approach is based on the Boltzmann transport equation (BTE) [86]. This approach provides greater computational flexibility and efficiency. It has been successfully applied to compute the effective thermal conductivity of complex materials including nanocomposites [81]. However, this approach does not include mechanical variables such as strain in the model. In this section, we present a computational approach combining a strain-dependent lattice dynamics with the BTE and calculate the thermal conductivity of strained nanocomposite materials.

15.2.1 Theoretical Model and Computational Procedure

Figure 15.2 illustrates the theoretical model of the analysis. In this approach, atomic interactions are described by using interatomic potentials. Mechanical strains are translated to crystal lattice deformation by applying the Cauchy–Born rule. For the deformed crystal lattice, we employ the lattice dynamics theory to compute the strain-dependent phonon scattering properties for both Silicon and Germanium, including the group velocity, specific heat and phonon mean free path. The strain-dependent phonon scattering properties are then incorporated into the BTE to describe the thermal transport with interface scattering in the strained nanocomposites. Along with the BTE, a diffuse mismatch model is adopted for the Si–Ge interface. In the numerical solution of BTE, a unit cell of the nanocomposite material is taken as the computational domain with a periodic boundary condition. The unit cell is discretized into unstructured triangular volumes. The BTE is solved over the unstructured mesh by using a finite volume formulation. Heat flux and effective temperature are calculated for the volumes and faces from the intensity solution of the BTE. The strain-dependent effective thermal conductivity can then be obtained.

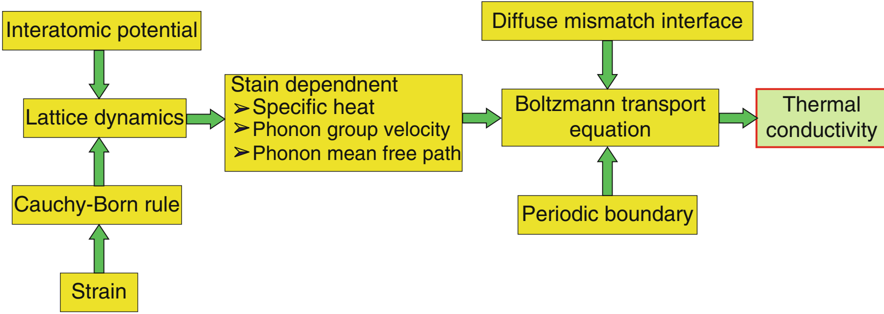

Fig. 15.2 Theoretical model of the analysis

Several assumptions are implied in the theoretical model described above: (1) Strain is assumed to be uniformly distributed throughout the nanocomposites, and residual strain is not considered between Si–Ge interfaces; (2) the BTE model employs a "gray" assumption with a single group velocity and single relaxation time [49]; (3) three-phonon scattering dominates the thermal transport within each material, and phonon scattering due to defects and/or impurities is neglected; (4) the scattering between Si–Ge interface is assumed to be diffuse.

15.2.2 Strain-Dependent Lattice Dynamics

At the atomistic level, interaction between atoms in diamond crystal lattices can be described by empirical interatomic potentials such as the Tersoff [66], Brenner [9], and Stillinger–Weber [62] potentials. Tersoff empirical interatomic potential is employed in this work for Si and Ge. Typically, the total potential energy U of a N-atom system is given by

$$U = \sum_{\alpha} U_{\alpha} = \frac{1}{2} \sum_{\alpha \neq \beta} V_{\alpha\beta} \tag{15.1}$$

where α and β are the atoms of the system and $V_{\alpha\beta}$ is the bond energy between atoms α and β given by

$$V_{\alpha\beta} = f_C(r_{\alpha\beta}) \left[a_{\alpha\beta} f_R(r_{\alpha\beta}) + b_{\alpha\beta} f_A(r_{\alpha\beta}) \right] \tag{15.2}$$

where $r_{\alpha\beta}$ is the distance between α and β, f_R and f_A denote the repulsive and attractive pair potentials defined as

$$f_R(r) = A e^{-\lambda_1 r} \tag{15.3}$$

$$f_A(r) = -B e^{-\lambda_2 r}, \tag{15.4}$$

respectively, $f_C(r_{\alpha\beta})$ is a smooth cutoff function going from 1 to 0 in a small range around the cutoff distance R_c, which is chosen to include only the first-neighbor shell for most structures of interest. $f_C(r)$ is defined as

$$f_C(r) = \begin{cases} 1 & r < R_c - D \\ \frac{1}{2} - \frac{1}{2}\sin\left(\frac{\pi(r-R_c)}{2D}\right) & R_c - D \le r \le R_c + D \\ 0 & r > R_c + D \end{cases} \quad (15.5)$$

In Eq. (15.2), $a_{\alpha\beta}$ is taken to be 1.0 for both Silicon and Germanium, $b_{\alpha\beta}$ is a measure of the bond order given by

$$b_{\alpha\beta} = \left(1+\mu^n \zeta_{\alpha\beta}^n\right)^{-1/2n}, \quad (15.6)$$

$$\zeta_{\alpha\beta} = \sum_{\chi \neq \alpha,\beta} f_C(r_{\alpha\chi}) g(\theta_{\alpha\beta\chi}) \exp\left(\lambda_3^3 (r_{\alpha\beta} - r_{\alpha\chi})^3\right), \quad (15.7)$$

$$g(\theta_{\alpha\beta\chi}) = 1 + c^2/d^2 - c^2/\left[d^2 + (h - \cos\theta_{\alpha\beta\chi})^2\right] \quad (15.8)$$

where χ denotes an atom, and $\theta_{\alpha\beta\chi}$ is the bond angle between the bonds $\alpha\beta$ and $\alpha\chi$. All remaining variables are constant parameters. For Silicon, the constants are summarized in the 3rd column of Table I in [66]. For Germanium, the constants are adopted from Table I in [67].

In the classical lattice dynamics, by using the periodicity of the crystal structure, the phonon frequency spectrum can be obtained by computing the eigenvalues of the dynamical matrix $\mathbf{D}(\mathbf{k})$ for each wave vector $\mathbf{k}$ in the first Brillouin zone, i.e. [85],

$$\mathbf{D}(\mathbf{k}) = \frac{1}{M}\begin{bmatrix} \sum_\beta \Phi_{j,k}^{11}(\alpha,\beta) e^{i\mathbf{k}\cdot(\mathbf{x}_\beta^0 - \mathbf{x}_\alpha^0)} & \sum_\beta \Phi_{j,k}^{12}(\alpha,\beta) e^{i\mathbf{k}\cdot(\mathbf{x}_\beta^0 - \mathbf{x}_\alpha^0)} \\ \sum_\beta \Phi_{j,k}^{21}(\alpha,\beta) e^{i\mathbf{k}\cdot(\mathbf{x}_\beta^0 - \mathbf{x}_\alpha^0)} & \sum_\beta \Phi_{j,k}^{22}(\alpha,\beta) e^{i\mathbf{k}\cdot(\mathbf{x}_\beta^0 - \mathbf{x}_\alpha^0)} \end{bmatrix} \quad j,k = 1,2,3 \quad (15.9)$$

where α and β denote the atoms in the unit cell, M is the mass of atom, $\mathbf{k}$ is wave vector, $\mathbf{x}_\alpha^0$ and $\mathbf{x}_\beta^0$ are the equilibrium positions of atom α and β, respectively, and $\Phi_{j,k}^{pq}(\alpha,\beta)$ is force constant defined by

$$\Phi_{j,k}^{pq}(\alpha,\beta) = \left.\frac{\partial^2 U(\mathbf{x})}{\partial \mathbf{x}_{\alpha j} \partial \mathbf{x}_{\beta k}}\right|_{\mathbf{x}=\mathbf{x}^0, \alpha \in B_p, \beta \in B_q} \quad j,k = 1,2,3;\ p,q = 1,2 \quad (15.10)$$

in which $\mathbf{x}_{\alpha j}$ and $\mathbf{x}_{\beta k}$ are the jth and the kth components of the position of atoms α and β, respectively. B_p and B_q are Bravais lattices p and q, respectively. Note that we choose α to be the center atom and loop atom β over all the atoms in the crystal lattice. The phonon frequencies can be calculated by $\omega_{s\mathbf{k}} = \sqrt{\lambda_{s\mathbf{k}}}$, where $\lambda_{s\mathbf{k}}$ are the eigenvalues of the 6×6 dynamical matrix $\mathbf{D}(\mathbf{k})$ and s is the index of the polarization.

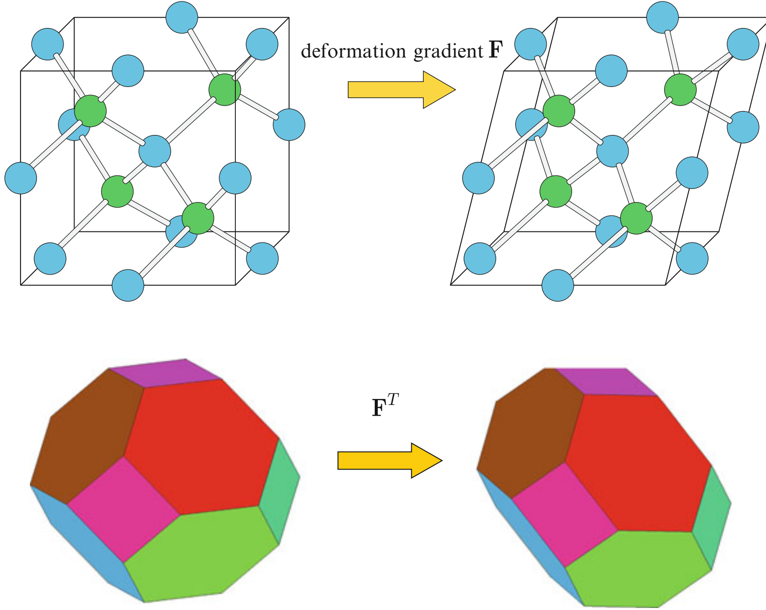

Fig. 15.3 *Top*: atom configuration and deformation for a diamond lattice. *Bottom*: corresponding deformation of the first Brillouin zone

When there is an applied strain, to relate the continuum level description of deformation to displacements of the atoms in the crystal lattice as shown in Fig. 15.3(top), we employ the hypotheses of the Cauchy–Born rule [8] which states that the crystal lattice is homogeneously distorted according to the deformation gradient. For Silicon/Germanium crystal, there exist additional inner displacements between the two Bravais lattices. The Cauchy–Born rule gives

$$\mathbf{x}_\beta^0 - \mathbf{x}_\alpha^0 = \mathbf{F}\left(\mathbf{X}_\beta^0 - \mathbf{X}_\alpha^0\right) + \xi \tag{15.11}$$

where $\mathbf{F}$ is the deformation gradient of the Bravais lattice, $\mathbf{X}_\alpha^0$ and $\mathbf{X}_\beta^0$ are the equilibrium positions of atom α and β in the undeformed configuration, respectively, and ξ is the inner displacement of the two FCC Bravais lattices. Note that $\mathbf{F} = \mathbf{I} + \partial\mathbf{u}/\partial\mathbf{X}^0$ where $\mathbf{u}$ is the displacement vector of an atom.

In the reciprocal lattice of a Bravais lattice, from Eq. (15.11), it is easy to show that, a given wave vector $\mathbf{k}^0$ in the undeformed configuration of the lattice deforms to $\mathbf{k}$ in the deformed configuration with the relation

$$\mathbf{k} = \mathbf{F}^{-T}\mathbf{k}^0 \tag{15.12}$$

as shown in Fig. 15.3(bottom). Substituting Eqs. (15.11, 15.12) into Eq. (15.9), the strain-dependent dynamical matrix can then be written as [85]

$$\mathbf{D}(\mathbf{k}) = \frac{1}{M}\left[\begin{array}{cc} \sum_{\beta}\overline{\Phi}^{11}_{jk}(\alpha,\beta)e^{i\mathbf{k}^0\cdot(\mathbf{X}^0_\beta-\mathbf{X}^0_\alpha)} & \sum_{\beta}\overline{\Phi}^{12}_{jk}(\alpha,\beta)e^{i\mathbf{k}^0\cdot(\mathbf{X}^0_\beta-\mathbf{X}^0_\alpha-\mathbf{F}^{-1}\xi)} \\ \sum_{\beta}\overline{\Phi}^{21}_{jk}(\alpha,\beta)e^{i\mathbf{k}^0\cdot(\mathbf{X}^0_\beta-\mathbf{X}^0_\alpha+\mathbf{F}^{-1}\xi)} & \sum_{\beta}\overline{\Phi}^{22}_{jk}(\alpha,\beta)e^{i\mathbf{k}^0\cdot(\mathbf{X}^0_\beta-\mathbf{X}^0_\alpha)} \\ & \alpha=1,\quad j,k=1,2,3 \end{array}\right] \tag{15.13}$$

where

$$\overline{\Phi}^{pq}_{j,k}(\alpha,\beta) = \left.\frac{\partial^2 U(\mathbf{x})}{\partial \mathbf{x}_{\alpha j}\partial \mathbf{x}_{\beta k}}\right|_{\mathbf{x}=\mathbf{x}^0(\mathbf{X}^0,\mathbf{F},\xi),\alpha\in B_p,\beta\in B_q} \qquad j,k=1,2,3;\ p,q=1,2 \tag{15.14}$$

and $\mathbf{F}^{-1}$ is the inverse of $\mathbf{F}$. The phonon frequencies of the strained bulk crystal Si and Ge, $\omega_{s\mathbf{k}}(\mathbf{F}, \xi)$, can be obtained by computing the eigenvalues of Eq. (15.13). After the phonon frequency spectrum is obtained, the Helmholtz free energy A of the system can be calculated by

$$A = U(\mathbf{X}^0,\mathbf{F},\xi) + \frac{1}{2}\sum_{\mathbf{k}}\sum_{s=1}^{6}\hbar\omega_{s\mathbf{k}}(\mathbf{F},\xi) + k_B T\sum_{\mathbf{k}}\sum_{s=1}^{6}\ln\left(1-e^{-\frac{\hbar\omega_{s\mathbf{k}}(\mathbf{F},\xi)}{k_B T}}\right) \tag{15.15}$$

where $U(\mathbf{X}^0, \mathbf{F}, \xi)$ is the total potential energy of the system at the deformed equilibrium position, $\hbar$ is the reduced Planck's constant, k_B is the Boltzmann constant, and T is temperature. For a given deformation gradient $\mathbf{F}$, the inner displacement ξ can be determined by minimizing the Helmholtz free energy, i.e.,

$$\frac{\partial A}{\partial \xi} = 0 \tag{15.16}$$

15.2.3 Strain-Dependent Thermodynamic and Phonon Scattering Properties

For a given deformation gradient $\mathbf{F}$, we compute the phonon frequency spectrum of Si and Ge lattices by sampling the $\mathbf{k}$ points in the first Brillouin zone. Once the phonon frequency spectrum is obtained, the bulk thermodynamic and phonon scattering properties of Si and Ge can be calculated. Of particular interest are the specific heat, the average phonon group velocity and the average phonon mean free path. As will be described later, they are the physical variables used in the BTE for the analysis of thermal transport in the Si–Ge nanocomposites. To compute these thermodynamic and phonon scattering properties, we first compute the bulk thermal conductivity of Si and Ge as a function of $\mathbf{F}$ by using the Slack relation [31, 60]. The Slack relation is suitable for calculating the thermal conductivity of nonmetallic

crystals at high temperatures (above 1/5 of the Debye temperature) where heat is mainly carried by acoustic phonons and the scattering is mainly intrinsic three-phonon process. The bulk thermal conductivity is given by [31, 60]

$$k_b = \frac{3.1 \times 10^7 < M > \delta T_D^3}{T < \gamma^2 > N_c^{2/3}} \tag{15.17}$$

where $<M>$ is the average atomic mass of the crystal, δ^3 is the average volume per atom, N_c is the number of atoms in a primitive cell, and T_D is high-temperature limit of the Debye temperature defined by

$$T_D^2 = \frac{5h^2 \int_0^\infty \omega^2 D_p(\omega) \mathrm{d}\omega}{3k_B^2 \int_0^\infty D_p(\omega) \mathrm{d}\omega} \tag{15.18}$$

in which h is Planck's constant, ω is the frequency, and $D_p(\omega)$ is phonon density of states. $<\gamma^2>$ is mode-averaged square of the Grüneisen parameter given by

$$< \gamma^2 > = \frac{1}{C} \sum_{\mathbf{k}} \sum_{s=1}^{6} (\gamma_{s\mathbf{k}})^2 C_{s\mathbf{k}} \tag{15.19}$$

where the Grüneisen parameter $\gamma_{s\mathbf{k}}$ for the s-th mode of a given wave vector $\mathbf{k}$ is defined as

$$\gamma_{s\mathbf{k}} = -\frac{\partial \ln \omega_{s\mathbf{k}}}{\partial \ln V}, \tag{15.20}$$

where V is the volume per atom, $C_{s\mathbf{k}}$ is the phonon specific heat given by

$$C_{s\mathbf{k}} = k_B \frac{\left(\frac{\hbar\omega_{s\mathbf{k}}}{k_B T}\right)^2 e^{\frac{\hbar\omega_{s\mathbf{k}}}{k_B T}}}{\left(e^{\frac{\hbar\omega_{s\mathbf{k}}}{k_B T}} - 1\right)^2}, \tag{15.21}$$

and C is the total specific heat given by

$$C = \sum_{\mathbf{k}} \sum_{s=1}^{6} C_{s\mathbf{k}}. \tag{15.22}$$

Noted that since the phonon frequencies $\omega_{s\mathbf{k}}(\mathbf{F}, \xi)$ depend on the applied strain, thermodynamic properties such as T_D, γ, C, and k_b are all functions of strain. For the simplicity of notation, "$(\mathbf{F}, \xi)$" is not shown explicitly for these quantities. After the bulk thermal conductivity k_b is obtained, the average phonon mean free path (MFP) can be calculated from approximated Kinetic theory by [16]

$$k_b \approx \frac{\Lambda}{3} \sum_{\mathbf{k}} \sum_{s=1}^{3} C_{s\mathbf{k}} v_{s\mathbf{k}} \quad s \in \text{acoustic phonon branches} \tag{15.23}$$

where $v_{s\mathbf{k}}$ is the acoustic phonon group velocity given by

$$v_{s\mathbf{k}} = \left| \frac{\partial \omega_{s\mathbf{k}}}{\partial \mathbf{k}} \right|. \tag{15.24}$$

Note that, in Eq. (15.23), only the acoustic branches of the phonon dispersion are included. The optical phonons are excluded for a better approximation of the average phonon MFP since they contribute little to the thermal conductivity at room temperature for Si and Ge due to their small group velocities. More detailed justification for this choice can be found in [15, 16]. The average phonon group velocity is then obtained from the average phonon MFP as

$$v = \frac{3k_b}{C^a \Lambda} \tag{15.25}$$

where C^a is the acoustic phonon specific heat which is obtained by summing $C_{s\mathbf{k}}$ over the acoustic branches. Again, the phonon scattering properties Λ and v are all function of the strain.

15.2.4 Boltzmann Transport Equation Model for Nanocomposites

Once the strain-dependent phonon thermal properties of the bulk Si and Ge are obtained, the effective thermal conductivity of nanocomposites can then be calculated by using a thermal transport model. Among various models that can be used to predict the thermal conductivity of nanocomposites [1, 10, 84], BTE-based thermal modeling approaches have been developed and applied to thermal transport analysis in various applications with demonstrated accuracy and efficiency (see [49] for a review). In this work, we adopt the "gray" BTE approach for the computational thermal transport analysis of Si–Ge nanocomposites. The BTE model under "gray" assumption can be expressed in terms of total phonon intensity as [14, 43]

$$\nabla \cdot (I(\mathbf{r}, \mathbf{s}) \cdot \mathbf{s}) = -\frac{I(\mathbf{r}, \mathbf{s}) - I_0(\mathbf{r})}{\Lambda} \tag{15.26}$$

where $I(\mathbf{r}, \mathbf{s})$ is the total phonon intensity at a spatial position $\mathbf{r} = \{x, y, z\}$ over a path length ds in the direction of unit vector $\mathbf{s}$. As shown in Fig. 15.4, $\mathbf{s}$ is defined by

$$\mathbf{s} = \sin\theta \cos\phi \mathbf{e}_x + \sin\theta \sin\phi \mathbf{e}_y + \cos\theta \mathbf{e}_z \tag{15.27}$$

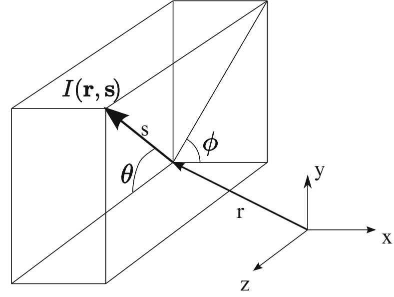

Fig. 15.4 Directional phonon intensity

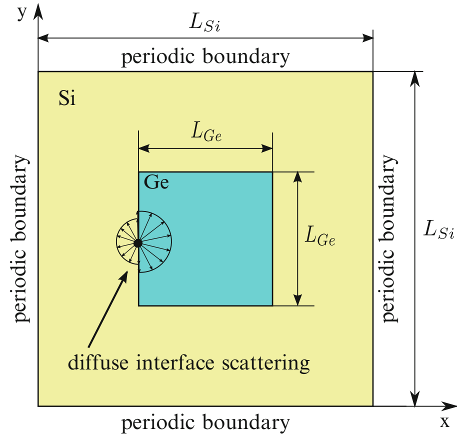

Fig. 15.5 Unit cell of $Si_{1-x}Ge_x$ nanocomposites for numerical solution of the BTE and calculation of the phonon thermal conductivity of the materials

where $\theta \in [0, \pi]$ and $\phi \in [0, 2\pi]$ represent polar and azimuthal angles, respectively, and $\mathbf{e}_x$, $\mathbf{e}_y$, and $\mathbf{e}_z$ are the unit vectors in the x, y, and z directions, respectively. $I_0(\mathbf{r})$ is the equivalent equilibrium phonon intensity which is given by

$$I_0(\mathbf{r}) = \frac{1}{4\pi} \int_0^{2\pi} \int_0^{\pi} I(\mathbf{r}, \mathbf{s}) \sin\theta \mathrm{d}\theta \mathrm{d}\phi \tag{15.28}$$

Assuming a uniform distribution of the Si nanowires, the BTE can be solved in a 2-D unit cell of the nanocomposite material as shown in Fig. 15.5. The edge length of the unit cell is denoted as L. The phonon intensities in the Si–Ge domains are determined by the BTE. Periodic boundary conditions are employed on the outer boundary of the unit cell. The phonon scattering at the Si–Ge interface is assumed to be diffuse. In this work, the boundary and interface models developed by Yang and Chen [81] for nanocomposites are adopted and implemented using the finite volume method. The boundary and interface conditions are briefly summarized as follows. For the top $(y = L)$ and bottom $(y = 0)$ edges, the periodic boundary condition can be written as

$$I(x, L, \mathbf{s}) = I(x, 0, \mathbf{s}), \tag{15.29}$$

for all x and $\mathbf{s}$. For the right ($x = 0$) and left ($x = L$) edges, the periodic boundary condition implies that the difference between the phonon intensities in any given direction at the right and left edges is independent of y. This constant difference is imposed by a temperature drop, ΔT, between the left and right edges. The magnitude of ΔT, however, does not affect the result of the thermal conductivity. The periodic boundary condition is given by

$$I(0, y, \mathbf{s}) - I(L, y, \mathbf{s}) = \frac{v_{\mathrm{Ge}} C_{\mathrm{Ge}}^{a} \Delta T}{4\pi}, \tag{15.30}$$

where v_{Ge} and C_{Ge}^{a} denote the group velocity and acoustic specific heat of Germanium, respectively. The diffuse interface scattering is represented by a simple diffuse mismatch model which assumes, at the interface, part of the phonons are transmitted through and the rest are reflected back. The transmitted and reflected phonons are evenly distributed across all angles on each side of the interface, as shown in Fig. 15.5. From the energy conservation, the relation of reflectivity R and transmissivity T is given by

$$T_{\mathrm{GS}} = R_{\mathrm{SG}} = 1 - T_{\mathrm{SG}}, \tag{15.31}$$

where the subscript GS denotes from Ge into Si and vice versa, and T_{GS} is given by [16]

$$T_{\mathrm{GS}} = \frac{C_{\mathrm{Si}}^{a} v_{\mathrm{Si}}}{C_{\mathrm{Ge}}^{a} v_{\mathrm{Ge}} + C_{\mathrm{Si}}^{a} v_{\mathrm{Si}}}. \tag{15.32}$$

By solving the BTE in both Si and Ge domains with the boundary and interface conditions, the phonon intensity $I(x, y, \mathbf{s})$ can be obtained. It is then straightforward to calculate the effective temperature distribution, heat flux, and thermal conductivity. Note that, since the local thermal equilibrium condition breaks down in nanostructures, an effective temperature is used to represent the local energy density, i.e.,

$$T(x, y) = \frac{4\pi I_0(x, y)}{C^{a} v} \tag{15.33}$$

The average temperature at each $y{-}z$ plane along the x-direction is then obtained as

$$\bar{T}(x) = \frac{1}{L} \int_0^L T(x, y) \mathrm{d}y \tag{15.34}$$

The heat flux in the x-direction, q_x, is computed by integrating the x-component of the phonon intensity over the entire solid angle

$$q_x(x,y) = \int_0^{2\pi} \int_0^{\pi} I(x,y,\mathbf{s}) \sin^2\theta \cos\phi \mathrm{d}\theta \mathrm{d}\phi \tag{15.35}$$

The effective thermal conductivity is then calculated by using Fourier's law.

$$k_e = \frac{\int_0^L q_x(x,y)\mathrm{d}y}{\bar{T}(0) - \bar{T}(L)} \tag{15.36}$$

Note that k_e is guaranteed to be constant along the x-axis by the periodic boundary conditions imposed by Eq. (15.29).

15.2.5 Finite Volume Solution of BTE

Due to the similarity between the thermal radiative transfer equation (RTE) and the BTE, numerical methods for solving RTE are often applicable to BTE. Among a variety of numerical methods that are used to solve the RTE, the discrete ordinates method (DOM) and the finite volume method (FVM) are most popular. The DOM is known for its simplicity and efficiency. However, like the finite difference method, the DOM typically requires a structured grid, which imposes a major difficulty for problems involving complex geometries. In comparison, the FVM can be easily applied to unstructured meshes. Thus it provides greater flexibility in treating complex geometries. In addition, integration over the control angles is calculated exactly and heat flux in control volumes is automatically conserved in FVM [54]. Due to these attractive properties, the FVM has been employed for radiative thermal transport analysis in various applications [11, 19, 35, 46]. It has also been applied to obtain BTE solution for heat transfer analysis of submicron structures [48]. In this work, as the Si–Ge nanocomposites to be investigated contain Si nanowires with different shaped cross sections as shown in Fig. 15.1, the FVM is employed in the computational analysis. One difficulty in the FVM solution of the BTE on an unstructured mesh is that the control angles may overlap with the control volume boundaries. In such cases, the overlapping control angle contains both the outgoing and incoming phonons. Several authors have addressed this issue for radiative heat transfer problems [3, 35, 46]. We employ an exact treatment proposed in [3]. This treatment is found to be effective to resolve the problem for our calculations.

As shown in Fig. 15.6, the 2-D domain of the Si–Ge unit cell is discretized into non-overlapping triangular volumes (or elements). The volume of a given triangular element is denoted as ΔV. The length of the edges is denoted as ΔA_i, $i = 1, 2, 3$. Within each triangular volume, the phonon intensity is defined on the center node of

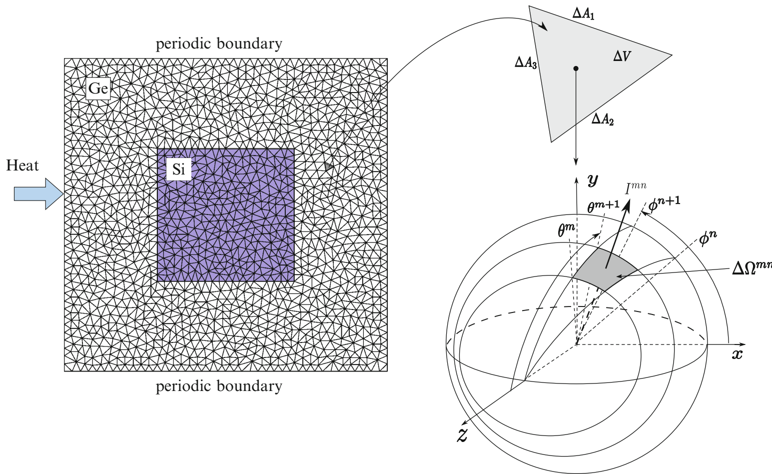

Fig. 15.6 Spatial and angular discretization

the triangular volume. The total solid angle, 4π, of the center node is discretized into $N_\theta \times N_\phi$ control angles along θ and ϕ directions. The control angles are denoted as $\Delta\Omega^{mn}$ ($1 \leq m \leq N_\theta$, $1 \leq n \leq N_\phi$) with the polar and azimuthal angles spanning from θ^m to θ^{m+1} and ϕ^n to ϕ^{n+1}, respectively, as shown in Fig. 15.6. Within each control volume and control angle $\Delta\Omega^{mn}$, the phonon intensity is assumed to be constant and denoted as I^{mn}. For each control volume and control angle, the governing BTE, Eq. (15.26), is integrated over ΔV and $\Delta\Omega^{mn}$ to yield

$$\int_{\Delta\Omega^{mn}} \int_{\Delta V} \nabla \cdot (I\mathbf{s})\, \mathrm{d}V\, \mathrm{d}\Omega = \int_{\Delta\Omega^{mn}} \int_{\Delta V} \left(-\frac{I - I_0}{\Lambda} \right) \mathrm{d}V\, \mathrm{d}\Omega \tag{15.37}$$

Applying the divergence theorem, Eq. (15.37) can be rewritten as

$$\int_{\Delta\Omega^{mn}} \int_{\Delta A} I\mathbf{s} \cdot \mathbf{n}\, \mathrm{d}A\, \mathrm{d}\Omega = \int_{\Delta\Omega^{mn}} \int_{\Delta V} \left(-\frac{I - I_0}{\Lambda} \right) \mathrm{d}V\, \mathrm{d}\Omega \tag{15.38}$$

For a given triangular control volume with a center node P, the phonon intensity in the control angle $\Delta\Omega^{mn}$ is denoted as $I_P{}^{mn}$. Assuming that for a given control angle, facial intensities are constant on each boundary face of the volume, the following finite-volume formulation can be obtained from Eq.(15.38) as

$$\sum_{i=1,2,3} I_i^{mn}\, \Delta A_i D_{\mathrm{C}i}^{mn} = \frac{1}{\Lambda} \left(-I_P^{mn} + (I_0^{mn})_P \right) \Delta V\, \Delta\Omega^{mn}, \tag{15.39}$$

where I_i^{mn} is the facial intensity on ΔA_i, $i = 1, 2, 3$, and the directional weight $D_{\mathrm{C}i}{}^{mn}$ is given by

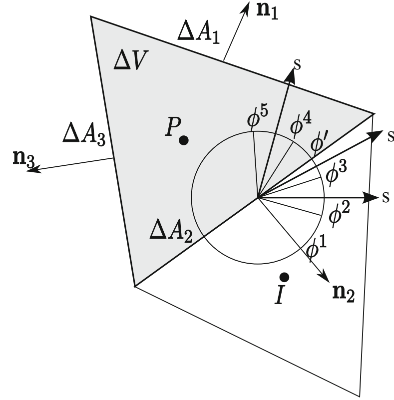

Fig. 15.7 Step scheme for the facial intensity

$$D_{\mathrm{Ci}}^{mn} = \int_{\theta^m}^{\theta^{m+1}} \int_{\phi^n}^{\phi^{n+1}} (\mathbf{s} \cdot \mathbf{n}_i) \sin\theta \mathrm{d}\theta \, \mathrm{d}\phi, \quad i = 1, 2, 3, \tag{15.40}$$

where $\mathbf{s}$ is given by Eq. (15.27) and $\mathbf{n}_i$ is the outward normal of the i-th face of the control volume. For 2-D problems, ${D_{\mathrm{Ci}}}^{mn}$ can be obtained as

$$\begin{aligned} {D_{\mathrm{Ci}}}^{mn} = & \left[\frac{\Delta\theta}{2} - \frac{1}{4}(\sin 2\theta^{m+1} - \sin 2\theta^m)\right] \\ & \times [n_x(\sin\phi^{n+1} - \sin\phi^n) - n_y(\cos\phi^{n+1} - \cos\phi^n)] \end{aligned} \tag{15.41}$$

where n_x and n_y are the x- and y-components of $\mathbf{n}_i$. In Eq. (15.40), the sign of ${D_{\mathrm{Ci}}}^{mn}$ (or equivalently, the sign of $\mathbf{s} \cdot \mathbf{n}_i$) determines whether the phonons are incoming or outgoing across the faces of control volume.

The facial intensity I_i^{mn} is then related to the nodal intensity by a step scheme assuming a downstream facial intensity is equal to the upstream nodal intensity. For example, as shown in Fig. 15.7, for face 2 of the control volume of node P, if the azimuthal angle of $\mathbf{s}$ is between ϕ^2 and ϕ^3, one obtains $\mathbf{s} \cdot \mathbf{n}_2 > 0$, i.e., phonons are outgoing and P is the upstream node. Therefore, $I_{i=2}^{mn} = I_P^{mn}$. If $\mathbf{s}$ is between ϕ^4 and ϕ^5, then $\mathbf{s} \cdot \mathbf{n}_2 < 0$ and the node I of the neighbor control volume is the upstream node. Therefore, $I_{i=2}^{mn} = I_I^{mn}$. However, as shown in Fig. 15.7, the control angle from ϕ_3 to ϕ_4 overlaps with the face and contains both incoming and outgoing phonons. It is more involved to determine the facial intensity in this situation. The solution to this control angel overlap problem has been summarized in [35]. In this work, we employ an exact treatment described in [3] which splits the control angle into [ϕ^3, ϕ'] and [ϕ', ϕ^4] as shown in Fig. 15.7 and integrates the two resultant control angle separately. The facial intensity can be expressed by the following general expression as

$$I_i^{mn} D_{\mathrm{ci}}^{mn} = I_P^{mn} D_{\mathrm{ci,out}}^{mn} + I_I^{mn} D_{\mathrm{ci,in}}^{mn} \tag{15.42}$$

where, for a non-overlapping control angle,

$$\text{if} \quad \mathbf{s}\cdot\mathbf{n}_i > 0, \quad \text{then} \quad D^{mn}_{\text{Ci,out}} = \int_{\theta^m}^{\theta^{m+1}} \int_{\phi^n}^{\phi^{n+1}} (\mathbf{s}\cdot\ \mathbf{n}_i)\sin\theta \mathrm{d}\theta\,\mathrm{d}\phi, \quad D^{mn}_{\text{Ci,in}} = 0, \tag{15.43}$$

$$\text{if} \quad \mathbf{s}\cdot\mathbf{n}_i < 0, \quad \text{then} \quad D^{mn}_{\text{Ci,in}} = \int_{\theta^m}^{\theta^{m+1}} \int_{\phi^n}^{\phi^{n+1}} (\mathbf{s}\cdot\ \mathbf{n}_i)\sin\theta \mathrm{d}\theta\,\mathrm{d}\phi, \quad D^{mn}_{\text{Ci,out}} = 0, \tag{15.44}$$

For an overlapping control angle, without loss of generality, assuming $\mathbf{s}\cdot\mathbf{n}_i > 0$ in $[\phi^n, \phi']$ and $\mathbf{s}\cdot\mathbf{n}_i < 0$ in $[\phi', \phi^{n+1}]$, we have

$$\begin{aligned} D^{mn}_{\text{Ci,out}} &= \int_{\theta^m}^{\theta^{m+1}} \int_{\phi^n}^{\phi'} (\mathbf{s}\cdot\ \mathbf{n}_i)\sin\theta \mathrm{d}\theta\mathrm{d}\phi, \\ D^{mn}_{\text{Ci,in}} &= \int_{\theta^m}^{\theta^{m+1}} \int_{\phi'}^{\phi^{n+1}} (\mathbf{s}\cdot\ \mathbf{n}_i)\sin\theta \mathrm{d}\theta\,\mathrm{d}\phi. \end{aligned} \tag{15.45}$$

When a control volume face is on the Si–Ge interface, the interface condition given in Eq. (15.31) is applied by replacing I_I^{mn} in Eq. (15.42) with

$$I_I^{mn} = \frac{R_{PI}}{\pi} \sum_{mn} I_P^{mn} D^{mn}_{\text{Ci,out}} - \frac{T_{IP}}{\pi} \sum_{mn} I_I^{mn} D^{mn}_{\text{Ci,in}} \tag{15.46}$$

where R_{PI} is the reflectivity from medium of node P to the medium of node I, and T_{IP} is the transmissivity from medium of node I to the medium of node P. It should be noted that the interface condition only modifies I_I^{mn} in Eq. (15.42) and I_P^{mn} remains the same. Otherwise, the transmission and reflection of the phonons would be double counted and the energy conservation condition would be violated. Substituting Eq. (15.42) into Eq. (15.39), the finite-volume formulation of the BTE for each control volume and control angle can be obtained as

$$\begin{aligned} &\left(\sum_i \Delta A_i D^{mn}_{\text{Ci,out}} + \frac{\Delta V}{\Lambda}\,\Delta\Omega^{mn} - \frac{\Delta V}{4\pi\Lambda}\,(\Delta\Omega^{mn})^2 \right) I_P^{mn} \\ &\qquad = -\sum_i \Delta A_i D^{mn}_{\text{Ci,in}} I_I^{mn} + \frac{\Delta V}{4\pi\Lambda} \left(\sum_{m'n' \neq mn} I_P^{m'n'}\,\Delta\Omega^{m'n'} \right) \Delta\Omega^{mn} \end{aligned} \tag{15.47}$$

For the global system, there are a total of $N_V \times N_\phi \times N_\theta$ equations, where N_V is the number of control volumes. This set of equations are solved iteratively by using the Gauss–Seidel method. Note that, like the DOM, in Gauss–Seidel iterations, the nodal intensities are calculated in each control volume and control angle by using

Table 15.1 Room temperature thermodynamic properties of bulk Si

$C(\frac{J}{m^3K})$	$T_D(K)$	γ	$v_{\text{LA}}^{\Gamma}(\frac{m}{s})$	$v_{\text{TA}}^{\Gamma}(\frac{m}{s})$	$v_{\text{LA}}^{X}(\frac{m}{s})$	$k_b(\frac{W}{mK})$
1.59×10^6	720	0.79	8,705	5,470	4,540	167.6
1.65×10^6 [25]	645[36]	0.8[52]	8,480[13]	5,860[13]	4,240[13]	156[27]

the values obtained from the last iteration. No global matrix storage is required. The iteration stops when the following convergence condition is reached:

$$\max\left(\left|I_P^{mn} - (I^{mn})_P^{\text{old}}\right| / I_P^{mn}\right) \leq 10^{-6}. \tag{15.48}$$

15.2.6 Strain Effect on Thermal Properties of Bulk Si and Ge

We first investigate the strain effect on thermodynamic properties of bulk Si and Ge. From the lattice dynamics with Tersoff potential, various thermodynamic properties of bulk Si and Ge can be calculated. A few thermodynamic properties that are used in the calculation of the thermal conductivity are first calculated under unstrained condition. These results are compared with the experimental data and other theoretical results. Table 15.1 lists the specific heat (C), Debye temperature (T_D), Grüneisen parameter (γ), longitudinal acoustic group velocity at Γ point in the first Brillouin zone (v_{LA}^{Γ}), transverse acoustic group velocity at Γ point (v_{TA}^{Γ}), longitudinal acoustic group velocity at X point (v_{LA}^{X}), and the bulk thermal conductivity (k_b) of Silicon. The comparison shows that the Tersoff potential gives reasonable estimates to the thermodynamic properties, including the bulk thermal conductivity.

We considered a maximum of 2 % length change caused by four types of strains: hydrostatic compressive, hydrostatic tensile, uniaxial compressive, and uniaxial tensile. In Sects. 15.2.6 and 15.2.7, if not otherwise specified, the strains correspond to a 2 % length change, i.e., (1) $F_{ii} = 0.98$, $i = 1, 2, 3$, and $F_{ij} = 0$, $i \neq j$ for hydrostatic compressive strain, (2) $F_{ii} = 1.02$, $i = 1, 2, 3$, and $F_{ij} = 0$, $i \neq j$ for hydrostatic tensile strain, (3) $F_{11} = 0.98$, $F_{22} = F_{33} = 1.0$, and $F_{ij} = 0$, $i \neq j$ for uniaxial compressive strain, and (4) $F_{11} = 1.02$, $F_{22} = F_{33} = 1.0$, and $F_{ij} = 0$, $i \neq j$ for uniaxial tensile strain. Figure 15.8 shows the strain effect on the phonon density of states (PDOS) of Si under hydrostatic compressive and tensile strains. A direct sampling method is used in the calculation of PDOS, which generates $100 \times 100 \times 100$ uniformly distributed **k**-points in the first Brillouin zone and approximates the PDOS by a normalized histogram. It is shown that a shift of optical phonons to the left occurs when the tensile strain is applied, while a shift to the right occurs for the compressive strain. In other words, compared to the unstrained case, most optical phonons will be at a lower (or higher) energy when tensile (or compressive) strain is applied. Note that there are similar peak shifts for longitudinal acoustic (LA) phonons, indicating that the hydrostatic strain has a

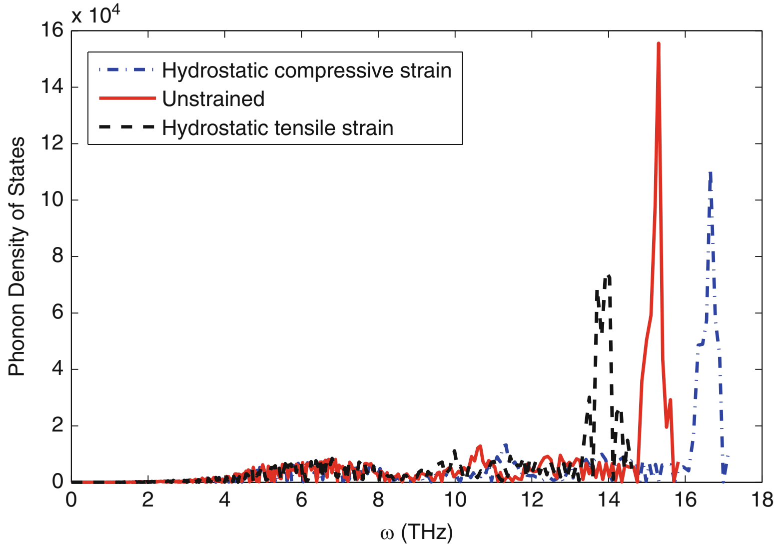

Fig. 15.8 Hydrostatic strain-induced variation of Si phonon density of states at $T = 300$ K

significant effect on them as well. Variations of transverse phonons are also observed, although not equally significant compared to the LA and optical phonons. Similar behavior of the PDOS is observed for Ge under strain (not shown). The different frequency shift direction of the PDOS is largely due to the change of the stiffness of the atomic bonds which is represented by the force constants given in Eq. (15.14), i.e., a compressive (tensile) strain increases (decreases) the force constants and consequently increases (decreases) the vibration frequencies of the atoms. Figure 15.9 shows the overall Grüneisen parameter under hydrostatic strain at different temperatures. It's shown that Grüneisen parameter increases when temperature increases and when tensile strain is applied. Again, similar behavior of the Grüneisen parameter of Ge is observed.

Figure 15.10 shows the Debye temperature of bulk Si crystal under hydrostatic compressive, uniaxial compressive, hydrostatic tensile, and uniaxial tensile strains at the temperature range 200–500 K comparing to the results of the unstrained case. The Debye temperature is almost independent of temperature but shows a strong dependence on strains. Debye temperature's increase with compressive strains and its decrease with the tensile strains can be explained from the PDOS variation as shown in Fig. 15.8. In addition, it's shown in the figure that hydrostatic strains produce a larger effect on T_D than the uniaxial strains.

With the decrease in Grüneisen parameter and the increase in Debye temperature for compressive strains, the Slack relation given in Eq. (15.17) predicts a increase in bulk phonon thermal conductivity. Similarly, a reduction of thermal conductivity

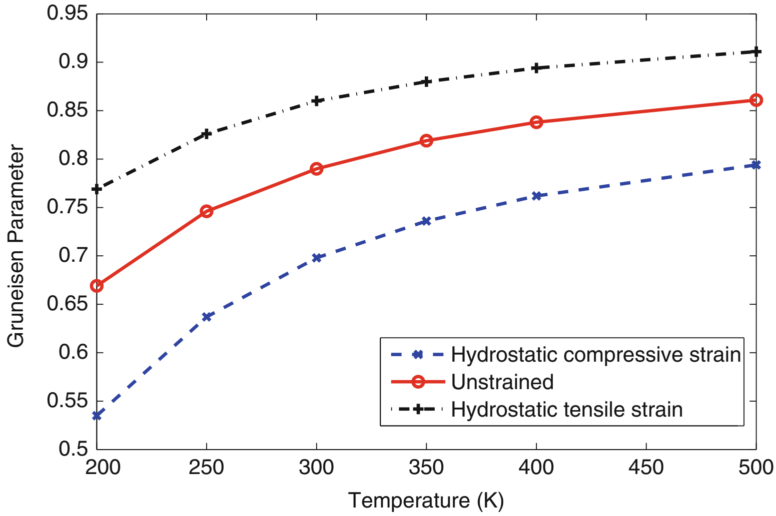

Fig. 15.9 Hydrostatic strain-induced variation of Grüneisen parameter of Si

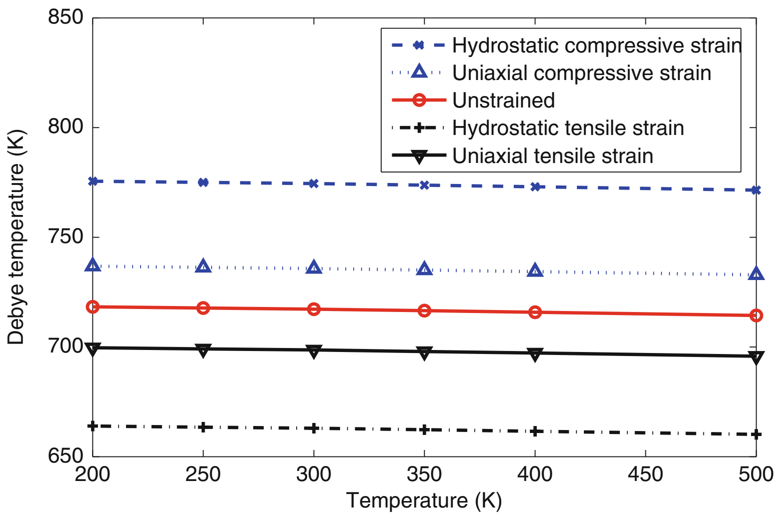

Fig. 15.10 Debye temperature variation of Si due to uniaxial and hydrostatic strains

is predicted for tensile strains. Same conclusions can be obtained for Ge. Figure 15.11 shows the bulk thermal conductivity of Si with respect to temperature and strain. In [60], Slack has qualitatively explored the strain effect on bulk thermal conductivity of crystalline solids by assuming possible changes in Debye temperature and Grüneisen parameter due to strain. Our calculations have confirmed his prediction quantitatively. Figure 15.11 shows that hydrostatic strains

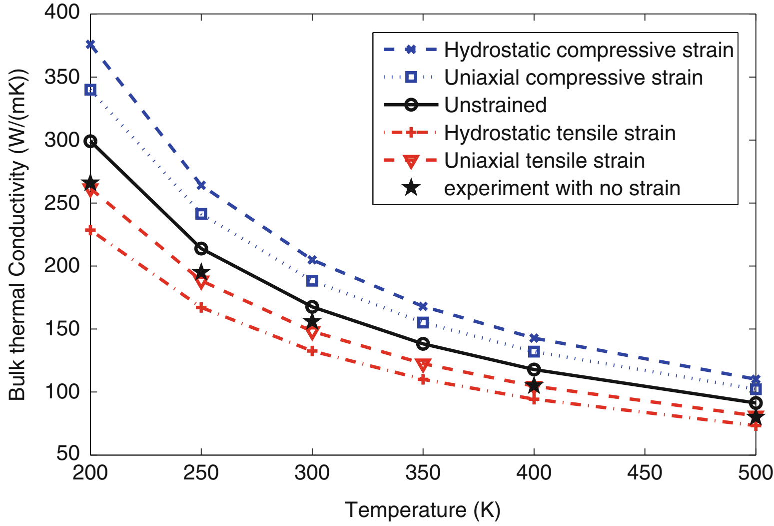

Fig. 15.11 Strain-dependent bulk thermal conductivity of Si between 200 and 500 K

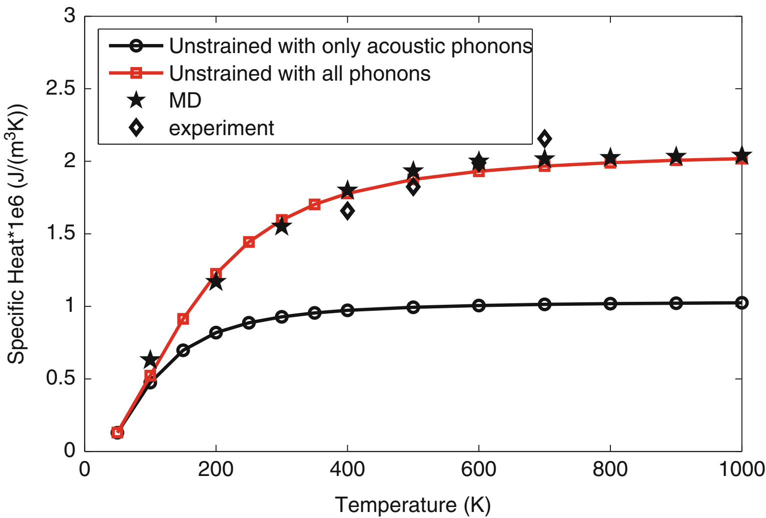

Fig. 15.12 Specific heat of Si

have a stronger effect on bulk thermal conductivity than the uniaxial strains. The stars in the figure show the experiment data of unstrained bulk Silicon taken from Table I of [27]. The calculated unstrained bulk thermal conductivities are higher than experiment results but in reasonable agreement.

Figure 15.12 shows the contribution of optical phonons to the overall specific heat. It is shown that, at low temperatures ($T < 100$ K), acoustic phonons are the

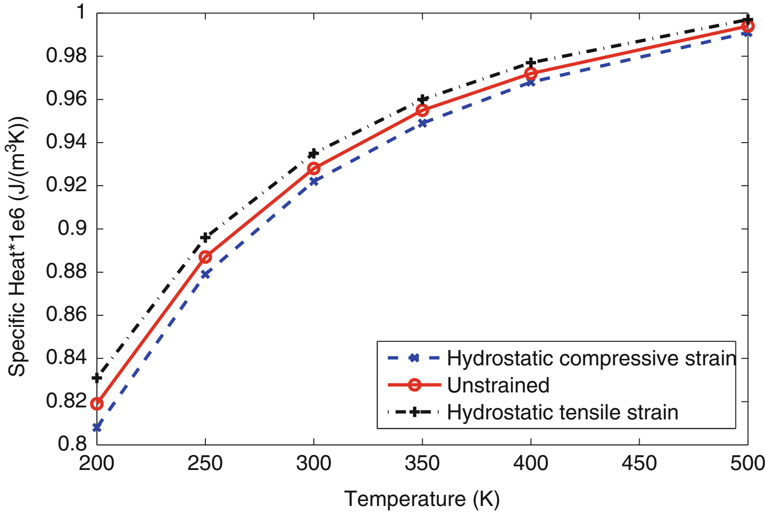

Fig. 15.13 Strain-dependent acoustic specific heat of Si between 200 and 500 K

major contributors to specific heat but at high temperatures ($T > 400$ K), optical phonons contribute about half of the total specific heat. Similar results have been obtained in [16]. Since the optical phonons contribute little to heat transfer due to their small group velocities, it is justifiable to exclude the optical phonons in the calculation of the phonon mean free path and average group velocity as shown in Eqs. (15.23), (15.25). MD data taken from Fig. 10 of [85] and experiment data taken from Fig. 1 of [28] are also shown in Fig. 15.12. The strain and temperature dependence of the acoustic specific heat is shown in Fig. 15.13, where a compressive strain decreases the specific heat and a tensile strain increases it. Once again, the results for Ge are similar. The results are not shown for the sake of brevity.

Figure 15.14 shows the variation of average group velocity with respect to strain-induced volume change. For the small strains considered here, the group velocity shows a nearly linear dependence on the volume change, for both hydrostatic and uniaxial cases. For the same volume change, hydrostatic strain leads to a larger variation than uniaxial strain. The group velocities of unstrained Si and Ge at room temperature are calculated to be 3,143 m/s and 2,233 m/s, respectively. In [81], the group velocities of Si and Ge were calculated by approximating the phonon dispersion using a simple sine function. The results are 1,804 m/s for Si and 1,042 m/s for Ge. It should be noted that this discrepancy is largely due to the differences in the phonon dispersion and the PDOS given by the Tersoff potential and the sine function.

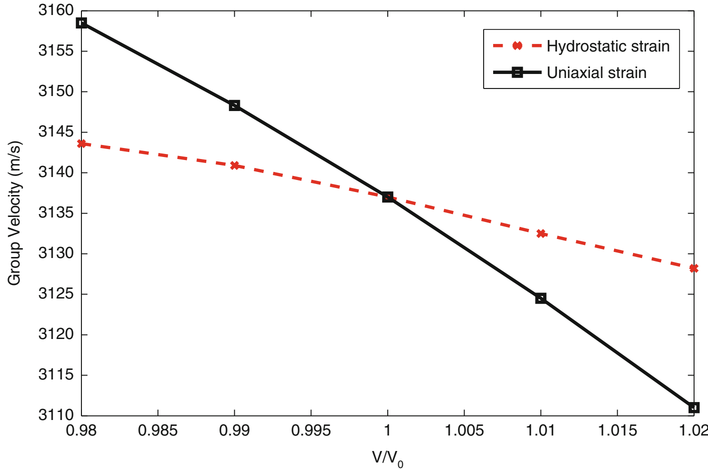

Fig. 15.14 Average group velocity of Si as a function of strain-induced volume change (V_0 is the undeformed volume)

15.2.7 Strain Effect on Thermal Conductivity of Si/Ge Nanocomposites

Having calculated the thermal properties of bulk Si and Ge as functions of strain, the effective thermal conductivity is computed for the Si–Ge nanocomposites as shown in Fig. 15.1 by using the FVM and solving the BTE over unstructured triangle meshes as shown in Fig. 15.6. In this section, the atomic percentage of Si is fixed at 20 %, i.e., the nanocomposites are $Si_{0.2}Ge_{0.8}$. In all calculations, θ is discretized uniformly into 12 angles from 0 and π while ϕ is discretized into 24 angles from 0 and 2π.

Figure 15.15 shows the size and temperature effects on phonon thermal conductivity of the $Si_{0.2}Ge_{0.8}$ nanocomposite with square-cross-section Si nanowires. The x-coordinate is the characteristic length of the Si nanowire, denoted as L_{Si}, which is the width of the square cross section. Thermal conductivity of the nanocomposite decreases when the temperature increases or when size decreases. The large reduction of the thermal conductivity with the decreasing characteristic length is due to the dominance of the interface scattering over the ballistic transport in nanocomposites [81]. Figure 15.15 shows that this interface scattering-induced thermal conductivity reduction holds over a wide range of temperatures while the effect is more significant at low temperatures.

Figure 15.16 shows the numerical results of x-directional heat flux at $T = 300$ K in unstrained $Si_{0.2}Ge_{0.8}$ nanocomposites with Si nanowires having square, circular, and diamond cross sections. For comparison, we keep the atomic percentage of the Si nanowires at 20 % and the characteristic length of the cross sections to be 10 nm.

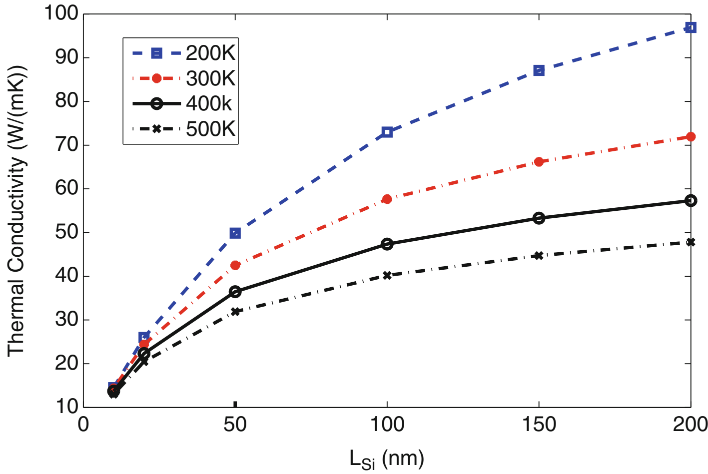

Fig. 15.15 Thermal conductivity of $Si_{0.2}Ge_{0.8}$ nanocomposites with respect to temperature (square Si nanowire cross section)

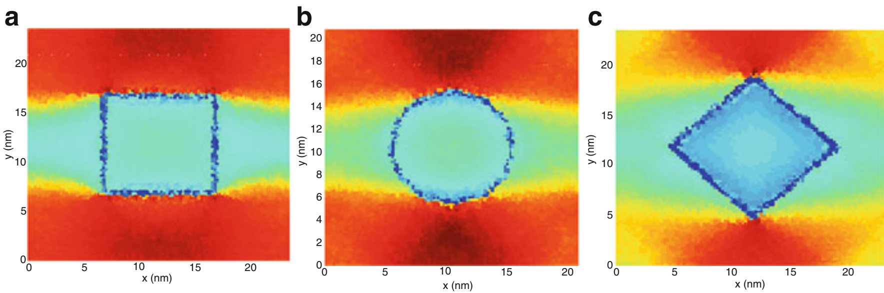

Fig. 15.16 Heat flux profile of unstrained $Si_{0.2}Ge_{0.8}$ at 300 K: (**a**) square Si nanowire with 10×10 nm square cross section; (**b**) circular Si nanowire cross section, the characteristic length of 10 nm; (**c**) diamond-shaped Si nanowire cross section, the characteristic length of 10 nm

Note that, for circular cross sections, the characteristic length of square, circular, and diamond cross sections refers to the width (or height), diameter, and length of the edges, respectively. The low heat flux along the path blocked by the Si wire is clearly due to the phonon scattering at the Si–Ge interface.

The effect of strain along with the size effect on the effective thermal conductivity is shown in Figs. 15.17 and 15.18. It is shown that strain has a significant effect on the thermal conductivity of the nanocomposite. Depending on the characteristic length of the Silicon nanowire, with a volume change of 2 %, an applied hydrostatic tensile or compressive strain can reduce or increase the thermal conductivity up to 15 %, while uniaxial tensile or compressive strain can reduce or increase the thermal conductivity by as much as 8 %. More importantly, the strain effect on the thermal conductivity of bulk materials is largely preserved in the composite configuration

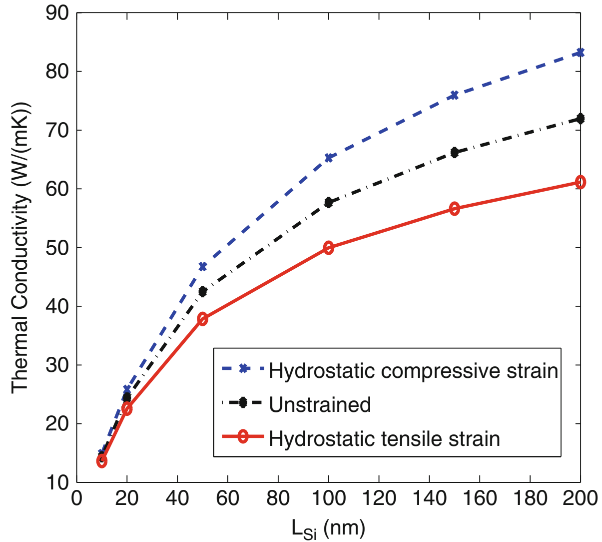

Fig. 15.17 Thermal conductivity of $Si_{0.2}Ge_{0.8}$ under hydrostatic strain (2 % volume change of the material) at 300K (square Si nanowire cross section)

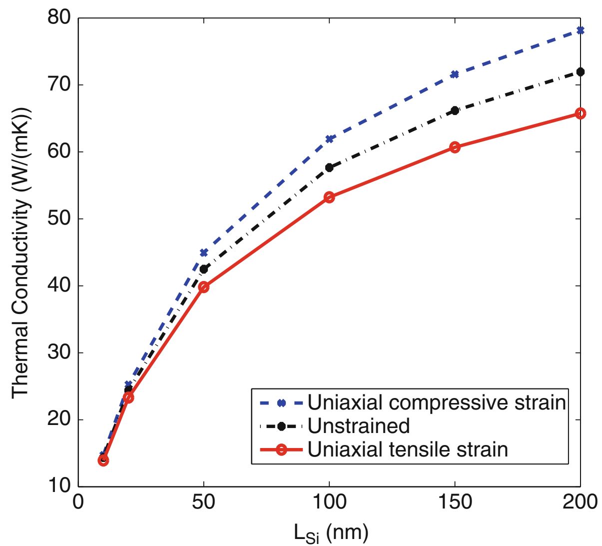

Fig. 15.18 Thermal conductivity of $Si_{0.2}Ge_{0.8}$ under uniaxial strain (2 % volume change of the material) at 300K (square Si nanowire cross section)

over all the sizes. This result shows that the mechanical effect can be combined with structural effects such as size and composition effects to further manipulate and control the thermal conductivity of nanomaterials and nanostructures.

Although, as shown in Fig. 15.16, the difference in the heat flux profiles corresponding to different nanowire cross section shapes is obvious, it is observed from calculations that the thermal conductivity curves of circular and diamond-shaped nanowires are very similar to those shown in Figs. 15.17 and 15.18, except

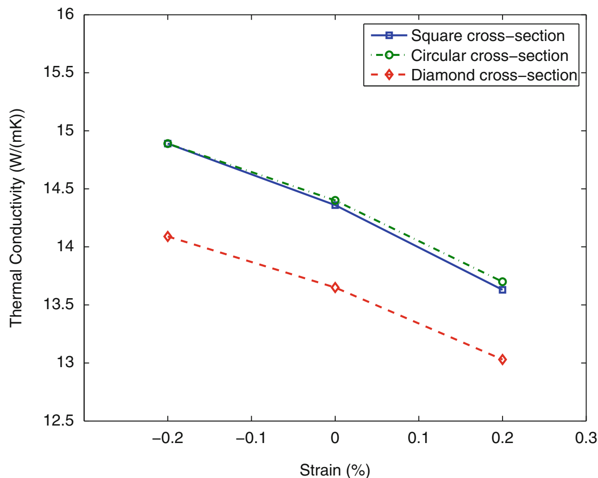

Fig. 15.19 Thermal conductivity of $Si_{0.2}Ge_{0.8}$ with different cross-section shapes of Si nanowire

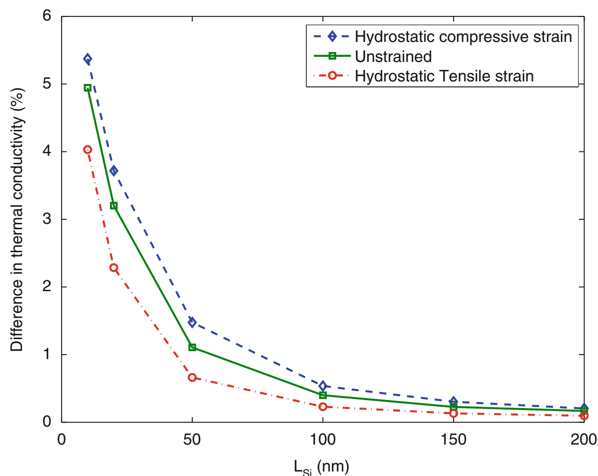

Fig. 15.20 Difference in thermal conductivity between diamond-shaped and square cross sections as a function of characteristic length

at the lower limit of the characteristic length. Figure 15.19 shows the thermal conductivities for the three types of Si nanowires at the characteristic length of 10 nm. The strain effect is almost the same for the three nanocomposites. The circular and square cases have very close thermal conductivities, with or without strain. The magnitude of the thermal conductivity for diamond-shaped cross section is appreciably lower (about 5 %). Figure 15.19 shows the difference in thermal conductivity for diamond and square cross sections over the characteristic length from 10 to 200 nm. The thermal conductivity difference between the two nanocomposites drops exponentially. These results show that, with the same atomic percentage of Si, the cross-sectional shape makes little difference when the characteristic length increases. However, for very small systems (e.g., characteristic length < 10 nm), the cross-sectional shape starts to play a role (Fig. 15.20).

15.3 Strain Effect on Electron Transport in Si/Ge Nanocomposites

Strain effect on the lineup band offsets of different semiconductor materials has been studied extensively in the literature [32, 39, 50, 75]. While most of the existing strain effect analysis has been focused on the strains at hetero-junctions due to lattice mismatch of dissimilar crystalline semiconductor materials, variation of electron transport properties due to externally applied mechanical strains has not been studied in details especially for nanocomposite semiconductor materials. In this section, we investigate the strain effect on electron transport in Si/Ge nanocomposites by incorporating strain-induced band shift and effective mass variation into an analytical model derived from the BTE under the relaxation-time approximation.

15.3.1 Strain-Dependent Band Structure of Si and Ge

To evaluate the strain effect on electron transport in Si/Ge nanocomposites, it is first necessary to study band structures of Si and Ge under different strain conditions. Taking Si as an example, in unstrained *n*-type Si, electrons fill Δ valleys before Λ valleys. Generally, the Λ valleys can be ignored for electron transport simulations in Si at relatively low temperatures. In an unstrained Si crystal, there are six degenerate Δ valleys with the same minimum energy located near the X point at the conduction band. The distribution of electrons in these valleys can be considered the same since in semiconductors such as Si, the x, y, z directions are equivalent in the first Brillouin zone. However, advantageous strain reduces the symmetry of those valleys, which changes the relative population of electrons, causing subband splitting. In addition, strains along a low-symmetry axis further break crystal symmetry and result in the warping of the energy surface of subbands, leading to the effective mass variation [41, 69, 73]. In short, mechanical strains cause band energy splitting and warping, resulting in the variation of the conduction band minima and effective mass, thus leading to changes on transport properties. Figure 15.21 shows a diagram of band structure change under uniaxial stress for bulk n-type Si. The longitudinal tensile strain in [100] direction splits the six originally equivalent subbands, causing the Δ_4 subbands to shift down and the Δ_2 subbands to shift up and leading to electron re-population from the Δ_2 valleys to Δ_4 valleys. If the current transports in [100] direction, since the valleys in [010] and [001] directions with lower conductivity effective mass have relatively higher electron mobility compared to the other two valleys in [100] direction, with more electrons distributed in the four-fold valleys, the conductivity will be increased.

In unstrained Ge, the lowest conduction bands lie at L point along Λ valleys with four degenerate valleys. However, for $Si_{1-x}Ge_x$ alloys, generally the band structure

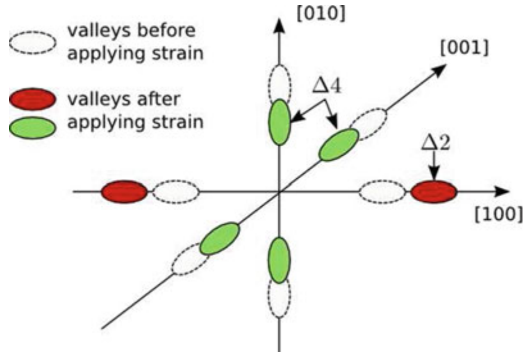

Fig. 15.21 Simplified band structure change under uniaxial strain for bulk n-type Si

and electronic properties can be modeled as Si-like with the lowest conduction minima near the X-point in the Brillouin zone for $x < 0.85$ and as Ge-like with conduction band minima at the L-point for $x > 0.85$ [38]. Further, in highly strained Ge grown on $Si_{1-x}Ge_x$ with $x < 0.40$, the conduction band minimum locates on the Δ valleys [57]. Here we assume that the lowest conduction band of $Si_{0.8}Ge_{0.2}$ nanocomposites lies at the $0.85X$ points of Δ valleys, the same as that in Si.

The total energy of an electron in a semiconductor, E_t, is the sum of the carrier's potential energy, E_C, and kinetic energy, E:

$$E_t = E_C + E, \tag{15.49}$$

where E_C is the conduction band minima and E is defined by

$$E(1 + \alpha E) = \frac{\hbar^2 k_l^2}{2m_l} + \frac{\hbar^2 k_{t1}^2}{2m_{t1}} + \frac{\hbar^2 k_{t2}^2}{2m_{t2}} \ , \tag{15.50}$$

in the ellipsoidal coordinate system (ECS), which is usually spanned by three unit vectors $\hat{\mathbf{k}}_\mathbf{l}$, $\hat{\mathbf{k}}_{\mathbf{t1}}$, and $\hat{\mathbf{k}}_{\mathbf{t2}}$ along the principal axes of a constant-energy ellipsoid. In this dispersion equation, the nonparabolicity and anisotropicity have been accounted to increase the accuracy, $\hbar$ is the reduced Planck's constant, and $k_l\,/\,k_t$ are longitudinal/transverse component of the wave vector.

As discussed earlier, strain typically introduces band shift and effective mass variation. Deformation potential theory was developed to describe energy shift introduced by strain. The energy shift of the n-th conduction band valley due to applied strain, ΔE_C^n, is given by [4],

$$\Delta E_C^n = \Xi_d \cdot (\varepsilon_{xx} + \varepsilon_{yy} + \varepsilon_{zz}) + \Xi_u \cdot \left(\hat{\mathbf{k}} \cdot \varepsilon_{ij} \cdot \hat{\mathbf{k}}\right) \ , \tag{15.51}$$

where ε denotes the mechanical strain, Ξ_d and Ξ_u are the dilation and uniaxial-shear deformation potential of the conduction band, respectively, which can be calculated

from theoretical methods or fitted by experimental results. In Eq. (15.51), i and j represent x, y, z and $\hat{\mathbf{k}}$ is the unit vector parallel to the valley n. Note that Eq. (15.51) holds for arbitrary stress/strain conditions. However, since the Δ valleys are along $< 100 >$ directions, the effect of shear strains is lost in Eq. (15.51). In order to account for energy shift due to shear strain, we follow a degenerate $\mathbf{k} \cdot \mathbf{p}$ theory at the zone-boundary X point proposed by Ungersboeck et al. [70]. Note that an $x-y$ plane shear strain ε_{xy} only shifts the band energy of z-direction valleys with [70],

$$\Delta E_{C,\text{shear}}^{\pm z} = \begin{cases} -\kappa^2 \varepsilon_{xy}^2 \Delta/4, & \kappa|\varepsilon_{xy}| < 1 \\ -(2\kappa|\varepsilon_{xy}| - 1)\Delta/4, & \kappa|\varepsilon_{xy}| > 1 \end{cases}, \tag{15.52}$$

where Δ is the band separation between the two lowest conduction bands of the unstrained lattice at the X point, and $\kappa = 4\Xi_p/\Delta$ with Ξ_p being the deformation potential responsible for the band splitting of the two lowest conduction bands at the zone boundary due to a shear in $x-y$ plane.

From full band calculations, the effect of normal stress on effective masses can be ignored but the shear strain ε_{xy} will affect the effective masses of valleys in z-directions (Figs. 11–13 of [69]). This is because the energy surface of two-fold valleys in z-directions is warped due to ε_{xy} (Fig. 14 of [69] and Fig. 2 of [63]), which has been experimentally demonstrated using UTB (ultrathin-body) FETs (Field-effect-transistors) [69]. From the same degenerate two-band $\mathbf{k} \cdot \mathbf{p}$ theory, we have [70]

$$m_{l,[001]}/m_l^* = \begin{cases} \left(1-\kappa^2\varepsilon_{xy}^2\right)^{-1}, & \kappa|\varepsilon_{xy}| < 1 \\ \left(1 - 1/\kappa|\varepsilon_{xy}|\right)^{-1}, & \kappa|\varepsilon_{xy}| > 1 \end{cases}, \tag{15.53}$$

$$m_{t,[110]}/m_t^* = \begin{cases} \left(1 + \eta\kappa\varepsilon_{xy}\right)^{-1}, & \kappa|\varepsilon_{xy}| < 1 \\ \left(1 + \eta sgn(\varepsilon_{xy})\right)^{-1}, & \kappa|\varepsilon_{xy}| > 1 \end{cases}, \tag{15.54}$$

$$m_{t,[\bar{1}10]}/m_t^* = \begin{cases} \left(1 - \eta\kappa\varepsilon_{xy}\right)^{-1}, & \kappa|\varepsilon_{xy}| < 1 \\ \left(1 - \eta sgn(\varepsilon_{xy})\right)^{-1}, & \kappa|\varepsilon_{xy}| > 1 \end{cases}. \tag{15.55}$$

Here sgn denotes the signum function, m_l and m_t are electron longitudinal and transverse effective masses with strain, respectively, $m_l{}^*$ and $m_t{}^*$ are electron longitudinal and transverse effective masses without strain, respectively, and $\eta \approx 1 - m_t^*/m_0$ [64] with m_0 being the free electron mass. Note that, when there is no shear strain, $m_l = m_l{}^*$ and $m_t = m_t{}^*$.

In addition, the nonparabolicity coefficient in the two valleys along z-direction is also a function of ε_{xy}, i.e. [63],

$$\alpha^{\pm z} = \alpha_0 \frac{1 + 2(\eta\kappa\varepsilon_{xy})^2}{1 - (\eta\kappa\varepsilon_{xy})^2} \tag{15.56}$$

where α_0 is the nonparabolicity coefficient when no strain is applied, which is chosen to be 0.5 eV^{-1} for intrinsic Si and 1.25 eV^{-1} for $Si_{0.8}Ge_{0.2}$ nanocomposites when doping density is high.

In summary, in the current model, ε_{xy} introduces band shift, effective masses variation and nonparabolicity coefficient change of the valley pairs along z direction only. Similarly, ε_{yz} and ε_{zx} alter band dispersion relations for valley pairs along x and y directions, respectively.

15.3.2 Electron Transport Model for Strained Si/Ge Nanocomposites

The change of dispersion relation changes electron transport properties. The i-direction electrical conductivity of the n-th valley σ_i^n can be calculated from an analytical model based on BTE under relaxation-time approximation [17]:

$$\sigma_i^n = -\frac{e^2}{3} \int_0^\infty {}^\tau n(E)[v_i^n(E)]^2 \frac{\partial f^n(E, E_F)}{\partial E} g^n(E)\mathrm{d}E, \tag{15.57}$$

where e is the electrical carrier charge, τ is the momentum relaxation time, and v_i^n is the group velocity of charge carriers in i-direction defined by [44]

$$v_i^n = \frac{\sqrt{2E(1+\alpha^n E)}}{\sqrt{m_i^n}(1 + 2\alpha^n E)}, \tag{15.58}$$

with m_i^n the i-direction effective mass of n-th valley. In Eq. (15.57), f is the Fermi-Dirac distribution function defined by $f^n = \left[e^{(E+E_C^n-E_F)/k_BT} + 1\right]^{-1}$ where E_F is the Fermi level. For a given carrier concentration, N, the Fermi level is calculated from [44]

$$N = \sum_n \int_0^\infty g^n(E)f^n(E, E_F)dE, \tag{15.59}$$

with $g^n(E)$ being the density of states(DOS) for the n-th valley given by [56]

$$g^n(E) = 2\sqrt{E(1+\alpha^n E)}(1 + 2\alpha^n E)(m_{d1}^n)^{3/2}/(\pi^2\hbar^3). \tag{15.60}$$

where m_{d1} is DOS effective mass for valley n: $m_{d1}^n = (m_l m_{t1} m_{t2})^{1/3}(1 + 2\alpha^n E)$ [56].

The total relaxation time is calculated by using Matthiessen's rule to combine the influences from the ionized impurity, phonon deformation potential (DP), and grain boundary (interface) scattering mechanisms. Ionized impurity scattering rate is calculated from [40]

$$\tau_{II}^{-1} = \frac{Ne^4\mathscr{H}(1+2\alpha E)}{16\pi\sqrt{2m_{d1}}\varepsilon^2[E(1+\alpha E)]^{2/3}}, \tag{15.61}$$

with $\mathscr{H} = ln(1+\gamma) - \frac{\gamma}{1+\gamma}$ where $\gamma = 4k^{*\,2}L_D{}^2$. Here k^* is effective wave vector defined by $k^* = \frac{\sqrt{2m_{d1}E(1+\alpha E)}}{\hbar}$ [56] and L_D is screening length obtained from $L_D = \frac{(\pi)^{2/3}\ \varepsilon^{1/2}\ \hbar}{(3N)^{1/6}\ m_{d1}^{1/2}\ e}$ [82].

For electron–phonon DP scattering rate, we employ a model proposed in [56],

$$\tau_{DP}^{-1} = \frac{\pi\ k_B T\ D_c^2\ g(E)}{\hbar\ K}\left\{\left[1 - \frac{\alpha E}{1+2\alpha E}\left(1 - \frac{D_v}{D_c}\right)\right]^2 - \frac{8}{3}\frac{\alpha E(1+\alpha E)}{(1+2\alpha E)^2}\frac{D_v}{D_c}\right\}. \tag{15.62}$$

In addition to the electron–phonon DP scattering, inter-valley optical phonon scattering can be significant. Unfortunately, inter-valley scattering parameters for single crystal silicon and germanium cannot be used to explain the experimental data for Si/Ge alloys and nanocomposites. Due to the lack of relevant experimental data of optical phonon modes, it is difficult to estimate the inter-valley scattering parameters for Si/Ge alloys and nanocomposites. In this work, we follow the approach proposed by Minnich et al. [45]. In their approach, based on the observation that the acoustic phonon scattering and the inter-valley scattering have the same energy dependence, the effects of both scattering processes are combined in a single set of effective deformation potentials. In this work, we fit effective deformation potentials, D_c and D_v, in Eq. (15.62) to the electrical conductivity experimental data of Si/Ge alloys and nanocomposites with different doping densities to account for both acoustic phonon and inter-valley scattering. Detailed discussion on this issue can be found in [45].

For grain boundary scattering rate, a model proposed in [45] is used, i.e.,

$$\tau_{\mathrm{GB}}^{-1} = 8\pi^2 U_0^2 z_0^2 r_0^4 g(E) N_g \mathscr{I}/\hbar, \tag{15.63}$$

with number density of interface N_g being $N_g = 4\ L_{\mathrm{Ge}}/(\pi\ r_0^2\ L_{\mathrm{Si}}^2)$ and $\mathscr{I}$ being Eq. (22) in [45]. Other parameters can be found in Table 15.2. For $Si_{1-x}Ge_x$ alloy and nanocomposites, the effective properties such as the bulk modulus, K, the low frequency permittivity, ε, and the deformation potentials, E_d and E_u, are calculated as functions of x from a first order (linear) interpolation [38]. For E_p, the value of Si is used.

Table 15.2 Parameters used to calculate electron transport properties for n-type Si and $Si_{1-x}Ge_x$ nanocomposites

m_l^* / m_t^* [57]	$0.92 / 0.19\ m_0$
E_d[24]	$(1.1 + 3.4x)$ eV
E_u[24]	$(10.5 - 0.75x)$ eV
E_p[70]	7.0 eV
Δ[70]	0.53 eV
Low frequency permittivity[38]	$\varepsilon = (11.7 + 4.5x)\varepsilon_0$ [a]
Electron/hole deformation potential (heavily doped $Si_{1-x}Ge_x$)	$D_c = 12.5$ eV, $D_v = 5.0$ eV
Electron/hole deformation potential (intrinsic Si)	$D_c = 9.0$ eV, $D_v = 5.0$ eV
Bulk modulus[38]	$K = (97.9 - 22.8x)$ GPa
Grain boundary potential parameters[45]	$U_0 = 45$ meV, $z_0 = 2.0$ nm, $r_0 = 1.0$ nm

[a]ε_0:vacuum permittivity.

The total electrical conductivity is obtained by summing contribution of electrons from all the six valleys [47]. Since these valleys are differently oriented, it's convenient to introduce a reference coordinate system defining some general directions. Here the crystal coordinate system (CCS) is chosen, which consists of lattice basis vectors $\hat{\mathbf{k}}_1$, $\hat{\mathbf{k}}_2$, and $\hat{\mathbf{k}}_3$, oriented along the three orthogonal [100] crystallographic directions of the underlying material. The CCS and the ECS are related in the reciprocal space. The direct relation between them depends on the material under consideration. For a given conduction band ellipsoid in a given material, the unit basis vector $\hat{\mathbf{k}}_l$, $\hat{\mathbf{k}}_{t1}$, and $\hat{\mathbf{k}}_{t2}$ in the ECS can be expressed in the CCS, thus forms a rotation matrix $\mathfrak{R}_{E \leftarrow C}$, which defines the direction cosine of the principal axes of this ellipsoid with respect to the coordinates of the CCS. Different ellipsoid transformation matrices at unstrained case have been shown in [53] for sixfold-degenerate Δ and the eightfold-degenerate Λ valleys. For Si, there are six degenerate constant energy Δ valley conduction band ellipsoids, as shown in Fig. 15.22. The basis vectors are unique for each ellipsoid in the ECS, with $\hat{\mathbf{k}}_l$ along the major axis and $\hat{\mathbf{k}}_{t1}$, $\hat{\mathbf{k}}_{t2}$ perpendicular to it. There is a unique transformation matrix $\mathfrak{R}_{E \leftarrow C}$ for each ellipsoid, with the rows coming from the components of $\hat{\mathbf{k}}_l$, $\hat{\mathbf{k}}_{t1}$, and $\hat{\mathbf{k}}_{t2}$. For instance, for ellipsoid 1 in Fig. 15.22, $\hat{\mathbf{k}}_l = (1\ 0\ 0)$, $\hat{\mathbf{k}}_{t1} = (0\ 1\ 0)$, and $\hat{\mathbf{k}}_{t2} = (0\ 0\ 1)$, thus,

$$\mathfrak{R}_{E \leftarrow C}^{\Delta_1} = \begin{bmatrix} 1 & 0 & 0 \\ 0 & 1 & 0 \\ 0 & 0 & 1 \end{bmatrix}. \tag{15.64}$$

Transformation matrix for other ellipsoids can be obtained similarly. In all our simulations, the CCS is fixed in real space, and the ECS depends on the specific material and is unique to each ellipsoid.

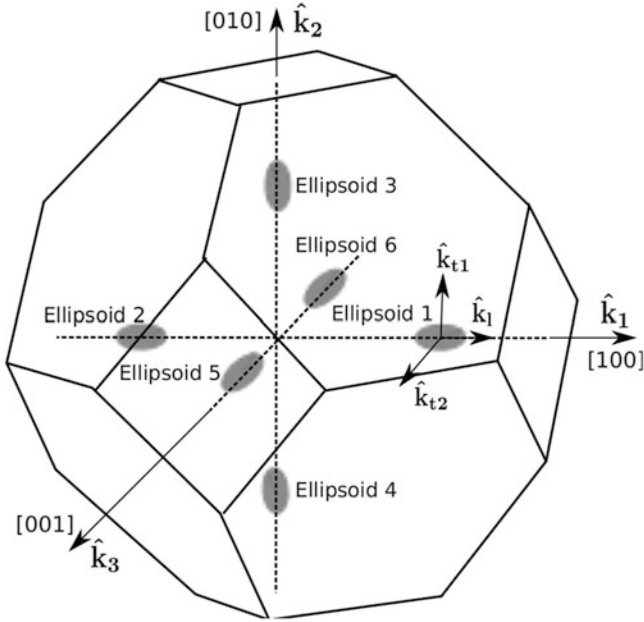

Fig. 15.22 Conduction band constant energy ellipsoids along Δ for Si

When strains are applied, the wave vectors between deformed and undeformed crystal configuration is related by $\mathbf{F}^{-T}$ where $\mathbf{F}$ is the deformation gradient tensor. Accordingly, after deformation, the directional cosines matrix C becomes $C = \mathbf{F}^{-T} \mathfrak{R}^{-1}_{E \leftarrow C}$.

The total conductivity is then calculated as,

$$\sigma_{ij} = \sum_{n}^{6} \sum_{p}^{3} c_{ip}^{n} \sigma_{p}^{n} \left[c_{pj}^{n} \right]^{-1} , \tag{15.65}$$

where $c_{i\,p}^{\,n}$ and $[c_{pj}^{n}]^{-1}$ are components of the n-th directional cosines matrix C^n and its inverse matrix.

The Seebeck coefficient is then calculated by

$$S_{ij} = \frac{\sum_{n}^{6} \sum_{p}^{3} c_{ip}^{n} S_{p}^{n} \sigma_{p}^{n} [c_{pj}^{n}]^{-1}}{\sigma_{ij}}, \tag{15.66}$$

with

$$S_i^n = -\frac{1}{eT} \frac{\int_0^\infty \tau^n(E) [v_i^n(E)]^2 \frac{\partial f^n(E, E_F)}{\partial E} (E - E_F) g^n(E) \mathrm{d}E}{\int_0^\infty \tau^n(E) [v_i^n(E)]^2 \frac{\partial f^n(E, E_F)}{\partial E} g^n(E) \mathrm{d}E}. \tag{15.67}$$

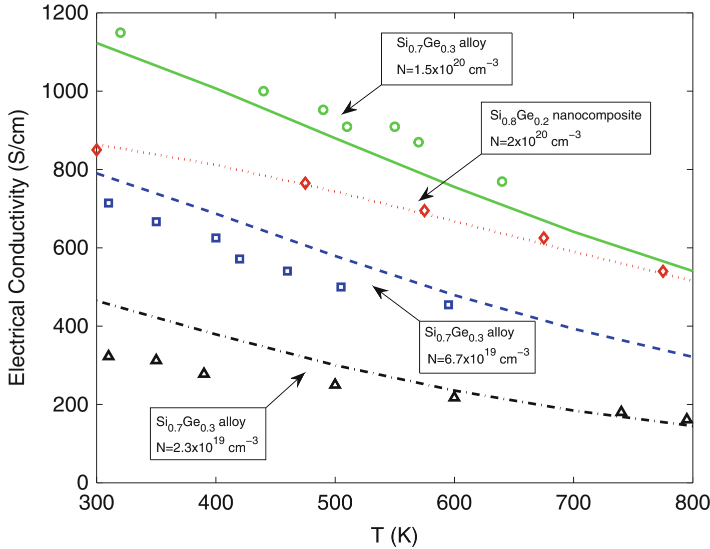

Fig. 15.23 Experimental (*symbols*) and computed (*curves*) electrical conductivity of $Si_{70}Ge_{30}$ alloy and $Si_{0.8}Ge_{0.2}$ nanocomposite as a function of temperature

Note that, while phonon-drag effects can be large at low temperatures in silicon (around 1/5 of the Debye temperature), they are generally reduced by alloying and increasing temperature [72]. For the temperature range (300–800 K) we consider in this work, phonon-drag effects are not included in the calculations.

The electronic thermal conductivity, k_e, is calculated from the Wiedemann–Franz law, $k_e = \sigma L_z T$, where L_z is the Lorenz number. For metals, $L_z = 2.45 \times 10^8$ WΩK^2. For doped Si/Ge nanocomposites, L_z depends on doping for semiconductors [17]. As Si/Ge nanocomposites considered for thermoelectric energy conversion applications are typically heavily doped. In this case, the semiconductors become metal-like and L_z for metals is used.

15.3.3 *Strain Effect on Electrical Transport Properties of Si and Si/Ge Nanocomposites*

This section investigates the strain effect on electrical properties of bulk Si and $Si_{1-x}Ge_x$ nanocomposites. As a validation of the electrical conductivity model described above, we calculated electrical conductivities of unstrained $Si_{0.7}Ge_{0.3}$ alloys and $Si_{0.8}Ge_{0.2}$ nanocomposites with different doping densities and compared them with available experimental data obtained from [45, 72] and [21], as shown in Fig. 15.23. The computational results show a good agreement with the experiment data.

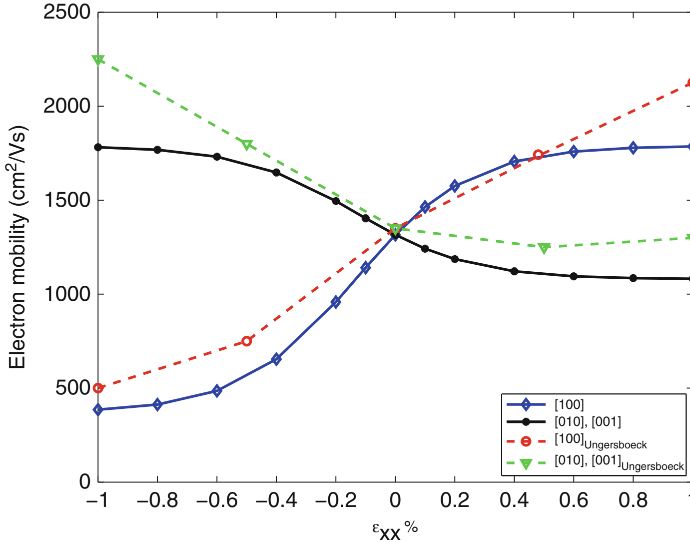

Fig. 15.24 Bulk electron mobility of intrinsic Si as a function of strain for stress direction along [100]

The strain effect on electrical conductivity is verified by comparing the electron mobility of intrinsic Si for [100] uniaxial strain with data from Ungersboeck et al.'s work [70], as shown in Fig. 15.24. Results show similar dependence on strain compared with Ungersboeck's results although they are not exactly the same. The difference comes from the different modeling approaches and different scattering mechanisms considered. Our results are based on an analytical model derived from BTE with several fitting parameters. The results in [70] were calculated numerically by solving the semiclassical BTE using a Monte Carlo method. We considered ionized impurity and phonon deformation potential scatterings while Ungersboeck's models contained ionized impurity scattering, phonon scattering, alloy scattering, and impact ionization scattering. Figure 15.25 shows electron mobility enhancement of intrinsic Si as a function of strain for stress direction along [100] calculated from our model and experimental results obtained from [69]. Our results show similar trends as experimental data. From the two figures, we observe that uniaxial tensile strain along [100] direction increases electron mobility in the same direction but decreases them in the two perpendicular directions, which implies possible change in thermoelectric power factor.

Seebeck coefficient of unstrained bulk Si with doping density from 10^{16}/cm^3 to 10^{19}/cm^3 is shown in Fig. 15.26. Solid lines are Seebeck coefficient calculated from our model and dashed lines are from Fig. 3.8 of [74]. The results indicate that Seebeck coefficient decreases with increasing temperature and further decreases with decreasing doping density.

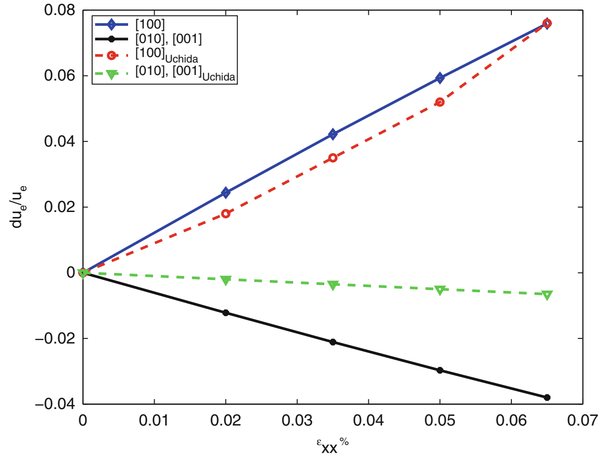

Fig. 15.25 Electron mobility enhancement of intrinsic Si as a function of strain for stress direction along [100]

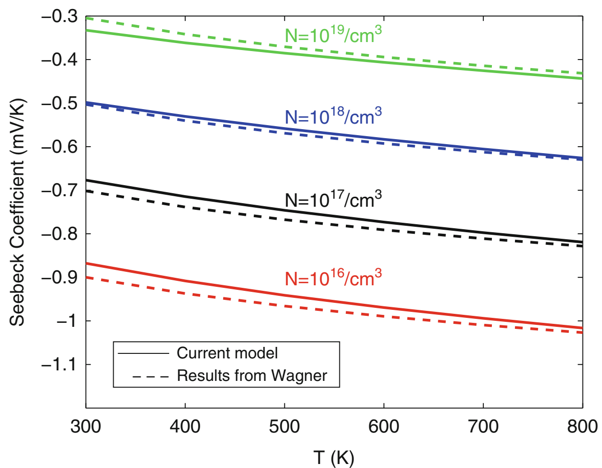

Fig. 15.26 Temperature and doping dependence of Seebeck coefficient of Si. *Solid curves*: results from current model. *Dashed curves*: results from Wagner [74]

15.4 Strain Effect on Figure of Merit of $Si_{0.8}Ge_{0.2}$ Nanocomposites

Having obtained strain-dependent phonon thermal conductivity and electrical properties, the calculation of dimensionless figure of merit of nanocomposite thermoelectric materials is straightforward, i.e., $ZT = S^2\sigma T/(k_p + k_e)$.

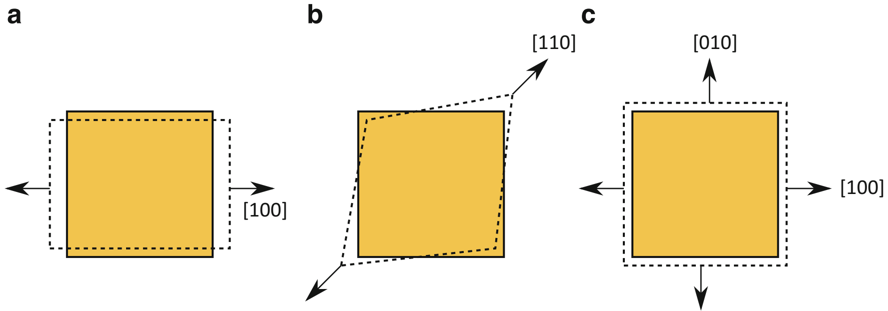

Fig. 15.27 Three types of stresses applied on the $Si_{0.8}Ge_{0.2}$ nanocomposites: (**a**) uniaxial stress in [100] direction, (**b**) uniaxial stress in [110] direction producing a shear strain on (001) plane, and (**c**) biaxial stress in [100] and [010] directions

In this section, three types of stresses are applied in the transverse plane (assumed to be (001) plane) of the $Si_{0.8}Ge_{0.2}$ nanocomposites to study strain effect on their thermoelectric properties. As shown in Fig. 15.27, the applied stresses are (1) uniaxial stress in [100] direction, (2) uniaxial stress in [110] direction, and (3) biaxial stress in [100] and [010] directions. These stresses are applied such that the resultant strains are, respectively, (1) 1 % normal strain in [100] direction, (2) a shear strain of 0.01 on (001) plane, and (3) 1 % biaxial normal strain in [100] and [010] directions. In addition, to show the size effect of Ge nanowires, $L_{Ge} = 10$ nm and $L_{Ge} = 20$ nm are used in the calculations while the atomic percentage of Si and Ge remains fixed. The doping density of the $Si_{0.8}Ge_{0.2}$ nanocomposites is set to be $N = 10^{19}\ \text{cm}^{-3}$.

The calculated Seebeck coefficient, electrical conductivity, phonon thermal conductivity, and figure of merit are shown in Figs. 15.28–15.30 for $L_{Ge} = 10$ nm and Figs. 15.31–15.33 for $L_{Ge} = 20$ nm. For the two nanowire sizes, as shown in Figs. 15.28 and 15.31, the tensile strain along [100] direction increases electrical conductivity and Seebeck coefficient, and at the same time, decreases thermal conductivity along the direction in which the stress is applied, resulting an increase in dimensionless figure of merit along the applied stress direction. The compressive strain in [100] direction largely decreases electrical conductivity and at the same time increases the phonon thermal conductivity. Under the compressive strain in [100] direction, the decreasing rate of Seebeck coefficient with temperature increase is higher than that in the tensile strain case. Even though Seebeck coefficient increases with compressive strain at low temperatures, ZT still decreases under a compressive strain in [100] direction. Figures 15.29 and 15.32 show that the shear strain due to the applied stresses along [110] direction largely decreases electrical conductivity and increases Seebeck coefficient in [100] direction, for both tension and compression loads. Note that in *n*-type semiconductors, Seebeck coefficients are

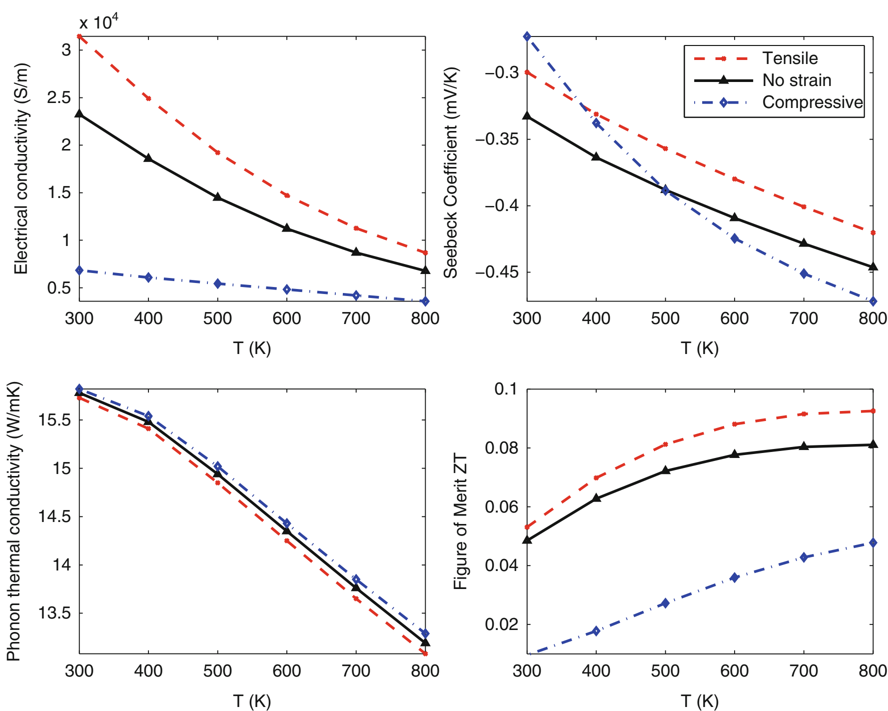

Fig. 15.28 Thermoelectric properties of $Si_{0.8}Ge_{0.2}$ with $N = 10^{19}\ cm^{-3}$ under 1 % normal strain in [100] direction when $L_{Ge} = 10$ nm

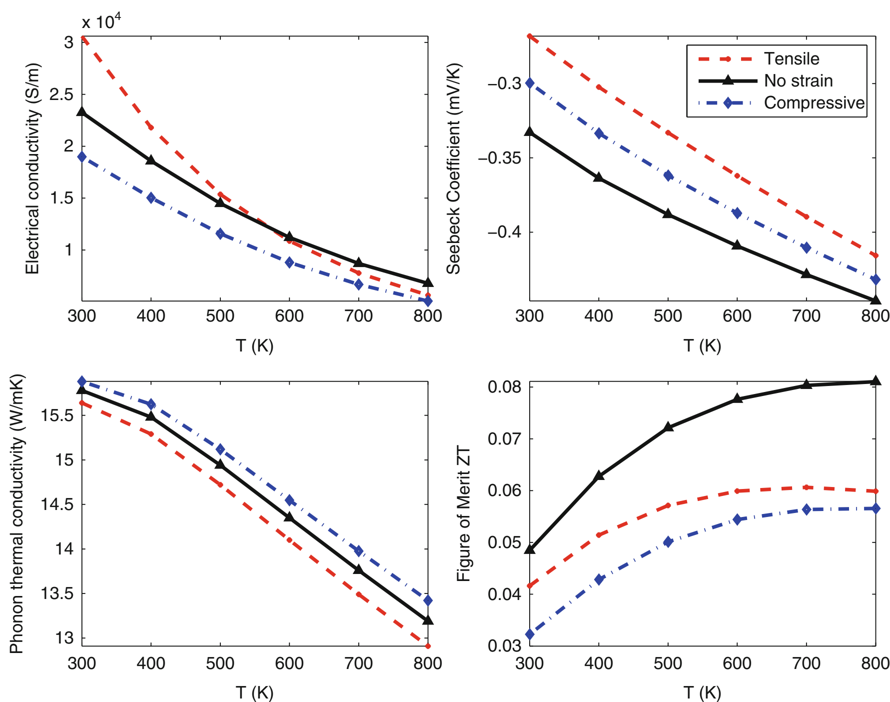

Fig. 15.29 Thermoelectric properties of $Si_{0.8}Ge_{0.2}$ with $N = 10^{19}\ cm^{-3}$ under a shear strain of 0.01 when $L_{Ge} = 10$ nm

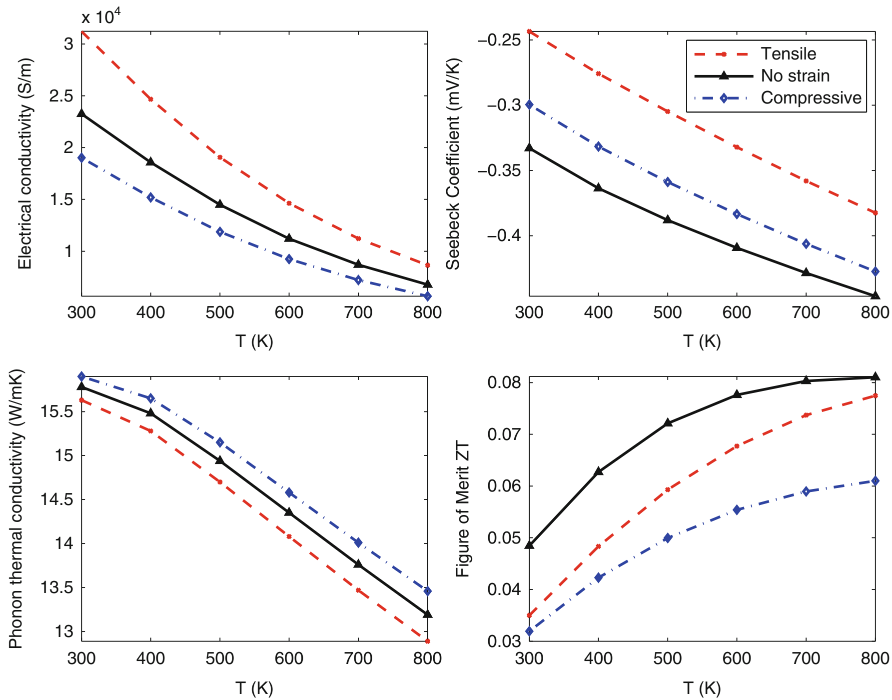

Fig. 15.30 Thermoelectric properties of $Si_{0.8}Ge_{0.2}$ with $N = 10^{19}\ cm^{-3}$ under 1 % biaxial strain when $L_{Ge} = 10$ nm

negative. The resultant power factor is decreased by the shear strain. At the same time, tension/compression loads in [110] direction decrease/increase the phonon thermal conductivity in [100] direction. Due to the combined effect, the shear strain leads to a drop in ZT in [100] direction. Figures 15.30 and 15.33 show strain effect on thermoelectric properties of $Si_{0.8}Ge_{0.2}$ nanocomposites along [100] and [010] directions in which biaxial normal strain occurs. The results indicate that biaxial tensile strain increases electrical conductivity and Seebeck coefficient while biaxial compressive strain decreases electrical conductivity but increases Seebeck coefficient. Phonon thermal conductivity is decreased by tensile strain and increased by compressive strain. Combining these effects together, we observed that the ZT decreases under the biaxial normal strain.

Comparing the figure of merit under different strains, the uniaxial tensile strain is the only case that leads to the increase of figure of merit. And this increase becomes clearer when the temperature increases. At 800 K, 1 % uniaxial tensile strain

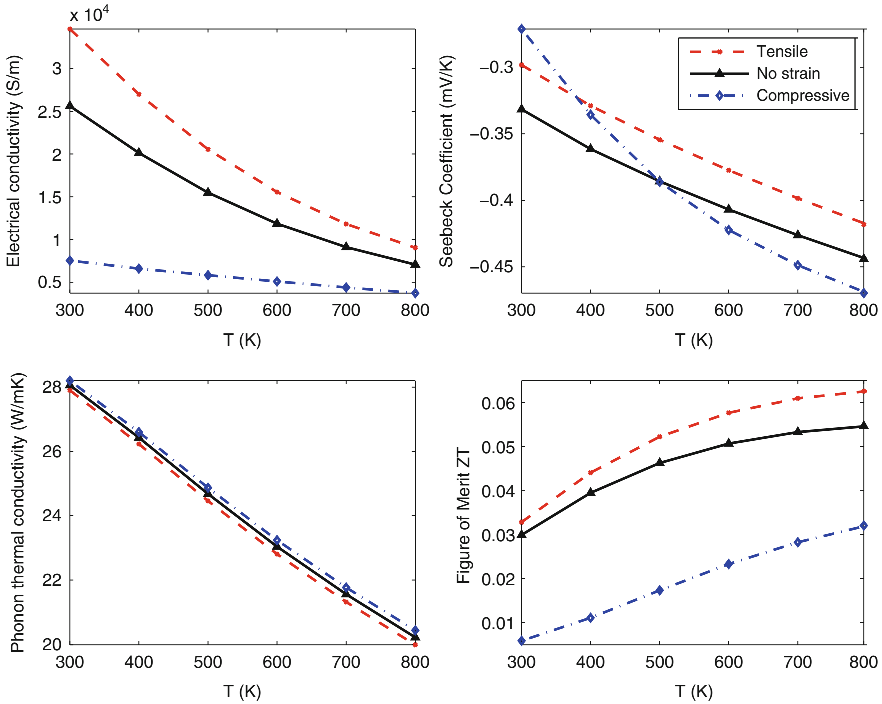

Fig. 15.31 Thermoelectric properties of $Si_{0.8}Ge_{0.2}$ with $N = 10^{19}$ cm^{-3} under 1 % normal strain in [100] direction when $L_{Ge} = 20$ nm

results in 15 % increase of dimensionless figure of merit in $Si_{0.8}Ge_{0.2}$ nanocomposites. The corresponding dimensionless figure of merit is 0.093.

Comparing the results for the two Ge nanowire sizes, $L_{Ge} = 10$ nm and $L_{Ge} = 20$ nm, it is shown that the decrease of Ge nanowire size causes a larger reduction in phonon thermal conductivity than in electrical conductivity, leading to a higher ZT. Taking Figs. 15.28 and 15.31 for example, when L_{Ge} decreases from 20 to 10 nm, the phonon thermal conductivity decreases by about 40 % but the electrical conductivity decreases by less than 10 %. This behavior is due to the stronger phonon scattering at Si/Ge interfaces when the characteristic length of the material components decreases, as many authors have pointed out in the literature [33, 71, 76, 83]. In addition, our results show that the strain effect on the thermoelectric properties is similar for the two Ge nanowire sizes, which implies that the strain effect is insensitive to the characteristic length of the material components.

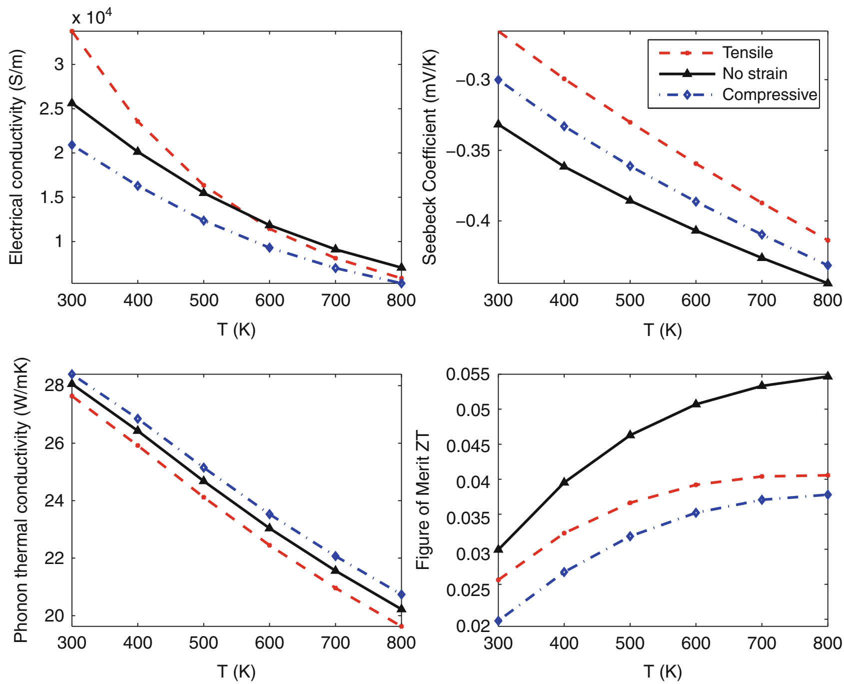

Fig. 15.32 Thermoelectric properties of $Si_{0.8}Ge_{0.2}$ with $N = 10^{19}$ cm^{-3} under a shear strain of 0.01 when $L_{Ge} = 20$ nm

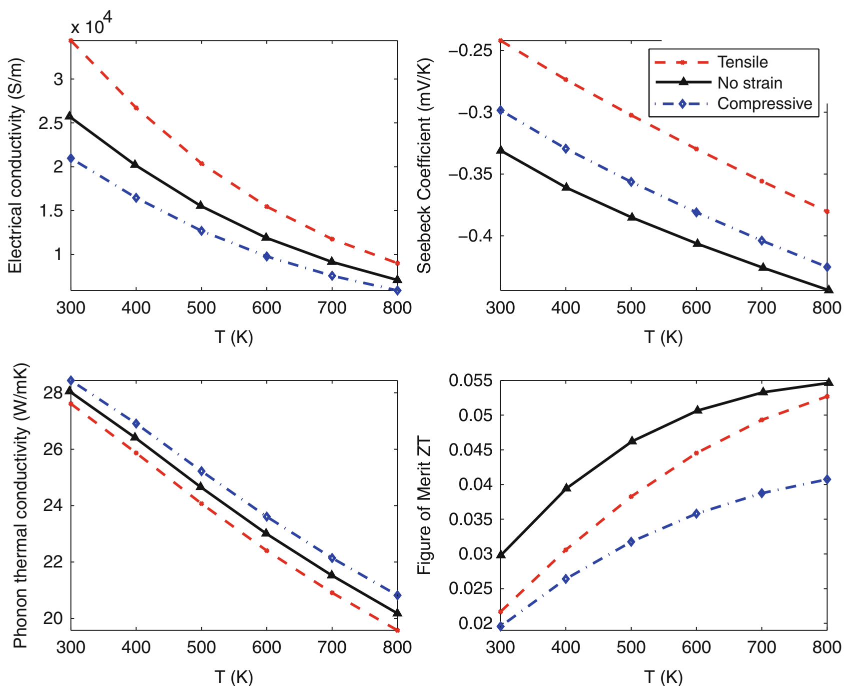

Fig. 15.33 Thermoelectric properties of $Si_{0.8}Ge_{0.2}$ with $N = 10^{19}$ cm^{-3} under 1 % biaxial strain when $L_{Ge} = 20$ nm

15.5 Conclusion

Strain effect on thermoelectric properties of Si/Ge nanocomposites has been investigated in this chapter. Strain effect on electron transport was studied by using an analytical model derived from BTE with band structures obtained from a degenerate $\mathbf{k} \cdot \mathbf{p}$ theory. Strain effect on thermal transport was studied by solving phonon BTE using strain-dependent phonon scattering properties calculated from lattice dynamics. Our results confirm that nanocomposites are better thermoelectric materials compared to their alloys. In the 300–800 K temperature range, uniaxial tensile strain along [100] direction can improve ZT parallel to the tension direction. Compressive strain in [100] direction, biaxial strain along [100] and [010] directions and uniaxial stress along [110] decrease ZT. At 800 K with electron concentration of $10^{19}/\text{cm}^3$, 1 % uniaxial tensile strain along [100] direction can increase figure of merit of $Si_{0.8}Ge_{0.2}$ nanocomposites by 15 % to ZT = 0.093. While the results have shown strong strain effects on the figure of merit of Si/Ge nanocomposites and demonstrated the possibility of tuning ZT by using externally applied mechanical strains, further studies are necessary to identify the optimal component material atomic percentage, nanowire size, and combination of the strains for obtaining the maximum improvement of the ZT.

Acknowledgements We gratefully acknowledge support by the National Science Foundation under Grants CMMI-0800474 and CBET-0955096.

References

1. Abramson, A.R., Tien, C.L., Majumdar, A.: Interface and strain effects on the thermal conductivity of heterostructures: A molecular dynamics study. J. Heat Transfer **124**, 970 (2002)
2. Arico, A.S., Bruce, P., Scrosati, B., Tarascon, J.M., Schalkwijk, W.V.: Nanostructured materials for advanced energy conversion and storage devices. Nat. Mater. **4**, 366–377 (2005)
3. Baek, S.W., Kim, M.Y., Kim, J.S.: Nonorthogonal finite-volume solutions of radiative heat transfer in a three-dimensional enclosure. Numer. Heat Transfer B **34**, 419–437 (1998)
4. Balslev, I.: Influence of uniaxial stress on the indirect absorption edge in silicon and germanium. Phys. Rev. **143**(2), 636–647 (1966)
5. Bardy, E.R., Mollendorf, J.C., Pendergast, D.R.: Thermal conductivity and compressive strain of aerogel insulation blankets under applied hydrostatic pressure. J. Heat Transfer **129**, 232–235 (2007)
6. Bell, L.E.: Cooling, heating, generating power, and recovering waste heat with thermoelectric systems. Science **321**(5895), 1457–1461 (2008)
7. Borca-Tasciuc, T., Liu, W., Liu, J., Zeng, T., Song, D.W., Moore, C.D., Chen, G., Wang, K.L., Goorsky, M.S., Radetic, T., Gronsky, R., Koga, T., Dresselhaus, M.S.: Thermal conductivity of symmetrically strained Si/Ge superlattices. Superlattices Microstructures **28**(3), 199–206 (2000)
8. Born, M., Huang, K.: Dynamical Theory of Crystal Lattices. Clarendon, Oxford (1954)
9. Brenner, D.W.: Empirical potential for hydrocarbons for use in simulating the chemical vapor deposition of diamond films. Phys. Rev. B **42**, 9458–9471 (1990)

10. Broido, D.A., Malorny, M., Birner, G., Mingo, N., Stewart, D.A.: Intrinsic lattice thermal conductivity of semiconductors from first principles. Appl. Phys. Lett. **91** (2007)
11. Chai, J.C., Lee, H.S., Patankar, S.V.: Finite volume method for radiation heat transfer. J. Thermophys. Heat Transfer **8**, 419–425 (1994)
12. Challis, L.J., Haseler, S.C.: The effect of uniaxial stress on the thermal conductivity of p-Ge. J. Phys. C Solid State Phys. **11**, 4681–4694 (1978)
13. Chantrenne, P., Barrat, J.L., Blase, X., Gale, J.D.: An analytical model for the thermal conductivity of silicon nanostructures. J. Appl. Phys. **97**, 1043,318 (2005)
14. Chen, G.: Nonlocal and nonequilibrium heat conduction in the vicinity of nanoparticles. J. Heat Transfer **118**(3), 539–545 (1996)
15. Chen, G.: Size and interface effects on thermal conductivity of superlattices and periodic thin-film structures. J. Heat Transfer **119**(2), 220–229 (1997)
16. Chen, G.: Thermal conductivity and ballistic-phonon transport in the cross-plane direction of superlattices. Phys. Rev. B **57**(23), 14,958–14,973 (1998)
17. Chen, G.: Nanoscale Energy Transport and Conversion: A Parallel Treatment of Electrons, Molecules, Phonons, and Photons. Oxford University Press, Oxford (2005)
18. Chen, G., Dresselhaus, M.S., Dresselhaus, G., Fleurial, J.P., Caillat, T.: Recent developments in thermoelectric materials. Int. Mater. Rev. **48**(1), 45–66 (2003)
19. Chui, E.H., Raithby, G.D., Hughes, P.M.J.: Prediction of radiative transfer in cylindrical enclosures with the finite volume method. J. Thermophysics Heat Transfer **6**, 605–611 (1992)
20. DiSalvo, F.J.: Thermoelectric cooling and power generation. Science **285**(5428), 703–706 (1999)
21. Dismukes, J.P., Ekstrom, L., Steigmeier, E.F., Kudman, I., Beers, D.S.: Thermal and electrical properties of heavily doped Ge-Si alloys up to 1300K. J. Appl. Phys. **35**(10), 2899–2907 (1964)
22. Etessam-Yazdani, K., Yang, Y., Asheghi, M.: Ballistic phonon transport and self-heating effects in strained-silicon transistors. IEEE Trans. Components Pack. Tech. **29**(2), 254–260 (2006)
23. Fischetti, M.V., Laux, S.E.: Monte carlo study of electron transport in Si inversion layers. Phys. Rev. B **48**, 2244 (1993)
24. Fischetti, M.V., Laux, S.E.: Band structure, deformation potentials, and carrier mobility in strained Si, Ge and SiGe alloys. J. Appl. Phys. **80**, 2234–2252 (1996)
25. Flubacher, P., Leadbetter, A.J., Morrison, J.A.: The heat capacity of pure silicon and germanium and properties of their vibrational frequency spectra. Philosophical Mag. **4**(39), 273–294 (1959)
26. Gehr, R.J., Boyd, R.W.: Optical properties of nanostructured optical materials. Chem. Mater. **8** (8), 1807–1819 (1996)
27. Glassbrenner, C.J., Slack, G.A.: Thermal conductivity of silicon and germanium from 3K to the melting point. Phys. Rev. **134**, A1058–A1069 (1964)
28. Glazov, V.M., Pashinkin, A.S., Mikhailova, M.S.: Heat capacity of silicon in the range 350–770 K. Scand. J. Metall. **30**, 388–390 (2001)
29. Goldsmid, H.J.: Thermoelectric Refrigeration. Plenum Press, New York (1964)
30. Hammond, P.T.: Form and function in multilayer assembly: New applications at the nanoscale. Adv. Mater. **16**(15), 1271–1293 (2004)
31. Huang, B.L., Kavianya, M.: Structural metrics of high-temperature lattice conductivity. J. Appl. Phys. **100**, 123,507 (2006)
32. Huang, S., Yang, L.: Strain Engineering of Band Offsets in Si/Ge Core-Shell Nanowires. Appl. Phys. Lett. **98**, 093,114 (2011)
33. Joshi, G., Lee, H., Lan, Y., Wang, X., Zhu, G., Wang, D., Gould, R.W., Cuff, D.C., Tang, M. Y., Dresselhaus, M.S., Chen, G., Ren, Z.: Enhanced thermoelectric figure-of-merit in nanostructured p-type silicon germanium bulk alloys. Nano Lett. **8**(12), 4670–4674 (2008)
34. Keyes, R.W., Sladek, R.J.: Piezo-thermal conductivity effect in germanium. Phys. Rev. **125** (2), 478–483 (1962)

35. Kim, M.Y., Baek, S.W., Park, J.H.: Unstructured finite-volume method for radiative heat transfer in a complex two-dimensional geometry with obstacles. Numer. Heat Transfer B **39**, 617–635 (2001)
36. Kittel, C.: Introduction to Solid State Physics. Wiley, New York (1995)
37. Lauer, I., Antoniadis, D.A.: Enhancement of Electron Mobility in Ultrathin-Body Silicon-on-Insulator MOSFETs with Uniaxial Strain. IEEE. Electron Dev. Lett. **26**(5), 314–316 (2005)
38. Levinshtein, M.E., Rumyantsev, S.L., Shur, M.S.: Properties of Advanced Semiconductor Materials: GaN, AlN, InN, BN, SiC, SiGe. Chapter 6, p. 149–187. Wiley, New York (2001)
39. Liu, L., Lee, G.S., Marshak, A.H.: Band Discontinuities of Si Ge Heterostructures. Solid State Electron. **37**(3), 421–425 (1994)
40. Lundstrom, M.: Fundamentals of Carrier Transport. Cambridge University Press, Cambridge (2000)
41. Maegawa, T., Yamauchi, T., Hara, T., Tsuchiya, H., Ogawa, M.: Strain effects on electronic bandstructures in nanoscaled silicon: from bulk to nanowire. IEEE Trans. Electron Dev. **56**(4), 553–559 (2009)
42. Mahan, G., Sales, B., Sharp, J.: Thermoelectric materials: New approaches to an old problem. Phys. Today **50**(3), 42–47 (1997)
43. Majumdar, A.: Microscale heat conduction in dielectric thin films. J. Heat Transfer **115**(1), 7–16 (1993)
44. Minnich, A.: Modeling the thermoelectric properties of bulk and nanocomposite thermoelectric materials. Master thesis, Massachusetts Institute of Technology. Department of Mechanical Engineering (2008)
45. Minnich, A.J., Lee, H., Wang, X.W., Joshi, G., Dresselhaus, M.S., Ren, Z.F., Chen, G., Vashaee, D.: Modeling study of thermoelectric SiGe nanocomposites. Phys. Rev. B **80**(15), 155,327 (2009)
46. Murthy, J.Y., Mathur, S.R.: Finite volume method for radiative heat transfer using unstructured meshes. J. Thermophysics Heat Transfer **12**, 313–321 (1998)
47. Nag, B.R.: Electron Transport in Compound Semiconductors, vol. 11 of Springer Series in Solid-State Sciences. Springer, New York (1980)
48. Narumanchi, S.V.J., Murthy, J.Y., Amon, C.H.: Submicron heat transport model in silicon accounting for phonon dispersion and polarization. J. Heat Transfer **126**, 946–955 (2004)
49. Narumanchi, S.V.J., Murthy, J.Y., Amon, C.H.: Boltzmann transport equation-based thermal modeling approaches for hotspots in microelectronics. Heat Mass Transfer **42**(6), 478–491 (2006)
50. People, R.: Indirect band gap and band alignment for coherently strained Si xGe1-x bulk alloys on germanium ¡001¿ substrates. Phys. Rev. B **34**(4), 2508–2510 (1986)
51. Picu, R.C., Borca-Tasciuc, T., Pavel, M.C.: Strain and size effects on heat transport in nanostructures. J. Appl. Phys. **93**(6), 3535–3539 (2003)
52. Porter, L.J., Yip, S., Yamaguchi, M., Kaburaki, H., Tang, M.: Empirical bond-order potential description of thermodynamic properties of crystalline silicon. J. Appl. Phys. **81**(1), 96–106 (1997)
53. Rahman, A., Lundstrom, M.S., Ghosh, A.W.: Generalized effective-mass approach for n-type metal-oxide-semiconductor field-effect transistors on arbitrarily oriented wafers. J. Appl. Phys. **97**(5), 053,702 (2005)
54. Raithby, G.D.: Discussion of the finite-volume method for radiation, and its application using 3D unstructured meshes. Numer. Heat Transfer B **35**, 389–405 (1999)
55. Ramdane, A., Salce, B., Challis, L.J.: Stress dependence of the thermal conductivity of Cr-doped GaAs. Phys. Rev. B **27**(4), 2554–2557 (1983)
56. Ravich, Y.I., Efimova, B.A., Tamarchenko, V.I.: Scattering of current carriers and transport phenomena in lead chalcogenides. Phys. Status Solidi (B): Basic Solid State Phys. **43**, 11–33 (1971)
57. Rieger, M.M., Vogl, P.: Electronic-band parameters in strained $Si_{1x}Ge_x$ alloys on $Si_{1_y}Ge_y$ substrates. Phys. Rev. B **48**, 14,276–14,287 (1993)

58. Rim, K., Koester, S., Hargrove, M., Chu, J., Mooney, P.M., Ott, J., Kanarsky, T., Ronsheim, P., M. Ieong, A.G., Wong, H.S.P.: Strained Si NMOSFETs for High Performance CMOS technology. VLSI Technology Digest of Technical Papers, pp. 59–60 (2001)
59. Singh, J.: Physics of Semiconductors and their Heterostructures. McGraw-Hill, New York (1993)
60. Slack, G.A.: The thermal conductivity of nonmetallic crystals. Solid State Phys. **34**, 1–71 (1979)
61. Sood, K.C., Roy, M.K.: Phonon conductivity of doped germanium under uniaxial stress in the [110] direction. Phys. Rev. B **46**(12), 7486–7495 (1992)
62. Stillinger, F.H., Weber, T.A.: Computer simulation of local order in condensed phases of silicon. Phys. Rev. B **31**, 5262–5271 (1985)
63. Sverdlov, V., Ungersboeck, E., Kosina, H., Selberherr, S.: Effects of shear strain on the conduction band in silicon: An efficient two-band k ·p theory. 2007 I.E. 37th European Solid State Device Research Conference, pp. 386–389 (2007)
64. Sverdlov, V., Windbacher, T., Selberherr, S.: Mobility enhancement in thin silicon films: Strain and thickness dependences of the effective masses and non-parabolicity parameter. 2008 I.E. Simulation of Semiconductor Processes and Devices, pp. 145–148 (2008)
65. Takagi, S., Mizuno, T., Tezuka, T., Sugiyama, N., Nakaharai, S., Numata, T., Koga, J., Uchida, K.: Sub-band structures engineering for advanced CMOS channels. Solid State Electron. **49**(5), 684–694 (2005)
66. Tersoff, J.: Empirical interatomic potential for silicon with improved elastic properties. Phys. Rev. B **38**(14), 9902–9905 (1988)
67. Tersoff, J.: Modeling solid-state chemistry: interatomic potentials for multicomponent systems. Phys. Rev. B **39**(8), 5566–5568 (1989)
68. Thacher, E.F., Helenbrook, B.T., Karri, M.A., Richter, C.J.: Testing of an automobile exhaust thermoelectric generator in a light truck. Proc. Institution Mech. Eng. D J. Automobile Eng. **221** (2007)
69. Uchida, K., Krishnamohan, T., Saraswat, K., Nishi, Y.: Physical mechanisms of electron mobility enhancement in uniaxial stressed MOSFETs and impact of uniaxial stress engineering in ballistic regime. 2005 I.E. International Electron Devices Meeting, pp. 129–132 (2005)
70. Ungersboeck, E., Dhar, S., Karlowatz, G., Sverdlov, V., Kosina, H., Selberherr, S.: The effect of general strain on the band strucutre and electron mobility of silicon. IEEE Trans. Electron Dev. **54**, 2183–2190 (2007)
71. Venkatasubramanian, R., Siivola, E., Colpitts, T., O'Quinn, B.: Thin-film thermoelectric devices with high room-temperature figures of merit. Nature **413**(6856), 597–602 (2001)
72. Vining, C.B.: A model for the high-temperature transport properties of heavily doped n-type silicon-germanium alloys. J. Appl. Phys. **69**, 331–341 (1991)
73. Vogelsang, T., Hofmann, K.R.: Electron Transport in Strained Si Layers on Si_xGe_{1-x} Substrates. Appl. Phys. Lett. **63**(2), 186–188 (1993)
74. Wagner, M.: Simulation of Thermoelectric Devices. PhD thesis, Vienna University of Technology (2007)
75. de Walle, C.G.V.: Band Lineups and Deformation Potentials in the Model-Solid Theory. Phys. Rev. B **39**(3), 1871–1883 (1989)
76. Wang, X.W., Lee, H., Lan, Y.C., Zhu, G.H., Joshi, G., Wang, D.Z., Yang, J., Muto, A.J., Tang, M.Y., Klatsky, J., Song, S., Dresselhaus, M.S., Chen, G., Ren, Z.F.: Enhanced thermoelectric figure of merit in nanostructured n-type silicon germanium bulk alloy. Appl. Phys. Lett. **93** (19), 193,121 (2008)
77. Wong, W.A., Anderson, D.J., Tuttle, K.L., Tew, R.C.: Status of NASA's advanced radioisotope power conversion technology research and development. AIP Conf. Proc. **813**(1), 340–347 (2006)
78. Xia, Y., Yang, P., Sun, Y., Wu, Y., Mayers, B., Gates, B., Yin, Y., Kim, F., Yan, H.: One-dimensional nanostructures: Synthesis, characterization, and applications. Adv. Mater. **15**, 353–389 (2003)

79. Xu, Y., Li, G.: Strain effect analysis on phonon thermal conductivity of two-dimensional nanocomposites. J. Appl. Phys. **106**(11), 114,302 (2009)
80. Xu, Y., Li, G.: Strain effect analysis on the thermoelectric figure of merit in n-Type Si/Ge nanocomposites. J. Appl. Phys. **111**, 054,318 (2012)
81. Yang, R., Chen, G.: Thermal conductivity modeling of periodic two-dimensional nanocomposites. Phys. Rev. B **69**, 195,316 (2004)
82. Zawadzki, W., Szymańska, W.: Elastic electron scattering in InSb-type semiconductors. Phys. Status Solidi B Basic Solid State Phys. **45**, 415–432 (1971)
83. Zhang, B., He, J., Ji, X., Tritt, T., Kumbhar, A.: Controlled two-dimensional coated nanostructures for bulk thermoelectric composites. Appl. Phys. Lett. **89**(16), 163,114 (2006)
84. Zhang, W., Fisher, T.S., Mingo, N.: The atomistic Green's function method: An efficient simulation approach for nanoscale phonon transport. Numer. Heat Transfer B **51**(4), 333–349 (2007)
85. Zhao, H., Tang, Z., Li, G., Aluru, N.R.: Quasiharmonic models for the calculation of thermodynamic properties of crystalline silicon under strain. J. Appl. Phys. **99**(6), 064,314 (2006)
86. Ziman, J.M.: Electrons and Phonons. Oxford University Press, Oxford (1960)

Chapter 16
SiGe Nanowires for Thermoelectrics Applications

Michele Amato, Maurizia Palummo, Stefano Ossicini, and Riccardo Rurali

Abstract The possibility to reduce the thermal conductivity leaving essentially unaltered the electron transport makes semiconducting nanowires ideal materials for the engineering of high-efficiency thermoelectric devices. A simple and appealing route to achieve these goals is bringing together Si and Ge, giving rise to $Si_{1-x}Ge_x$ alloy nanowires with tunable Ge concentration, core–shell structures and multiple axial junctions, i.e. superlattices. In this chapter we review the most recent progresses in this field.

M. Amato (✉)
Institut d'Electronique Fondamentale, UMR8622, CNRS, Universitè Paris-Sud, 91405 Orsay, France
e-mail: michele.amato@u-psud.fr

M. Palummo
Dipartimento di Fisica, European Theoretical Spectroscopy Facility (ETSF), Università di Roma, "Tor Vergata", Via della Ricerca Scientifica 1, 00133 Roma, Italy
e-mail: maurizia.palummo@roma2.infn.it

S. Ossicini
"Centro S3", CNR-Istituto di Nanoscienze, Via Campi 213/A, 41125 Modena, Italy

Dipartimento di Scienze e Metodi dell'Ingegneria, Centro Interdipartimentale En&Tech, Universitá di Modena e Reggio Emilia, Via Amendola 2 Pad. Morselli, I-42100 Reggio Emilia, Italy
e-mail: stefano.ossicini@unimore.it

R. Rurali
Institut de Ciència de Materials de Barcelona (CSIC), Campus de Bellaterra, 08193 Bellaterra, Spain
e-mail: rrurali@icmab.es

X. Wang and Z.M. Wang (eds.), *Nanoscale Thermoelectrics*, Lecture Notes in Nanoscale Science and Technology 16, DOI 10.1007/978-3-319-02012-9_16,
© Springer International Publishing Switzerland 2014

16.1 Introduction

In the quest for renewable sources of energy that would be compatible with a sustainable development, thermoelectricity is one of the most intriguing alternatives and has long been sought for. Heat is the most pervasive form that energy takes in our world, but regretfully is also the one that we are less able to govern. As a matter of fact, despite its ubiquitousness, heat is normally related to the concept of *dissipation* and is regarded as a source of loss. The conversion of heat into electricity is possibly the ideal paradigm of a clean energy source: heat is freely available and is often the product of other energy conversion processes, such as the friction within the bearings of a mechanical engine or Joule heating in an electric circuit.

The thermoelectric effect is the direct conversion of a temperature gradient into an electric voltage and vice versa. The Seebeck effect is the kind of thermoelectricity we are concerned here: the conversion of heat into electricity. It is particularly appealing to implement such conversion scheme in semiconducting materials, which are the natural backbone of electronic devices. In these materials electrons do not contribute to the thermal transport and heat is entirely carried by phonons, the vibrations of the lattice. The thermoelectric efficiency of a semiconductor is then given by the dimensionless figure of merit:

$$\mathrm{ZT} = S^2 T \frac{\sigma}{\kappa} \tag{16.1}$$

where S is the Seebeck coefficient or thermoelectric power, T is the temperature, and σ and κ are electrical conductivity and thermal conductivity, respectively.

Apparently the increase of the efficiency of a semiconductor as thermoelectric material is not difficult and it boils down to trying to increase the electrical conductivity or decrease the thermal conductivity. Or doing both things at the same time. Unfortunately, things are more complicated than that. The electrical and the thermal conductivities are magnitudes that normally exhibit a high degree of correlation and materials that are good at conducting electricity tend to do well also at conducting heat; similarly, poor electrical conductors are usually also poor thermal conductors. This means that attempts of increasing σ lead to an increase κ and, vice versa, a decrease of κ goes normally together with a decrease of σ as well.

One-dimensional materials seem to offer a way out of this problem, as first proposed in their seminal paper back in 1993 by Hicks and Dresselhaus [1]. Electrons and phonon are scattered in different ways, thus the electrical conductivity and the thermal conductivity might be decoupled via an appropriate nanostructuring of the system. While electrons are confined to one-dimensional motion along the conductor axis, phonons still move in three dimensions and can be scattered off the surface. It follows that, as the conductor size shrinks down, surface scattering becomes increasingly important for phonon mobility, pushing it down, while electrical conductivity will be mostly insensitive. Hicks and Dresselhaus

showed that in the limit case of a square one-dimensional Bi_2Te_3 conductor of 5Å × 5Å, ZT would be as high as 14, to be compared to 0.5 for the bulk counterpart.

The advent of semiconducting nanowires (NWs) [2–5] marked a resurgent interest in the prediction of Hicks and Dresselhaus. Thin, cylindrical conductors approaching the size domain relevant to their proposal became available, thanks to the outstanding progresses in the bottom-up growth techniques. The vapor–liquid–solid (VLS) method—where a metallic nanoparticle that catalyzes the decomposition of a gas precursors is the vehicle of the nanowire nucleation—played a crucial role in the controlled synthesis of these nanostructures and wires with diameters below 10 nm have been successfully grown by several groups [6–14].

In 2008 two groups at UC Berkeley [15] and Caltech [16] independently reported Si NWs with ZT $\sim$ 1, causing a great excitement. Instead of simply improving the efficiency of a good thermoelectric, nanowires proved to be capable of making a thermoelectric out of a material that in its bulk form was not such. And that material was silicon! These studies showed that, exactly like theory predicted 15 years before, with nanowires it was possible to greatly reduce the thermal conductivity without much affecting the Seebeck coefficient and electrical resistivity. To understand the excitement generated by these results it should be stressed that the values of ZT reported represent an approximately 100-fold improvement over bulk Si and are of the order of the best performing bulk thermoelectrics, such as Bi_2Te_3 and Bi_2Se_3.

These works stimulated an extraordinary interest around nanowires and their potential as thermoelectric materials. Many efforts were devoted to either try to increase those unprecedented efficiencies or maintaining them in thicker nanowires that could be grown in a more reproducible way. Given a semiconductor, a rigorous approach to the increase of ZT would be invoking isotope blends, either disordered or in the form of ordered superlattices. Isotopes have different masses, but the same electronic structure. Hence, by definition, the electrical conductivity is strictly preserved, while, as by adding different isotopes one is adding scattering centers for the incoming phonons, κ will decrease, leading to the corresponding increase of ZT.

However, controlling the isotopic composition of a material is not practical and in many cases the difference in the mass that can be achieved is rather modest. For instance, Si has three known stable isotopes whose masses differ at most of 7 % [17], which suggests that the associated phonon scattering will be moderate.

An appealing alternative is mixing Si and Ge. These two elements have the same valence electronic structure ($3s^2 3p^2$ and $4s^2 4p^2$), but Ge mass is $\sim$2.5 larger than Si (72.63 vs 28.085), being a close approximation of the isotope mixing described above. Si and Ge both crystallize in the zincblende structure, thus obtaining stable $Si_{1-x}Ge_x$ alloys is rather straightforward. Heterojunctions required in superlattice structures, on the other hand, are more problematic, because the 4 % lattice mismatch prevent defect-free 2D interfaces. Luckily, this problem virtually vanishes with nanowires, where the strain can be released laterally.

In the remaining part of this chapter we describe the state-of-the art and the most cutting-edge challenges of SiGe nanowire research for thermoelectric applications. The chapter will be organized as follows: in Sect. 16.2 we will give a brief overview on the growth techniques, in Sect. 16.3 we will focus on the experimental characterization of thermal and electron transport properties of SiGe NWs, while in Sect. 16.4 we discuss the most recent progress concerning the theoretical modeling. In Sect. 16.5 we present our conclusions.

16.2 Growth Methods

The enormous interest in the thermoelectric device application of SiGe NWs has been boosted by the recent advances in synthesis, processing, and characterization. Though some preliminary attempts to produce cylindrical shaped structures have been proposed in the 1960s [18], the last 15 years have seen a noticeable improvement of the experimental techniques to produce SiGe nanowires with different composition and interfaces. The latter assumes a particular importance in the case of thermoelectrics, since it is well known that phonon and electron scattering are strongly influenced by the thickness and the quality of the interface. The main aim of thermoelectric design, namely the decoupling of electronic and thermal conductivity to optimize ZT, can be reached only if a total control on the geometry and interface can be obtained. As we discuss below, this goal can be achieved, opening new and exciting paths for one-dimensional nanostructures SiGe systems.

The most used method to produce SiGe NWs is the VLS growth. This method, originally developed for the synthesis of pure Si and pure Ge NWs, implies the growth of the NW through the decomposition of a gas precursor on a metal nanoparticle catalyst. The basic idea of the process is quite simple in the case of a pure Si NW: first a metal nanoparticle (usually Au) is deposited onto an Si substrate and metal–Si liquid droplets are formed. Then the gas precursor (silane) is introduced into the growth chamber. This gas starts to diffuse into the metal/Si droplets. By choosing the opportune thermodynamic conditions, the eutectic state for the metal–Si liquid alloy can be reached. After this point, Si atoms diffusing into the droplets reach supersaturation and start to precipitate forming a Si NW. This basic mechanism has been slightly modified by (changing the type of precursor gas or the catalyst) and used for the growth of a lot of different types of NWs, but preserving the main concept: the process always relies on the catalyzed decomposition of a precursor on a liquid metal droplet, which permits the growth only along one direction suppressing growth mechanism in the other two directions. Many different *flavors* of the VLS method have been reported [Chemical Vapor Deposition (CVD), laser ablation, Molecular Beam Epitaxy (MBE)] [6, 7, 19, 20] and the interested reader is referred to the focused review of Schmidt et al. [21].

As we will see below, in the case of SiGe NWs the possibility of switching the precursor gas from silane to germane or using them combined together has been revealed to be fundamental for the growth of these kinds of wires. The main

objective of this section is to review the main achievements and challenges concerning the growth of SiGe NWs. The most used methods to produce different types of SiGe NWs will be discussed, trying to point out the role of controlling morphology and interfaces for thermoelectrics.

SiGe alloyed NWs represent one of the most attracting nanostructures for thermoelectrics. The possibility of playing with phonon boundary and alloying scattering seems a promising tool to modulate the thermal conductivity of the material and hence the figure of merit ZT. The basic idea to grow a NW in which both Si and Ge are randomly distributed into the wire was developed immediately after the first experiments on VLS growth. Since both Si and Ge have the same eutectic temperature, the technique of growing an NW containing both the species presents only some modifications with respect to the growth of a pure wire. The first to accomplish this task were Duan and Lieber [19] who proposed a method in which, by using laser assisted catalytic growth, Si and Ge gas precursors are introduced into growth chamber and then incorporated into droplets. This permits the precipitation and the nucleation of the SiGe wire. This method offers the possibility of growing SiGe alloyed NWs whose composition, however, cannot be controlled. In fact the different thermal stabilities of SiH_4 and GeH_4 and the nonuniform temperature distribution into the growth chamber create Si-rich NWs in the hotter central region while Ge-rich NWs were obtained at the colder end. The control of composition assumes a particular importance, also in view of thermoelectric applications, and for this reason several efforts were proposed to overcome this limit.

An important step in this direction was taken by Lew et al. [22] who, by using CVD growth, optimize the temperature and the inlet gas ratio between SiH_4 and GeH_4 to produce wires with uniform composition and diameter. In particular at temperature between 350 and 400 °C they obtained wires with uniform composition x up to 0.66. Although the technique proposed by Lew et al. [22] gave a good control over the composition, the work of Givan and Patolsky [23] showed that another useful way to reach uniform composition was playing with the total growth pressure. In particular, by keeping low the temperature and the gas inlet ratio to minimize the tapering, it is possible to modulate the composition by modifying the total pressure. The intrinsic advantage of the method consists in the fact that the control on x, in the optimal range of temperature and gas inlet ratio, can be reached by varying only one parameter, i.e. the pressure. The authors showed that for values $<$ 500 Torr, the Ge content increases sharply with the pressure, while for values $>$ 500 Torr, a milder linear dependence was observed.

Axial SiGe nanowires, namely wires in which there is a planar interface between Si and Ge along the direction of growth, are particularly interesting for thermoelectrics since they present some intriguing coherence effects in both thermal and electronic transport which constitute a useful playground to engineer thermoelectric performances. In this context the possibility to have a wire with a sharp interface between Si and Ge is of primary interest. Preliminary works [24–29] showed that, though in principle is possible to obtain axial SiGe wires with the standard VLS-CVD growth or MBE growth methods, the results are quite poor in terms of

sharpness of the interfaces. In fact, in all the above-mentioned works the obtained interfaces were very diffuse, mining their application as electronic or thermoelectric devices. This limit is related to the fact that when the gas precursor is switched from silane to germane to build a sharp Si/Ge interface, the droplet must be cleaned of all the Si before a pure Ge NW can be grown. Recently, several works have been carried to overcome VLS limits in producing Si/Ge abrupt interfaces. Perea et al. [30] proposed a way in which the solubility of semiconductors precursors into the droplet can be changed by playing on the composition of the metal nanoparticle. In particular, they showed that the eutectic solubility of Ge into an $Au_{1-x}Ga_x$ droplet can be varied by changing the Ga concentration x of the alloyed catalyst. Following this idea, they applied this procedure: (1) first, they grew the Ge segment on a pure Au droplet; (2) then, when the Si/Ge interface had to be built, Ga alloying into Au droplets was induced, by changing gas precursor. Ge diffusion was inhibited because Ge atoms have very low solubility into the new formed droplets; (3) finally, the Ge-based and Ga-based gas were removed and SiH_4 was introduced to form the Si segment. With this method interfaces less than 11 nm were achieved.

Another workaround attempting to obtain sharp interfaces beyond the limits of the reservoir effect was reported by Wen et al. [31], who achieved the sharpest interfaces between Si and Ge segments thus far. Conscious of the limits of VLS growth, they decided to follow a completely different strategy of growth. Their interesting solution, with which heterojunction as sharp as 1 nm for wires can be obtained, is based on a combination of VLS and vapor–solid–solid (VSS) growth. In particular, they (1) start the growth of the Si segment with a standard VLS method; (2) then, lower the temperature and started the VSS growth; (3) when the droplet is emptied of its Si content, they switch from SiH_4 to GeH_4 and start growing the Ge segment. The only limit of the present method consists in the fact that, due to the low growth rate of VSS process (incompatible with a technological large scale production), this noticeable abruptness can be obtained only when short Ge segments have to be grown.

Another important geometry of SiGe nanowires is represented by radial heterostructures like core–shell SiGe NWs. This type of wires has attracted a lot of interest from a technological point of view, thanks to the excellent electronic properties they present with respect to the pure Si and pure Ge NWs. The carrier confinement properties and the higher mobility if compared to pure wires have been shown to lead to field-effect transistors (FETs) with significantly better performances than FETs based on single-element Ge or Si nanowires [32]. The first experimental demonstration of the synthesis of radial SiGe heterostructures was reported by Lauhon et al. [33] who performed axial VLS growth of a Ge or an Si NW followed by uncatalyzed, homogeneous vapor-phase deposition on the nanowire sidewalls of the complementary chemical species. They demonstrated the possibility of heteroepitaxial growth of crystalline Ge–Si and Si–Ge core–shell NWs as well as the synthesis of multi-structure with an interface that is less than 1 nm.

After this pioneering work, several efforts have been focused on optimizing growth conditions to obtain more uniform and defect-free structures. Most of the works focused on the Ge-core/Si-shell geometry that is the most interesting one for device applications. The first main problem arising from the growth of such kind of nanostructures is related to the different optimal growth temperatures of Si and Ge. In order to favor the radial deposition of Si (Ge) when the axial segment of Ge (Si) is grown the temperature has to be changed. However, this cannot avoid the growth of an additional segment on the top of the wire (Si or Ge). This problem was solved by Goldthorpe et al. [34]: before depositing the Si-shell, they etched the Au nanoparticle from the Ge NW tip avoiding any type of additional VLS growth on the top of the catalyst.

An important issue related to the growth of core–shell NWs deals is the smoothness of the Si shells. Due to the critical impact that it has on device performances many efforts have been devoted to the minimization of the shell roughening that derives from the accommodation of Si/Ge lattice misfit. In particular in the work of Goldthorpe et al. [35] the authors proposed a strategy to obtain uniform Si shells: starting from the observation that the roughening of the shell observed derives from the low stability of {112} facets, they thought to replace them with lower energy planes to minimize mechanical and energetic distortions. In this way, by playing on the surface energy they were able to eliminate the facet break-up. More recently, Zhao et al. [36] meticulously characterized the impact of the shell morphology on the transport regime in SiGe NW-based FETs, showing how without a proper degree of crystallinity of the shell doping impurities therein could not be properly activated (see Fig. 16.1).

16.3 Experimental

As discussed in Sect. 16.1 the energy conversion efficiency of thermoelectric devices is determined by the figure of merit $\mathrm{ZT} = \frac{S^2 \sigma T}{k}$. This is a dimensionless parameter that has no direct physical meaning, but plays an important role in the maximum thermodynamic efficiency expression:

$$n_{\max} = \frac{T_H - T_C}{T_H} \frac{\sqrt{1 + \mathrm{ZT}} - 1}{\sqrt{1 + \mathrm{ZT}} + \frac{T_C}{T_H}}$$

where the first fraction is the usual Carnot efficiency, with T_H and T_C being the hot and cold temperatures. Therefore a higher ZT corresponds to an efficiency closer to the Carnot one. However, since the electrical conductivity σ and the electronic contribution κ_e to the thermal conductivity $\kappa = \kappa_e + \kappa_L$ (where κ_L is the lattice thermal vibrations, i.e. phonons, contribution) are linked by the Wiedemann–Franz law, the maximum ZT is limited and a reduction of the lattice contribution to the thermal conductivity is the first possible way to further improve the efficiency.

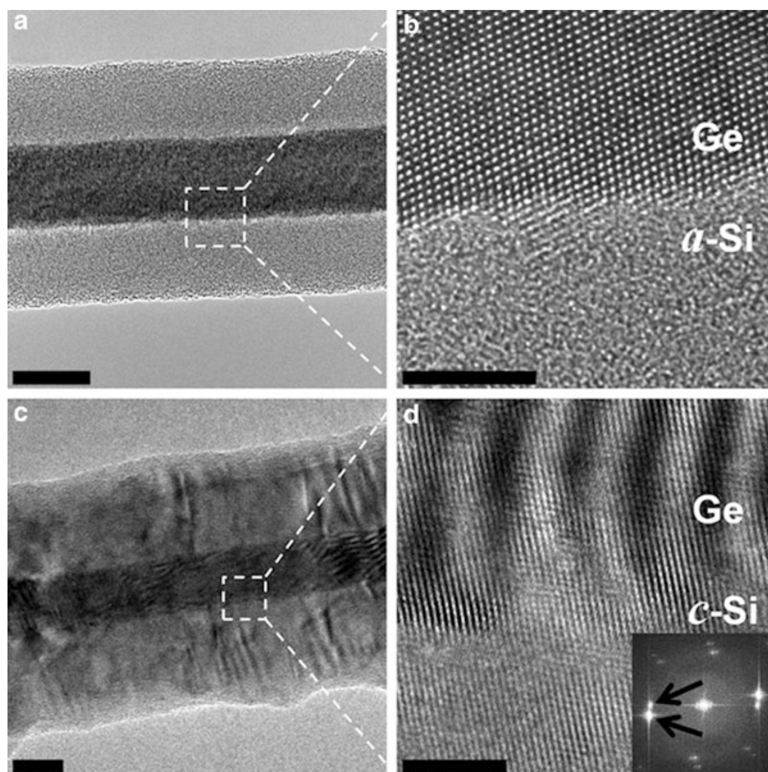

Fig. 16.1 (**a**) Transmission electron microscopy (TEM) image of a Ge-core amorphous Si-shell NW. (**b**) High-resolution TEM (HRTEM) image at the Ge/Si interface of panel (**a**). (**c**) TEM image of a Ge-core Si-shell NW with crystalline shell. (**d**) HRTEM image at the Ge/Si interface of panel (**c**). Scale bars for (**a–d**) are 20, 5, 20, and 5 nm, respectively. Reprinted with permission from Zhao et al., Nano Lett. **11**(4), 1406. Copyright 2011 American Chemical Society

In this context SiGe NWs represent a promising strategy to greatly enhance ZT, thanks to the combination of the scaling down of the material size (using the quantum-confinement effects that should increase S and σ and reduce the thermal conductivity k, due to an increased phonons scattering rate) and of alloying (which mimics an isotope mixing). Since nanostructuring affects much more the thermal than the electrical conductivity (because electrons have much smaller mean free paths than phonons at room temperature), in the majority of the experiments the main task has been to reduce the thermal conductivity. Only few works have been devoted to the simultaneous measurement of all the thermoelectric properties in order to reach an accurate determination of the figure of merit.

16.3.1 Thermal Transport

Since a reduction in the thermal conductivity can be related to increased phonon scattering as consequence of alloying, nanostructuring, and surface boundaries, all these issues have been investigated in the last years.

Li et al. [37] have synthesized high crystalline Si/SiGe (111) superlattice NWs with diameters between 53 and 83 nm and Ge concentration from 5 to 10 %, using a hybrid pulsed laser ablation/CVD method. They have observed a reduction of thermal conductivity (values around $6\,\mathrm{W\,m^{-1}\,K^{-1}}$ at 300 K) with respect to both pure Si NWs of similar diameter and 2D Si/SiGe superlattice films. Decreasing the diameter results in a slight reduction of k, while the interface scattering is not very significant. From these results it is possible to conclude that the alloy scattering mechanism in SiGe regions is the main sources of thermal conductivity reduction in these nanowires, while boundary effects contribute to further decrease k.

This alloy effect has been observed also by Kim et al. [38]. They have showed that the thermal conductivity of $Si_{1-x}Ge_x$ NW alloys decreases with increasing the Ge concentration, whereas, on decreasing the NW diameter, the reduction of the thermal conductivity is not as evident as in pure Si NWs.

More recently Yin et al. [39] have studied the influence of phonon scattering on the thermal conductivity of VLS grown SiGe NWs of different diameter and length, variable Ge concentration and amorphous silicon oxide shell thickness. A small dependence on the wire length and a small influence from the oxide layer is observed and this is explained in terms of the shortened phonon characteristic lengths due to the high Ge concentration present in the NWs. The thermal conductivities measured from 60 to 450 K approach the minimum values, around 1–2 $\mathrm{W\,m^{-1}\,K^{-1}}$ at 300 K, for diameter of the order of 40–60 nm and with Si:Ge ratios around the unit.

Another source of thermal conductivity reduction, originated by carrier-phonon scattering of low-frequency modes, has been individuated by Martinez et al. [40] in B-doped SiGe alloy NWs. The measured values of the order of $1.1\,\mathrm{W\,m^{-1}\,K^{-1}}$ at 300 K, comparable to bulk silica and more than a factor 2 smaller than single-crystal alloys. Measurements at room temperature show that the largest reduction of k is reached for the most heavily doped NWs, suggesting that, in addition to boundary and alloy scattering, also the carrier-phonon scattering mechanism is present. Moreover the temperature dependence of k confirms the role of hole-phonon scattering as a mechanism of increasing importance, reducing T. Indeed in the most heavily doped samples a strong reduction of k is observed below room temperature, while in less doped NWs a weak temperature dependence, characteristic of alloy scattering, is observed.

The role of surface roughness on thermal conductivity has been studied by Kim et al. [41] in VLS grown $Si_{1-x}Ge_x$ nanowires, with diameters around 200–300 nm. The thermal conductivity of rough $Si_{0.96}Ge_{0.04}$ nanowires is a factor 4 smaller than that of corresponding smooth nanowires and also an order of magnitude smaller than the bulk alloy as shown in Fig. 16.2.

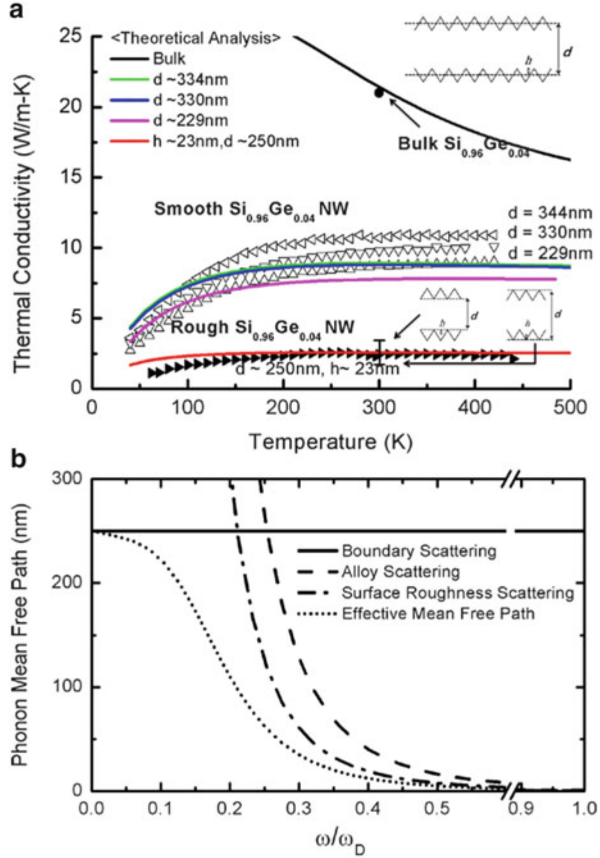

Fig. 16.2 (**a**) Temperature-dependent thermal conductivities of $Si_{0.96}Ge_{0.04}$ crystals in bulk, smooth NWs and rough NWs. *Dot* and *triangular markers* are based on experimental data in the literature, whereas *lines* are based on model calculation. Thermal conductivities of 250 nm rough SiGe NWs with surface roughness, *h*, of 23 nm are presented. (**b**) Phonon mean free path of various scattering mechanism vs normalized phonon frequency. ω_d is the Debye frequency. With kind permission from Springer Science+Business Media: Appl. Phys. A, Effect of surface roughness on thermal conductivity of VLS-grown rough $Si_{1-x}Ge_x$ nanowires, **104**, 2011, 23, Kim, Park, Kim, Kim, Choi, and Kim, Fig. 3

Recently Lee et al. [42] have produced and studied several $[\bar{1}1\bar{1}]$ oriented SiGe NWs with different diameter and Ge concentration. They have observed a reduction of the thermal conductivity mainly due to surface-boundary scattering for NWs with diameter over $\simeq$ 100 nm, while alloying plays an important role in suppressing phonon transport for smaller diameters.

In the last years, the interest has shifted to Ge/Si core shell NWs due to their remarkable properties. In particular Wingert et al. [43] have measured the thermal conductivity of Ge/Si core–shell NWs (diameters in the range 10–20 nm) with a new apparatus able to measure very low thermal conductivities of the order of 0.1 $\mathrm{nW\,m^{-1}\,K^{-1}}$, at least one order of magnitude smaller than the traditional measurement sensitivity. Their results show that the phonon confinement starts to play a role beyond the diffusive scattering limit when the NW diameter is of the order of the phonon wavelength. The measured thermal conductivity of their Ge/Si core–shell NWs is of the order of 1–2 $\mathrm{W\,m^{-1}\,K^{-1}}$ at room temperature and it is

rather independent of the temperature. Comparing these results with those measured in pure Ge NWs an increase below 220 K is observed while, at room and higher temperature, a reduction of about 1 W m^{-1} K^{-1} is found. Furthermore, at room temperature, k is lower both than the corresponding bulk alloy and than that measured in larger diameter SiGe alloy NWs. In agreement with theoretical simulations [44], this reduction has been attributed to the altered vibration modes of the phonons responsible of transport heat through the lattice.

16.3.2 Electronic Transport and the Determination of ZT

To determine the figure of merits ZT it is necessary to measure simultaneously all the thermoelectric properties, including the electrical conductivity.

Using a thermoelectric platform produced by photolithography processes and a homemade nanomanipulator Martinez et al. [40] were able, in the case of B-doped SiGe alloy NWs, to measure the electric and thermal conductivity on suspended wires of two different diameters (100 and 300 nm) and variable dopants concentration (1.2×10^{19} and 3.8×10^{19} cm^3). Measurements at room temperature of the electrical and thermal conductivity result in a figure of merit ZT close to 0.18 at room temperature, more than a factor 2 higher than bulk SiGe alloy. An enhancement mostly due to the enhanced thermal properties.

By simultaneously measuring the thermal conductivity, the electrical conductivity and the thermopower of several SiGe NWs with different diameter and Ge concentration, Lee et al. [42] reported a large improvement in the figure of merit with respect to reference bulk material and to Si NWs. Due to the short electron mean free paths, the measured electrical conductivities, different from the thermal ones, do not show a strong dependence on the nanowire diameter and on the Ge concentration. Thus the authors conclude that the measured improvement of ZT is mainly due to the reduction of the thermal conductivity. A maximum and significative value of ZT $\simeq$ 0. 46 is reached at 450 K.

Finally Moon et al. [45] presented a study of the gate modulated thermoelectric power factor $S^2\sigma$ for single Ge/Si core–shell NWs with Ge core diameters ranging from 11 to 25 nm. The Seebeck coefficient has a dependence on the carrier concentration similar to that of bulk Ge, showing that the quantum confinement effect is not significant at room temperature for the investigated diameters. The behavior of the power factor $S^2\sigma$ vs carrier concentration is reported in Fig. 16.3.

The results for SiGe NWs are compared with that of bulk Ge. Similar to bulk Ge there is an optimal carrier concentration for the peak power factor. The highest results (more than 30 % larger that of p-type bulk Ge) are those related to the NWs, that show the highest mobility, suggesting the promising possibility of exploiting the high carrier mobility of the hole gas in core–shell Si/Ge NWs.

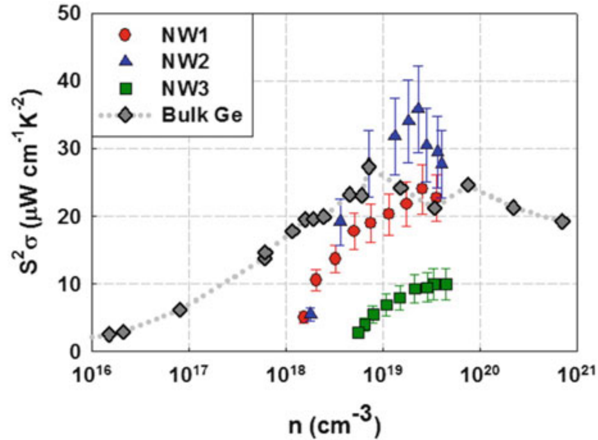

Fig. 16.3 Power factor vs carrier concentration of Ge/Si NWs and bulk p-Ge. Similar to bulk Ge, there is an optimal carrier concentration for the peak power factor for the NWS. Reprinted with permission from Moon et al. [45]

16.4 Theoretical

As mentioned in the introduction, in the last decade SiGe nanowires started to play an important role for the envisaged good performances as thermoelectric devices. Beyond SiGe nanostructured alloys and thanks to the enormous progress in nanowire's synthesis, axial and radial heterostructures can be grown with Si/Ge interfaces less than 1 nm wide. Both of these geometries have been individuated as particular promising for thermoelectric applications.

Indeed, as we have seen before, nanostructuring offers the possibility to improve the thermoelectric figure of merit $ZT = \frac{S^2 \sigma T}{\kappa_e + \kappa_L}$, by reducing the lattice thermal conductivity κ_L, without a corresponding reduction of the electric conductivity σ and the Seebeck coefficient S. Moreover, these one-dimensional systems offer the possibility of engineering phonon dispersion and thermal conductivity by playing not only on the NW cross section but also on the specific atomic arrangement of Si and Ge species. Several authors [46] have shown that (1) as in bulk systems, the temperature modulates the magnitude of atomic displacements influencing the thermal transport; (2) the NW diameter, when comparable to the phonons mean free path, determines the phonon boundary scattering and the propagation of heat in the wire; (3) the relative amplitude of Si and Ge regions is a fundamental parameter which influences the thermal conductance.

Beyond several experimental works, an increasing number of theoretical investigations are appeared in the last years on SiGe NWs to calculate and explain their thermoelectric features. The role of theoretical modeling in nanoscience is each day more important, as simulating a nanomaterial in well-defined conditions provides great insight on its most fundamental properties, whose direct measurement is often complicated by a number of factors, such as the intrinsic uncertainty and the difficulty of having well-controlled experimental conditions or pure samples.

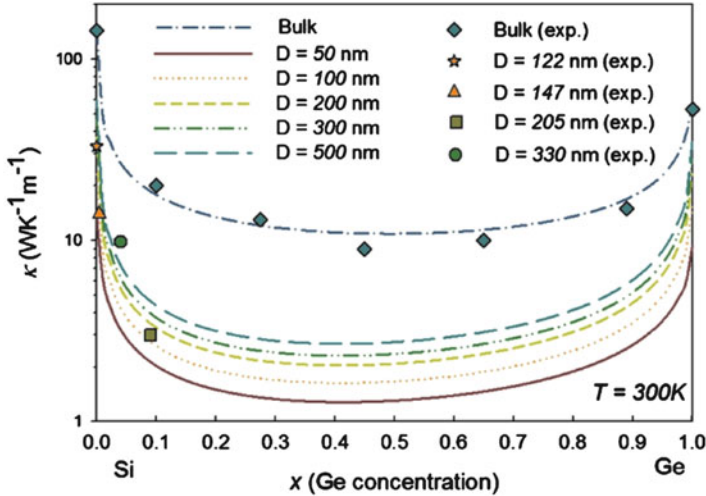

Fig. 16.4 Thermal conductivity as a function of the Ge concentration x for a $Si_{1-x}Ge_x$ bulk alloy and NWs with different diameters. The *lines* show calculation results using an analytical expression (see [47]), and the *symbols* are experimental data [38, 48]. Reprinted with permission from Wang and Mingo, Appl. Phys. Lett. **97**(10), 101903. Copyright 2010, American Institute of Physics

The study of nanoscale thermal transport is no exception and, in view of the relevance of practical applications such as thermoelectricity, many studies have been reported recently.

The important case of SiGe alloy nanowires has been tackled recently by Wang and Mingo [47] who computed the thermal conductivity as a function of nanowire diameter. In this work the scattering rate is calculated as sum of anharmonic, alloy and boundary scattering contributions. In fair agreement with experimental observation [38, 48], a weak dependence as compared to pure Si nanowires is reported. For small diameter κ is proportional to D, while this dependence becomes slower as D increases. At larger Ge concentration the deviation from linear dependence occurs at smaller diameters. This slower dependence is related to the fact that the thermal conductivity of an alloy, due to the presence of the alloy scattering which proportional to ω^4, is dominated by low frequency modes, while for very small D the boundary scattering term dominates over alloy and anharmonic terms at all frequencies. The thermal conductivity for $Si_{1-x}Ge_x$ bulk and NWs of different diameter as function of x is reported in Fig. 16.4 showing a good agreement of theoretical results with available experimental data.

In SiGe superlattices NWs three different types of thermal resistance can be individuated: the space resistance R_S, originated by the sidewall phonons scattering, the transmission resistance R_T, related to Si/Ge interface phonon boundary scattering and finally the volumetric resistance, R_V, which is due to defects, impurities, grain boundary.

Dames and Chen [49] provided one of the first examples of thermal conductivity calculations of SiGe superlattice nanowires. Their model considers the three mechanisms described above completely decoupled and, similarly to [47], uses a simple Matthiessen's rule to derive the three effective independent mean free paths. It neglects confinement effects and it is based on the assumption that thermal transport is mainly dominated by diffuse scattering of incoherent phonons in agreement with several experimental observations [50, 51]. Notably in this work, a fair agreement with experimental data [37] for Si/$Si_{0.9}Ge_{0.1}$ superlattice nanowires of 58 and 83 nm in the temperature range 30–150 K is reported. Additionally, their results, valid in the diffusive scattering regime, show that the thermal conductivity κ decreases reducing wire diameter, Si or Ge segment length and intersegment transmission. Three distinct scattering regimes can be individuated: the small diameter regime where the dominant scattering mechanism is due to the wire's sidewalls, the short segment regime where the thermal resistance of the Si/Ge interface plays the major role and finally the bulk regime when both the diameter and the segment length are much larger than the mean free path of the bulk phonons and then nanostructuring is not any more relevant. Other studies [44, 52, 53], appeared recently in the literature, focus on the study of the thermal behavior of ultrathin nanowires taking into account quantum confinement and coherence interference effects and are mainly based on atomistic calculations of the thermal conductance.

Since various experimental results have shown that κ depends not only from the size of the SiGe alloy NW but also from the arrangement of atoms therein, Chan et al. [54] investigated this aspect using equilibrium classical MD simulations, joined to coarse grained cluster expansion and genetic algorithm optimization. Although limited to the case of $\langle 111 \rangle$ $Si_{1-x}Ge_x$ NWs with $0.03 < x < 0.2$ with $D = 1.5$ nm, their results clearly indicate that configurations with complete planes of Ge atoms along the NW axis, have the lowest κ, close to the bulk amorphous limit, which is explained by the suppression of long-range order in the simulations.

Non-equilibrium Molecular Dynamics calculations have been used by Hu and Poulikakos [46] to investigate the dependence of thermal conductivity of $\langle 100 \rangle$ SiGe superlattice NWs on diameter, periodic length, and temperature. Actually three different types of NWs are analyzed: pure, superlattices, and random alloys. A strong reduction of thermal conductivity in superlattices with respect to pure Si NW is observed and a non-monotonic behavior is found varying the superlattice periodic length. The values of thermal conductivity for pure Si NW, random alloyed SiGe and SiGe superlattice NWs and fully amorphous Si NW are 45.3, 6.03, 4.44 and $1.35\,\mathrm{W\,m^{-1}\,K^{-1}}$, respectively, indicating that more the system is heterostructured more the thermal conductivity is reduced. The sound velocity reduction, the phonon interface and boundary scattering, are the main reasons of the k reduction found in SiGe NWs. The non-monotonic behavior of the thermal conductance with periodic length is explained by the fact that at small periodic lengths, coherence effects become dominant and a constructive interference phenomenon suppresses the interface scattering and facilitates the thermal transport

along the wire. These findings have been confirmed by Shi et al. [52], who, by combining Density Functional Theory calculations and non-equilibrium Green's Function simulations for ⟨100⟩ SiGe superlattice NWs, found the same non-monotonic behavior for the thermal conductance dependence on the periodic length. Another interesting result of [46] is that, at fixed periodic length of 4.34 nm, the thermal conductivity is a non-monotonic function of the wire diameter. While the initial thermal conductance decrease is explained, according to the Boltzmann equation, with the calculated reduction of heat capacity, at small diameters the heat conduction is facilitated by the fact that the long-wave length surface modes become predominant due to the high surface–volume ratio. Finally in the 50–650 K range, a negligible dependence of the heat conduction by temperature is reported.

By using a combination of first-principles simulations, interatomic potentials and Landauer–Büttiker approach, Shelley and Mostofi [53] evaluated the thermal transport for axial SiGe ⟨111⟩, ⟨110⟩, and ⟨112⟩ heterostructures in the coherent regime. Beyond pristine nanowires they studied superlattices with random, Fibonacci chain and periodic distribution of Ge layers along the wire axis, evaluating the thermal conductivity both in the ohmic and in the coherent regimes. They confirmed the strong decrease of thermal conduction when the heterostructure is created and, moreover, they report a further reduction when disorder is increased, especially when the ohmic regime is considered. This study is of special interest because it is one of the few that addresses thermal and electronic transport in an SiGe NW at the same time. Most of the theoretical works, on the other hand (another noticeable exception is [55]), are focused on the engineering of the phonon transport. Single alloyed inclusions were studied by Amato et al. [56] within a first-principles formalisms, focusing on the change of the ballistic conductivity as the Ge content increases.

As described above, SiGe core–shell NWs are radial heterostructures which are made up by two coaxial cylinders, the internal one, the core, is made up by one type of material while the external one, the shell, is made up by the other material. Like in the superlattice geometry the presence of at least one dimension of the order of the phonon mean free path and of interface between Si and Ge offers the right conditions to modulate phonon scattering and, hence, heat conduction.

In particular, several works have shown how the deposition of a Ge or Si coating on the top of a pure Si or Ge NW can strongly modify normal modes of the system and give rise up to unusual coherent resonance effects.

Hu et al. [44] have reported one of the first detailed investigations of thermal processes in SiGe core–shell nanowires by using Molecular Dynamics simulations in ⟨100⟩ oriented NWs up to 7.7 nm of diameter. The influence of thermal conductivity from the dimension of the shell, the diameter, and the length of the wire is discussed.

The addition of a Ge shell substantially lowers the phonon transport with respect to the pure Si NW. This reduction of thermal conductivity is preserved also if the cross-section width and length of the wire are varied. A slight non-monotonic behavior has been found increasing the number of Ge shells because the value of

κ increases as a consequence of the larger contribution of the Ge part of the wire to the overall heat conduction.

The authors demonstrate that when a Ge layer is added on the surface of a pure Si NW there is a suppression of low frequency vibrational modes of the Si surface atoms. While oscillations of Si core atoms are not modified by the presence of Ge atoms, in the case of Si surface atoms the bonds with the heavier Ge atoms strongly depress low frequency vibrational modes. It is well known that low frequency modes are very delocalized and hence their contribution to heat conduction is very large. For this reason the suppression of these modes, by adding Ge layers, is the main cause of thermal conduction reduction with respect to the pure system. Finally, the authors demonstrate that another contribution to the thermal conductivity reduction comes from the depression of high frequency phonons, which usually can carry heat in core–shell structure.

All the above-mentioned effects have been better highlighted in the works of Chen et al. [57, 58] who have investigated the nature of coherent resonance in Ge-core/Si-shell NWs. By using Molecular Dynamics simulations of Ge-core/Si-shell NWs, they have shown that the low values of thermal conductivity are associated with the strong localization of longitudinal phonon modes originating by a coherent resonance effect due to a coupling between longitudinal and transversal vibrational modes. Indeed, while in pristine nanowires the longitudinal and transversal modes are completely decoupled due to the sound velocity that is the same for all the atoms, this is not true in SiGe core–shell NWs where, induced by the stretching of the atoms belonging to the Si/Ge interfaces, a coupling between longitudinal and transversal oscillations occurs. Consequently the non-propagating nature of transversal modes is transferred to the longitudinal ones, strongly depressing the overall heat conduction in the nanowire.

Chen et al. [57] have recently analyzed how the thermal-conductivity of a Ge NW changes when coated with Si shells. Their results demonstrate that κ can be reduced of more than 25 % with respect to the pristine wire, but that a critical thickness coating exists beyond which the thermal conductivity grows back. Moreover, they have shown that a disordered interface, at a given coating thickness, can further reduce the value of κ. This behavior is explained in terms of vibrational eigenmode analysis and is due to the fact that coating induces localization for low-frequency phonons with wavelength comparable to NW diameter, while interface roughness localizes the high-frequency phonons.

By means of atomistic calculations based on semi-empirical methods and Green's Function Theory, Markussen [55] has reached similar conclusions studying the thermoelectric properties of Ge-core Si-shell nanowires with surface disorder (a sketch of the wires studied is given in Fig. 16.5). Due to the decoupling of the electronic and phonon transport a very promising thermoelectric figure of merit ZT > 2 has been predicted for Ge/Si core/shell NWs with high-degree of surface roughness disorder. Charge carrier flow in the wire's core, due to the confinement potential of the shell and are thus insensitive to the surface structure (see Fig. 16.6). Phonons, on the other hand, suffer a considerable surface scattering, thus leading to an increased value of ZT.

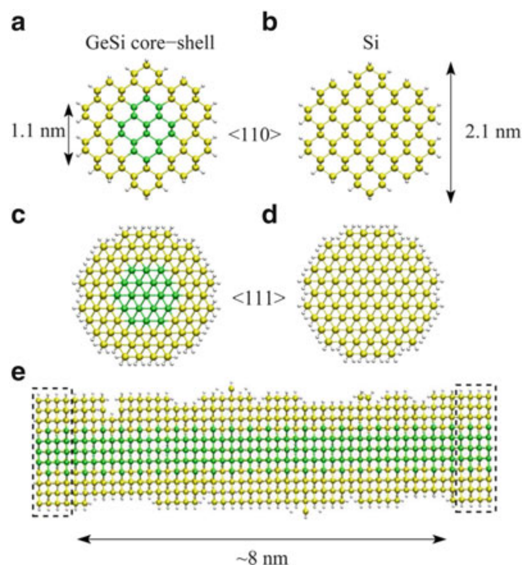

Fig. 16.5 (**a**, **b**) ⟨110⟩ and (**c**, **d**) ⟨111⟩ nanowires. The ZT figure of merit of core–shell NWs (**a**, **c**) is compared against that of pure Si NWs (**b**, **d**). The scattering region with the rough Si-shell is shown in panel (**e**). Reprinted with permission from Markussen, Nano Lett. **12**(9), 4698. Copyright 2012 American Chemical Society

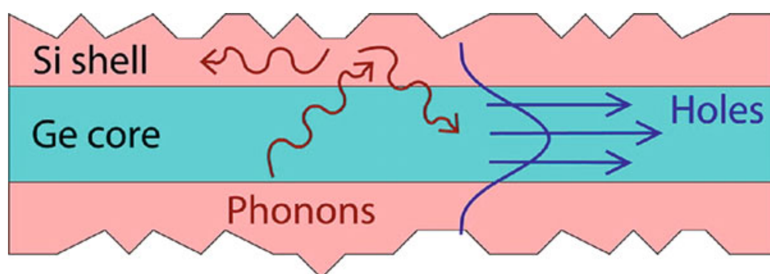

Fig. 16.6 Schematic representation of a core–shell NW in which charge carriers flow in the Ge core because of the shell confinement, while phonons are scattered at the rough shell surface, leading to an increased value of ZT. Reprinted with permission from Markussen, Nano Lett. **12**(9), 4698. Copyright 2012 American Chemical Society

16.5 Conclusions

Semiconducting nanowires are among the most firm candidates to provide the paradigm shift needed to continue improving the efficiency of electronic devices, beyond the limits that the heuristic and well-known Moore's law starts facing. More recently, however, a wealth of applications with a broader scope are being investigated and thermoelectricity is proving to be one of the most fertile. The marriage

of Si and Ge is an old-classic in conventional planar electronics, but it is at the nanoscale that it is free to flourish and express its full potential. SiGe nanowires are extremely versatile and thier tailor-made properties can be tuned by playing with the composition, with the interfaces or with the periodicity with which these two materials are alternated. The development in the growth techniques has been crucial to obtain properties that were previously predicted, but that rely critically on the atomic scale details of the nanowire geometry, such as the sharpness of the interfaces or the homogeneous distribution of the species in an alloy. In this chapter we have shown that these properties can now be controlled with an increasingly high degree of precision and that efficient thermoelectric devices based on SiGe nanowires are on their way to have an impact on practical applications for the generation of clean energy.

Acknowledgements We acknowledge the funding of the Spanish Ministry of Science and Technology under contracts FIS2009-12721-C04-03, CSD2007-00041, and FIS2012-37549-C05-05. M.A. acknowledges the support from the European Union through the FP7 Marie Curie Intra-European Fellowship No. 326794 (EXPRESS project).

References

1. Hicks, L.D., Dresselhaus, M.S.: Phys. Rev. B **47**, 16631 (1993)
2. Xia, Y., Yang, P., Sun, Y., Wu, Y., Mayers, B., Gates, B., Yin, Y., Kim, F., Yan, H.: Adv. Mater. **15**(5), 353 (2003)
3. Lu, W., Lieber, C.M.: J. Phys. D: Appl. Phys. **39**(21), R387 (2006)
4. Wu, X., Kulkarni, J.S., Collins, G., Petkov, N., Almécija, D., Boland, J.J., Erts, D., Holmes, J.D.: Chem. Mater. **20**(19), 5954 (2008)
5. Rurali, R.: Rev. Mod. Phys. **82**(1), 427 (2010)
6. Morales, A.M., Lieber, C.M.: Science **279**(5348), 208 (1998)
7. Holmes, J.D., Johnston, K.P., Doty, R.C., Korgel, B.A.: Science **287**(5457), 1471 (2000)
8. Cui, Y., Lauhon, L.J., Gudiksen, M.S., Wang, J., Lieber, C.M.: Appl. Phys. Lett. **78**(15), 2214 (2001)
9. Coleman, N.R.B., Morris, M.A., Spalding, T.R., Holmes, J.D.: J. Am. Chem. Soc. **123**(1), 187 (2001)
10. Coleman, N.R.B., O'Sullivan, N., Ryan, K.M., Crowley, T.A., Morris, M.A., Spalding, T.R., Steytler, D.C., Holmes, J.D.: J. Am. Chem. Soc. **123**(29), 7010 (2001)
11. Ma, D.D.D., Lee, C.S., Au, F.C.K., Tong, S.Y., Lee, S.T.: Science **299**(5614), 1874 (2003)
12. Cui, Y., Zhong, Z., Wang, D., Wang, W., Lieber, C.: Nano Lett. **3**(2), 149 (2003)
13. Wu, Y., Cui, Y., Huynh, L., Barrelet, C., Bell, D., Lieber, C.: Nano Lett. **4**(3), 433 (2004)
14. Zhong, Z., Fang, Y., Lu, W., Lieber, C.M.: Nano Lett. **5**(6), 1143 (2005)
15. Boukai, A.I., Bunimovich, Y., Tahir-Kheli, J., Yu, J.K., Goddard III, W.A., Heath, J.R.: Nature **451**(7175), 168 (2008)
16. Hochbaum, A.I., Chen, R., Delgado, R.D., Liang, W., Garnett, E.C., Najarian, M., Majumdar, A., Yang, P.: Nature **451**(7175), 163 (2008)
17. de Laeter, J.R., Böhlke, J.K., De Bièvre, P., Hidaka, H., Peiser, H.S., Rosman, K.J.R., Taylor, P.D.P.: Pure Appl. Chem. **75**(6), 683 (2003)
18. Wagner, R.S., Ellis, W.C.: Appl. Phys. Lett. **4**(5), 89 (1964)
19. Duan, X., Lieber, C.M.: Adv. Mater. **12**(4), 298 (2000)
20. Wang, N., Tang, Y.H., Zhang, Y.F., Lee, C.S., Lee, S.T.: Phys. Rev. B **58**(24), R16024 (1998)

21. Schmidt, V., Wittemann, J.V., Senz, S., Gösele, U.: Adv. Mater. **21**(25–26), 2681 (2009)
22. Lew, K.K., Pan, L., Dickey, E., Redwing, J.: Adv. Mater. **15**(24), 2073 (2003)
23. Givan, U., Patolsky, F.: Nano Lett. **9**(5), 1775 (2009)
24. Wu, Y., Fan, R., Yang, P.: Nano Lett. **2**(2), 83 (2002)
25. Redwing, J.M., Lew, K.K., Bogart, T.E., Pan, L., Dickey, E.C., Carim, A.H., Wang, Y., Cabassi, M.A., Mayer, T.S.: Proc. SPIE **5361**(1), 52 (2004)
26. Dujardin, R., Poydenot, V., Devillers, T., Favre-Nicolin, V., Gentile, P., Barski, A.: Appl. Phys. Lett. **89**(15), 153129 (2006)
27. Zakharov, N., Werner, P., Gerth, G., Schubert, L., Sokolov, L., Gösele, U.: J. Cryst. Growth **290**(1), 6 (2006)
28. Mouchet, C., Latu-Romain, L., Cayron, C., Rouviere, E., Celle, C., Simonato, J.P.: Nanotechnology **19**(33), 335603 (2008)
29. Clark, T.E., Nimmatoori, P., Lew, K.K., Pan, L., Redwing, J.M., Dickey, E.C.: Nano Lett. **8**(4), 1246 (2008)
30. Perea, D.E., Li, N., Dickerson, R.M., Misra, A., Picraux, S.T.: Nano Lett. **11**(8), 3117 (2011)
31. Wen, C.Y., Reuter, M.C., Bruley, J., Tersoff, J., Kodambaka, S., Stach, E.A., Ross, F.M.: Science **326**(5957), 1247 (2009)
32. Xiang, J., Lu, W., Hu, Y., Wu, Y., Yan, H., Lieber, C.M.: Nature **441**(7092), 489 (2006)
33. Lauhon, L.J., Gudiksen, M.S., Wang, D., Lieber, C.M.: Nature **420**(6911), 57 (2002)
34. Goldthorpe, I.A., Marshall, A.F., McIntyre, P.C.: Nano Lett. **8**(11), 4081 (2008)
35. Goldthorpe, I.A., Marshall, A.F., McIntyre, P.C.: Nano Lett. **9**(11), 3715 (2009)
36. Zhao, Y., Smith, J.T., Appenzeller, J., Yang, C.: Nano Lett. **11**(4), 1406 (2011)
37. Li, D., Wu, Y., Fan, R., Yang, P., Majumdar, A.: Appl. Phys. Lett. **83**(15), 3186 (2003)
38. Kim, H., Kim, I., jin Choi, H., Kim, W.: Appl. Phys. Lett. **96**(23), 233106 (2010)
39. Yin, L., Lee, E.K., Lee, J.W., Whang, D., Choi, B.L., Yu, C.: Appl. Phys. Lett. **101**, 043114 (2012)
40. Martinez, J.A., Provencio, P.P., Picraux, S.T., Sullivan, J.P., Swartzentruber, B.S.: J. Appl. Phys. **110**(7), 074317 (2011)
41. Kim, H., Park, Y.H., Kim, I., Kim, J., Choi, H.J., Kim, W.: Appl. Phys. A **104**, 23 (2011)
42. Lee, E.K., Yin, L., Lee, Y., Lee, J.W., Lee, S.J., Lee, J., Cha, S.N., Whang, D., Hwang, G.S., Hippalgaonkar, K., Majumdar, A., Yu, C., Choi, B.L., Kim, J.M., Kim, K.: Nano Lett. **12**, 2918 (2012)
43. Wingert, M.C., Chen, Z.C.Y., Dechaumphai, E., Moon, J., Kim, J.H., Xiang, J., Chen, R.: Nano Lett. **11**, 5507 (2011)
44. Hu, M., Giapis, K.P., Goicochea, J.V., Zhang, X., Poulikakos, D.: Nano Lett. **11**(2), 618 (2011)
45. Moon, J., Kim, J.H., Chen, Z.C., Xiang, J., Chen, R.: Nano Lett. **13**(3), 1196 (2013)
46. Hu, M., Poulikakos, D.: Nano Lett. **12**(11), 5487 (2012)
47. Wang, Z., Mingo, N.: Appl. Phys. Lett. **97**(10), 101903 (2010)
48. Steele, M.C., Rosi, F.D.: J. Appl. Phys. **29**(11), 1517 (1958)
49. Dames, C., Chen, G.: J. Appl. Phys. **95**(2), 682 (2004)
50. Tighe, T.S., Worlock, J.M., Roukes, M.L.: Appl. Phys. Lett. **70**(20), 2687 (1997)
51. Fon, W., Schwab, K.C., Worlock, J.M., Roukes, M.L.: Phys. Rev. B **66**, 045302 (2002)
52. Shi, L., Jiang, J., Zhang, G., Li, B.: Appl. Phys. Lett. **101**(23), 233114 (2012)
53. Shelley, M., Mostofi, A.A.: Europhys. Lett. **94**(6), 67001 (2011)
54. Chan, M.K.Y., Reed, J., Donadio, D., Mueller, T., Meng, Y.S., Galli, G., Ceder, G.: Phys. Rev. B **81**, 174303 (2010)
55. Markussen, T.: Nano Lett. **12**(9), 4698 (2012)
56. Amato, M., Ossicini, S., Rurali, R.: Nano Lett. **12**(6), 2717 (2012)
57. Chen, J., Zhang, G., Li, B.: Nano Lett. **12**(6), 2826 (2012)
58. Chen, J., Zhang, G., Li, B.: J. Chem. Phys. C **135**(10), 104508 (2011)

Index

A

Alloy, 32, 42, 52, 60, 62, 68, 70, 82, 85, 142, 146, 152, 162, 164, 171, 203, 204, 238–240, 242, 255–259, 262, 264, 266, 267, 269, 275, 277, 328–330, 332, 335, 339–348, 434, 437, 452, 476, 480, 483, 484, 491, 499–501, 505–510
Anodic aluminum oxide (AAO), 239, 240, 242, 243, 247, 248
Antimony, 165, 256, 257

B

Ball milling (BM), 150, 257, 261, 265, 266, 271, 276–278, 285, 292, 293, 323, 330, 331, 344, 353
BiSb, 256–262, 264, 266, 267, 341
Bismuth (Bi), 165, 236–250, 256, 257, 265, 267, 343, 428
Bi_2Te_3, 33, 86, 142, 146, 149, 163, 239, 240, 243, 244, 247, 248, 272, 329, 330, 334, 339, 346, 499
Boltzmann transport equation (BTE), 1–37, 43, 60, 98, 104, 120, 141, 153, 162, 166, 188, 201, 245, 334, 451, 453–455, 460–464, 466, 472, 476, 479, 484, 491

C

Carbon nanotubes, 102, 163, 363–389
Carbon nanowires (CNWs), 363, 364, 383–389
Carrier concentration, 4, 20, 60, 165, 167, 172, 177, 201, 202, 258, 260, 262–264, 269, 289, 290, 306–308, 314, 315, 317, 322, 333, 364, 373, 380, 385, 387, 479, 507, 508
Carrier mobility, 42, 89, 159, 166, 167, 173–175, 262, 272, 274, 290, 302, 339, 435, 440, 507
Cerium, 255–269
Core-shell, 41, 43, 65–74, 86, 89, 153, 185, 195–200, 208, 387, 502, 503, 506, 507, 511–513
$CoSb_3$, 272, 273, 276–278, 283, 291, 293, 301–323

D

Doping, 33, 42, 48, 49, 58, 64, 70, 72, 82–85, 89, 152, 157, 165, 167, 169, 175–177, 191–192, 203, 255–266, 269, 272, 284, 289, 310, 330, 333, 335, 342, 348, 353, 354, 367, 372–377, 379–381, 383, 385–389, 405, 437, 438, 440, 479, 480, 483–486, 503

E

Electrical resistivity, 257, 260, 265, 282, 287, 288, 292–294, 302, 305–307, 313, 314, 318, 319, 499
Electrical transport, 166, 245, 263, 304, 332, 452, 483–485
Electrodeposition, 238–240, 242, 343
Electronic transport, 2, 3, 240, 242, 364–366, 372, 375, 376, 379, 380, 385, 389, 411, 415, 416, 418, 429, 501, 507–508, 511
Electron-phonon interaction, 2, 96, 106, 107, 114, 120, 135, 233, 414
Electron scattering times, 14, 43, 349
Electron transport, 41–90, 157, 163, 226, 334, 335, 394, 399–401, 409, 411, 452, 453, 476–485, 491, 500

X. Wang and Z.M. Wang (eds.), *Nanoscale Thermoelectrics*, Lecture Notes in Nanoscale Science and Technology 16, DOI 10.1007/978-3-319-02012-9,
© Springer International Publishing Switzerland 2014

F

Figure of Merit, 31, 42, 65, 74, 80–84, 142–146, 177, 187, 200–207, 214, 228, 229, 233, 234, 237, 248, 255, 272, 302, 304, 309, 316, 321, 323, 329, 332–334, 344, 346–348, 354, 363, 366, 370, 381, 400, 404–406, 408, 410, 412–415, 417–419, 434, 436, 451–492, 498, 501, 503, 504, 507, 508, 512, 513, 3238

G

Gallium (Ga), 280, 303, 309–315, 323, 348, 502
Grain boundary, 152, 158, 159, 162, 168–172, 267, 351, 352, 355, 480, 481, 509
Graphene, 208, 378, 393–420, 432
Graphene nanojunctions (GNJs), 394, 406–419
Graphene nanoribbons (GNRs), 364, 377–383, 385, 393–420
Group 13 elements, 301–323

H

Hall, 62, 75, 77, 78, 174, 176, 257, 258, 262, 290, 306–308, 314, 317, 420
Heat transfer, 463, 471
Hetero-interfaces, 43, 55, 58, 86
High pressure torsion (HPT), 148, 281–282, 286–288, 292
Holmium, 255–269
Hydrothermal, 149, 282–283, 292, 344, 346

I

In-situ, 244, 280–281, 292

L

Lattice thermal conductivity, 3, 18–20, 35, 36, 42, 49, 61, 62, 81, 82, 84, 85, 142, 145, 146, 150, 152, 159–161, 166, 167, 171–174, 177, 203, 239, 240, 242, 267, 268, 272–274, 282, 284, 286, 292–294, 308, 309, 315, 321, 322, 333, 338–341, 454, 508
Linear response, 213, 227–230, 233, 314, 334, 373
Long range disorder, 211–234

M

Magnesium silicide (Mg_2Si), 43, 75, 82–85, 89, 143, 147, 164–166, 168, 170–177
Magnetic susceptibility, 258, 260
Melt spinning, 279, 280, 292, 330, 339, 342, 344
Modeling, 27, 47, 76, 78, 95–97, 108, 117, 141–178, 267, 334–335, 451–492, 500, 508

N

Nano, 141–178, 187, 188, 204, 215, 234, 293, 344, 353, 508
Nano bulk, 141–178
Nanocomposites, 42, 62–65, 82, 93–136, 143, 152, 163, 204, 271–294, 420, 451–492
Nanofabrication, 202, 436
Nanoparticles, 43, 50, 51, 53–75, 78, 86, 89, 96, 98, 99, 105, 121, 123, 135, 146, 149, 152, 153, 162, 169, 170, 177, 276, 280, 282–284, 286, 287, 291, 292, 318, 321–323, 340, 341, 344, 346, 499, 500, 502, 503
Nanoscale effects, 144, 146, 200
Nanostructures, 3, 16, 17, 21, 28, 30, 32, 33, 36, 37, 41–90, 107, 143, 145, 149–151, 156, 162, 163, 165, 177, 187, 188, 199, 200, 207, 237–250, 274, 275, 284–292, 302, 316, 322, 329, 333, 335–355, 364, 365, 389, 413, 419, 427–448, 452, 454, 462, 474, 499–501, 503
Nanostructuring, 82, 143, 144, 146, 147, 164–177, 274, 277, 284, 287, 292–294, 323, 337, 342, 347, 429, 434, 436–438, 448, 498, 504, 505, 508, 510
Nanotubes, 102, 163, 193, 238, 240–242, 244–247, 275, 363–389, 393, 416, 452
Nanowires, 2, 98, 185, 211, 238, 274, 329, 364, 411, 429, 453, 497
Narrow band gap, 258
Nonequilibrium Green's function (NEGF), 163, 206, 364–366, 372, 379, 380, 388, 394, 397, 398, 420
Nonequilibrium molecular dynamics (NEMD), 163, 364, 365, 367, 372, 380, 386, 389
Nonlinear response, 214

O
One-dimensional, 128, 159, 187, 201, 215, 237–250, 363–389, 498–500, 508
Oxide thermoelectric, 332, 355

P
Particle-particle interaction, 126, 127, 132, 135, 136
Particulate nanocomposites, 93–136
Phonon scattering, 2, 20, 35, 42, 50, 60–62, 64, 65, 70, 74, 75, 77, 82, 87, 88, 144, 147, 152, 156, 158, 159, 162, 168, 170–172, 192–195, 208, 213, 239, 256, 264, 267, 268, 272–274, 284–286, 292, 303, 320–323, 333, 336, 338, 341–343, 348, 351, 352, 354, 355, 437, 453–455, 458–461, 473, 480, 484, 489, 491, 499, 505, 511
Phonon transport, 2, 37, 42, 98, 150–165, 190, 199, 207, 208, 282, 333–335, 337, 348, 364, 367, 372, 380, 386, 397, 399, 413, 416, 454, 506, 511, 512
Polycrystalline, 151, 157, 240, 241, 243, 250, 256, 257, 285, 289, 304–323, 332, 342, 344, 347
Precipitation, 151, 243, 314, 343, 345, 347, 501

Q
Quantum confinement, 17, 144, 202, 288, 333, 340, 364, 412, 504, 507, 510

R
Roughness, 27, 157, 160–162, 188–191, 199, 200, 208, 214, 222–226, 337, 340–342, 350, 384, 386, 416–418, 437, 505, 506, 512

S
Samarium, 255–269
Scattering in waveguides, 214–217
Seebeck coefficient, 3, 42, 142, 187, 227, 237, 263, 272, 302, 331, 363, 400, 430, 452, 498
Self-assembly, 342, 345–346
Semiconductor, 1, 13–17, 30, 36, 43–53, 57, 59–62, 65, 70, 74, 77, 86, 89, 98, 130, 158, 246, 262, 272, 273, 275, 284, 289, 313, 315, 320, 332, 366, 394, 403, 406, 413, 420, 428, 431, 433, 435, 437, 452, 453, 476, 477, 483, 486, 498, 499, 502
Semiconductor nanowires, 185–209
SiGe nanowires, 203–205, 497–514
Silicon germanium, 164–166, 203, 205–207, 457
Silicon nanowires, 21, 36, 37, 187–208, 211–213, 226–234, 386, 429, 438–442, 445, 447, 448, 473
Size effect, 17, 36, 95, 98–106, 145, 155, 188, 201, 208, 245, 386, 473, 486
Skutterudite, 144, 160, 271–294, 301–323, 328, 331, 333, 387
Solvothermal, 244, 282–283, 346
Strain effects, 451–492
Superlattice nanowires (SLNWs), 242, 331, 346, 510
Synthesis, 82, 150, 164, 165, 177, 178, 239, 244, 250, 276, 279, 280, 282–284, 288, 292, 293, 329–331, 342–347, 452, 499, 500, 502, 508

T
Thallium, 429
Thermal conductivity, 3, 42, 93, 142, 185, 237, 256, 272, 302, 331, 364, 401, 428, 452, 498
Thermal transport, 27, 36, 154, 162, 163, 166, 199, 208, 255, 257, 339, 365, 380, 394, 397–399, 406, 411–413, 415, 416, 420, 453–475, 491, 498, 505–511
Thermoelectricity, 3, 400, 446, 498, 509, 513
Thermoelectric properties, 42–47, 62, 63, 83, 89, 144, 153, 162, 166, 187, 200–208, 238, 244–250, 255–257, 271–294, 301–323, 330, 335–346, 363–389, 393–420, 486–491, 504, 507, 512
Thermopower, 33, 233, 263, 272, 332, 333, 335, 353, 403, 404, 409–411, 415, 507